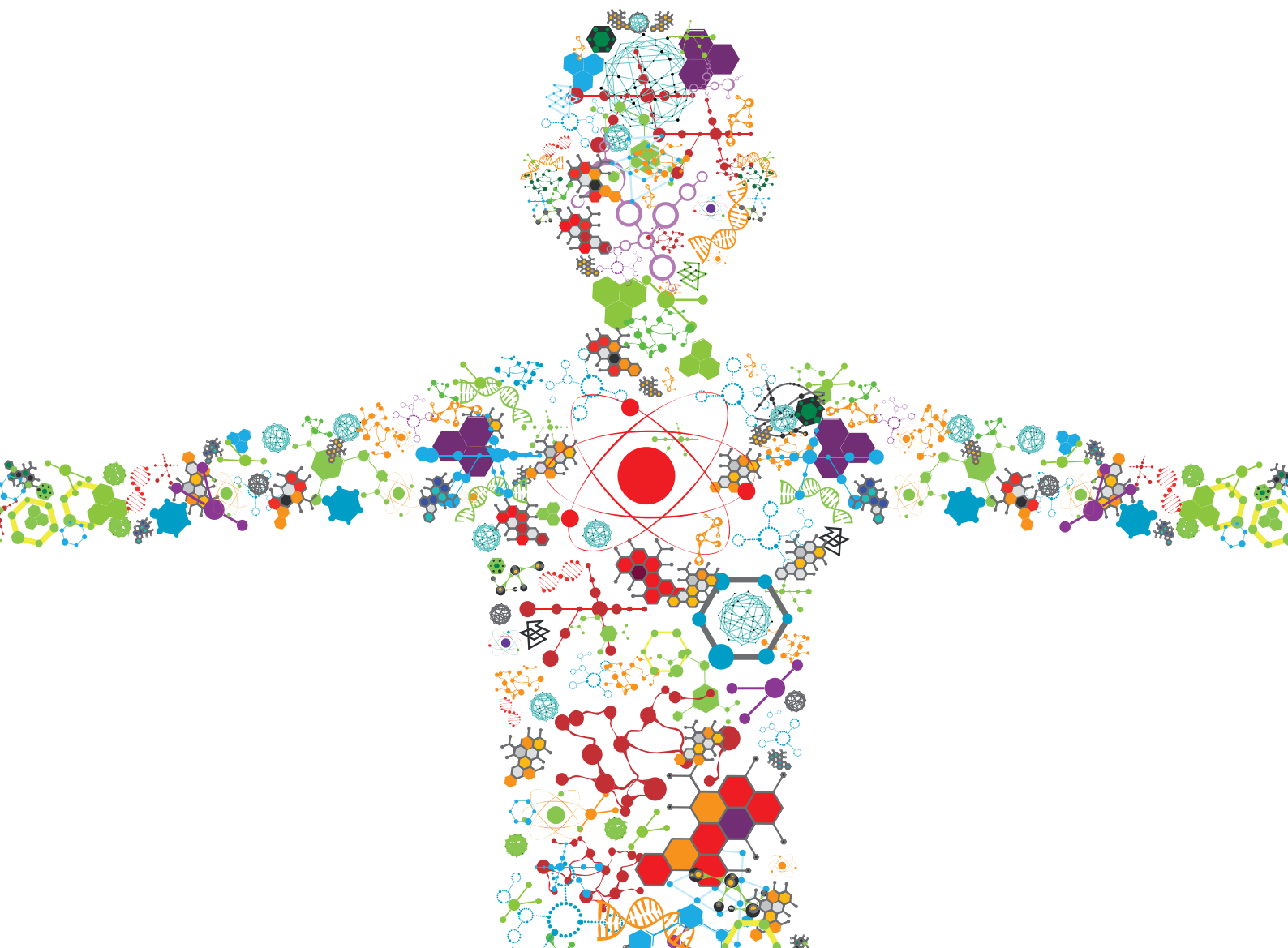


METALLIC BIOMATERIALS FOR MEDICAL APPLICATIONS

EDITED BY: Liqiang Wang, Chaozong Liu and Lechun Xie
PUBLISHED IN: Frontiers in Bioengineering and Biotechnology and
Frontiers in Materials





frontiers

Frontiers eBook Copyright Statement

The copyright in the text of individual articles in this eBook is the property of their respective authors or their respective institutions or funders. The copyright in graphics and images within each article may be subject to copyright of other parties. In both cases this is subject to a license granted to Frontiers.

The compilation of articles constituting this eBook is the property of Frontiers.

Each article within this eBook, and the eBook itself, are published under the most recent version of the Creative Commons CC-BY licence.

The version current at the date of publication of this eBook is CC-BY 4.0. If the CC-BY licence is updated, the licence granted by Frontiers is automatically updated to the new version.

When exercising any right under the CC-BY licence, Frontiers must be attributed as the original publisher of the article or eBook, as applicable.

Authors have the responsibility of ensuring that any graphics or other materials which are the property of others may be included in the CC-BY licence, but this should be checked before relying on the CC-BY licence to reproduce those materials. Any copyright notices relating to those materials must be complied with.

Copyright and source acknowledgement notices may not be removed and must be displayed in any copy, derivative work or partial copy which includes the elements in question.

All copyright, and all rights therein, are protected by national and international copyright laws. The above represents a summary only. For further information please read Frontiers' Conditions for Website Use and Copyright Statement, and the applicable CC-BY licence.

ISSN 1664-8714

ISBN 978-2-88974-047-5

DOI 10.3389/978-2-88974-047-5

About Frontiers

Frontiers is more than just an open-access publisher of scholarly articles: it is a pioneering approach to the world of academia, radically improving the way scholarly research is managed. The grand vision of Frontiers is a world where all people have an equal opportunity to seek, share and generate knowledge. Frontiers provides immediate and permanent online open access to all its publications, but this alone is not enough to realize our grand goals.

Frontiers Journal Series

The Frontiers Journal Series is a multi-tier and interdisciplinary set of open-access, online journals, promising a paradigm shift from the current review, selection and dissemination processes in academic publishing. All Frontiers journals are driven by researchers for researchers; therefore, they constitute a service to the scholarly community. At the same time, the Frontiers Journal Series operates on a revolutionary invention, the tiered publishing system, initially addressing specific communities of scholars, and gradually climbing up to broader public understanding, thus serving the interests of the lay society, too.

Dedication to Quality

Each Frontiers article is a landmark of the highest quality, thanks to genuinely collaborative interactions between authors and review editors, who include some of the world's best academicians. Research must be certified by peers before entering a stream of knowledge that may eventually reach the public - and shape society; therefore, Frontiers only applies the most rigorous and unbiased reviews. Frontiers revolutionizes research publishing by freely delivering the most outstanding research, evaluated with no bias from both the academic and social point of view. By applying the most advanced information technologies, Frontiers is catapulting scholarly publishing into a new generation.

What are Frontiers Research Topics?

Frontiers Research Topics are very popular trademarks of the Frontiers Journals Series: they are collections of at least ten articles, all centered on a particular subject. With their unique mix of varied contributions from Original Research to Review Articles, Frontiers Research Topics unify the most influential researchers, the latest key findings and historical advances in a hot research area! Find out more on how to host your own Frontiers Research Topic or contribute to one as an author by contacting the Frontiers Editorial Office: frontiersin.org/about/contact

METALLIC BIOMATERIALS FOR MEDICAL APPLICATIONS

Topic Editors:

Liqiang Wang, Shanghai Jiao Tong University, China

Chaozong Liu, University College London, United Kingdom

Lechun Xie, Wuhan University of Technology, China

Citation: Wang, L., Liu, C., Xie, L., eds. (2022). Metallic Biomaterials for Medical Applications. Lausanne: Frontiers Media SA. doi: 10.3389/978-2-88974-047-5

Table of Contents

- 05 Editorial: Metallic Biomaterials for Medical Applications**
Liqiang Wang, Chaozong Liu and Lechun Xie
- 07 The Toxicity Phenomenon and the Related Occurrence in Metal and Metal Oxide Nanoparticles: A Brief Review From the Biomedical Perspective**
Shokouh Attarilar, Jinfan Yang, Mahmoud Ebrahimi, Qingge Wang, Jia Liu, Yujin Tang and Junlin Yang
- 30 Cold Rolling Deformation Characteristic of a Biomedical Beta Type Ti–25Nb–3Zr–2Sn–3Mo Alloy Plate and Its Influence on α Precipitated Phases and Room Temperature Mechanical Properties During Aging Treatment**
Jun Cheng, Jinshan Li, Sen Yu, Zhaoxin Du, Xiaoyong Zhang, Wen Zhang, Jinyang Gai, Hongchuan Wang, Hongjie Song and Zhentao Yu
- 44 Influence of Strontium phosphate Coating on the Degradation of Physical Vapor Deposition Sprayed Mg Coating on Ti6Al4V Substrate to Promote Bone Tissue Healing**
Muhammad Ibrahim, Xiaoming Yu, Lili Tan and Ke Yang
- 52 Research Progress of Titanium-Based High Entropy Alloy: Methods, Properties, and Applications**
Ning Ma, Shifeng Liu, Wei Liu, Lechun Xie, Daixiu Wei, Liqiang Wang, Lanjie Li, Beibei Zhao and Yan Wang
- 70 Surface Modification Techniques of Titanium and its Alloys to Functionally Optimize Their Biomedical Properties: Thematic Review**
Tong Xue, Shokouh Attarilar, Shifeng Liu, Jia Liu, Xi Song, Lanjie Li, Beibei Zhao and Yujin Tang
- 89 Nano-Modified Titanium Implant Materials: A Way Toward Improved Antibacterial Properties**
Jianqiao Liu, Jia Liu, Shokouh Attarilar, Chong Wang, Maryam Tamaddon, Chengliang Yang, Kegong Xie, Jinguang Yao, Liqiang Wang, Chaozong Liu and Yujin Tang
- 119 Copper-Containing Alloy as Immunoregulatory Material in Bone Regeneration via Mitochondrial Oxidative Stress**
Daorong Xu, Jikun Qian, Xin Guan, Ling Ren, Kaifan Yang, Xuan Huang, Shuyuan Zhang, Yu Chai, Xiaohu Wu, Hangtian Wu, Xianrong Zhang, Ke Yang and Bin Yu
- 131 Functional Gradient Metallic Biomaterials: Techniques, Current Scenery, and Future Prospects in the Biomedical Field**
Hongyuan Shi, Peng Zhou, Jie Li, Chaozong Liu and Liqiang Wang
- 157 Influence of Isothermal ω Transitional Phase-Assisted Phase Transition From β to α on Room-Temperature Mechanical Performance of a Meta-Stable β Titanium Alloy Ti–10Mo–6Zr–4Sn–3Nb (Ti-B12) for Medical Application**
Jun Cheng, Jinshan Li, Sen Yu, Zhaoxin Du, Xiaoyong Zhang, Wen Zhang, Jinyang Gai, Hongchuan Wang, Hongjie Song and Zhentao Yu

- 170** *A Novel Design of Temporomandibular Joint Prosthesis for Lateral Pterygoid Muscle Attachment: A Preliminary Study*
Luxiang Zou, Yingqian Zhong, Yinze Xiong, Dongmei He, Xiang Li, Chuan Lu and Huimin Zhu
- 181** *Characteristics of Passive Films Formed on As-Cast Ti–6Al–4V in Hank’s Solution Before and After Transpassivation*
Guo Yi, Xinxin Liu, Chuanbo Zheng, Hongyue Zhang, Cheng Xu, Yu-Wei Cui and Shuan Li
- 192** *Elastically Graded Titanium Alloy Produced by Mechanical Surface Deformation*
Stéphanie Delannoy, Sarah Baïz, Pascal Laheurte, Laurence Jordan and Frédéric Prima
- 201** *Mg/ZrO₂ Metal Matrix Nanocomposites Fabricated by Friction Stir Processing: Microstructure, Mechanical Properties, and Corrosion Behavior*
Ke Qiao, Ting Zhang, Kuaishe Wang, Shengnan Yuan, Shengyi Zhang, Liqiang Wang, Zhi Wang, Pai Peng, Jun Cai, Chaozong Liu and Wen Wang
- 217** *Metal Material, Properties and Design Methods of Porous Biomedical Scaffolds for Additive Manufacturing: A Review*
Yuting Lv, Binghao Wang, Guohao Liu, Yujin Tang, Eryi Lu, Kegong Xie, Changgong Lan, Jia Liu, Zhenbo Qin and Liqiang Wang
- 233** *Enhancement of Bone Regeneration on Calcium-Phosphate-Coated Magnesium Mesh: Using the Rat Calvarial Model*
Shuang Wu, Yong-Seok Jang and Min-Ho Lee



Editorial: Metallic Biomaterials for Medical Applications

Liqiang Wang^{1*}, Chaozong Liu² and Lechun Xie^{3,4}

¹State Key Laboratory of Metal Matrix Composites, School of Materials Science and Engineering, Shanghai Jiao Tong University, Shanghai, China, ²Institute of Orthopaedic and Musculoskeletal Science, University College London, Royal National Orthopaedic Hospital, Stanmore, United Kingdom, ³Hubei Key Laboratory of Advanced Technology for Automotive Components, Wuhan University of Technology, Wuhan, China, ⁴Hubei Collaborative Innovation Center for Automotive Components Technology, Wuhan, China

Keywords: biomaterials, medical applications, metal, titanium, magnesium

Editorial on the Research Topic

Metallic Biomaterials for Medical Applications

Biomaterials are natural or artificial materials used to make structures or implants to replace lost or diseased biological structures to restore form and function. In actual clinical situation, they are used in the complex environment of body fluid, so the requirements for the structure and properties of biomaterials are very strict. Biomaterials require great physical and chemical stability, however, some alloy elements, toxic and biological incompatible, harm the human body and some metals' mechanical properties don't match the human body. Therefore, for further improving the biological and mechanical properties of metallic biomaterials, many attempts have been adopted to design novel metallic biomaterials and different advanced processing and preparation technologies have been developed in the content of this topic.

Titanium alloys are widely used for dental and implant materials because of their superior biocompatibility, corrosion resistance and specific strength compared with other metallic implant materials. In the aspect of Ti alloys, Liu et al. investigated the antibacterial properties of various surface nano-modification of Ti implant materials and the related procedures, and the surface nano-modification of Ti materials were discussed from three aspects: nanostructures formation procedures, nanomaterials loading, and nano-morphology. Cheng et al. investigated a biomedical beta type Ti-25Nb-3Zr-2Sn-3Mo alloy plate *via* cold rolling deformation, and the alloy plates possessed various mechanical properties owing to the different morphology, size and volume fraction of α precipitated phases, which would be deemed as a potential material in the orthopedic field. Cheng et al. also investigated the microstructure evolution and mechanical properties of metastable beta type titanium alloy (Ti-B12) after different aging treatments. MTT test with L929 cells showed that the cytotoxicity of Ti-B12 was better than that of Ti-6Al-4V, which was suitable for biomedical application.

As lightweight alloys with mechanical properties close to human bone and degradable in the human environment, magnesium alloys have good biocompatibility and are widely used in load-bearing implants and degradable stents. In terms of Mg alloys, Ibrahim et al. introduced a Mg/SrP composite coating on Ti-6Al-4V in order to promote the bone tissue healing and shorten the healing cycle; the results revealed that Mg/SrP coating shows more suitable degradation rate than pure Mg, with no cytotoxicity and higher proliferation compared with the culture medium. Qiao et al. fabricated Mg/ZrO₂ metal matrix nanocomposites by friction stir processing (FSP), and the Mg/ZrO₂ achieved homogenization, densification, and grain refinement after FSP, which are due to the grain refinement and Orowan strengthening. Wu et al. used calcium phosphates (CaPs) coated on the surface of pure Mg through a simple alkali-hydrothermal treatment, and the CaP coating of Mg favors cell attachment and cell

OPEN ACCESS

Edited and reviewed by:

Hasan Uludag,
University of Alberta, Canada

*Correspondence:

Liqiang Wang
wang_liqiang@sjtu.edu.cn

Specialty section:

This article was submitted to
Biomaterials,
a section of the journal
Frontiers in Materials

Received: 15 October 2021

Accepted: 05 November 2021

Published: 23 November 2021

Citation:

Wang L, Liu C and Xie L (2021)
Editorial: Metallic Biomaterials for
Medical Applications.
Front. Mater. 8:795642.
doi: 10.3389/fmats.2021.795642

spreading, which can endow Mg with higher surface energy and osteogenesis capability and lower degradation than pristine Mg.

In order to meet the biological, chemical, and mechanical properties of actual clinical needs, it is necessary to perform surface modification treatment on the above-mentioned metallic biomaterials. Surface treatment methods are very important methods to modify the physical and mechanical properties of biomaterials. Xue et al. reviewed the main physical and chemical surface modification techniques for Ti related biomaterials, such as plasma spray, PIII, PIII&D, PVD, CVD, sol-gel and MAO, and future studies were introduced and should be focused on designing the basic new methods or the combination of modification methods to play a synergistic effect and combine their advantages to conquer the deficiencies. Delannoy et al. developed a thermo-mechanical strategy to create a radial elasticity gradient in a β metastable Ti-Nb-Zr alloy, and shot-peening enabled to locally induce martensitic transformation on surface, and a decrease in indentation elastic modulus; this combination of material and process could be suitable to produce dental implants with mechanically enhanced biocompatibility. Yi et al. studied the characteristics of passive films formed on as-cast Ti-6Al-4V before and after transpassivation by electrochemical methods, which advance the understanding of as-cast Ti-6Al-4V polarized under different potentials for potential biomedical applications.

In addition to mainstream titanium alloys and magnesium alloys, efforts should be made to develop novel metallic biomaterials. In the aspects of new alloys and manufacturing methods, Ma et al. provided an insight into the development of Ti-based high entropy alloy (HEA), and the emergence of HEAs has brought great room for development in the field of medical implant materials. Shi et al. reviewed the current scenery of functional gradient metallic materials (FGM) in the biomedical field, specifically its dental and orthopedic applications; any improvement in FGM can lead to big steps toward its industrialization and most notably for much better implant designs with more biocompatibility and similarity to natural tissues. Xu et al. investigated the copper-containing alloy as immunoregulatory material in bone regeneration via mitochondrial oxidative stress, and the copper-containing metal promoted the evolution of callus through the generation of type H vessels during the process of bone repair by upregulating the expression of PDGF-BB derived from M2a macrophages. Attarilar et al. reviewed the related factors in toxicity of nanoparticles such as size, concentration, etc. with an emphasis on metal and metal oxide nanoparticles, which can highlight their potential hazard and the advancement of green non-cytotoxic nanomaterials with safe threshold dose levels to resolve the toxicity issues.

With the maturity of additive manufacturing technology, we should focus on developing complex, gradient and multi-scale structures to customize medical devices. Some special structures were utilized to realize the medical application. Lv et al. reviewed the research progress of porous metal scaffolds, and introduced the additive manufacturing technology used in porous metal scaffolds, which provided unprecedented opportunities for production of customized biomedical implants. Zou et al. studied a novel design of temporomandibular joint (TMJ), and an artificial TMJ prosthesis designed with a porous structure on the condylar neck region for lateral pterygoid muscle (LPM) attachment was fabricated by a 3D printed Ti alloy; The TMJ prosthesis can help LPM attach to its porous titanium scaffold structure area for future function.

The contributions of above work were summarized as following: the important metallic biomaterials, especially Ti and Mg alloys; the surface treatments on biomaterials; some new alloys and manufacturing methods; and some special structures for special application. This research topic focused on the recent development of metallic biomaterials for medical applications, and all results would promote the development of metallic biomaterials.

DATA AVAILABILITY STATEMENT

The original contributions presented in the study are publicly available in NCBI under accession number PRJNA591354.

AUTHOR CONTRIBUTIONS

LW, CL, and LX wrote the original manuscript and revised the manuscript. They contribute equally.

Conflict of Interest: The authors declare that the research was conducted in the absence of any commercial or financial relationships that could be construed as a potential conflict of interest.

Publisher's Note: All claims expressed in this article are solely those of the authors and do not necessarily represent those of their affiliated organizations, or those of the publisher, the editors and the reviewers. Any product that may be evaluated in this article, or claim that may be made by its manufacturer, is not guaranteed or endorsed by the publisher.

Copyright © 2021 Wang, Liu and Xie. This is an open-access article distributed under the terms of the Creative Commons Attribution License (CC BY). The use, distribution or reproduction in other forums is permitted, provided the original author(s) and the copyright owner(s) are credited and that the original publication in this journal is cited, in accordance with accepted academic practice. No use, distribution or reproduction is permitted which does not comply with these terms.



The Toxicity Phenomenon and the Related Occurrence in Metal and Metal Oxide Nanoparticles: A Brief Review From the Biomedical Perspective

Shokouh Attarilar^{1†}, Jinfan Yang^{2†}, Mahmoud Ebrahimi³, Qingge Wang⁴, Jia Liu⁵, Yujin Tang^{5*} and Junlin Yang^{1*}

OPEN ACCESS

Edited by:

Lechun Xie,
Wuhan University of Technology,
China

Reviewed by:

Jian Wang,
Xihua University, China
Ke Zhan,
University of Shanghai for Science
and Technology, China

*Correspondence:

Yujin Tang
tangyujin196709@163.com
Junlin Yang
yjunlin@126.com

[†]These authors have contributed
equally to this work

Specialty section:

This article was submitted to
Biomaterials,
a section of the journal
Frontiers in Bioengineering and
Biotechnology

Received: 25 May 2020

Accepted: 26 June 2020

Published: 17 July 2020

Citation:

Attarilar S, Yang J, Ebrahimi M,
Wang Q, Liu J, Tang Y and Yang J
(2020) The Toxicity Phenomenon
and the Related Occurrence in Metal
and Metal Oxide Nanoparticles:
A Brief Review From the Biomedical
Perspective.
Front. Bioeng. Biotechnol. 8:822.
doi: 10.3389/fbioe.2020.00822

¹ Department of Pediatric Orthopaedics, Xin Hua Hospital Affiliated to Shanghai Jiao Tong University School of Medicine, Shanghai, China, ² Department of Spine Surgery, Xin Hua Hospital Affiliated to Shanghai Jiao Tong University School of Medicine, Shanghai, China, ³ National Engineering Research Center of Light Alloy Net Forming, School of Materials Science and Engineering, Shanghai Jiao Tong University, Shanghai, China, ⁴ School of Metallurgical Engineering, Xi'an University of Architecture and Technology, Xi'an, China, ⁵ Affiliated Hospital of Youjiang Medical University for Nationalities, Baise, China

Thousands of different nanoparticles (NPs) involve in our daily life with various origins from food, cosmetics, drugs, etc. It is believed that decreasing the size of materials up to nanometer levels can facilitate their unfavorable absorption since they can pass the natural barriers of live tissues and organs even, they can go across the relatively impermeable membranes. The interaction of these NPs with the biological environment disturbs the natural functions of cells and its components and cause health issues. In the lack of the detailed and comprehensive standard protocols about the toxicity of NPs materials, their control, and effects, this review study focuses on the current research literature about the related factors in toxicity of NPs such as size, concentration, etc. with an emphasis on metal and metal oxide nanoparticles. The goal of the study is to highlight their potential hazard and the advancement of green non-cytotoxic nanomaterials with safe threshold dose levels to resolve the toxicity issues. This study supports the NPs design along with minimizing the adverse effects of nanoparticles especially those used in biological treatments.

Keywords: non-cytotoxic materials, nanomaterials, cytotoxicity, nanomedicine, metal oxide nanoparticles, nanotoxicology

INTRODUCTION

Nanoparticles (NPs) are defined as materials with two dimensions in the range of 1–100 nm (10^{-9} m), while nanomaterials are determined as materials possessing just one dimension in that range according to ASTM E2456 standard (ASTM, 2012). These NPs can have a variety of shapes with different aspect ratios including nanorods with <10 aspect ratio, spherical, cubical, and other possible shapes. Owing to this nanometric size level, NPs can have versatile size-dependent and special properties such as catalytic, electrochemical, optical, magnetic features as well as increased surface to volume ratios which in turn make them the unique materials for modern applications.

Metal oxide nanoparticles are amongst the most widely used NPs in a variety of applications including cosmetics (Waghmode et al., 2019), drug and medicine industry (Klębowski et al., 2018), detergents, agricultural systems (Chen, 2018), environment (Kanchi and Ahmed, 2018), antibacterial agents (Mordorski and Friedman, 2017), paints and textiles (Vigneshwaran et al., 2010). Nowadays, some metallic NPs including gold NPs (Au NPs), silver NPs (Ag NPs), and metallic magnetic NPs such as iron-oxide NPs (IONPs) are frequently utilized and improved in order to intensify their functions as diagnostic and remedial agents. **Table 1** lists some applications of the common metallic NPs.

Metallic NPs' design and their modification can be done through versatile surface functionalities so they can be conjoined with antibodies, ligands, and drugs, consequently raise their potential applications in biotechnology, drug and gene delivery, magnetic separation and imaging, besides the favorable characteristics they have a potential to cause harmful effects if they enter to live biological systems and tissues (Yang et al., 2018; Gu et al., 2019; Liu et al., 2019; Wang L. et al., 2019). Unfortunately, there are many ways for unwanted and spontaneous entry of NPs to the body system, whether through the air we breathe or the water we drink, also foods, medicines, clothes, and cosmetics are no exception. The main entry routes can be considered as inhalation through the respiratory tract, by transudation through the skin and by ingestion through the digestive tract (Zoroddu et al., 2014). Therefore, nanomaterials released into the body environment seem to be inevitable and may have some unforeseen harmful effects hence it is of crucial importance to study their toxicity-related issues. This subject becomes of more paramount importance if we know that their nanoscale size facilitates their penetration to different live tissues and enables possible interaction with the same sized organs like cells, proteins, and antibodies also they can accumulate in organs and tissues as a foreign body (Nemmar et al., 2002; Nel et al., 2006). This arises from the high surface area for example in the case of two NPs with the same mass, smaller NPs have a larger specific surface area and thus provide a more available area to cellular interactions with nucleic acids, proteins, fatty acids, and carbohydrates (Huang et al., 2017). Considering the so-called issues, a new branch of research was introduced and entitled "Nanotoxicology" which deals with the nanomaterials toxicity (Pacheco et al., 2007). Unfortunately, there have not been yet any comprehensive and precise standard protocols for cytotoxicity of various materials, however, about the NPs, the concentration, composition, size, charge, and other physicochemical factors are considered for material selection and their possible utilization. Various methods are used in order to estimate the cytotoxicity levels of NPs which is categorized into two main groups of *in vitro* and *in vivo* methods. In this regard, the *in vitro* group includes dye exclusion assays (trypan blue exclusion and erythrosin B dye exclusion assays), colorimetric assays (MTT, WST-1, neutral red uptake and lactate dehydrogenase assays), fluorescence-based assays (Alamar blue and protease-based viability assays), luminometric methods (Adenosine triphosphate based method), cell viability test in real-time (estimation of oxidative stress, ROS level measurement, lipid peroxidation, glutathione estimation), apoptosis based assays (Annexin-V FITC/propidium Iodide

and TUNEL assays. For determining the level of genotoxicity of nanoparticles *in vitro*, micronucleus formation, cytokinesis block micronucleus, flow micronucleus, and comet assays can be utilized. *In vivo* characterization of toxicity can be done through quantitation and bio-distribution of NPs from tissues, electron microscopy and detection of NPs accumulation, liquid scintillation counting, and NPs' quantification by drug loading and release. Also, the whole body imaging-based methods are utilized for estimation of NPs' toxicity and bio-distribution such as *in vivo* optical imaging, computed tomography, magnetic resonance, and nuclear medicine imaging, for more information about cytotoxicity assessment, the readers can refer to (Shah et al., 2020). The main objective of these nanotoxicology experiments and studies is the comprehensive understanding in relation to the toxicity of quantum size effects, shape, and high surface area to volume ratio of nanomaterials in biological environments. In this regard and considering the generally used metal and metal oxide NPs, this review paper focuses on the nanotoxicology of these materials with special attention to the physical properties of NPs and their effects on toxicity. Also, the involved mechanisms in relation to nanotoxicology will be addressed.

MECHANISMS OF NANOTOXICOLOGY

A lot of toxicity mechanism is involved with NPs and the most common types can be listed as below and are shown in **Figure 1**. As shown in **Figure 1**, NPs have the ability to interact with most of the cell components from DNA and various proteins to mitochondria, they can lead to reactive oxide species (ROS) formation and affect the different functions of cell. In this regard, DNA damage, lysosomal hydrolases, ROS generation, mitochondrial dysfunction, apoptosis, cell membrane damage, cytoplasm impairment, alterations in ATP, and permeability of cell membrane, accumulation of NPs in Golgi and variations in proteins all can be attributed to NPs interaction.

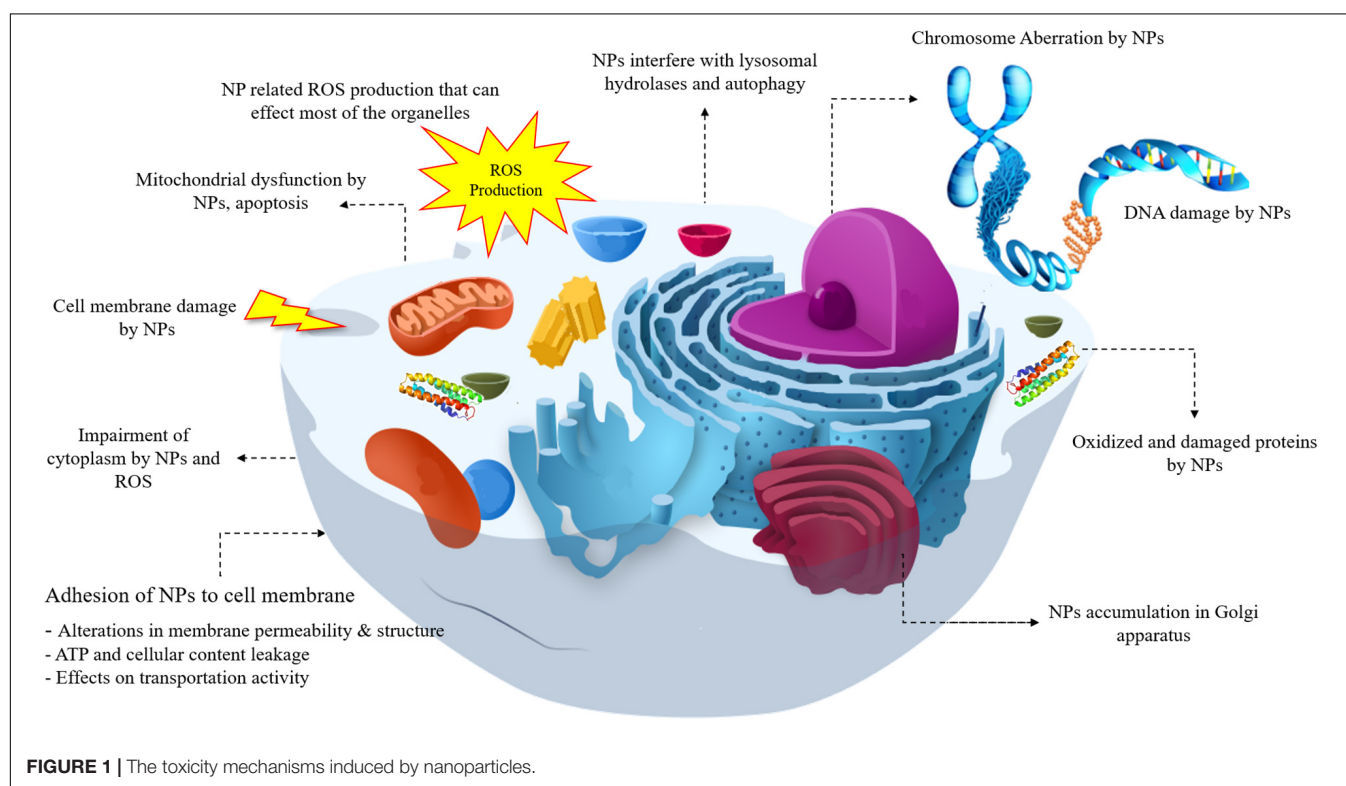
Reactive Oxygen Species Formation

The imbalance between production and accumulation of oxygen reactive species (ROS) leads to the occurrence of oxidative stress in cells and live tissues. ROS generates by mitochondria during both physiological and pathological conditions and they are considered as the metabolic by-products of biological systems (Pizzino et al., 2017). They can also be referred to as free radicals and have favorable functions at low or moderate concentrations, they fight with pathogens and are necessary to cell signaling and synthesize various cellular structures and proteins (Dröge, 2002). However, in high concentrations, oxidative stress (OS) condition takes place in which ROS suppress the live cells and organs' ability to detoxify and unfortunately, it can damage proteins, lipids, and nucleic acids, and severely leads to cell death and disease development including cancer (Katerji et al., 2019).

Oxidative stress biomarkers can be categorized in two groups of (a) ROS modified molecules generation and (b) deterioration or derivation of enzymes or antioxidants, the trace of these biomarkers can be detected in body fluids (Tsukahara, 2007). Although due to its unstable condition it

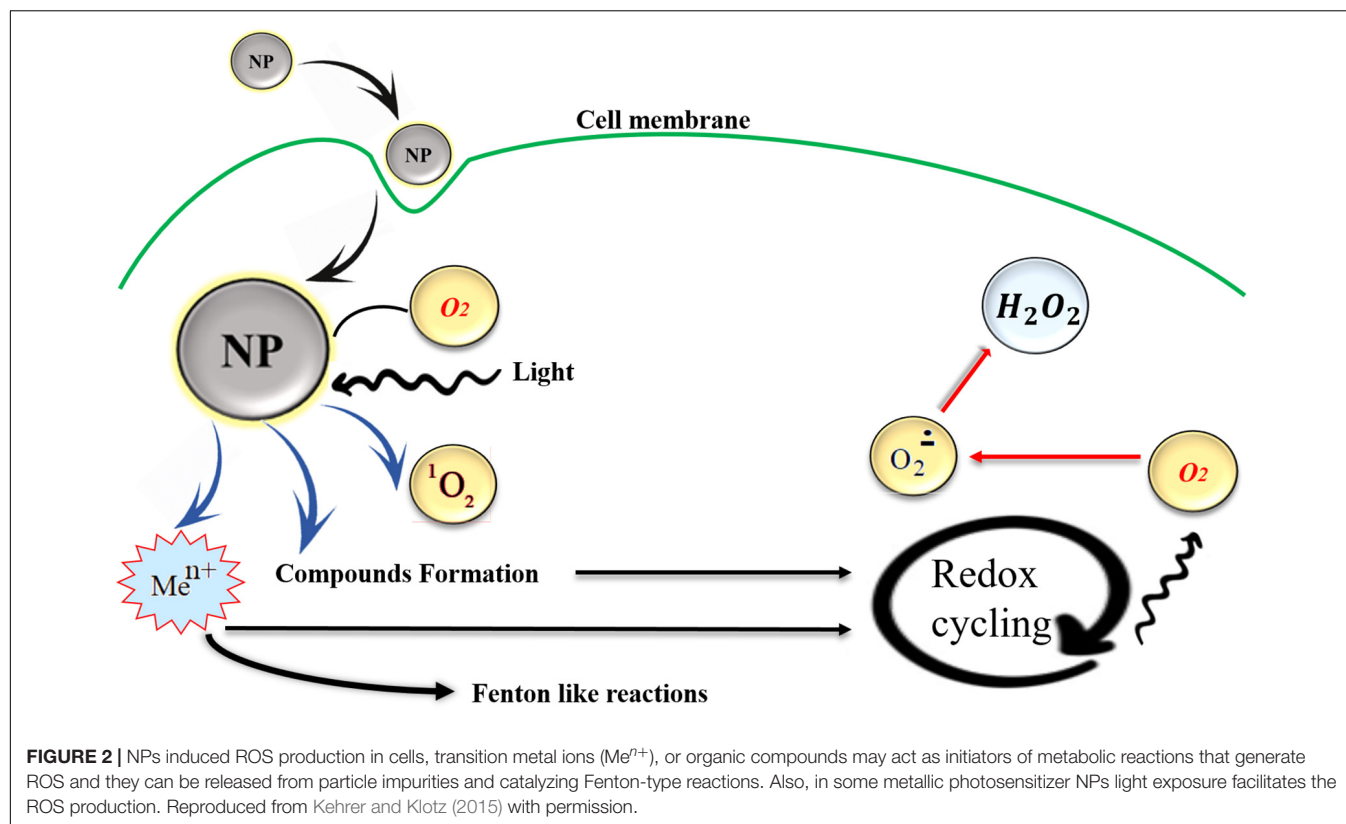
TABLE 1 | Application of some metallic and metal oxide nanoparticles.

Metals	Application of metallic and metal oxide nanoparticles
Titanium dioxide (Ti)	Solar cells, food wraps, medicines, pharmaceuticals, lacquers, construction, medical devices, gas sensing, photocatalyst, agriculture, paint, food, cosmetic, sterilization, antibacterial coatings (Waghmode et al., 2019).
Zinc and Zinc oxide (Zn)	Medical and healthcare goods, sunscreens, packaging, UV-protective materials such as textiles.
Aluminum (Al)	Automobile industry, aircraft, heat shielding coatings, military application, corrosion, fuel additive/propellant.
Gold (Au)	Sensory probes, cellular imaging, electronic conductors, drug delivery, therapeutic agents, organic photovoltaics, catalysis, nanofibers, textiles.
Iron (Fe)	Magnetic imaging, environmental remediation, glass and ceramic industry, memory tape, resonance imaging, plastics, nanowires, coatings, textiles, alloy and catalyst applications.
Silica (Si)	Drug and gene delivery, adsorbents, electronic, sensor, catalysis, remediation of the environment pollutants, additive in rubber and plastic industry, filler, electric and thermal insulators.
Silver (Ag)	Antimicrobial coatings, textiles, batteries, surgery, wound dressings, biomedical devices, photography, electrical devices, dental work, burns treatment.
Copper (Cu)	Biosensors and electrochemical sensors, plastic additives like anti-biotic, anti-microbial, and anti-fungal agent, coatings, textiles, nanocomposite coating, catalyst, lubricants, inks, filler.
Cerium (Ce)	Chemical mechanical polishing/planarization, computer chip, corrosion, solar cells, fuel oxidation catalysis, automotive exhaust treatment (Dhall and Self, 2018).
Manganese and its oxides (Mn)	Molecular meshing, solar cells, batteries, catalysts, optoelectronics, drug delivery ion-sieves, imaging agents, magnetic storage devices, water treatment and purification (Hoseinpour and Ghaemi, 2018; Wang W. et al., 2019).
Nickel (Ni)	Fuel cells, membrane fuel cells, automotive catalytic converters, plastics, nanowires, nanofibers, textiles, coatings, conduction, magnetic properties, catalyst, batteries, printing inks.



is very hard to determine the exact level of ROS, its cellular levels can be measured through various methods such as fluorogenic and fluorescent probes, also hydrogen peroxide (H_2O_2), hydroxyl radicals (OH^\cdot), and peroxy radicals (ROO^\cdot) can be estimated by staining methods. In addition, ROS molecules like hydroperoxides (R-OOH) can be quantified by performing the (D-Roms) test through reactive oxygen

metabolites derivatives. ROS with a potent chemically reactive characteristic contain oxygen and can be found as superoxides, peroxides, hydroxyl radical, singlet and alpha-oxygen, **Figure 2** schematically shows ROS production by NPs, it was believed that some NPs are photosensitizers and they facilitate ROS formation with the light assistance but for the case of tissues which are not exposed to daylight other mechanisms are involved such as



organic material released from combustion derived NPs. Also, transition metal ions can be released from particle impurities and catalyzing Fenton-type reactions, for more details about ROS production see Kehrer and Klotz (2015), Saliani et al. (2016), and Flores-López et al. (2019). The ROS produced as one of the natural byproducts of the normal oxygen metabolism and they affect the cell signaling and homeostasis (Devasagayam et al., 2004). In addition to positive functions of ROS formation in cells, their excess generation by external inputs such as NPs can also lead to some harmful effects like apoptosis (programmed cell death) and may induce damages on RNA or DNA (Wan et al., 2012), lipid peroxidation, amino acids oxidation in proteins and deactivation of enzymes by oxidation of co-factors are other unfavorable results of NPs induced ROS generation (Brooker, 2018). The mechanism of ROS production by metallic NPs depends on particle size, shape, surface area, and chemistry. ROS have a key role in multiple cell functions and its biology. ROS generation plays a crucial role in toxicity issues aroused from NPs application, as well as other related phenomena like cellular signaling fluctuations involved in cell death, proliferation, and differentiation (Dayem et al., 2017).

Cell Damages Through NPs Induced Membrane Perforation

Some metallic NPs like Au NPs can be used in order to maintain unspecific attachment to the cell membrane and activated the interim and cell membrane permeabilization in a spatial manner (Heinemann et al., 2013). Unfortunately, this characteristic can

also cause cell damages, for instance Ag NPs with lower than 10 nm diameter have a potential to bind with the cell walls in *Escherichia coli* bacteria and finally leads to cell death (Gogoi et al., 2006). It was observed (Gopinath et al., 2008) that Ag NPs are able to cause cell apoptosis and damage the mitochondrial membrane during cell apoptosis with cell membrane perforation intervention.

Cytoskeleton Components Damage

Cytoskeleton acts as a footstone of the cell architecture hence the NPs' influence on the cytoskeleton network must be carefully considered. Actin and intermediate filaments, microtubules, and different types of proteins are among the most important components of the cytoskeleton (Ispanixtlahuatl-Meráz et al., 2018). Despite the proven non-toxicity of TiO_2 in most studies (Ding et al., 2016; Zhang et al., 2017) it was reported that TiO_2 NPs led to actin and tubulin disassembly and some alterations in the cytoskeleton and its proteins (Vuong et al., 2016). TiO_2 NPs treated epithelial cell line BEAS-2B confirms the expression alterations in mRNAs and miRNAs which is possibly in relation to the cytoskeleton (Thai et al., 2015). The epithelial cells co-culturing and their proteomic analysis indicated that Ag NPs readjust different types of cyokeratins and gelsolin, in contrast to α - and β -tubulin together with actin which were downregulated, and strong dissolution of Ag confirmed the strong effects of NPs rather than Ag ions (Georgantzopoulou et al., 2016). The ZnO NPs can be internalized by endosomes and in turn move to lysosomes, also the existence of zinc ions causes cytotoxicity

and actin rearrangement in cell bundles. Besides, this effected tubulin network by ZnO NPs can generate wrapped bundles in the periphery of the nucleus and these improper chromosomes and spindles can subsequently distribute all over the cytoplasm region and cause harmful effects (García-Hevia et al., 2016). Xu F. et al. (2013) reported the cytoskeleton component failure like and filamentous actin (*F*-actin) and the β -tubulin Ag NPs treated samples, it was also demonstrated that they led to the dramatic reduction in the number of synaptic clusters of the presynaptic vesicle protein synaptophysin, and the postsynaptic receptor density protein PSD-95 and lastly Ag NPs cause mitochondria dysfunction in rat cortical cells.

DNA and Transcription Damage by NPs and Mutagenesis Acceleration

Application of Co NPs within the non-toxic dose range and their exposure to human lung epithelial cell line A549 demonstrated the ROS generation which finally ended to DNA damage. Subsequently, this DNA damage led to ataxia-telangiectasia mutated (ATM) protein activation and increase the phosphorylation of p53 and Rad 51 protein expression, TiO₂ NPs did not indicate any considerable cytotoxic effects. In addition, Co NPs induced DNA damage is able to actuate various cellular reactions such as apoptosis, cell cycle arrest, and importantly the DNA repair (Wan et al., 2012). The effects of Cu NPs on transcriptional responses of zebrafish embryos confirmed the up-regulation of genes in the healing of wounds and stimulus reactions but it was seen that the genes which are responsible for phototransduction and metabolisms were acted in downward fashion (Zhang et al., 2018). It seems that Cu NPs together with Cu²⁺ ions induce gene transcription damages to Zebrafish embryos (Zhang et al., 2018). The study about the mitotic and meiotic effects of Cu and CdS NPs indicated higher degrees of cytotoxicity in Cu NPs than CdS ones, the mitotic aberrations can be in the result of several phenomena such as (1) DNA depolymerization and sticking of chromosomes bundles, (2) chromosome breakages leading to the generation of rings, bridges, fragments, and micronuclei, (3) prevention of the centromeric division which leads to diplochromosomes formation, (4) spindle apparatus variations which promotes the polyploid cells and laggards. Different mitotic cycles have the potential to initiate the meiotic cell division, NPs inducing aberrations seem to be significant since their consistent changes can cause heritable alterations in the genotype (Kumbhakar et al., 2016).

Mitochondria Damage

Mitochondria is among the most important organelles of the cells; it chiefly engages in energy supply and differentiation procedure and unfortunately it can be mischievously affected by NPs related toxicity. Mitochondrial permeability transition (PT) occurrence is one of the prime causes of cell death in which a sudden permeability increase in the inner mitochondrial membrane to small size solutes leads to apoptosis, for example, Au NPs with 1.4 nm diameter showed to cause oxidative stress leading to mitochondrial PT in which the higher permeability

of mitochondrial membrane toward 1.4 nm Au NPs triggered the cell death by necrosis (Pan et al., 2009). Gallud et al. (2019) also proved the mitochondrial dysfunction in ammonium-modified Au NPs, these cationic Au NPs stimulated autophagy in macrophage-like reporter cells, and cell death can be deteriorated by autophagy inhibition and in general mitochondria-dependent effects of cationic Au NPs induce the quick perish in cells. Yu et al. (2013) reported that ZnO NPs have a capability to affect the mitochondrial membrane potential, also mitochondrial ATP level was significantly diminished in the presence of these ZnO NPs. In addition, interruption of mitochondria, dysfunction, and fall of mitochondrial membrane potential after ZnO NPs treatment to normal skin cells was proven and these NPs adversely influence the mitochondrial network and biogenesis (Yu et al., 2013). Iron-based NPs like Fe₃O₄ NPs also can lead to dysfunctions in the mitochondrial activity, increase the ROS production in cells and leads to the draft decrease of ATP level even it can induce autophagy by reduction of cytoplasmic energy (Zhang et al., 2016). These harmful effects are also seen in TiO₂ NPs and it was reported that TiO₂ NPs can cause severe mitochondrial dysfunction, the increment of ROS levels, reduction of ATP generation, mitochondrial phospholipids and metabolic fluxes (Chen et al., 2018). TiO₂ NPs can also affect the dynamic of the mitochondria and leads to its dynamic imbalances and damages in HT22 Cells and it can also activate the mitochondrial-related apoptosis pathways (Zhao et al., 2019). In the Ag NPs treatment with a diameter of 10 nm it was seen that these NPs are able to impair mitochondrial function and in turn induce cell dysfunctions (Bressan et al., 2013).

The Effect of NPs on Lysosomes

Lysosomes are defined as membrane-bound organelles comprising hydrolases that act in the deterioration process of macromolecules transported by various pathways including the endocytic, phagocytic, and autophagic ones (Luzio et al., 2014) and they are considered as acute intracellular organelles controlling the cytotoxicity of nanomaterials (Fröhlich, 2013). Metallic NPs like Ag NPs can be taken up by different cell types and they are able to deposit as agglomerates or aggregates in endosomes or lysosomes of the cytoplasm (Guo et al., 2015; Xu et al., 2015). It was shown (Miyayama and Matsuoka, 2016) that Ag NPs exposure on cells can lead to a reduction of Ag dissolution rate (pH-dependent behavior) and MT expression which in turn induce damages on pulmonary epithelial cells. The lysosome impairment was also seen in Fe₃O₄ NPs (Zhang et al., 2016), metallic NPs can lead to ROS production and its transportation into lysosomes which finally interfering with the lysosomal hydrolases and induce the autophagy process (Halamoda Kenzaoui et al., 2012). It was seen that TiO₂ NPs can be responsible for the increment of lysosomal activities mainly caused by oncogenic transformations (Zhu et al., 2012; Lammel et al., 2019). Also, the strength of lysosomal membrane can be significantly decreased by TiO₂ NPs since they could easily get access into digestive cells, in the next step they can accumulate in lysosomes and then released to the alveolar lumen by apocrine extrusion of residual bodies or by holocrine elimination of dead cells (Jimeno-Romero et al., 2016). The Au NPs can also

decrease the lysosomal functions by alkalization of the lysosomal lumen which in turn induce the autophagosomes accumulation and leads to a reduction of cellular degradative capacity and low efficiency in damaged mitochondria release. In fact, these unstable cellular changes absolutely have an influence on the cell functionality, for instance in Au NPs-marked cells, cell migration and invasion were hindered (Manshian et al., 2018).

PHYSICOCHEMICAL PROPERTIES OF NANOPARTICLES

The potency of NPs to enter certain organs across specific pathways and their propensity whether to be accumulated in cell organelles or transported to other organelles is affected by both physical and chemical properties of related NPs. In addition, the physicochemical properties of NPs have a great impact on their toxicity since they can change the mechanism of toxicological response and NPs' accumulation, uptake, and translocation (Zoroddu et al., 2014). For instance, the same material with different shapes and sizes can considerably change the response of live tissue and identify the destiny of NPs as a safe or toxic one. The important physicochemical properties related to the cytotoxicity of nanomaterials are morphological features like size, shape, roughness and surface area, uniformity of agglomerates and the aggregate formation, mass of NPs, exact chemical composition, concentration or dose of NPs, surface charge, hydrophilicity, solubility and geometrical properties all can influence the behavior of material (Zoroddu et al., 2014).

Figure 3 schematically shows some major physical properties related to the toxicity of metal-based NPs in different categories of dimension, agglomerate condition, shape, and size of NPs and the surface charge, also each of which consisted of various states that finally led to toxicity or safety of NPs.

Size-Dependent Toxicity in Nanoparticles

The NPs' Size and surface area act as a key factor in its interaction with live tissues, the nanometric size level of NPs are almost in the same range of protein globules ranging from 2 to 10 nm, DNA helix about just two nanometers and cell membrane thickness with 10 nm, so they can easily pass the barriers of cells and enter to cell organelles (Sukhanova et al., 2018). It was shown (De Jong et al., 2008) that the distribution of gold NPs in organs are highly size-dependent, an obvious difference was detected between the distribution of the 10 nm and the larger particles. Ten nm NPs were found in most of the organs whereas the larger NPs distribution was seen in the limited organs of rats. Actually, gold NPs with 6 nm size can freely enter to cell nucleus while these NPs in the size range of 10–16 nm can only be found in cytoplasm and cell membranes which shows the higher toxicity of gold NPs with less than 10 nm size (Huo et al., 2014). Also, it was reported (Pan et al., 2007) that gold NPs with 15 nm size is about sixty times less toxic than 1.4 nm NPs especially for fibroblasts, epithelial cells, macrophages, and melanoma cells. In addition, NPs size can effectively determine and control the interactions between transport and cell defense systems which finally influences the kinetics of NPs distribution and concentration. It is believed that

(Zhang S. et al., 2015). NPs with smaller than 5 nm diameter generally can defeat cell entrance barriers and they are able to pass through cell membranes by translocation, while the larger NPs get into the cells by phagocytosis and other possible transportation mechanisms. The *in vivo* experiments (De Jong et al., 2008) confirmed that large NPs can be easily recognized by the immune system and prevents their entrance to the body. The surface area as one of the important factors in NPs cytotoxicity warrants the effective adsorption of NPs on the surface of cell organelles.

The Effect of Nanoparticles' Shape on Toxicity

Nanoparticles can have a variety of shapes and geometries including spheres, ellipsoids, cylinders, sheets, cubes, spikes, and rods which considerably affect the toxicity. In this relation, the round-shaped NPs are more susceptible to endocytosis than NPs with fiber and tube geometry (Champion and Mitragotri, 2006). Also, it was indicated that (Zhao et al., 2013) plate-like and needle-like NPs induce larger necrosis proportions than other spherical and rod-like NPs since these shapes have more capacity to induce physical damages to cells and live tissues by direct contact. In addition in gold NPs, geometry and shape of the NPs have an impact on the accumulation kinetics and its excretion and only star-like shapes can be stored in the lung, also it was confirmed that shape and geometrical variations do not considerably increase their chance to pass the blood-brain barriers (Talamini et al., 2017).

Chemical Composition

Along with other critical factors like shape and size, the chemical composition also must be considered with full attention. Inorganic NPs with the same physical condition but distinct chemical composition confirmed to have different toxicological behaviors. One of the examples is the different toxicity of SiO₂ and ZnO NPs with 20 nm size in which SiO₂ induce oxidative stress while ZnO influences the DNA structure (Yang H. et al., 2009). The induced toxicity related to chemical composition mainly arises from metallic ions' leakage into cells, also some of these metallic NPs are actually has a toxic nature such as As, Pb, Cd, Hg, and Ag since they can damage the cells (Roane et al., 2009). On the other hand, some metals like Fe and Zn are useful from the biological aspect of view but they can be harmful at high concentrations and cause toxicity reactions. Most of the mentioned issues can be solved by coating the NPs cores with polymeric shells, silica layers, or new NPs synthesis methods with non-toxic compounds which can lead to enhanced safety and chemical stability against metal ionic leakages and degradations (Soenen et al., 2015).

The Effect of Crystal Structure on the Toxicity of NPs

It was shown that the different crystal structures of the same NPs can make alterations in the toxicity response. One of the good examples is TiO₂ owing to its various crystal structures entitled rutile (TiO₂ with prism shape), anatase (octahedral crystals), and brookite (orthorhombic crystals). It was reported

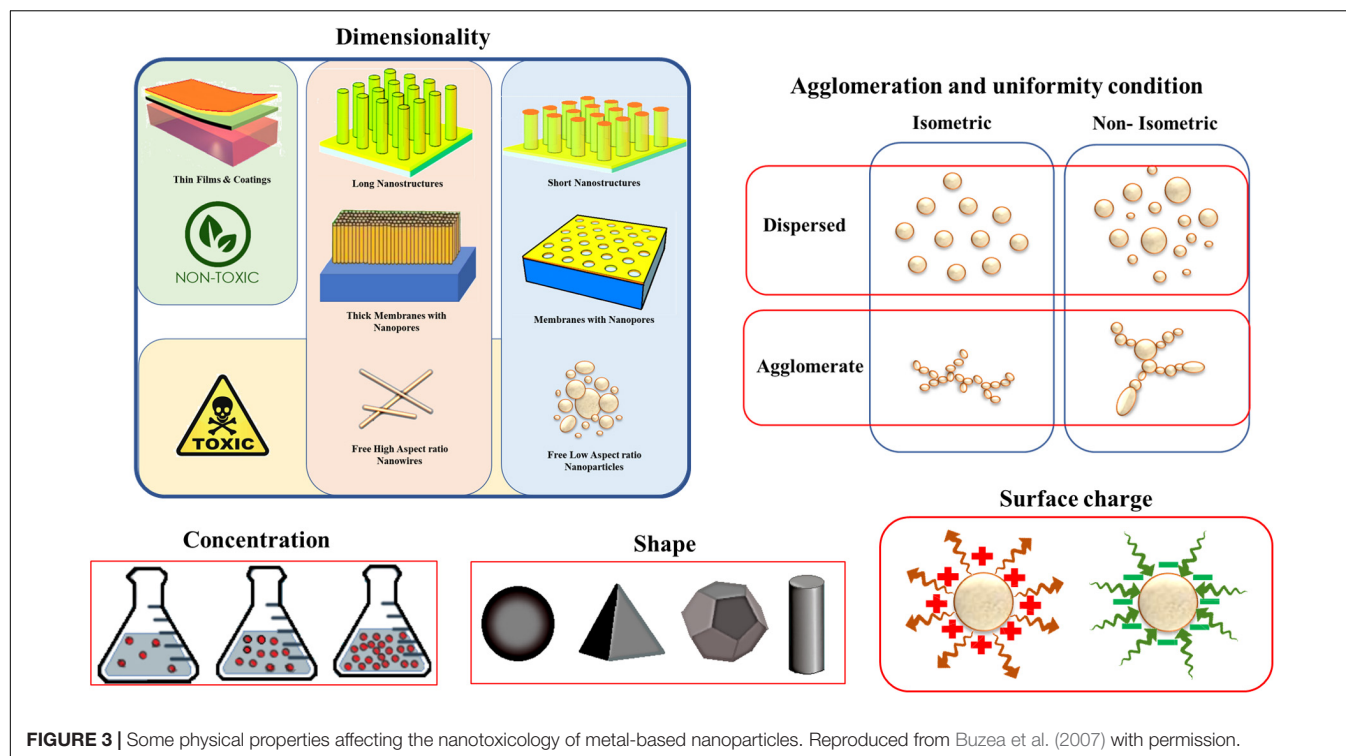


FIGURE 3 | Some physical properties affecting the nanotoxicology of metal-based nanoparticles. Reproduced from Buzea et al. (2007) with permission.

(Gurr et al., 2005) that 200 nm TiO₂ NPs with rutile structure caused hydrogen peroxide and oxidative DNA damage, lipid peroxidation, micronuclei formation, and the signs of abnormal chromosome segregation during mitosis process while in the anatase form there was not any considerable toxicity.

The Effect of Surface Charge on Toxicity

Ionic charges can affect the interaction between the NPs with cells hence having a great impact on toxicity related mechanisms. The surface charge of NPs can be described by zeta potential which is explained as the potential variation among the mobile dispersion medium and the stationary layer of the dispersion medium that is in attachment with the dispersed particle (Lu and Gao, 2010). **Figure 4** schematically shows the zeta potential.

The movement of particles in a fluid cause a net surface charge generation which can be defined by zeta potential hence the constancy of particles dispersion can be determined from zeta potential, NPs with a zeta potential value higher than 130 mV or lower than 230 mV are unlikely to aggregate (Khan, 2020), while NPs with lower zeta potential values are prone to stick to each other, entitled as aggregation in which the particles are firmly bonded, or agglomeration if the particles are weakly bonded due to van der Waal's forces. It was proved that the physical interaction between cellular membrane and NPs is mainly governed by surface charge of NPs and it was also indicated that other toxicity factors like shape and size of NPs have minimal impact on the toxicity of Ag NPs unless the electrostatic barrier between the NPs and cells are overcome. It was shown that positively charged coated Ag NPs are more toxic than that of the negatively charged NPs (El

Badawy et al., 2011). Thevenot et al. (2008) demonstrated that negative charged COOH treated TiO₂ NPs had not an impact on the cell viability because they can easily be absorbed into the cells without any membrane binding. In fact, the positively charged particles are more toxic and the variance surface charge determines the cellular uptake, the positively charged ZnO NPs show increased toxicity values compared to negatively charged NPs (Kim et al., 2014).

The Effect of NPs Solubility

The metallic NPs that have penetrated the cell is a source for supplying the metal ions and have the potential to constantly release these ions to cytoplasm environment. This metallic ion release is directly dependent on the NPs' dissolution rate (Khan, 2020). Despite the low dissolution, some metallic ions can show a very toxic behavior in physiological mediums, for example, ZnO NPs with just 10 mg/L dissolved zinc are highly toxic because of its critical concentration and dose range (Khan, 2020) so they should be used in the safe range and the minimum allowed limit must be considered. Horie et al. (2009) reported that NiO NPs have more activity compared to NiO fine particles because the NPs can release higher amounts of Ni²⁺ in the medium while fine particles do not have this capability. In addition, again because of this solubility effect of metallic ions cupric oxide CuO NPs are considerably more toxic than the same amount of CuCl₂ (Karlsson et al., 2008). It was believed that NPs have higher solubility rate than the bulk materials, this finding can only be correct for NPs in the special size condition (less than 100 nm size) hence particle sizes more than 100 nm fail to enhance the saturation solubility in the low solubility compounds, even if

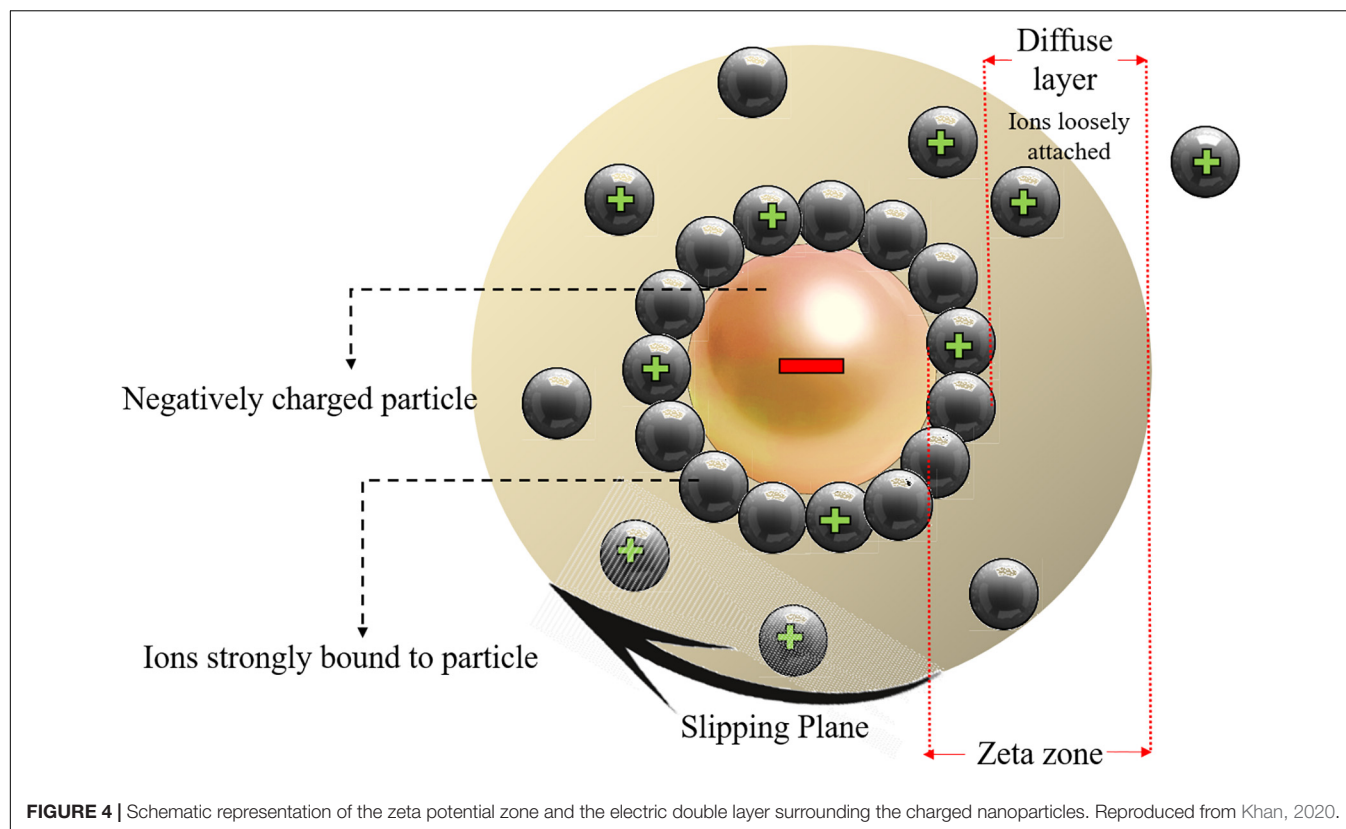


TABLE 2 | Effect of particle size on the solubility behavior and dissolution rate (He, 2009).

Size of particle	Solubility ratio (S/S_{∞})*	Variations in dissolution rate
10 μm	1	No considerable effect
1 μm	1.01	10-fold increase
100 nm	1.13	113- fold increase
10 nm	3.32	3320-fold increase

(S/S_{∞})*: the ratio of solid solubility to be dissolved with that of the substance having infinitely large solubility.

the rate of dissolution is increased, **Table 2** shows this situation in more details.

TOXICITY OF COMMON METALLIC AND METAL OXIDE NPs

The toxicity phenomenon is a very complicated issue that is dependent on lots of physicochemical parameters, hence different metallic NPs with their special nature would have various toxicity mechanisms and indicate alterations in toxicity amount. It was known that usually as the atomic number of the element increases, cytotoxicity increases (Huang et al., 2017), possibly due to band-gap energy. Also, it was shown that different materials activate certain toxicity mechanisms. In this relation, the present study discusses the involved nanotoxicology mechanisms of

common metallic and metal oxide NPs including Ti, Ag, Au, Zn, and Cu, and their effects on biological environments.

Titanium Dioxide TiO_2 NPs Toxicity; *in vitro* and *in vivo*

Titanium oxide NPs are among the most manufactured NPs with approximately 10,000 tons yearly production, owing to its unique properties such as suitable strength and Young's modulus (Ansarian et al., 2019; Attarilar et al., 2020), biocompatibility (Attarilar et al., 2019), corrosion resistance (Gode et al., 2015), solubility properties, surface structure, and the related aggregation manner so it has a lot of applications in industry as listed in **Table 1**. This wide use of TiO_2 NPs and its post disposal in the environment may arise the health and ecosystem issues hence its impact on live organisms *in vitro* and *in vivo* must be studied and considered.

The impact of TiO_2 NPs' shape on toxicity was examined in BEAS-2B cells, the shape of NPs was selected as bipyramids, rods, and platelets. It was seen that the rod-shaped NPs induced the most amount of toxicity, but in the platelets the genotoxicity and oxidative DNA damage were seen and their accumulation was higher than the rod and bipyramid-shaped NPs (Gea et al., 2019). It seems that among different crystal structures of TiO_2 , the anatase form has more toxicity. De Matteis et al. (2016) indicated that titanium ions are more prone to release in anatase rather than rutile form, also anatase form leads to more ROS production in MCF-7 cell line. Consequently, anatase influences the mitochondrial membrane and is more prone to activate the

apoptosis pathway. TiO₂ NPs treated Caco-2 cell indicated the affected intestinal epithelium layer after 24 h exposure and the cell viability shows the 13% reduction compared to the control sample (Pedata et al., 2019). Transmission electron microscope (TEM) observations showed that TiO₂ NPs were selectively accumulated in Caco-2 monolayers, as indicated in **Figure 5**. Also, it was proved that titanium ions have the potential to trigger the production of the pro-inflammatory cytokines and led to some toxic effects on the intestinal epithelium layer (Pedata et al., 2019). Experiments on the A549 cell line (human lung epithelial cells) confirmed the significant cytotoxic effects of citrate-coated TiO₂ NPs also the DNA damage experiments by comet assay indicated the increasing genotoxic effects in these citrate coated NPs. In fact, variation in the physicochemical properties of NPs by variation in the surface of coating affected the NPs' toxicity (Stoccoro et al., 2017).

An *in vivo* study about TiO₂ NPs was done by Fabian et al. (2008), TiO₂ NPs (<100 nm) were injected to Wistar rats. They did not find any sign of TiO₂ NPs accumulation in brain and lymph nodes, blood cells, and plasma, the most

bioaccumulation of NPs was seen in the liver and lower values of NPs were detected in the kidney, lung, and spleen. TiO₂ NPs injection into rats at a moderate dose of 20 mg/kg for 20 days had some effects on liver including congestion, prominent vasodilatation, and vacuolization that finally led to liver dysfunction, TiO₂ NPs injection at high doses (1387 mg/kg body weight) led to mortality of rats after 2 days of injection whereas the low dose injections (in the range of 10 mg/kg body weight) induced toxicity related signs such as decreased water and food consumption, increased number of white blood cells (Ben Younes et al., 2015). Xu J. et al. (2013) showed that TiO₂ NPs treatment induced some damages in the kidney, lung, brain, spleen, and liver of rats but no considerable pathological effects were detected in rats' heart. In another study, the rutile TiO₂ NPs treated rats indicated normal external lung morphology while TiO₂ NPs in crystalline form with 80% anatase and 20% rutile content showed pulmonary toxicity (Abdelgied et al., 2019). Briefly, it can be said that shape, higher dose, crystalline structure, and phases have the potential to cause toxicity in both *in vitro* and *in vivo* studies hence

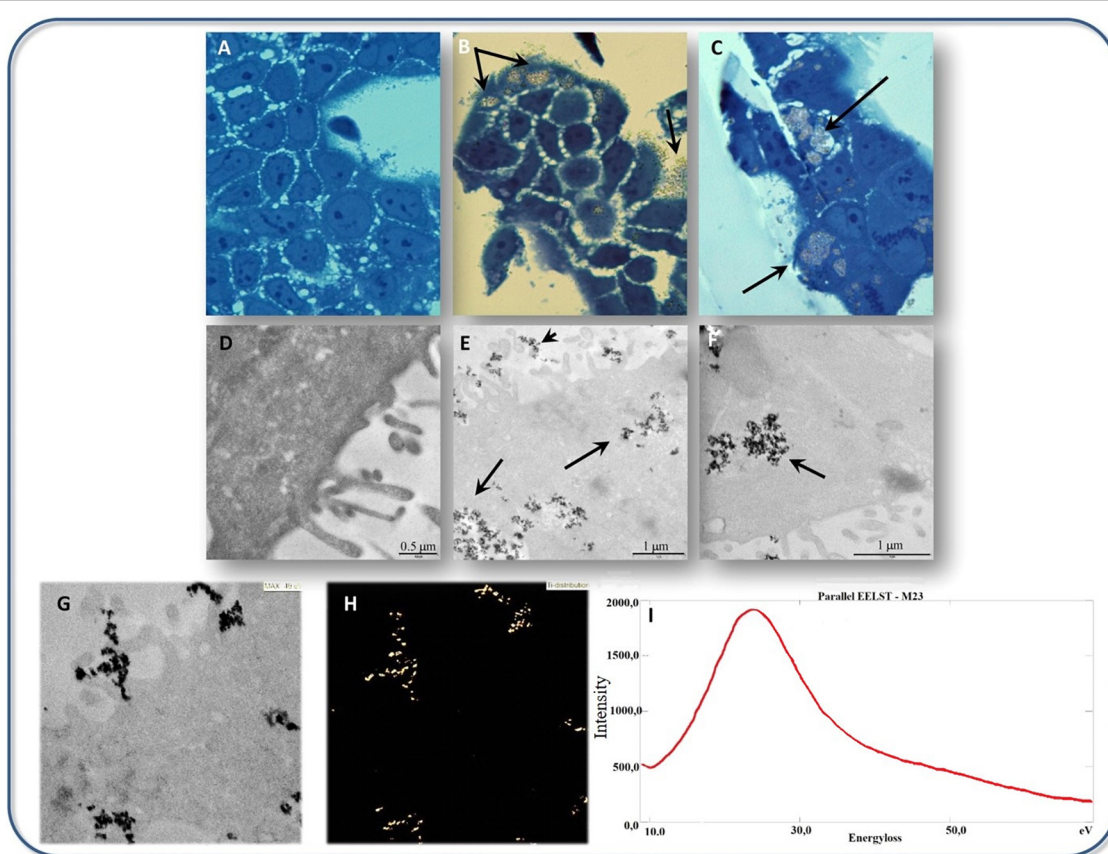


FIGURE 5 | Transmission electron microscope micrographs of TiO₂ NPs interaction with cultured Caco-2 cells, **(A–C)** Bright field optical microscopy analysis of Caco-2 cells cultured **(A)** without, **(B,C)** with 500 µg/mL TiO₂ NPs. Black arrows indicate TiO₂ NPs accumulation observable on the surface of cells as well as in the cytoplasm. **(D–F)** TEM analysis of Caco-2 cells cultured with **(E,F)** or without **(D)** 500 µg/mL TiO₂ NPs. Black arrows in **(E,F)** indicate TiO₂ NPs accumulation. **(G,H)** The ultrastructural appearance of Caco-2 cells cultured with 500 µg/mL TiO₂ NPs **(G)** with the respective map of Ti localization (ESI analysis) is shown in panel **(H)**. **(I)** Electron energy loss spectrum (EELS), withdrawn from the same sample regions of **(G,H)**, is shown. A peak at 25 eV compatible with the TiM_{2,3} edge electron energy loss was detected. Adapted from Pedata et al. (2019) with permission from Elsevier.

the careful control of TiO₂ NPs would be led to more safe utilization of these NPs.

Silver Nanoparticles and Their Toxicity

Silver as a noble metal in nanoparticle condition is the most widespread antibacterial agent, also Ag salts are utilized as agents for the treatment of different bacterial infections. Consequently,

Ag NPs are vastly utilized as bactericides due to its attainment in antibiotic resistance by various bacteria (Sintubin et al., 2012). Ag NPs have the potential to attach to the cell membrane of bacteria or fungi and induce damages on cell membrane structure, intracellular components leakage and in the end cell death (Yamanaka et al., 2005), they can also produce free radicals and cause oxidative stress (Park et al., 2009). Ag NPs are able to

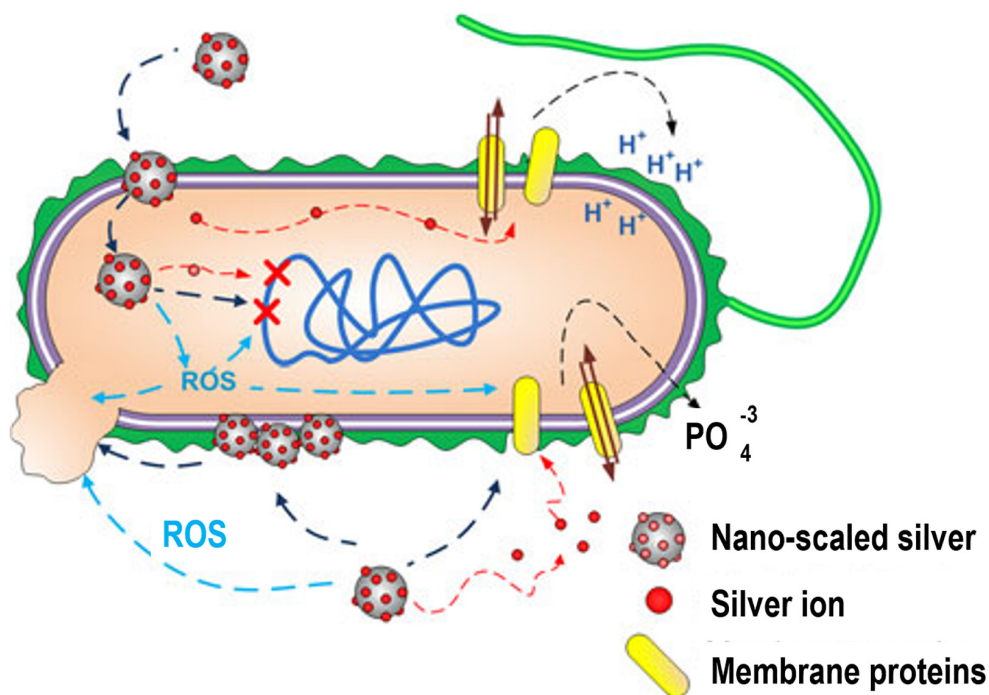


FIGURE 6 | Ag NPs interaction with bacterial cells. Ag NPs can induce (1) Ag ions leakage and ROS generation, (2) membrane proteins dysfunction, (3) accumulation in cell membrane influencing the membrane permeability, (4) DNA damage. Adapted from Marambio-Jones and Hoek (2010) with permission.

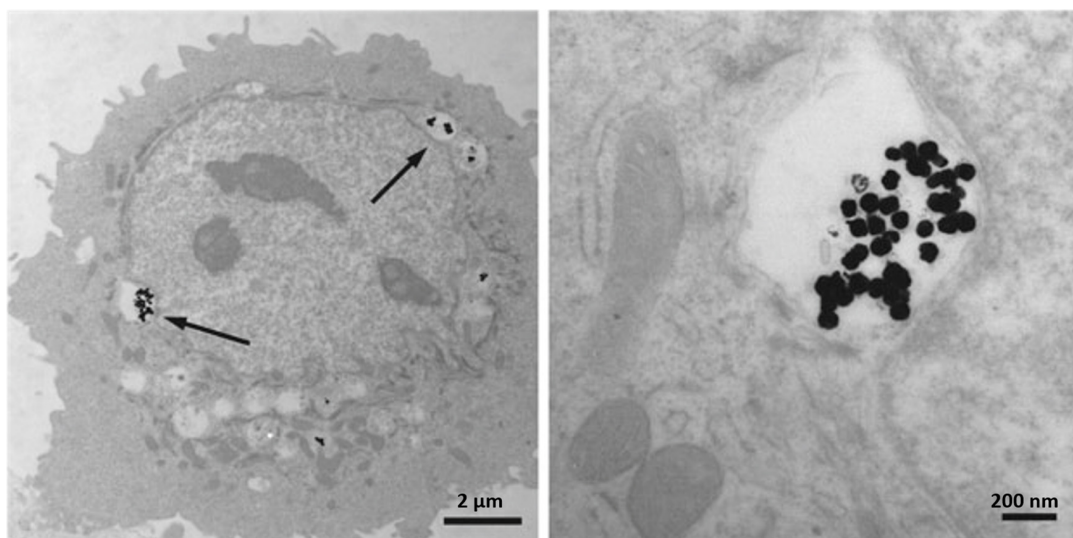


FIGURE 7 | Transmission electron micrographs depicting Ag NPs uptake into HEK cells. (A) 80 nm Ag NPs within cytoplasmic vacuoles of a HEK; (B) higher magnification of the (A). Arrows point to Ag NPs. Adapted from Deyhle et al. (2012).

construct destructive binding with genomic DNA and prevent the direct replication (Yang W. et al., 2009), it can also decrease the activity of enzymes and other proteins in the transcription stage (Yamanaka et al., 2005). **Figure 6** shows Ag NPs interaction with bacterial cells (Marambio-Jones and Hoek, 2010).

The dose of Ag NPs utilization for inhibition of microbial growth must be kept under the range of human cell cytotoxicity. *In vitro* cell studies indicated the dependence of cytotoxicity on the size of Ag NPs and related ROS generation in different cell lines including fibrosarcoma, skin carcinoma, fibroblast, glioblastoma, hepatoma, alveolar, and keratinocyte (Wijnhoven et al., 2009; Samberg et al., 2010). In addition to size, the cytotoxicity and genotoxicity of Ag NPs are associated with its coating, concentration, exposure time, environmental factors, particle aggregation, surface oxidation to form silver oxides, etc. (Akter et al., 2018). Both Ag and its oxides have the potential to release Ag^+ and Ag^0 into media which consequently results in ionic Ag concentration in the environmental media and causes some degree of dysfunctions in mitochondria (Reidy et al., 2013). Subsequently, the interaction of Ag NPs with cell membrane proteins can lead to activation of signaling pathways for ROS generation and eventually cause proteins and nucleic acids destruction because of the potent affinity of silver for sulfur, at the end all of these events led to apoptosis and reductions in cell proliferation (Haase et al., 2012). **Figure 7** shows the TEM images indicating Ag NPs uptake in HEK cells.

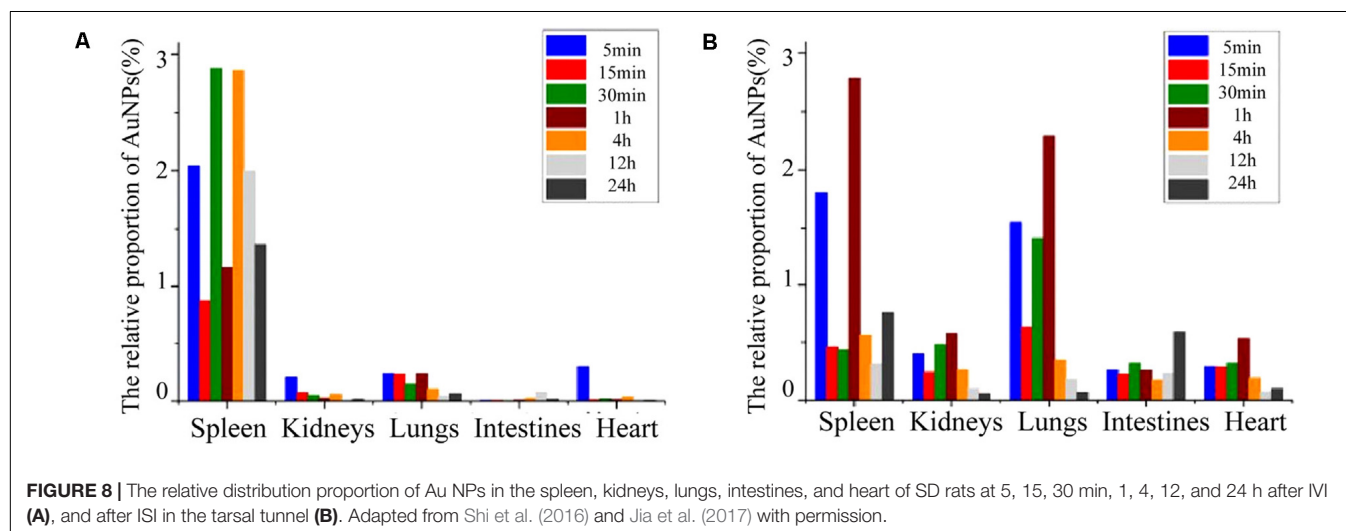
There are some limited *in vivo* studies about the Ag NPs toxicity, it was shown that these NPs induced some harmful impacts on reproduction, malformations, and various morphological destructions in different animal models (Zhang X.F. et al., 2015). Drinking Ag NPs contained water to rats for 1–2 weeks duration, indicated Ag NPs distribution in musculus soleus, cerebellum, spleen, duodenum, and myocardial muscle (Pelkonen et al., 2003), also a dose-dependent Ag NPs accumulation in the liver of rats was reported (Kim et al., 2008). Prolonged intake of Ag NPs in the salt form with low concentrations led to fatty degeneration in the liver and kidneys together with variations in blood cells (Wijnhoven et al., 2009).

Intravenous Ag NPs injection in rats showed 40 mg/kg dose (higher than 20 mg/kg dose values considered as toxic in rat models) can cause a considerable increase in liver enzymes whereas ROS increasing was detected in blood serum also TEM micrographs indicated the particle deposition in the liver and kidney of rats (Tiwari et al., 2011).

Gold Nanoparticles and Their Toxicity

Gold (Au) NPs are also having a place between widespread NPs since they can be used in order to evaluate the cellular uptake and tissue distribution of particles, due to their easy to detect nature by electron microscopy and it has other applications as listed in **Table 1**. In addition, gold salts such as sodium gold thiomalate are utilized as decisive disease-modifying antirheumatic agents (Fadeel and Garcia-Bennett, 2010) but its long-term accumulation in the body can cause cytotoxic effects.

It was confirmed that the cellular response to Au NPs is size-dependent. For instance, 1.4 nm Au NPs is among the most toxic conditions of these NPs and results in rapid cell death by necrosis (Pan et al., 2007) while it seems to be non-toxic in 15 nm condition (Chen et al., 2009). *In vitro* studies about the Au NPs (35 nm) indicated its low toxicity for murine RAW macrophages with no considerable cell functionality blockage (Shukla et al., 2005). Coradeghini et al. (2013) investigated the effect of 5–20 nm Au NPs on human fetal lung fibroblast cells (MRC-5) and no considerable effect on the viability of MRC-5 cells was detected but cell proliferation was inhibited. Also, the oxidative DNA damage was confirmed due to NPs' destructive effects on DNA. The smaller the Au NPs, the higher its tendency to induce toxicity since smaller NPs can easily bind on cellular surfaces. For example, Au NPs with 1.4 nm diameter are capable to bind with DNA and influence genes (mutation) compared to their larger counterparts (Yah, 2013). The dose of NPs has a crucial role in cytotoxicity, for example, Au NPs with a size range of 2–40 nm are biologically safe to MRC-5 cells but in exceeded dosage range (10 ppm dosage) apoptosis and up-regulated expression of pro-inflammatory genes and tumor necrosis was reported (Yen et al., 2009).



The Au NPs (5 nm) can preferentially bind to specified growth factors like vascular endothelial growth factor (VEGF) perhaps by cysteine residues of the heparin-binding domain and cause the inhibition of angiogenesis in a mouse model (Fadeel and Garcia-Bennett, 2010). Intravenous implementation of Au NPs (18 nm diameter) in rats showed that NPs were selectively accumulated within the liver and spleen, while NPs with 1 nm size were secreted in urine and feces. In addition, 3.7% of 1 nm sized particles remained in the blood at the first 24 h hence Au NPs interaction is size-dependent (Semmler-Behnke et al., 2008). Sonavane et al. (2008) studied the tissue distribution of Au NPs in rats, NPs intravenous exposure confirmed the highest accumulation in the liver and with lower amounts in the lung,

kidney, and spleen. The smaller NPs with 15 and 50 nm size even can be found in the brain which indicates its ability to pass the blood-brain barrier hence they have the potential to get into the brain through neuronal transport. Au NPs with 20 nm size entry via inhalation can concentrate in the olfactory bulb of rats (Yu et al., 2007). **Figure 8** shows the relative distribution proportion of the Au NPs in the various organs of rats including spleen, kidneys, lungs, intestines, and heart at different time durations.

Berce et al. (2016) investigated the bone marrow toxicity of Au NPs in rats, it was shown that Au NPs accumulated in the hematopoietic bone tissue and unfortunately resulting in severe side effects such as leucopoiesis and megakaryopoiesis and also increased levels of white blood cell and platelet were found in Au

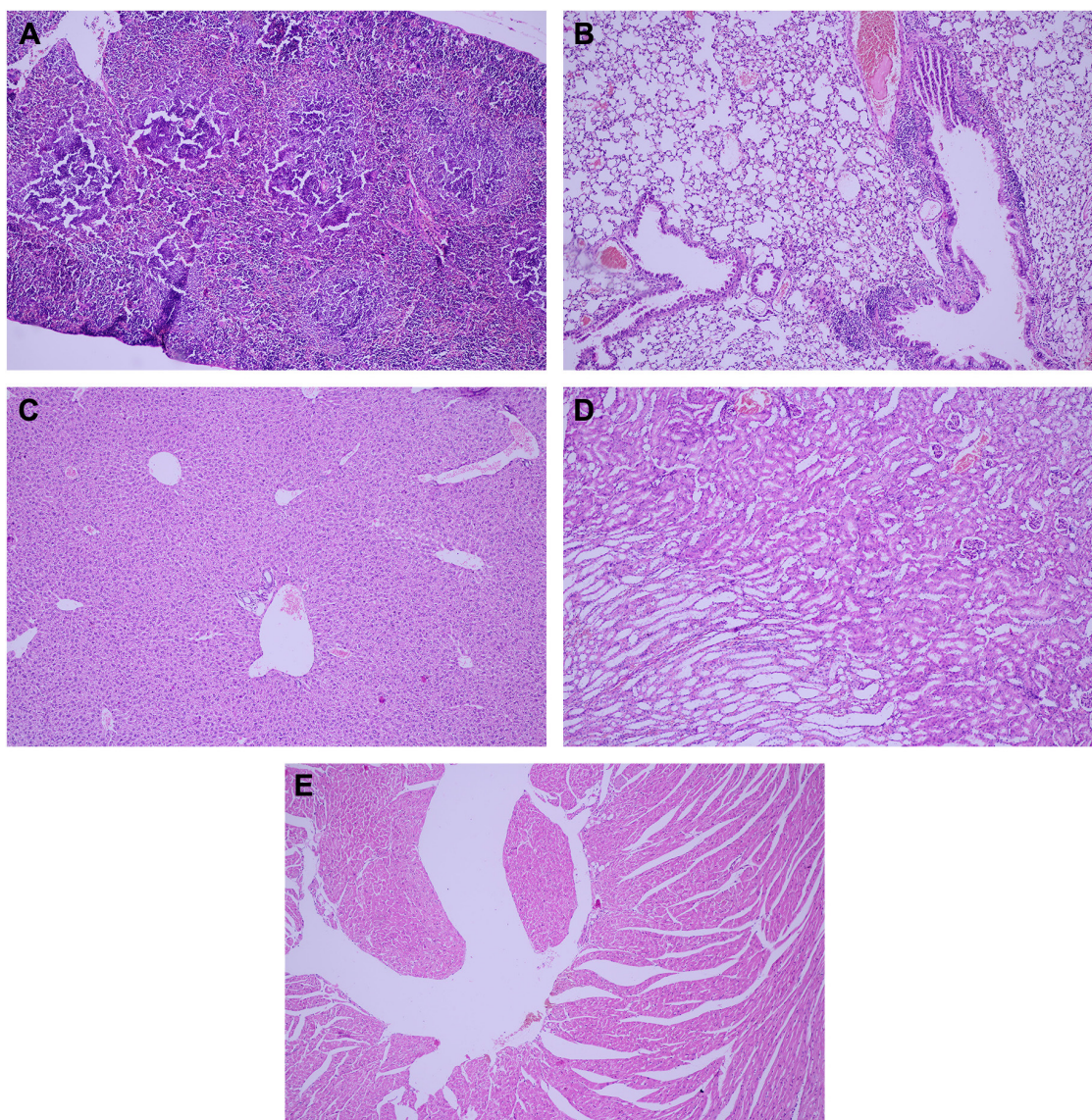


FIGURE 9 | The pathology examination of the Au NPs treated rat organs, in 1,100 $\mu\text{g/kg}$ dosage the pathology examination of the organs showed no degenerative, inflammatory, vascular, necrotic, or apoptotic lesions over the spleen (A), lung (B), liver (C), kidney (D), and heart (E). Adapted from Berce et al. (2016) with permission from Dove Medical Press.

NPs treated rats compared to control ones, indicating its toxic effects. **Figure 9** shows the pathology examination of the Au NPs treated rat organs as it was seen in the 1,100 $\mu\text{g/kg}$ dosage no considerable sign of degenerative, inflammatory, vascular, necrotic, or apoptotic lesions was detected. While the pathology experiments through bone marrow and sternum in **Figure 10** showed that the mice which got the daily iv Tween® 20-GNPs had increased megakaryopoiesis as opposed to the control group. **Figures 10A,B** shows the increased megakaryopoiesis as opposed to the control group in **Figures 10C,D**, but no bone marrow fibrosis was detected.

Zinc and Zinc Oxide Cytotoxicity

The zinc and zinc oxides were listed as safe substances in a US Food and Drug Administration (USFDA) (U.S. Food Drug Administration, 2019), while in the NPs condition it can induce toxicity into the surrounding environment. *In vitro* toxicity investigations of ZnO NPs in the size range of 40–48 nm in exposure to *Chlorella Vulgaris* indicated the reduction in viability, superoxide dismutase (SOD), and glutathione (GSH) and also increment of lactate dehydrogenase (LDH) (Suman et al., 2015). This finding indicates the considerable impact of ROS production in the cytotoxicity of ZnO NPs. Together with shape and concentration, the surface charge of ZnO NPs has a key

role in its toxicity. It was believed that the positively charged NPs induce more toxicity and it can affect the cellular uptake and intracellular location (Asati et al., 2010; De Angelis et al., 2013). Kim et al. (2014) also proved the higher cytotoxicity of positively charged ZnO NPs in comparison to the negatively charged ones. In addition, genotoxicity and DNA damage was seen in ZnO treated MRC5 lung cells along with the high secretion of extracellular LDH and reduction in cell viability (Ng et al., 2017). Also, the Zn^{2+} release in ZnO NPs could lead to free radical emissions from the NPs surface and resulted in metabolic disbalance and fluctuation in ionic state of cells related to the deterrence of ion transport and defects in ionic homeostasis (Namvar et al., 2015; Suman et al., 2015).

ZnO NPs treatment of rats with 300 mg/kg dose showed the NPs concentration in the liver which led to cell trauma also a considerable DNA lesion in the liver was seen which resulting in oxidative stress caused DNA damage (Sharma et al., 2012), **Figure 11** shows the pathological alterations in the liver and kidney of rats, treated with ZnO NPs for 14 consecutive days and also the control samples. The intraperitoneal injection with 50–200 mg of ZnO NPs/kg body dosage in Wistar rats indicated the dose-dependent toxicity behavior of ZnO NPs with considerable ROS generation also a major enhancement in liver enzymes at the concentration of 100 mg/kg animal body weight was

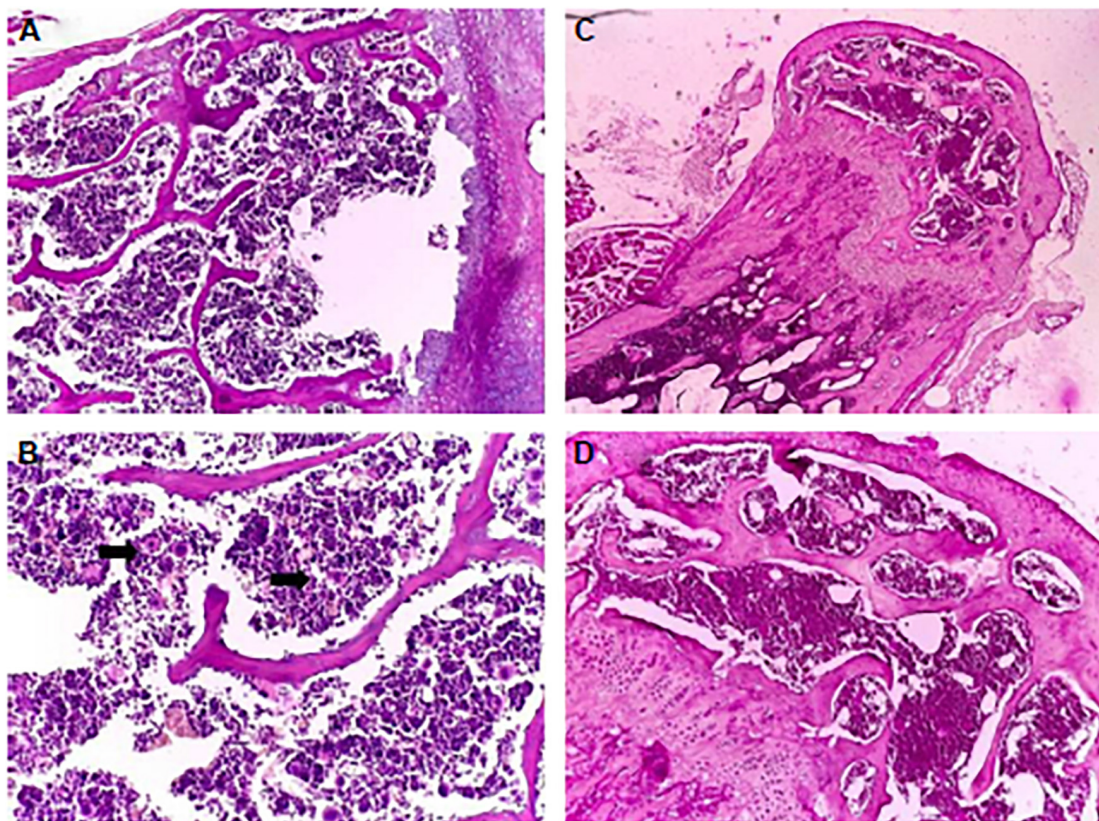


FIGURE 10 | The pathology experiment of the bone marrow of the mice treated with Tween 20-GNPs (**A,B**) and of the control group (**C,D**). In (**A,C**) the magnification was $\times 4$, and in (**B,D**) $\times 20$ magnification was used. The black arrows indicate the megakaryocytes. Adapted from Berce et al. (2016) with permission from Dove Medical Press.

reported (Abbasalipourkabar et al., 2015). ZnO NPs exposed liver tissue of animals indicated inflammation, increased congestion, chromatin condensation, and apoptosis, the tissue distribution analysis of ZnO NPs confirmed the increasing zinc dosages in the liver, large intestine, small intestine, and feces and some degree of hyperkeratosis and papillomatosis were detected in the skin (Ryu et al., 2014). Hence, ZnO NPs have toxic effects in both *in vitro* and *in vivo* studies including cytotoxicity, oxidative stress, and genotoxicity thus exposure to ZnO NPs should be considered and controlled precisely.

Toxicity of Copper and Copper Oxide NPs

Copper oxide (CuO) NPs have special characteristics like spin dynamics, high-temperature superconductivity, and electron correlation effects (El-Trass et al., 2012). Copper can be found in two ionic conditions Cu^{1+} and Cu^{2+} hence it can be interacting with biochemical reactions both as a reducing or oxidizing agent, nevertheless, it is not favorable from the toxicity aspect since copper ions are capable to induce oxidative stress (Valko

et al., 2005), genotoxicity (Adeyemi et al., 2020), and free radical production (Fahmy et al., 2020).

In vitro examinations on the toxicity of CuO NPs on human breast cancer MCF-7 cells had shown some morphological changes in cells, also autophagic vacuoles were detected and the cell cycle arrest caused apoptosis (Laha et al., 2014). The study about lung epithelial cells treated with CuO NPs with 9.2 nm size with at various concentrations indicated that these NPs led to a reduction of cell cytotoxicity and increased level of dose-dependent oxidative stress (Jing et al., 2015). The effect of size and shapes on the toxicity of CuO NPs was investigated by Thit et al. (2015), two sizes of CuO NPs with 6 nm and 100 nm larger polydispersed CuO NPs, also microparticles and Cu ions were examined in epithelial kidney cells. The most toxic state belongs to the polydispersed CuO NPs and they induced a considerable increment in intracellular ROS generation, DNA damage, and cell death, **Figure 12** schematically presents the *in vitro* toxicity model of CuO NPs.

In vivo studies in mouse models have shown that CuO NPs induced obviously epigenetic changes (Lu et al., 2016). Oral exposure of CuO NPs into rats showed the NP uptake in spleen,

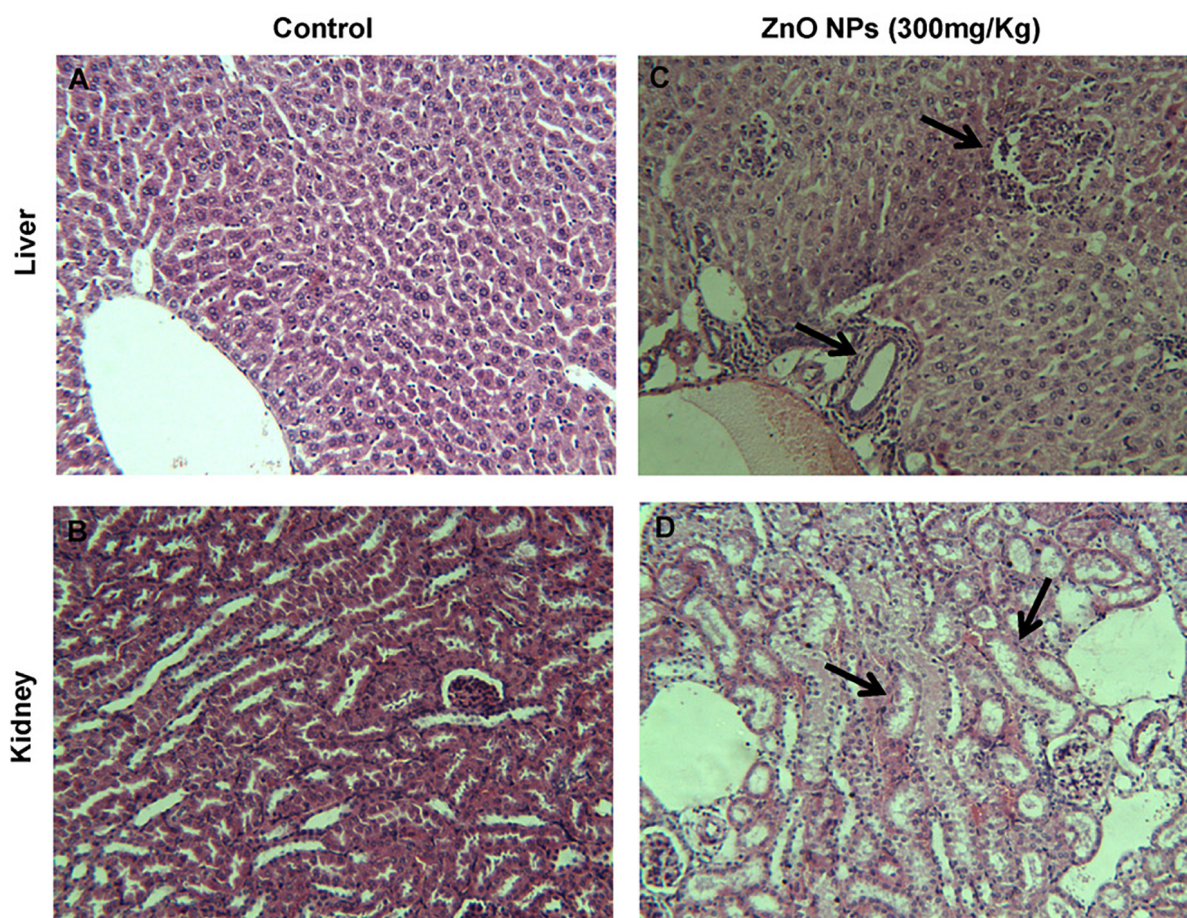


FIGURE 11 | Histopathology of liver and kidney tissues in mice, ZnO NPs treated for 14 consecutive days. **(A,B)** Control group showing normal liver and kidney, **(C,D)** pathological alterations in the liver and kidney of ZnO NPs (300 mg/kg) treated group (indicated by arrow); magnification (200×). Adapted from Sharma et al. (2012) with permission.

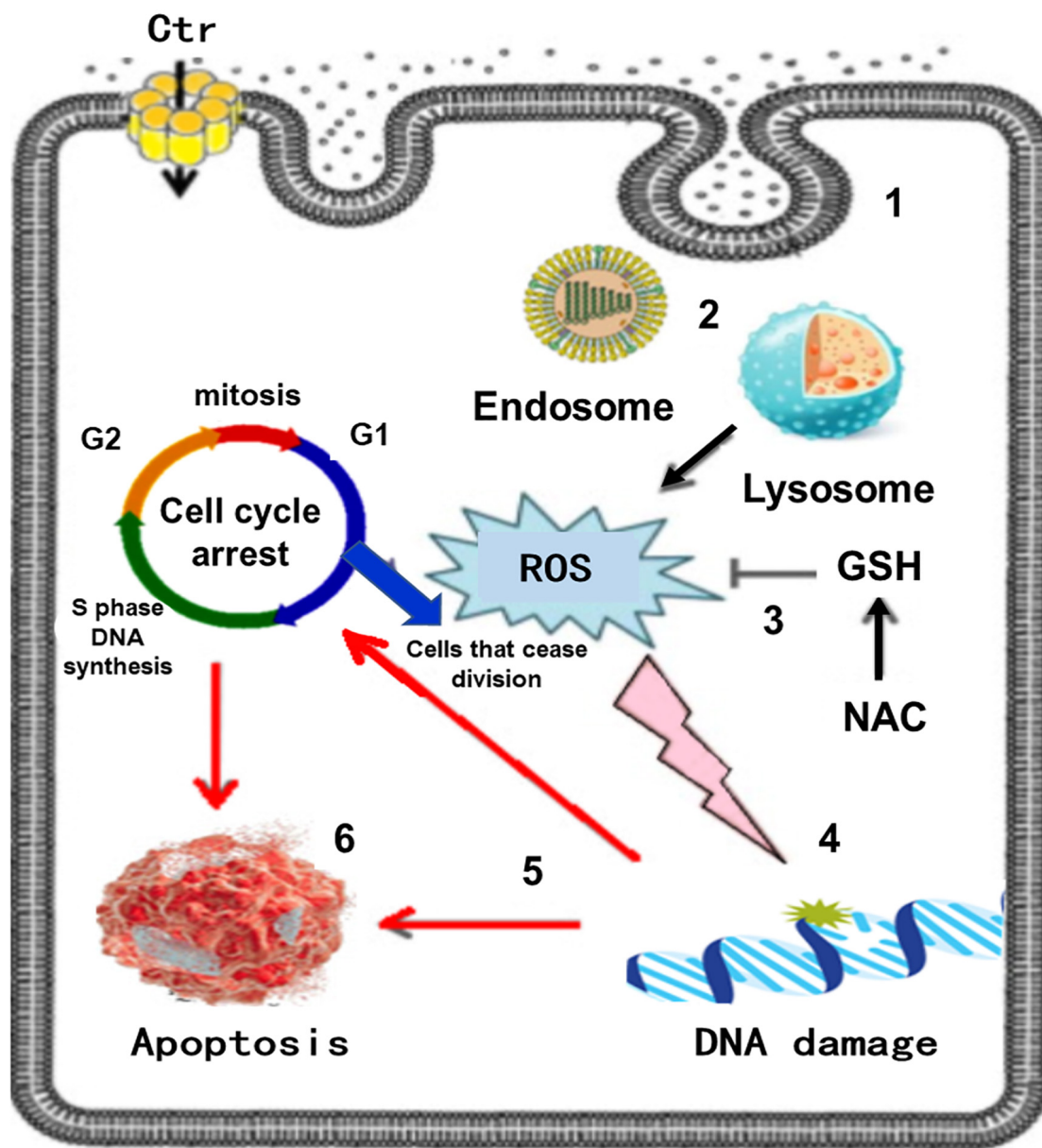


FIGURE 12 | *In vitro* toxicity model of CuO NPs, the sequence of events in Poly toxicity. **(1)** CuO NPs are taken up via endocytosis, **(2)** Endocytotic vesicles are converted to lysosomes via autophagy, **(3)** ROS generation, other molecules can be oxidized mitigated by the antioxidant GSH and its precursor NAC, **(4)** ROS attacks DNA in the nucleus, **(5)** DNA damage activates signaling systems that induce cell cycle arrest, **(6)** Cell death by apoptosis. Reproduced from Thit et al. (2015) with permission.

liver, kidney, brain, blood, lung, heart, urine, and feces (Lee et al., 2016). The CuO NPs exposed rats for up to 26 days showed some signs of increased Alanine Aminotransferase (ALT) levels as a liver damage index, also in 512 mg/kg dosage, no variations of histopathology were detected in liver, bone marrow, and stomach. The released Cu ions interfered with the immune system by lymphoid cell depletion in thymus and spleen organs, it should be said that the dissolution and biodistribution of NPs have a potential to act as a key factor in the toxic behavior of CuO treated

samples (De Jong et al., 2019). Other studies in relation to the toxicity issues of metal and metal oxide NPs are listed in **Table 3**.

Toxicity Prevention in Metallic and Metal Oxide NPs

The size, morphology, concentration, aggregation mode, charge, surface properties all have an impact on toxicity and must be considered in order to prevent the harmful effects of NPs. It

TABLE 3 | *In vitro* and *in vivo* nanotoxicology studies of metal and metal oxide nanoparticles.

Material	Condition	Properties	Cell line or animal model	Conclusion	References
Ag	<i>In vitro</i>	20–30 nm	Caco-2, SW480	No significant ROS generation, increased inflammation, increased cell death and cell stress.	Abbott Chalew and Schwab, 2013
		Two nano-sized and two micro-sized	Human red blood cells	NPs were more hemolytic than micron-sized particles at equivalent mass concentrations > 220 µg/ml and at surface area concentrations > 10 cm (2)/ml, NPs released more Ag ions than micro-sized particles.	Choi et al., 2011
	<i>In vivo</i>	Silver-coated wound dressing Acticoat (1 week) 30, 300 or 1000 mg/kg/day for 28 days (60 nm in size) per oral	Human burns patient Sprague-Dawley rats	Hepatotoxicity and argyria-like symptoms, Ag increase in plasma, urine and liver enzymes. Higher than 300 mg of NPs may result in slight liver damage, do not induce genetic toxicity, a gender-related difference in the accumulation of silver was noted in the kidneys, with a twofold increase in the female kidneys.	Trop et al., 2006 Kim et al., 2008
Al	<i>In vitro</i>	<500 nm	A549, THP-1	Low toxicity in MTT assay.	Lanone et al., 2009
Ni	<i>In vitro</i>	<500 nm	A549, THP-1	Low to moderate toxicity in MTT assay.	Lanone et al., 2009
Co	<i>In vitro</i>	<500 nm	A549, THP-1	Co NPs induced toxicity only when incorporated as a Nickel–Cobalt–Manganese mixed variant.	Lanone et al., 2009
Au	<i>In vitro</i>	Nanorods with 4:1 length-to-diameter ratio	HT29	Cytotoxicity caused by free CTAB, overcoating with polymer is useful.	Alkilany et al., 2009
	<i>In vivo</i>	8 mg/kg/week (3–100 nm in size) (4 weeks) intraperitoneal	BALB/C mice	NPs ranging from 8 to 37 nm induced severe sickness, fatigue, loss of appetite, change of fur color, and weight loss, from day 14 they exhibited a camel-like back and crooked spine. Pathological studies showed an increase of Kupffer cells in the liver, loss of structural integrity in the lungs, and diffusion of white pulp in the spleen.	Chen et al., 2009
		0.17, 0.85, and 4.26 mg/kg body weight (13 nm in size), (30 min after injection for 7 days) Intravenous, coated with PEG (12.5 nm in size) (40, 200, or 400 µg/kg/day for 8 days), intraperitoneal	BALB/C mice C57/BL6 mice	Acute inflammation and apoptosis in the liver, NPs accumulate in the liver and spleen for up to 7 days with long blood circulation times, NPs presence in cytoplasmic vesicles and lysosomes of liver Kupffer cells and spleen macrophages. NPs internalized inside the cell via a mechanism involving pinocytosis, also NPs internalization in lysosomal bodies arranged in perinuclear fashion, Au NPs were non-cytotoxic, non-immunogenic, and biocompatible properties.	Cho W.S. et al., 2009 Shukla et al., 2005
Ti and TiO₂	<i>In vitro</i>	10–300 nm	Caco-2	DNA damage dependency on sample processing conditions, cytotoxic in LDH and WST-1 assay.	Gerloff et al., 2009
		21 nm	Caco-2, SW480	No significant ROS generation, increased inflammation, increased cell death and cell stress.	Abbott Chalew and Schwab, 2013
		21 nm	16HBE, A549	No considerable effect on 16-HBE or A549 cell viability, strong aggregation in culture media.	Guadagnini et al., 2015
ZnO	<i>In vitro</i>	<500 nm	A549, THP-1	Moderate toxicity in MTT assay.	Lanone et al., 2009
		NPs containing sunscreen, mean particle size of 20 nm	Human volunteers	NPs penetrate deeper into human skin from an oily dispersion than from an aqueous one.	Bennat and Müller-Goymann, 2000
		20 nm	Caco-2, SW480	Toxic but no significant ROS generation, increased inflammation, increased cell death and cell stress.	Abbott Chalew and Schwab, 2013
		10–20 nm	Caco-2	DNA damage, cytotoxic in LDH and WST-1 assay.	Gerloff et al., 2009

(Continued)

TABLE 3 | Continued

Material	Condition	Properties	Cell line or animal model	Conclusions	References
MgO SiO and SiO₂	<i>In vivo</i>	<500 nm 288.2 and 265.7	A549, THP-1 Alveolar type II epithelial cells N10	High toxicity in MTT assay. Oxidative stress generation induced by Zn ions, Decrease in cell viability after 6 and 24 h of incubation.	Lanone et al., 2009 Xie et al., 2012
		Coated and uncoated NPs with 74.0 nm and 65.0 nm size	Human volunteers	NPs did not enter or cause cellular toxicity in the viable epidermis, Zinc ion concentrations slightly increased, repeated application of ZnO NPs to the skin, as used in sunscreen products was determined as safe.	Mohammed et al., 2019
	<i>In vitro</i>	8 nm	Caco-2	No cytotoxicity in LDH and WST-1 assay.	Gerloff et al., 2009
	<i>In vitro</i>	14 nm	Caco-2	Glutathione depletion, DNA damage, cytotoxic in LDH and WST-1 assay.	Gerloff et al., 2009
		25 and 50 nm, modified and not modified with sodium oleate	16HBE, A549	Dose, time and size dependent effects, 25 nm NPs are more toxic than 50 nm ones at lower concentrations, ROS generation ROS at toxic concentrations.	Guadagnini et al., 2015
		100 nm	HeLa, 3T3	Cell viability and survival decreased only about 20% at high concentration of 100 µg/mL, no significant toxic effects.	Xia et al., 2013
	<i>In vivo</i>	20 mg/animal (1 or 2 months), intratracheal instillation	Wistar rats	Changes in pathology and fibrotic grade, the lung/body coefficient and hydroxyproline content of SiO ₂ NPs were lower than micro-sized SiO ₂ .	Chen et al., 2004
		50 mg/kg (50, 100 or 200 nm in size), (12, 24, 48 and 72 h, 7 days) intravenous	BALB/C mice	NPs trapped by macrophages in the spleen and liver and remained there until 4 weeks after the single injection, Macrophage mediated frustrated phagocytosis of larger NPs resulted in release of pro-inflammatory cytokines and cell infiltrates within hepatic parenchyma.	Cho M. et al., 2009
Cu, CuO and CuS	<i>In vitro</i>	2 mg/kg (20-25 nm in size) (24 h), intravenous	Nude mice	Higher accumulation of NPs in liver, spleen, and stomach than in kidney, heart, and lungs, hepatobiliary excretion of NPs after 15 days.	Kumar et al., 2010
		50 and 100 nm, surface charge	Caco-2	Positively charged NPs have higher toxicity and cell uptake, NPs transfer is a dynamin-dependent process.	Bannunah et al., 2014
		50 nm	A549, SAEC	Cell cycle arrest by Cu ions, highly toxic, inhibition of cell proliferation genes, apoptosis.	Hanagata et al., 2011
	<i>In vivo</i>	<500 nm	A549, THP-1	High toxicity in MTT assay.	Lanone et al., 2009
		Length of 59.4 nm and thickness of 23.8 nm	HUVECs, RAW 264.7, KB, HeLa	Cell viability reduction in HUVECs at higher than 100 µg/mL dosages, toxicity to HUVEC and RAW 264.7 cells, NPs uptake in RAW 264.7 cells, no considerable change in cytoskeleton components.	Feng et al., 2015
FeO and Fe₃O₄	<i>In vivo</i>	Micro-Cu (1 µm), and nano-Cu (80–100 nm),	Sprague-Dawley rats	Cu NPs changed the immune function of the spleen, Alteration in the number of blood cells in rats and lymphocyte subpopulation in the spleen, antibody production and obvious histopathology changes.	Zhou et al., 2019
	<i>In vitro</i>	10 nm, without and with polyethylenoxide (PEO) coating	PC3, C4-2, HUVECs	Viability reduction, coated NPs uptake by cells, the surface-modified NPs are more toxic than NPs without shells.	Häfelí et al., 2009
		8 nm, modified and not modified with sodium oleate	16HBE, A549	Sodium oleate coating led to an increase in cytotoxicity, strong aggregation in culture media, toxic and inducing cytotoxicity in a dose, time and coating dependent manner.	Guadagnini et al., 2015
	<i>In vivo</i>	Ferrite and manganese ferrite oxide with sizes between 3 and 20 nm	Zebrafish embryos and mice	In manganese-based NPs concentrations above 100 µg/mL showed a low survival rate (<50%), absence of toxicity in mice	Caro et al., 2019
	<i>In vitro</i>	15, 25, 30, and 45 nm	BEAS-2B	ROS generation led to cell death, NPs absorption by cells and localized in the perinuclear space	Park et al., 2008

was known that toxicity of metallic and metal oxide NPs is directly related to its surface properties hence alterations in the surface of these NPs can be a good idea for mitigating their possible harmful effects. In this regard, various safe surface designs are the spotlights and can be listed as utilization of surface coatings (Osmond-McLeod et al., 2013), core-shell structures (Davidson et al., 2015), doping-based methods (Wang et al., 2012), geometric control (Ji et al., 2012), and surface passivation methods (Cai et al., 2017). Among these methods, the coating approaches seem to be simpler and more controllable and it is almost applicable to every metallic NPs. These methods can affect the surface reactivity and ion outlet in order to avoid any cytotoxic occurrence. One of the coating and surface passivation methods is sulfidation, for example, the existence of sulfide can avoid AgNO₃ toxicity (Bowles et al., 2002). Also, Levard et al. (2013) reported that sulfidation of silver NPs can hinder Ag ion mobility and reduce its dissolution rate. Considering gastrointestinal digestion impact, Martirosyan et al. (2014) used food matrix component phenolic compounds (PCs) to prevent from the toxicology of Ag NPs. In this regard, two major factors involving in the toxicity of Ag NPs (the release of Ag⁺ and ROS) were studied. Results showed that two PCs, quercetin and kaempferol, relatively defended the Caco-2 cells from Ag NPs induced toxicity and these PCs protected the epithelial barrier integrity which disrupted by NPs. Future investigations seem to be necessary to find more sophisticated methods in order to precise and complete toxicity prevention.

CONCLUSION

Nanotechnology as one of the exciting and modern branches of science found a lot of applications in various technologies from the food and cosmetic industry to medicine and agriculture, hence humanity is in direct contact with these nanoparticles (NPs). Although, the nanosized materials have many benefits compared to coarse sizes they can also have unfavorable effects since they have the potential to pass the natural barriers of live cells and tissues and cause toxic and inflammatory issues. Because of these problems, a new branch of science entitled nanotoxicology has emerged with the aim to elucidate the possible effects of NPs and the related parameters affecting the cytotoxicity of nanomaterials. Metal and metal oxide materials are among the most used NPs so this review paper dedicated to analyze the key factors influencing the toxicity of these NPs and review the *in vitro* and *in vivo* studies to find out the possible hazards of NPs and found a detailed guideline to control and decrease the adverse effects of metal and metal oxide NPs. In order to attain this goal, firstly the toxicity mechanisms including reactive oxygen species (ROS) generation, the effect of NPs on cell membranes, cytoskeleton components, DNA, mitochondria, and lysosomes was discussed. Secondly, because of the obvious effects of physical and chemical characteristics on toxicity, they were carefully reviewed. It was found that the size of NPs has a significant effect since its nano-sized range by increasing the specific surface area led to more cellular interactions and

toxicity. The other key factors affecting the cytotoxicity of NPs are shape and dimensionality, chemical composition and NPs concentration or dosage, crystalline structures, solubility, hydrophilicity, surface charge, and agglomeration condition. In this regard, it was believed that it is critical to control the physicochemical properties of NPs in order to achieve more safe and reliable NPs since even natural non-toxic and even antibacterial materials such as Ag, Cu, Ti, and Zn can induce toxicity in some ranges of size, dosage and surface charges. Overall, it seems that violating the cell passage system for example by decreasing the size of NPs to smaller than cellular subunits, organelles, and cells and letting them permeate and enter into the biological structures should be strictly prevented. Thirdly, some highlight findings of *in vitro* and *in vivo* studies about the toxicity of metal and metal oxide NPs were discussed to determine key factors. In the end, it is hoped that increasing the awareness and information about this subject opens a new horizon to understand more about the nanotoxicology and design the modern materials and procedures with the safe thresholds. These modern NPs should be designed meticulously by taking into account all the intriguing and complex aspects that arise from nanometric size ranges and also the other affecting factors.

The emerging trends and prospects in metallic NPs' toxicity studies are quite broad including modern NPs designs with optimal properties, enhancing their favorable effects and minimizing the potential toxicity, detection of toxicity transmitting species and targets by considering their life cycle, incorporation of various coating and surface treatments to decrease the harmful results while maintaining the favorable properties. Many aspects of these issues are still unsolved and need further studies in the future to overcome the toxicity limitations of metallic NPs and other present to-date barriers. In this regard, methods based on the simultaneous use of NPs with antitoxic strategies seem to be more promising. Also, in future studies, more attention should be paid to possible effects of biological fluids and surrounding tissues, biokinetics, involved mechanisms, and other chemical and biological factors. Moreover, there is a demand for more sophisticated and validated *in vitro* models that are prognostic of *in vivo* experiments outcomes. Finally, the resultant guidelines should have a potency to underlie the exact NPs' interactions with biological systems in order to support a complete correct risk assessment. Hence, various scientific disciplines including chemistry, physics, medicine, and biology should be involved and interact together to shade light on all the complex cellular-molecular events.

AUTHOR CONTRIBUTIONS

SA wrote the main part of the manuscript. QW and JuY greatly contributed to the titanium and copper parts. ME made major contributions particularly in choosing the figures. SA, JiY, ME, and JL made significant contribution to the revision stage. YT and SA prepared and formulated the references. All the authors contributed to the article and approved the submitted version.

FUNDING

The authors would like to acknowledge the financial supports provided by National Natural Science Foundation of China under Grant Nos. 51674167 and 81828007, High-level Innovation team

and Outstanding Scholars Program of Colleges and University in Guangxi: Innovative team of basic and Clinical Comprehensive Research on Bone and Joint Degenerative Diseases, and Open Foundation of Guangxi Key Laboratory of Processing for Non-ferrous Metals and Featured Materials (2019GXYSOF01).

REFERENCES

- Abbasalipourkabir, R., Moradi, H., Zarei, S., Asadi, S., Salehzadeh, A., Ghafourikhoshroshahi, A., et al. (2015). Toxicity of zinc oxide nanoparticles on adult male Wistar rats. *Food Chem. Toxicol.* 84, 154–160. doi: 10.1016/j.fct.2015.08.019
- Abbott Chalew, T. E., and Schwab, K. J. (2013). Toxicity of commercially available engineered nanoparticles to Caco-2 and SW480 human intestinal epithelial cells. *Cell Biol. Toxicol.* 29, 101–116. doi: 10.1007/s10565-013-9241-6
- Abdelgied, M., El-Gazzar, A. M., Alexander, D. B., Alexander, W. T., Numano, T., Iigou, M., et al. (2019). Pulmonary and pleural toxicity of potassium octatitanate fibers, rutile titanium dioxide nanoparticles, and MWCNT-7 in male Fischer 344 rats. *Arch. Toxicol.* 93, 909–920. doi: 10.1007/s00204-019-02410-z
- Adeyemi, J. A., Machado, A. R. T., Ogunjimi, A. T., Alberici, L. C., Antunes, L. M. G., and Barbosa, F. (2020). Cytotoxicity, mutagenicity, oxidative stress and mitochondrial impairment in human hepatoma (HepG2) cells exposed to copper oxide, copper-iron oxide and carbon nanoparticles. *Ecotoxicol. Environ. Saf.* 189:109982. doi: 10.1016/j.ecoenv.2019.109982
- Akter, M., Sikder, M. T., Rahman, M. M., Ullah, A. K. M. A., Hossain, K. F. B., Banik, S., et al. (2018). A systematic review on silver nanoparticles-induced cytotoxicity: physicochemical properties and perspectives. *J. Adv. Res.* 9, 1–16. doi: 10.1016/j.jare.2017.10.008
- Alkilany, A. M., Nagaria, P. K., Hexel, C. R., Shaw, T. J., Murphy, C. J., and Wyatt, M. D. (2009). Cellular uptake and cytotoxicity of gold nanorods: molecular origin of cytotoxicity and surface effects. *Small* 5, 701–708. doi: 10.1002/sml.200801546
- Ansarian, I., Shaeri, M. H., Ebrahimi, M., Minárik, P., and Bartha, K. (2019). Microstructure evolution and mechanical behaviour of severely deformed pure titanium through multi directional forging. *J. Alloys Compd.* 776, 83–95. doi: 10.1016/j.jallcom.2018.10.196
- Asati, A., Santra, S., Kaftanis, C., and Perez, J. M. (2010). Surface-charge-dependent cell localization and cytotoxicity of cerium oxide nanoparticles. *ACS Nano* 4, 5321–5331. doi: 10.1021/nn100816s
- ASTM (2012). *ASTM E2456-06, Standard Terminology Relating to Nanotechnology*. West Conshohocken, PA: ASTM International.
- Attarilar, S., Djevanroodi, F., Irfan, O. M., Al-Mufadi, F. A., Ebrahimi, M., and Wang, Q. D. (2020). Strain uniformity footprint on mechanical performance and erosion-corrosion behavior of equal channel angular pressed pure titanium. *Results Phys.* 17:103141. doi: 10.1016/j.rinp.2020.103141
- Attarilar, S., Salehi, M. T., Al-Fadhalah, K. J., Djevanroodi, F., and Mozafari, M. (2019). Functionally graded titanium implants: characteristic enhancement induced by combined severe plastic deformation. *PLoS One* 14:e0221491. doi: 10.1371/journal.pone.0221491
- Bannunah, A. M., Vllasaliu, D., Lord, J., and Stolnik, S. (2014). Mechanisms of nanoparticle internalization and transport across an intestinal epithelial cell model: effect of size and surface charge. *Mol. Pharm.* 11, 4363–4373. doi: 10.1021/mp500439c
- Ben Younes, N. R., Amara, S., Mrad, I., Ben-Slama, I., Jeljeli, M., and Omri, K. (2015). Subacute toxicity of titanium dioxide (TiO₂) nanoparticles in male rats: emotional behavior and pathophysiological examination. *Environ. Sci. Pollut. Res.* 22, 8728–8737. doi: 10.1007/s11356-014-4002-5
- Bennat, C., and Müller-Goymann, C. C. (2000). Skin penetration and stabilization of formulations containing microfine titanium dioxide as physical UV filter. *Int. J. Cosmet. Sci.* 22, 271–283. doi: 10.1046/j.1467-2494.2000.00009.x
- Berce, C., Lucan, C., Petrushev, B., Boca, S., Miclean, M., Sarpataki, O., et al. (2016). In vivo assessment of bone marrow toxicity by gold nanoparticle-based bioconjugates in CrL:CD1(ICR) mice. *Int. J. Nanomedicine* 11, 4261–4273. doi: 10.2147/IJN.S108711
- Bowles, K. C., Bianchini, A., Brauner, C. J., Kramer, J. R., and Wood, C. M. (2002). Evaluation of the effect of reactive sulfide on the acute toxicity of silver (I) to *Daphnia magna*. Part 1: description of the chemical system. *Environ. Toxicol. Chem.* 21, 1286–1293.
- Bressan, E., Ferroni, L., Gardin, C., Rigo, C., Stocchero, M., Vindigni, V., et al. (2013). Silver nanoparticles and mitochondrial interaction. *Int. J. Dentistry* 2013, 1–8.
- Brooker, R. J. (2018). *Genetics: Analysis & Principles*, 6th Edn. New York, NY: McGraw-Hill Science.
- Buza, C., Pacheco, I. I., and Robbie, K. (2007). Nanomaterials and nanoparticles: sources and toxicity. *Biointerphases* 2, MR17–MR71. doi: 10.1116/1.2815690
- Cai, X., Lee, A., Ji, Z., Huang, C., Chang, C. H., Wang, X., et al. (2017). Reduction of pulmonary toxicity of metal oxide nanoparticles by phosphonate-based surface passivation. *Part Fibre Toxicol.* 14, 1–11. doi: 10.1186/s12989-017-0193-5
- Caro, C., Egea-Benavente, D., Polvillo, R., Royo, J. L., Pernia Leal, M., and García-Martín, M. L. (2019). Comprehensive toxicity assessment of PEGylated magnetic nanoparticles for in vivo applications. *Colloids Surfaces B Biointerfaces* 177, 253–259. doi: 10.1016/j.colsurfb.2019.01.051
- Champion, J. A., and Mitragotri, S. (2006). Role of target geometry in phagocytosis. *Proc. Natl. Acad. Sci. U.S.A.* 103, 4930–4934. doi: 10.1073/pnas.0600997103
- Chen, H. (2018). Metal based nanoparticles in agricultural system: behavior, transport, and interaction with plants. *Chem. Speciat. Bioavailab.* 30, 123–134. doi: 10.1080/09542299.2018.1520050
- Chen, Q., Wang, N., Zhu, M., Lu, J., and Zhong, H. (2018). Redox Biology TiO₂ nanoparticles cause mitochondrial dysfunction, activate in inflammatory responses, and attenuate phagocytosis in macrophages: a proteomic and metabolomic insight. *Redox Biol.* 15, 266–276. doi: 10.1016/j.redox.2017.12.011
- Chen, Y., Chen, J., Dong, J., and Jin, Y. (2004). Comparing study of the effect of nanosized silicon dioxide and microsilicon dioxide on fibrogenesis in rats. *Toxicol. Ind. Health* 20, 21–27. doi: 10.1191/0748233704th190oa
- Chen, Y.-S., Hung, Y.-C., Liao, I., and Huang, G. S. (2009). Assessment of the in vivo toxicity of gold nanoparticles. *Nanoscale Res. Lett.* 4, 858–864. doi: 10.1007/s11671-009-9334-6
- Cho, M., Cho, W.-S., Choi, M., Kim, S. J., Han, B. S., Kim, S. H., et al. (2009). The impact of size on tissue distribution and elimination by single intravenous injection of silica nanoparticles. *Toxicol. Lett.* 189, 177–183. doi: 10.1016/j.toxlet.2009.04.017
- Cho, W.-S., Cho, M., Jeong, J., Choi, M., Cho, H.-Y., and Han, B. S. (2009). Acute toxicity and pharmacokinetics of 13 nm-sized PEG-coated gold nanoparticles. *Toxicol. Appl. Pharmacol.* 236, 16–24. doi: 10.1016/j.taap.2008.12.023
- Choi, J., Reipa, V., Hitchins, V. M., Goering, P. L., and Malinauskas, R. A. (2011). Physicochemical characterization and in vitro hemolysis evaluation of silver nanoparticles. *Toxicol. Sci.* 123, 133–143. doi: 10.1093/toxsci/kfr149
- Coradeghini, R., Gioria, S., García, C. P., Nativio, P., Franchini, F., Gilliland, D., et al. (2013). Size-dependent toxicity and cell interaction mechanisms of gold nanoparticles on mouse fibroblasts. *Toxicol. Lett.* 217, 205–216. doi: 10.1016/j.toxlet.2012.11.022
- Davidson, D. C., Derk, R., He, X., Stueckle, T. A., Cohen, J., Pirela, S. V., et al. (2015). Direct stimulation of human fibroblasts by nCeO₂ in vitro is attenuated with an amorphous silica coating. *Part. Fibre Toxicol.* 13:23. doi: 10.1186/s12989-016-0134-8
- Dayem, A. A., Hossain, M. K., Bin Lee, S., Kim, K., Saha, S. K., Yang, G., et al. (2017). The role of reactive oxygen species (ROS) in the biological activities of metallic nanoparticles. *Int. J. Mol. Sci.* 18, 1–21. doi: 10.3390/ijms18010120
- De Angelis, I., Barone, F., Zijno, A., Bizzarri, L., Russo, M. T., Pozzi, R., et al. (2013). Comparative study of ZnO and TiO₂ nanoparticles: physicochemical characterisation and toxicological effects on human colon carcinoma cells. *Nanotoxicology* 7, 1361–1372. doi: 10.3109/17435390.2012.741724
- De Jong, W. H., De Rijk, E., Bonetto, A., Wohlleben, W., Stone, V., Brunelli, A., et al. (2019). Toxicity of copper oxide and basic copper carbonate nanoparticles after short-term oral exposure in rats. *Nanotoxicology* 13, 50–72. doi: 10.1080/17435390.2018.1530390

- De Jong, W. H., Hagens, W. I., Krystek, P., Burger, M. C., Sips, A. J. A. M., and Geertsma, R. E. (2008). Particle size-dependent organ distribution of gold nanoparticles after intravenous administration. *Biomaterials* 29, 1912–1919. doi: 10.1016/j.biomaterials.2007.12.037
- De Matteis, V., Cascione, M., Brunetti, V., Toma, C. C., and Rinaldi, R. (2016). Toxicity assessment of anatase and rutile titanium dioxide nanoparticles: the role of degradation in different pH conditions and light exposure. *Toxicol. Vitro* 37, 201–210. doi: 10.1016/j.tiv.2016.09.010
- Devasagayam, T. P. A., Tilak, J. C., Boloor, K. K., Sane, K., Ghaskadbi, S., and Lele, R. (2004). Free radicals and antioxidants in human health: current status and future prospects. *J. Assoc. Physicians India* 52, 794–804.
- Deyhle, H., Schulz, G., and Bert, M. (2012). *Encyclopedia of Nanotechnology*. Berlin: Springer Netherlands. Dordrecht.
- Dhall, A., and Self, W. (2018). Cerium oxide nanoparticles: a brief review of their synthesis methods and biomedical applications. *Antioxidants* 7, 1–13. doi: 10.3390/antiox7080097
- Ding, Z., Zhang, C., Xie, L., Zhang, L.-C., Wang, L., and Lu, W. (2016). Effects of friction stir processing on the phase transformation and microstructure of TiO₂-compounded Ti-6Al-4V alloy. *Metall. Mater. Trans. A* 47, 5675–5679. doi: 10.1007/s11661-016-3809-8
- Dröge, W. (2002). Free radicals in the physiological control of cell function. *Physiol. Rev.* 82, 47–95. doi: 10.1152/physrev.00018.2001
- El Badawy, A. M., Silva, R. G., Morris, B., Scheckel, K. G., Suidan, M. T., and Tolaymat, T. M. (2011). Surface charge-dependent toxicity of silver nanoparticles. *Environ. Sci. Technol.* 45, 283–287. doi: 10.1021/es1034188
- El-Trass, A., ElShamy, H., El-Mehasseb, I., and El-Kemary, M. (2012). CuO nanoparticles: synthesis, characterization, optical properties and interaction with amino acids. *Appl. Surf. Sci.* 258, 2997–3001. doi: 10.1016/j.apsusc.2011.11.025
- Fabian, E., Landsiedel, R., Ma-Hock, L., Wiench, K., Wohleben, W., and van Ravenzwaay, B. (2008). Tissue distribution and toxicity of intravenously administered titanium dioxide nanoparticles in rats. *Arch. Toxicol.* 82, 151–157. doi: 10.1007/s00204-007-0253-y
- Fadeel, B., and Garcia-Bennett, A. E. (2010). Better safe than sorry: understanding the toxicological properties of inorganic nanoparticles manufactured for biomedical applications. *Adv. Drug Deliv. Rev.* 62, 362–374. doi: 10.1016/j.addr.2009.11.008
- Fahmy, H. M., Ebrahim, N. M., and Gaber, M. H. (2020). In-vitro evaluation of copper/copper oxide nanoparticles cytotoxicity and genotoxicity in normal and cancer lung cell lines. *J. Trace Elem. Med. Biol.* 60:126481. doi: 10.1016/j.jtemb.2020.126481
- Feng, W., Nie, W., Cheng, Y., Zhou, X., Chen, L., Qiu, K., et al. (2015). In vitro and in vivo toxicity studies of copper sulfide nanoplates for potential photothermal applications, Nanomedicine Nanotechnology. *Biol. Med.* 11, 901–912. doi: 10.1016/j.nano.2014.12.015
- Flores-López, L. Z., Espinoza-Gómez, H., and Somanathan, R. (2019). Silver nanoparticles: electron transfer, reactive oxygen species, oxidative stress, beneficial and toxicological effects. Mini review, *J. Appl. Toxicol.* 39, 16–26. doi: 10.1002/jat.3654
- Fröhlich, E. (2013). Cellular targets and mechanisms in the cytotoxic action of non-biodegradable engineered nanoparticles. *Curr. Drug Metab.* 14, 976–988. doi: 10.2174/1389200211314090004
- Gallud, A., Klöditz, K., Ytterberg, J., Östberg, N., Katayama, S., Skoog, T., et al. (2019). Cationic gold nanoparticles elicit mitochondrial dysfunction: a multi-omics study. *Sci. Reports* 9, 1–19. doi: 10.1038/s41598-019-40579-6
- García-Hevia, L., Valiente, R., Martín-Rodríguez, R., Renero-Lecuna, C., González, J., Rodríguez-Fernández, L., et al. (2016). Nano-ZnO leads to tubulin microtubule assembly and actin bundling, triggering cytoskeletal catastrophe and cell necrosis. *Nanoscale* 8, 10963–10973. doi: 10.1039/C6NR00391E
- Gea, M., Bonetta, S., Iannarelli, L., Giovannozzi, A. M., Maurino, V., Bonetta, S., et al. (2019). Shape-engineered titanium dioxide nanoparticles (TiO₂-NPs): cytotoxicity and genotoxicity in bronchial epithelial cells. *Food Chem. Toxicol.* 127, 89–100. doi: 10.1016/j.fct.2019.02.043
- Georgantzopoulou, A., Serchi, T., Cambier, S., Leclercq, C. C., Renaut, J., and Shao, J. (2016). Effects of silver nanoparticles and ions on a co-culture model for the gastrointestinal epithelium. *Part. Fibre Toxicol.* 13:9. doi: 10.1186/s12989-016-0117-9
- Gerloff, K., Albrecht, C., Boots, A. W., Frster, I., and Schins, R. P. F. (2009). Cytotoxicity and oxidative DNA damage by nanoparticles in human intestinal Caco-2 cells. *Nanotoxicology* 3, 355–364. doi: 10.3109/17435390903276933
- Gode, C., Attarilar, S., Eghbali, B., and Ebrahimi, M. (2015). “Electrochemical behavior of equal channel angular pressed titanium for biomedical application,” in *AIP Conference Proceedings*, College Park, MD: AIP.
- Gogoi, S. K., Gopinath, P., Paul, A., Ramesh, A., Ghosh, S. S., and Chattopadhyay, A. (2006). Green fluorescent protein-expressing *Escherichia coli* as a model system for investigating the antimicrobial activities of silver nanoparticles. *Langmuir* 22, 9322–9328. doi: 10.1021/la060661v
- Gopinath, P., Gogoi, S. K., Chattopadhyay, A., and Ghosh, S. S. (2008). Implications of silver nanoparticle induced cell apoptosis for in vitro gene therapy. *Nanotechnology* 19:075104. doi: 10.1088/0957-4484/19/7/075104
- Gu, H., Ding, Z., Yang, Z., Yu, W., Zhang, W., and Lu, W. (2019). Microstructure evolution and electrochemical properties of TiO₂/Ti-35Nb-2Ta-3Zr micro/nano-composites fabricated by friction stir processing. *Mater. Des.* 169:107680. doi: 10.1016/j.matdes.2019.107680
- Guadagnini, R., Moreau, K., Hussain, S., Marano, F., and Boland, S. (2015). Toxicity evaluation of engineered nanoparticles for medical applications using pulmonary epithelial cells. *Nanotoxicology* 9, 25–32. doi: 10.3109/17435390.2013.855830
- Guo, D., Zhang, J., Huang, Z., Jiang, S., and Gu, N. (2015). Colloidal silver nanoparticles improve anti-leukemic drug efficacy via amplification of oxidative stress. *Colloids Surf. B Biointerfaces* 126, 198–203. doi: 10.1016/j.colsurfb.2014.12.023
- Gurr, J. R., Wang, A. S. S., Chen, C. H., and Jan, K. Y. (2005). Ultrafine titanium dioxide particles in the absence of photoactivation can induce oxidative damage to human bronchial epithelial cells. *Toxicology* 213, 66–73. doi: 10.1016/j.tox.2005.05.007
- Haase, A., Rott, S., Mantion, A., Graf, P., Plendl, J., Thünemann, A. F., et al. (2012). Effects of silver nanoparticles on primary mixed neural cell cultures: uptake. Oxidative stress and acute calcium responses. *Toxicol. Sci.* 126, 457–468. doi: 10.1093/toxsci/kfs003
- Häfel, U. O., Riffle, J. S., Harris-Shekhawat, L., Carmichael-Baranaskas, A., Mark, F., Dailey, J. P., et al. (2009). Cell uptake and in vitro toxicity of magnetic nanoparticles suitable for drug delivery. *Mol. Pharm.* 6, 1417–1428. doi: 10.1021/mp900083m
- Halamoda Kenzaoui, B., Chapuis Bernasconi, C., Guney-Ayra, S., and Juillerat-Jeanneret, L. (2012). Induction of oxidative stress, lysosome activation and autophagy by nanoparticles in human brain-derived endothelial cells. *Biochem. J.* 441, 813–821. doi: 10.1042/BJ20111252
- Hanagata, N., Zhuang, F., Connolly, S., Li, J., Ogawa, N., and Xu, M. (2011). Molecular responses of human lung epithelial cells to the toxicity of copper oxide nanoparticles inferred from whole genome expression analysis. *ACS Nano* 5, 9326–9338. doi: 10.1021/nn202966t
- He, X. (2009). “Chapter 18 - integration of physical, chemical, mechanical, and biopharmaceutical properties in solid oral dosage form development,” in *Developing Solid Oral Dosage Forms*, eds Y. Qiu, Y. Chen, G. Zhang, and G. Z. Liu (San Diego: Academic Press), 407–441.
- Heinemann, D., Schomaker, M., Kalies, S., Schieck, M., Carlson, R., Escobar, H. M., et al. (2013). Gold nanoparticle mediated laser transfection for efficient siRNA mediated gene knock down. *PLoS One* 8:e58604. doi: 10.1371/journal.pone.0058604
- Horie, M., Nishio, K., Fujita, K., Kato, H., Nakamura, A., and Kinugasa, S. (2009). Ultrafine NiO particles induce cytotoxicity in vitro by cellular uptake and subsequent Ni(II) release. *Chem. Res. Toxicol.* 22, 1415–1426. doi: 10.1021/tx900171n
- Hoseinpour, V., and Ghaemi, N. (2018). Green synthesis of manganese nanoparticles: applications and future perspective—A review. *J. Photochem. Photobiol. B Biol.* 189, 234–243. doi: 10.1016/j.jphotobiol.2018.10.022
- Huang, Y. W., Cambre, M., and Lee, H. J. (2017). The toxicity of nanoparticles depends on multiple molecular and physicochemical mechanisms. *Int. J. Mol. Sci.* 18:2702. doi: 10.3390/ijms18122702
- Huo, S., Jin, S., Ma, X., Xue, X., Yang, K., Kumar, A., et al. (2014). Ultrasmall gold nanoparticles as carriers for nucleus-based gene therapy due to size-dependent nuclear entry. *ACS Nano* 8, 5852–5862. doi: 10.1021/nn5008572

- Ispanixtlahuatl-Meráz, O., Schins, R. P. F., and Chirino, Y. I. (2018). Cell type specific cytoskeleton disruption induced by engineered nanoparticles. *Environ. Sci. Nano* 5, 228–245. doi: 10.1039/c7en00704c
- Ji, Z., Wang, X., Zhang, H., Lin, S., Meng, H., Sun, B., et al. (2012). Designed synthesis of CeO 2 nanorods and nanowires for studying toxicological effects of high aspect ratio nanomaterials. *ACS Nano* 6, 5366–5380. doi: 10.1021/nn3012114
- Jia, Y. P., Ma, B. Y., Wei, X. W., and Qian, Z. Y. (2017). The in vitro and in vivo toxicity of gold nanoparticles. *Chinese Chem. Lett.* 28, 691–702. doi: 10.1016/j.ccl.2017.01.021
- Jimeno-Romero, A., Oron, M., Cajaraville, M. P., Soto, M., and Marigómez, I. (2016). Nanoparticle size and combined toxicity of TiO₂ and DSLS (surfactant) contribute to lysosomal responses in digestive cells of mussels exposed to TiO₂ nanoparticles. *Nanotoxicology* 10, 1168–1176. doi: 10.1080/17435390.2016.1196250
- Jing, X., Park, J. H., Peters, T. M., and Thorne, P. S. (2015). Toxicity of copper oxide nanoparticles in lung epithelial cells exposed at the air–liquid interface compared with in vivo assessment. *Toxicol. Vitro* 29, 502–511. doi: 10.1016/j.tiv.2014.12.023
- Kanchi, S., and Ahmed, S. (eds) (2018). *Green Metal Nanoparticles*. Hoboken, NJ: John Wiley & Sons, Inc.
- Karlsson, H. L., Cronholm, P., Gustafsson, J., and Möller, L. (2008). Copper oxide nanoparticles are highly toxic: a comparison between metal oxide nanoparticles and carbon nanotubes. *Chem. Res. Toxicol.* 21, 1726–1732. doi: 10.1021/tx800064j
- Katerji, M., Filippova, M., and Duerksen-Hughes, P. (2019). Approaches and methods to measure oxidative stress in clinical samples: research applications in the cancer field. *Oxid. Med. Cell. Longev.* 2019, 1–29. doi: 10.1155/2019/1279250
- Kehrer, J. P., and Klotz, L.-O. (2015). Free radicals and related reactive species as mediators of tissue injury and disease: implications for Health. *Crit. Rev. Toxicol.* 45, 765–798. doi: 10.3109/10408444.2015.1074159
- Khan, S. A. (2020). *Metal Nanoparticles Toxicity: Role of Physicochemical Aspects*. Amsterdam: Elsevier Inc.
- Kim, C.-S., Nguyen, H.-D., Ignacio, R. M., Kim, J.-H., Cho, H.-C., and Maeng, E. H. (2014). Immunotoxicity of zinc oxide nanoparticles with different size and electrostatic charge. *Int. J. Nanomedicine* 9(Suppl. 2), 195–205. doi: 10.2147/IJN.S57935
- Kim, Y. S., Kim, J. S., Cho, H. S., Rha, D. S., Kim, J. M., Park, J. D., et al. (2008). Twenty-eight-day oral toxicity, genotoxicity, and gender-related tissue distribution of silver nanoparticles in sprague-dawley rats. *Inhal. Toxicol.* 20, 575–583. doi: 10.1080/08958370701874663
- Kłębowski, B., Depciuch, J., Parlińska-Wojtan, M., and Baran, J. (2018). Applications of noble metal-based nanoparticles in medicine. *Int. J. Mol. Sci.* 19:4031. doi: 10.3390/ijms19124031
- Kumar, R., Roy, I., Ohulchanskyy, T. Y., Vathy, L. A., Bergey, E. J., Sajjad, M., et al. (2010). In vivo biodistribution and clearance studies using multimodal organically modified silica nanoparticles. *ACS Nano* 4, 699–708. doi: 10.1021/nn901146y
- Kumbhakar, D. V., Datta, A. K., Mandal, A., Das, D., Gupta, S., Ghosh, B., et al. (2016). Effectivity of copper and cadmium sulphide nanoparticles in mitotic and meiotic cells of *Nigella sativa* L. (black cumin) – can nanoparticles act as mutagenic agents? *J. Exp. Nanosci.* 11, 823–839. doi: 10.1080/17458080.2016.1149236
- Laha, D., Pramanik, A., Maity, J., Mukherjee, A., Pramanik, P., Laskar, A., et al. (2014). Interplay between autophagy and apoptosis mediated by copper oxide nanoparticles in human breast cancer cells MCF7. *Biochim. Biophys. Acta Gen. Subj.* 1840, 1–9. doi: 10.1016/j.bbagen.2013.08.011
- Lammel, T., Mackevica, A., Johansson, B. R., and Sturve, J. (2019). Endocytosis, intracellular fate, accumulation, and agglomeration of titanium dioxide (TiO₂) nanoparticles in the rainbow trout liver cell line RTL-W1. *Environ. Sci. Pollut. Res.* 26, 15354–15372. doi: 10.1007/s11356-019-04856-1
- Lanone, S., Rogerieux, F., Geys, J., Dupont, A., Maillot-Marechal, E., Boczkowski, J., et al. (2009). Comparative toxicity of 24 manufactured nanoparticles in human alveolar epithelial and macrophage cell lines. *Part. Fibre Toxicol.* 6:14. doi: 10.1186/1743-8977-6-14
- Lee, I. C., Ko, J. W., Park, S. H., Shin, N. R., Shin, I. S., Moon, C., et al. (2016). Comparative toxicity and biodistribution assessments in rats following subchronic oral exposure to copper nanoparticles and microparticles. *Part. Fibre Toxicol.* 13, 1–16. doi: 10.1186/s12989-016-0169-x
- Levard, C., Hotze, E. M., Colman, B. P., Dale, A. L., Truong, L., Yang, X. Y., et al. (2013). Sulfidation of silver nanoparticles: natural antidote to their toxicity. *Environ. Sci. Technol.* 47, 13440–13448. doi: 10.1021/es403527n
- Liu, W., Liu, S., and Wang, L. (2019). Surface modification of biomedical titanium alloy: micromorphology. Microstructure evolution and biomedical applications. *Coatings* 9:249. doi: 10.3390/coatings9040249
- Lu, G. W., and Gao, P. (2010). “CHAPTER 3 - emulsions and microemulsions for topical and transdermal drug delivery,” in *Handbook of Non-Invasive Drug Delivery Systems*, ed. V. S. Kulkarni (Boston: William Andrew Publishing), 59–94.
- Lu, X., Miousse, I. R., Pirela, S. V., Moore, J. K., Melnyk, S., Koturbash, I., et al. (2016). In vivo epigenetic effects induced by engineered nanomaterials: a case study of copper oxide and laser printer-emitted engineered nanoparticles. *Nanotoxicology* 10, 629–639. doi: 10.3109/17435390.2015.1108473
- Luzio, J. P., Hackmann, Y., Dieckmann, N. M. G., and Griffiths, G. M. (2014). The biogenesis of lysosomes and lysosome-related organelles. *Cold Spring Harb. Perspect. Biol.* 6:a016840. doi: 10.1101/cshperspect.a016840
- Manshian, B. B., Pokhrel, S., Mädler, L., and Soenen, S. J. (2018). The impact of nanoparticle-driven lysosomal alkalization on cellular functionality. *J. Nanobiotechnol.* 16, 1–13. doi: 10.1186/s12951-018-0413-7
- Marambio-Jones, C., and Hoek, E. M. V. (2010). A review of the antibacterial effects of silver nanomaterials and potential implications for human health and the environment. *J. Nanoparticle Res.* 12, 1531–1551. doi: 10.1007/s11051-010-9900-y
- Martirosyan, A., Bazes, A., and Schneider, Y. J. (2014). In vitro toxicity assessment of silver nanoparticles in the presence of phenolic compounds-preventive agents against the harmful effect? *Nanotoxicology* 8, 573–582. doi: 10.3109/17435390.2013.812258
- Miyayama, T., and Matsuoka, M. (2016). Involvement of lysosomal dysfunction in silver nanoparticle-induced cellular damage in A549 human lung alveolar epithelial cells. *J. Occup. Med. Toxicol.* 11:1. doi: 10.1186/s12995-016-0090-0
- Mohammed, Y. H., Holmes, A., Haridass, I. N., Sanchez, W. Y., Studier, H., Grice, J. E., et al. (2019). Support for the safe use of zinc oxide nanoparticle sunscreens: lack of skin penetration or cellular toxicity after repeated application in volunteers. *J. Invest. Dermatol.* 139, 308–315. doi: 10.1016/j.jid.2018.08.024
- Mordorski, B., and Friedman, A. (2017). “Metal nanoparticles for microbial infection,” in *Functionalized Nanomaterials for the Management of Microbial Infection*, eds R. Boukherroub, S. Szunerits, and D. Dridier (Amsterdam: Elsevier), 77–109.
- Namvar, F., Rahman, H. S., Mohamad, R., Azizi, S., Tahir, P. M., Chartrand, M. S., et al. (2015). Cytotoxic effects of biosynthesized zinc oxide nanoparticles on murine cell lines. evidence-based complement. *Altern. Med.* 2015:593014. doi: 10.1155/2015/593014
- Nel, L. N., Xia, A., Mädler, L., and Li, N. (2006). Toxic potential of materials at the nanolevel. *Science* 311, 622–627. doi: 10.1126/science.1114397
- Nemmar, A., Hoet, P. H. M., Vanquickenborne, B., Dinsdale, D., Thomeer, M., Hoylaerts, M. F., et al. (2002). Passage of inhaled particles into the blood circulation. *Hum. Circ.* 106, 411–414. doi: 10.1161/01.CIR.0000037134.24080.42
- Ng, C. T., Yong, L. Q., Hande, M. P., Ong, C. N., Yu, L. E., Bay, B. H., et al. (2017). Zinc oxide nanoparticles exhibit cytotoxicity and genotoxicity through oxidative stress responses in human lung fibroblasts and *Drosophila melanogaster*. *Int. J. Nanomedicine* 12, 1621–1637. doi: 10.2147/IJN.S124403
- Osmond-McLeod, M. J., Osmond, R. I., Oytam, Y., McCall, M. J., Feltis, B., Mackay-Sim, A., et al. (2013). Surface coatings of ZnO nanoparticles mitigate differentially a host of transcriptional, protein and signalling responses in primary human olfactory cells. *Part. Fibre Toxicol.* 10:54. doi: 10.1186/1743-8977-10-54
- Pacheco, I. I., Robbie, K., and Buzea, C. (2007). Nanomaterials and nanoparticles. *Sour. Toxic.* 2, 17–71.
- Pan, Y., Leifert, A., Ruau, D., Neuss, S., Bornemann, J., Schmid, G., et al. (2009). Gold nanoparticles of diameter 1.4 nm trigger necrosis by oxidative stress and mitochondrial damage. *Small* 5, 2067–2076. doi: 10.1002/smll.200900466

- Pan, Y., Neuss, S., Leifert, A., Fischler, M., Wen, F., Simon, U., et al. (2007). Size-dependent cytotoxicity of gold nanoparticles. *Small* 3, 1941–1949. doi: 10.1002/smll.200700378
- Park, E.-J., Choi, J., Park, Y.-K., and Park, K. (2008). Oxidative stress induced by cerium oxide nanoparticles in cultured BEAS-2B cells. *Toxicology* 245, 90–100. doi: 10.1016/j.tox.2007.12.022
- Park, H.-J., Kim, J. Y., Kim, J., Lee, J.-H., Hahn, J.-S., Gu, M. B., et al. (2009). Silver-ion-mediated reactive oxygen species generation affecting bactericidal activity. *Water Res.* 43, 1027–1032. doi: 10.1016/j.watres.2008.12.002
- Pedata, P., Ricci, G., Malorni, L., Venezia, A., Cammarota, M., Volpe, M. G., et al. (2019). In vitro intestinal epithelium responses to titanium dioxide nanoparticles. *Food Res. Int.* 119, 634–642. doi: 10.1016/j.foodres.2018.10.041
- Pelkonen, K. H. O., Heinonen-Tanski, H., and Hänninen, O. O. P. (2003). Accumulation of silver from drinking water into cerebellum and musculus soleus in mice. *Toxicology* 186, 151–157. doi: 10.1016/S0300-483X(02)00743-6
- Pizzino, G., Irrera, N., Cucinotta, M., Pallio, G., Mannino, F., Arcoraci, V., et al. (2017). Oxidative stress: harms and benefits for human health. *Oxid. Med. Cell. Longev.* 2017, 1–13. doi: 10.1155/2017/8416763
- Reidy, B., Haase, A., Luch, A., Dawson, K. A., and Lynch, I. (2013). Mechanisms of silver nanoparticle release, transformation and toxicity: a critical review of current knowledge and recommendations for future studies and applications. *Materials* 6, 2295–2350. doi: 10.3390/ma6062295
- Roane, T. M., Rensing, C., Pepper, I. L., and Maier, R. M. (2009). “Chapter 21 - Microorganisms and Metal Pollutants,” in *Environmental Microbiology*, 2nd Edn, eds I. L. Pepper, C. P. Gerba, T. J. Gentry, and R. M. Maier (San Diego: Academic Press), 421–441.
- Ryu, H.-W., Lee, D. H., Florens, L., Swanson, S. K., Washburn, M. P., and Kwon, S. H. (2014). Analysis of the heterochromatin protein 1 (HP1) interactome in *Drosophila*. *J. Proteomics* 102, 137–147. doi: 10.1016/j.jprot.2014.03.016
- Saliani, M., Jalal, R., and Goharshadi, E. K. (2016). Mechanism of oxidative stress involved in the toxicity of ZnO nanoparticles against eukaryotic cells. *Nanomedicine J.* 3, 1–14. doi: 10.7508/nmj.2016.01.001
- Samberg, M. E., Oldenburg, S. J., and Monteiro-Riviere, N. A. (2010). Evaluation of silver nanoparticle toxicity in skin in vivo and keratinocytes in vitro. *Environ. Health Perspect.* 118, 407–413. doi: 10.1289/ehp.0901398
- Semmler-Behnke, M., Kreyling, W. G., Lipka, J., Fertsch, S., Wenk, A., Takenaka, S., et al. (2008). Biodistribution of 1.4- and 18-nm gold particles in rats. *Small* 4, 2108–2111. doi: 10.1002/smll.200800922
- Shah, J., Bhagat, S., and Singh, S. (2020). “Standard biological assays to estimate nanoparticle toxicity and biodistribution,” in *Nanotoxicity*, eds S. Rajendran, A. Mukherjee, T. A. Nguyen, C. Godugu, and R. K. Shukla (Amsterdam: Elsevier), 71–104.
- Sharma, V., Singh, P., Pandey, A. K., and Dhawan, A. (2012). Induction of oxidative stress, DNA damage and apoptosis in mouse liver after sub-acute oral exposure to zinc oxide nanoparticles. *Mutat. Res. Genet. Toxicol. Environ. Mutagen.* 745, 84–91. doi: 10.1016/j.mrgentox.2011.12.009
- Shi, X., Zhu, Y., Hua, W., Ji, Y., Ha, Q., Han, X., et al. (2016). An in vivo study of the biodistribution of gold nanoparticles after intravaginal space injection in the tarsal tunnel. *Nano Res.* 9, 2097–2109. doi: 10.1007/s12274-016-1100-3
- Shukla, R., Bansal, V., Chaudhary, M., Basu, A., Bhonde, R. R., and Sastry, M. (2005). Biocompatibility of gold nanoparticles and their endocytotic fate inside the cellular compartment: a microscopic overview. *Langmuir* 21, 10644–10654. doi: 10.1021/la0513712
- Sintubin, L., Verstraete, W., and Boon, N. (2012). Biologically produced nanosilver: current state and future perspectives. *Biotechnol. Bioeng.* 109, 2422–2436. doi: 10.1002/bit.24570
- Soenen, S. J., Parak, W. J., Reijman, J., and Manshian, B. (2015). (Intra)cellular stability of inorganic nanoparticles: effects on cytotoxicity, particle functionality, and biomedical applications. *Chem. Rev.* 115, 2109–2135. doi: 10.1021/cr400714j
- Sonavane, G., Tomoda, K., and Makino, K. (2008). Biodistribution of colloidal gold nanoparticles after intravenous administration: effect of particle size. *Colloids Surf. B Biointerfaces* 66, 274–280. doi: 10.1016/j.colsurf.2008.07.004
- Stocco, A., Di Bucchanico, S., Coppedè, F., Ponti, J., Uboldi, C., and Blois, M. (2017). Multiple endpoints to evaluate pristine and remediated titanium dioxide nanoparticles genotoxicity in lung epithelial A549 cells. *Toxicol. Lett.* 276, 48–61. doi: 10.1016/j.toxlet.2017.05.016
- Sukhanova, A., Bozrova, S., Sokolov, P., Berestovoy, M., Karaulov, A., and Nabiev, I. (2018). Dependence of nanoparticle toxicity on their physical and chemical properties. *Nanoscale Res. Lett.* 13:44. doi: 10.1186/s11671-018-2457-x
- Suman, T. Y., Radhika Rajasree, S. R., and Kirubakaran, R. (2015). Evaluation of zinc oxide nanoparticles toxicity on marine algae *Chlorella vulgaris* through flow cytometric, cytotoxicity and oxidative stress analysis. *Ecotoxicol. Environ. Saf.* 113, 23–30. doi: 10.1016/j.ecoenv.2014.11.015
- Talamini, L., Violatto, M. B., Cai, Q., Monopoli, M. P., Kantner, K., Krpetiæ, Ž, et al. (2017). Influence of size and shape on the anatomical distribution of endotoxin-free gold nanoparticles. *ACS Nano* 11, 5519–5529. doi: 10.1021/acsnano.7b00497
- Thai, S. F., Wallace, K. A., Jones, C. P., Ren, H., Prasad, R. Y., Ward, W. O., et al. (2015). Signaling pathways and microRNA changes in nano-TiO₂ treated human lung epithelial (BEAS-2B) cells. *J. Nanosci. Nanotechnol.* 15, 492–503. doi: 10.1166/jnn.2015.9202
- Thevenot, P., Cho, J., Wavhal, D., Timmons, R. B., and Tang, L. (2008). Surface chemistry influences cancer killing effect of TiO₂ nanoparticles. *Nanomedicine* 4, 226–236. doi: 10.1016/j.nano.2008.04.001
- Thit, A., Selck, H., and Bjerregaard, H. F. (2015). Toxic mechanisms of copper oxide nanoparticles in epithelial kidney cells. *Toxicol. Vitro.* 29, 1053–1059. doi: 10.1016/j.tiv.2015.03.020
- Tiwari, D. K., Jin, T., and Behari, J. (2011). Dose-dependent in-vivo toxicity assessment of silver nanoparticle in Wistar rats. *Toxicol. Mech. Methods* 21, 13–24. doi: 10.3109/15376516.2010.529184
- Trop, M., Novak, M., Rodl, S., Hellbom, B., Kroell, W., and Goessler, W. (2006). Silver-coated dressing acticoat caused raised liver enzymes and argyria-like symptoms in burn patient. *J. Trauma Acute Care Surg.* 60:1024.
- Tsukahara, H. (2007). Biomarkers for oxidative stress: clinical application in pediatric medicine. *Curr. Med. Chem.* 14, 339–351. doi: 10.2174/092986707779941177
- U.S. Food and Drug Administration (2019). *USFDA, Code of Federal Regulations*. Silver Spring, FL: Food and drug, 21.
- Valko, M., Morris, H., and Cronin, M. T. D. (2005). Metals, toxicity and oxidative stress. *Curr. Med. Chem.* 12, 1161–1208. doi: 10.2174/0929867053764635
- Vigneshwaran, N., Varadarajan, P. V., and Balasubramanya, R. H. (2010). “Application of Metallic Nanoparticles in Textiles,” in *Nanotechnologies Life Science*, ed. P. Ram (Weinheim: Wiley-VCH Verlag GmbH & Co. KGaA).
- Vuong, N. Q., Gogan, P., Mohottalage, S., Breznar, D., Ariganello, M., Williams, A., et al. (2016). Proteomic changes in human lung epithelial cells (A549) in response to carbon black and titanium dioxide exposures. *J. Proteomics* 149, 53–63. doi: 10.1016/j.jprot.2016.03.046
- Waghmode, M. S., Gunjal, A. B., Mulla, J. A., Patil, N. N., and Nawani, N. N. (2019). Studies on the titanium dioxide nanoparticles: biosynthesis, applications and remediation. *SN Appl. Sci.* 1:310. doi: 10.1007/s42452-019-0337-3
- Wan, R., Mo, Y., Feng, L., Chien, S., Tollerud, D. J., and Zhang, Q. (2012). DNA damage caused by metal nanoparticles: the involvement of oxidative stress and activation of ATM Rong. *Chem Res Toxicol.* 25, 1402–1411. doi: 10.1021/tx200513t
- Wang, L., Xie, L., Shen, P., Fan, Q., Wang, W., Wang, K., et al. (2019). Surface microstructure and mechanical properties of Ti-6Al-4V/Ag nanocomposite prepared by FSP. *Mater. Charact.* 153, 175–183. doi: 10.1016/j.matchar.2019.05.002
- Wang, W., Han, P., Peng, P., Zhang, T., Liu, Q., and Yuan, S.-N. (2019). Friction stir processing of magnesium alloys: a review. *Acta Metall. Sin. English Lett.* 33, 43–57. doi: 10.1007/s40195-019-00971-7
- Wang, X., Xia, T., Duch, M. C., Ji, Z., Zhang, H., Li, R., et al. (2012). Pluronic F108 coating decreases the lung fibrosis potential of multiwall carbon nanotubes by reducing lysosomal injury. *Nano Lett.* 12, 3050–3061. doi: 10.1021/nl300895y
- Wijnhoven, S. W. P., Peijnenburg, W. J. G. M., Herberths, C. A., Hagens, W. I., Oomen, A. G., Heugens, E. H. W., et al. (2009). Nano-silver – a review of available data and knowledge gaps in human and environmental risk assessment. *Nanotoxicology* 3, 109–138. doi: 10.1080/17435390902725914
- Xia, Y., Li, M., Peng, T., Zhang, W., Xiong, J., Hu, Q., et al. (2013). In vitro cytotoxicity of fluorescent silica nanoparticles hybridized with aggregation-induced emission luminogens, for living cell imaging. *Int. J. Mol. Sci.* 14, 1080–1092. doi: 10.3390/ijms14011080
- Xie, Y., Williams, N. G., Tolic, A., Chrisler, W. B., Teeguarden, J. G., Maddux, B. L. S., et al. (2012). Aerosolized ZnO nanoparticles induce toxicity in alveolar

- type II epithelial cells at the air-liquid interface. *Toxicol. Sci.* 125, 450–461. doi: 10.1093/toxsci/kfr251
- Xu, F., Piett, C., Farkas, S., Qazzaz, M., and Syed, N. I. (2013). Silver nanoparticles (AgNPs) cause degeneration of cytoskeleton and disrupt synaptic machinery of cultured cortical neurons. *Mol. Brain* 6:29. doi: 10.1186/1756-6606-6-29
- Xu, J., Shi, H., Ruth, M., Yu, H., Lazar, L., Zou, B., et al. (2013). Acute toxicity of intravenously administered titanium dioxide nanoparticles in mice. *PLoS One* 8:e70618. doi: 10.1371/journal.pone.0070618
- Xu, L., Shi, C., Shao, A., Li, X., Cheng, X., Ding, R., et al. (2015). Toxic responses in rat embryonic cells to silver nanoparticles and released silver ions as analyzed via gene expression profiles and transmission electron microscopy. *Nanotoxicology* 9, 513–522. doi: 10.3109/17435390.2014.948942
- Yah, C. S. (2013). The toxicity of gold nanoparticles in relation to their physiochemical properties. *Biomed. Res.* 24, 400–413.
- Yamanaka, M., Hara, K., and Kudo, J. (2005). Bactericidal actions of a silver ion solution on *Escherichia coli* Studied by energy-filtering transmission electron microscopy and proteomic analysis. *Appl. Environ. Microbiol.* 71, 7589–7593. doi: 10.1128/AEM.71.11.7589-7593.2005
- Yang, H., Liu, C., Yang, D., Zhang, H., and Xi, Z. (2009). Comparative study of cytotoxicity, oxidative stress and genotoxicity induced by four typical nanomaterials: the role of particle size, shape and composition. *J. Appl. Toxicol.* 29, 69–78. doi: 10.1002/jat.1385
- Yang, W., Shen, C., Ji, Q., An, H., Wang, J., Liu, Q., et al. (2009). Food storage material silver nanoparticles interfere with DNA replication fidelity and bind with DNA. *Nanotechnology* 20:085102. doi: 10.1088/0957-4484/20/8/085102
- Yang, Z., Gu, H., Sha, G., Lu, W., Yu, W., Zhang, W., et al. (2018). TC4/Ag metal matrix nanocomposites modified by friction stir processing: surface characterization, antibacterial property, and cytotoxicity in vitro. *ACS Appl. Mater. Interfaces* 10, 41155–41166. doi: 10.1021/acsami.8b16343
- Yen, H.-J., Hsu, S., and Tsai, C.-L. (2009). Cytotoxicity and immunological response of gold and silver nanoparticles of different sizes. *Small* 5, 1553–1561. doi: 10.1002/sml.200900126
- Yu, K., Yoon, T., Minai-tehrani, A., Kim, J., Jin, S., Sook, M., et al. (2013). Toxicology in Vitro Zinc oxide nanoparticle induced autophagic cell death and mitochondrial damage via reactive oxygen species generation. *Toxicol. Vitro* 27, 1187–1195. doi: 10.1016/j.tiv.2013.02.010
- Yu, L. E., Lanry Yung, L.-Y., Ong, C.-N., Tan, Y.-L., Suresh Balasubramaniam, K., and Hartono, D. (2007). Translocation and effects of gold nanoparticles after inhalation exposure in rats. *Nanotoxicology* 1, 235–242. doi: 10.1080/17435390701763108
- Zhang, C., Ding, Z., Xie, L., Zhang, L.-C., Wu, L., Fu, Y., et al. (2017). Electrochemical and in vitro behavior of the nanosized composites of Ti-6Al-4V and TiO₂ fabricated by friction stir process. *Appl. Surf. Sci.* 423, 331–339. doi: 10.1016/j.apsusc.2017.06.141
- Zhang, S., Gao, H., and Bao, G. (2015). Physical principles of nanoparticle cellular endocytosis. *ACS Nano* 9, 8655–8671. doi: 10.1021/acsnano.5b03184
- Zhang, X., Zhang, H., Liang, X., Zhang, J., Tao, W., Zhu, X., et al. (2016). Iron oxide nanoparticles induce autophagosome accumulation through multiple mechanism: lysosome impairment, mitochondrial damage and ER stress. *Mol. Pharm.* 13, 2578–2587. doi: 10.1021/acs.molpharmaceut.6b00405
- Zhang, X.-F., Gurunathan, S., and Kim, J.-H. (2015). Effects of silver nanoparticles on neonatal testis development in mice. *Int. J. Nanomedicine* 10, 6243–6256. doi: 10.2147/IJN.S90733
- Zhang, Y., Ding, Z., Zhao, G., Zhang, T., Xu, Q., Cui, B., et al. (2018). Transcriptional responses and mechanisms of copper nanoparticle toxicology on zebrafish embryos. *J. Hazard. Mater.* 344, 1057–1068. doi: 10.1016/j.jhazmat.2017.11.039
- Zhao, H., Chen, L., Zhong, G., Huang, Y., Zhang, X., Chu, C., et al. (2019). Titanium dioxide nanoparticles induce mitochondrial dynamic imbalance and damage in HT22 cells. *J. Nanomater.* 2019, 1–16. doi: 10.1155/2019/4607531
- Zhao, X., Ng, S., Heng, B. C., Guo, J., Ma, L., and Tan, T. T. Y. (2013). Cytotoxicity of hydroxyapatite nanoparticles is shape and cell dependent. *Arch. Toxicol.* 87, 1037–1052. doi: 10.1007/s00204-012-0827-1
- Zhou, X., Zhao, L., Luo, J., Tang, H., Xu, M., Wang, Y., et al. (2019). The toxic effects and mechanisms of nano-cu on the spleen of rats. *Int. J. Mol. Sci.* 20:1469. doi: 10.3390/ijms20061469
- Zhu, Y., Eaton, J. W., and Li, C. (2012). Titanium dioxide (TiO₂) nanoparticles preferentially induce cell death in transformed cells in a Bak/Bax-independent fashion. *PLoS One* 7:e50607. doi: 10.1371/journal.pone.0050607
- Zoroddu, M. A., Medici, S., Ledda, A., Nurchi, V. M., Lachowicz, J. I., and Peana, M. (2014). Toxicity of nanoparticles. *Curr. Med. Chem.* 21, 3837–3853. doi: 10.2174/0929867321666140601162314

Conflict of Interest: The authors declare that the research was conducted in the absence of any commercial or financial relationships that could be construed as a potential conflict of interest.

Copyright © 2020 Attarilar, Yang, Ebrahimi, Wang, Liu, Tang and Yang. This is an open-access article distributed under the terms of the Creative Commons Attribution License (CC BY). The use, distribution or reproduction in other forums is permitted, provided the original author(s) and the copyright owner(s) are credited and that the original publication in this journal is cited, in accordance with accepted academic practice. No use, distribution or reproduction is permitted which does not comply with these terms.



Cold Rolling Deformation Characteristic of a Biomedical Beta Type Ti–25Nb–3Zr–2Sn–3Mo Alloy Plate and Its Influence on α Precipitated Phases and Room Temperature Mechanical Properties During Aging Treatment

OPEN ACCESS

Edited by:

Liqiang Wang,
Shanghai Jiao Tong University, China

Reviewed by:

Linjiang Chai,
Chongqing University of Technology,
China
Fuping Li,
Xi'an University of Technology, China

*Correspondence:

Jun Cheng
524161386@qq.com
Jinshan Li
ljsh@nwpu.edu.cn

Specialty section:

This article was submitted to
Biomaterials,
a section of the journal
Frontiers in Bioengineering and
Biotechnology

Received: 24 August 2020

Accepted: 22 September 2020

Published: 19 October 2020

Citation:

Cheng J, Li J, Yu S, Du Z,
Zhang X, Zhang W, Gai J, Wang H,
Song H and Yu Z (2020) Cold Rolling
Deformation Characteristic of a
Biomedical Beta Type
Ti–25Nb–3Zr–2Sn–3Mo Alloy Plate
and Its Influence on α Precipitated
Phases and Room Temperature
Mechanical Properties During Aging
Treatment.
Front. Bioeng. Biotechnol. 8:598529.
doi: 10.3389/fbioe.2020.598529

**Jun Cheng^{1,2*}, Jinshan Li^{1*}, Sen Yu², Zhaoxin Du³, Xiaoyong Zhang⁴, Wen Zhang²,
Jinyang Gai⁴, Hongchuan Wang⁵, Hongjie Song² and Zhentao Yu⁶**

¹ State Key Laboratory of Solidification Processing, Northwestern Polytechnical University, Xi'an, China, ² Shaanxi Key Laboratory of Biomedical Metal Materials, Northwest Institute for Non-ferrous Metal Research, Xi'an, China, ³ School of Materials Science and Engineering, Inner Mongolia University of Technology, Hohhot, China, ⁴ State Key Laboratory of Powder Metallurgy, Central South University, Changsha, China, ⁵ School of Material Science and Engineering, Northeastern University, Shenyang, China, ⁶ Institute of Advanced Wear and Corrosion Resistant and Functional Materials, Jinan University, Guangzhou, China

The microstructure characteristics and texture evolution of a biomedical metastable beta Ti–25Nb–3Zr–2Sn–3Mo (TLM; wt%) titanium alloy plate cold rolled at various reductions were studied in this article. $\langle 110 \rangle$ texture was easily formed in the TLM alloy plates, and a large number of dislocation tangles were generated in the β matrix in the process of cold rolling deformation. The dislocation lines, dislocation cells, subgrain boundaries, and other crystal defects introduced during cold rolling had a great impact on the morphological characteristics and volume fraction of precipitated phases during aging. These typical crystal defects could be considered as the major triggers of the formation of second phases, and they could also shorten the time of $\beta \rightarrow \alpha$ phase transformation. α precipitated phases, with a size range of 150–500 nm, were formed within the β matrix in the cold deformed 34% in conjunction with the aging specimen, resulting in the relatively high tensile strength of 931 MPa and the acceptable elongation of 6.9%. When the TLM alloy plate was cold rolled at a reduction of 60% in conjunction with aging, the maximum value of ultimate strength (1,005 MPa) was achieved, but the elongation value was relatively low owing to the formation of α precipitated phases with a large size around the subgrain boundaries. In this paper, the influence of crystal defects and subgrain boundaries on the morphology characteristics and volume fraction of α precipitated phases and mechanical properties will be discussed in detail.

Keywords: Cold deformation, biomedical β -type titanium alloy, α precipitated phases, mechanical properties, texture evolution

INTRODUCTION

Compared with other noble metals (Au, Ag), medical stainless steel (316L), magnesium alloys (Mg-4Y-3RE), and Co-Cr-Mo alloys (Co-28Cr-6Mo), Ti, and its alloys possess more outstanding comprehensive performances in the metallic implant material family (Rack and Qazi, 2006; Niinomi et al., 2012; Zhang and Chen, 2019; Liu et al., 2020). Both large application potential and commercial values exist in hard tissue reconstruction and replacement due to their attractive characteristics, including low modulus, excellent mechanical properties, as well as superior biofunctions and biocompatibility (Niinomi, 2002; Geetha et al., 2009; Niinomi and Nakai, 2011; Zhang et al., 2020). Hence, Ti and Ti alloys are extensively applied in the processing and manufacturing of dental implants, bone plates, spinal internal fixation devices, orthodontic wires, intramedullary nails, as well as other orthopedic repair devices (Taddei et al., 2004; Li Y. et al., 2014; Duraccio et al., 2015). Currently, commercial Ti64 and Ti-13Nb-13Zr are mainly applied to produce devices for joint prosthesis. However, commercial Ti64 contains toxic elements, such as Al and V, which may cause Alzheimer's disease after long-term implantation in the patient's body (Gepreel and Niinomi, 2013; Abdelrhman et al., 2019). The biomedical β Ti alloy is predominantly composed of biocompatible components, including Nb, Zr, Sn, Mo, Ta, and Fe (Wang L. et al., 2010; Malek et al., 2012). In general, the strength level in biomechanical properties is crucial for the long-term service and safety of metallic implant materials and their devices (Goriainov et al., 2014). Notably, β Ti alloys can achieve a comprehensive matching degree with high strength, good biocompatibility, and acceptable ductility through optimized processing (Niinomi, 2008; Ramezannejad et al., 2019). In addition, based on the effect of precipitation strengthening, the strength level of β -type Ti alloy can be significantly improved after solution treatment followed by rapid cooling and aging (Banerjee et al., 2004; Chen et al., 2014; Xu et al., 2019b). Up to now, several typical metastable β Ti alloys, for instance, Ti-Mo, Ti-Nb, Ti-V, and Ti-Ta-based alloys, have received considerable attention due to their controllable microstructures and performances (Mantani and Tajima, 2006; Sun et al., 2010; Min et al., 2012). A detailed investigation of the influences of heat treatment on microstructural evolution, phase transitions, mechanical properties, and deformation mechanisms has been carried out for metastable β Ti alloys. Moreover, for β -type Ti alloys, a suitable heat treatment process is beneficial to produce fine, uniform, and dispersed α precipitates in the β matrix, thereby improving the mechanical properties of β -type Ti alloys (Jaworski and Ankem, 2005; Qazi et al., 2005). It is significant to note that the density, distribution, and length-to-diameter ratio for secondary phases are considered to be the primary factors affecting the strength level of β -type Ti alloys. Previous studies indicated that the improvement of strength for Ti alloys can be achieved using the composite processing of cold rolling followed by aging at a certain condition (Malinov et al., 2003). A large number of dislocation tangles/proliferation, nucleation sites, and sub-boundaries (interfaces) would be introduced into the deformed microstructure of β -type Ti alloy during the

plastic deformation. The presence of defects is considered to be beneficial for the refinement and uniform distribution of precipitation phases. Meanwhile, grain refinement is apparent (Xu et al., 2016a). In general, the crystal defects introduced during plastic deformation are mainly composed of dislocations, twins, and interfaces, etc., which can facilitate the $\beta \rightarrow \alpha$ phase transition (Wang et al., 2009; Karthikeyan et al., 2010). The primary reason is that the presence of defects is able to reduce the driving force and barrier required to the occurrence of the phase transition to some extent.

Until now, a large number of groups are persistently focusing on the microstructural controlling, the mechanical property optimization, and the relationship between them, resulting in a lot of representative studies (Ivasishin et al., 2005; Xu et al., 2016b). Li T. et al. (2014) prepared β -type Ti-15Nb-2Mo-2Zr-1Sn alloy with ultrafine grains using hot or cold working followed by aging. Finer precipitates were prone to be generated at the elongated grain boundaries or subgrain boundaries, resulting in a significant improvement of the room temperature strength level. Karthikeyan et al. (2010) studied the influence of cooling rate on texture feature and variant selection in phase transition for Ti-5Ta-1.8Nb alloy during aging. They found that the effect of cold rolling on the microstructure and phase transition in the subsequent annealing has a significant inheritability. Song et al. (2010) discussed the influence of predeformation in conjunction with aging on the microstructural features and room-temperature mechanical properties for β -type Ti-10Mo-8V-1Fe-3.5Al alloy. The results showed that the alloy is only subjected to predeformation and single aging. Although higher strength of the alloy could be achieved at room temperature, the ductility would be very poor. The final dislocation density could be reduced, and the plasticity level could be further enhanced after a lower-temperature pre-aging followed by a higher-temperature secondary aging treatment. Guo et al. (Qiang et al., 2011) revealed the precipitation progress and mechanism of the secondary phase and its effect on the mechanical properties of TB5 (nominal composition: Ti-15V-3Cr-3Sn-3Al) alloy after severe plastic deformation. They found that finer precipitates are generated within the region of severe deformation and evenly distributed within the β grains, while in other transition regions, the newly precipitated phases are thick lamellar or in a shuttle-like shape with relatively large size. Therefore, in the processing of the semifinished products made of β -type Ti alloys, the finer and uniformly dispersed precipitates can be obtained using a composite preparation method of cold deformation in conjunction with aging treatment, leading to an obvious improvement in strength level. However, the strengthening mechanism of biomedical β -type Ti-Nb-Zr-Sn-Mo-based Ti alloys subjected to cold deformation in conjunction with aging has not been definitely investigated and proposed until now. Although biomedical β -type Ti alloys have superior cold workability compared with α - and ($\alpha + \beta$)-type alloys, their plastic deformation behavior is extraordinarily complicated. The deformation mechanism is not only related to phase stability but also to the reduction of deformation (Wang et al., 2015; Hafeez et al., 2020). Mechanical properties of β type Ti alloy are associated with multiple deformation

modes including dislocation slip, mechanical twinning, stress-induced martensitic transformation, kinking deformation, and dislocation-free plastic deformation, etc. (Xiang et al., 2020; Zheng et al., 2020). Hence, the investigation on cold deformation behavior of β -type Ti alloys has extremely important practical significance for the development of biofunctional Ti alloys with an excellent matching degree of lower modulus and higher strength.

Ti-25Nb-3Zr-2Sn-3Mo (TLM) alloy, a type of metastable β -type titanium alloy, is independently developed for surgical implants by Shaanxi Key Laboratory of Biomedical Metal Materials (Kent et al., 2010; Yu et al., 2011, 2014). The α precipitates are generated in β grains and along with grain boundaries after solution treatment followed by aging, leading to an obvious increase in the strength level of the alloy (Salib et al., 2013). Malinov et al. (2003) revealed the phase transformation mechanism of β -21s Ti alloy under constant temperature conditions at a temperature ranging from 400°C to 750°C with the assistance of experimental research and computer simulation methods. Meanwhile, the corresponding thermodynamic, and kinetic models were established, respectively. Xu et al. (2015) investigated the effect of various heat treatments on phase transition mechanism, microstructural features, and room temperature mechanical properties for the TB8 alloy. They found that the location and morphological features of precipitates are closely related to the aging temperature and time. In addition, finer and more uniform secondary phases can be obtained by adopting an appropriate solution treatment followed by aging, leading to a significant increase in the strength level. Meanwhile, Xu et al. (2016b) investigated the microstructural features and phase transition mechanism in the two-stage aging process. They found that the isothermal omega transition phases precipitated in a single aging process could provide more nucleation sites for α phases, resulting in an apparent refinement of α phases. Kent et al. (2011) investigated the microstructural features and phase transition behavior of Ti-25Nb-3Zr-2Sn-3Mo alloy using accumulative roll bonding (ARB) processing technology. The ultrafine-grained alloy was prepared, and α precipitates with nanosize were generated along with the grain boundaries, leading to the increment in the strength level. In summary, for the biomedical metastable β -type Ti alloy, the microstructure morphology and texture component would simultaneously change during cold deformation (Ma et al., 2018; Vajpai et al., 2018; Ozan et al., 2019). This will induce the presence of preferred orientation and the increase in the dislocation density, resulting in the changing in the nucleation and growth rates of precipitates during aging. In the meanwhile, the driving force and barrier would be reduced when the phase transition of $\beta \rightarrow \alpha$ occurs.

This work will mainly focus on the microstructure evolution and phase transition of TLM alloy plates after cold rolling in conjunction with aging treatment. The effects of cold deformation-induced dislocations and subgrain boundaries on the formation mechanism of precipitates and mechanical properties are also discussed. This work will provide the theoretical guidance and technology optimization for the precise

control of microstructures and properties for high-performance biomedical β -type Ti alloys, which has important scientific significance and engineering value.

EXPERIMENTAL MATERIALS AND METHODS

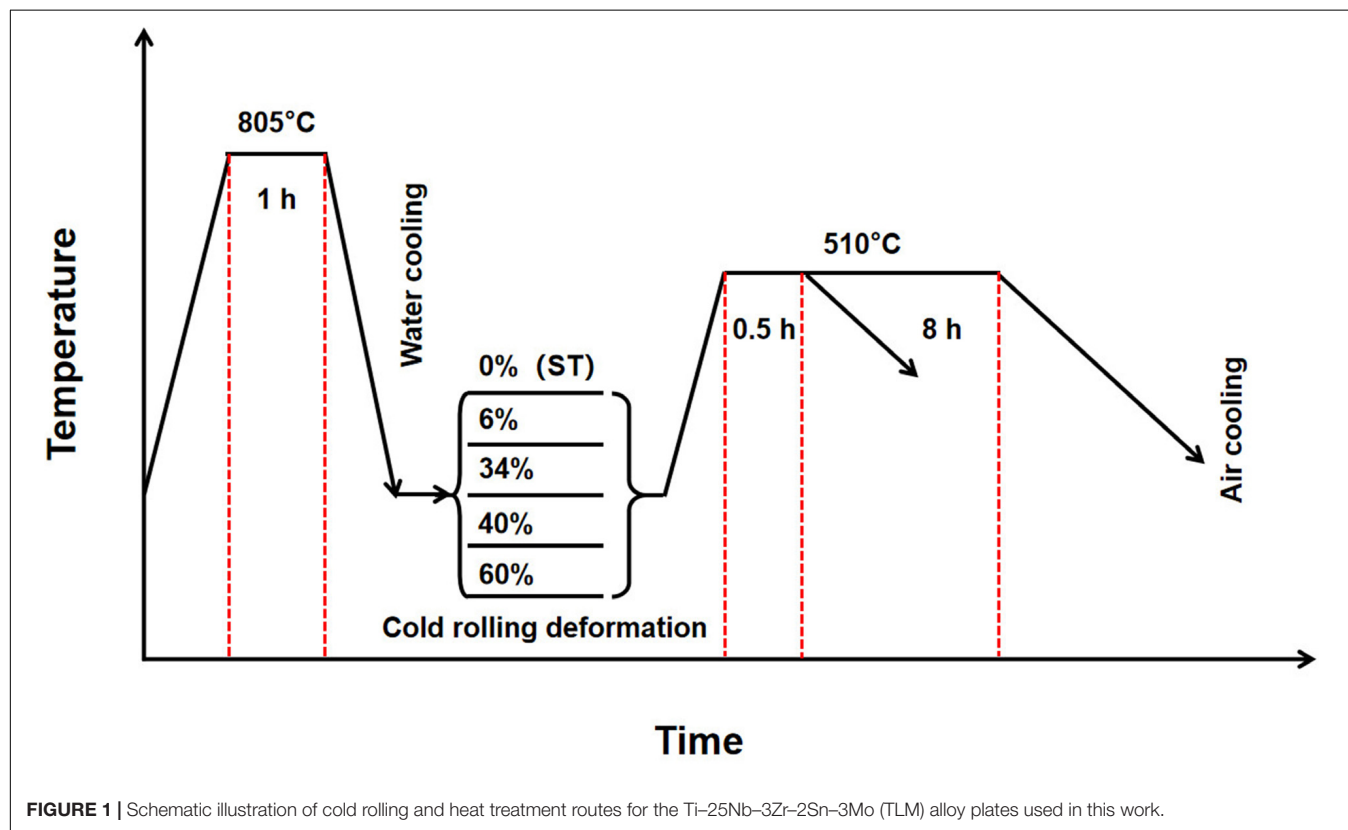
The TLM (Ti-25Nb-3Zr-2Sn-3Mo, wt%) alloy ingot was produced by VAR (vacuum arc remelting) three times. The sponge titanium (grade 0, 3–12.7 mm), sponge zirconium (industrial grade, Zr-1), Nb-47Ti, Ti-80Sn, and Ti-2Mo binary master alloys (chips) were used as raw materials. Consumable electrode blocks were prepared using a 1,000-ton four-column hydraulic press. Both the alloy ingots and master alloys were fabricated by NIN BRC SKLBMM (Northwest Institute for Non-ferrous Metal Research, Biomaterial Research Center, Shaanxi Key Laboratory of Biomedical Metal Materials, Xi'an, China). Clean turning scraps and bulk samples for testing were machined from ingot at two various positions. The surface of the machined sample is smooth and free of burrs. The chemical compositions of TLM alloy were examined using the inductively coupled plasma optical emission spectroscopy (ICPOES, for the metallic main elements including Mo, Zr, Sn, Fe, and Nb) and infrared absorption method (IR absorption, for the interstitial elements including N, O, H, and C). The chemical compositions of TLM alloy ingot at two different positions are listed in **Table 1**. The ingot with a dimension of $\Phi 160 \text{ mm} \times 500 \text{ mm}$ was multistep hot forged in order to break down the coarse grains after homogenization treatment at 1,150°C for 8 h. The TLM alloy billets were hot rolled at 750°C into plates with 5 mm in thickness using 2,000 tons of reversing rolling plate equipment. First, the hot-rolled plate billet was leveled and straightened by the automatic plate-leveling machine. Subsequently, the oxide layer of the plate was efficiently removed using sandblasting and mechanical polishing. The surface of the alloy plate was polished in the end. Then the alloy plates were solution treated (ST) at 805°C for 1 h followed by water cooling and cold rolled with reductions of 6, 34, 40, and 60% in thickness by 650-type rolling plate equipment. For the cold-rolled specimens, aging treatments were performed at 510°C for 8 h in the muffle furnace. Both the oxide layer and the micrometallurgical defects were removed by NC machines. The schematic illustration of cold rolling and heat treatment routes for the TLM alloy plates in this work is shown in **Figure 1**.

Figure 2 shows microstructures of the TLM alloy plate ST at 805°C for 1 h followed by water cooling and aging-treated at 510°C for 8 h after solution treatment. The inverse pole figure (IPF) map and transmission electron microscope (TEM) images for the ST TLM alloy plate indicate that the microstructures are constituted by β phase, as presented in **Figures 2A,B**. The α precipitates generated during one step aging after solution treatment exhibit a needle shape within the β matrix, as shown in **Figure 2C**.

The uniaxial tensile test was carried out using an INSTRON 598X (maximum load: 250 kN) machine at a constant strain

TABLE 1 | Chemical compositions of TLM (Ti–25Nb–3Zr–2Sn–3Mo, wt%) alloy ingot at two different positions.

Position	Ti	Nb	Zr	Sn	Mo	Fe	C	N	O	H
Upper	Bal.	25.5	3.05	2.05	3.05	0.02	0.01	0.003	0.049	0.0006
Bottom	Bal.	25.8	2.96	2.03	3.08	0.02	0.02	0.003	0.044	0.0006

**FIGURE 1** | Schematic illustration of cold rolling and heat treatment routes for the Ti–25Nb–3Zr–2Sn–3Mo (TLM) alloy plates used in this work.

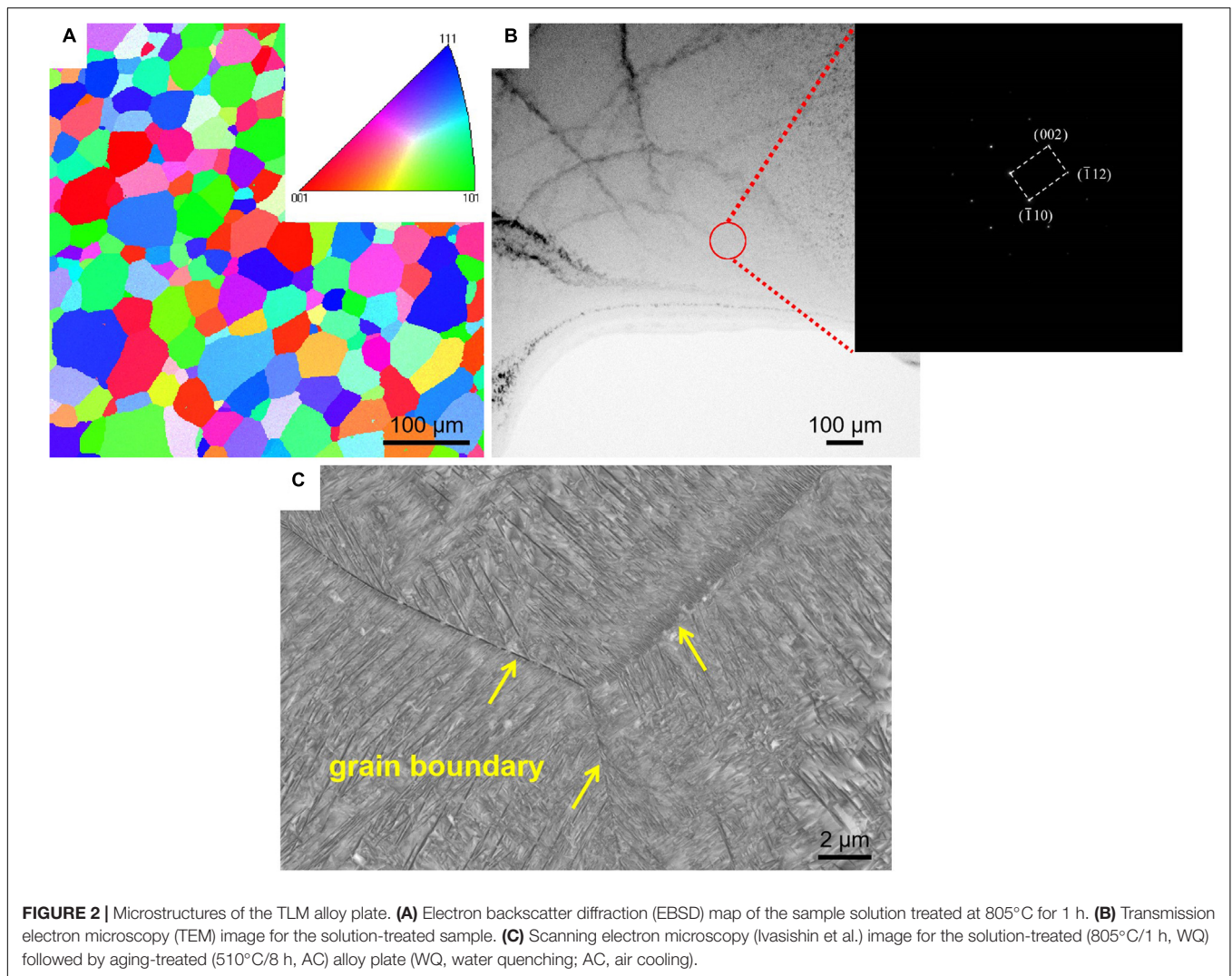
rate of $5 \times 10^{-3} \text{ s}^{-1}$ at room temperature. Tensile samples were machined from TLM alloy plates in compliance with ASTM E8/E8M-13a (width: $6.0 \pm 0.1 \text{ mm}$, gage length: $25 \pm 0.1 \text{ mm}$). The optical microstructures (OMs) were examined by a LEICA microscope. Metallographic samples were etched using Kroll's reagent (10 vol% HF + 10 vol% HNO₃ + 80 vol% H₂O). X-ray diffraction (XRD) analysis was performed by BRUKER D8 ADVANCE machine equipped with copper K α radiation. The acceleration voltage and operating current were set at 40 kV and 40 mA, respectively. The XRD was conducted at 2 theta angle of 20–90°, a step size of 0.02°, and a scanning speed of 6°/min. The texture analysis was carried out using high-resolution XRD (XPert Pro MRD). The fracture morphology and microstructure morphology were observed and analyzed by a FEI Quanta 650F SEM. electron backscattered diffraction (EBSD) characterization was conducted by AZtech (Oxford Instrument, HKL Channel 5 data analysis software) with an accelerating voltage of 20 kV. The microstructural morphology of high magnification was observed using FEI Tecnai G2 F20 TEM operating at 200 kV. TEM specimens were mechanically ground to a thickness of approximately 40 μm using SiC abrasive paper (400, 600, 800, 1,000, 1,200, 1,500, and 2,000 grit). The ion

milling was performed for the preparation and observation of the TEM samples.

RESULTS AND DISCUSSION

Cold Rolling and Texture Analysis

In the process of plastic deformation of metal materials, both the dislocation density and residual stress are extremely high in the area with a large degree of deformation, which leads to a significant reduction in the calibration rate of EBSD. The quality of the obtained images is poor, and the grain shape and crystallographic orientation cannot be achieved. On the contrary, the calibration rate is higher, and the image quality is relatively better in some areas with a smaller degree of deformation. Furthermore, the calibration rate is also relatively low due to the high density of defects or dislocations at grain boundaries. In the early stage of the investigation, it was found that higher residual stress would significantly affect the calibration rate (less than 50%) in cold deformed samples using EBSD technique, resulting in blurry Kikuchi patterns. Compared with the EBSD technique, the sample preparation of XRD is simple. The specimen is



irradiated with characteristic X-rays, and the texture analysis is carried out according to the difference in the diffraction intensity in different characteristic directions. The evaluation of macroscopic properties for crystalline materials is unique. Therefore, the XRD technique can effectively make up for the shortcomings of a lower calibration rate in cold deformed metallic samples. Meanwhile, this technique is more suitable for the investigation of texture evolution and crystallographic orientation relationship of titanium and its alloys during cold deformation, such as cold rolling and cold drawing.

Figure 3 shows the pole figures (PF) of TLM alloy plates cold deformed with 6, 34, and 60% reductions in thickness measured by XRD. It can be seen from **Figure 3A** that when the TLM alloy plate is cold rolled with a 6% reduction, the β grains present a kind of relatively random orientation distribution characteristic, and only a small part of the β grains is rotated during cold rolling. The main reason for the rotation of the β grains is that dislocation tangles are dominant for the TLM alloy plate during cold rolling at a relatively small reduction. The elongated β grains can be observed in the cold-rolled alloy plates, and few secondary phases

or recrystallized grains were generated. In addition, as seen from the PF in **Figures 3B,C**, with the increased degree of cold rolling deformation, the $\langle 110 \rangle$ texture gradually appears and increases. As shown in **Figure 3B**, when the TLM alloy plate is cold deformed with 34% reduction, the intensity of both $\langle 200 \rangle$ and $\langle 110 \rangle$ textures increase. Meanwhile, when the reduction is raised to 60%, the TLM alloy plate has an obvious $\langle 110 \rangle$ texture. It can be reasonably inferred that the β grains tend to rotate to the $\langle 110 \rangle$ direction instead of $\langle 211 \rangle$ during cold rolling. Generally, for β -type titanium alloys with a body-centered cubic (BCC) structure, with the increase in the cold reduction, the $\langle 110 \rangle$ texture is easier to be presented due to the tightness of atomic arrangements and slip systems on the close-packed plane during the plastic deformation (tension, compression, and rolling) at room temperature.

Cold Rolling, Dislocation Distribution, and Substructure

X-ray diffraction patterns of the TLM specimen ST at 805°C for 1 h followed by water quenching and cold rolling at

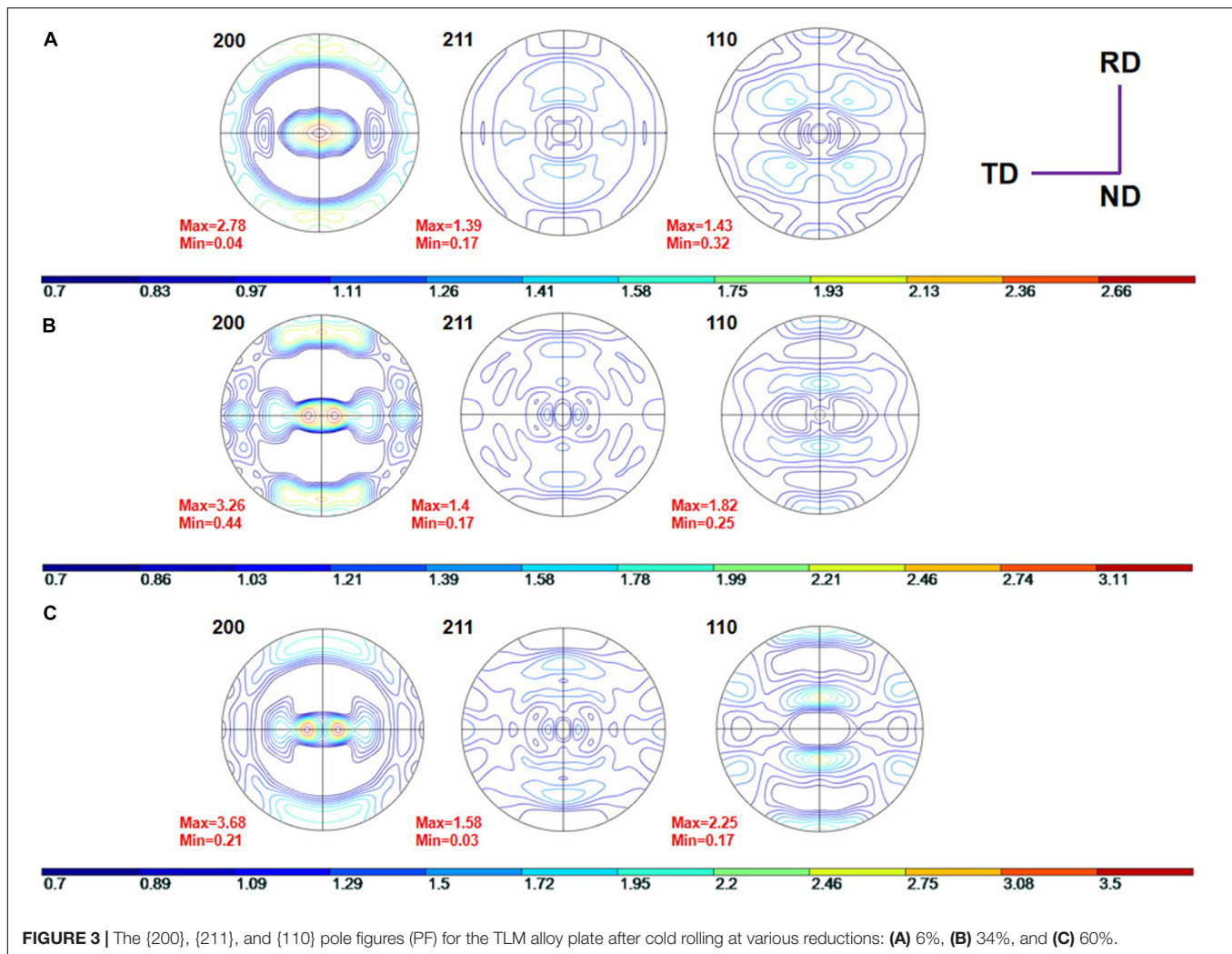


FIGURE 3 | The {200}, {211}, and {110} pole figures (PF) for the TLM alloy plate after cold rolling at various reductions: **(A)** 6%, **(B)** 34%, and **(C)** 60%.

various reductions are indicated in **Figure 4**. Diffraction peaks of orthorhombic α' phases are obviously detected in the alloy plate ST at 805°C for 1 h. Meanwhile, a few stress-induced martensite α' phases gradually appear after cold rolling with various reductions at room temperature. It can be inferred that the phase transition of stress-induced martensite from β phase to α' is promoted after cold deformation. In addition, the intensity and quantity of diffraction peaks for α' phase gradually increases with the increase in the degree of reduction owing to the martensite phase transition that is prone to be promoted after cold rolling. It can be observed that $(110)_\beta$, $(200)_\beta$, $(211)_\beta$, and $(220)_\beta$ diffraction peaks are detected in all specimens. Moreover, with the increase in the cold reduction, the intensity of $(200)_\beta$ diffraction peak first decreases up to the reduction of 34% and subsequently increases up to the reduction of 40% and then decreases again after 60% reduction. The ratios of β $(200)/\beta$ (110) are calculated to be 0.209, 0.037, 0.029, 0.055, and 0.018, respectively. This finding demonstrates that the texture varies with the reduction in the cold deformation; the textures of cold-deformed TLM alloy plate gradually transform into the $\langle 110 \rangle$ orientation during cold working. Generally,

the full width half maximum (FWHM) in XRD patterns of deformed metals is used to analyze the lattice distortion owing to the dislocation movement, deformation twins, and kinking, etc. The FWHM value of β (110) diffraction peak obtained using Jade 6.0 are 0.494, 0.527, 0.597, and 0.697 for the samples cold deformed at 0 (solution-treated), 6, 34, 40, and 60% rolling reduction, respectively. It is clearly seen that with increasing cold-deformed reduction, the values of FWHM of β (110) diffraction peak show a rising tendency. Furthermore, the change in the FWHM of β (110) diffraction peak in various cold-deformed samples illustrates that dislocation tangles and substructures are the predominant deformation mechanisms in severe plastic deformation samples. The cold-rolled TLM alloy plate with a large number of dislocation tangles tends to inhibit the generation of dislocation cells and subgrains, especially in BCC alloys. A lot of deformation bands are generated within the deformed microstructures for the coordination deformation. Therefore, the deformed grains and newly formed substructures, such as subgrains, subgrain boundaries, and deformation twins, could be found in the TLM specimens after severe plastic deformation (Hao et al., 2012; Xu et al., 2019a).

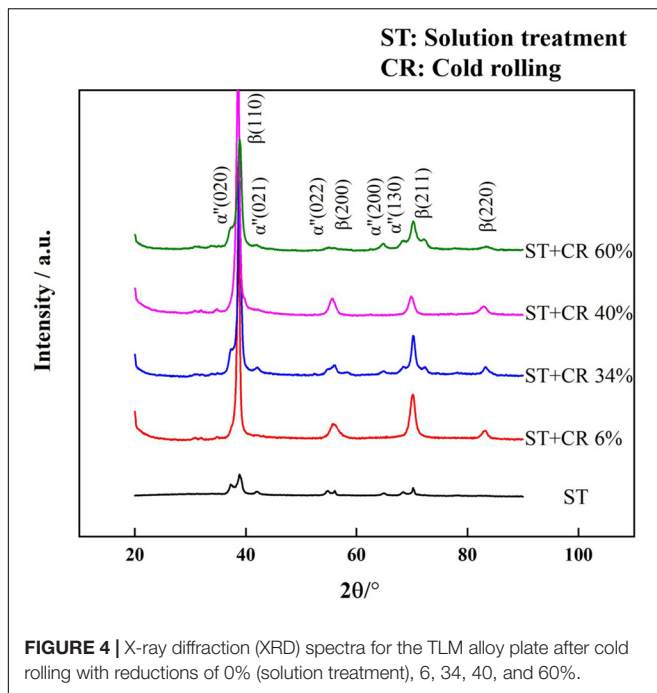


FIGURE 4 | X-ray diffraction (XRD) spectra for the TLM alloy plate after cold rolling with reductions of 0% (solution treatment), 6, 34, 40, and 60%.

Transmission electron microscope micrographs for the TLM alloy plate after cold rolling at 34 and 60% reduction. Bright-field images (BF) are used to reveal the crystallographic misorientation and characteristics of cold-deformed microstructures. Dislocation density in the cold-deformed TLM specimen (**Figure 5**) is higher than that in the solution-annealed alloy (**Figure 2B**). Therefore, it could be deduced that the dislocation multiplication, mutual reactions, and movement play significant roles in the cold rolling of TLM alloy plate. It can be seen from the SAED pattern (**Figure 5A**) that the black bands scattered within the cold-deformed TLM alloy are not newly formed phases or other structures but the dislocation tangles generated in the process of cold rolling. The density of dislocation increases visibly after cold rolling at 34% reduction. Bright-field image taken from another region of the 34% cold-deformed TLM alloy plate is presented in **Figure 5B**, which displays the dislocation pile-up near the grain boundaries as well as in the grain interior. As seen from the SAED patterns (**Figure 5B**), phase transition and newly formed substructures are observed in the region of black and white bands. This interesting phenomenon was previously found by Takemoto in the investigation of tensile deformation behavior and cold rolling at various reductions for the titanium–molybdenum alloy (Takemoto et al., 2004). The formation of bands is attributed to the dislocation movement and tangle non-uniformity to some extent. Additionally, it can be observed that the extension and growth of bands are suppressed by the grain boundary. The bright-field (BF) image and SAED patterns for the 60% cold-deformed TLM alloy plate are displayed in **Figures 5C,D**. We can also see that a severe deformation area is primarily composed of dislocation tangle and 112 <111> type deformation twins near the grain boundary. Generally, the ω phases induced by stress during cold rolling

were not detected by XRD and TEM in the cold-deformed TLM alloy (Cheng et al., 2020). One of the reasons is that the contents of β stable elements, such as Nb, Zr, Sn, and Mo, are so high that the formation of ω precipitates is suppressed to a large extent. This kind of ω phase can be considered as stress-induced omega (SIO) phase transformation triggered by the recombination of solute atoms in the {112} lattice planes with the orientation of <111> crystallographic direction families. The mechanism of dislocation motion and tangles can also be clarified by the replacement of solute atoms in {112} lattice planes in the direction of <111> during cold deformation. Moreover, the degree of dislocation pile up improves obviously with the increment in the reductions, which may result in the generation of new boundaries for the β -type Ti alloys (Wu et al., 2014; Yang et al., 2018; Rabadia et al., 2019a,b).

Aging Treatment, Precipitation Phases, and Mechanical Properties

In general, the $\beta \rightarrow \alpha$ phase transformation could be triggered in the TLM alloy during the solution treatment plus aging. **Figure 6** presents the morphology (SEM and TEM) of the precipitation phases for the alloy after cold rolling at various reductions plus 510°C aging treatment. As can be seen from **Figures 6C,F**, compared with the size of precipitated phases in the single aging-treated sample, the precipitations formed in the TLM alloy subjected to cold rolling in conjunction with the same aging should be refined to a large extent. When the TLM alloy plate is cold rolled at a reduction of 34% in conjunction with aging treatment for 8 h, the length of precipitation phases is approximately 150–500 nm, which is much thinner than that of a single aged one. The formation of dislocation lines or dislocation cells introduced by cold rolling deformation plays a very important role in the emergence of precipitates during aging treatment. **Figure 6B** presents the dark-field (DF) TEM picture of the morphology for the tiny precipitations generated in the process of cold rolling at a 34% reduction followed by short-time aging treatment. As seen from the SAED pattern, the white precipitation phases should be α phase. Systematic research on α precipitation phases with nanometer dimensions of the initial sample, such as β 21s, subjected to certain aging heat treatment was carried out. However, α phases were hardly observed in the β matrix using an electron microscope (Malinov et al., 2003; Banerjee and Williams, 2013). The reason for this interesting phenomenon is that the crystal defects, such as dislocation lines, sub-boundaries, phase interface, and twin boundaries, can promote the phase transition of $\beta \rightarrow \alpha$ and reduce the time of subsequent aging simultaneously (Wang Y. B. et al., 2010; Guo et al., 2013). **Figures 6A,B** present that the length of α precipitated phases is approximately 15–90 nm in the sample cold rolled at 34% reduction followed by aging treatment for 0.5 h. After rolling, a large number of dislocations were introduced into the initial microstructure, which is favorable for the homogeneous nucleation process of $\beta \rightarrow \alpha$ phase transition during aging, resulting in the refinement of α precipitations. More and more nucleation sites in the β matrix will be conducive to suppress the rapid growth of the α phase. Furthermore, a

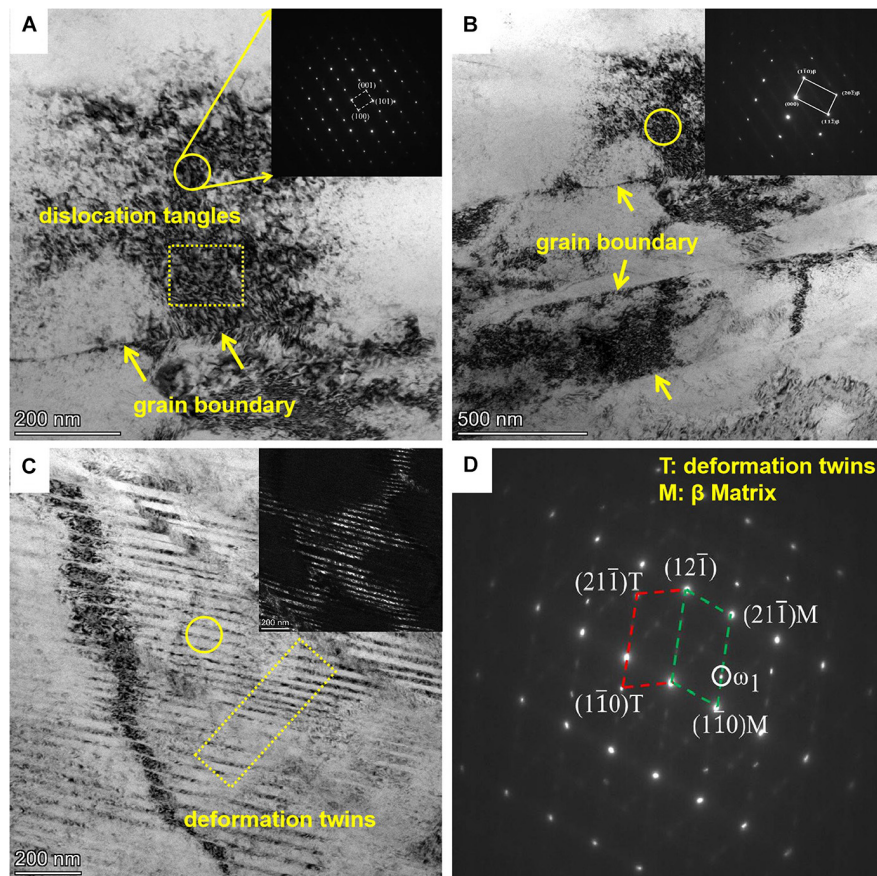


FIGURE 5 | TEM analyses of the TLM alloy plates cold rolled with various reductions. **(A,B)** Bright-field (BF) micrographs and SAED patterns for the specimen cold deformed with the reduction of 34%. **(C,D)** Bright-field (BF) micrographs and SAED patterns for the specimen cold deformed at a reduction of 60%.

large number of newly generated interfaces were introduced into the deformed specimen. These new interfaces accelerate the precipitation of lamellar α phases, which may result in a decrease in the plasticity of aged specimens. The newly generated grain boundaries contribute to the homogeneous nucleation and dispersed precipitation of α phase in the process cold rolling at various reductions. Moreover, it can be seen from **Figures 6D–F** that the newly generated grain boundaries appear during cold rolling at a relatively large reduction (60%), resulting in the linear dispersion of secondary phases along with them after aging treatment.

Previous studies have shown that the dislocation density of alloy is approximately $1.0 \times 10^9 \text{ mm}^{-2}$ after plastic deformation (Azushima et al., 2008; Cheong, 2008). During cold rolling processing, the formation of dislocations in the TLM alloy plate could provide the driving force for $\beta \rightarrow \alpha$ transformation after aging, which contributes to the refinement of the α phase. Therefore, the strengthening mechanisms for the TLM alloy plate cold rolled with various reductions followed by aging could be clarified using the above theory. This kind of finer α phase can offer more phase interfaces, which will be regarded as one type of powerful dislocation obstacles, and can also help to obtain the enhancement of strength for the TLM alloy.

A schematic diagram of microstructural evolution and precipitating process for the TLM alloy plates cold rolled with reductions of 0, 6, 36, 40, and 60% followed by aging treatment at 510°C for 8 h is presented in **Figure 7**. The morphology of the α phases shows a remarkable difference at various cold-rolling reductions. Meanwhile, a large number of slip bands and newly generated grain boundaries gradually emerge during cold deformation. To the author's knowledge, they are considered as a typically inferior microstructural characteristic, which is prone to be changed into coarse lamellar α precipitates after following aging treatment. The dislocation slip or motion is suppressed by this microstructure coarsening, and the ductility is simultaneously weakened during tensile deformation at room temperature. In addition, when the plate is cold rolled with a reduction of 60% in conjunction with aging treatment at 510°C for 8 h, the maximum strength value (tensile strength: 1,005 MPa) is achieved under this condition.

The tensile curves for TLM plate ST at 805°C for 1 h followed by water quenching and cold rolled with various reductions in conjunction with aging treatment at 510°C for 8 h are displayed in **Figure 8**. For the β solution-treated ($805^\circ\text{C}/1 \text{ h}$, WQ) condition, the curve demonstrates a so-called “double yielding” effect during the tensile deformation. The reason for

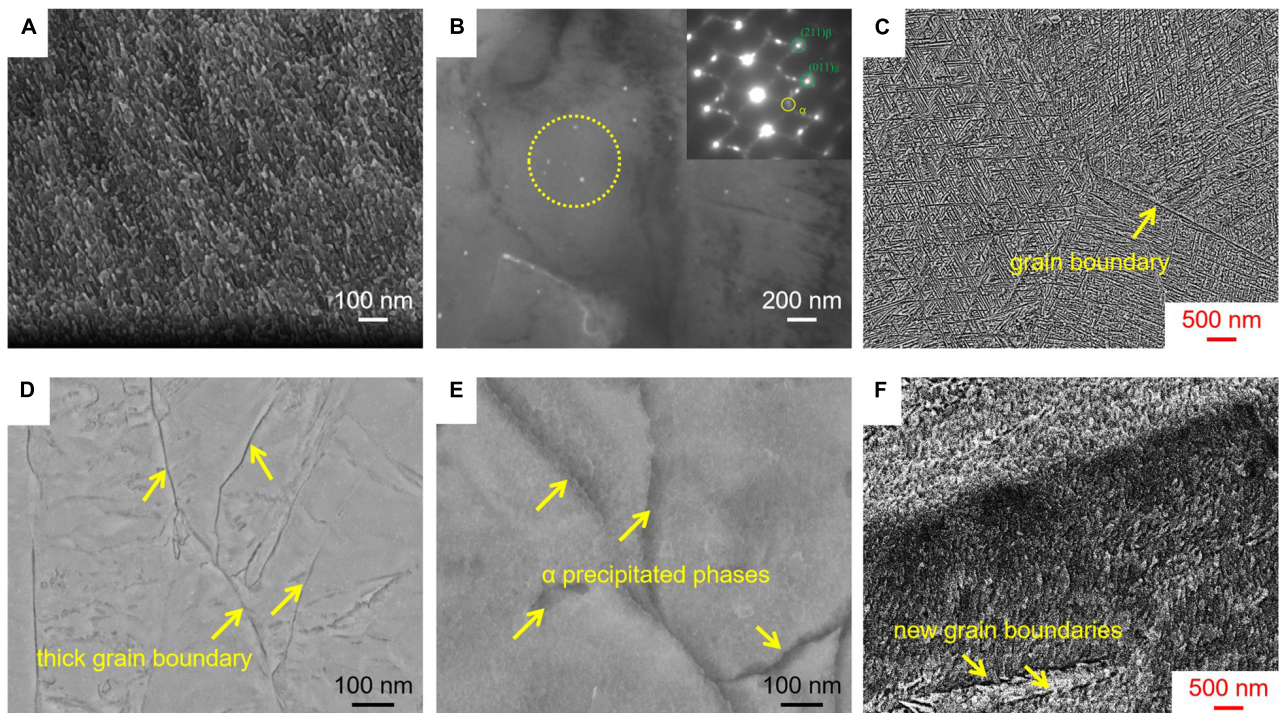


FIGURE 6 | Micrographs of the TLM alloy plate cold rolled with various reductions in conjunction with aging treated at 510°C. **(A,B)** SEM image, dark-field TEM micrograph, and SAED pattern for the sample after cold rolling at a reduction of 34% in conjunction with aging treatment for 0.5 h. **(C)** SEM image for the sample after cold rolling at a reduction of 34% in conjunction with aging treatment for 8 h. **(D,E)** SEM images for the sample after cold rolling at a reduction of 60% in conjunction with aging treatment for 0.5 h. **(F)** SEM image for the sample after cold rolling at a reduction of 60% in conjunction with aging treatment for 8 h.

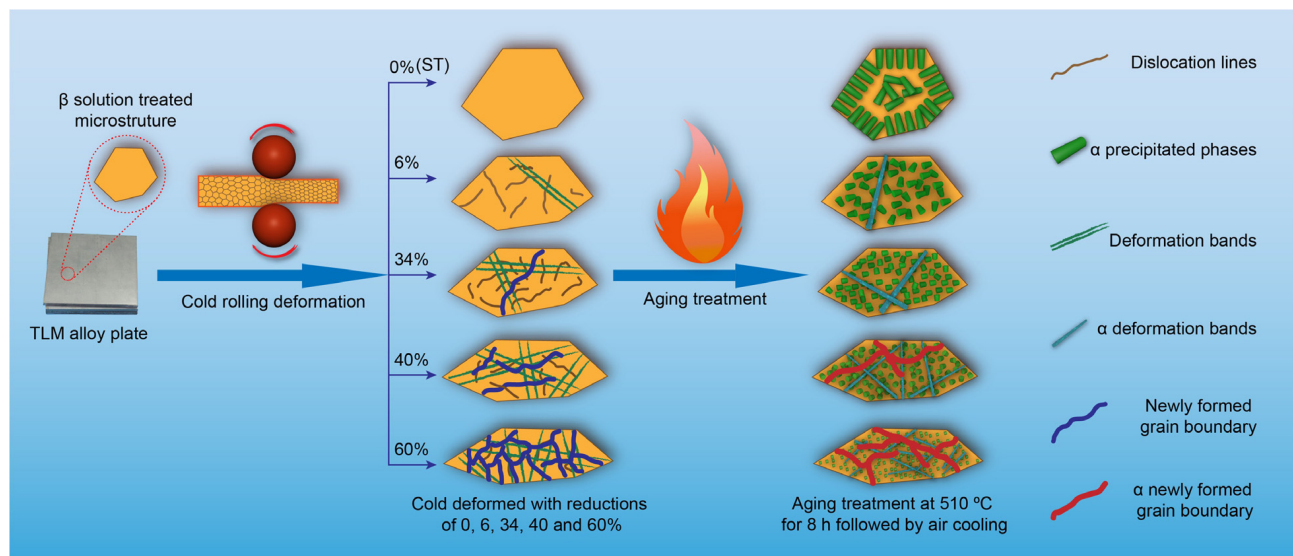


FIGURE 7 | A schematic diagram of microstructural evolution and precipitating process for the TLM alloy plates cold rolled with reductions of 0, 6, 36, 40, and 60% followed by aging treatment at 510°C for 8 h.

this phenomenon is that when the temperature is selected in the beta phase region, the beta phase is in a relatively metastable condition, and the precipitation of martensite phase (α'') is prone to be promoted. The stress-strain curve with a fairly low

value of apparent yielding stress is caused by the nucleation of the martensite phase and inheritance of room temperature deformation modes. Meanwhile, the emergence of the second yield point is attributed to the applied stress needed for the

activation of certain slip systems, which could suppress the movement of the martensite laths during deformation. The tensile strength and elongation of the TLM alloy ST at 805°C for 1 h followed by water cooling are 609 MPa and 43.7%, respectively. Moreover, the tensile strength gradually increases with the increment in the reductions, while the elongation decreases with the increment in the reduction of cold rolling. The maximum value of tensile strength is as high as 1,005 MPa at cold rolling with a 60% reduction followed by aging treatment. However, the elongation of the TLM alloy plate is only about 4.5% in this condition. The TLM alloy plate has not visibly demonstrated the characteristic of plastic deformation. It can be inferred that the tensile strength and elongation of the TLM alloy plate are obviously different because of the volume percentage, size, and shape of α phases formed after cold deformation followed by aging treatment. The TLM alloy having finer α precipitations formed, based on the assisted nucleation and growth of dislocation tangles, or pile up during cold deformation with a reduction of 34%, possesses a higher tensile strength level. The main reason for this is considered to be the following factors including the geometrical size and volume percentage of α phase as well as the quantity and density of α phase interfaces, which are significantly influenced by the degree of cold-rolling deformation. Based on the precipitation strengthening criterion, the α precipitated phase refinement contributes to the enhancement of tensile strength for the TLM alloy (Gao et al., 2019; Bermingham et al., 2020). Furthermore, it can be noted that the room temperature elongation of the alloy plate subjected to solution annealing plus direct aging treatment is approximately 24%, and the tensile strength is about 660 MPa. The reason is that the formation of α precipitation phases with thick lamellar is suppressed owing to the lack of newly formed interfaces within the (ST + AG) sample, while they will be precipitated within the alloy plates after cold rolling in conjunction with aging treatment. These abundant newly formed α interfaces will hinder the dislocation slip or movement and result in the decrease in elongation at room temperature. Moreover, the tensile strength and elongation for the TLM alloy plate subjected to cold rolling at a reduction of 6% followed by 510°C aging treatment for 8 h are 882 MPa and 6.5%, respectively.

The OM of the TLM alloy plates subjected to cold rolling with a reduction of 0% (solution treated), 34%, and 60% followed by 510°C aging treatment for 8 h and their corresponding fracture surfaces after tensile deformation are presented in **Figure 9**. In general, the OM and fracture surfaces are often used to analyze and characterize the details of microstructural evolution for the experimental alloy plates according to the morphology features and deformation behaviors to be predicted. **Figures 9A,B** indicate that α phases are precipitated in the β matrix, and a very small amount of micro precipitate-free zones (PFZ) can be observed in the TLM alloy plate subjected to solution annealing plus direct aging treatment. Interestingly, from **Figures 9C,D**, it can be observed that more and more α precipitations with smaller size form in the TLM alloy plate subjected to cold rolling at a reduction of 34% and followed by aging treatment. It is believed that the cold rolling plays a significant role in the uniform distribution and refinement of α precipitations and

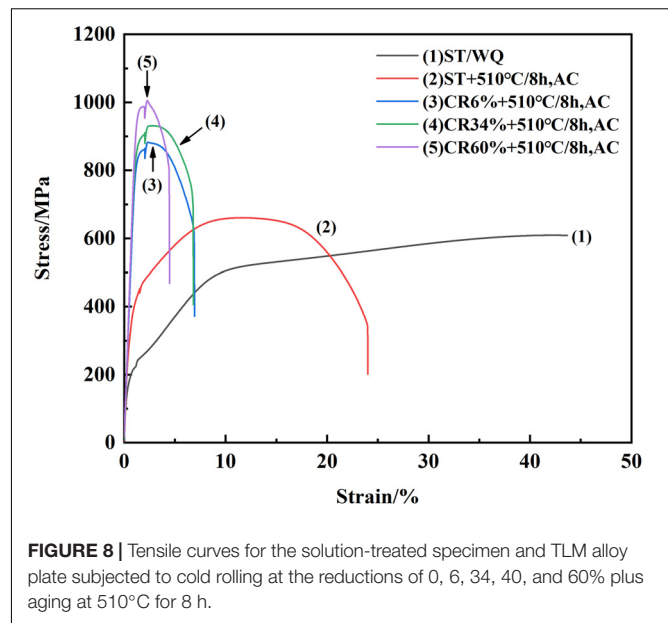


FIGURE 8 | Tensile curves for the solution-treated specimen and TLM alloy plate subjected to cold rolling at the reductions of 0, 6, 34, 40, and 60% plus aging at 510°C for 8 h.

increasing in the number of secondary phases. As for the TLM alloy plate subjected to cold rolling at a reduction of 34%, many crystal defects induced by plastic deformation, such as dislocation tangles or pile up, contribute to provide more nucleation sites and suppress the over quick coarsening and growth of secondary phases during aging. Furthermore, it can be obviously observed in **Figure 9D** that the intergranular fracture mode is dominant in the TLM alloy plate subjected to cold rolling at a reduction of 34% followed by aging treatment. As seen from the details of fracture surface morphology, the alloy plate shows ductile fracture characteristic to some extent. The fracture surface is composed of massive dimples with a size of approximately 5–11 μm . This fracture mode is associated with the more uniform and smaller secondary phases precipitated in the β grains and the acceptable ductility with 6.9% at room temperature. The finer scale of secondary phases precipitated in the process of aging treatment after cold rolling will result in the formation of plenty of interfaces between alpha and beta phases. These interfaces can be considered as a lot of effective obstacles to dislocation movement and cause visible increase in the tensile strength for the TLM and other titanium alloys (Cai et al., 2013; Ozan et al., 2019). The OM and fracture surface (SEM image) for the TLM alloy plate subjected to cold rolling at a reduction of 60% and followed by aging treatment are presented in **Figures 9E,F**. The fracture surface shows the evidence of brittle failure to some extent due to the formation of a thick lath-like α phase in the grain boundary, which could result in a decrease in elongation after tensile deformation at room temperature.

CONCLUSION

The microstructure characteristics of the TLM alloy plates cold deformed at various reductions and its influence on precipitated phases during aging treatment were mainly studied in this work.

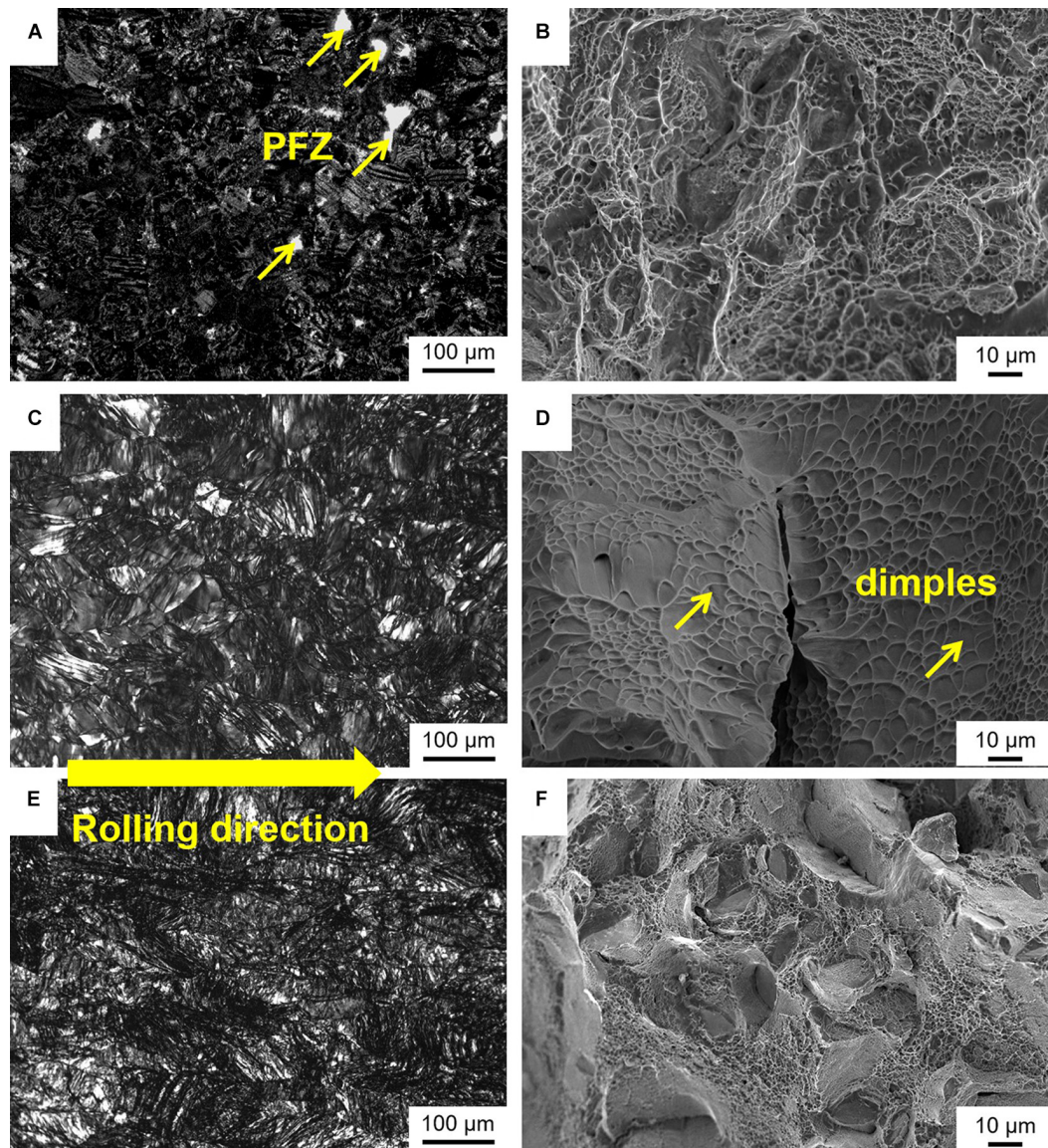


FIGURE 9 | Microstructures and fracture surfaces for the TLM alloy plates subjected to cold rolling at various reductions followed by aging treatment at 510°C for 8 h: (A,B) 0% reduction. (C,D) 34% reduction; (E,F) 60% reduction.

The TLM alloy plates possessed various mechanical properties owing to the different morphology, size, and volume fraction of α precipitated phases after cold-rolling deformation with various reductions (0, 6, 34, 40, and 60%) in conjunction with aging treatment at 510°C for 8 h. These main conclusions could be summarized from this work:

- (1) The $\langle 110 \rangle$ texture was prone to form in the β solution-treated TLM alloy plates subjected to cold-rolling deformation with various reductions at room temperature. Dislocation tangles were visibly observed in the β matrix after cold rolling.
- (2) The α precipitated phases formed after cold rolling with various reductions (0, 34, and 60%) in conjunction with aging treatment possessed various characteristics. The dimension of α precipitated phases in the alloy plate subjected to cold rolling was smaller than that of the α phases transformed after a direct solution treatment in conjunction with aging.
- (3) When the alloy plate was subjected to cold rolling at a reduction of 60% in conjunction with aging, the maximum tensile strength could be achieved, while the elongation was relatively low. A large number of newly generated subgrain boundaries and interfaces were prone to be formed after cold deformation with various reductions at room temperature. The precipitated phases with thick lamellar were formed, which could be considered as one of the principal reasons for the relatively low elongation.

- (4) When the alloy plate was subjected to cold rolling at a reduction of 34% in conjunction with aging, the smaller α precipitated phases could be formed within the β matrix, resulting in the relatively high tensile strength of 931 MPa and the acceptable elongation of 6.9%. Therefore, the TLM alloy will be deemed as a potential material in the orthopedic field.

DATA AVAILABILITY STATEMENT

The raw data supporting the conclusions of this article will be made available by the authors, without undue reservation.

AUTHOR CONTRIBUTIONS

JC took charge of the manuscript writing and data analysis. JL took charge of the technical guidance and supervision. SY took charge of literature research and

providing research idea. ZD and XZ took charge of the microstructure characterization. WZ took charge of the mechanical properties testing. JG and HW took charge of the preparation of specimens. HS took charge of the cold rolling of alloy plates. ZY took charge of the texture analysis. All authors contributed to the article and approved the submitted version.

FUNDING

This work was financially supported by the National Natural Science Foundation of China (Nos. 51901193, 51861029, 51801162, and 32071327), Key Research and Development Program of Shaanxi (Program Nos. 2019GY-151, 2019GY-178, and 2020GY-251), Science and Technology Plan Project of Weiyang District in Xi'an City (201905), and Xi'an Science and Technology Project (2020KJRC0141). JC was the leader of the funding.

REFERENCES

- Abdelrhman, Y. M., Gepreel, M. A., Kobayashi, S., Okano, S., and Okamoto, T. (2019). Biocompatibility of new low-cost ($\alpha + \beta$)-type Ti-Mo-Fe alloys for long-term implantation. *Mater. Sci. Eng. C* 99, 552–562. doi: 10.1016/j.msec.2019.01.133
- Azushima, A., Kopp, R., Korhonen, A. S., Yang, D., Micari, F., Lahoti, G., et al. (2008). Severe plastic deformation (SPD) processes for metals. *CIRP Ann. Manuf. Technol.* 57, 716–735.
- Banerjee, D., and Williams, J. C. (2013). Perspectives on titanium science and technology. *Acta Mater.* 61, 844–879. doi: 10.1016/j.actamat.2012.10.043
- Banerjee, R., Nag, S., Stechschulte, J., and Fraser, H. L. (2004). Strengthening mechanisms in Ti-Nb-Zr-Ta and Ti-Mo-Zr-Fe orthopaedic alloys. *Biomaterials* 25, 3413–3419. doi: 10.1016/j.biomaterials.2003.10.041
- Bermingham, M. J., Kent, D., Pace, B., Cairney, J. M., and Dargusch, M. S. (2020). High strength heat-treatable β -titanium alloy for additive manufacturing. *Mater. Sci. Eng. A* 791:139646. doi: 10.1016/j.msea.2020.139646
- Cai, S., Daymond, M. R., Ren, Y., Bailey, D. M., and Kay, L. E. (2013). Influence of short time anneal on recoverable strain of beta III titanium alloy. *Mater. Sci. Eng. A Struct. Mater.* 562, 172–179. doi: 10.1016/j.msea.2012.11.005
- Chen, Y., Du, Z., Xiao, S., Xu, L., and Tian, J. (2014). Effect of aging heat treatment on microstructure and tensile properties of a new β high strength titanium alloy. *J. Alloys Compd.* 586, 588–592. doi: 10.1016/j.jallcom.2013.10.096
- Cheng, J., Li, J., Yu, S., Du, Z., Zhang, X., Gai, J., et al. (2020). Room temperature deformation and superelastic behavior of TLM titanium alloy under different solution conditions. *Front. Mater.* 7:114. doi: 10.3389/fmats.2020.00114
- Cheong, K. (2008). The role of dislocations in cyclically deformed metal polycrystals. *Curr. Appl. Phys.* 8, 436–439. doi: 10.1016/j.cap.2007.10.068
- Duraccio, D., Mussano, F., and Faga, M. G. (2015). Biomaterials for dental implants: current and future trends. *J. Mater. Sci.* 50, 4779–4812. doi: 10.1007/s10853-015-9056-3
- Gao, J., Knowles, A. J., Guan, D., and Rainforth, W. M. (2019). ω phase strengthened 1.2GPa metastable β titanium alloy with high ductility. *Scr. Mater.* 162, 77–81. doi: 10.1016/j.scriptamat.2018.10.043
- Geetha, M., Singh, A. K., Asokamani, R., and Gogia, A. K. (2009). Ti based biomaterials, the ultimate choice for orthopaedic implants – a review. *Prog. Mater. Sci.* 54, 397–425. doi: 10.1016/j.pmatsci.2008.06.004
- Gepreel, M. A., and Niinomi, M. (2013). Biocompatibility of Ti-alloys for long-term implantation. *J. Mech. Behav. Biomed. Mater.* 20, 407–415. doi: 10.1016/j.jmbbm.2012.11.014
- Goriainov, V., Cook, R., Latham, J. M., Dunlop, D. G., and Oreffo, R. O. C. (2014). Bone and metal: an orthopaedic perspective on osseointegration of metals. *Acta Biomater.* 10, 4043–4057. doi: 10.1016/j.actbio.2014.06.004
- Guo, S., Meng, Q., Hu, L., Liao, G., Zhao, X., and Xu, H. (2013). Suppression of isothermal ω phase by dislocation tangles and grain boundaries in metastable β -type titanium alloys. *J. Alloys Compd.* 550, 35–38. doi: 10.1016/j.jallcom.2012.09.081
- Hafeez, N., Liu, J., Wang, L., Wei, D., Tang, Y., Lu, W., et al. (2020). Superelastic response of low-modulus porous beta-type Ti-35Nb-2Ta-3Zr alloy fabricated by laser powder bed fusion. *Addit. Manuf.* 34:101264. doi: 10.1016/j.addma.2020.101264
- Hao, Y., Zhang, Z., Li, S., and Yang, R. (2012). Microstructure and mechanical behavior of a Ti-24Nb-4Zr-8Sn alloy processed by warm swaging and warm rolling. *Acta Mater.* 60, 2169–2177. doi: 10.1016/j.actamat.2012.01.003
- Ivasishin, O. M., Markovsky, P. E., Semiatin, S. L., and Ward, C. H. (2005). Aging response of coarse- and fine-grained β titanium alloys. *Mater. Sci. Eng. A Struct. Mater.* 405, 296–305. doi: 10.1016/j.msea.2005.06.027
- Jaworski, A., and Ankem, S. (2005). The effect of α phase on the deformation mechanisms of β titanium alloys. *J. Mater. Eng. Perform.* 14, 755–760. doi: 10.1361/105994905x75565
- Karthikeyan, T., Dasgupta, A., Khatirkar, R. K., Saroja, S., Samajdar, I., and Vijayalakshmi, M. (2010). Effect of cooling rate on transformation texture and variant selection during $\beta \rightarrow \alpha$ transformation in Ti-5Ta-1.8Nb alloy. *Mater. Sci. Eng. A Struct. Mater.* 528, 549–558. doi: 10.1016/j.msea.2010.09.055
- Kent, D., Wang, G., Yu, Z., and Dargusch, M. S. (2010). Pseudoelastic behaviour of a β Ti-25Nb-3Zr-3Mo-2Sn alloy. *Mater. Sci. Eng. A Struct. Mater.* 527, 2246–2252. doi: 10.1016/j.msea.2009.11.059
- Kent, D., Wang, G., Yu, Z., Ma, X., and Dargusch, M. S. (2011). Strength enhancement of a biomedical titanium alloy through a modified accumulative roll bonding technique. *J. Mech. Behav. of Biomed. Mater.* 4, 405–416. doi: 10.1016/j.jmbbm.2010.11.013
- Li, T., Kent, D., Sha, G., Dargusch, M. S., and Cairney, J. M. (2014). Precipitation of the α -phase in an ultrafine grained beta-titanium alloy processed by severe plastic deformation. *Mater. Sci. Eng. A Struct. Mater.* 605, 144–150. doi: 10.1016/j.msea.2014.03.044

- Li, Y., Yang, C., Zhao, H., Qu, S., Li, X., and Li, Y. (2014). New developments of Ti-based alloys for biomedical applications. *Materials* 7, 1709–1800. doi: 10.3390/ma7031709
- Liu, S., Liu, J., Wang, L., Ma, R. L., Zhong, Y., Lu, W., et al. (2020). Superelastic behavior of in-situ eutectic-reaction manufactured high strength 3D porous NiTi-Nb scaffold. *Scr. Mater.* 181, 121–126. doi: 10.1016/j.scriptamat.2020.02.025
- Ma, Y., Du, Z., Cui, X., Cheng, J., Liu, G., Gong, T., et al. (2018). Effect of cold rolling process on microstructure and mechanical properties of high strength β titanium alloy thin sheets. *Prog. Nat. Sci. Mater. Int.* 28, 711–717. doi: 10.1016/j.pnsc.2018.10.004
- Malek, J., Hnilica, F., Veselý, J., Smola, B., Bartakova, S., and Vaník, J. (2012). The influence of chemical composition and thermo-mechanical treatment on Ti-Nb-Ta-Zr alloys. *Mater. Des.* 35, 731–740. doi: 10.1016/j.matdes.2011.10.030
- Malinov, S., Sha, W., and Markovsky, P. E. (2003). Experimental study and computer modelling of the $\beta \rightarrow \alpha + \beta$ phase transformation in $\beta 21s$ alloy at isothermal conditions. *J. Alloys Compd.* 348, 110–118.
- Mantani, Y., and Tajima, M. (2006). Phase transformation of quenched α' martensite by aging in Ti-Nb alloys. *Mater. Sci. Eng. A* 438, 315–319. doi: 10.1016/j.msea.2006.02.180
- Min, X., Tsuzaki, K., Emura, S., and Tsuchiya, K. (2012). Heterogeneous twin formation and its effect on tensile properties in Ti-Mo based β titanium alloys. *Mater. Sci. Eng. A Struct. Mater.* 554, 53–60. doi: 10.1016/j.msea.2012.06.009
- Niinomi, M. (2002). Recent metallic materials for biomedical applications. *Metall. Mater. Trans. A* 33:477. doi: 10.1007/s11661-002-0109-2
- Niinomi, M. (2008). Mechanical biocompatibilities of titanium alloys for biomedical applications. *J. Mech. Behav. Biomed. Mater.* 1, 30–42. doi: 10.1016/j.jmbbm.2007.07.001
- Niinomi, M., and Nakai, M. (2011). Titanium-based biomaterials for preventing stress shielding between implant devices and bone. *Int. J. Biomater.* 2011:836587.
- Niinomi, M., Nakai, M., and Hieda, J. (2012). Development of new metallic alloys for biomedical applications. *Acta Biomater.* 8, 3888–3903. doi: 10.1016/j.actbio.2012.06.037
- Ozan, S., Lin, J., Zhang, Y., Li, Y., and Wen, C. (2019). Cold rolling deformation and annealing behavior of a β -type Ti-34Nb-25Zr titanium alloy for biomedical applications. *J. Mater. Res. Technol.* 9, 2308–2318. doi: 10.1016/j.jmrt.2019.12.062
- Qazi, J. I., Marquardt, B., Allard, L. F., and Rack, H. J. (2005). Phase transformations in Ti-35Nb-7Zr-5Ta-(0.06–0.68)O alloys. *Mater. Sci. Eng. C* 25, 389–397. doi: 10.1016/j.msec.2005.01.022
- Qiang, G., Qing, W., Xiuli, H., Xuekun, L., Dongli, S., and Gaohui, W. (2011). Precipitation behavior of α phase and mechanical properties in severely plastic deformed Ti-15-3 alloy. *Rare Metal Mater. Eng.* 40, 377–383. doi: 10.1016/S1875-5372(11)60019-2
- Rabadia, C., Liu, Y., Chen, L., Jawed, S. F., Wang, L., Sun, H., et al. (2019a). Deformation and strength characteristics of Laves phases in titanium alloys. *Mater. Des.* 179:107891. doi: 10.1016/j.matdes.2019.107891
- Rabadia, C., Liu, Y., Zhao, C. H., Wang, J., Jawed, S. F., Wang, L., et al. (2019b). Improved trade-off between strength and plasticity in titanium based metastable beta type Ti-Zr-Fe-Sn alloys. *Mater. Sci. Eng. A Struct. Mater.* 766:138340. doi: 10.1016/j.msea.2019.138340
- Rack, H. J., and Qazi, J. I. (2006). Titanium alloys for biomedical applications. *Mater. Sci. Eng. C* 26, 1269–1277.
- Ramezannejad, A., Xu, W., Xiao, W. L., Fox, K., Liang, D., and Qian, M. (2019). New insights into nickel-free superelastic titanium alloys for biomedical applications. *Curr. Opin. Solid State Mater. Sci.* 23:100783. doi: 10.1016/j.cossms.2019.100783
- Salib, M., Teixeira, J., Germain, L., Lamielle, E., Gey, N., and Aebygaudier, E. (2013). Influence of transformation temperature on microtexture formation associated with α precipitation at β grain boundaries in a β metastable titanium alloy. *Acta Mater.* 61, 3758–3768. doi: 10.1016/j.actamat.2013.03.007
- Song, Z., Sun, Q., Xiao, L., Liu, L., and Sun, J. (2010). Effect of prestrain and aging treatment on microstructures and tensile properties of Ti-10Mo-8V-1Fe-3.5Al alloy. *Mater. Sci. Eng. A Struct. Mater.* 527, 691–698. doi: 10.1016/j.msea.2009.09.046
- Sun, F., Prima, F., and Gloriant, T. (2010). High-strength nanostructured Ti-12Mo alloy from ductile metastable beta state precursor. *Mater. Sci. Eng. A Struct. Mater.* 527, 4262–4269. doi: 10.1016/j.msea.2010.03.044
- Taddei, E. B., Henriques, V. A. R., Silva, C. R. M., and Cairo, C. A. A. (2004). Production of new titanium alloy for orthopedic implants. *Mater. Sci. Eng. C* 24, 683–687. doi: 10.1016/j.msec.2004.08.011
- Takemoto, Y., Shimizu, I., Sakakibara, A., Hida, M., and Mantani, Y. (2004). Tensile behavior and cold workability of Ti-Mo alloys. *Mater. Trans.* 45, 1571–1576. doi: 10.2320/matertrans.45.1571
- Vajpai, S. K., Sharma, B., Ota, M., and Ameyama, K. (2018). Effect of cold rolling and heat-treatment on the microstructure and mechanical properties of β -titanium Ti-25Nb-25Zr alloy. *Mater. Sci. Eng. A Struct. Mater.* 736, 323–328. doi: 10.1016/j.msea.2018.09.002
- Wang, L., Lu, W., Qin, J., Zhang, F., and Zhang, D. (2009). Effect of precipitation phase on microstructure and superelasticity of cold-rolled beta titanium alloy during heat treatment. *Mater. Des.* 30, 3873–3878. doi: 10.1016/j.matdes.2009.03.042
- Wang, L., Lu, W., Qin, J., Zhang, F., and Zhang, D. (2010). The characterization of shape memory effect for low elastic modulus biomedical β -type titanium alloy. *Mater. Charact.* 61, 535–541. doi: 10.1016/j.matchar.2010.02.009
- Wang, L., Qu, J., Chen, L., Meng, Q., Zhang, L., Qin, J., et al. (2015). Investigation of deformation mechanisms in β -Type Ti-35Nb-2Ta-3Zr alloy via FSP leading to surface strengthening. *Metall. Mater. Trans. A* 46, 4813–4818. doi: 10.1007/s11661-015-3089-8
- Wang, Y. B., Zhao, Y., Lian, Q., Liao, X. Z., Valiev, R. Z., Ringer, S. P., et al. (2010). Grain size and reversible beta-to-omega phase transformation in a Ti alloy. *Scr. Mater.* 63, 613–616. doi: 10.1016/j.scriptamat.2010.05.045
- Wu, S. Q., Ping, D. H., Yamabe-Mitarai, Y., Xiao, W. L., Yang, Y., Hu, Q. M., et al. (2014). {112}<111> twinning during $\bar{\epsilon}$ to body-centered cubic transition. *Acta Mater.* 62, 122–128. doi: 10.1016/j.actamat.2013.09.040
- Xiang, K., Chai, L., Wang, Y., Wang, H., Guo, N., Ma, Y., et al. (2020). Microstructural characteristics and hardness of CoNiTi medium-entropy alloy coating on pure Ti substrate prepared by pulsed laser cladding. *J. Alloys Compd.* 849:156704. doi: 10.1016/j.jallcom.2020.156704
- Xu, T., Kou, H., Li, J. S., Zhang, F. S., and Feng, Y. (2015). Effect of phase transformation conditions on the microstructure and tensile properties of Ti-3Al-15Mo-3Nb-0.2Si alloy. *J. Mater. Eng. Perform.* 24, 3018–3025. doi: 10.1007/s11665-015-1583-1
- Xu, T., Li, J. S., Zhang, S., Zhang, F., and Liu, X. (2016a). Cold deformation behavior of the Ti-15Mo-3Al-2.7Nb-0.2Si alloy and its effect on α precipitation and tensile properties in aging treatment. *J. Alloys Compd.* 682, 404–411. doi: 10.1016/j.jallcom.2016.04.293
- Xu, T., Zhang, S. S., Zhang, F., Kou, H., and Li, J. S. (2016b). Effect of $\bar{\epsilon}$ -assisted precipitation on $\beta \rightarrow \alpha$ transformation and tensile properties of Ti-15Mo-2.7Nb-3Al-0.2Si alloy. *Mater. Sci. Eng. A Struct. Mater.* 654, 249–255. doi: 10.1016/j.msea.2015.12.052
- Xu, T., Zhang, S., Cui, N., Cao, L., and Wan, Y. (2019a). Effects of strain rate and annealing temperature on the evolution of microstructure and texture in pure niobium. *Metall. Mater. Trans. A Phys. Metall. Mater. Sci.* 50, 5297–5313. doi: 10.1007/s11661-019-05425-4
- Xu, T., Zhang, S., Cui, N., Cao, L., and Wan, Y. (2019b). Precipitation behavior of Ti15Mo alloy and effects on microstructure and mechanical performance. *J. Mater. Eng. Perform.* 28, 7188–7197. doi: 10.1007/s11665-019-04456-7
- Yang, Y., Castany, P., Bertrand, E., Cornen, M., Lin, J. X., and Gloriant, T. (2018). Stress release-induced interfacial twin boundary ω phase formation in a β type Ti-based single crystal displaying stress-induced α' martensitic transformation. *Acta Mater.* 149, 97–107. doi: 10.1016/j.actamat.2018.02.036
- Yu, S., Yu, Z., Wang, G., Han, J., Ma, X., and Dargusch, M. S. (2011). Biocompatibility and osteoconduction of active porous calcium-phosphate films on a novel Ti-3Zr-2Sn-3Mo-25Nb biomedical alloy. *Colloids Surf. B Biointerfaces* 85, 103–115. doi: 10.1016/j.colsurf.2011.02.025
- Yu, Z., Zhang, M., Tian, Y., Cheng, J., Ma, X., Liu, H., et al. (2014). Designation and development of biomedical Ti alloys with finer biomechanical compatibility in

- long-term surgical implants. *Front. Mater. Sci.* 8, 219–229. doi: 10.1007/s11706-014-0254-8
- Zhang, L., Chen, L., and Wang, L. (2020). Surface modification of titanium and titanium alloys: technologies, developments, and future interests. *Adv. Eng. Mater.* 22:1901258. doi: 10.1002/adem.201901258
- Zhang, L.-C., and Chen, L.-Y. (2019). A review on biomedical titanium alloys: recent progress and prospect. *Adv. Eng. Mater.* 21:1801215. doi: 10.1002/adem.201801215
- Zheng, Z., Chai, L., Xiang, K., Huang, W., Wang, Y., Liu, L., et al. (2020). Typical microstructural characteristics of Ti–5Al–5Mo–5V–3Cr–1Fe metastable β Ti alloy forged in $\alpha+\beta$ region. *Acta Metall. Sin.* doi: 10.1007/s40195-020-01115-y

Conflict of Interest: The authors declare that the research was conducted in the absence of any commercial or financial relationships that could be construed as a potential conflict of interest.

Copyright © 2020 Cheng, Li, Yu, Du, Zhang, Zhang, Gai, Wang, Song and Yu. This is an open-access article distributed under the terms of the Creative Commons Attribution License (CC BY). The use, distribution or reproduction in other forums is permitted, provided the original author(s) and the copyright owner(s) are credited and that the original publication in this journal is cited, in accordance with accepted academic practice. No use, distribution or reproduction is permitted which does not comply with these terms.



Influence of Strontium phosphate Coating on the Degradation of Physical Vapor Deposition Sprayed Mg Coating on Ti6Al4V Substrate to Promote Bone Tissue Healing

Muhammad Ibrahim^{1,2}, Xiaoming Yu³, Lili Tan^{1*} and Ke Yang^{1*}

¹ Institute of Metal Research, Chinese Academy of Science, Shenyang, China, ² School of Materials Science and Engineering, University of Science and Technology of China, Shenyang, China, ³ School of Material Science and Engineering, Shenyang Ligong University, Shenyang, China

OPEN ACCESS

Edited by:

Lechun Xie,
Wuhan University of Technology,
China

Reviewed by:

Shokouh Attarilar,
Shanghai Jiao Tong University, China
Liang-Yu Chen,
Jiangsu University of Science and
Technology, China

*Correspondence:

Lili Tan
ltan@imr.ac.cn
Ke Yang
keyang@imr.ac.cn

Specialty section:

This article was submitted to
Biomaterials,
a section of the journal
Frontiers in Materials

Received: 14 July 2020

Accepted: 18 August 2020

Published: 05 November 2020

Citation:

Ibrahim M, Yu X, Tan L and Yang K
(2020) Influence of Strontium
phosphate Coating on the Degradation
of Physical Vapor Deposition Sprayed
Mg Coating on Ti6Al4V Substrate to
Promote Bone Tissue Healing.
Front. Mater. 7:583240.
doi: 10.3389/fmats.2020.583240

Ti6Al4V is one of the commonly used orthopedic metallic materials, but its bioactivity is weak, which makes it challenging to produce bone integration between material and bone tissue. In this study, an Mg/SrP composite coating was prepared on Ti6Al4V, to promote bone tissue healing and shorten the healing cycle. The surface characterization, *in vitro* degradation performance and bioactivity of the composite coating, were investigated. The results revealed that Mg/SrP composite coating has more suitable degradation rate than Pure Mg, no cytotoxicity was found on the Mg/SrP composite coated samples, higher proliferation compared with the culture medium was found, indicating that the Mg/SrP composite coating is a candidate coating on Ti6Al4V to improve the bioactivity.

Keywords: Ti alloy, Mg/SrP coating, degradation, biocompatibility, Mg coating

INTRODUCTION

Ti-based metal is one of the metallic materials used in dentistry and orthopedic surgery to enhance or support or to replace an existing biological structure (Zhang and Chen, 2019; Hafeez et al., 2020; Liu et al., 2020). Most of these medical devices are made of pure Ti and its alloy, because of their excellent biocompatibility, enhanced corrosion resistance, and unique mechanical properties (Liu et al., 2004; Gode et al., 2015; Yu et al., 2018b; Ebrahimi et al., 2019; Ibrahim et al., 2020). In the 1950s, Per-Ingvar Branemark discovered the principles of osteointegration for the first time (Le et al., 2014). However, Ti-based metal has still some shortcomings yet to be resolved. The major challenge for Ti is to improve the osteointegration and enhance the bioactivity of the implants for bone regeneration and healing (Drago and Howell, 2012; Attarilar et al., 2019; Wang et al., 2020). 3D printed porous structure and surface modification are the conventional approaches to improve bone growth and enhance the bioactivity of Ti. Surface modifications such as CaP coating could accelerate bone growth, and the physicochemical changes of the implant could induce a firm bonding with the bone (Li et al., 2017).

Recently, Mg-based metals have shown great potential to be used as biocompatible and biodegradable materials, because of their excellent properties, including relatively close elastic modulus and density (41–45 GPa, 1.7–2.0 g/cm³) to the human bones (10–40 GPa, 1.8–2.1 g/cm³) (Staiger et al., 2006; Witte et al., 2006; Kraus et al., 2012; Sun et al., 2012; Yu et al., 2018a). Mg also exhibits a positive effect on bone tissue, which could improve the reconstruction and healing of the associated bone. Witte (2015) reported that Mg-based metals

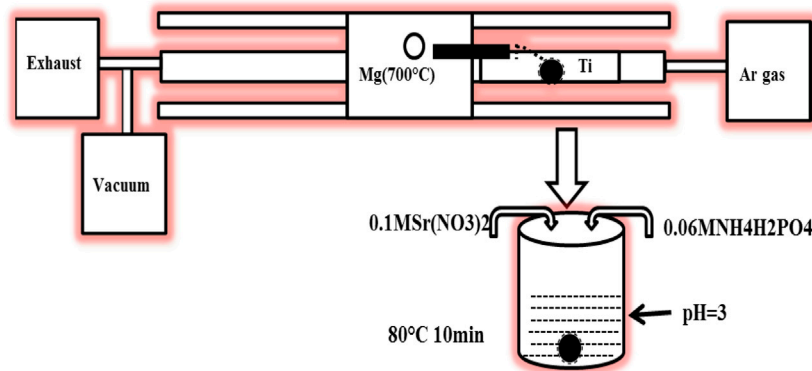


FIGURE 1 | The schematic diagram for Mg and Mg/SrP coatings.

showed a positive impact on the bone tissue, and high Mg ions activated the surrounding bone cells (Wang et al., 2015). Zhai et al. (2014) found that Mg also has a strong effect on the apoptosis of osteoclasts and osteoblast, and influences the proliferation. Therefore, Mg coating on Ti can enhance its osteointegration properties. The main problem that exists for Mg coating is its fast degradation (Salunke et al., 2011), mainly when applied on implants with large surface area exposed to the body fluid, leading to large pieces of layer peeling off the substrate and the high alkaline environment around the implants limits its application as a bone implant coating.

Strontium phosphate (SrP) a biocompatible coating was used to control the degradation rate of pure Mg. Sr^{2+} ions have the function to reduce bone resorption and cause to promote bone regeneration (Boyd et al., 2015). Further SrP coating has excellent corrosion rate and has been developed explicitly for biocompatible orthopedic implants (Ke et al., 2014). The morphology, size, concentration, charge, and surface properties; all of them have a high impact on preventing toxicity and harmful effects (Attarilar et al., 2020). To improve the biological function of Ti6Al4V alloys, some nanoscale (Mg, Sr)-HA powders were coated on its surface (Cao et al., 2019).

Therefore, in this work, a Mg/SrP composite coating was deposited on the surface of the Ti alloy, to regulate the degradation behavior of Mg-based metal coating, further promote the bone tissue healing and shorten the healing cycle of Ti alloy with the Mg^{2+} ions release from the surface. The biocompatibility and corrosion resistance of Mg/SrP composite coating on Ti alloy was also studied.

EXPERIMENTAL DETAILS

Materials and Methods

The schematic diagram of the Mg and Mg/SrP coatings preparation process is shown in **Figure 1**. Mg coatings were deposited on Ti6Al4V samples with a dimension of $\phi 10 \text{ mm} \times 3 \text{ mm}$ by Physical Vapor Deposition (PVD) method. Firstly Ti6Al4V substrate was polished, washed, ultrasonically cleaned, and then dried. The vapor generated from the source

of pure Mg (99.99 wt%) at 700°C was carried by an Ar flow of 250 sccm and deposited on the substrate at a temperature of 300°C . The vacuum pumps allowed the pressure of 10^{-1} Torr to collect the high purity Mg. In the designing or optimization of PVD, the coating thickness varies with the variation of source and substrate distance. So it is essential to control the gap between the source and substrate to control its depth because the coating with higher thickness lowered the coating adhesion and possibly may affect the bone tissue healing.

Mg coated samples were then treated with SrP coating. The SrP coating solution consisted of 0.06 M $\text{NH}_4\text{H}_2\text{PO}_4$ and 0.1 M $\text{Sr}(\text{NO}_3)_2$. The dilute HNO_3 was used to adjust the pH to 3, and then the samples were immersed in the solution for 10 min at 80°C . The coated samples were washed with ethanol and then warmly dried.

Characterization of Coatings

The surface and cross-section morphology of Mg and Mg/SrP coatings were observed by scanning electron microscope (SEM, S-3400 N) equipped with a dispersive energy spectrum (EDS). Furthermore, the compositions of the layers were characterized by X-ray diffractometry (XRD, Bruker D8 ADVANCE) using the CuK α line generated at 40 kV and 35 mA.

Electrochemical Test

A Gamry instrument (Reference 600) was used to examine the electrochemical corrosion test. The samples used for this purpose had an exposed area of 0.785 cm^2 and were molded in the epoxy resin. D-Hank's was used to perform the test at a temperature of 37°C . The composition of D-Hank's solution was listed in Table 1. The three-electrode cell used for this purpose consists of platinum as the counter electrode; a saturated calomel electrode as a reference electrode and the coated samples were working electrode. After the 1800 s, the test started at an open-circuit potential (OCP). At a frequency range of 100 kHz to 10 MHz, the electrochemical impedance spectroscopy (EIS) was carried out at the OCP. Concerning OCP, the potentiodynamic polarization test started at a scan rate of 0.5 mV/s and a voltage of -0.25 to 0.35 V . For each coated sample the experiment was repeated three

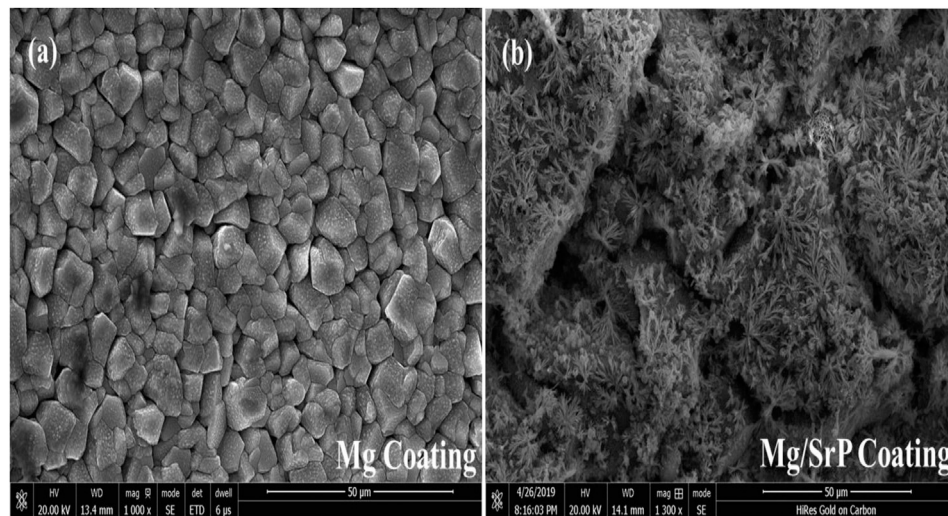


FIGURE 2 | Surface morphologies of the coatings of Mg **(A)** and Mg/SrP **(B)**.

times. The corrosion rate of Mg and Mg/SrP coating was measured with the following equation (Chen et al., 2019). I_{corr} the corrosion current density of the coating is measured by Tafel extrapolation of polarization curve, I_{corr} is related to P_i (average corrosion rate) in mm/year using the equation.

$$P_i = 22.85 I_{corr} \quad (1)$$

Immersion Test and Mg^{2+} Release

Mg and Mg/SrP coated samples with a size of $\phi 10 \text{ mm} \times 3 \text{ mm}$ were immersed in D-Hank's solution for nine days at the ratio of $1.25 \text{ cm}^2/\text{ml}$. The immersion solution was changed after each 24 h to keep it fresh. The pH value was recorded every 24 h before refreshing the solution. The release of Mg^{2+} from each sample in

D-Hank's solution at 1, 2, 3, 4, 5, 6, and 7 days were determined by using inductive-coupled plasma mass spectrometry (ICP-MS, Thermo, United States).

Cell Proliferation

MC3T3-E1 mouse preosteoblast cells were purchased from the College of Stomatology, Fourth Military Medical University, Xi'an, China. The α -MEM complete medium supplemented with 10% heat-inactivated fetal bovine serum, 100 U/ml penicillin, and 100 mg/ml streptomycin, were used for cell culture under the condition of 5% CO_2 at 37°C . MC3T3-E1 incubated cells were seeded on Mg and Mg/SrP coated samples in a 96-well plate with an initial density of 4×10^4 cells. Kit-8 (CCK-8, Japan) was used for this purpose. The cultured medium at the time point of 1, 3, and 5 days was transferred to new 96-well culture plates. CCK-8 solution (10% volume) was added onto the plates and incubated for 3 h at 37°C . A microplate reader was then used to quantify the absorbance of the solutions at 450 nm wavelength with a plate reader.

Statistical Analysis

Data were expressed in standard deviation (SD) and statistically, one-way analysis of variance (ANOVA) was analyzed with a post-hoc Tukey test. The significant P values of less than 0.05 were considered.

RESULTS AND DISCUSSION

Characterization of Coatings

Figure 2 presents the surface morphology of Mg and Mg/SrP coatings on the Ti substrate. Mg coating deposited smoothly and densely with an average particle size of $7 \mu\text{m}$ (Figure 2A). From the Mg/SrP composite coating observation, a small crystal-like

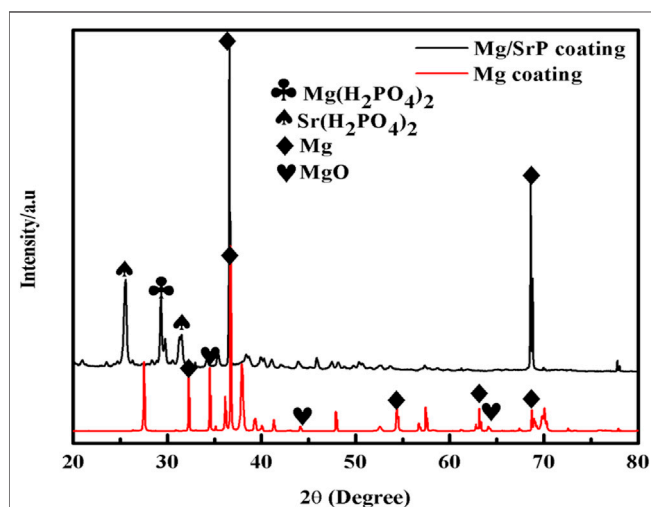


FIGURE 3 | XRD pattern of Mg and Mg/SrP coatings on Ti alloy.

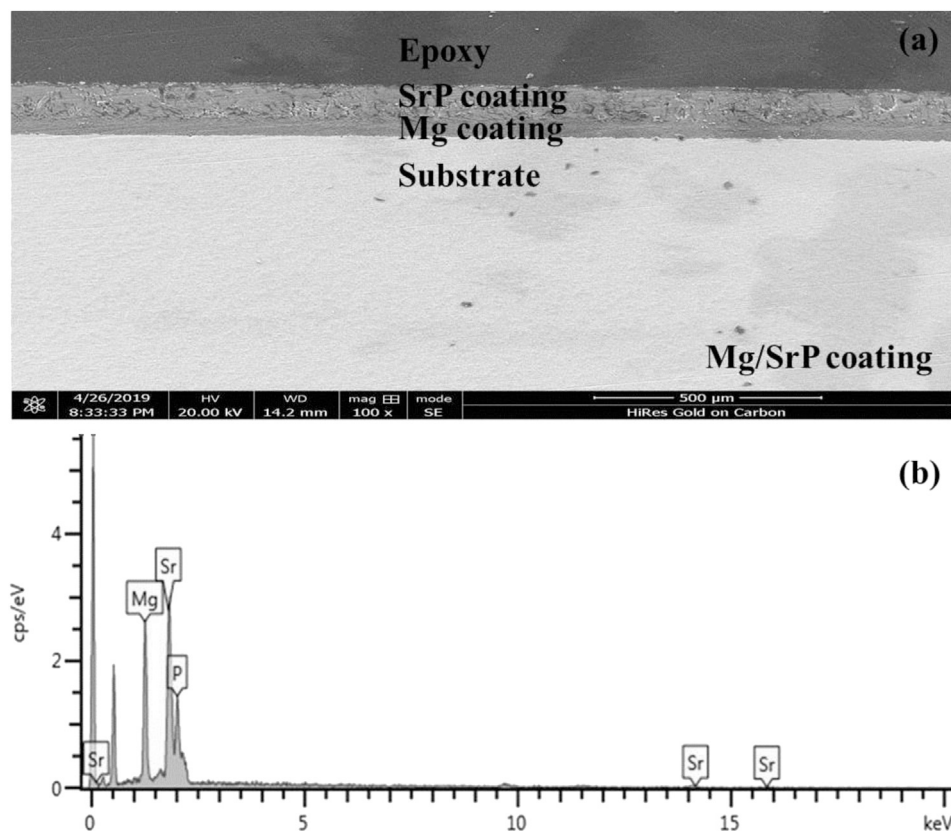


FIGURE 4 | Cross-section morphology (A) and EDS (B) results of the Mg/SrP coating.

pattern was observed (**Figure 2B**). From EDS analysis, there are Mg, Sr, and P elements in the Mg/SrP coating. Further analysis of the coating layer was carried out from the XRD pattern (**Figure 3**). The Mg coating consists of both Mg and MgO. In the Mg/SrP coating, in addition to the diffraction peak of the Mg, the existence of diffraction peaks belonging to $\text{Sr}(\text{H}_2\text{PO}_4)_2$ and $\text{Mg}(\text{H}_2\text{PO}_4)_2$ indicates the presence of crystallization in the coating, which arguments the strength of the coating with substrate because the coating strength with the substrate is a key factor for evaluation of its performance. Also, the low adhesion strength possibly delaminates the coating layer from the surface, which may cause the failure of the implant. Previous studies also reported the importance of coating strength with the substrate (Cao et al., 2019).

From the cross-section morphology of the coating shown in **Figure 4**, it can be seen that the thickness of Mg coating was about 50–52 μm and that of Mg/SrP was 99–101 μm (**Figure 4A**).

Electrochemical Measurements

The electrochemical corruptions of Mg and Mg/SrP coatings were characterized by potentiodynamic polarization curves and electrochemical impedance spectrometry. **Figure 5** showed the polarization curves and impedance spectra in D-Hank's solution at 37°C for both Mg and Mg/SrP coatings. **Table 2** presents the Tafel fitting results of both kinds of coating

surfaces. From the results we can see that the Mg/SrP coating exhibited a lower current density of $0.700 \pm 0.02 \mu\text{A}/\text{cm}^2$ compared to that of Mg coating ($3.400 \pm 1.01 \mu\text{A}/\text{cm}^2$), the corrosion rate of Mg/SrP coating is approximately $0.103 \pm 0.01 \text{ mm/year}$, also less than that of Mg ($0.52 \pm 0.21 \text{ mm/year}$). Similarly, from electrochemical impedance spectrometry (EIS), the higher the arc in the impedance spectrometry is, the higher the corrosion resistance of the material is. Hence, the corrosion resistance of the Mg/SrP coating is significantly higher than that of Mg coating (**Figure 5B**), which is also consistent with the potentiodynamic polarization curve. It implies that the SrP coating shows more resistant to corrosion than the Mg coating.

Figure 6 shows the equivalent circuit of Mg and Mg/SrP coating and **Table 3** shows the fitted data obtained with ZSimp Win software. C is the double-layer capacitance of solution and coating surface, Y04 is the constant phase element, whereas R_1 and R_2 show the solution and charge transfer resistance, respectively. From **Table 3** R_2 shows better corrosion resistance. The corrosion resistance of coating increases with SrP. To analyze the degradation of coating impedance is usually adopted. From impedance curves in **Figure 5**, one capacitive loop can be found on the Nyquist plot of the coating with Mg and Mg/SrP coating. Usually, a larger diameter of the circuit and higher impedance means better corrosion resistance of the

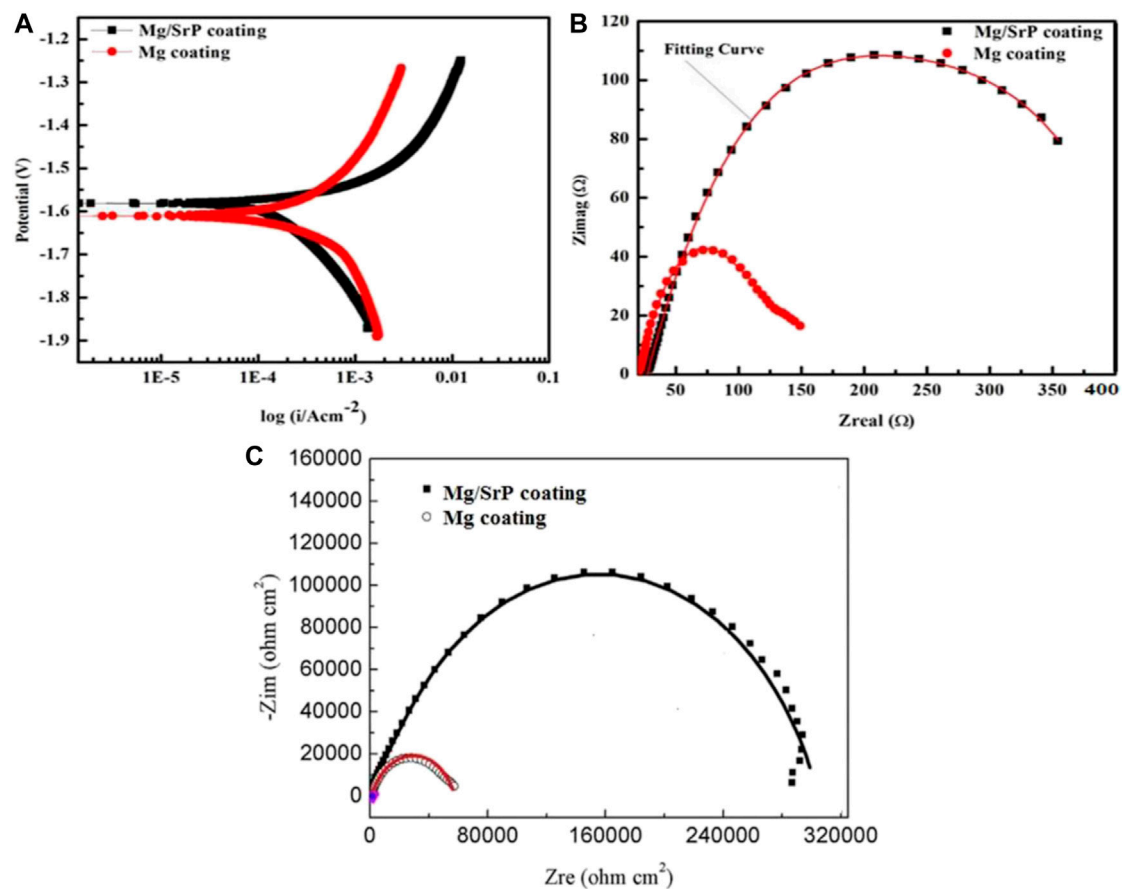


FIGURE 5 | Potentiodynamic polarization (A) electrochemical impedance spectroscopy (B) Nyquist curves (C) curves of Mg and Mg/SrP coatings in D-Hank's solution.

coating **Table 3**. Therefore Mg/SrP coating exhibited the highest degradation resistance.

Immersion Test

Biodegradable materials are implant materials gradually corroded *in vivo*, with the release of corrosion products, which dissolve completely and assist the healing tissue without implant residues (Li et al., 2014a). Biodegradable Mg-based materials have been investigated widely, due to its unique degradation in the physiological environment, to avoid the repeated surgery of

implants (Staiger et al., 2006; Chai et al., 2012; Zheng et al., 2014). Mg having similar mechanical properties with human bones and have a positive effect on the growth of bone tissue (Witte et al., 2008). The pH and Mg^{2+} ion release results of the coated samples immersed in D-Hank's solution shown in **Figure 7**. The products arising from the degradation of Mg influence apoptosis of osteoclasts and proliferation of osteoblasts has been observed to activate bone cell (Witte et al., 2005; Li et al., 2014b).

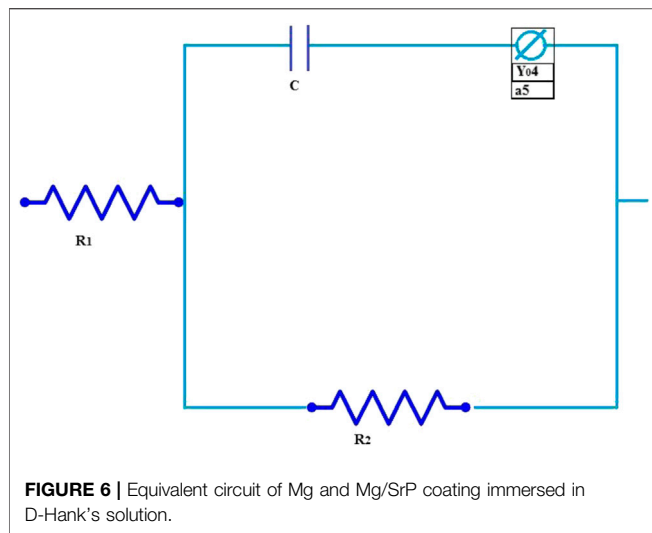
From the variation of pH, it can be seen that the pH value of Mg coated sample rises rapidly on the first day of immersion in D-Hank's solution to around 11, reaching a maximum, and this is significantly higher than the Mg/SrP coated sample and the blank control sample. In the following days, the pH value is on a downward trend, and the overall pH value drops rapidly. The pH of the Mg/SrP coated sample shifts up quickly to 9.75 after

TABLE 1 | The composition of D-Hank's solution (g/L).

KCl	KH_2PO_4	NaCl	$Na_2HPO_4 \cdot 7H_2O$	$NaHCO_3$	$C_{19}H_{14}O_5S$
0.4	0.06	8	0.06	0.35	0.02

TABLE 2 | Tafel fitting results based on potentiodynamic polarizations tested in D-Hank's solution.

Samples	Potential (V)	Current density ($\mu A/cm^2$)	Corrosion rate (mm/year)
Mg coating	-1.620 ± 0.02	3.400 ± 1.01	0.521 ± 0.21
Mg/SrP coating	-1.580 ± 0.01	0.700 ± 0.02	0.103 ± 0.01

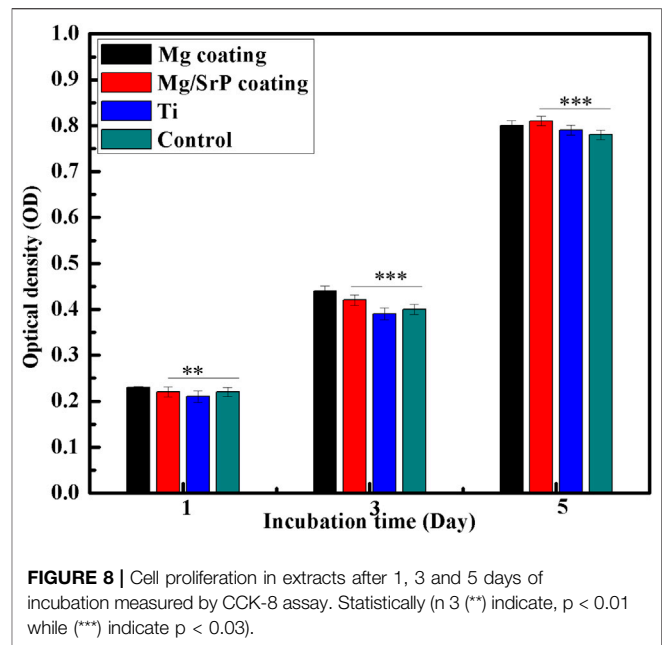


immersion on the first day, much lower than that of Mg coating on the first day, after that, its downward pH trend is much slower than that of Mg coating, showing more Mg coating left in the Mg/SrP coating and presenting higher pH values in a more extended degradation period.

The deposition of SrP coating protected the Mg coating from degradation, but the existence of small non-uniform pores permeated the solution to inert the inner layer, and the degradation of Mg coating occurred. When Mg^{2+} ions dissolved into the solution, the cation reacted with OH^- to

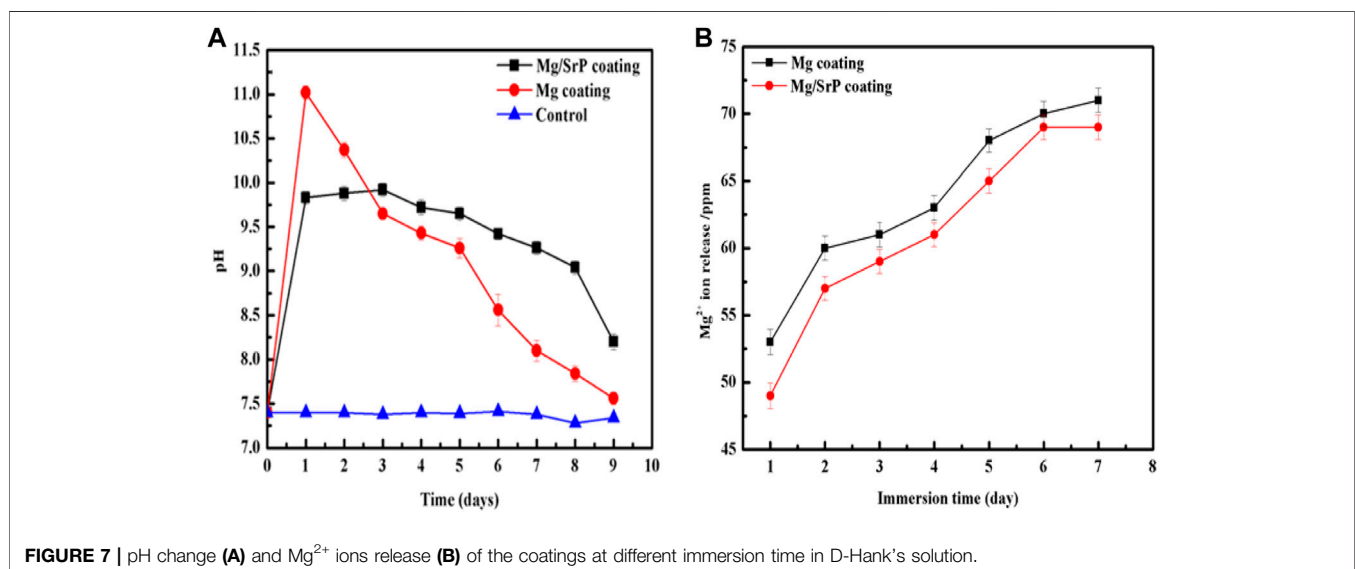
TABLE 3 | Fitting results of Mg and Mg/SrP coatings immersed in D-Hank's solution.

Samples	R_1 (ohm)	$Y04$ ($S \cdot s^{-1} \cdot n$)	C (F)	R_2 (ohm)
Mg coating	22.23	2.963×10^{-4}	0.543	7,160
Mg/SrP coating	18.34	2.123×10^{-4}	0.632	7,533



form $Mg(OH)_2$ in the solution. There is a release of Mg^{2+} ions during a different period, with both Mg coated and Mg/SrP coated samples indicating a rising tendency. After 7 days of immersion, the numbers of ions gradually rise to 73 and 69 ppm respectively, which is an indication of the continuous degradation of Mg coating.

Although Mg coating has well-established biocompatibility, its uncontrolled degradation and corrosion in the body fluid are the main factors affecting its reliability to support bone growth or tissues healing process. Also, the degradation of Mg causes hydrogen evolution (Witte et al., 2008). Both the formation of hydrogen gas cavities and the alkalization of the body fluid around the tissues interfere with the adhesion of the cell to



the implants. The presence of SrP coating on pure Mg coated implants reduced these phenomena. The release of Mg^{2+} ions around the implant overlaps the osteoblastic lineage and cell proliferation, which leads to the regeneration of bone tissues.

Cell Proliferation

Mg-Sr alloy containing a trace element of strontium may stimulate and increase the formation of new bone (Gu et al., 2012; Tie et al., 2016).

Figure 7 shows the cell proliferation assessment during the first 5 days. At 1st day, Mg/SrP coating cultured with cells showed relatively comparable absorbance, while Mg coating had a relatively lower absorbance in comparison with the control group. However, the absorbance, after 3 days, increased drastically for the entire group. At Day 3 and 5, Mg/SrP showed a relative increase in cell proliferation as compared to Mg coating and Ti groups. At day one, it is revealed from **Figure 8** that Mg coating shows a lower value of Optical Density (OD) as compared to the control, meaning that cell proliferation was inhibited because of the slight increase in pH value of the medium (Yang et al., 2013) which is not suitable for murine BMSCs to be adapted in the early stage. But cytoplasmic membrane would not disrupt due to the variation of pH. It's because the human body fluid is a considerable buffer system, which can very well adjust the pH of the physiological system. After 3 and 5 days, the absorbance measurements increased drastically for all groups, and no noticeable change was found. The results of 5 days demonstrate no cytotoxicity effect for both Mg and Mg/SrP coated implants. Furthermore, the overall proliferation of Mg/SrP group is better than the other group, due to the controlled release of ions and slower degradation of the coating. Mg^{2+} and Sr^{2+} ions in the coating surface have been found to accelerate diffusion, cell adhesion which favor effect on the mineralization and to improve cell proliferation (Cao et al., 2019).

REFERENCES

- Attarilar, S., Salehi, M. T., Al-Fadhalah, K. J., Djavanroodi, F., and Mozafari, M. (2019). Functionally graded titanium implants: characteristic enhancement induced by combined severe plastic deformation. *PLoS One*. 14 (8), e0221491. doi:10.1371/journal.pone.0221491
- Attarilar, S., Yang, J., Ebrahimi, M., Wang, Q., Liu, J., Tang, Y., et al. (2020). The toxicity phenomenon and the related occurrence in metal and metal oxide nanoparticles: a brief review from the biomedical perspective. *Front. Bioeng. Biotechnol.* 8, 822. doi:10.3389/fbioe.2020.00822
- Boyd, A. R., Rutledge, L., Randolph, L., Mutreja, I., and Meenan, B. J. (2015). The deposition of strontium-substituted hydroxyapatite coatings. *J. Mater. Sci. Mater. Med.* 26 (2), 65. doi:10.1007/s10856-014-5377-z
- Cao, L., Ullah, I., Li, N., Niu, S., Sun, R., Xia, D., et al. (2019). Plasma spray of biofunctional (Mg, Sr)-substituted hydroxyapatite coatings for titanium alloy implants. *J. Mater. Sci. Technol.* 35 (5), 719–726. doi:10.1016/j.jmst.2018.10.020
- Chai, H., Guo, L., Wang, X., Gao, X., Liu, K., Fu, Y., et al. (2012). *In vitro* and *in vivo* evaluations on osteogenesis and biodegradability of a β -tricalcium phosphate coated magnesium alloy. *J. Biomed. Mater. Res.* 100A (2), 293–304. doi:10.1002/jbm.a.33267
- Chen, J., Zhang, Y., Ibrahim, M., Etim, I. P., Tan, L., and Yang, K. (2019). *In vitro* degradation and antibacterial property of a copper-containing micro-arc

CONCLUSION

In the present work, Mg/SrP composite coating was prepared on Ti6Al4V alloy. Mg/SrP coating initiated from the formation of $MgO/Mg(OH)_2$ carrying SrP. After immersion in the solution containing ammonium dihydrogen phosphate and strontium, the conversion reaction developed, $MgO/Mg(OH)_2$ -SrP flakes into duplex coating, which cover the entire Mg coating after 10 min. Such coating system reduced the degradation rate of pure Mg coating and will serve in the future to control the degradation of Mg base coating. Further Mg/SrP coating cultured extract show high proliferation of MC3T3-E1 cells compared with normal culture medium. These results revealed that the Mg/SrP composite coating showed a higher corrosion resistance and exhibited significant biocompatibility compared with pure Mg coating on Ti alloy.

DATA AVAILABILITY STATEMENT

The raw data supporting the conclusions of this article will be made available by the authors, without undue reservation.

AUTHOR CONTRIBUTIONS

MI and XY performed the experiments and wrote the manuscript. KY and LT revised it.

FUNDING

This work was supported by National Key R&D Program of China (No. 2016YFC1101804) 2016YFC1100604) and National Natural Science Foundation of China (51971222, 51631009, 51801220).

- oxidation coating on Mg-2Zn-1Gd-0.5Zr alloy. *Colloids Surf. B Biointerfaces*. 179, 77–86. doi:10.1016/j.colsurfb.2019.03.023
- Drago, C., and Howell, K. (2012). Concepts for designing and fabricating metal implant frameworks for hybrid implant prostheses. *J. Prosthodont.* 21 (5), 413–424. doi:10.1111/j.1532-849x.2012.00835.x
- Ebrahimi, M., Attarilar, S., Shaeri, M. H., Gode, C., Armoon, H., and Djavanroodi, F. (2019). An investigation into the effect of alloying elements on corrosion behavior of severely deformed Cu-Sn alloys by equal channel angular pressing. *Arch. Civ. Mech. Eng.* 19, 842–850. doi:10.1016/j.acme.2019.03.009
- Gode, C., Attarilar, S., Eghbali, B., and Ebrahimi, M. (2015). "Electrochemical behavior of equal channel angular pressed titanium for biomedical application," AIP Conference Proceeding. 020041, 1–9. doi:10.1063/1.4914232
- Gu, X., Xie, X., Li, N., Zheng, Y., and Qin, L. (2012). *In vitro* and *in vivo* studies on a Mg-Sr binary alloy system developed as a new kind of biodegradable metal. *Acta Biomaterialia*. 8 (6), 2360–2374. doi:10.1016/j.actbio.2012.02.018
- Hafeez, N., Liu, J., Wang, L., Wei, D., Tang, Y., Lu, W., et al. (2020). Superelastic response of low-modulus porous beta-type Ti-35Nb-2Ta-3Zr alloy fabricated by laser powder bed fusion. *Addit. Manuf.* 34, 101264. doi:10.1016/j.addma.2020.101264
- Ibrahim, M., Yu, X., Chen, J., Etim, I. P., Misra, R. D. K., Tan, L., et al. (2020). Fabrication of biodegradable $MgXCu(X=0, 0.1, 0.4, 0.7)$ coating on Ti6Al4V alloy with enhanced antibacterial property. *Mater. Technol.*, 1–10. doi:10.1080/10667857.2020.1738672

- Ke, C., Pohl, K., Birbilis, N., and Chen, X.-B. (2014). Protective strontium phosphate coatings for magnesium biomaterials. *Mater. Sci. Technol.* 30 (5), 521–526. doi:10.1179/1743284714y.0000000508
- Kraus, T., Fischerauer, S. F., Hänzli, A. C., Uggowitz, P. J., Löffler, J. F., and Weinberg, A. M. (2012). Magnesium alloys for temporary implants in osteosynthesis: in vivo studies of their degradation and interaction with bone. *Acta Biomater.* 8 (3), 1230–1238. doi:10.1016/j.actbio.2011.11.008
- Le, V. Q., Pourroy, G., Cochis, A., Rimondini, L., Abdel-Fattah, W. I., Mohammed, H. I., et al. (2014). Alternative technique for calcium phosphate coating on titanium alloy implants. *Biomater.* 4 (1), e28534. doi:10.4161/biom.28534
- Li, H., Zheng, Y., and Qin, L. (2014a). Progress of biodegradable metals. *Prog. Nat. Sci.: Materials International.* 24 (5), 414–422. doi:10.1016/j.pnsc.2014.08.014
- Li, R. W., Kirkland, N. T., Truong, J., Wang, J., Smith, P. N., Birbilis, N., et al. (2014b). The influence of biodegradable magnesium alloys on the osteogenic differentiation of human mesenchymal stem cells. *J. Biomed. Mater. Res.* 102 (12), 4346–4357. doi:10.1002/jbm.a.35111
- Li, X. K., Gao, P., Wan, P., Pei, Y. F., Shi, L., Fan, B., et al. (2017). Novel bio-functional magnesium coating on porous Ti6Al4V orthopaedic implants: in vitro and in vivo study. *Sci. Rep.* 7, 40755. doi:10.1038/srep40755
- Liu, S., Liu, J., Wang, L., Ma, R. L.-W., Zhong, Y., Lu, W., et al. (2020). Superelastic behavior of *in-situ* eutectic-reaction manufactured high strength 3D porous NiTi-Nb scaffold. *Scripta Mater.* 181, 121–126. doi:10.1016/j.scriptamat.2020.02.025
- Liu, X., Chu, P., and Ding, C. (2004). Surface modification of titanium, titanium alloys, and related materials for biomedical applications. *Mater. Sci. Eng. R Rep.* 47 (3), 49–121. doi:10.1016/j.mser.2004.11.001
- Salunke, P., Shanov, V., and Witte, F. (2011). High purity biodegradable magnesium coating for implant application. *Mater. Sci. Eng., B* 176 (20), 1711–1717. doi:10.1016/j.mseb.2011.07.002
- Staiger, M. P., Pietak, A. M., Huadmai, J., and Dias, G. (2006). Magnesium and its alloys as orthopedic biomaterials: a review. *Biomaterials* 27 (9), 1728–1734. doi:10.1016/j.biomaterials.2005.10.003
- Sun, Y., Zhang, B., Wang, Y., Geng, L., and Jiao, X. (2012). Preparation and characterization of a new biomedical Mg-Zn-Ca alloy. *Mater. Des.* 34, 58–64. doi:10.1016/j.matdes.2011.07.058
- Tie, D., Guan, R., Liu, H., Cipriano, A., Liu, Y., Wang, Q., et al. (2016). An *in vivo* study on the metabolism and osteogenic activity of bioabsorbable Mg-1Sr alloy. *Acta Biomater.* 29, 455–467. doi:10.1016/j.actbio.2015.11.014
- Wang, J., Witte, F., Xi, T., Zheng, Y., Yang, K., Yang, Y., et al. (2015). Recommendation for modifying current cytotoxicity testing standards for biodegradable magnesium-based materials. *Acta Biomater.* 21, 237–249. doi:10.1016/j.actbio.2015.04.011
- Wang, Q., Zhou, P., Liu, S., Attarilar, S., Ma, R. L.-W., Zhong, Y., et al. (2020). Multi-scale surface treatments of titanium implants for rapid osseointegration: a review. *Nanomaterials* 10 (6), 1244. doi:10.3390/nano10061244
- Witte, F. (2015). Reprint of: the history of biodegradable magnesium implants: a review. *Acta Biomater.* 23, S28–S40. doi:10.1016/j.actbio.2015.07.017
- Witte, F., Fischer, J., Nellesen, J., Crostack, H.-A., Kaese, V., Pisch, A., et al. (2006). *In vitro* and *in vivo* corrosion measurements of magnesium alloys. *Biomaterials* 27 (7), 1013–1018. doi:10.1016/j.biomaterials.2005.07.037
- Witte, F., Hort, N., Vogt, C., Cohen, S., Kainer, K. U., Willumeit, R., et al. (2008). Degradable biomaterials based on magnesium corrosion. *Curr. Opin. Solid State Mater. Sci.* 12 (5–6), 63–72. doi:10.1016/j.cossms.2009.04.001
- Witte, F., Kaese, V., Haferkamp, H., Switzer, E., Meyer-Lindenberg, A., Wirth, C., et al. (2005). *In vivo* corrosion of four magnesium alloys and the associated bone response. *Biomaterials* 26 (17), 3557–3563. doi:10.1016/j.biomaterials.2004.09.049
- Yang, X., Li, M., Lin, X., Tan, L., Lan, G., Li, L., et al. (2013). Enhanced *in vitro* biocompatibility/bioactivity of biodegradable Mg-Zn-Zr alloy by micro-arc oxidation coating contained Mg₂SiO₄. *Surf. Coating. Technol.* 233, 65–73. doi:10.1016/j.surfcoat.2013.01.052
- Yu, X., Ibrahim, M., Liu, Z., Yang, H., Tan, L., and Yang, K. (2018a). Biofunctional Mg coating on PEEK for improving bioactivity. *Bioact. Mater.* 3 (2), 139–143. doi:10.1016/j.bioactmat.2018.01.007
- Yu, X., Ibrahim, M., Lu, S., Yang, H., Tan, L., and Yang, K. (2018b). MgCu coating on Ti6Al4V alloy for orthopedic application. *Mater. Lett.* 233, 35–38. doi:10.1016/j.matlet.2018.08.063
- Zhai, Z., Qu, X., Li, H., Yang, K., Wan, P., Tan, L., et al. (2014). The effect of metallic magnesium degradation products on osteoclast-induced osteolysis and attenuation of NF- κ B and NFATc1 signaling. *Biomaterials* 35 (24), 6299–6310. doi:10.1016/j.biomaterials.2014.04.044
- Zhang, L. C., and Chen, L. Y. (2019). A review on biomedical titanium alloys: recent progress and prospect. *Adv. Eng. Mater.* 21 (4), 1801215. doi:10.1002/adem.201801215
- Zheng, Y. F., Gu, X. N., and Witte, F. (2014). Biodegradable metals. *Mater. Sci. Eng. R Rep.* 77, 1–34. doi:10.1016/j.mser.2014.01.001

Conflict of Interest: The authors declare that the research was conducted in the absence of any commercial or financial relationships that could be construed as a potential conflict of interest.

Copyright © 2020 Tan, Ibrahim, Yu and Yang. This is an open-access article distributed under the terms of the Creative Commons Attribution License (CC BY). The use, distribution or reproduction in other forums is permitted, provided the original author(s) and the copyright owner(s) are credited and that the original publication in this journal is cited, in accordance with accepted academic practice. No use, distribution or reproduction is permitted which does not comply with these terms.



Research Progress of Titanium-Based High Entropy Alloy: Methods, Properties, and Applications

Ning Ma¹, Shifeng Liu^{1*}, Wei Liu¹, Lechun Xie^{2*}, Daixiu Wei^{3*}, Liqiang Wang⁴, Lanjie Li⁵, Beibei Zhao⁵ and Yan Wang^{1*}

¹ School of Metallurgical Engineering, Xi'an University of Architecture and Technology, Xi'an, China, ² Hubei Key Laboratory of Advanced Technology for Automotive Components, Wuhan University of Technology, Wuhan, China, ³ Institute for Materials Research, Tohoku University, Sendai, Japan, ⁴ State Key Laboratory of Metal Matrix Composites, School of Material Science and Engineering, Shanghai Jiao Tong University, Shanghai, China, ⁵ Chengsteel Group Co., Ltd., HBIS Group Co., Ltd., Chengde, China

OPEN ACCESS

Edited by:

T. S. Sampath Kumar,
Indian Institute of Technology Madras,
India

Reviewed by:

Peter K. Liaw,
The University of Tennessee,
Knoxville, United States
Demircan Canadinc,
Koç University, Turkey

*Correspondence:

Shifeng Liu
liushifeng66@xauat.edu.cn
Lechun Xie
xielechun@whut.edu.cn
Daixiu Wei
wei1987xiu@imr.tohoku.ac.jp
Yan Wang
wangyan140511@xauat.edu.cn

Specialty section:

This article was submitted to
Biomaterials,
a section of the journal
Frontiers in Bioengineering and
Biotechnology

Received: 07 September 2020

Accepted: 19 October 2020

Published: 11 November 2020

Citation:

Ma N, Liu S, Liu W, Xie L, Wei D,
Wang L, Li L, Zhao B and Wang Y
(2020) Research Progress
of Titanium-Based High Entropy Alloy:
Methods, Properties,
and Applications.
Front. Bioeng. Biotechnol. 8:603522.
doi: 10.3389/fbioe.2020.603522

With the continuous progress and development in the biomedicine field, metallic biomedical materials have attracted the considerable attention of researchers, but the related procedures need to be further developed. Since the traditional metal implant materials are not highly compatible with the human body, the modern materials with excellent mechanical properties and proper biocompatibility should be developed urgently in order to solve any adverse reactions caused by the long-term implantations. The advent of the high-entropy alloy (HEA) as an innovative and advanced idea emerged to develop the medical implant materials through the specific HEA designs. The properties of these HEA materials can be predicted and regulated. In this paper, the progression and application of titanium-based HEAs, as well as their preparation and biological evaluation methods, are comprehensively reviewed. Additionally, the prospects for the development and use of these alloys in implant applications are put forward.

Keywords: titanium-based high entropy alloy, biomedical application, implant, complex alloys, multi-principal element alloys

INTRODUCTION

In recent decades, bio-medical materials are widely used in implants and repair surgeries due to their high strength, wear, corrosion resistance, and biocompatibility (Saini, 2015). In order to improve the bone tissue rehabilitation in biomedical applications, a kind of materials should be selected that possess similar properties to the natural bone so it can maintain the cell adhesion function after implantation, promote the tissue repair, and accelerate the healing process. Among all the biomedical implant materials, metallic ones are the most widely used material group in the clinical practices. The metallic biomaterials include stainless steel, CoCrMo alloy, NiTi shape memory alloy, magnesium alloy, titanium, and its alloys (Saini, 2015; Liu et al., 2020; Wang W. et al., 2020). Titanium and its traditional alloys are ideal biomedical materials with good mechanical properties, biocompatibility, and corrosion resistance. These materials are mostly used in orthopedics and dental implants (Niinomi, 2003, 2008; Geetha et al., 2009; Zhu et al., 2016;

Zhang et al., 2017; Rabadia et al., 2018), such as plates, stents, hip and knee joint replacements, dental roots, etc. However, pure titanium and its alloys also have some limitations such as poor wear resistance in which the material wears out and produces some metallic particles and debris under long-term and repeated stress conditions. These metallic particles and debris can cause local tissue lesions and inflammation. The Ti-6Al-4V and Ti-6Al-7Nb alloys are known as the traditional Ti alloys (Kobayashi et al., 1998; Tamilselvi et al., 2006; Assis and Costa, 2007; Ding et al., 2016; Wang H. et al., 2019). These two materials fulfill the strength requirement of the implant, but the alloying elements such as the Al and V can cause toxic effects and adversely influence the live tissues and organs. The Al element can accumulate in the brain, liver, spleen, kidney, thyroid, and other tissues and organs and cause some degree of damages (Attarilar et al., 2020). Also, the V element may cause bone softening, anemia, and nerve disorders. Moreover, the elastic modulus of these two titanium alloys (about 120 GPa) is still very high compared to natural bone (10~35 GPa). Niinomi (2008) found that titanium alloys with low elastic modulus have better load transfer characteristics than the alloys with high elastic modulus. The dense metal implant bears most of the applied load and leads to a significant reduction of stress level in the periphery of bone tissue, hence the density and strength of the bone tissue gradually decrease. This phenomenon is known as the stress shielding effect, which causes slow bone healing, bone resorption, implant loosening, and failure.

Recently, high-entropy alloys (HEAs) are known as novel metallic functional materials and they attract considerable attention. HEAs have great potential in the field of biomedicine and seem to find lots of applications in the medical industry (Yan and Zhang, 2020). The concept of HEA was originated from increasing the number of elements to increase the mixing entropy of the material to achieve the purpose of a stable solid solution alloy formation. They are also called multi-principal element alloys (MPEAs) or compositionally complex alloys (CCAs) (Miracle and Senkov, 2017; George et al., 2020). Based on the multiple element principal, HEAs are the representative of a new class of alloys that provide better performance through composition adjustment and the controlling methods, in which the phase composition encountered some transitions from a single-phase solid solution toward a variety of complex phase compositions. Moreover, researchers have divided a large number of HEAs into two main categories and analyzed their deformation mechanisms (Brechtel et al., 2020). The first one is based on the crystallographic structure of the phase and includes FCC-based, BCC-based, HCP-based, amorphous, and intermetallic HEAs. The second one is categorized according to the phase types and includes single-phase, dual-phase, eutectic and multi-phase HEAs. The HEAs had attracted substantial attention due to their excellent properties, such as high strength/hardness, high wear resistance, high fracture toughness, excellent low temperature performance and structural stability, good corrosion resistance, oxidation resistance, etc. (Juan et al., 2015; Xu et al., 2015; Shang et al., 2017; Chen J. et al., 2018; Jin et al., 2018; Qiu, 2018; Sharma et al., 2018; Shuang et al., 2019; Tian et al., 2019; George et al., 2020; Yao et al., 2020). For instance, Průša et al. (2020)

investigated the strengthening mechanism of ultrafine-grained CoCrFeNiNb HEA by mechanical alloying and spark plasma sintering that showed ultra-high strength of 2412 MPa and high hardness of 798 ± 9 HV at 1000°C. Furthermore, researchers have also realized that rapid oxidation under high temperature conditions limits the high-temperature applicability of HEAs. The addition and content of alloying elements are the key factors affecting the oxidation resistance and application of HEAs. Recent research have confirmed that the addition of Al and Cr to the alloy can effectively improve the oxidation resistance of HEAs, and the formation of some complex oxides can also provide better protection for the alloy (Waseem and Ryu, 2020).

This new type of alloy and its modern concept breaks the bottleneck of traditional material design and introduce new ideas for the research and development of high-performance metallic materials. Therefore, the design of Ti-HEAs materials with excellent biocompatibility and good mechanical properties is of great significance for the advancement of medical implants.

EMERGENCE AND DEVELOPMENT OF TITANIUM-BASED HEAS

Yeh et al. (2004) and Yeh (2006) introduced the HEAs in 2004, this new class of metallic materials usually composed of 5 or more metallic elements in nearly equiatomic proportions (Cantor et al., 2004; Miracle and Senkov, 2017; Zhang et al., 2018). Although the composition of high entropy alloys is very complex, it is usually composed of a single phase or two phase structures with proper stability and flexibility (George et al., 2020).

The HEA design is based on the four effects, including the high-entropy effect, the lattice distortion, sluggish diffusion, and the “cocktail” effect (Zhang et al., 2014). The high entropy effect is the landmark concept of HEAs. Initially, scholars believe that the alloy which contains the multi-principal elements will be led to the production of various intermetallic compounds and or complex microstructures. However, after a while, they have discovered a special phenomenon in which HEAs do not form a large number of intermetallic compounds, rather they tend to form a simple BCC, HCP, and FCC phase or even amorphous structures after solidification, this phenomenon is defined as the high-entropy effect. Due to this high-entropy effect, the high mixing entropy strengthens the mutual dissolution between elements and thereby hindering the formation of intermetallic compounds. In general, HEAs include five or more elements that each of them has the same probability of occupying lattice points. The difference in atomic sizes during the formation of the solid solution will cause lattice distortion in the crystal structure, which is called the lattice distortion effect. When the lattice distortion energy is too high, the crystal cannot maintain a stable structure, and the distorted lattice will collapse to form an amorphous phase or intermetallic compounds. But, whether in crystal or amorphous state, this distortion effect will affect the mechanical properties, electrical properties, optical properties, and even chemical properties of the material. The sluggish diffusion effect is attributed to the fact that in the casting process of HEAs, the coordinated diffusion of multiple

elements gets more difficult due to the liquid-solid phase changes, and severe lattice distortion will slow down the diffusion rate of the elements. Therefore, the phase separation rate at high temperature is slow, even suppressed at low temperatures, which is the major cause of nano-precipitate formation in the as-cast HEAs. The “cocktail” effect refers to a combination effect due to the multi-element interaction of the HEAs, which combines the original characteristics of various elements and relatively eliminates their shortcomings. Considering the “four core” effect, it is easy to obtain solid solution phases, nanostructures, and even amorphous structures with high thermal stability in HEAs (Yeh, 2006; Zhang et al., 2014), and they can be regarded as the composite materials on the atomic scale. Moreover, the HEA design is not a simple mixing of elements, it is necessary to consider the interaction between elements that will affect the overall performance of the obtained alloy (George et al., 2020). At present, the HEA design firstly is done through computer simulations in which the influence of thermodynamics and kinetics of the alloy needed to determine, also the impact of phase formation laws must be considered (Koval et al., 2019). Computer simulation generally uses first-principle calculations and phase diagram calculations to predict the structure, phase stability, and mechanical properties of HEAs. Ge H. et al. (2017) used the first principle calculations to predict the elastic and thermal properties of ternary or quaternary refractory HEAs containing Al, Ti, V, Cr, Nb, and Mo elements. They found that the calculated properties by simulations are consistent with the experimental results. In recent years, the Hume-Rothery criterion and the valence electron concentration criterion are often used to study the phase and formation possibility of HEAs. Yao et al. (2017) used the three parameters Ω , δ , and ΔH of common solid solutions, intermetallic compounds, and NbTaV- (Ti, W) series alloys to predict the phase formation of the designed alloy.

In the recent research reports, the most HEAs used in medical implants consist of refractory elements with non-toxic and hypoallergenic nature (Stiehler et al., 2008; Yurchenko et al., 2020). Biomedical HEAs usually employ Ti and non-toxic and hypoallergenic elements of group IV and group V as main components with the addition of Cu and Co elements on the matrix. Discovery of the latest three TiTaHf-based HEAs that showed significant biocompatibility in immersion experiments has demonstrated the potential of these novel HEAs can be utilized as long-term implant materials (Gurel et al., 2020). Among them, the presence of Nb and Zr elements have made enormous contributions to the enhancement of material corrosion performance. Yuan et al. (2019) prepared a series of TiZrHfNbTa HEAs with low modulus, good biocompatibility, and low magnetic susceptibility. In addition, they systematically analyzed and summarized the performance of HEAs with the addition of any element. It is found that Young's modulus in HEAs is relatively easier to control than the traditional implant metals, and the comparison between Ti-based HEAs and other metallic biomaterials are indicated in **Figure 1**. It provides more possibilities to utilize HEAs as biomedical implant materials in the future. Ching et al. (2020) reported a theoretical modeling technique to predict the properties of HEAs; they analyzed and predicted the performance of thirteen biocompatible HEAs.

Their proposed technology is based on the quantum mechanical measurements, total bond order density (TBOD), and partial bond order density (PBOD). It can deeply analyze the electronic structure and interatomic bonding of HEAs and has an important guiding significance for the design and application of medical HEAs in the future.

FABRICATION METHODS OF TITANIUM BASED HEAS

The HEA preparation methods mainly include ingot metallurgy, powder metallurgy, selective laser melting, laser cladding, magnetron sputtering, etc. Among them, ingot metallurgy, powder metallurgy, and selective laser melting are the most used techniques to prepare the bulk HEAs, while laser cladding and magnetron sputtering methods are commonly used in order to prepare HEA thin films or coatings. The advantages and limitations of various HEA preparation methods are listed in **Table 1**.

Preparation of Bulk HEAs Arc Melting

Arc melting is currently one of the most commonly used preparation methods for the production of bulk HEAs (Baldenebro-Lopez et al., 2015; Chen Y. et al., 2018; Hou et al., 2019; Zhang J. et al., 2020). The process involves pouring a certain proportion of metallic materials into the tongs. Then, after repeatedly vacuuming, the vacuum furnace fills with the protective argon gas. Subsequently, the elements are completely melted by the plasma arc heating of the electrode, then the water-cooled rapid cooling process solidifies the whole melt into an alloy. The schematic of arc melting is shown in **Figure 2**.

Recently, Wang and Xu (2017) prepared a TiZrNbTaMo equiatomic HEA by arc-melting, which contains BCC1 and BCC2 dual phases, and it shows a good corrosion resistance in phosphate buffer solution. Dirras et al. (2016) explored the necking and fracture surfaces of the as-cast TiHfZrTaNb HEA, and they revealed a combination of multiple slip bands, grain boundary distortion, as well as shallow and deep dimples, which exhibited the high tensile plastic behavior. Yuan et al. (2019) developed the TiZrHfNbTa HEAs, and they focus on Ti₂₅Zr₂₅Nb₂₅Ta₂₅, Ti₄₅Zr₄₅Nb₅Ta₅, and Ti₁₅Zr₁₅Nb₃₅Ta₃₅ HEA. The transmission electron microscopy (TEM) and SEM images of three HEAs are shown in **Figure 3**. Typical dendritic morphology enriched with Nb and Ta are shown in **Figure 3A,C**, while the equiaxed grains is shown in **Figure 3B**. Furthermore, Ti₄₅Zr₄₅Nb₅Ta₅ HEA exhibited lower modulus values (57 Gpa) than the equiatomic TiZrHfNbTa HEA, which is similar to Young's modulus of cortical bone (10~30 Gpa). The mechanical properties of HEAs prepared by arc-melting are shown in **Table 2**. In addition, to further explore the corrosion resistance and wear resistance of the TiZrTaHfNb HEA, Motalebzadeh et al. (2019) made a comparison of TiZrTaHfNb and Ti_{1.5}ZrTa_{0.5}Hf_{0.5}Nb_{0.5} HEA with 316L, CoCrMo, and Ti6Al4V alloys. The corrosion product morphologies of the samples after the electrochemical test in the phosphate buffer saline (PBS) electrolyte are shown

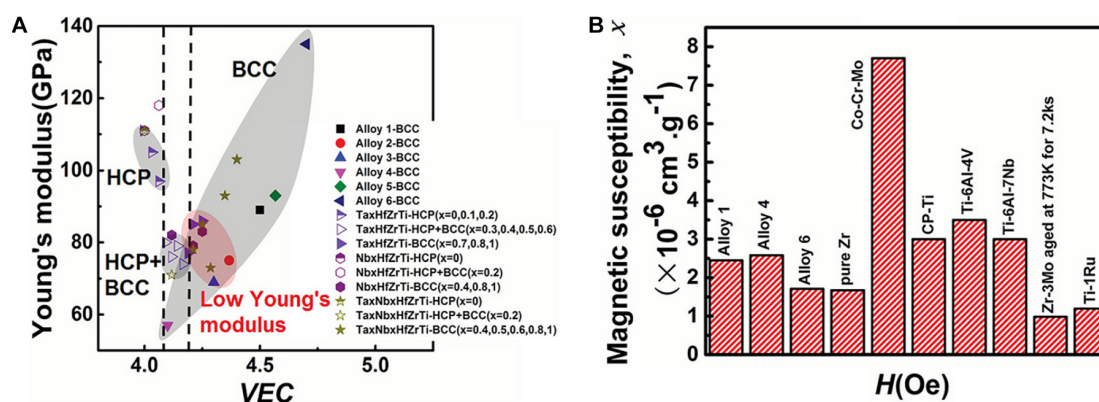


FIGURE 1 | Performance comparison of titanium-based HEAs and other metallic alloys, **(A)** Dependence of Young's modulus and crystalline phase structure on VEC in all the HEAs investigated. **(B)** Comparison of magnetic susceptibilities of alloys 1, 4, 6, and pure Zr with the alloys commonly used in medical devices. (Alloy 1: $\text{Ti}_{25}\text{Zr}_{25}\text{Nb}_{25}\text{Ta}_{25}$; Alloy 2: $\text{Ti}_{31.67}\text{Zr}_{31.67}\text{Nb}_{31.66}\text{Ta}_5$; Alloy 3: $\text{Ti}_{35}\text{Zr}_{35}\text{Nb}_{25}\text{Ta}_5$; Alloy 4: $\text{Ti}_{45}\text{Zr}_{45}\text{Nb}_5\text{Ta}_5$; Alloy 5: $\text{Ti}_{21.67}\text{Zr}_{21.67}\text{Nb}_{21.66}\text{Ta}_{35}$; Alloy 6: $\text{Ti}_{15}\text{Zr}_{15}\text{Nb}_{35}\text{Ta}_{35}$) (Yuan et al., 2019). Reproduced from Yuan et al. (2019) with permission.

TABLE 1 | The advantages and limitations of HEAs preparations.

Preparation methods	Advantages	Limitations	References
Arc Melting	<ul style="list-style-type: none"> ➢ Simple process ➢ Wide range of applications 	<ul style="list-style-type: none"> ➢ Exist casting defects such as composition segregation, coarse structure, internal shrinkage cavity etc. 	Zhang J. et al., 2020
Powder Metallurgy	<ul style="list-style-type: none"> ➢ Near net shape forming ➢ Higher utilization of material ➢ Uniform composition ➢ Save metals and reduce costs 	<ul style="list-style-type: none"> ➢ Poor toughness ➢ Higher die cost 	Ge W. et al., 2017; Wang et al., 2017
Magnetron sputtering	<ul style="list-style-type: none"> ➢ Film thickness can be controlled by adjusting sputtering parameters. ➢ Low requirements on target composition ➢ High sputtering rate, and low base temperature can obtain a dense film surface 	<ul style="list-style-type: none"> ➢ Higher preparation cost. ➢ Complex equipment ➢ Lower target utilization 	Yan et al., 2018; Zhang et al., 2018
Laser cladding	<ul style="list-style-type: none"> ➢ High melting and cooling rate ➢ Small heat affected zone ➢ Metallurgical combination of coating and substrate 	<ul style="list-style-type: none"> ➢ The cladding layer is easy to crack ➢ Uneven distribution of composition 	Xingwu et al., 2018; Yan et al., 2018; Liu J. et al., 2019

in **Figure 4**. It can be seen that significant pitting corrosion was detected on the surfaces of 316L, CoCrMo, and Ti6Al4V alloy. On the contrary, there are not any clear hints of pit formation on TiZrTaHfNb and $\text{Ti}_{1.5}\text{ZrTa}_{0.5}\text{Hf}_{0.5}\text{Nb}_{0.5}$ HEA surfaces. Annealing can effectively improve the mechanical properties of the alloy. Researchers have investigated the effect of annealing on the microstructure and properties of titanium based HEA. Nagase et al. (2020) have studied the microstructure of equiatomic and non-equiatomic TiNbTaZrMo HEA, the dendrite coarsening and element segregation can be observed after annealing operation.

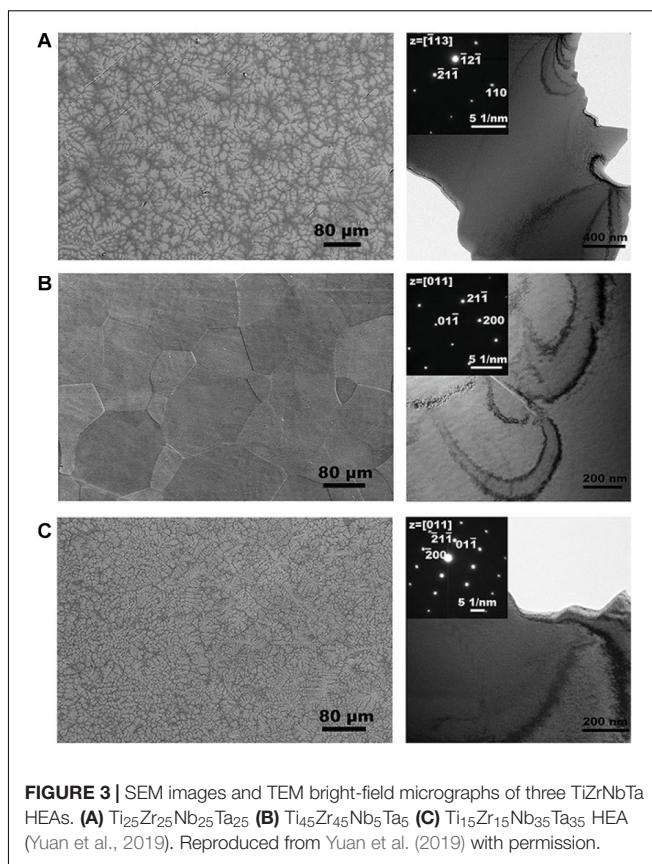
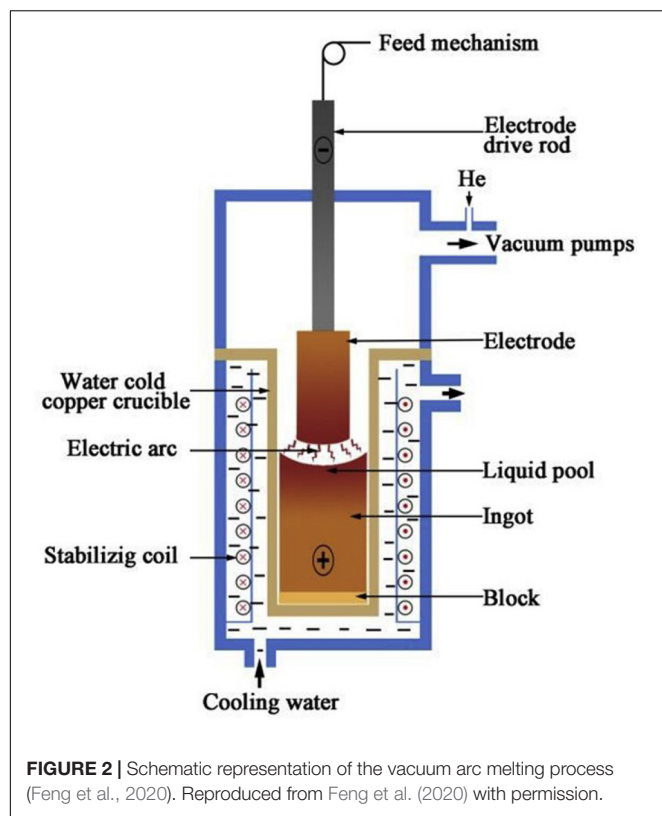
As one of the most important methods for preparing HEAs, a class of titanium-based HEAs prepared by arc melting, they believed to have excellent biological properties. However, the cytotoxicity assessment of Ti-based HEAs is still under study, and more *in vivo* and *in vitro* experiments are needed to confirm its biological behavior. Furthermore, mechanical properties are also one of the significant aspects of HEAs in evaluating the functionality of orthopedic materials. The yield strength and Vickers hardness of as-cast titanium-based HEAs are significantly

higher than that of 316Lstainless steel, CoCrMo alloy, and Ti6Al4V alloy, which seems promising to increase the longevity of orthopedic implants.

Powder Metallurgy

The HEA prepared by powder metallurgy (PM) generally uses elemental powders or pre-alloyed powders as the raw materials (Rao et al., 2014; Wang et al., 2017,a,b). Then, the bulk HEA is prepared through the steps of ball milling/mixing, pressing, sintering, and subsequent processing. Compared with the casting method, PM application can effectively decrease the segregation of alloy components, also it can eliminate the coarse and uneven metal casting structures and significantly improve the optimum raw material consumption (Málek et al., 2019a). However, there are limited studies on the preparation of HEAs by powder metallurgy, at present.

In addition to traditional mechanical processing methods, there are more and more researches and applications of powder metallurgy technology in biomedical metals. According to the recently reported studies about titanium-based HEA alloys,



Ti-Nb-Zr, Ti-Mo-Nb, Ti-Nb-Ag, Ti-Nb-Ta-Zr, Ti-Nb-Ta-Mn, Ti-Nb-Ta-V, Ti-Al-Ni-Co-Fe, and Ti-Nb-Hf-Zr-Ta systems (Sakaguchi et al., 2005; Gabriel et al., 2012; Wen et al., 2014; Hussein et al., 2015; Nazari et al., 2015; Aguilar et al., 2016; Anand Sekhar et al., 2019; Guo et al., 2019; Málek et al., 2019a,b) were prepared by PM. Wen et al. (2014) conducted a comparative analysis of Ti-Nb-Ag alloy after vacuum sintering and spark plasma sintering. The sample sintered in the vacuum furnace has some pores, while the samples sintered by SPS showed a dense structure on the surface. Additionally, in order to study the relationship between structure and mechanical properties with sintering time in HEAs prepared by PM, Málek et al. (2019b) found that HfNbTaTiZr alloy had better resistance to grain coarsening after sintering compared with the alloy obtained by arc melting, which had a small amount of porosity after sintering,

and the porosity is eliminated in the subsequent heat treatment process. Guo et al. (2019) have studied NbTaTiV alloy prepared by PM, which showed excellent properties, higher hardness of 510 HV, yield strength of 1.37 GPa, and compressive fracture strength of 2.19 GPa at room temperature.

Among these alloys, the Ti-Nb-Ta-Zr system alloys found many applications in the biomedical field (Wang et al., 2009, 2015, 2017; Wei et al., 2011; Liu et al., 2015; Ran et al., 2018; Gu et al., 2019; Hafeez et al., 2019, 2020). Sakaguchi et al. (2005) studied the deformation mechanism of Ti-Nb-Ta-Zr alloys with different Nb contents. At the same time, in order to further explore Ti-based HEA with biomedical prospects, the biological properties of other elements added to Ti-Nb-Ta-Zr HEA were studied by Stráský et al. (2017). Besides, Popescu et al. (2018)

TABLE 2 | Mechanical properties of HEA prepared by arc-melting and powder metallurgy.

Alloy	Procedures	Young's modulus (Gpa)	Yield strength (Mpa)	Elongation (%)	Hardness (Gpa)	References
Ti-Zr-Nb-Ta	Arc-melting	89	970	23	~	Yuan et al., 2019
Ti-Zr-Hf-Ta	Arc-melting	86	1367	4.07	~	Yuan et al., 2019
Ti-Zr-Hf-Nb	Arc-melting	83	728	18.7	~	Yuan et al., 2019
TiZrHfNbTa	Arc-melting	80	800~985	~	3.80	Senkov et al., 2011; Dirras et al., 2016
TiZrNbTaMo	Arc-melting	153	1390	~	4.90	Wang and Xu, 2017
TiZrHfCrMo	Arc-melting	~	1250	~	5.20	Nagase et al., 2020
TiNbTaZrFe	Powder metallurgy	52	2425	~	0.95	Popescu et al., 2018
TiNbTaZrCr	Arc-melting	~	~	~	6.16	Poletti et al., 2016

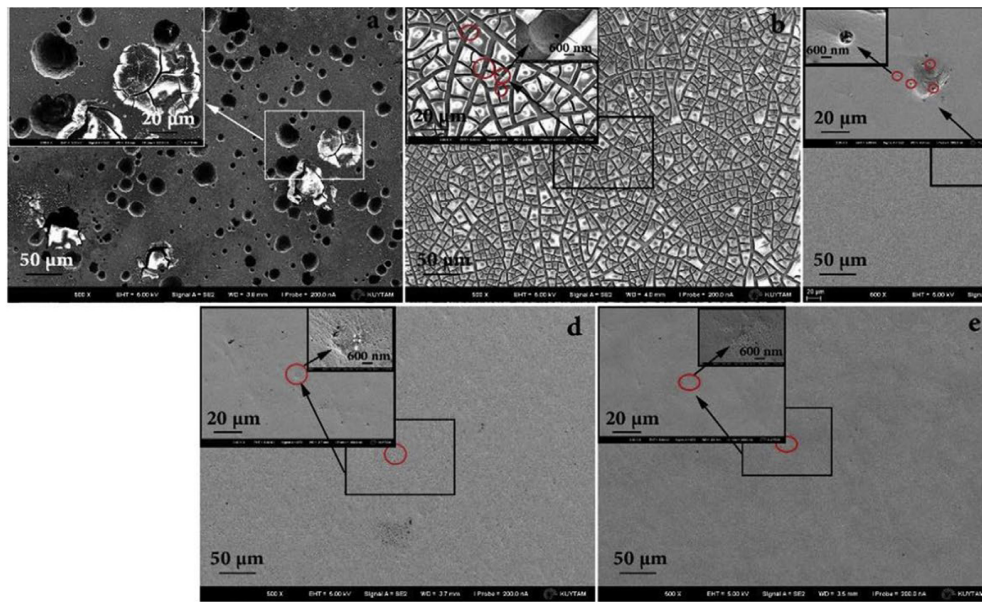


FIGURE 4 | FESEM images of different alloys after the potentiodynamic tests in PBS electrolyte at 37°C. **(a)** 316L, **(b)** CoCrMo alloy, **(c)** Ti6Al4V, **(d)** TiZrTaHfNb HEA, and **(e)** Ti_{1.5}ZrTa_{0.5}Hf_{0.5}Nb_{0.5} HEA (Motallebzadeh et al., 2019). Reproduced from Motallebzadeh et al. (2019) with permission.

prepared a novel Ti₄₀Nb₂₀Zr₂₀Ta₁₀Fe₁₀ HEA that was showed the outstanding corrosion resistance compared with Ti6Al4V. Cao et al. (2020) prepared TiNbTa_{0.5}ZrA_{0.5} HEA by PM and found that after hot-working, the TiNbTa_{0.5}ZrA_{0.5} HEA transformed from the initial BCC phase to BCC and HCP phase with 1740 MPa high-pressure yield strength (Chen et al., 2019).

From the above, it can be seen that powder metallurgy also can be an excellent alternative process to produce Ti-based alloys. This method can manufacture porous titanium parts at a lower processing temperature and allows more precise control of process variables and pore size, as well as physical and chemical properties. In the currently existing research, it is found that the Ti-based HEA prepared by powder metallurgy has excellent corrosion resistance in simulated body fluids (SBFs) and may become a potential biomedical substitute. In particular, TiNbZrTaFe HEA has ultra-low Young's modulus and better corrosion resistance than traditional mental implant materials. Especially with the development of laser 3D printing technology, personalized metal implants will gradually be promoted in clinics application. However, there are not many studies on the preparation of Ti-based HEAs by powder metallurgy, and follow-up on this method will continue to focus on its biomedical research.

Preparation of Thin Film HEAs

According to the reported methods for preparing HEA coatings, the surface modification techniques include electrochemical deposition (Soare et al., 2015), physical vapor deposition (PVD) (Khan et al., 2020; Xia et al., 2020), laser cladding (Zhang et al., 2017; Guo et al., 2018; Wang L. et al., 2019), plasma cladding (Anupam et al., 2019; Peng et al., 2019; Zhu et al., 2020), and thermal spraying (Wang et al., 2011; Vallimanalan et al., 2020),

etc. Particularly, the magnetron sputtering and laser cladding in the biomedical field are two relatively promising technologies for the preparation of HEA coatings. The properties of titanium-based HEA coatings prepared by two different methods are listed in Table 3.

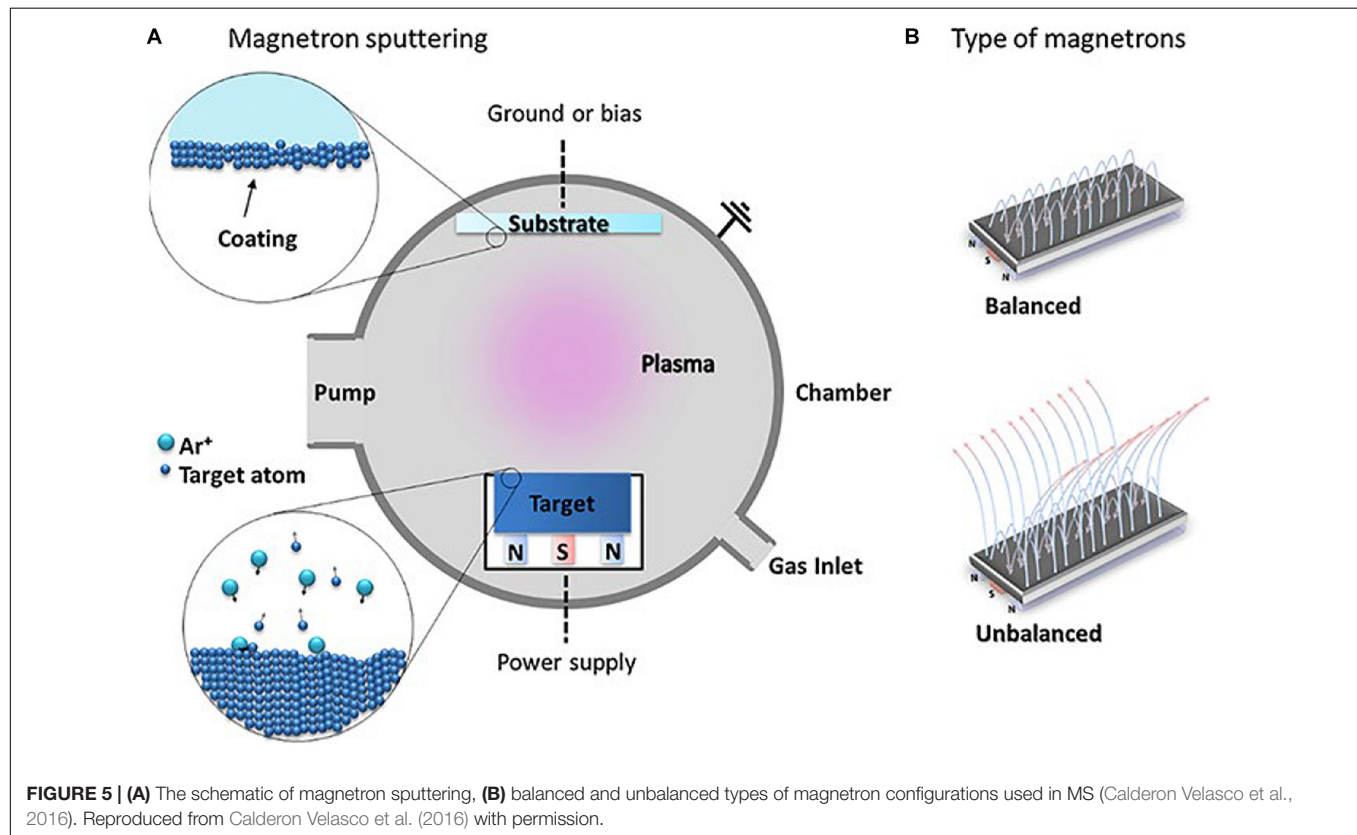
Magnetron Sputtering

As a significant surface modification technology, magnetron sputtering has been widely used in various fields. Magnetron sputtering, divided into direct current (DC) magnetron sputtering and radio frequency (RF) magnetron sputtering by the power supply type that is one of the PVD methods (Yan et al., 2018; Deng et al., 2020). This method utilizes the plasma phenomenon to bombard the target material in order to separate metal atoms from the surface of the target and deposit a thin film on the substrate surface. The argon (Ar) and nitrogen (N₂) gases are often used as the working gases for the preparation of HEA films. A schematic diagram of this process is shown in Figure 5 (Calderon Velasco et al., 2016). The working gas types and its parameters have an extensive impact on the structure and performance of the prepared HEA films.

Cui et al. (2020) studied the effect of different nitrogen contents on the microstructure and mechanical properties of the deposited HEA films, prepared the (AlCrTiZrHf)N film by RF magnetron sputtering. They found that the hardness and friction coefficient of the HEA film changed as the nitrogen flow increased and the film transformed from the initial amorphous state to the columnar structure with the FCC structure, this exhibits the low friction coefficient and excellent wear resistance. Liang et al. (2011) found that in the nitrogen flow rate of 4 SCCM, the hardness and elastic modulus of (TiVCrZrHf)N coatings reach respectively to their maximum values of about

TABLE 3 | Structural features and properties of HEA coatings prepared by laser cladding and magnetron sputtering.

Alloy	Substrates	Procedures	Phases	Young's modulus (GPa)	Hardness (GPa)	References
(TiVCrZrHf)N	Si	Magnetron sputtering	FCC	~267.3	23.8	Liang et al., 2011
(TiZrNbHfTa)C	M2 steel	Magnetron sputtering	FCC	~	~28	Braic et al., 2012
(TiZrNbHfTa)N	C45 steel	Magnetron sputtering	FCC	~	~33	Braic et al., 2012
TiTaHfNbZr	Ti-6Al-4V	Magnetron sputtering	Amorphous	~	12.51	Tüten et al., 2019
VAITiCrCu	Q235 steel	Magnetron sputtering	BCC	~	12	Chen et al., 2019
(TiHfZrVNb)N	Steel	Cathode vacuum-arc	FCC	~384	44.3	Pogrebnjak et al., 2014
TiZrNbWMo	45 steel	Laser Cladding	BCC+ β -Ti _x W _{1-x}	~	12.74	Zhang et al., 2017
TiAlNiSiV	Ti-6Al-4V	Laser Cladding	BCC	~	11.27~13.2	Zhang L.-C. et al., 2020
Ni-Cr-Co-Ti-V	Ti-6Al-4V	Laser Cladding	BCC	~	6.86	Cai et al., 2018

**FIGURE 5 |** (A) The schematic of magnetron sputtering, (B) balanced and unbalanced types of magnetron configurations used in MS (Calderon Velasco et al., 2016). Reproduced from Calderon Velasco et al. (2016) with permission.

23.8 \pm 0.8 and 267.3 \pm 4.0 GPa. Furthermore, the corrosion resistance of the NbTiAlSiZrN_x HEA coating was prepared by Xing et al. (2019) under the various nitrogen flow rates is significantly different from that of 304 stainless steel. Lukáč et al. (2020) prepared the HfNbTaTiZr HEA film that presents a nano-cell structure with fine surface microstructure and uneven distribution of defects by DC magnetron sputtering. Chen et al. (2019) have studied the mechanical properties and tribo-corrosion behavior of VAlTiCrCu HEA thin film deposited on the surface of 304 stainless steel at different deposition temperatures by magnetron sputtering. The film showed excellent corrosion resistance in the H₂SO₄ solution, and the hardness of the film at the deposition temperature of 300°C was 10.93 \pm 1.07 GPa, and the elastic modulus was 230.04 \pm 56.03 GPa.

Recently, Scholars have discovered that HEA or medium-entropy alloy films are expected to become the potential materials to be used as surface modification coatings on implants (Nguyen et al., 2018; Chen et al., 2020; Wang S. et al., 2020). Chen et al. (2020) prepared TiTaNb medium entropy alloy films by magnetron sputtering, which has excellent bio-corrosion, higher wear resistance, and higher hardness. In addition to spraying or depositing HEA coating on the surface of the implant material, depositing a hydroxyapatite layer on the surface of the implant material can also improve the biocompatibility of metal material by using the magnetron sputtering method. The deposition parameters can be controlled to obtain a thin, flawless, and uniform layer, with tight adhesion to the substrate, low roughness, corrosion and abrasion resistance, which are essential characteristics in medical applications. Despite the

higher Young's modulus of the HEA film compared to human bones, its application as a surface coating does not affect Young's modulus of the implant material.

Laser Cladding

Laser cladding, as a well-known surface modification process, mainly improves the hardness, wear resistance, and corrosion resistance of the surface of the substrate by cladding the alloy powder on the substrate. At present, the common substrate materials which were selected include Q235, Al, titanium, magnesium alloys, and tool steel (Zhang et al., 2017, 2019; Zhang J. et al., 2020; Tian et al., 2019; Wang L. et al., 2019). The principle diagram of laser cladding is shown in **Figure 6**. Moreover, the fundamental process parameters of laser cladding from several aspects are laser power size, powder feeding method, scanning speed, spot diameter, and overlap ratio (Shu et al., 2019).

In order to study the effect of the Ti element on the wear resistance of the coating prepared by laser cladding, Wang X. et al. (2020) studied CoCrFeNiTiX HEA coatings with different Ti content and found that the hardness and corrosion resistance of the coatings increased with the addition of Ti content. Furthermore, the main corrosion mechanism of CoCrFeNiTiX high entropy coatings in 3.5wt% NaCl solution is pitting corrosion. Cai et al. (2018) conducted an in-depth analysis of the phase composition and wear resistance of the Ni-Cr-Co-Ti-V HEA coating after the laser surface modification. The coating after the cladding and remelting process contains the Ti-rich phase and BCC phase with the excellent wear resistance. Zhang L.-C. et al. (2020) prepared Ti-based high entropy coatings (TiAlNiSiV) deposited on Ti-6Al-4V alloy, which showed the BCC structure and 1151~1357 HV hardness in the coating. In addition, the authors analyzed the coating strengthening

mechanism and found that solid solution strengthening and the dispersion strengthening are the main reasons for the hardness increase in the coating. Zhang et al. (2017) characterized the microstructure of the TiZrNbWMo HEA coating prepared by laser cladding. The microstructure mainly consists of dendrites and interdendritic structures. Also, through TEM characterization, nano-precipitates were found in this coating that can be explained by the high-entropy and slow diffusion effect of the HEA. Therefore, the combination of laser cladding technology on HEA is a new attempt in surface modification technology to improve the excellent performance of HEAs.

A great deal of research has focused on exploring the effects of surface morphology and composition on implants. The biomimetic design of the coating roughness and porosity without affecting the chemical structure of the substrate can accurately control the mechanical properties and biological reactions of the coating. Laser cladding is a flexible and effective method to obtain the desired properties by mixing different powder materials to form a special biological coating on the surface of the part. However, due to the inconsistency between the thermal expansion coefficient of the cladding layer and the matrix, surface quality problems such as cracks and pores in the cladding layer may be difficult to be accurately controlled.

In recent years, several concerns have been raised on the surface modification of titanium alloy (Liu W. et al., 2019; Wang Q. et al., 2020; Zhang L.-C. et al., 2020), which illustrates that the surface modification technologies play a significant role in improving the surface properties of the implant. In addition, surface modification methods have certain limitations because the antibacterial coatings deposited on the surface of the implant does not have long-term antibacterial performance due to the poor wear resistance and weak bonding forces between

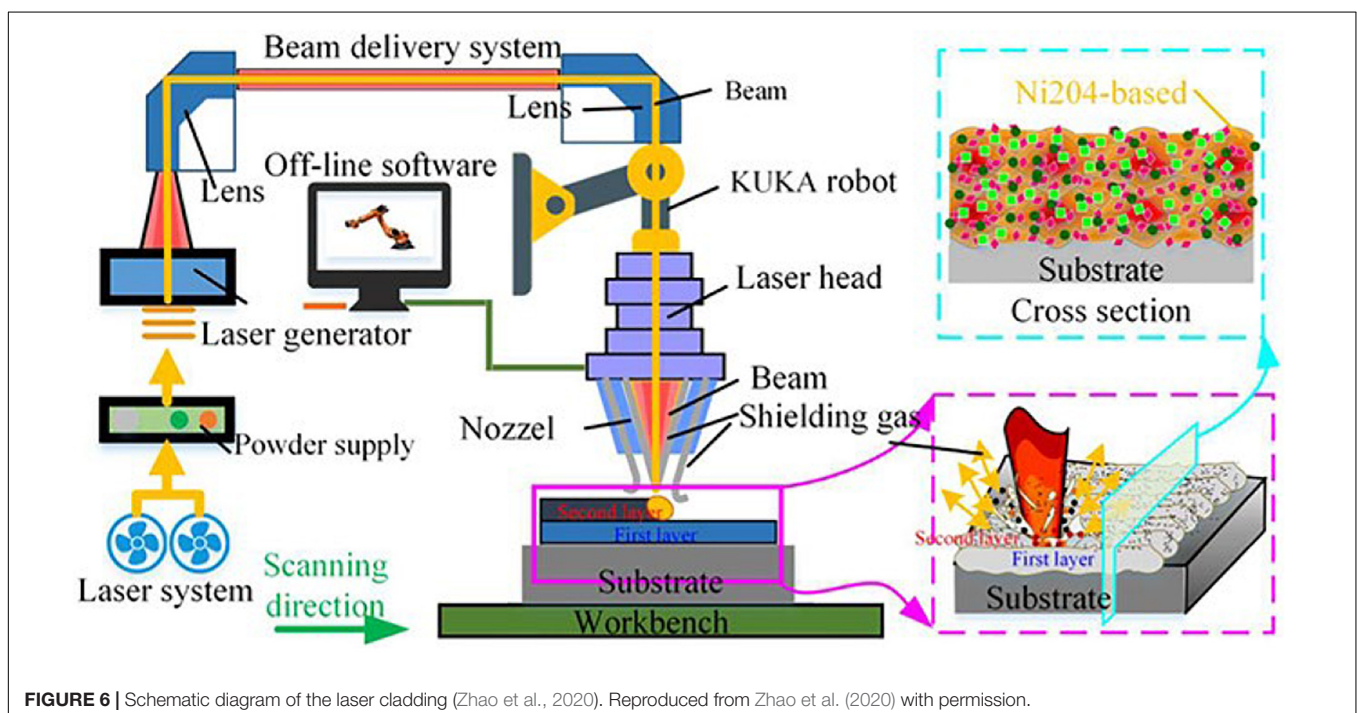


FIGURE 6 | Schematic diagram of the laser cladding (Zhao et al., 2020). Reproduced from Zhao et al. (2020) with permission.

the substrates. The titanium-based HEA coatings deposited by laser cladding and magnetron sputtering exhibit good corrosion resistance and wear resistance, hence HEAs can be used as a potential coating on the surface of long-term implants. However, the application of titanium-based HEA coatings in medical implants is still in its infancy, and more *in-vivo* experiments are needed in the later stages to ensure its potential use in cardiovascular or oral implants.

BIOMEDICAL APPLICATIONS

The biomedical materials can be divided into several groups, including metallic, polymer, ceramic, and bio-composite materials (Chen and Thouas, 2015). Among them, ceramic materials are favored in the clinical use of artificial joints, dental restorations, and cardiovascular system restoration operations due to their good wear properties, chemical stability, high hardness, and good biocompatibility. Biopolymer materials are widely used for drug release carriers, non-permanent implantable devices, tissue induced regeneration, and tissue engineering. In recent years, bioceramics have been widely used in orthopedic clinics due to their excellent biocompatibility, corrosion resistance, and rigidity. Patients can benefit from ceramic components to replace damaged bone tissue and fill bone defects with bioceramic particles. However, in the context of bone tissue engineering, ceramic scaffolds are easy to become brittle, and like metal scaffolds, its degradation rate is also difficult to accurately control. Therefore, the development of ceramic/polymer composite scaffolds with excellent mechanical properties has caused more and more researchers to pay more attention. On the other hand, the release of ions in ceramic materials can inhibit the inflammatory response of macrophages, which is believed to strongly affect the biological activity of cells and tissue regeneration. The hydrophobicity of the polymer makes it lack of cell adsorption capacity, which limits its application in medical implants without secondary modification (Lozano et al., 2010; Chen and Liu, 2016; Huang et al., 2018). Therefore, a secondary chemical treatment is introduced to treat the surface of the polymer-based scaffold and use organic solvents to increase micropores. Usually, surface modification or the addition of biologically active substances helps cell adhesion and proliferation. Therefore, the development of new biomaterials is very urgent, and the emergence of titanium-based HEAs is expected to meet actual clinical needs. It is very necessary to carry out corresponding *in vivo* and *in vitro* experiments.

In-vivo Evaluation

Before the implant material is officially put into clinical use, it is necessary to evaluate its biological safety both *in vivo* and *in vitro*. The most effective method for biocompatibility assessment is to conduct *in vivo* test but unfortunately, the direct biocompatibility test on the human body is risky, so animal implantation tests are usually used to evaluate the biological safety of materials. In particular, the possible applicability in human tissues should be interpreted with caution because the results of animal models may not necessarily predict the results of human use.

Guo et al. (2013) evaluated the biocompatibility of $\text{Ti}_{35}\text{Nb}_2\text{Ta}_3\text{Zr}$ alloy both *in vivo* and *in vitro* conditions and found that the degree of new bone formation around $\text{Ti}_{35}\text{Nb}_2\text{Ta}_3\text{Zr}$ implants is equivalent to that around Ti6Al4V implants, which showed excellent bone tissue compatibility *in vivo*. Stenlund et al. (2015) evaluated the osseointegration ability of Ti-Nb-Ta-Zr alloy that exhibits the same biological properties with implanted pure titanium in the rat tibial model. The light micrographs of undecalcified ground sections of the bone interface of Ti implants and Ti-Ta-Nb-Zr implants are shown in Figure 7. It could be observed that the osteoblasts arranged as a woven bone in the periphery of implanted material and indicated bone formation.

The medical research on Ti-based HEAs has remained in the material selection stage. As far as the authors of this article know, there is not any comprehensive *in vivo* evaluation study about Ti-based HEAs as implants. *In vivo* tests generally evaluate the following aspects: biomechanics, histology, histomorphometry, and ultrastructure, as well as gene expression. It is necessary to conduct in-depth research on the *in vivo* evaluation of Ti-based HEAs in the future.

In-vitro Evaluation

Antibacterial Test

According to reports, titanium alloys and other metallic materials as implants are susceptible to bacterial infections after surgery in the human body. At present, in addition to the use of antibiotics, implants with antibacterial properties are used in order to reduce the rate of bacterial infections during implant repair surgery. Once a bacterial infection occurs, the implant may be loosened from its place, and it may fail. The patient usually needs to take antibiotics for a long time or even undergo multiple operations to heal, which will increase the mental and financial burden for both patients and the medical system. Therefore, biomedical material researchers have been committed to developing some new materials with antibacterial function. The medical field also urgently needs to develop new biomedical materials that can play a long-term anti-infection function, thereby reducing the possibility of infection and reducing the abuse of antibiotics. It is of far-reaching significance to alleviate the suffering of patients and improve people's quality of life. In the previous research literature (Wu et al., 2006), some researchers tested the antibacterial properties of HEA by inoculating *Staphylococcus aureus*, *Escherichia coli*, *Klebsiella pneumoniae*, and *Pseudomonas aeruginosa* bacteria on the surface of HEA coating. After 24 h, it was found that the HEA coating had a significant inhibitory effect on the bacterial colony formation, and the antibacterial rate reached 99.99%, which indicated that the HEA coatings had positive antibacterial properties.

Generally, a small number of antibacterial elements such as Cu and Ag will be added to the antibacterial metal material to enhance its mechanical properties and the antibacterial activity (Liu et al., 2014; Han et al., 2020; Wang Y. et al., 2020). In recent years, some scholars have studied the antibacterial properties of copper-containing Ti-based HEAs and copper-containing HEAs. Ke et al. (2019) prepared a medical Ti-13Nb-13Zr-10Cu alloy

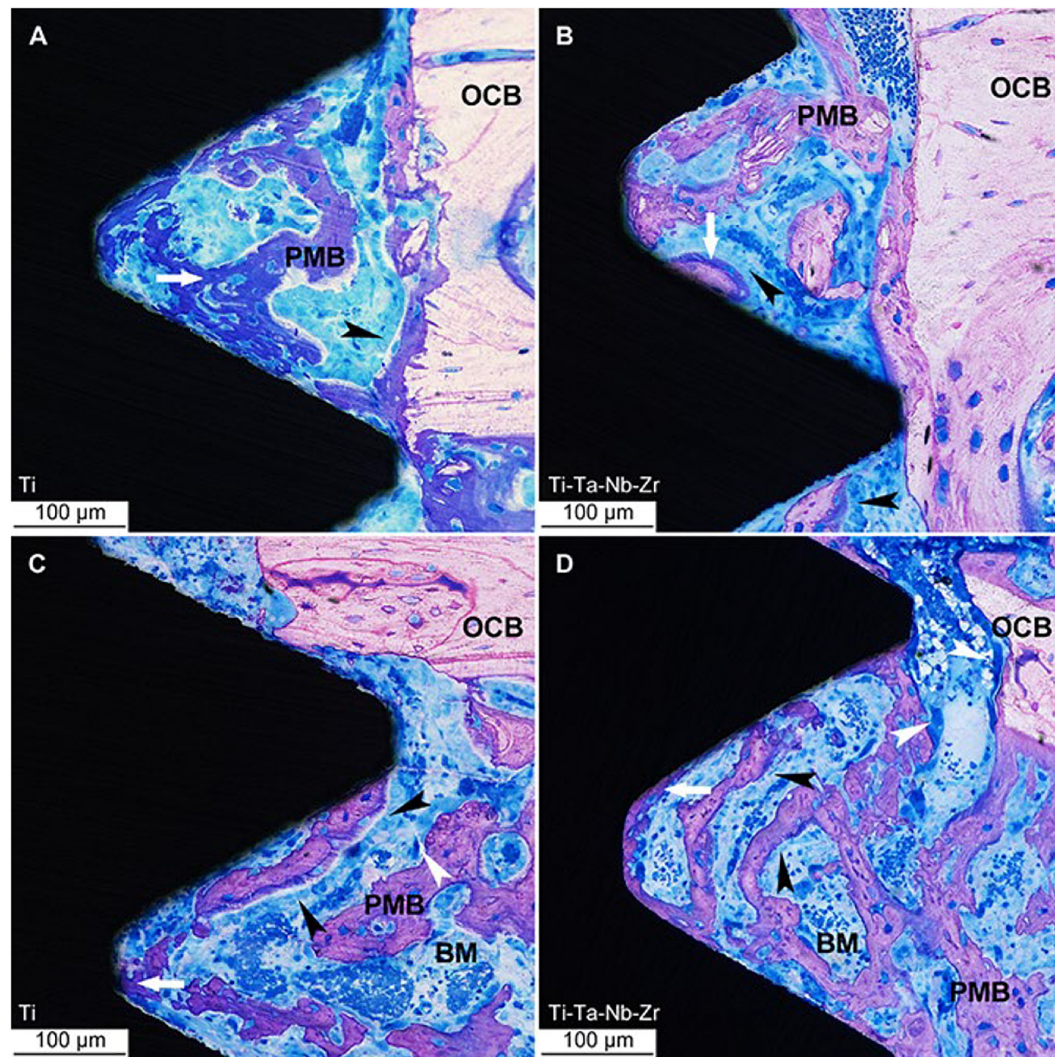


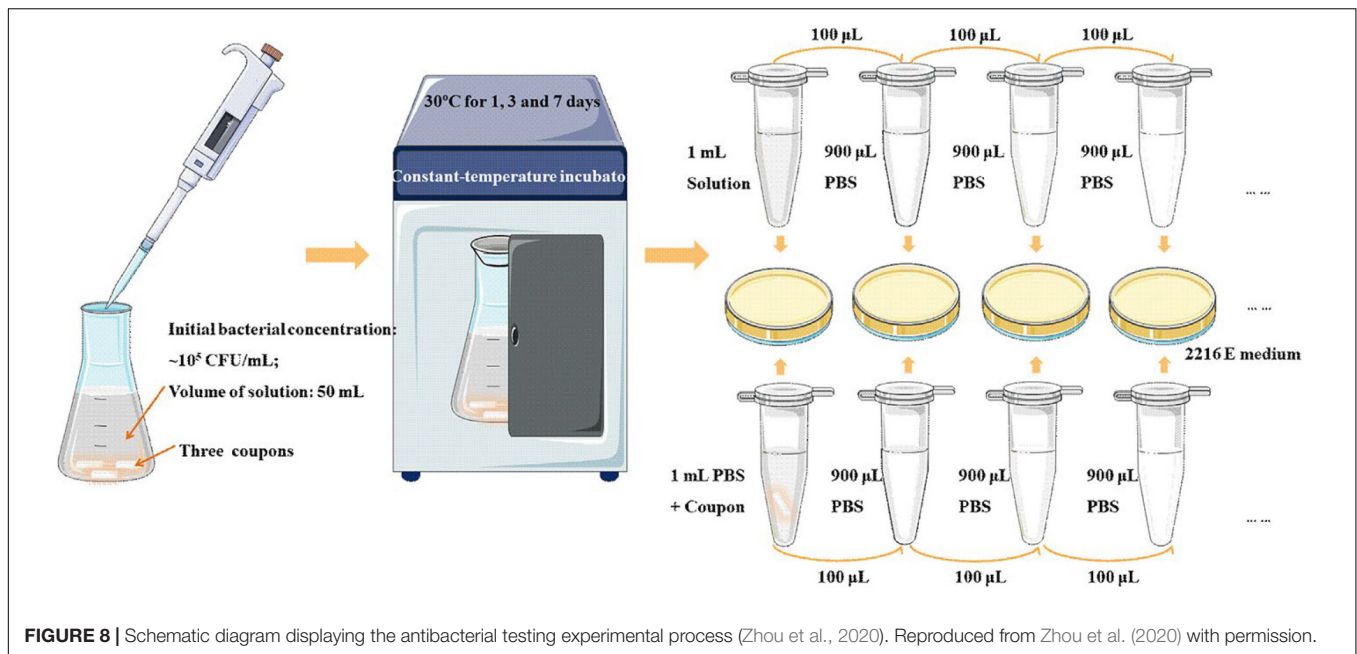
FIGURE 7 | Light micrographs of undecalcified ground sections of bone interface to Ti implants. (A–C) and Ti-Ta-Nb-Zr implants (B–D) after 7 days' healing. OCB, original cortical bone; PMB, partially mineralized bone; BM, bone marrow; white arrow = osteoid, white arrowhead = osteoclast and the black arrowheads = osteoblast seams (Stenlund et al., 2015). Reproduced from Stenlund et al. (2015) with permission.

that its elastic modulus was significantly lower than CP-Ti, and showed significant antibacterial activity after 24 h of *S. aureus* culture. In addition, Zhou et al. (2020) designed a novel Cu-bearing $\text{Al}_{0.4}\text{CoCrCuFeNi}$ high-entropy alloy (AHEA) that was used to prevent the growth of bio-corrosive marine bacteria. At the same time, the antibacterial properties of different samples (HEA and 304 stainless steel, and copper-containing 304 stainless steel and pure copper) were compared by three marine bacteria. The antibacterial test process is shown in Figure 8. After 1, 3, and 7 days of cultivation in the medium, the bacterial colonies on the HEA have significantly reduced, and the antibacterial effect was similar to pure copper (Figure 9).

Electrochemical Test

In recent years, due to the widespread use of metallic implant materials in the medical field, researchers have tried to observe

and investigate patients after repair surgery. They found that the implant material can be corroded due to complex body fluids interaction. Also, stress wear between bones can happen. As a consequence, the material will plastically deform, and its properties are affected finally, the implant will fail, and the patients may undergo multiple repair operations in severe cases. At the same time, the implant materials wear with the surrounding tissues of the human body leads to the formation of metallic debris formation that may cause tissue infection and allergic effects. Furthermore, corrosion and stress wear of implants can cause the precipitation of some toxic metal ions, which in turn can trigger toxic and allergic reactions. In order to reduce the harmful effects of implants in the human body, the production of novel implant materials with excellent comprehensive performance is necessary. Therefore, in the current research of implant materials, the corrosion resistance



and friction and wear properties of implants are a focus of researchers (Ghiban et al., 2018).

Due to a certain effect of the pH value of the simulated physiological environment on the corrosion behavior of metal implants, many researchers have explored the corrosion behavior of titanium-based HEAs as potential implant materials in simulated physiological environments. Song and Xu (2020) investigated the $(\text{TiZrNbTa})_{90}\text{Mo}_{10}$ HEA electrochemical properties in Ringer's solution and used XPS to characterize the passive film formation on the surface of $(\text{TiZrNbTa})_{90}\text{Mo}_{10}$ HEA. In addition, $(\text{TiZrNbTa})_{90}\text{Mo}_{10}$ HEA exhibits robust corrosion resistance far better than CoCrMo alloys and stainless steel. Braic et al. (2012) prepared $(\text{TiZrNbHfTa})\text{N}$ and $(\text{TiZrNbHfTa})\text{C}$ coatings by DC magnetron sputtering on Ti6Al4V alloy. They examined the processed samples by the corrosion and tribological tests in SBFs, as well as cell viability tests. These films exhibited good protective properties and did not induce any cytotoxic response by osteoblasts (24 and 72 h), with good morphology of the attached cells. Aksoy et al. (2019) have studied the deposition of TiTaHfNbZr HEA films on NiTi shape memory alloy by RF magnetron sputtering, then they immersed it into artificial saliva (AS) and gastric fluid (GF) solutions. This study demonstrates that TiTaHfNbZr HEA coatings have a significant inhibitory effect toward the release of Ni ions. Therefore, TiTaHfNbZr HEA thin films can serve as a potential biomedical coating on NiTi implants to prevent the release of Ni ions. Tüten et al. (2019) prepared TiTaHfNbZr HEA coatings on Ti-6Al-4V substrates by RF magnetron sputtering, which are considered an effective coating for long-term orthopedic implants with a protective effect on surface wear and cracking.

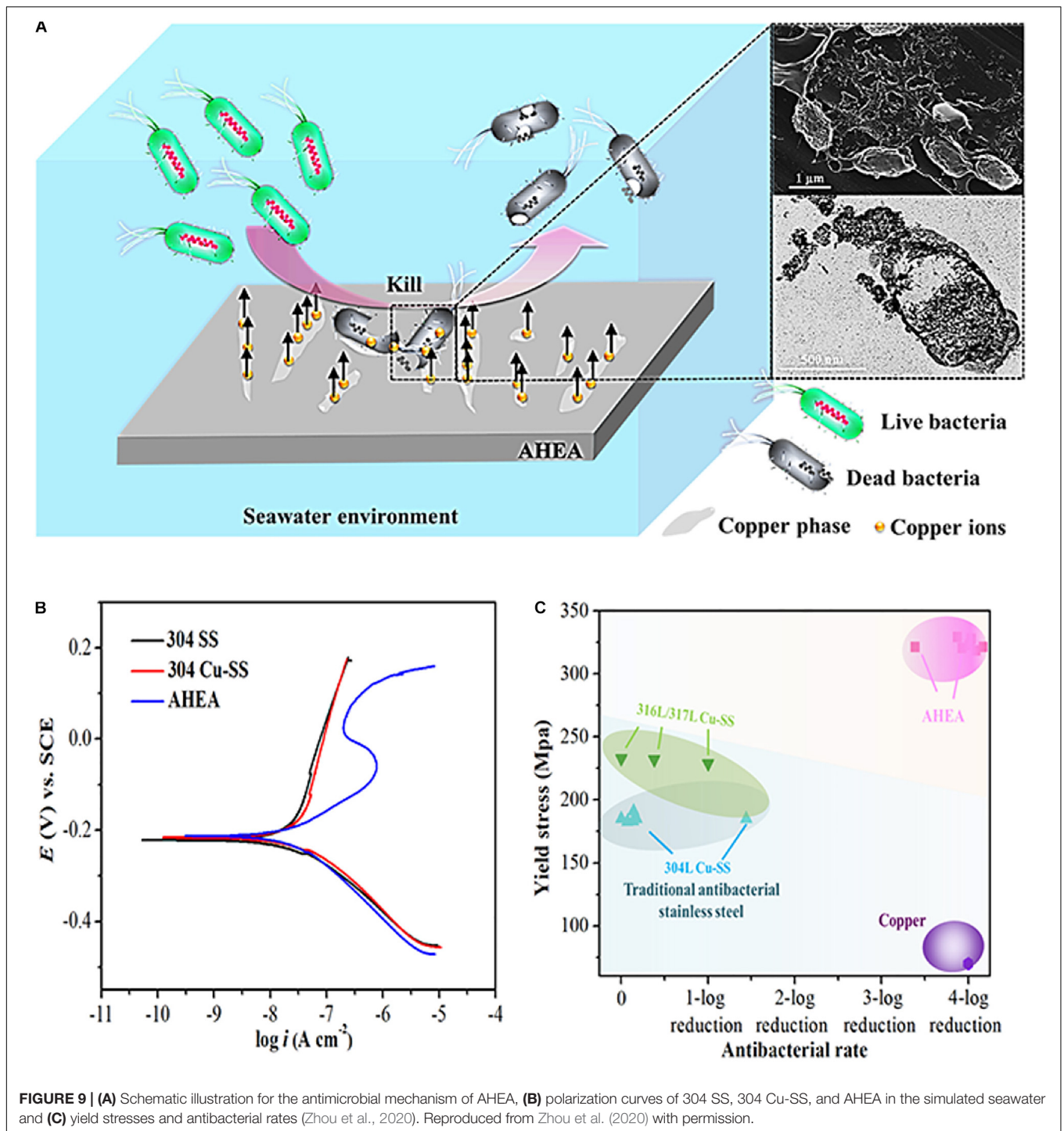
Cell Adhesion and Cytotoxicity Assay

Cell adhesion is the basic condition for maintaining the stability of tissue structure, and it is also the regulator factor of cell

movement and function that has a significant influence on cell proliferation and differentiation (Yang et al., 2011). Cytotoxicity assay is usually used to evaluate the effect of alloy on cell growth activity that represents one of the most key indicators in the *in vitro* evaluation (Rincic Mlinaric et al., 2019). Cytotoxicity is the process of chemical substances, drugs, or physiological action of cells acting on the basic structure. These processes include cell membrane or cytoskeleton structure, cell metabolism process, synthesis, degradation, or release of cell components or products, ion regulation, and cell division, etc. finally leading to cell survival, proliferation, or functional disorders that result in adverse reactions.

In recent years, researchers have found in the follow-up study of patients after implant repair surgery that long-term implantation of metal materials in the human body will cause a series of biological problems. For example, the metal elements such as Co and Ni in cobalt-based alloys have serious sensitization problems, as well as the long-term implantation of Al and V elements in the commonly used Ti-6Al-4V implants will exert influence on human organs and functions. Therefore, the detection of cytotoxicity and the activity of metal implant materials is of great significance before implantation and repair surgery in humans. Cytotoxicity and cell activity assays are mainly based on the function of individual cells and they can change in cell membrane permeability. According to scholars' previous research, cytotoxicity and activity detection methods are divided into the following four types: dye exclusion assays, colorimetric assays, fluorometric assays, luminometric assays (Aslantürk, 2018). Among them, MTT assay, XTT assay, LDP assay of colorimetric assays are among the most commonly used techniques in cell detection.

In order to evaluate the adhesion effect of osteoblasts on the surface of HEA immunocytochemical methods were used to observe the cell adhesion behavior. Hori et al. (2019)



designed a series of novel non-equiatomic Ti-Nb-Ta-Zr-Mo HEAs. They demonstrated that this HEA system promoted the maturation of local adhesion spots in osteoblasts. As shown in **Figure 10**, it can be seen that the number of osteoblasts adhesion on the two HEAs, including $Ti_{1.4}Zr_{1.4}Nb_{0.6}Ta_{0.6}$, and $Ti_{0.6}Zr_{0.6}Nb_{1.4}Ta_{1.4}Mo_{1.4}$ is larger than SUS316L. Moreover, $Ti_{1.4}Zr_{1.4}Nb_{0.6}Ta_{0.6}Mo_{0.6}$ shows superior biocompatibility because of its fibric adhesion structure is significantly longer

than $Ti_{0.6}Zr_{0.6}Nb_{1.4}Ta_{1.4}Mo_{1.4}$. Nagase et al. (2020) found that Ti-Zr-Hf-Cr-Mo and Ti-Zr-Hf-Co-Cr-Mo HEAs showed excellent biocompatibility compared with CP-Ti. Edalati et al. (2020) have studied TiAlFeCoNi HEA exhibited ultra-high hardness and favorable cellular activity by a combination of MTT assay and microhardness measurements. Todai et al. designed a new TiNbTaZrMo HAE that shows good biocompatibility compares to Cp-Ti. The osteoblasts on the as-cast and annealed

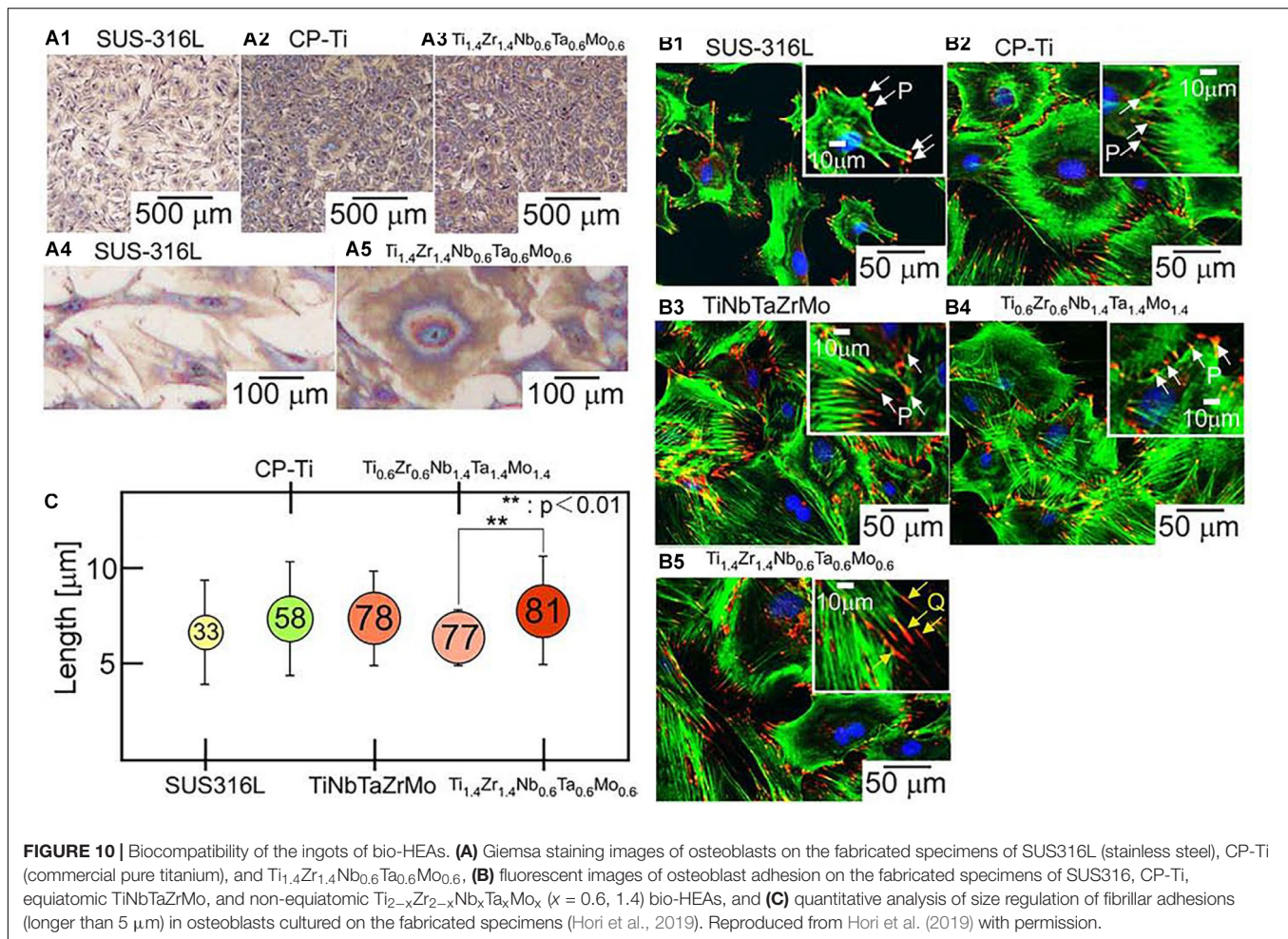


FIGURE 10 | Biocompatibility of the ingots of bio-HEAs. **(A)** Giemsa staining images of osteoblasts on the fabricated specimens of SUS316L (stainless steel), CP-Ti (commercial pure titanium), and $\text{Ti}_{1.4}\text{Zr}_{1.4}\text{Nb}_{0.6}\text{Ta}_{0.6}\text{Mo}_{0.6}$, **(B)** fluorescent images of osteoblast adhesion on the fabricated specimens of SUS316, CP-Ti, equiatomic TiNbTaZrMo, and non-equiatomic $\text{Ti}_{2-x}\text{Zr}_{2-x}\text{Nb}_x\text{Ta}_x\text{Mo}_x$ ($x = 0.6, 1.4$) bio-HEAs, and **(C)** quantitative analysis of size regulation of fibrillar adhesions (longer than 5 μm) in osteoblasts cultured on the fabricated specimens (Hori et al., 2019). Reproduced from Hori et al. (2019) with permission.

TiNbTaZrMo HEA surface show a wide range of morphology, which is similar to the osteoblasts on the Cp-Ti surface. On the other hand, the distribution of osteoblasts on 316L stainless steel shows a smaller number of various morphologies. Osteoblasts on TiNbTaZrMo HEAs and Cp-Ti are very advantageous in the bone matrix formation.

It can be understood from the above-mentioned explains that Ti-based HEAs have a great potential to become a biomedical material due to their excellent antibacterial ability, wear resistance, and corrosion resistance, as well as lower cytotoxicity. In particular, Ti-Nb-Ta-Zr HEAs and TiTaHf-based HEAs have considerable biocompatibility compared with Cp-Ti and attracts lots of attention from research communities. Generally, implantable devices made of biomaterials aim to improve the quality of life and extend the life of patients. After long-term use of plastic surgical prostheses made of biologically inert materials, the current focus is on materials that promote the proliferation and differentiation of osteoblasts and activate tissue repair mechanisms (called biologically active materials). In addition, regarding the biocompatibility of implantable alloys, it is necessary to ensure improved corrosion resistance in corrosive physiological environments (Yang et al., 2020). Therefore, more attention should be focused on the Ti-Nb-Ta-Zr system HEAs in

the future. Furthermore, the HEA design is also a critical factor in determining its performance, and researchers should focus on the establishment of the proper design principles and criteria to develop the novel bio-HEAs.

CONCLUSION

In this review, an insight into the development of Ti-based HEAs is provided, and it summarizes the current methods in HEAs fabrication, HEA blocks or coatings, and analysis its properties and biological applications. Metallic implant materials usually are made of traditional titanium alloy, 316L stainless steel, and CoCrMo alloys, and they have less harmful effects on the human body after the surgery. In order to develop implant materials with excellent functional properties, many scholars began to turn their attention to HEAs, which have a wide range of applications resulting from its exceptional physical, chemical, magnetization, and mechanical properties. The emergence of HEAs has brought great room for development in the field of medical implant materials. This HEA design concept overturns the principles of traditional alloy design, and it emphasizes multiple principal elements as the basis. Also, a small number of modified elements

were utilized to mutually control the structure and mechanical properties of the alloy.

PROSPECTS

In recent years, due to the continuous improvement of medical science and technology, the performance requirements of implant materials for revision and implantation operations have become more and more significant. Ti-based HEAs have recently emerged as alternative implant materials to address some of the unresolved issues in terms of performance and biocompatibility. Compared with traditional alloys, the complexity of various chemical elements in HEAs makes them functional. The combination of chemical elements can induce excellent mechanical properties also it ensures functionality and biocompatibility. Moreover, it is suitable for use as a new type of biocompatible metal material. Although titanium-based HEAs are among the new potential metallic implant material, its cytotoxicity and biological evaluation and research on its implantation in animals are in the initial stage and Ti-based HEAs still have not been used clinically. Therefore, the future development of titanium-based HEAs still needs a lot of experimental research and further in-depth exploration.

REFERENCES

- Aguilar, C., Guzman, P., Lascano, S., Parra, C., Bejar, L., Medina, A., et al. (2016). Solid solution and amorphous phase in Ti-Nb-Ta-Mn systems synthesized by mechanical alloying. *J. Alloys Compounds* 670, 346–355. doi: 10.1016/j.jallcom.2015.12.173
- Aksoy, C. B., Canadinc, D., and Yagci, M. B. (2019). Assessment of Ni ion release from TiTaHfNbZr high entropy alloy coated NiTi shape memory substrates in artificial saliva and gastric fluid. *Mater. Chem. Phys.* 236:121802. doi: 10.1016/j.matchemphys.2019.121802
- Anand Sekhar, R., Samal, S., Nayan, N., and Bakshi, S. R. (2019). Microstructure and mechanical properties of Ti-Al-Ni-Co-Fe based high entropy alloys prepared by powder metallurgy route. *J. Alloys Compounds* 787, 123–132. doi: 10.1016/j.jallcom.2019.02.083
- Anupam, A., Kottada, R. S., Kashyap, S., Meghwal, A., Murty, B. S., Berndt, C. C., et al. (2019). Understanding the microstructural evolution of high entropy alloy coatings manufactured by atmospheric plasma spray processing. *Appl. Surf. Sci.* 505:144117. doi: 10.1016/j.apsusc.2019.144117
- Aslantürk, Ö. (2018). *In Vitro Cytotoxicity and Cell Viability Assays: Principles, Advantages, and Disadvantages*. London: In Tech.
- Assis, S. L., and Costa, I. (2007). Electrochemical evaluation of Ti-13Nb-13Zr, Ti-6Al-4V and Ti-6Al-7Nb alloys for biomedical application by long-term immersion tests. *Mater. Corrosion* 58, 329–333. doi: 10.1002/maco.200604027
- Attarilar, S., Yang, J., Ebrahimi, M., Wang, Q., Liu, J., Tang, Y., et al. (2020). The toxicity phenomenon and the related occurrence in metal and metal oxide nanoparticles: a brief review from the biomedical perspective. *Front. Bioeng. Biotechnol.* 8:822. doi: 10.3389/fbioe.2020.00822
- Baldenebro-Lopez, F. J., Herrera-Ramírez, J. M., Arredondo-Rea, S. P., Gómez-Esparza, C. D., and Martínez-Sánchez, R. (2015). Simultaneous effect of mechanical alloying and arc-melting processes in the microstructure and hardness of an AlCoFeMoNiTi high-entropy alloy. *J. Alloys Compounds* 643, S250–S255. doi: 10.1016/j.jallcom.2014.12.059
- Braic, V., Balaceanu, M., Braic, M., Vladescu, A., Panseri, S., and Russo, A. (2012). Characterization of multi-principal-element (TiZrNbHfTa)N and (TiZrNbHfTa)C coatings for biomedical applications. *J. Mech. Behav. Biomed. Mater.* 10, 197–205. doi: 10.1016/j.jmbbm.2012.02.020

AUTHOR CONTRIBUTIONS

NM wrote the main part of the manuscript. SL and WL greatly contributed to the fabrication methods parts. NM and BZ made a contribution to data curation. LX, DW, LW, and YW made significant contributions particularly in revising the manuscript. NM, LL, and WL prepared and formulated the references. All the authors contributed to the manuscript and approved the submitted version.

FUNDING

This research was funded by the National Natural Science Foundation of China (Nos. 51671152 and 51874225), the Industrialization Project of Shaanxi Education Department (18JC019), the funding 2020ZDLGY13-10 and the funding 2020KJRC0048.

ACKNOWLEDGMENTS

The authors sincerely thank Shokouh Attarilar, Xintao Li, Tong Xue, and Qingge Wang from Xi'an University of Architecture and Technology for data analysis of this paper.

- Brecht, J., Chen, S., Lee, C., Shi, Y., Feng, R., Xie, X., et al. (2020). A review of the serrated-flow Phenomenon and its role in the deformation behavior of high-entropy alloys. *Metals* 10:1101. doi: 10.3390/met10081101
- Cai, Z., Cui, X., Liu, Z., Li, Y., Dong, M., and Jin, G. (2018). Microstructure and wear resistance of laser clad Ni-Cr-Co-Ti-V high-entropy alloy coating after laser remelting processing. *Optics Laser Technol.* 99, 276–281. doi: 10.1016/j.optlastec.2017.09.012
- Calderon Velasco, S., Cavaleiro, A., and Carvalho, S. (2016). Functional properties of ceramic-Ag nanocomposite coatings produced by magnetron sputtering. *Prog. Mater. Sci.* 84, 158–191. doi: 10.1016/j.pmatsci.2016.09.005
- Cantor, B., Chang, I. T. H., Knight, P., and Vincent, A. J. B. (2004). Microstructural development in equiatomic multicomponent alloys. *Mater. Sci. Eng. A* 375–377, 213–218. doi: 10.1016/j.msea.2003.10.257
- Cao, Y., Liu, Y., Li, Y., Liu, B., Fu, A., and Nie, Y. (2020). Precipitation behavior and mechanical properties of a hot-worked TiNbTa_{0.5}ZrAl_{0.5} refractory high entropy alloy. *Int. J. Refract. Metals Hard Mater.* 86:105132. doi: 10.1016/j.jrmhm.2019.105132
- Chen, F. M., and Liu, X. (2016). Advancing biomaterials of human origin for tissue engineering. *Prog. Polym. Sci.* 53, 86–168. doi: 10.1016/j.progpolymsci.2015.02.004
- Chen, J., Zhou, X., Wang, W., Liu, B., Lv, Y., Yang, W., et al. (2018). A review on fundamental of high entropy alloys with promising high-temperature properties. *J. Alloys Compounds* 760, 15–30. doi: 10.1016/j.jallcom.2018.05.067
- Chen, Q., and Thouas, G. A. (2015). Metallic implant biomaterials. *Mater. Sci. Eng. Rep.* 87, 1–57. doi: 10.1016/j.mser.2014.10.001
- Chen, S., Cai, Z., Lu, Z., Pu, J., Chen, R., Zheng, S., et al. (2019). Tribo-corrosion behavior of VAlTiCrCu high-entropy alloy film. *Mater. Charact.* 157:109887. doi: 10.1016/j.matchar.2019.109887
- Chen, Y., Zhu, S., Wang, X., Yang, B., Han, G., and Qiu, L. (2018). Microstructure evolution and strengthening mechanism of Al_{0.4}CoCu_{0.6}NiSix (x = 0–0.2) high entropy alloys prepared by vacuum arc melting and copper injection fast solidification. *Vacuum* 150, 84–95. doi: 10.1016/j.vacuum.2018.01.031
- Chen, Y. H., Chuang, W. S., Huang, J. C., Wang, X., Chou, H. S., Lai, Y. J., et al. (2020). On the bio-corrosion and biocompatibility of TiTaNb medium entropy alloy films. *Appl. Surf. Sci.* 508:145307. doi: 10.1016/j.apsusc.2020.145307

- Ching, W.-Y., San, S., Brecht, J., Sakidja, R., Zhang, M., and Liaw, P. K. (2020). Fundamental electronic structure and multiautomic bonding in 13 biocompatible high-entropy alloys. *NPJ Comp. Mater.* 6:45. doi: 10.1038/s41524-020-0321-x
- Cui, P., Li, W., Liu, P., Zhang, K., Ma, F., Chen, X., et al. (2020). Effects of nitrogen content on microstructures and mechanical properties of (AlCrTiZrHf)N high-entropy alloy nitride films. *J. Alloys Compounds* 834:155063. doi: 10.1016/j.jallcom.2020.155063
- Deng, Y., Chen, W., Li, B., Wang, C., Kuang, T., and Li, Y. (2020). Physical vapor deposition technology for coated cutting tools: a review. *Ceram. Int.* 46(11 Pt. B), 18373–18390. doi: 10.1016/j.ceramint.2020.04.168
- Ding, Z., Zhang, C., Xie, L., Zhang, L.-C., Wang, L., and Lu, W. (2016). Effects of friction stir processing on the phase transformation and microstructure of TiO₂-Compounded Ti-6Al-4V Alloy. *Metall. Mater. Trans. A* 47, 5675–5679. doi: 10.1007/s11661-016-3809-8
- Dirras, G., Lilensten, L., Djemia, P., Laurent-Brocq, M., Tingaud, D., Couzinié, J. P., et al. (2016). Elastic and plastic properties of as-cast equimolar TiHfZrTaNb high-entropy alloy. *Mater. Sci. Eng. A* 654, 30–38. doi: 10.1016/j.msea.2015.12.017
- Edalati, P., Floriano, R., Tang, Y., Mohammadi, A., Pereira, K. D., Luchessi, A. D., et al. (2020). Ultrahigh hardness and biocompatibility of high-entropy alloy TiAlFeCoNi processed by high-pressure torsion. *Mater. Sci. Eng. C Mater. Biol. Appl.* 112:110908. doi: 10.1016/j.msec.2020.110908
- Feng, J., Song, K., Liang, S., Guo, X., and Jiang, Y. (2020). Electrical wear of TiB₂ particle-reinforced Cu and Cu–Cr composites prepared by vacuum arc melting. *Vacuum* 175:109295. doi: 10.1016/j.vacuum.2020.109295
- Gabriel, S. B., Panaino, J. V. P., Santos, I. D., Araujo, L. S., Mei, P. R., de Almeida, L. H., et al. (2012). Characterization of a new beta titanium alloy, Ti–12Mo–3Nb, for biomedical applications. *J. Alloys Compounds* 536, S208–S210. doi: 10.1016/j.jallcom.2011.11.035
- Ge, H., Tian, F., and Wang, Y. (2017). Elastic and thermal properties of refractory high-entropy alloys from first-principles calculations. *Comp. Mater. Sci.* 128, 185–190. doi: 10.1016/j.commatsci.2016.11.035
- Ge, W., Wu, B., Wang, S., Xu, S., Shang, C., Zhang, Z., et al. (2017). Characterization and properties of CuZrAlTiNi high entropy alloy coating obtained by mechanical alloying and vacuum hot pressing sintering. *Adv. Powder Technol.* 28, 2556–2563. doi: 10.1016/j.appt.2017.07.006
- Geetha, M., Singh, A. K., Asokamani, R., and Gogia, A. K. (2009). Ti based biomaterials, the ultimate choice for orthopaedic implants – A review. *Prog. Mater. Sci.* 54, 397–425. doi: 10.1016/j.pmatsci.2008.06.004
- George, E. P., Curtin, W. A., and Tassan, C. C. (2020). High entropy alloys: a focused review of mechanical properties and deformation mechanisms. *Acta Mater.* 188, 435–474. doi: 10.1016/j.actamat.2019.12.015
- Ghiban, B., Popescu, G., Lazar, C., Rosu, L., Constantin, I., Oлару, M., et al. (2018). Corrosion behaviour in human stimulation media of a high entropy titan-based alloy. *Mater. Sci. Eng.* 374:010024. doi: 10.1088/1757-899x/374/1/010024
- Gu, H., Ding, Z., Yang, Z., Yu, W., Zhang, W., Lu, W., et al. (2019). Microstructure evolution and electrochemical properties of TiO₂/Ti-35Nb-2Ta-3Zr micro/nano-composites fabricated by friction stir processing. *Mater. Des.* 169:107680. doi: 10.1016/j.matdes.2019.107680
- Guo, W., Liu, B., Liu, Y., Li, T., Fu, A., Fang, Q., et al. (2019). Microstructures and mechanical properties of ductile NbTaTiV refractory high entropy alloy prepared by powder metallurgy. *J. Alloys Compounds* 776, 428–436. doi: 10.1016/j.jallcom.2018.10.230
- Guo, Y., Chen, D., Cheng, M., Lu, W., Wang, L., and Zhang, X. (2013). The bone tissue compatibility of a new Ti35Nb2Ta3Zr alloy with a low Young's modulus. *Int. J. Mol. Med.* 31, 689–697. doi: 10.3892/ijmm.2013.1249
- Guo, Y., Shang, X., and Liu, Q. (2018). Microstructure and properties of in-situ TiN reinforced laser cladding CoCr2FeNiTi high-entropy alloy composite coatings. *Surf. Coat. Technol.* 344, 353–358. doi: 10.1016/j.surfcoat.2018.03.035
- Gurel, S., Yagci, M. B., Bal, B., and Canadinc, D. (2020). Corrosion behavior of novel Titanium-based high entropy alloys designed for medical implants. *Mater. Chem. Phys.* 254:123377. doi: 10.1016/j.matchemphys.2020.123377
- Hafeez, N., Liu, J., Wang, L., Wei, D., Tang, Y., Lu, W., et al. (2020). Superelastic response of low-modulus porous beta-type Ti-35Nb-2Ta-3Zr alloy fabricated by laser powder bed fusion. *Addit. Manufact.* 34:101264. doi: 10.1016/j.addma.2020.101264
- Hafeez, N., Liu, S., Lu, E., Wang, L., Liu, R., Lu, W., et al. (2019). Mechanical behavior and phase transformation of β -type Ti-35Nb-2Ta-3Zr alloy fabricated by 3D-Printing. *J. Alloys Compounds* 790, 117–126. doi: 10.1016/j.jallcom.2019.03.138
- Han, X., Ji, X., Zhao, M., and Li, D. (2020). Mg/Ag ratios induced in vitro cell adhesion and preliminary antibacterial properties of TiN on medical Ti-6Al-4V alloy by Mg and Ag implantation. *Surf. Coat. Technol.* 397:126020. doi: 10.1016/j.surfcoat.2020.126020
- Hori, T., Nagase, T., Todai, M., Matsugaki, A., and Nakano, T. (2019). Development of non-equiautomic Ti-Nb-Ta-Zr-Mo high-entropy alloys for metallic biomaterials. *Script. Mater.* 172, 83–87. doi: 10.1016/j.scriptamat.2019.07.011
- Hou, L., Hui, J., Yao, Y., Chen, J., and Liu, J. (2019). Effects of Boron Content on microstructure and mechanical properties of AlFeCoNiBx High Entropy Alloy Prepared by vacuum arc melting. *Vacuum* 164, 212–218. doi: 10.1016/j.vacuum.2019.03.019
- Huang, Y., Wu, C., Zhang, X., Chang, J., and Dai, K. (2018). Regulation of immune response by bioactive ions released from silicate bioceramics for bone regeneration. *Acta Biomater.* 66, 81–92. doi: 10.1016/j.actbio.2017.08.044
- Hussein, M. A., Suryanarayana, C., and Al-Aqeeli, N. (2015). Fabrication of nano-grained Ti-Nb-Zr biomaterials using spark plasma sintering. *Mater. Des.* 87, 693–700. doi: 10.1016/j.matdes.2015.08.082
- Jin, G., Cai, Z., Guan, Y., Cui, X., Liu, Z., Li, Y., et al. (2018). High temperature wear performance of laser-cladded FeNiCoAlCu high-entropy alloy coating. *Appl. Surf. Sci.* 445, 113–122. doi: 10.1016/j.apsusc.2018.03.135
- Juan, C.-C., Tsai, M.-H., Tsai, C.-W., Lin, C.-M., Wang, W.-R., Yang, C.-C., et al. (2015). Enhanced mechanical properties of HfMoTaTiZr and HfMoNbTaTiZr refractory high-entropy alloys. *Intermetallics* 62, 76–83. doi: 10.1016/j.intermet.2015.03.013
- Ke, Z., Yi, C., Zhang, L., He, Z., Tan, J., and Jiang, Y. (2019). Characterization of a new Ti-13Nb-13Zr-10Cu alloy with enhanced antibacterial activity for biomedical applications. *Mater. Lett.* 253, 335–338. doi: 10.1016/j.matlet.2019.07.008
- Khan, N. A., Akhavan, B., Zhou, C., Zhou, H., Chang, L., Wang, Y., et al. (2020). RF magnetron sputtered AlCoCrCu0.5FeNi high entropy alloy (HEA) thin films with tuned microstructure and chemical composition. *J. Alloys Compounds* 836:155348. doi: 10.1016/j.jallcom.2020.155348
- Kobayashi, E., Wang, T. J., Doi, H., Yoneyama, T., and Hamanaka, H. (1998). Mechanical properties and corrosion resistance of Ti-6Al-7Nb alloy dental castings. *Mater. Med.* 9, 567–574. doi: 10.1023/A:1008909408948
- Koval, N. E., Juaristi, J. I., Díez Muño, R., and Alducin, M. (2019). Elastic properties of the TiZrNbTaMo multi-principal element alloy studied from first principles. *Intermetallics* 106, 130–140. doi: 10.1016/j.intermet.2018.12.014
- Liang, S.-C., Tsai, D.-C., Chang, Z.-C., Sung, H.-S., Lin, Y.-C., Yeh, Y.-J., et al. (2011). Structural and mechanical properties of multi-element (TiVCrZrHf)N coatings by reactive magnetron sputtering. *Appl. Surf. Sci.* 258, 399–403. doi: 10.1016/j.apsusc.2011.09.006
- Liu, J., Li, F., Liu, C., Wang, H., Ren, B., Yang, K., et al. (2014). Effect of Cu content on the antibacterial activity of titanium–copper sintered alloys. *Mater. Sci. Eng. C* 35, 392–400. doi: 10.1016/j.msec.2013.11.028
- Liu, J., Liu, H., Chen, P., and Hao, J. (2019). Microstructural characterization and corrosion behaviour of AlCoCrFeNiTiX high-entropy alloy coatings fabricated by laser cladding. *Surf. Coat. Technol.* 361, 63–74. doi: 10.1016/j.surfcoat.2019.01.044
- Liu, S., Liu, J., Wang, L., Ma, R. L.-W., Zhong, Y., Lu, W., et al. (2020). Superelastic behavior of in-situ eutectic-reaction manufactured high strength 3D porous NiTi-Nb scaffold. *Script. Mater.* 181, 121–126. doi: 10.1016/j.scriptamat.2020.02.025
- Liu, W., Cheng, M., Wahafu, T., Zhao, Y., Qin, H., Wang, J., et al. (2015). The in vitro and in vivo performance of a strontium-containing coating on the low-modulus Ti35Nb2Ta3Zr alloy formed by micro-arc oxidation. *J. Mater. Sci. Mater. Med.* 26:203.
- Liu, W., Liu, S., and Wang, L. (2019). Surface modification of biomedical titanium alloy: micromorphology, microstructure evolution and biomedical applications. *Coatings* 9:249. doi: 10.3390/coatings9040249
- Lozano, D., Manzano, M., Doadrio, J. C., Salinas, A. J., Vallet-Regi, M., Gomez-Barrena, E., et al. (2010). Osteostatin-loaded bioceramics stimulate osteoblastic

- growth and differentiation. *Acta Biomater.* 6, 797–803. doi: 10.1016/j.actbio.2009.08.033
- Lukáč, F., Hruška, P., Cichoš, S., Vlasák, T., Čížek, J., Kmječ, T., et al. (2020). Defects in thin layers of high entropy alloy HfNbTaTiZr. *Acta Phys. Pol. A* 137, 219–221. doi: 10.12693/APhysPolA.137.219
- Málek, J., Zýka, J., Lukáč, F., ěížek, J., Kuněická, L., and Kocich, R. (2019a). Microstructure and mechanical properties of sintered and heat-treated HfNbTaTiZr high entropy alloy. *Metals* 9:1324. doi: 10.3390/met9121324
- Málek, J., Zýka, J., Lukáč, F., Vilemova, M., Vlasak, T., Cizek, J., et al. (2019b). The effect of processing route on properties of HfNbTaTiZr high entropy alloy. *Materials* 12:4022. doi: 10.3390/ma12234022
- Miracle, D. B., and Senkov, O. N. (2017). A critical review of high entropy alloys and related concepts. *Acta Mater.* 122, 448–511. doi: 10.1016/j.actamat.2016.08.081
- Motallebzadeh, A., Peighambaroust, N. S., Sheikh, S., Murakami, H., Guo, S., and Canadinc, D. (2019). Microstructural, mechanical and electrochemical characterization of TiZrTaHfNb and Ti1.5ZrTa0.5Hf0.5Nb0.5 refractory high-entropy alloys for biomedical applications. *Intermetallics* 113:106572. doi: 10.1016/j.intermet.2019.106572
- Nagase, T., Iijima, Y., Matsugaki, A., Ameyama, K., and Nakano, T. (2020). Design and fabrication of Ti-Zr-Hf-Cr-Mo and Ti-Zr-Hf-Co-Cr-Mo high-entropy alloys as metallic biomaterials. *Mater. Sci. Eng. C Mater. Biol. Appl.* 107:110322. doi: 10.1016/j.msec.2019.110322
- Nazari, K. A., Nouri, A., and Hilditch, T. (2015). Mechanical properties and microstructure of powder metallurgy Ti-xNb-yMo alloys for implant materials. *Mater. Des.* 88, 1164–1174. doi: 10.1016/j.matdes.2015.09.106
- Nguyen, V. T., Qian, M., Shi, Z., Song, T., Huang, L., and Zou, J. (2018). A novel quaternary equiatomic Ti-Zr-Nb-Ta medium entropy alloy (MEA). *Intermetallics* 101, 39–43. doi: 10.1016/j.intermet.2018.07.008
- Niinomi, M. (2003). Recent research and development in titanium alloys for biomedical applications and healthcare goods. *Sci. Technol. Adv. Mater.* 4, 445–454. doi: 10.1016/j.stam.2003.09.002
- Niinomi, M. (2008). Mechanical biocompatibilities of titanium alloys for biomedical applications. *J. Mech. Behav. Biomed. Mater.* 1, 30–42. doi: 10.1016/j.jmbbm.2007.07.001
- Peng, Y. B., Zhang, W., Li, T. C., Zhang, M. Y., Wang, L., Song, Y., et al. (2019). Microstructures and mechanical properties of FeCoCrNi high entropy alloy/WC reinforcing particles composite coatings prepared by laser cladding and plasma cladding. *Int. J. Refract. Metals Hard Mater.* 84:105044. doi: 10.1016/j.jirmhm.2019.105044
- Pogrebniak, A., Yakuschenko, I., Bagdasaryan, A., Bondar, O., Krause-Rehberg, R., Abadias, G., et al. (2014). Microstructure, physical and chemical properties of nanostructured (Ti-Hf-Zr-V-Nb)N coatings under different deposition conditions. *Mater. Chem. Phys.* 147, 1079–1091. doi: 10.1016/j.matchemphys.2014.06.062
- Poletti, M. G., Branz, S., Fiore, G., Szost, B. A., Crichton, W. A., and Battezzati, L. (2016). Equilibrium high entropy phases in X-NbTaTiZr (X = Al, V, Cr and Sn) multiprincipal component alloys. *J. Alloys Compounds* 655, 138–146. doi: 10.1016/j.jallcom.2015.09.118
- Popescu, G., Ghiban, B., Popescu, C. A., Rosu, L., Truscă, R., Carcea, I., et al. (2018). New TiZrNbTaFe high entropy alloy used for medical applications. *Mater. Sci. Eng.* 400:022049. doi: 10.1088/1757-899x/400/2/022049
- Průša, F., Cabibbo, M., Šenková, A., Kučera, V., Veselka, Z., Školáková, A., et al. (2020). High-strength ultrafine-grained CoCrFeNiNb high-entropy alloy prepared by mechanical alloying: properties and strengthening mechanism. *J. Alloys Compounds* 835:155308. doi: 10.1016/j.jallcom.2020.155308
- Qiu, X. (2018). Microstructure, hardness and corrosion resistance of Al₂CoCrCuFeNiTi_x high-entropy alloy coatings prepared by rapid solidification. *J. Alloys Compounds* 735, 359–364. doi: 10.1016/j.jallcom.2017.11.158
- Rabadia, C. D., Liu, Y. J., Wang, L., Sun, H., and Zhang, L. C. (2018). Laves phase precipitation in Ti-Zr-Fe-Cr alloys with high strength and large plasticity. *Mater. Des.* 154, 228–238. doi: 10.1016/j.matdes.2018.05.035
- Ran, R., Liu, Y., Wang, L., Lu, E., Xie, L., Lu, W., et al. (2018). α'' Martensite and amorphous phase transformation mechanism in TiNbTaZr Alloy Incorporated with TiO₂ particles during friction stir processing. *Metall. Mater. Trans. A* 49, 1986–1991. doi: 10.1007/s11661-018-4577-4
- Rao, X., Chu, C. L., and Zheng, Y. Y. (2014). Phase composition, microstructure, and mechanical properties of porous Ti-Nb-Zr alloys prepared by a two-step foaming powder metallurgy method. *J. Mech. Behav. Biomed. Mater.* 34, 27–36. doi: 10.1016/j.jmbbm.2014.02.001
- Rincic Mlinaric, M., Durgo, K., Katic, V., and Spalj, S. (2019). Cytotoxicity and oxidative stress induced by nickel and titanium ions from dental alloys on cells of gastrointestinal tract. *Toxicol. Appl. Pharmacol.* 383:114784. doi: 10.1016/j.taap.2019.114784
- Saini, M. (2015). Implant biomaterials: a comprehensive review. *World J. Clin. Cases* 3, 52–57. doi: 10.12998/wjcc.v3.i1.52
- Sakaguchi, N., Niinomi, M., Akahori, T., Takeda, J., and Toda, H. (2005). Relationships between tensile deformation behavior and microstructure in Ti-Nb-Ta-Zr system alloys. *Mater. Sci. Eng.* 25, 363–369. doi: 10.1016/j.msec.2004.12.014
- Senkov, O., Scott, J., Senkova, S., Miracle, D., and Woodward, C. (2011). Microstructure and Room Temperature Properties of a High-Entropy TaNbHfZrTi Alloy (Preprint). *J. Alloys Compounds* 509, 6043–6048. doi: 10.1016/j.jallcom.2011.02.171
- Shang, C., Axinte, E., Ge, W., Zhang, Z., and Wang, Y. (2017). High-entropy alloy coatings with excellent mechanical, corrosion resistance and magnetic properties prepared by mechanical alloying and hot pressing sintering. *Surf. Interf.* 9, 36–43. doi: 10.1016/j.surf.2017.06.012
- Sharma, A. S., Yadav, S., Biswas, K., and Basu, B. (2018). High-entropy alloys and metallic nanocomposites: processing challenges, microstructure development and property enhancement. *Mater. Sci. Eng.* 131, 1–42. doi: 10.1016/j.mser.2018.04.003
- Shu, F., Zhang, B., Liu, T., Sui, S., Liu, Y., He, P., et al. (2019). Effects of laser power on microstructure and properties of laser clad CoCrFeNiSi high-entropy alloy amorphous coatings. *Surf. Coat. Technol.* 358, 667–675. doi: 10.1016/j.surfcoat.2018.10.086
- Shuang, S., Ding, Z. Y., Chung, D., Shi, S. Q., and Yang, Y. (2019). Corrosion resistant nanostructured eutectic high entropy alloy. *Corrosion Sci.* 164:108315. doi: 10.1016/j.corsci.2019.108315
- Soare, V., Burada, M., Constantin, I., Mitrică, D., Bădiliță, V., Caragea, A., et al. (2015). Electrochemical deposition and microstructural characterization of AlCrFeMnNi and AlCrCuFeMnNi high entropy alloy thin films. *Appl. Surf. Sci.* 358, 533–539. doi: 10.1016/j.apsusc.2015.07.142
- Song, Q.-T., and Xu, J. (2020). (TiZrNbTa)90Mo10 high-entropy alloy: electrochemical behavior and passive film characterization under exposure to Ringer's solution. *Corrosion Sci.* 167:108513. doi: 10.1016/j.corsci.2020.108513
- Stenlund, P., Omar, O., Brohede, U., Norgren, S., Norlindh, B., Johansson, A., et al. (2015). Bone response to a novel Ti-Ta-Nb-Zr alloy. *Acta Biomater.* 20, 165–175. doi: 10.1016/j.actbio.2015.03.038
- Stiehler, M., Lind, M., Mygind, T., Baatrup, A., Dolatshahi-Pirouz, A., Li, H., et al. (2008). Morphology, proliferation, and osteogenic differentiation of mesenchymal stem cells cultured on titanium, tantalum, and chromium surfaces. *J. Biomed. Mater. Res. Part A* 86, 448–458. doi: 10.1002/jbm.a.31602
- Stráský, J., Harcuba, P., Václavová, K., Horváth, K., Landa, M., Srba, O., et al. (2017). Increasing strength of a biomedical Ti-Nb-Ta-Zr alloy by alloying with Fe, Si and O. *J. Mech. Behav. Biomed. Mater.* 71, 329–336. doi: 10.1016/j.jmbbm.2017.03.026
- Tamilselvi, S., Raman, V., and Rajendran, N. (2006). Corrosion behaviour of Ti-6Al-7Nb and Ti-6Al-4V ELI alloys in the simulated body fluid solution by electrochemical impedance spectroscopy. *Electrochim. Acta* 52, 839–846. doi: 10.1016/j.electacta.2006.06.018
- Tian, Y., Lu, C., Shen, Y., and Feng, X. (2019). Microstructure and corrosion property of CrMnFeCoNi high entropy alloy coating on Q235 substrate via mechanical alloying method. *Surf. Interf.* 15, 135–140. doi: 10.1016/j.surf.2019.02.004
- Tüten, N., Canadinc, D., Motallebzadeh, A., and Bal, B. (2019). Microstructure and tribological properties of TiTaHfNbZr high entropy alloy coatings deposited on Ti 6Al 4V substrates. *Intermetallics* 105, 99–106. doi: 10.1016/j.intermet.2018.11.015
- Vallimanalan, A., Kumares Babu, S. P., Muthukumar, S., Murali, M., Gaurav, V., and Mahendran, R. (2020). Corrosion behaviour of thermally sprayed Mo added AlCoCrNi high entropy alloy coating. *Mater. Today* 27, 2398–2400. doi: 10.1016/j.matpr.2019.09.149
- Wang, H., Liu, Q., Guo, Y., and Lan, H. (2019). MoFe1.5CrTiWAlNb_x refractory high-entropy alloy coating fabricated by laser cladding. *Intermetallics* 115:106613. doi: 10.1016/j.intermet.2019.106613

- Wang, L., Lu, W., Qin, J., Zhang, F., and Zhang, D. (2009). Influence of cold deformation on martensite transformation and mechanical properties of Ti-Nb-Ta-Zr alloy. *J. Alloys Compounds* 469, 512–518. doi: 10.1016/j.jallcom.2008.02.032
- Wang, L., Qu, J., Chen, L., Meng, Q., Zhang, L.-C., Qin, J., et al. (2015). Investigation of deformation mechanisms in β -Type Ti-35Nb-2Ta-3Zr Alloy via FSP Leading to Surface Strengthening. *Metall. Mater. Trans. A* 46, 4813–4818. doi: 10.1007/s11661-015-3089-8
- Wang, L., Xie, L., Lv, Y., Zhang, L.-C., Chen, L., Meng, Q., et al. (2017). Microstructure evolution and superelastic behavior in Ti-35Nb-2Ta-3Zr alloy processed by friction stir processing. *Acta Mater.* 131, 499–510. doi: 10.1016/j.actamat.2017.03.079
- Wang, L., Xie, L., Shen, P., Fan, Q., Wang, W., Wang, K., et al. (2019). Surface microstructure and mechanical properties of Ti-6Al-4V/Ag nanocomposite prepared by FSP. *Mater. Charact.* 153, 175–183. doi: 10.1016/j.matchar.2019.05.002
- Wang, L. M., Chen, C. C., Yeh, J. W., and Ke, S. T. (2011). The microstructure and strengthening mechanism of thermal spray coating Ni₃Co_{0.6}Fe_{0.2}CrySi₂AlTi_{0.2} high-entropy alloys. *Mater. Chem. Phys.* 126, 880–885. doi: 10.1016/j.matchemphys.2010.12.022
- Wang, Q., Zhou, P., Liu, S., Attarilar, S., Ma, R. L.-W., Zhong, Y., et al. (2020). Multi-scale surface treatments of titanium implants for rapid osseointegration: a review. *Nanomaterials* 10:1244. doi: 10.3390/nano10061244
- Wang, S., Wu, D., She, H., Wu, M., Shu, D., Dong, A., et al. (2020). Design of high-ductile medium entropy alloys for dental implants. *Mater. Sci. Eng.* 113:110959. doi: 10.1016/j.msec.2020.110959
- Wang, S. P., and Xu, J. (2017). TiZrNbTaMo high-entropy alloy designed for orthopedic implants: as-cast microstructure and mechanical properties. *Mater. Sci. Eng. C Mater. Biol. Appl.* 73, 80–89. doi: 10.1016/j.msec.2016.12.057
- Wang, W., Han, P., Peng, P., Zhang, T., Liu, Q., Yuan, S.-N., et al. (2020). Friction stir processing of magnesium alloys: a review. *Acta Metall. Sin.* 33, 43–57. doi: 10.1007/s40195-019-00971-7
- Wang, X., Liu, Q., Huang, Y., Xie, L., Xu, Q., and Zhao, T. (2020). Effect of Ti content on the microstructure and corrosion resistance of CoCrFeNiTi_x high entropy alloys prepared by laser cladding. *Materials* 13:2209. doi: 10.3390/ma13102209
- Wang, X.-R., Wang, Z.-Q., Li, W.-S., Lin, T.-S., He, P., and Tong, C.-H. (2017a). Preparation and microstructure of CuNiTiZr medium-entropy alloy coatings on TC11 substrate via electrospark – computer numerical control deposition process. *Mater. Lett.* 197, 143–145. doi: 10.1016/j.matlet.2017.03.109
- Wang, X.-R., Wang, Z.-Q., Lin, T.-S., and He, P. (2017b). Mass transfer trends of AlCoCrFeNi high-entropy alloy coatings on TC11 substrate via electrospark - computer numerical control deposition. *J. Mater. Process. Technol.* 241, 93–102. doi: 10.1016/j.jmatprotec.2016.09.012
- Wang, Y., Zhao, S., Li, G., Zhang, S., Zhao, R., Dong, A., et al. (2020). Preparation and in vitro antibacterial properties of anodic coatings co-doped with Cu, Zn, and P on a Ti-6Al-4V alloy. *Mater. Chem. Phys.* 241:122360. doi: 10.1016/j.matchemphys.2019.122360
- Waseem, O. A., and Ryu, H. J. (2020). Combinatorial synthesis and analysis of Al_xTa_yV_z-Cr₂₀Mo₂₀Nb₂₀Ti₂₀Zr₁₀ and Al₁₀Cr₁₀MoxNb₁₀Ti₁₀Zr₁₀ refractory high-entropy alloys: oxidation behavior. *J. Alloys Compounds* 828:154427. doi: 10.1016/j.jallcom.2020.154427
- Wei, Q., Wang, L., Fu, Y., Qin, J., Lu, W., and Zhang, D. (2011). Influence of oxygen content on microstructure and mechanical properties of Ti-Nb-Ta-Zr alloy. *Mater. Des.* 32, 2934–2939. doi: 10.1016/j.matdes.2010.11.049
- Wen, M., Wen, C., Hodgson, P., and Li, Y. (2014). Fabrication of Ti-Nb-Ag alloy via powder metallurgy for biomedical applications. *Mater. Des.* 56, 629–634. doi: 10.1016/j.matdes.2013.11.066
- Wu, W.-H., Yang, C.-C., and Yeh, J.-W. (2006). Industrial development of high-entropy alloys. *Ann. Chim. Sci. Matér.* 31, 737–747.
- Xia, A., Togni, A., Hirn, S., Bolelli, G., Lusvarghi, L., and Franz, R. (2020). Angular-dependent deposition of MoNbTaVW HEA thin films by three different physical vapor deposition methods. *Surf. Coat. Technol.* 385:125356. doi: 10.1016/j.surfcoat.2020.125356
- Xing, Q., Wang, H., Chen, M., Chen, Z., Li, R., Jin, P., et al. (2019). Mechanical Properties and Corrosion Resistance of NbTiAlSiZrNx High-Entropy Films Prepared by RF Magnetron Sputtering. *Entropy* 21:396. doi: 10.3390/e21040396
- Xingwu, Q., Mingjun, W., Yan, Q., Chungue, L., Yunpeng, Z., and Chongxiang, H. (2018). Microstructure and corrosion resistance of Al₂CrFeCoCuNi_xTi high entropy alloy coatings prepared by laser cladding. *Infrared Laser Eng.* 47:706008. doi: 10.3788/irla201847.0706008
- Xu, Y.-F., Xiao, Y.-F., Yi, D. Q., Liu, H.-Q., Wu, L., and Wen, J. (2015). Corrosion behavior of Ti-Nb-Ta-Zr-Fe alloy for biomedical applications in Ringer's solution. *Trans. Nonferrous Metals Soc. China* 25, 2556–2563. doi: 10.1016/s1003-6326(15)63875-4
- Yan, X., and Zhang, Y. (2020). Functional properties and promising applications of high entropy alloys. *Scripta Mater.* 187, 188–193. doi: 10.1016/j.scriptamat.2020.06.017
- Yan, X. H., Li, J. S., Zhang, W. R., and Zhang, Y. (2018). A brief review of high-entropy films. *Mater. Chem. Phys.* 210, 12–19. doi: 10.1016/j.matchemphys.2017.07.078
- Yang, C.-H., Wang, Y.-T., Tsai, W.-F., Ai, C.-F., Lin, M.-C., and Huang, H.-H. (2011). Effect of oxygen plasma immersion ion implantation treatment on corrosion resistance and cell adhesion of titanium surface. *Clin. Oral Implants Res.* 22, 1426–1432. doi: 10.1111/j.1600-0501.2010.02132.x
- Yang, W., Liu, Y., Pang, S., Liaw, P. K., and Zhang, T. (2020). Bio-corrosion behavior and in vitro biocompatibility of equimolar TiZrHfNbTa high-entropy alloy. *Intermetallics* 124:106845. doi: 10.1016/j.intermet.2020.106845
- Yao, H., Tan, Z., He, D., Zhou, Z., Zhou, Z., Xue, Y., et al. (2020). High strength and ductility AlCrFeNiV high entropy alloy with hierarchically heterogeneous microstructure prepared by selective laser melting. *J. Alloys Compounds* 813:152196. doi: 10.1016/j.jallcom.2019.152196
- Yao, H. W., Qiao, J. W., Hawk, J. A., Zhou, H. F., Chen, M. W., and Gao, M. C. (2017). Mechanical properties of refractory high-entropy alloys: experiments and modeling. *J. Alloys Compounds* 696, 1139–1150. doi: 10.1016/j.jallcom.2016.11.188
- Yeh, J.-W. (2006). Recent progress in high-entropy alloys. *Ann. Chim. Sci. Matér.* 31, 633–648. doi: 10.3166/acsm.31.633-8
- Yeh, J.-W., Chen, S. K., Lin, S.-J., Gan, J.-Y., Chin, T.-S., Shun, T., et al. (2004). Nanostructured high-entropy alloys with multiple principal elements: novel alloy design concepts and outcomes. *Advanced Engineering Materials* 6, 299–303. doi: 10.1002/adem.200300567
- Yuan, Y., Wu, Y., Yang, Z., Liang, X., Lei, Z., Huang, H., et al. (2019). Formation, structure and properties of biocompatible TiZrHfNbTa high-entropy alloys. *Mater. Res. Lett.* 7, 225–231. doi: 10.1080/21663831.2019.1584592
- Yurchenko, N., Panina, E., Tikhonovsky, M., Salishchev, G., Zhrebetsov, S., and Stepanov, N. (2020). A new refractory Ti-Nb-Hf-Al high entropy alloy strengthened by orthorhombic phase particles. *Int. J. Refract. Metals Hard Mater.* 92:105322. doi: 10.1016/j.ijrmhm.2020.105322
- Zhang, C., Ding, Z., Xie, L., Zhang, L.-C., Wu, L., Fu, Y., et al. (2017). Electrochemical and in vitro behavior of the nanosized composites of Ti-6Al-4V and TiO₂ fabricated by friction stir process. *Appl. Surf. Sci.* 423, 331–339. doi: 10.1016/j.apsusc.2017.06.141
- Zhang, H. X., Dai, J. J., Sun, C. X., and Li, S. Y. (2020). Microstructure and wear resistance of TiAlNiSiV high-entropy laser cladding coating on Ti-6Al-4V. *J. Mater. Process. Technol.* 282:116671. doi: 10.1016/j.jmatprotec.2020.116671
- Zhang, J., Hu, Y., Wei, Q., Xiao, Y., Chen, P., Luo, G., et al. (2020). Microstructure and mechanical properties of RexNbMoTaW high-entropy alloys prepared by arc melting using metal powders. *J. Alloys Compounds* 827:154301. doi: 10.1016/j.jallcom.2020.154301
- Zhang, L.-C., Chen, L.-Y., and Wang, L. (2020). Surface modification of titanium and titanium alloys: technologies, developments, and future interests. *Adv. Eng. Mater.* 22:1901258. doi: 10.1002/adem.201901258
- Zhang, M., Zhou, X., Yu, X., and Li, J. (2017). Synthesis and characterization of refractory TiZrNbWMo high-entropy alloy coating by laser cladding. *Surf. Coat. Technol.* 311, 321–329. doi: 10.1016/j.surfcoat.2017.01.012
- Zhang, W., Liaw, P. K., and Zhang, Y. (2018). Science and technology in high-entropy alloys. *Sci. China Mater.* 61, 2–22. doi: 10.1007/s40843-017-9195-8
- Zhang, Y., Han, T., Xiao, M., and Shen, Y. (2019). Effect of Nb content on microstructure and properties of laser cladding FeNiCoCrTi_{0.5}Nb_x high-entropy alloy coating. *Optik* 198:163316. doi: 10.1016/j.ijleo.2019.163316

- Zhang, Y., Zuo, T. T., Tang, Z., Gao, M. C., Dahmen, K. A., Liaw, P. K., et al. (2014). Microstructures and properties of high-entropy alloys. *Prog. Mater. Sci.* 61, 1–93.
- Zhao, Y., Yu, T., Sun, J., and Jiang, S. (2020). Microstructure and properties of laser cladded B4C/TiC/Ni-based composite coating. *Int. J. Refract. Metals Hard Mater.* 86:105112. doi: 10.1016/j.ijrmhm.2019.105112
- Zhou, E., Qiao, D., Yang, Y., Xu, D., Lu, Y., Wang, J., et al. (2020). A novel Cu-bearing high-entropy alloy with significant antibacterial behavior against corrosive marine biofilms. *J. Mater. Sci. Technol.* 46, 201–210. doi: 10.1016/j.jmst.2020.01.039
- Zhu, C., Lv, Y., Qian, C., Qian, H., Jiao, T., Wang, L., et al. (2016). Proliferation and osteogenic differentiation of rat BMSCs on a novel Ti/SiC metal matrix nanocomposite modified by friction stir processing. *Sci. Rep.* 6:38875. doi: 10.1038/srep38875
- Zhu, S., Yu, Y., Zhang, B., Zhang, Z., Yan, X., and Wang, Z. (2020). Microstructure and wear behaviour of in-situ TiN-Al₂O₃ reinforced CoCrFeNiMn high-entropy alloys composite coatings fabricated by plasma cladding. *Mater. Lett.* 272:127870. doi: 10.1016/j.matlet.2020.127870
- Conflict of Interest:** LL and BZ were employed by the company Chengsteel Group Co., Ltd., HBIS Group Co., Ltd.
- The remaining authors declare that the research was conducted in the absence of any commercial or financial relationships that could be construed as a potential conflict of interest.
- Copyright © 2020 Ma, Liu, Liu, Xie, Wei, Wang, Li, Zhao and Wang. This is an open-access article distributed under the terms of the Creative Commons Attribution License (CC BY). The use, distribution or reproduction in other forums is permitted, provided the original author(s) and the copyright owner(s) are credited and that the original publication in this journal is cited, in accordance with accepted academic practice. No use, distribution or reproduction is permitted which does not comply with these terms.



Surface Modification Techniques of Titanium and its Alloys to Functionally Optimize Their Biomedical Properties: Thematic Review

OPEN ACCESS

Edited by:

Lechun Xie,
Wuhan University of Technology,
China

Reviewed by:

Liang-Yu Chen,
Jiangsu University of Science
and Technology, China
Peng Fu,
Liaocheng University, China
Jiuxiao Li,
Shanghai University of Engineering
Sciences, China

*Correspondence:

Shifeng Liu
liushifeng66@xauat.edu.cn
Jia Liu
liujia0111@live.cn
Yujin Tang
tangyujin1967@163.com

[†]These authors have contributed
equally to this work

Specialty section:

This article was submitted to
Biomaterials,
a section of the journal
Frontiers in Bioengineering and
Biotechnology

Received: 05 September 2020

Accepted: 07 October 2020

Published: 11 November 2020

Citation:

Xue T, Attarilar S, Liu S, Liu J,
Song X, Li L, Zhao B and Tang Y
(2020) Surface Modification
Techniques of Titanium and its Alloys
to Functionally Optimize Their
Biomedical Properties: Thematic
Review.
Front. Bioeng. Biotechnol. 8:603072.
doi: 10.3389/fbioe.2020.603072

**Tong Xue^{1†}, Shokouh Attarilar^{2,3†}, Shifeng Liu^{1*}, Jia Liu^{4*}, Xi Song¹, Lanjie Li⁵,
Beibei Zhao⁵ and Yujin Tang^{4*}**

¹ School of Metallurgical Engineering, Xi'an University of Architecture and Technology, Xi'an, China, ² Department of Pediatric Orthopaedics, Xin Hua Hospital Affiliated to Shanghai Jiao Tong University School of Medicine, Shanghai, China, ³ State Key Laboratory of Metal Matrix Composites, School of Material Science and Engineering, Shanghai Jiao Tong University, Shanghai, China, ⁴ Affiliated Hospital of Youjiang Medical University for Nationalities, Baise, China, ⁵ Chengsteel Group Co., Ltd., HBIS Group Co., Ltd., Chengde, China

Depending on the requirements of specific applications, implanted materials including metals, ceramics, and polymers have been used in various disciplines of medicine. Titanium and its alloys as implant materials play a critical role in the orthopedic and dental procedures. However, they still require the utilization of surface modification technologies to not only achieve the robust osteointegration but also to increase the antibacterial properties, which can avoid the implant-related infections. This article aims to provide a summary of the latest advances in surface modification techniques, of titanium and its alloys, specifically in biomedical applications. These surface techniques include plasma spray, physical vapor deposition, sol-gel, micro-arc oxidation, etc. Moreover, the microstructure evolution is comprehensively discussed, which is followed by enhanced mechanical properties, osseointegration, antibacterial properties, and clinical outcomes. Future researches should focus on the combination of multiple methods or improving the structure and composition of the composite coating to further enhance the coating performance.

Keywords: titanium, surface modification, implant materials, osteogenesis properties, antibacterial function

INTRODUCTION

With the growing maturity of medical technologies, it is found that implanting biomaterials into the human body is an excellent way to treat some of the orthopedic and dental diseases (Lausmaa et al., 1990; Ohthuki et al., 1999). The commonly used metallic biomaterials are titanium (Ti) and its alloys (Wang et al., 2009; Guo et al., 2013; Jemat et al., 2015; Hafeez et al., 2019), 316L stainless steel (Singh et al., 2018), and cobalt-based alloys (Wang et al., 2014). Apart from these, shape memory alloys like magnesium (Mg) (Kirkland et al., 2010), NiTi (Bansiddhi et al., 2008; Wang et al., 2016; Wang et al., 2018; Liu et al., 2020a,b), and tantalum (Ta) are also potential candidates in biomedical applications (Balla et al., 2010). For the first time Ti was discovered in

the 1790s (Chouirfa et al., 2019). Nowadays, due to its high specific strength, strong corrosion resistance, and excellent biocompatibility (Jemat et al., 2015; Niinomi et al., 2016; Shi et al., 2017; Rabadia et al., 2018, 2019; Ran et al., 2018; Hafeez et al., 2020; Wang L. et al., 2020), titanium and its alloys have been widely used in the biomedical field (Wang et al., 2017), among which Ti-6Al-4V alloy applications account for more than 50% (Hu et al., 2012; Ding et al., 2016; Zhang et al., 2017). Although their beneficial properties (Matter and Burch, 1990), titanium and its alloys are considered as inert metals and cannot properly stimulate the proliferation of osteoblasts and bone cells (Zhu et al., 2016; Xiao et al., 2017; Souza et al., 2019). In addition, most of the failures are caused by implant-related infections, thus, lots of researches have been focused on improving the antibacterial ability of titanium implants (Yousefi et al., 2017; Ding et al., 2019; Liu et al., 2019; Wang et al., 2020). The exposed titanium alloy cannot resist the wear triggered by the relative movement between the implant and the bone, and external force and body fluid immersion will cause the disappearance of the passive film on the titanium alloy surface, resulting in a decrease in its corrosion performance (Zhang and Chen, 2019). The above problems can be solved by improving the surface properties of titanium and its alloys. Therefore, various surface modification methods have been used to improve the biological function, wear, and corrosion resistance of implants. In the last decade, coatings have been using in multiple applications to modify the surface of implants and, in some cases, to create new surfaces with exceptional properties that are very different from uncoated materials (Zhong, 1999, 2001; Wang et al., 2015; Wang et al., 2017; Gu et al., 2019). Furthermore, many studies proved that surface modifications techniques can minimize the bacterial adhesion on the implant substrate. They can also inhibit the biofilm formation and provide the effective bacterial removal, thus improving the performance of implanted biomaterials (Asri et al., 2017; Awad et al., 2017; Ahn et al., 2018; Zhang et al., 2020).

This review thematically focuses on surface modifications technologies such as plasma spray, plasma immersion ion implantation (PIII), plasma immersion ion implantation and deposition (PIII&D), physical vapor deposition (PVD), chemical vapor deposition (CVD), sol-gel, and micro-arc oxidation (MAO) methods. These methods are divided into two major parts: physical modification and chemical modification techniques. In the chemical methods, the surface is dipped into chemically active solutions, while in physical methods the surface is exposed to highly energetic charges or other physical species like a flame, plasma, etc. Certain technologies can have the involvement of multiple physical and chemical processes. Thus, it is impossible to strictly separate physical and chemical methods. The classification mainly depends on the main idea behind each technology. Moreover, this article summarizes the osteogenic and antibacterial properties achieved through surface technologies on Ti-based implant materials from these two aspects and provides a comprehensive incite to improve the surface techniques to manufacture the modern implant materials with improved properties. **Figure 1** shows all the surface treatment methods along with their pros and cons.

PHYSICAL MODIFICATION

The main idea of the physical modification method in Ti-based alloys is to treat and change the surface ultrastructure, and these methods include plasma spray technology, PIII, PIII&D, and PVD. The physical modification method is relatively cheap, and the preparation method and mechanism are simple. Correspondingly, the bonding force of the coating is weak, and it is slightly insufficient in the preparation of complex samples. **Table 1** gives a comparison of the main results of different physical methods.

Plasma Spray Technology

Plasma spray technology is a thermal spraying technique using plasma arc as the heat source, and it has been widely used to form coatings with excellent physical, chemical, and mechanical properties (Karthikeyan et al., 1997; Shaw et al., 2000), especially in the biomedical field. As shown in **Figure 2**, many parameters involved in this method, which can potentially affect the microstructure and properties of coatings, among them porosity is the most significant factor which determines the coating quality.

Hydroxyapatite (HA) coating is used to improve osteoconductivity and enhances osseointegration. Kotian et al. (2017) analyzed the production of HA coatings on Ti and Ti-6Al-4V under different plasma atmospheres. They proved that the atmosphere has a substantial influence on the composition, crystallinity, and the formation of microcracks of HA-coated implants. In order to obtain high-quality coatings, researchers need to control the temperature of the plasma gas to reduce microcracks. Besides, the atmosphere with argon and nitrogen gases showed the highest degree of crystallinity. Furthermore, according to Liu Y.-C. et al. (2020), a new vapor-induced pore-forming atmospheric plasma spraying (VIPF-APS) technique has great potential for producing bioactive porous HA coating which enhances osteoblast attachment and differentiation. Apart from the plasma spray technology, other strategies have been considered to improve the overall performance of the coating. Meanwhile, a new double-layer HA/Al₂O₃-SiO₂ coating was put forward by Ebrahimi et al. (2018), compared to monolayer HA, it has improved cell behavior and biocompatibility. Vahabzadeh et al. (2015) and Cao et al. (2019) doped Sr (Mg and Sr) into HA coating. In **Figure 3**, the formation of steroids is evident in the Sr-HA coating, which indicates that the bone regeneration of the Sr-HA coating is accelerated compared to uncoated Ti and HA coating implants. As for (Mg, Sr)-HA, on the fifth day, the visible cell adhesion prove its good biocompatibility on the surface of the coating, and it also showed high bonding strength. In another study, MgO, Ag₂O, and gradient HA were mixed in order to improve the biological and antibacterial properties (Ke et al., 2019). This novel method improves osseointegration and decreases the possibility of failure due to loosening or infection. Besides, Otsuka et al. (2016) clarified that due to the acceleration of dissolution at the interface, the delamination life of the HA coating immersed in the simulated body fluid (SBF) is shortened. Therefore, the delamination behavior of

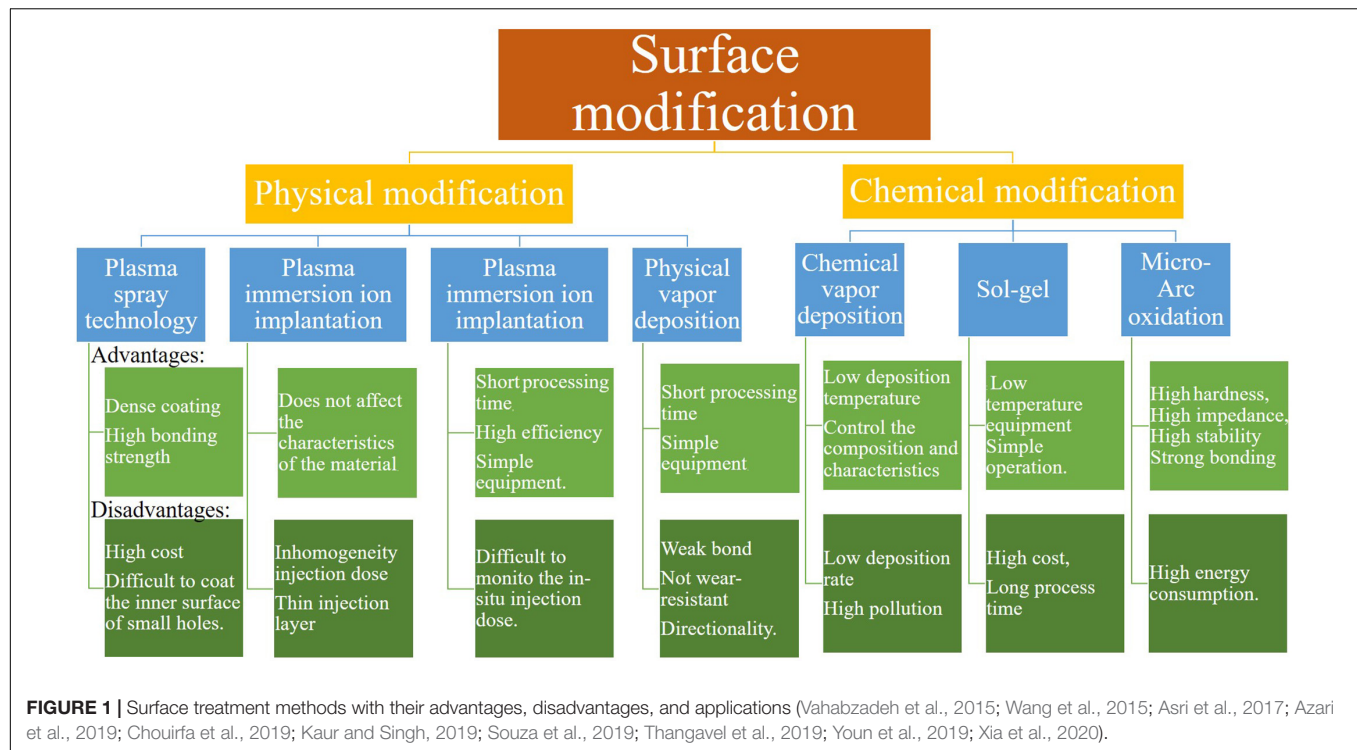


TABLE 1 | Main results of physical methods application on titanium and its alloys.

Methods	Coating quality	Process rate	Bond strength	Osteogenesis and antibacterial function	Applications
Plasma spray technology (Hanawa, 2019; Ke et al., 2019)	Dense coating, high bonding strength, difficult to oxidize spray material	Not available	20–80 MPa	Enhanced osseointegration, osteoblast proliferation and rapid bone repair.	Wide range of materials, suitable for a variety of coatings
Plasma immersion ion implantation (Yu et al., 2017; Shanaghi and Chu, 2019b)	Inert to surface thin injection layer, good biocompatibility.	Not available	Not available	Inhibition of <i>Staphylococcus aureus</i> and <i>Escherichia coli</i> (<i>E. coli</i>)	Used for large, heavy. and complex shaped workpieces
Plasma immersion ion implantation and deposition (Yang et al., 2007; Yu et al., 2017)	Easy composition control, improved density and adhesion, suitable for three-dimensional and complex surfaces	≈30–40 nm min ⁻¹ in thickness	Very high	Rapid osseointegration and continuous biomechanical stability, reduction of gram-negative <i>E. coli</i> and <i>Pseudomonas aeruginosa</i>	Used for precision parts with high added value to improve the wear resistance
Physical vapor deposition (Behera et al., 2020; Liu et al., 2020)	Uniform and dense film, strong bonding force	≈25–1,000 nm min ⁻¹ in thickness	Moderate	Surface modification to increase the contact area, good blood compatibility	Suitable for preparation of special functional composite membrane

extracorporeal circulation should be considered to extend the service life of HA coatings.

Researchers investigated the composite coatings for a decade, trying to improve the tribological behavior of implants, Ganapathy et al. (2015) prepared Al₂O₃ –40 wt.%8 YSZ on the biomedical grade Ti-6Al-4V alloy used for total joint prosthetic components through plasma spray. Another method, combined with the mutual effect of ceramics and metallic materials, have been investigated by Veerachamy et al. (2018). According to their research, Al₂O₃ +13 wt.% TiO₂/-YSZ BL can be deemed as a suitable coating on Ti-6Al-4V because of its high antibacterial activity and superior cell compatibility.

Furthermore, the bioactive glass-ceramic coating named M2 coating (including CaO–MgO–SiO₂) on Ti-6Al-4V alloy has shown good performance *in vitro*. In order to figure out its performance in osteogenesis and osseointegration, Zhang et al. (2019) implanted it into rabbits, it was verified that the M2 coated Ti-6Al-4V was provided with the better biological performance *in vivo* and could probable replace HA coating to repair load bearing bone implants. Many new coating materials have received extensive attention. For instance, tricalcium magnesium silicate is recommended as a new coating, which has almost the same thermal expansion properties as Ti-6Al-4V, also it has the potential to enhance the corrosion and biological behavior of

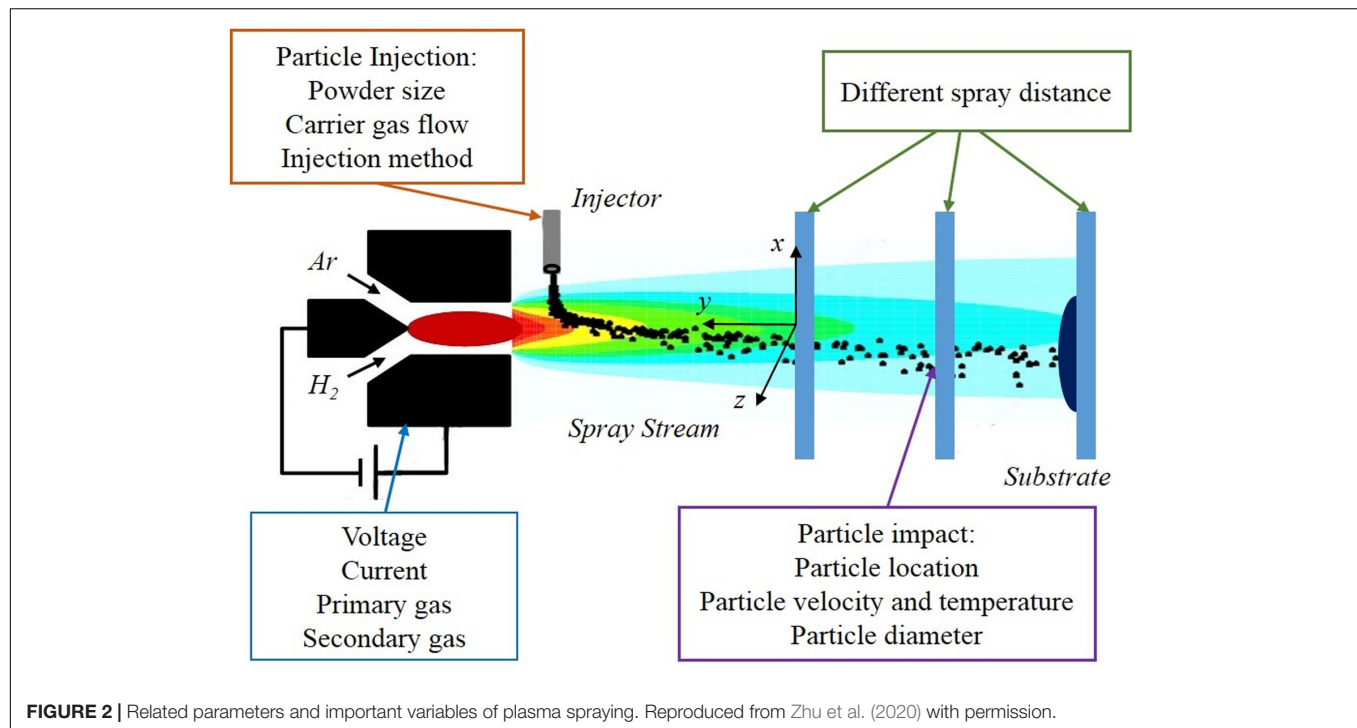


FIGURE 2 | Related parameters and important variables of plasma spraying. Reproduced from Zhu et al. (2020) with permission.

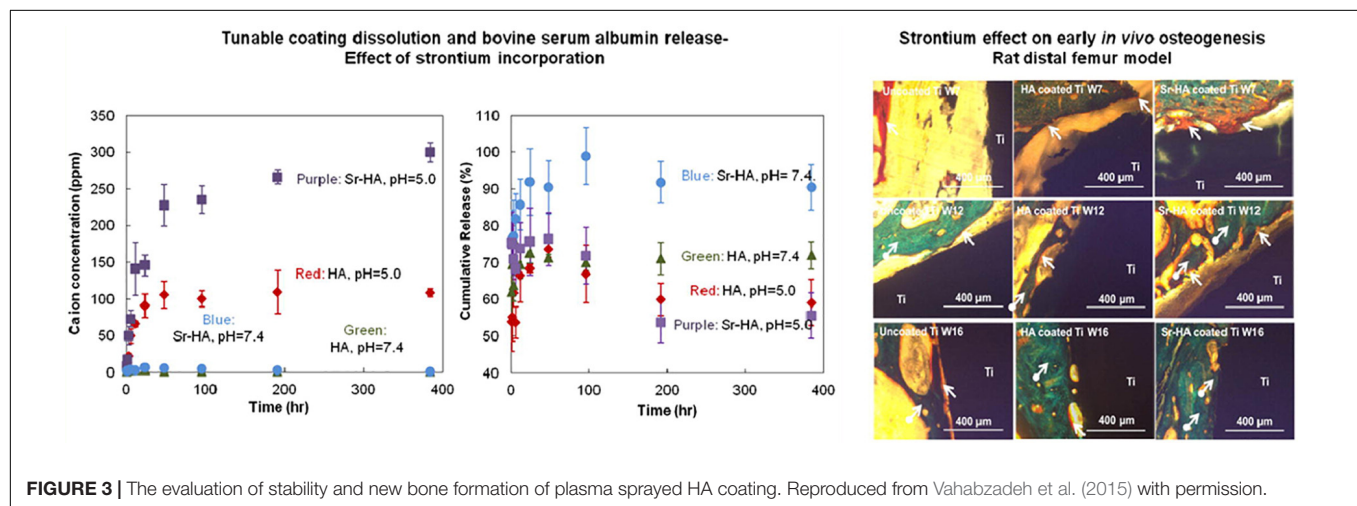


FIGURE 3 | The evaluation of stability and new bone formation of plasma sprayed HA coating. Reproduced from Vahabzadeh et al. (2015) with permission.

permanent metallic implants (Maleki-Ghaleh et al., 2015). At the same time, other metal elements with excellent bio-properties like tantalum (Kuo et al., 2019), have been deposited on titanium alloy implants.

Plasma spray technology provides a cost-effective, straightforward, and reliable approach to prepare coatings on titanium alloys. The gas atmosphere and temperature of plasma spraying will affect the thermal stress and crystallinity of the coating, which will affect the osteogenic activity and other properties. On the one hand, as the conventional coating material, HA needs to be upgraded by improving the production process or with doping new elements. On the other hand, novel coatings like metal composites should be considered. Although it was initially found that plasma sprayed TiO₂ and ZrO₂ coatings

have good biological activity and biocompatibility, the related mechanisms still need to be further explored. In addition, the plasma spraying temperature is extremely high, and the coating encounters large thermal stresses. Special attention should be paid to the bonding force between the coating and the substrate. Also, it still requires some improvement in the preparation of coatings on small and special-shaped workpieces.

Plasma Immersion Ion Implantation

Since the PIII technique enables to embed a great variety of elements into the near-surface region of the various substrates, it offers unique advantages for surface modification technologies of biomaterials (Lin et al., 2019). The most valuable feature of PIII is that the concentration and depth

distribution of the implanted ions in the substrate can be strictly controlled by adjusting the implantation parameters (Jin et al., 2014). In addition, it has been demonstrated that it can enhance the hardness, corrosion resistance, wear resistance, bioactivity, and antibacterial properties of biomaterials (Chen et al., 2020).

As the most common surface coating in Ti-based alloys, TiO_2 has attracted attention in the PIII method. PIII method and optical emission spectrometry (OES) was used to produce TiO_2 , which has the potential to improve the osseointegration of implants due to its super hydrophilicity (Lin et al., 2019). Shiau et al. (2019) and Chen et al. (2020) investigated the parameters of O-PIII respectively, the former proved that the applied voltage during O-PIII treatment promote blood-clotting and platelet activation, as shown in Figure 4, the latter indicates that the use of higher doses of oxygen ions can improve osteocytic differentiation and osseointegration of dental Ti implants *in vivo*. In addition to O-PIII, nitrogen plasma immersion ion implantation (N-PIII), carbon plasma immersion ion implantation (C-PIII), etc. were also widely used in fabricating coatings. Nitrogen was incorporated into TiO_2 coatings by N-PIII, which could effectively reduce the viability of bacteria in visible light (Zheng et al., 2020). Different from N-PIII, C-PIII was used to preparing coatings with increased mechanical properties and corrosion resistance (Shanaghi and Chu, 2019a). Unfortunately, it could also release the Ni element of NiTi alloys in the SBF solution (Shanaghi and Chu, 2019b).

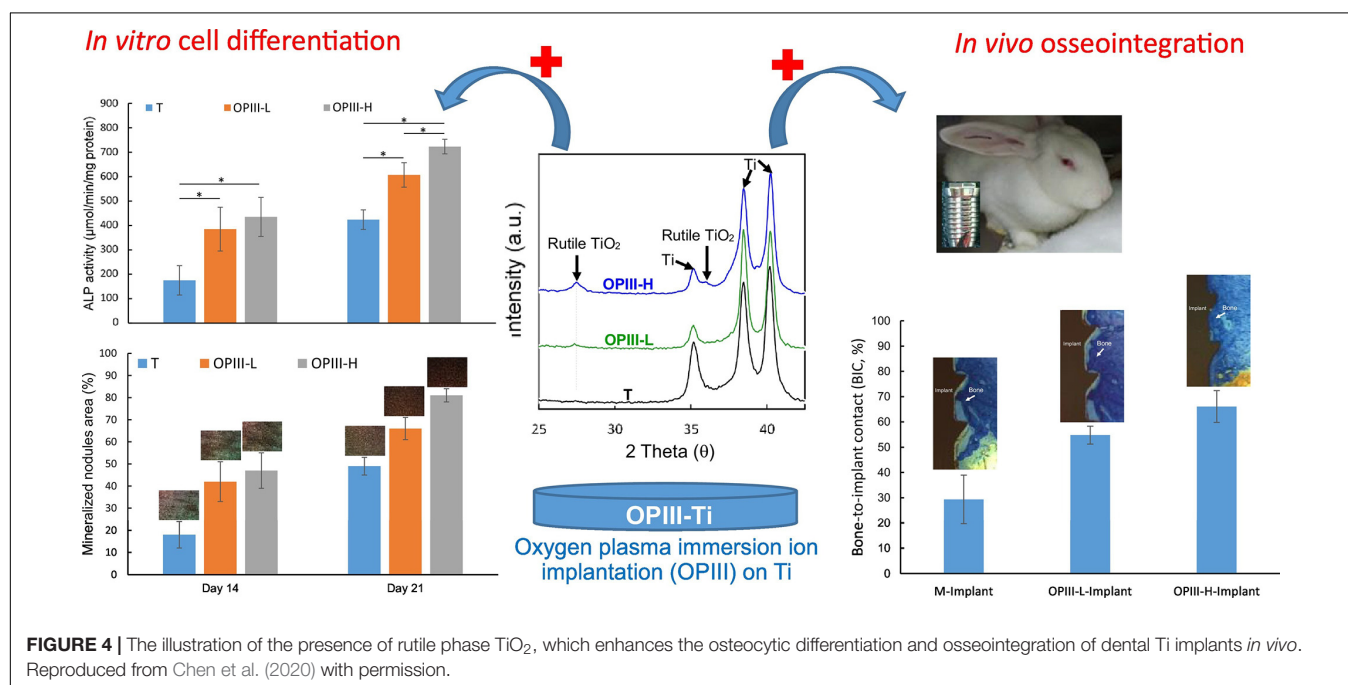
Besides, the TiN thin film can be formed on Ti-6Al-4V by N-PIII method (Huang et al., 2019), which could positively affect the surface hardness, corrosion resistance, cell responses, and antibacterial adhesion. Furthermore, Xu et al. (2015) added Ag into TiN films as an antibacterial agent, which has good cytocompatibility and retains the required mechanical properties.

The Zn-implanted Ti exhibits excellent osteogenic activity and partly antibacterial effect. It is worth noting that the depth profile of zinc in CP-Ti resembles a Gaussian distribution (Jin et al., 2014). Interestingly, Yu et al. (2017) developed dual Zn/Mg ion co-implanted titanium (Zn/Mg-PIII). Zinc is considered as an important and necessary trace element for bone metabolism and production, also Mg plays a critical role in the adhesion of osteoblasts and osteoblasts to orthopedic implants. Thus, due to the beneficial combination of Zn/Mg, the Zn/Mg-PIII implants present good osteoinductivity, pro-angiogenic and antibacterial effects and as shown in Figure 5, these implants can increase the rate of osseointegration and maintain biomechanical fixation.

In summary, with the ability to control the concentration and depth distribution of implanted ions, PIII shows the potential to implant single or multiple metal ions according to demand. Cell differentiation and osseointegration can be enhanced by injecting designated oxygen, nitrogen, or carbon ions. Additionally, O-PIII, N-PIII, C-PIII, etc. could contribute to essential elements for biocompatibility. Therefore, future research should focus on the procedures to achieve reasonable implantation of multiple metal ions by adjusting the PIII process parameters and to reduce the cytotoxicity caused by metal ion release.

Plasma Immersion Ion Implantation and Deposition

The PIII&D method, invented in 1987 by Conrad et al. (1987), it has become a routine surface modification method. It has the advantage to levitate the retained dose levels that were limited by the sputtering because of ion implantation. Therefore, using PIII&D with relatively low cost, a three-dimensional film with strong adhesion, thick and without stress is possible to be



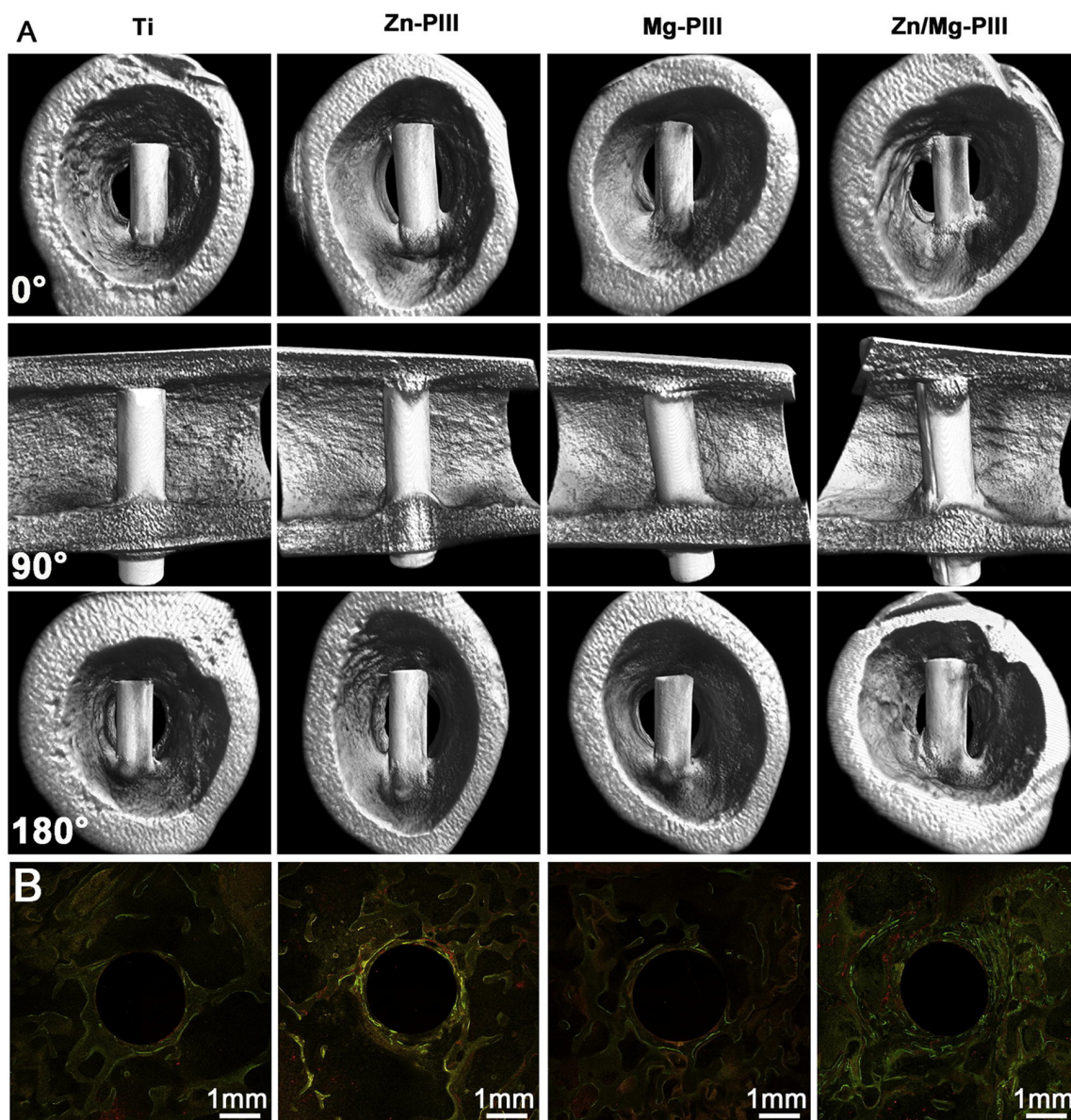
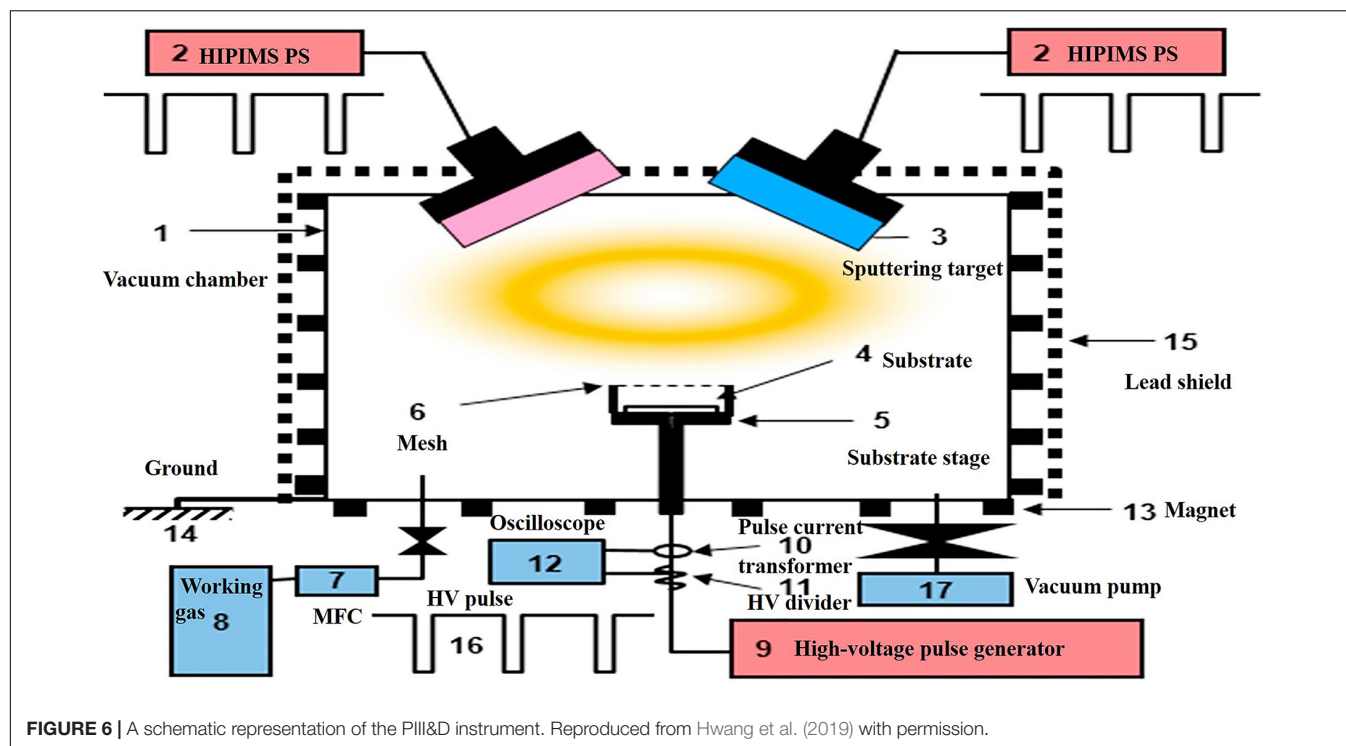


FIGURE 5 | Twelve weeks after implantation, newly formed around Zn/Mg-PIII implants and its sequential fluorescent labeling images. Reproduced from Yu et al. (2017) with permission. **(A)** Micro-CT 3D images of new bone formation around various implants in rabbit femur. **(B)** Sequential fluorescent labeling images of newly-formed bone around various implants in rabbit femoral condylar: Alizarin red S (red), tetracycline (yellow), Calcein (green).

produced (Yang et al., 2007). The schematic process of PIII&D was shown in **Figure 6**.

Facing a crucial problem namely thrombosis, blood-contacting biomaterials need to form an interface between the material and blood. Yang et al. (2007) modified the surface characteristics of biomaterial with the functional inorganic films of Ti-O, a-C: N:H, and Si-N synthesized using PIII-D, which can prevent the platelet adhesion/activation. Later in 2013, Ca film deposition has been completed on Ti for the applications of osseointegration in artificial components (Ueda et al., 2013), which is resulted in the formation of a well adherent Ca film. PIII&D was also used to improve the cell response to titanium,

Mg-Ag PIII&D treated Ti not only can inhibit the adhesion and proliferation of *Escherichia coli* bacteria but also promote the initial adhesion and alkaline phosphatase (ALP) expression of MG63 cells (Cao et al., 2014). Concurrently, an excellent compromise between the biocompatibility and cytotoxicity of incorporated metals (like Cu, Mn, etc.) is still required. Copper, a trace element that also exists in the human tissues, has a well-known antimicrobial activity. Hempel et al. (2014) testified that Cu doped and coated Ti can prevent and treat implant-associated infections. It's worth noting that the surface of overdosed Cu-bearing Ti exhibits negative biocompatibilities (Yu et al., 2016), except for the Cu coating. Yu et al. (2017)



investigated a stable Mn ion release on Ti, showing significantly enhanced osteogenesis-related gene expressions and providing a better understanding of relationships between the doped element and biological properties which are caused by additive induction. Aim to solve the bio-inertness of Ti, Ta-implanted entangled porous titanium (EPT) was constructed by the PIII&D method (Wang et al., 2016). As shown in **Figure 7**, compared with Ca-implanted EPTs, Ta-implanted EPTs shows more stable and continuous effects in the long-term utilization. Another study has deposited zirconium oxide nanostructured coating on the Ti-6Al-4V surface to improve the tribological properties (Saleem et al., 2017). Apart from these coatings, the penetration of nitrogen ions can also be used to support the stability of phospholipid artificial membranes (SLBs) with enhanced biocompatibility (Cisternas et al., 2020). Targeting improvement on the corrosion resistance and prolong the lifespan of Ti, carbon film deposition was accomplished by using a PIII&D system. Santos et al. (2019) verified the desirable properties of carbon films as coating, it can protect the titanium alloy tubes and also can provide new ideas in biology.

In summary, PIII&D technologies are widely used to form metal coatings on titanium and its alloys. Injecting metal ions into the surface of the Ti substrate through the PIII&D technology, since the metal phase tends to act as an anode to release metal ions, the antibacterial properties of the material can be improved. The PIII&D method generally deposits a single metal element on the titanium substrate, but the balance between toxicity and biocompatibility must be considered. PIII&D technology overcomes the apparent linearity problem of other physical deposition methods, and it is suitable for surface modification of complex-shaped workpieces but its biological safety should also

be scrutinized. In the future, the deposition of multiple metal elements or carbon nanomaterials must be investigated to further enhance the biocompatibility of the coatings.

Physical Vapor Deposition

Physical vapor deposition implies a physical coating strategy, involving the evaporation of solid metal under the vacuum environment and depositing it on a conductive substrate (Hauschild et al., 2015). Generally, vacuum evaporation, ion plating, and sputter coating, etc. are among the main methods of PVD. Among them, magnetron sputtering technology has been extensively studied and it results in the formation of high-quality films over a large area and at a relatively low substrate temperature (Nemati et al., 2018; Hamdi et al., 2019).

In the biomedical field, TiN coating concurrent with its favorable biocompatibility can be used as a desirable blood-contacting material. Prachar et al. (2015) compared the properties of TiN with ZrN on pure Ti, Ti-6Al-4V, and Ti35Nb6Ta titanium alloys. It was confirmed that TiN has higher cell colonization than ZrN. Furthermore, their color solves the issue of aesthetics in oral implantology because the color of these coatings prevents Ti visibility through the gingiva. Hussein et al. (2020) deposited TiN on Ti20Nb13Zr via cathodic arc PVD. The coated alloys show better corrosion protection behavior in both SBF and the artificial saliva medium. Wu et al. (2019) used the high-power impulse magnetron sputtering (HiPIMS) method which has high peak current and maximum power to deposit TiN on TiAl6V4. The 110 A deposited coating exhibits the highest cell viability. However, the biocompatibility of surface-modified Ti alloys mainly depends on the nitrogen content of the film, therefore in the work of Nemati et al. (2018), Ti_xNy are applied to Ti-6Al-4V

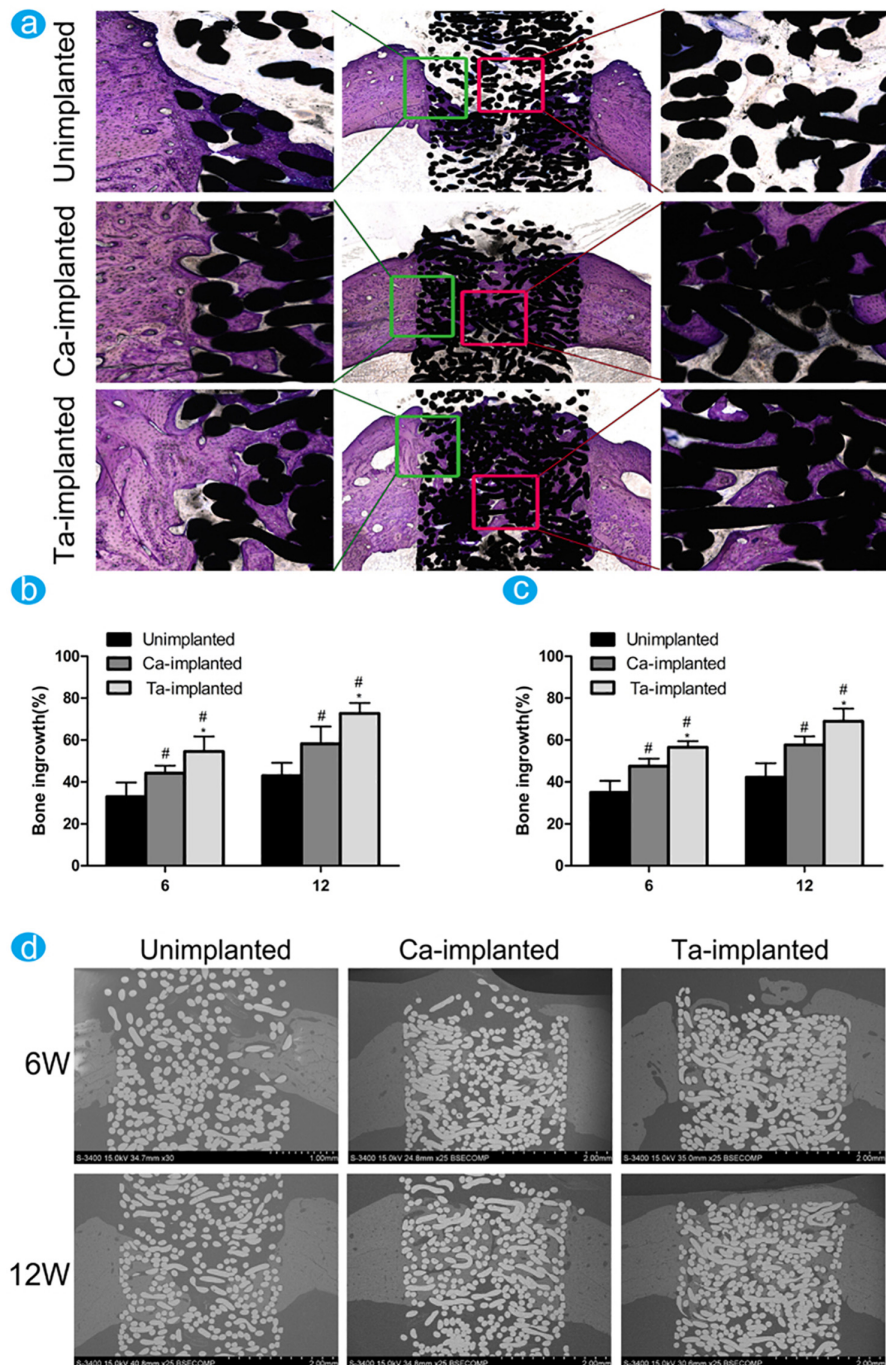


FIGURE 7 | The difference of new bone ingrowth was evaluated through histological observation and histomorphological measurement. Reproduced from Wang et al. (2016) with permission. **(a)** Undecalcified sections of samples were stained with toluidine blue at 12 weeks. The percentage of new bone ingrowth and pores in different EPT implants measured from toluidine blue staining **(b)** and back scattered SEM images **(c)** at 6 and 12 weeks. **(d)** The back scattered SEM images of new bone around and inside pores of EPT implants at 6 and 12 weeks.

substrates as thin films. They controlled the nitrogen partial pressure and prepared samples under a mixed atmosphere of Ar and N₂. Greater mechanical properties, corrosion resistance, and biocompatibility occurred with the upgrade of the N/Ti ratio. In the work of Bahi et al. (2020), two types of coatings

were studied: TiN as the top layer, while the upper layer of the others was TiO₂ with two different oxygen content. The TiN presents the best tribological performance in the multilayered film condition when its surface slide against the bovine cortical bone. Some researchers (Cui et al., 2019) found that compared

to TiN and ZrN coatings, partial replacement of Ti atoms with Zr provides excellent wear resistance and fracture toughness. The TiZrN graded coating which was prepared by Cui et al. (2019) is suitable for artificial joint applications that can endure large loads and resist serious wear conditions. Besides, Hauschild et al. (2015) put the Ag-coated cementless stem into the canine model and showed osseous integration *in vivo*, where toxic side effects did not appear. Afterward, Ag-doped NiTi (NiTi/Ag) coatings were prepared on pure Ti substrates by Thangavel et al. (2019). The NiTi/Ag coating with 3 at. % Ag showed the highest cell viability of human dermal fibroblast neonatal cells and showed a well-grown actin filament network. YSZ was deposited onto the titanium substrate in the study of Kaliaraj et al. (2016) unfortunately this coating couldn't inhibit bacterial growth but it could enhance the blood protein adhesion. Tantalum pentoxide nanotubes (Ta₂O₅ NTs) were prepared on biomedical grade Ti-6Al-4V alloy by Sarraf et al. (2017), results of the SBF tests exhibited that on the first day of immersion, a bone-like apatite layer has already formed on the coating of the nanotubular array, indicating the importance of nanotubular configuration for *in vitro* biological activity.

Nowadays, multi-layered coatings with prominent osseointegration properties and mechanical strength have become focused research areas. In this respect, HA bioceramics have good biocompatibility but the mechanical strength is weak. Hence, Hamdi et al. (2019) prepared triple-layered HA/Al₂O₃/TiO₂ coating on Ti-6Al-4V alloys. In this work, HA plays a critical role in biocompatibility, while others improve the corrosion behavior of the substrate, which prevents the entry of active ions from body fluids onto the surface. Chen et al. (2019) deposit a novel bio-functional bilayer coating consist of calcium phosphate and magnesium (CaP-Mg) on Ti. The CaP coating could inhibit the releasement of Mg, while the alkaline environment caused by Mg degradation has the potential to reduce the bacterial viability. Furthermore, BCP as a kind of CaP is the mixture of β -TCP, Behera et al. (2020) proved that BCP-TiO₂ film can be beneficial to improve the biological performance of implants. Nowadays, the development of amorphous carbon (a-C) films has received a lot of attention, Liu et al. (2020) successfully deposited Zr/a-C gradient multilayer films (GMFs), it comprised of three distinct layers. Zr/a-C GMFs modified Ti shows upgraded wettability, enhancing the proliferation and adhesion of osteoblast cells.

To sum up, PVD is used as a mature method to form a nearly perfect adhering layer of materials, which does not disintegrate nor affects the surface topography and shows good tribological properties. Due to the mismatch of the coefficient of thermal expansion between the coating and the substrate, their bonding force is weak, which limits the applications of this type of coating. At present, the transition layer or gradient coating deposition methods are generally used in order to reduce the mismatch of the crystal lattice and thermal stress between the coating and the substrate, thereby enhancing its binding force. TiN coatings with different element doped compositions seem to be the further research direction at present. It is necessary to consider the cell cytotoxicity, adhesion, activity, and antibacterial properties of the newly designed coating composition. In addition, multi-layered

coatings could provide proper performance, while researchers should rationally design multi-layer structures to maximize their respective advantages and avoid the possible adverse effects.

CHEMICAL MODIFICATION

The chemical modification changes the chemical properties of the carrier surface to produce specific interactions between cell surface molecules, which not only affect the cell surface properties but also cause closely related changes in the internal structure and function of cells. Chemical modifiers are relatively complex in preparation mechanisms and they are expensive. Current research focuses on composition control, multilayer structure design, multi-scale coatings, or coatings with novel surface morphologies. Table 2 gives a comparison of the main findings of different chemical methods.

Chemical Vapor Deposition

Chemical vapor deposition represents a coating method to form a thin film layer on the substrate surface by chemical reaction of one or several vapor compounds or elements that contain the final film elements (Marsh et al., 2010). It has been used in the inorganic synthetic chemistry to prepare inorganic materials like carbon nanotubes, graphene, TiO₂, etc. (Somani et al., 2006), the final product can be carefully controlled, both quantitatively and qualitatively. The facts have shown that the technology is very successful in industrial applications. However, their applications on titanium alloy substrate for biomedical surface modification is still limited.

Chemical vapor deposition methods are mainly used for complex workpieces and inner hole coating. Coatings prepared by the CVD method usually show high osteogenic activity, which has a certain potential for orthopedic applications. Giavaresi et al. (2003) used a metal-organic chemical vapor deposition (MOCVD) method to prepare the titanium oxide layer on pure titanium. Ti/MOCVD exhibited higher ALP activity than the control group, which means it has a higher potential for bone implantation. Subsequently, Du et al. (2016) successfully deposited Si-doped TiO₂ nanowires on the TiSi₂ layer by atmospheric pressure chemical vapor deposition (APCVD). It is not only showing higher hydrophilic activities but also has great importance in the field of doping. Related to the previous works, Xu et al. (2016) grafted a thin graphitic C₃N₄ (g-C₃N₄) layer on aligned TiO₂ nanotube arrays (TiNT) by CVD. The binary nanocomposite coating shows excellent bactericidal efficiency. Glycidyl methacrylate (GMA) is a chemically versatile reagent through a ring-opening reaction (Mao and Gleason, 2004; Kang et al., 2014). Hence, in the research of Park et al. (2015), dot-patterned GMA-coated titanium implants notably displayed higher ALP activities, while displayed increased protein adsorption and higher calcium deposition. Furthermore, based on the previous study, Youn et al. (2019) added recombinant human bone morphogenic protein-2 (rhBMP2) as osteoinductive agents on GMA-coated titanium. From *in vitro* analysis, they found its good osteogenic activity without any cytotoxicity. Scarce information exists on the effect of amino group

TABLE 2 | Main results of chemical methods application on titanium and its alloys.

Methods	Coating quality	Process rate	Bond strength	Osteogenesis and antibacterial function	Applications
Chemical vapor deposition (Du et al., 2016; Youn et al., 2019)	Good controlling on composition and characteristics of the film, flexibility	Deposition by chemical reaction at a high temperature	Not available	It positively affects the proliferation and activity of osteoblast-like cells, sterilization efficiency against <i>E. coli</i>	Used for complex workpieces and inner hole coating
Sol-gel (El hadad et al., 2020; Ziabka et al., 2020)	Easy to prepare uniform multi-component oxide film and quantitative doping, effective control on composition and microstructure	Several steps for the preparation of sol-gel, transfer of sol-gel to substrate, aging and drying	3–55 MPa	Bone-like apatite formation in SBF, good biological activity, antifungal effects	Used for preparing thin films, possible for coating on the surface of particles of powder materials
Micro-Arc oxidation (Sedelnikova et al., 2017; Li et al., 2018)	Suitable for ceramic membrane, firm bonding, dense and uniform ceramic membrane	$\approx 1\text{--}3\ \mu\text{m min}^{-1}$ in thickness	5–44 MPa	Improving the adhesion of cells. Good antibacterial ability against <i>E. coli</i> and <i>Staphylococcus aureus</i>	Used for improving the surface roughness

plasma-enhanced CVD on nerve regeneration. Hence, Zhao et al. (2018) introduced the amino group onto the titanium disk. Although, it exhibited the best cell attachment performance, it inhibited the expression of the key growth factors like glial cell-derived neurotrophic factor (GDNF) and neurotrophin nerve growth factor (NGF) *in vitro*, at least within a week. Tantalum coating on porous Ti-6Al-4V scaffold was investigated by Li et al. (2013), they found the better bone ingrowth within the coated scaffolds, indicating the potential for orthopedics. Interestingly, Ji et al. (2016) compared the adhesion of *Streptococcus mutans* on polished titanium (control group), magnetron sputtering titanium, and plasma nitriding modified titanium samples. There is not any clear difference between the treated samples and the control group. Gu et al. (2018) indicated the influence of heat treatment on the bonding strength and osteoinductive activity of monolayer graphene sheets with the antibacterial and osteoinductive properties.

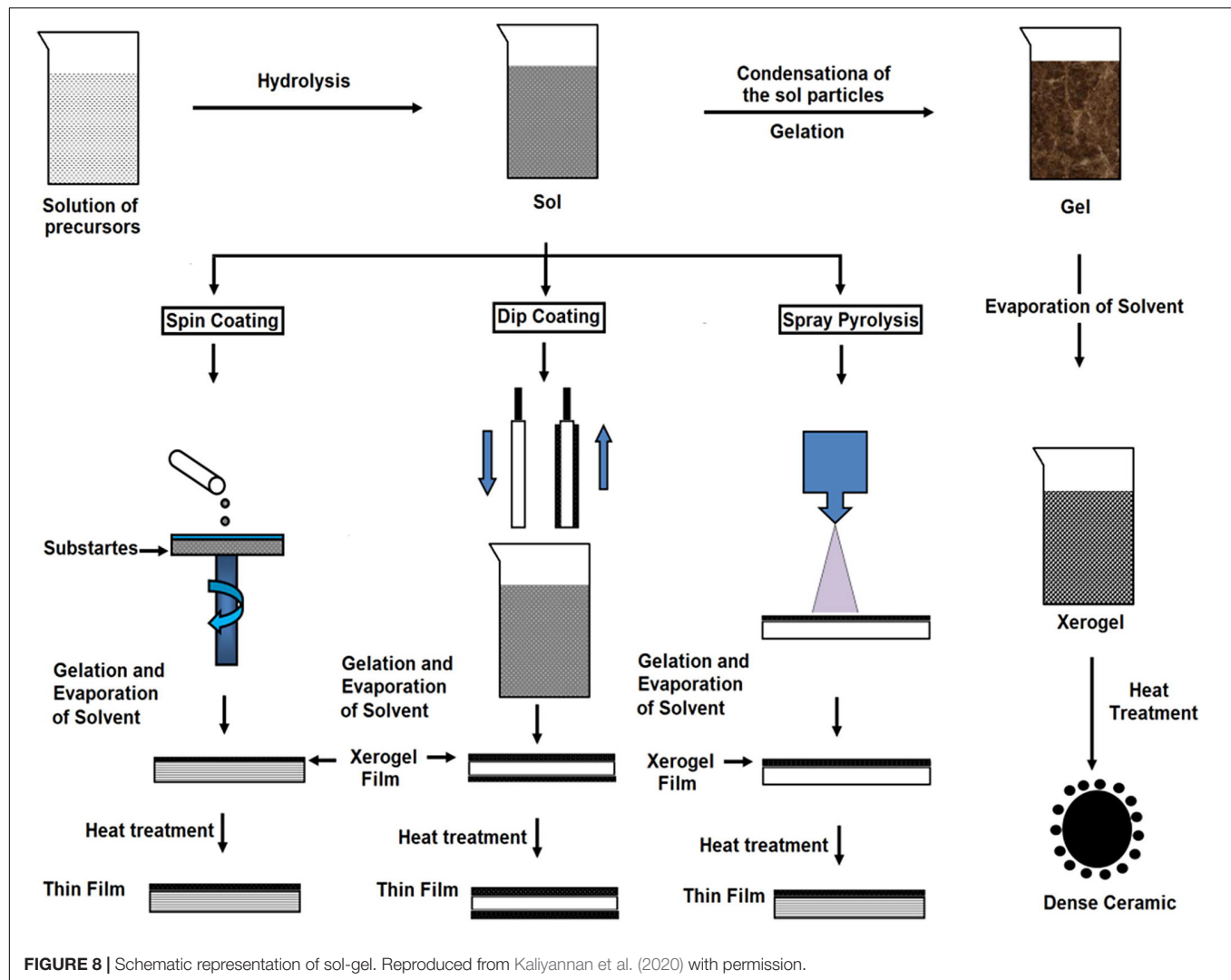
In summary, the utilization of the CVD methods is not as common as the physical methods mentioned earlier. It may be because of its high reaction temperature that leads to a low deposition rate, also in this method the gas source and exhaust gas have certain toxicity, which may be harmful to the subsequent implantation process. Despite this, the coatings made by CVD usually have good quality, and their purity and density can be controlled. It has been used in industries like electronics, automobiles, aviation, and aerospace. However, vapor deposition equipment is more expensive, and some processes have higher film forming temperatures, which may adversely affect the structure of the substrate. In addition, some process line-of-sight film forming methods are more difficult to form on small shaped parts and need to be improved. In the future, the preparation of copolymer and inorganic coatings by CVD should be studied in depth to form a bacteriostatic surface.

Sol-Gel

The Sol-gel technique is widely implemented to produce multifarious oxide films. This kind of method has the following advantages: simple fabrication environment, reliability of the

consuming equipment, high uniformity of films, and utilization of different sizes of the substrate (Hench and West, 1990). The main factor that affects the sol-gel method is pH, chemical equilibrium, substrate-precursor interface, time, etc. (Wang and Bierwagen, 2009). **Figure 8** is the schematic representation of sol-gel.

Ti, the dominant material for orthopedic application now, maybe impairing physical integrity like change its hardness and flexural modulus after sol-gel treatment. In order to solve this problem, Greer et al. (2016) evaluated coatings properties at different annealing temperatures and concluded that although the ductility decreased, 500°C was the optimal annealing temperature. TiO₂ coatings have good physical properties as follows: high surface hardness, good wear resistance, low friction coefficient, and excellent corrosion resistance. Çomaklı et al. (2018) compared TiO₂ films produced by sol-gel and successive ionic layer adsorption and reaction (SILAR) methods, the former exhibited better wear and corrosion resistance than the latter. Titania containing silver was deposited on TiSi alloys and commercially pure titanium (CP-Ti) by Horkavcova et al. (2017) and Yetim (2017), respectively. The results showed no cytotoxicity and excellent corrosion resistance, which means these materials are potential candidates for orthopedic application. Moreover, Ziabka et al. (2020) confirmed that this coating can be used in the veterinary treatment of bone fractures. In addition, doping with silver, TiO₂ often forms a double-layer coating with HA. As mentioned before, the use of HA promotes bone formation, and in addition, proper chemical homogeneity can be obtained through sol-gel technology (Domínguez-Trujillo et al., 2018). Mohammed Hussein and Talib Mohammed (2019) prepared bilayer TiO₂/HA coating, which has good corrosion protection with advanced crystallization and nano-scale homogeneous surface morphology. To enhance the adhesion strength of HA coatings sintered at low temperatures, Robertson et al. (2019) formed titania nanotubes through anodization. Azari et al. (2019) did further research and produced a functionally graded HA-TiO₂ on Ti-6Al-4V alloy substrate and improved the adhesion and cohesion of the single-layer coating.



Meanwhile, other strategies have been adopted to deal with the shortcomings of HA. Zinc substituted hydroxyapatite/bismuth (Zn-HA/Bi-HA) biphasic coatings were fabricated through sol-gel and dip-coating processes by Bi et al. (2020), which exhibited the most positive effect on osteoblast proliferation.

Moreover, bio-inert ceramics like silicon dioxide and zirconia attracts a wide range of attention because of their stability in the human body. It also exhibits excellent load-bearing capacity and high cell viability. Lee et al. (2017) made zirconia-coated porous-Ti (Z-P-Ti) by the hydrothermal method, and then the sol-gel method was used. Among the samples, Z-P-Ti_55 (Ti samples with 55 wt.% additions of NaCl) exhibited excellent load-bearing capacity and high cell viability. **Figure 9** is the mechanism of interaction between Z-P-Ti and the cell surface. Sandblasting Al_2O_3 combined with ZrO_2 sol-gel layer was obtained by Lubas et al. (2018), providing a stable bond. Romero-Gavilan et al. (2018) prepared silica hybrid sol-gel coating (35M35G30T) on Ti, it can adsorb a large number of complement proteins. These proteins are involved in maintaining cell renewal, healing, proliferation and regeneration, and many other processes, which

might be related to their intrinsic bioactivity. The addition of strontium (Sr) could affect their interactions with cells and proteins. Thus, Romero-Gavilan et al. (2019) applied a silica-hybrid sol-gel network doped with SrCl_2 as a coating on Ti. In *in vitro* analysis, the coating containing Sr is more abundant in proteins involved in the coagulation process. Besides, the gene expression of ALP and $\text{TGF}\beta$ was enhanced in the MC3T3-E1 cells.

Recently, organic-inorganic composite coatings have also received a lot of attention, which is a suitable candidate for metallic prosthetic equipment. Catauro et al. (2018) synthesized coating from a multicomponent solution. Higher vitality of cells seeded on the coated samples was recorded and the higher HA nucleation was detected on the CP-Ti surface after soaking in SBF, which was also happened in the research of Aghajanian et al. (2019). They coated the porous titanium surface with forsterite/poly-3-hydroxybutyrate (P3HB) nanobiocomposite, this coating inhibited the excessive pH increment of the SBF. Moreover, Palla-Rubio et al. (2019) found that different amounts of chitosan and tetraethyl orthosilicate (TEOS)

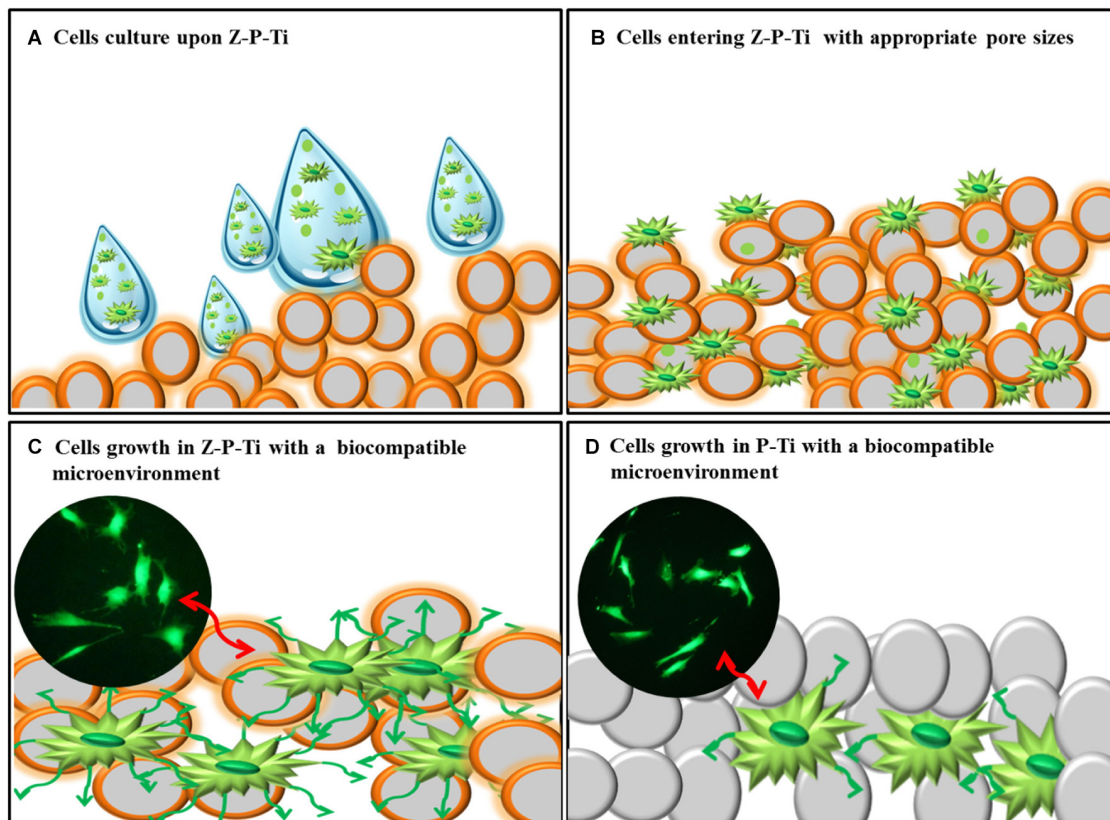


FIGURE 9 | The mechanism of interaction between Z-P-Ti and the cell surface. Reproduced from Lee et al. (2017) with permission. **(A)** Cells culture upon Z-P-Ti. **(B)** Cells entering Z-P-Ti with appropriate pore sizes. **(C)** Cells growth in Z-P-Ti with biocompatible microenvironment. **(D)** Cells growth in P-Ti with biocompatible microenvironment.

could modulate silicon release in hybrid silica-chitosan coatings, which plays a critical role in osteoregeneration. Based on the former research, Ballarre et al. (2020) added gentamicin to the chitosangelatin/silica, aimed at extending the bioactive effect. Based on, the sol consists of ZrO_2 , TiO_2 , Li^+ , and polyethylene glycol (PEG), Alcázar et al. (2019) evaluated the biocompatibility of hybrid coatings and found that the modified titanium surfaces have higher cellular growth. El hadad et al. (2020) have developed a new hybrid nanocomposite coating based on organofunctional alkoxysilanes precursors and phosphorus precursors, which prove that the presence of phosphorus at the molecular level can lead to the enhancement of biocompatibility. Simultaneously, Garcia-Casas et al. (2019) also deemed that an intermediate quantity of organophosphate showed the ability to enhance the mineralization of the substrate, which is why it was considered as the most suitable candidate for metallic prosthetic equipment. The drawbacks of pure HA were overcome by adding multi-minerals with the combination of PSSG polymer as hydroxyapatite/sorbitol sebacate glutamate (MHAP/PSSG) composite (Pan et al., 2019). Interestingly, Melatonin (MLT), used primarily to regulate the circadian rhythm and its role in bone regeneration and inflammation has been studied. Cerqueira et al. (2020) used sol-gel coatings as a release agent for MLT on a titanium substrate, they found that it

didn't improve the ALP activity, but has the potential in the activation and development of pathways. Based on the sol-gel coating, Toirac et al. (2020) added two different fungicides (fluconazole and anidulafungin) directly both of them exhibited anti-fungal properties.

At present, more research is conducted on the composition control of the sol-gel method than the process parameter control. These sol-gel coatings greatly enhance the corrosion protection and the migration of the metal matrix, thereby reducing the incidence of prosthesis rejection. Like other thermal deposition methods, it needs to consider the impact of thermal effects, so its current clinical use is subject to certain restrictions. There are extensive studies on the preparation of titanium dioxide, bio-inert ceramics, and organic-inorganic composite layers. For the titanium dioxide coating, the performance can be improved by doping other elements or improving the structural design of the composite coating with HA. For organic-inorganic composite coatings, in the future, it is possible to assess the comprehensive biocompatibility experiments by increasing the types of coating raw materials and adjusting the ratio.

Micro-Arc Oxidation

Micro-arc oxidation, is developed based on anodizing technology. The MAO process mainly relies on the matching

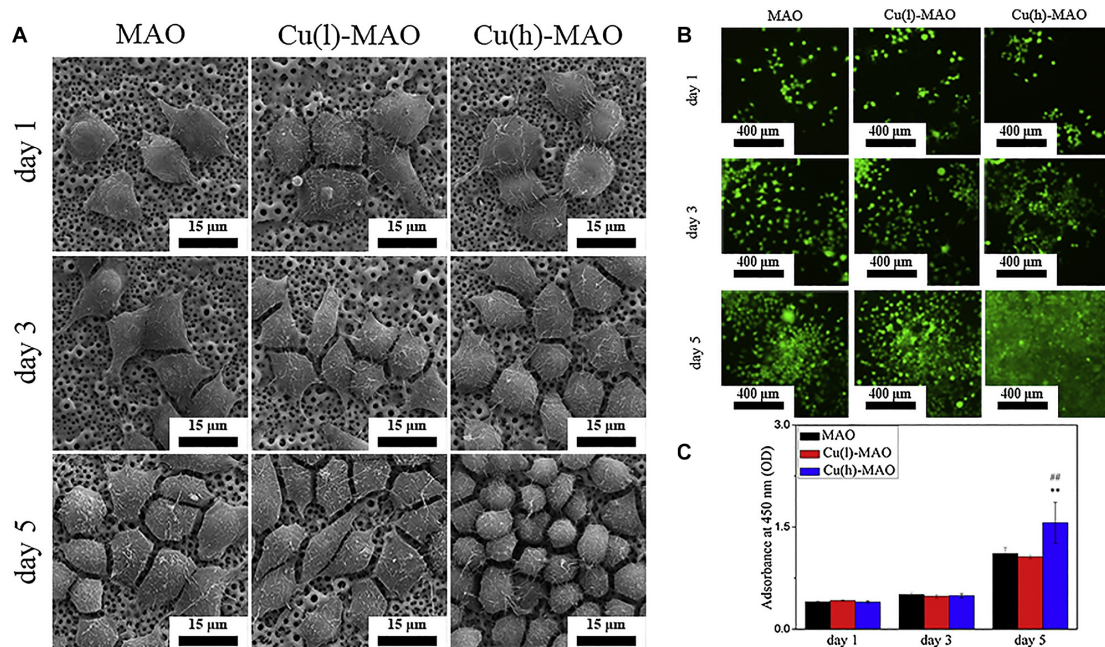


FIGURE 10 | (A) The morphology of macrophages cultured on the surface of various materials for 1, 3, and 5 days. **(B)** Calcein-AM staining and **(C)** CCK-8 results show that Cu(h)-MAO surface promotes the proliferation of macrophages. Reproduced from Huang et al. (2018) with permission.

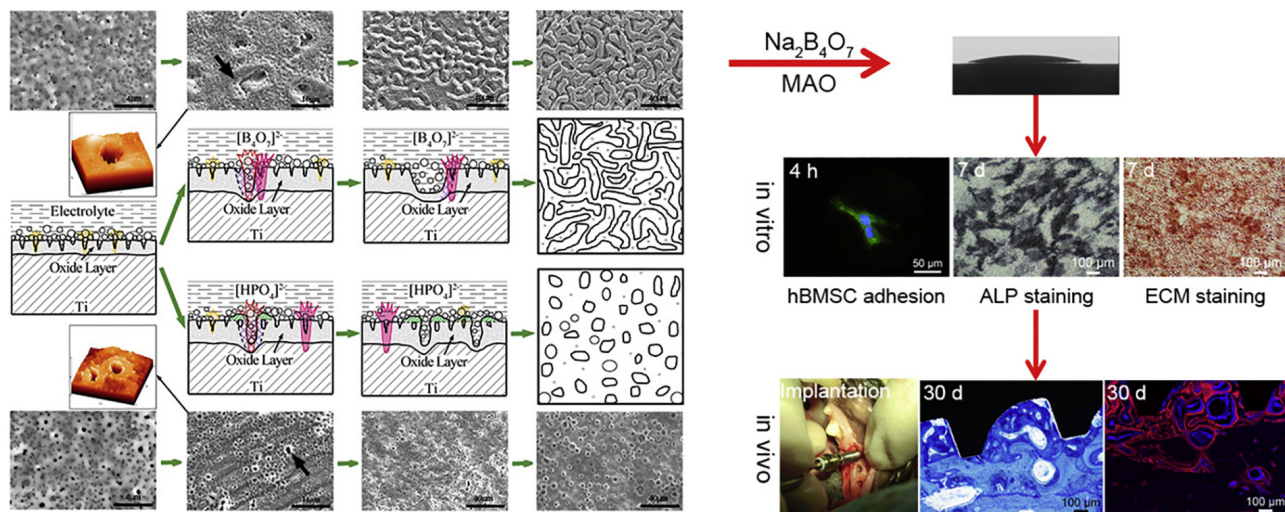


FIGURE 11 | The forming mechanism and biological performance evaluation of the micro-arc oxidized TiO₂ coatings with the “cortex-like” structure and the “volcanolike” structure. Reproduced from Li et al. (2018) with permission.

adjustment of the electrolyte and the electrical parameters. The process is done under the instantaneous high temperature and high pressure generated by the arc discharge, on the surface of Al, Mg, Ti, and other valve metals and their alloys. A modified ceramic coating produced by MAO is mainly composed of base metal oxides and supplemented with electrolyte components (Han et al., 2003; Li et al., 2004). It has the advantages of simple process, small area, strong processing capacity, high production efficiency, suitable for large industrial

production, environmental protection, etc. (Liu et al., 2015; Wang et al., 2015).

According to the principle of plasma-electrolytic oxidation, MAO can create a macro-porous and firmly adherent TiO₂ film on the Ti substrate, which got a lot of attention. Some organic substances coated on the layer can make a balance between antibacterial and cell compatibility (He et al., 2018). Additionally, bioactive elements, like B, Ag, Ca, and Sr can be incorporated with TiO₂ coating to enhance its bioactivity

and biological properties. Huang et al. (2016, 2018) prepared boron-incorporated TiO₂ coating (B-TiO₂ coating) and Cu-containing TiO₂ coatings successively. Specifically, the change of the chemical properties of the surface of B-TiO₂ coating and release of B ions from its surface is believed to be the main reason for the improvement of ALP activity and cell differentiation. In the latter research, although the incorporation of Cu did not change the surface morphology and roughness, it still improved the macrophage-mediated osteogenesis and sterilization ability (**Figure 10**). Zhang et al. (2020) also fabricated Cu-TiO₂ through a one-step MAO in a solution containing ethylene diamine tetraacetic acid cupric disodium (Na₂CuEDTA) that has a two-layered coating consisting of TiO₂ and porous Ca, P-rich outer layer containing nano-sized HA crystals. Subsequently, they investigated the enhanced antibacterial property and osteogenic activity of Zn-TiO₂ coating fabricated by one step MAO method (Zhang et al., 2019). This structure improved the proliferation and differentiation of osteoblasts and slightly enhanced the antibacterial capability relative to its relatively higher Cu content. Ag-incorporated TiO₂ coatings were prepared by Lv et al. (2019), the resultant film exhibits significantly improved antibacterial capability and bone-forming capacity with the increase of Ag₂O nanoparticles in the electrolyte, also it has a slightly upgraded cytotoxicity behavior relative to polished Ti substrate. Li et al. (2020) incorporated Ca and Sr, which are good for bone reconstruction, into the MAO coating. This coating has a highly porous and super-hydrophilic layered structure, which showed excellent promoting effects in the proliferation of human bone marrow-derived mesenchymal stem cells (hBMSC). It is also a good way to combine MAO with other processes to improve the performance of the coating. Therefore, Tang et al. (2020) prepared BaTiO₃ on the surface of TiO₂ produced by MAO through a hydrothermal reaction. In the early period after bone implantation, the piezoelectric effect of this coating may play a positive role in bone growth and bone integration. High energy shot peening (HESP) pretreatment can be used to enhance the stability and bioactivity of the TiO₂ coatings fabricated by MAO, Shen et al. (2020) used this method to increase the effective doping of Ca & P elements on the surfaces. Novel “cortex-like” coatings were investigated by Li et al. (2017, 2018), they have studied a macro/micro/nano triple hierarchical structure and micro/nano dual-scale structured TiO₂ coating on Ti. Results proved that the “cortex-like” structure significantly promotes the cell adhesion, diffusion, and differentiation and increases the matrix mineralization. The graphic abstract and schematic diagram of the “cortex-like” TiO₂ were shown in **Figure 11**.

The incorporation of Ca and P species into the TiO₂ surfaces can cause the biocompatible compound formation. Thus, plenty of studies focused on obtaining HA-containing coating on titanium and its alloys. Karbowniczek et al. (2017) proved that in the electrolyte containing disodium hydrogen phosphate and calcium acetate hydrate, with the Ca/P ratio of 2/1 the coated Ti6Al7Nb alloy achieved the best combination of bioactivity and mechanical properties. Through a two-step method, it is also possible to produce an oxide layer with micro-pores and bio-active elements by MAO on a surface with macro-porosity

(Costa et al., 2020). Similarly, Durdu et al. (2018) combined thermal evaporation-physical vapor deposition (TE-PVD) and MAO. In addition to higher hydrophilicity, the uniform and dense apatite distribution were observed on the Ag-incorporated coatings. Sedelnikova et al. (2017) deposited wollastonite-calcium phosphate (WeCaP) on the pure titanium, revealing the identical dependencies of coating thickness variation, surface roughness, and adhesion strength with process voltage. Interestingly, calcium-rich waste eggshell was used to produce HA coating on Ti-6Al-4V, which is in good agreement with that of bone.

As a hot spot technology for surface modification, MAO was used in lots of research schemes including the preparation of titanium dioxide and HA layers. The enhanced surface hydrophilicity of the porous coating prepared by the MAO method can stimulate the interaction between the implant and the surrounding biological environment, and it also brings excellent antibacterial properties due to the presence of metal ions. Although the anodic oxidation technology is convenient and economical, its bonding strength with the titanium matrix needs to be further improved. In future research, in addition to combining with other preparation methods, the structural design of the coating should be developed, such as the multi-level structure designs, multi-scale coating, or coating with novel surface morphology.

CONCLUSION

Titanium and its alloys are the most commonly used materials for permanent implants, especially in application with direct contact with the bone, teeth, and bodily fluid. Numerous techniques exist to modify titanium and its alloys surfaces, their different mechanisms, procedure, and targets were listed in this review and with the goal for further clarification of how to choose the corresponding surface modification process and to select its optimum parameters for different demands.

This article reviews the main physical and chemical surface modification techniques for Ti related biomaterials, such as plasma spray, PIII, PIII&D, PVD, CVD, sol-gel, and MAO. Although these methods have been applied in practice and achieved some results, they still have some deficiencies, like the bonding strength still needs to be improved, the influence of thermal effects is eliminated, and how to compromise between toxicity and biological performance, etc. Future studies must be focused on designing the basic new methods or the combination of a variety of surface modification methods to play a synergistic effect and combine their advantages to conquer the deficiencies. On the other hand, the structure and composition of the composite coating can be tailored in order to achieve excellent biomedical performance.

AUTHOR CONTRIBUTIONS

TX and SA wrote the main part of the manuscript. SL, JL, and YT greatly contributed to the physical methods parts. SA made major contributions particularly in planning the tables. TX, SA, and XS made significant contribution to the revision stage. TX, XS, LL,

and BZ prepared and formulated the references. All the authors contributed to the article and approved the submitted version.

FUNDING

This research was funded by the National Natural Science Foundation of China (Nos. 51671152 and 51874225), the Industrialization Project of Shaanxi Education Department

REFERENCES

- Aghajanian, A. H., Bigham, A., Khodaei, M., and Hossein Kelishadi, S. (2019). Porous titanium scaffold coated using forsterite/poly-3-hydroxybutyrate composite for bone tissue engineering. *Surf. Coat. Technol.* 378:124942. doi: 10.1016/j.surfcoat.2019.124942
- Ahn, T. K., Lee, D. H., Kim, T. S., Jang, G. C., Choi, S., Oh, J. B., et al. (2018). Modification of Titanium Implant and Titanium Dioxide for Bone Tissue Engineering. *Adv. Exp. Med. Biol.* 1077, 355–368. doi: 10.1007/978-981-13-0947-2_19
- Alcázar, J. C. B., Lemos, R. M. J., Conde, M. C. M., Chisini, L. A., Salas, M. M. S., NoreMBERG, B. S., et al. (2019). Preparation, characterization, and biocompatibility of different metal oxide/PEG-based hybrid coating synthesized by sol–gel dip coating method for surface modification of titanium. *Progr. Organic Coat.* 130, 206–213. doi: 10.1016/j.porgcoat.2019.02.007
- Asri, R. I. M., Harun, W. S. W., Samykano, M., Lah, N. A. C., Ghani, S. A. C., Tarlochan, F., et al. (2017). Corrosion and surface modification on biocompatible metals: a review. *Mater. Sci. Eng. C Mater. Biol. Appl.* 77, 1261–1274. doi: 10.1016/j.msec.2017.04.102
- Awad, N. K., Edwards, S. L., and Morsi, Y. S. (2017). A review of TiO₂ NTs on Ti metal: electrochemical synthesis, functionalization and potential use as bone implants. *Mater. Sci. Eng. C Mater. Biol. Appl.* 76, 1401–1412. doi: 10.1016/j.msec.2017.02.150
- Azari, R., Rezaie, H. R., and Khavandi, A. (2019). Investigation of functionally graded HA–TiO₂ coating on Ti–6Al–4V substrate fabricated by sol–gel method. *Ceramics Int.* 45, 17545–17555. doi: 10.1016/j.ceramint.2019.05.317
- Bahi, R., Nouveau, C., Beliardouh, N. E., Ramoul, C. E., Meddah, S., and Ghelloudj, O. (2020). Surface performances of Ti–6Al–4V substrates coated PVD multilayered films in biological environments. *Surf. Coat. Technol.* 385:125412. doi: 10.1016/j.surfcoat.2020.125412
- Balla, V. K., Bose, S., Davies, N. M., and Bandyopadhyay, A. (2010). Tantalum—A bioactive metal for implants. *JOM* 62, 61–64. doi: 10.1007/s11837-010-0110-y
- Ballarre, J., Aydemir, T., Liverani, L., Roether, J. A., Goldmann, W. H., and Boccaccini, A. R. (2020). Versatile bioactive and antibacterial coating system based on silica, gentamicin, and chitosan: improving early stage performance of titanium implants. *Surf. Coat. Technol.* 381:125138. doi: 10.1016/j.surfcoat.2019.125138
- Bansiddhi, A., Sargeant, T., Stupp, S. I., and Dunand, D. (2008). Porous NiTi for bone implants: a review. *Acta Biomater.* 4, 773–782. doi: 10.1016/j.actbio.2008.02.009
- Behera, R. R., Das, A., Hasan, A., Pamu, D., Pandey, L. M., and Sankar, M. R. (2020). Effect of TiO₂ addition on adhesion and biological behavior of BCP–TiO₂ composite films deposited by magnetron sputtering. *Mater. Sci. Eng. C* 114:111033. doi: 10.1016/j.msec.2020.111033
- Bi, Q., Song, X., Chen, Y., Zheng, Y., Yin, P., and Lei, T. (2020). Zn–HA/Bi–HA biphasic coatings on Titanium: fabrication, characterization, antibacterial and biological activity. *Colloids Surf. B Biointerf.* 189:110813. doi: 10.1016/j.colsurf.2020.110813
- Cao, H., Cui, T., Jin, G., and Liu, X. (2014). Cellular responses to titanium successively treated by magnesium and silver PIII&D. *Surf. Coat. Technol.* 256, 9–14. doi: 10.1016/j.surfcoat.2013.11.006
- Cao, L., Ullah, I., Li, N., Niu, S., Sun, R., Xia, D., et al. (2019). Plasma spray of biofunctional (Mg, Sr)-substituted hydroxyapatite coatings for titanium alloy implants. *J. Mater. Sci. Technol.* 35, 719–726. doi: 10.1016/j.jmst.2018.10.020
- (18JC019), and the funding 2020ZDLGY13-10 and 2020KJRC0048.
- ## ACKNOWLEDGMENTS
- We sincerely thank Ning Ma, Qingge Wang, and Wei Liu from Xi'an University of Architecture and Technology for data analysis of this article.
- Catauro, M., Bollino, F., and Papale, F. (2018). Surface modifications of titanium implants by coating with bioactive and biocompatible poly (ε-caprolactone)/SiO₂ hybrids synthesized via sol–gel. *Arab. J. Chem.* 11, 1126–1133. doi: 10.1016/j.arabjc.2015.02.010
- Cerqueira, A., Romero-Gavilán, F., Araújo-Gomes, N., García-Arnáez, I., Martínez-Ramos, C., Özturan, S., et al. (2020). A possible use of melatonin in the dental field: protein adsorption and in vitro cell response on coated titanium. *Mater. Sci. Eng. C* 2020:111262. doi: 10.1016/j.msec.2020.111262
- Chen, C.-S., Chang, J.-H., Srimaneepong, V., Wen, J.-Y., Tung, O.-H., Yang, C.-H., et al. (2020). Improving the in vitro cell differentiation and in vivo osseointegration of titanium dental implant through oxygen plasma immersion ion implantation treatment. *Surf. Coat. Technol.* 399:126125. doi: 10.1016/j.surfcoat.2020.126125
- Chen, L., Yan, X., Tan, L., Zheng, B., Muhammed, F. K., Yang, K., et al. (2019). In vitro and in vivo characterization of novel calcium phosphate and magnesium (CaP–Mg) bilayer coated titanium for implantation. *Surf. Coat. Technol.* 374, 784–796. doi: 10.1016/j.surfcoat.2019.06.023
- Chouirfa, H., Bouloussa, H., Migonney, V., and Falentin-Daudre, C. (2019). Review of titanium surface modification techniques and coatings for antibacterial applications. *Acta Biomater.* 83, 37–54. doi: 10.1016/j.actbio.2018.10.036
- Cisternas, M., Bhuyan, H., Retamal, M. J., Casanova-Morales, N., Favre, M., Volkmann, U. G., et al. (2020). Study of nitrogen implantation in Ti surface using plasma immersion ion implantation & deposition technique as biocompatible substrate for artificial membranes. *Mater. Sci. Eng. C Mater. Biol. Appl.* 113:111002. doi: 10.1016/j.msec.2020.111002
- Çomaklı, O., Yazıcı, M., Kovacı, H., Yetim, T., Yetim, A. F., and Çelik, A. (2018). Tribological and electrochemical properties of TiO₂ films produced on Cp–Ti by sol–gel and SILAR in bio-simulated environment. *Surf. Coat. Technol.* 352, 513–521. doi: 10.1016/j.surfcoat.2018.08.056
- Conrad, J. R., Radtke, J. L., Dodd, R. A., Worzala, F. J., and Tran, N. C. (1987). Plasma source ion-implantation technique for surface modification of materials. *J. Appl. Phys.* 62, 4591–4596. doi: 10.1063/1.339055
- Costa, A. I., Sousa, L., Alves, A. C., and Toptan, F. (2020). Tribocorrosion behaviour of bio-functionalized porous Ti surfaces obtained by two-step anodic treatment. *Corrosion Sci.* 166:108467. doi: 10.1016/j.corsci.2020.108467
- Cui, W., Cheng, J., and Liu, Z. (2019). Bio-tribocorrosion behavior of a nanocrystalline TiZrN coating on biomedical titanium alloy. *Surf. Coat. Technol.* 369, 79–86. doi: 10.1016/j.surfcoat.2019.04.036
- Ding, Z., Fan, Q., and Wang, L. (2019). A review on friction stir processing of titanium alloy: characterization, method, microstructure, properties. *Metallurgical Mater. Trans. B* 50, 2134–2162. doi: 10.1007/s11663-019-01634-9
- Ding, Z., Zhang, C., Xie, L., Zhang, L.-C., Wang, L., and Lu, W. (2016). Effects of Friction Stir Processing on the Phase Transformation and Microstructure of TiO₂-Compounded Ti–6Al–4V Alloy. *Metallurgical Mater. Trans. A* 47, 5675–5679. doi: 10.1007/s11661-016-3809-8
- Dominguez-Trujillo, C., Peón, E., Chicardi, E., Pérez, H., Rodríguez-Ortiz, J. A., Pavón, J. J., et al. (2018). Sol-gel deposition of hydroxyapatite coatings on porous titanium for biomedical applications. *Surf. Coat. Technol.* 333, 158–162. doi: 10.1016/j.surfcoat.2017.10.079
- Du, J., Li, X., Li, K., Gu, X., Qi, W., and Zhang, K. (2016). High hydrophilic Si-doped TiO₂ nanowires by chemical vapor deposition. *J. Alloys Compounds* 687, 893–897. doi: 10.1016/j.jallcom.2016.06.182
- Durdu, S., Aktug, S. L., Korkmaz, K., Yalcin, E., and Aktas, S. (2018). Fabrication, characterization and in vitro properties of silver-incorporated TiO₂ coatings on

- titanium by thermal evaporation and micro-arc oxidation. *Surf. Coat. Technol.* 352, 600–608. doi: 10.1016/j.surfcoat.2018.08.050
- Ebrahimi, N., Zadeh, A. S. A. H., Vaezi, M. R., and Mozafari, M. (2018). A new double-layer hydroxyapatite/alumina-silica coated titanium implants using plasma spray technique. *Surf. Coat. Technol.* 352, 474–482. doi: 10.1016/j.surfcoat.2018.08.022
- El hadad, A. A., García-Galván, F. R., Mezour, M. A., Hickman, G. J., Soliman, I. E., Jiménez-Morales, A., et al. (2020). Organic-inorganic hybrid coatings containing phosphorus precursors prepared by sol-gel on Ti6Al4V alloy: electrochemical and in-vitro biocompatibility evaluation. *Prog. Organic Coat.* 148:105834. doi: 10.1016/j.porgcoat.2020.105834
- Ganapathy, P., Manivasagam, G., Rajamanickam, A., and Natarajan, A. (2015). Wear studies on plasma-sprayed Al₂O₃ and 8mole% of Yttrium-stabilized ZrO₂ composite coating on biomedical Ti-6Al-4V alloy for orthopedic joint application. *Int. J. Nanomed.* 10(Suppl. 1), 213–222. doi: 10.2147/IJN.S79997
- García-Casas, A., Aguilera-Correa, J. J., Mediero, A., Esteban, J., and Jimenez-Morales, A. (2019). Functionalization of sol-gel coatings with organophosphorus compounds for prosthetic devices. *Colloids Surf. B Biointerf.* 181, 973–980. doi: 10.1016/j.colsurfb.2019.06.042
- Giavaresi, G., Giardino, R., Ambrosio, L., Battiston, G., Gerbasio, R., Fini, M., et al. (2003). In vitro biocompatibility of titanium oxide for prosthetic devices nanostructured by low pressure metal-organic chemical vapor deposition. *Int. J. Artif. Organs.* 26, 774–780. doi: 10.1177/039139880302600811
- Greer, A. I., Lim, T. S., Brydone, A. S., and Gadegaard, N. (2016). Mechanical compatibility of sol-gel annealing with titanium for orthopaedic prostheses. *J. Mater. Sci. Mater. Med.* 27:21. doi: 10.1007/s10856-015-5611-3
- Gu, H., Ding, Z., Yang, Z., Yu, W., Zhang, W., Lu, W., et al. (2019). Microstructure evolution and electrochemical properties of TiO₂/Ti-35Nb-2Ta-3Zr micro/nano-composites fabricated by friction stir processing. *Mater. Design* 169:107680. doi: 10.1016/j.matdes.2019.107680
- Gu, M., Lv, L., Du, F., Niu, T., Chen, T., Xia, D., et al. (2018). Effects of thermal treatment on the adhesion strength and osteoinductive activity of single-layer graphene sheets on titanium substrates. *Sci. Rep.* 8:8141. doi: 10.1038/s41598-018-26551-w
- Guo, Y., Chen, D., Cheng, M., Lu, W., Wang, L., and Zhang, X. (2013). The bone tissue compatibility of a new Ti35Nb2Ta3Zr alloy with a low Young's modulus. *Int. J. Mol. Med.* 31, 689–697. doi: 10.3892/ijmm.2013.1249
- Hafeez, N., Liu, J., Wang, L., Wei, D., Tang, Y., Lu, W., et al. (2020). Superelastic response of low-modulus porous beta-type Ti-35Nb-2Ta-3Zr alloy fabricated by laser powder bed fusion. *Addit. Manufact.* 34:101264. doi: 10.1016/j.addma.2020.101264
- Hafeez, N., Liu, S., Lu, E., Wang, L., Liu, R., Lu, W., et al. (2019). Mechanical behavior and phase transformation of β -type Ti-35Nb-2Ta-3Zr alloy fabricated by 3D-Printing. *J. Alloys Compounds* 790, 117–126. doi: 10.1016/j.jallcom.2019.03.138
- Hamdi, D. A., Jiang, Z.-T., No, K., Rahman, M. M., Lee, P.-C., Truc, L. N. T., et al. (2019). Biocompatibility study of multi-layered hydroxyapatite coatings synthesized on Ti-6Al-4V alloys by RF magnetron sputtering for prosthetic-orthopaedic implant applications. *Appl. Surf. Sci.* 463, 292–299. doi: 10.1016/j.apsusc.2018.08.157
- Han, Y., Hong, S.-H., and Xu, K. (2003). Structure and in vitro bioactivity of titania-based films by micro-arc oxidation. *Surf. Coat. Technol.* 168, 249–258. doi: 10.1016/S0257-8972(03)00016-1
- Hanawa, T. (2019). Titanium-tissue interface reaction and its control with surface treatment. *Front. Bioeng. Biotechnol.* 7:170. doi: 10.3389/fbioe.2019.00170
- Hauschild, G., Harges, J., Gosheger, G., Stoeppeler, S., Ahrens, H., Blaske, F., et al. (2015). Evaluation of osseous integration of PVD-silver-coated hip prostheses in a canine model. *Biomed. Res. Int.* 2015:292406. doi: 10.1155/2015/292406
- He, Y., Zhang, Y., Shen, X., Tao, B., Liu, J., Yuan, Z., et al. (2018). The fabrication and in vitro properties of antibacterial polydopamine-LL-37-POPC coatings on micro-arc oxidized titanium. *Colloids Surf. B Biointerf.* 170, 54–63. doi: 10.1016/j.colsurfb.2018.05.070
- Hempel, F., Finke, B., Zietz, C., Bader, R., Weltmann, K. D., and Polak, M. (2014). Antimicrobial surface modification of titanium substrates by means of plasma immersion ion implantation and deposition of copper. *Surf. Coat. Technol.* 256, 52–58. doi: 10.1016/j.surfcoat.2014.01.027
- Hench, L. L., and West, J. K. (1990). The sol-gel process. *Chem. Rev.* 90, 33–72.
- Horkavcova, D., Novak, P., Fialova, I., Cerny, M., Jablonska, E., Lipov, J., et al. (2017). Titania sol-gel coatings containing silver on newly developed TiSi alloys and their antibacterial effect. *Mater. Sci. Eng. C Mater. Biol. Appl.* 76, 25–30. doi: 10.1016/j.msec.2017.02.137
- Hu, Y., Cai, K., Luo, Z., Zhang, Y., Li, L., Lai, M., et al. (2012). Regulation of the differentiation of mesenchymal stem cells in vitro and osteogenesis in vivo by microenvironmental modification of titanium alloy surfaces. *Biomaterials* 33, 3515–3528. doi: 10.1016/j.biomaterials.2012.01.040
- Huang, H.-H., Shiau, D.-K., Chen, C.-S., Chang, J.-H., Wang, S., Pan, H., et al. (2019). Nitrogen plasma immersion ion implantation treatment to enhance corrosion resistance, bone cell growth, and antibacterial adhesion of Ti-6Al-4V alloy in dental applications. *Surf. Coat. Technol.* 365, 179–188. doi: 10.1016/j.surfcoat.2018.06.023
- Huang, Q., Elkhooly, T. A., Liu, X., Zhang, R., Yang, X., Shen, Z., et al. (2016). SaOS-2 cell response to macro-porous boron-incorporated TiO₂ coating prepared by micro-arc oxidation on titanium. *Mater. Sci. Eng. C Mater. Biol. Appl.* 67, 195–204. doi: 10.1016/j.msec.2016.05.051
- Huang, Q., Li, X., Elkhooly, T. A., Liu, X., Zhang, R., Wu, H., et al. (2018). The Cu-containing TiO₂ coatings with modulatory effects on macrophage polarization and bactericidal capacity prepared by micro-arc oxidation on titanium substrates. *Colloids Surf. B Biointerf.* 170, 242–250. doi: 10.1016/j.colsurfb.2018.06.020
- Hussein, M. A., Adesina, A. Y., Kumar, A. M., Sorour, A. A., Ankan, N., and Al-Aqeeli, N. (2020). Mechanical, in-vitro corrosion, and tribological characteristics of TiN coating produced by cathodic arc physical vapor deposition on Ti20Nb13Zr alloy for biomedical applications. *Thin. Solid Films* 709:138183. doi: 10.1016/j.tsf.2020.138183
- Hwang, S., Lim, S. H., and Han, S. (2019). Highly adhesive and bioactive Ti-Mg alloy thin film on polyether ether ketone formed by PIII&D technique. *Appl. Surf. Sci.* 471, 878–886. doi: 10.1016/j.apsusc.2018.12.080
- Jemat, A., Ghazali, M. J., Razali, M., and Otsuka, Y. (2015). Surface Modifications and Their Effects on Titanium Dental Implants. *Biomed. Res. Int.* 2015:791725. doi: 10.1155/2015/791725
- Ji, M. K., Lee, M. J., Park, S. W., Lee, K., Yun, K. D., Kim, H. S., et al. (2016). Evaluation of antibacterial activity of titanium surface modified by PVD/PACVD process. *J. Nanosci. Nanotechnol.* 16, 1656–1659. doi: 10.1166/jnn.2016.11924
- Jin, G., Cao, H., Qiao, Y., Meng, F., Zhu, H., and Liu, X. (2014). Osteogenic activity and antibacterial effect of zinc ion implanted titanium. *Colloids Surf. B Biointerf.* 117, 158–165. doi: 10.1016/j.colsurfb.2014.02.025
- Kaliaraj, G. S., Bavanilathamuthiah, M., Kirubakaran, K., Ramachandran, D., Dharini, T., Viswanathan, K., et al. (2016). Bio-inspired YSZ coated titanium by EB-PVD for biomedical applications. *Surf. Coat. Technol.* 307, 227–235. doi: 10.1016/j.surfcoat.2016.08.039
- Kaliyannan, G. V., Palanisamy, S. V., Priyanka, E. B., Thangavel, S., Sivaraj, S., and Rathanasamy, R. (2020). Investigation on sol-gel based coatings application in energy sector – A review. *Mater. Today Proc.* doi: 10.1016/j.matpr.2020.03.484
- Kang, B.-J., Kim, H., Lee, S. K., Kim, J., Shen, Y., Jung, S., et al. (2014). Umbilical-cord-blood-derived mesenchymal stem cells seeded onto fibronectin-immobilized polycaprolactone nanofiber improve cardiac function. *Acta Biomater.* 10, 3007–3017. doi: 10.1016/j.actbio.2014.03.013
- Karbowiczek, J., Muhaffel, F., Cempura, G., Cimenoglu, H., and Czyrska-Filemonowicz, A. (2017). Influence of electrolyte composition on microstructure, adhesion and bioactivity of micro-arc oxidation coatings produced on biomedical Ti6Al7Nb alloy. *Surf. Coat. Technol.* 321, 97–107. doi: 10.1016/j.surfcoat.2017.04.031
- Karthikeyan, J., Berndt, C., Tikkanen, J., Reddy, S., and Herman, H. (1997). Plasma spray synthesis of nanomaterial powders and deposits. *Mater. Sci. Eng. A* 238, 275–286. doi: 10.1016/S0921-5093(96)10568-2
- Kaur, M., and Singh, K. (2019). Review on titanium and titanium based alloys as biomaterials for orthopaedic applications. *Mater. Sci. Eng. C Mater. Biol. Appl.* 102, 844–862. doi: 10.1016/j.msec.2019.04.064
- Ke, D., Vu, A. A., Bandyopadhyay, A., and Bose, S. (2019). Compositionally graded doped hydroxyapatite coating on titanium using laser and plasma spray deposition for bone implants. *Acta Biomater.* 84, 414–423. doi: 10.1016/j.actbio.2018.11.041

- Kirkland, N., Lespagnol, J., Birbilis, N., and Staiger, M. (2010). A survey of bio-corrosion rates of magnesium alloys. *Corrosion Sci.* 52, 287–291. doi: 10.1016/j.corsci.2009.09.033
- Kotian, R., Rao, P. P., and Madhyastha, P. (2017). X-ray diffraction analysis of hydroxyapatite-coated in different plasma gas atmosphere on Ti and Ti-6Al-4V. *Eur. J. Dent.* 11, 438–446. doi: 10.4103/ejd.ejd_100_17
- Kuo, T.-Y., Chin, W.-H., Chien, C.-S., and Hsieh, Y.-H. (2019). Mechanical and biological properties of graded porous tantalum coatings deposited on titanium alloy implants by vacuum plasma spraying. *Surf. Coat. Technol.* 372, 399–409. doi: 10.1016/j.surfcoat.2019.05.003
- Lausmaa, J., Kasemo, B., and Mattsson, H. (1990). Surface spectroscopic characterization of titanium implant materials. *Appl. Surf. Sci.* 44, 133–146. doi: 10.1016/0169-4332(90)90100-e
- Lee, H., Liao, J.-D., Sivashanmugan, K., Liu, B. H., Weng, S.-L., Juang, Y.-D., et al. (2017). Dual properties of zirconia coated porous titanium for a stiffness enhanced bio-scaffold. *Mater. Design* 132, 13–21. doi: 10.1016/j.matdes.2017.06.053
- Li, L.-H., Kong, Y.-M., Kim, H.-W., Kim, Y.-W., Kim, H.-E., Heo, S.-J., et al. (2004). Improved biological performance of Ti implants due to surface modification by micro-arc oxidation. *Biomaterials* 25, 2867–2875. doi: 10.1016/j.biomaterials.2003.09.048
- Li, X., Wang, L., Yu, X., Feng, Y., Wang, C., Yang, K., et al. (2013). Tantalum coating on porous Ti6Al4V scaffold using chemical vapor deposition and preliminary biological evaluation. *Mater. Sci. Eng. C Mater. Biol. Appl.* 33, 2987–2994. doi: 10.1016/j.msec.2013.03.027
- Li, Y., Wang, W., Duan, J., and Qi, M. (2017). A super-hydrophilic coating with a macro/micro/nano triple hierarchical structure on titanium by two-step micro-arc oxidation treatment for biomedical applications. *Surf. Coat. Technol.* 311, 1–9. doi: 10.1016/j.surfcoat.2016.12.065
- Li, Y., Wang, W., Liu, H., Lei, J., Zhang, J., Zhou, H., et al. (2018). Formation and in vitro/in vivo performance of “cortex-like” micro/nano-structured TiO₂ coatings on titanium by micro-arc oxidation. *Mater. Sci. Eng. C Mater. Biol. Appl.* 87, 90–103. doi: 10.1016/j.msec.2018.02.023
- Li, Y., Wang, W., Yu, F., Wang, D., Guan, S., Li, Y., et al. (2020). Characterization and cytocompatibility of hierarchical porous TiO₂ coatings incorporated with calcium and strontium by one-step micro-arc oxidation. *Mater. Sci. Eng. C Mater. Biol. Appl.* 109:110610. doi: 10.1016/j.msec.2019.110610
- Lin, Z., Li, S.-J., Sun, F., Ba, D.-C., and Li, X.-C. (2019). Surface characteristics of a dental implant modified by low energy oxygen ion implantation. *Surf. Coat. Technol.* 365, 208–213. doi: 10.1016/j.surfcoat.2018.09.003
- Liu, D., Yang, T., Ma, H., and Liang, Y. (2020). The microstructure, bio-tribological properties, and biocompatibility of titanium surfaces with graded zirconium incorporation in amorphous carbon bioceramic composite films. *Surf. Coat. Technol.* 385:125391. doi: 10.1016/j.surfcoat.2020.125391
- Liu, S., Han, S., Zhang, L., Chen, L.-Y., Wang, L., Zhang, L., et al. (2020a). Strengthening mechanism and micropillar analysis of high-strength NiTi-Nb eutectic-type alloy prepared by laser powder bed fusion. *Composites Part B Eng.* 200:108358. doi: 10.1016/j.compositesb.2020.108358
- Liu, S., Liu, J., Wang, L., Ma, R. L.-W., Zhong, Y., Lu, W., et al. (2020b). Superelastic behavior of in-situ eutectic-reaction manufactured high strength 3D porous NiTi-Nb scaffold. *Scripta Mater.* 181, 121–126. doi: 10.1016/j.scriptamat.2020.02.025
- Liu, Y.-C., Lin, G.-S., Lee, Y.-T., Huang, T.-C., Chang, T.-W., Chen, Y.-W., et al. (2020). Microstructures and cell reaction of porous hydroxyapatite coatings on titanium discs using a novel vapour-induced pore-forming atmospheric plasma spraying. *Surf. Coat. Technol.* 393:125837. doi: 10.1016/j.surfcoat.2020.125837
- Liu, W., Cheng, M., Wahafu, T., Zhao, Y., Qin, H., Wang, J., et al. (2015). The in vitro and in vivo performance of a strontium-containing coating on the low-modulus Ti35Nb2Ta3Zr alloy formed by micro-arc oxidation. *J. Mater. Sci. Mater. Med.* 26:203. doi: 10.1007/s10856-015-5533-0
- Liu, W., Liu, S., and Wang, L. (2019). Surface modification of biomedical titanium alloy: micromorphology, microstructure evolution and biomedical applications. *Coatings* 9:249. doi: 10.3390/coatings9040249
- Lubas, M., Jasinski, J. J., Jelen, P., and Sitarz, M. (2018). Effect of ZrO₂ sol-gel coating on the Ti 99.2 – Porcelain bond strength investigated with mechanical testing and Raman spectroscopy. *J. Mol. Struct.* 1168, 316–321. doi: 10.1016/j.molstruc.2018.04.086
- Lv, Y., Wu, Y., Lu, X., Yu, Y., Fu, S., Yang, L., et al. (2019). Microstructure, bio-corrosion and biological property of Ag-incorporated TiO₂ coatings: influence of Ag₂O contents. *Ceramics Int.* 45, 22357–22367. doi: 10.1016/j.ceramint.2019.07.265
- Maleki-Ghaleh, H., Hafezi, M., Hadipour, M., Nadernezhad, A., Aghaie, E., Behnamian, Y., et al. (2015). Effect of tricalcium magnesium silicate coating on the electrochemical and biological behavior of Ti-6Al-4V Alloys. *PLoS One* 10:e0138454. doi: 10.1371/journal.pone.0138454
- Mao, Y., and Gleason, K. K. (2004). Hot filament chemical vapor deposition of poly (glycidyl methacrylate) thin films using tert-butyl peroxide as an initiator. *Langmuir* 20, 2484–2488. doi: 10.1021/la0359427
- Marsh, E. P., Quick, T., Uhlenbrock, S., and Kraus, B. (2010). *Deposition Systems, ALD Systems, CVD Systems, Deposition Methods, ALD Methods and CVD Methods*. U.S. Patent No:US20100075037A1. Washington, DC: U.S. Patent and Trademark Office.
- Matter, P., and Burch, H. (1990). Clinical experience with titanium implants, especially with the limited contact dynamic compression plate system. *Arch. Orthopaedic Trauma Surg.* 109, 311–313. doi: 10.1007/bf00636167
- Mohammed Hussein, S., and Talib Mohammed, M. (2019). Pure and bilayer sol-gel nanolayers derived on a novel Ti surface for load bearing applications. *Mater. Today Proc.* 18, 2217–2224. doi: 10.1016/j.matpr.2019.07.001
- Nemati, A., Saghaei, M., Khamseh, S., Alibakhshi, E., Zarrintaj, P., and Saeb, M. R. (2018). Magnetron-sputtered Ti_xNy thin films applied on titanium-based alloys for biomedical applications: composition-microstructure-property relationships. *Surf. Coat. Technol.* 349, 251–259. doi: 10.1016/j.surfcoat.2018.05.068
- Niinomi, M., Liu, Y., Nakai, M., Liu, H., and Li, H. (2016). Biomedical titanium alloys with Young's moduli close to that of cortical bone. *Regen. Biomater.* 3, 173–185. doi: 10.1093/rb/rbw016
- Ohthuki, C., Osaka, A., Iida, H., and Ohta, K. (1999). *Biocompatible Titanium Implant*. U.S. Patent No: US 6544288 B2. Washington, DC: U.S. Patent and Trademark Office.
- Otsuka, Y., Kawaguchi, H., and Mutoh, Y. (2016). Cyclic delamination behavior of plasma-sprayed hydroxyapatite coating on Ti-6Al-4V substrates in simulated body fluid. *Mater. Sci. Eng. C Mater. Biol. Appl.* 67, 533–541. doi: 10.1016/j.msec.2016.05.058
- Palla-Rubio, B., Araujo-Gomes, N., Fernandez-Gutierrez, M., Rojo, L., Suay, J., Gurruchaga, M., et al. (2019). Synthesis and characterization of silica-chitosan hybrid materials as antibacterial coatings for titanium implants. *Carbohydr. Polym.* 203, 331–341. doi: 10.1016/j.carbpol.2018.09.064
- Pan, J., Prabakaran, S., and Rajan, M. (2019). In-vivo assessment of minerals substituted hydroxyapatite / poly sorbitol sebacate glutamate (PSSG) composite coating on titanium metal implant for orthopedic implantation. *Biomed. Pharmacother.* 119:109404. doi: 10.1016/j.biopha.2019.109404
- Park, S. W., Lee, D., Lee, H. R., Moon, H. J., Lee, B. R., Ko, W. K., et al. (2015). Generation of functionalized polymer nanolayer on implant surface via initiated chemical vapor deposition (iCVD). *J. Colloid Interf. Sci.* 439, 34–41. doi: 10.1016/j.jcis.2014.10.018
- Prachar, P., Bartakova, S., Brezina, V., Cvrcek, L., and Vanek, J. (2015). Cytocompatibility of implants coated with titanium nitride and zirconium nitride. *Bratisl. Lek. Listy* 116, 154–156. doi: 10.4149/bll_2015_031
- Rabadia, C. D., Liu, Y. J., Chen, L. Y., Jawed, S. F., Wang, L. Q., Sun, H., et al. (2019). Deformation and strength characteristics of Laves phases in titanium alloys. *Mater. Design* 179:107891. doi: 10.1016/j.matdes.2019.107891
- Rabadia, C. D., Liu, Y. J., Wang, L., Sun, H., and Zhang, L. C. (2018). Laves phase precipitation in Ti-Zr-Fe-Cr alloys with high strength and large plasticity. *Mater. Design* 154, 228–238. doi: 10.1016/j.matdes.2018.05.035
- Ran, R., Liu, Y., Wang, L., Lu, E., Xie, L., Lu, W., et al. (2018). α' Martensite and amorphous phase transformation mechanism in tinbraz alloy incorporated with tio2 particles during friction stir processing. *Metallurgical Mater. Trans. A* 49, 1986–1991. doi: 10.1007/s11661-018-4577-4
- Robertson, S. F., Bandyopadhyay, A., and Bose, S. (2019). Titania nanotube interface to increase adhesion strength of hydroxyapatite sol-gel coatings on Ti-6Al-4V for orthopedic applications. *Surf. Coat. Technol.* 372, 140–147. doi: 10.1016/j.surfcoat.2019.04.071
- Romero-Gavilan, F., Araujo-Gomes, N., Garcia-Arnez, I., Martinez-Ramos, C., Elortza, F., Azkargorta, M., et al. (2019). The effect of strontium incorporation

- into sol-gel biomaterials on their protein adsorption and cell interactions. *Colloids Surf. B Biointerf.* 174, 9–16. doi: 10.1016/j.colsurfb.2018.10.075
- Romero-Gavilan, F., Araujo-Gomes, N., Sanchez-Perez, A. M., Garcia-Arnez, I., Elortza, F., Azkargorta, M., et al. (2018). Bioactive potential of silica coatings and its effect on the adhesion of proteins to titanium implants. *Colloids Surf. B Biointerfaces* 162, 316–325. doi: 10.1016/j.colsurfb.2017.11.072
- Saleem, S., Ahmad, R., Ayub, R., Ikhlaiq, U., Jin, W., and Chu, P. K. (2017). Investigation of nano-structured Zirconium oxide film on Ti6Al4V substrate to improve tribological properties prepared by PIII&D. *Appl. Surf. Sci.* 394, 586–597. doi: 10.1016/j.apsusc.2016.09.091
- Santos, N. M., Mariano, S. F. M., and Ueda, M. (2019). Carbon films deposition as protective coating of titanium alloy tube using PIII&D system. *Surf. Coat. Technol.* 375, 164–170. doi: 10.1016/j.surfcoat.2019.03.083
- Sarraf, M., Razak, B. A., Nasiri-Tabrizi, B., Dabbagh, A., Kasim, N. H. A., Basirun, W. J., et al. (2017). Nanomechanical properties, wear resistance and in-vitro characterization of Ta2O5 nanotubes coating on biomedical grade Ti-6Al-4V. *J. Mech. Behav. Biomed. Mater.* 66, 159–171. doi: 10.1016/j.jmbbm.2016.11.012
- Sedelnikova, M. B., Komarova, E. G., Sharkeev, Y. P., Tolkacheva, T. V., Khlusov, I. A., Litvinova, L. S., et al. (2017). Comparative investigations of structure and properties of micro-arc wollastonite-calcium phosphate coatings on titanium and zirconium-niobium alloy. *Bioact. Mater.* 2, 177–184. doi: 10.1016/j.bioactmat.2017.01.002
- Shanaghi, A., and Chu, P. K. (2019a). Enhancement of mechanical properties and corrosion resistance of NiTi alloy by carbon plasma immersion ion implantation. *Surf. Coat. Technol.* 365, 52–57. doi: 10.1016/j.surfcoat.2018.04.027
- Shanaghi, A., and Chu, P. K. (2019b). Investigation of corrosion mechanism of NiTi modified by carbon plasma immersion ion implantation (C-PIII) by electrochemical impedance spectroscopy. *J. Alloys Compounds* 790, 1067–1075. doi: 10.1016/j.jallcom.2019.03.272
- Shaw, L. L., Goberman, D., Ren, R., Gell, M., Jiang, S., Wang, Y., et al. (2000). The dependency of microstructure and properties of nanostructured coatings on plasma spray conditions. *Surf. Coat. Technol.* 130, 1–8. doi: 10.1016/s0257-8972(00)00673-3
- Shen, X., Ping, L., Wang, L., Liu, C., Liu, J., and Deng, Z. (2020). Improving the stability and bioactivity of micro-arc oxidized calcium phosphate/titania porous coatings by high energy shot peening pretreatment. *Ceramics Int.* 46, 2041–2048. doi: 10.1016/j.ceramint.2019.09.183
- Shi, Q., Qian, Z., Liu, D., and Liu, H. (2017). Surface modification of dental titanium implant by layer-by-layer electrostatic self-assembly. *Front. Physiol.* 8:574. doi: 10.3389/fphys.2017.00574
- Shiau, D.-K., Yang, C.-H., Sun, Y.-S., Wu, M.-F., Pan, H., and Huang, H.-H. (2019). Enhancing the blood response and antibacterial adhesion of titanium surface through oxygen plasma immersion ion implantation treatment. *Surf. Coat. Technol.* 365, 173–178. doi: 10.1016/j.surfcoat.2018.05.029
- Singh, D., Singh, R., Boparai, K., Farina, I., Feo, L., and Verma, A. K. (2018). In-vitro studies of SS 316 L biomedical implants prepared by FDM, vapor smoothing and investment casting. *Composites Part B Eng.* 132, 107–114. doi: 10.1016/j.compositesb.2017.08.019
- Somani, P. R., Somani, S. P., and Umeno, M. (2006). Planer nano-graphenes from camphor by CVD. *Chem. Phys. Lett.* 430, 56–59. doi: 10.1016/j.cplett.2006.06.081
- Souza, J. C. M., Sordi, M. B., Kanazawa, M., Ravindran, S., Henriques, B., Silva, F. S., et al. (2019). Nano-scale modification of titanium implant surfaces to enhance osseointegration. *Acta Biomater.* 94, 112–131. doi: 10.1016/j.actbio.2019.05.045
- Tang, Y., Wu, C., Tian, P., Zhao, K., and Wu, Z. (2020). Fabrication and induced mineralization of bio-piezoelectric ceramic coating on titanium alloys. *Ceramics Int.* 46, 4006–4014. doi: 10.1016/j.ceramint.2019.10.040
- Thangavel, E., Dhandapani, V. S., Dharmalingam, K., Marimuthu, M., Veerapandian, M., Arumugam, M. K., et al. (2019). RF magnetron sputtering mediated NiTi/Ag coating on Ti-alloy substrate with enhanced biocompatibility and durability. *Mater. Sci. Eng. C Mater. Biol. Appl.* 99, 304–314. doi: 10.1016/j.msec.2019.01.099
- Toirac, B., Garcia-Casas, A., Cifuentes, S. C., Aguilera-Correa, J. J., Esteban, J., Mediero, A., et al. (2020). Electrochemical characterization of coatings for local prevention of Candida infections on titanium-based biomaterials. *Progr. Organic Coat.* 146:105681. doi: 10.1016/j.porgcoat.2020.105681
- Ueda, M., Oliveira, R. M., Rossi, J. O., Mello, C. B., Rangel, R. C. C., and Vieira, M. S. (2013). Improvements of plasma immersion ion implantation (PIII) and deposition (PIII&D) processing for materials surface modification. *Surf. Coat. Technol.* 229, 97–104. doi: 10.1016/j.surfcoat.2012.06.057
- Vahabzadeh, S., Roy, M., Bandyopadhyay, A., and Bose, S. (2015). Phase stability and biological property evaluation of plasma sprayed hydroxyapatite coatings for orthopedic and dental applications. *Acta Biomater.* 17, 47–55. doi: 10.1016/j.actbio.2015.01.022
- Veerachamy, S., Hameed, P., Sen, D., Dash, S., and Manivasagam, G. (2018). Studies on mechanical, biocompatibility and antibacterial activity of plasma sprayed nano/micron ceramic bilayered coatings on Ti-6Al-4V alloy for biomedical application. *J. Nanosci. Nanotechnol.* 18, 4515–4523. doi: 10.1166/jnn.2018.15332
- Wang, D., and Bierwagen, G. P. (2009). Sol-gel coatings on metals for corrosion protection. *Progr. Organic Coat.* 64, 327–338. doi: 10.1016/j.porgcoat.2008.08.010
- Wang, L., Lu, W., Qin, J., Zhang, F., and Zhang, D. (2009). Influence of cold deformation on martensite transformation and mechanical properties of Ti-Nb-Ta-Zr alloy. *J. Alloys Compounds* 469, 512–518. doi: 10.1016/j.jallcom.2008.02.032
- Wang, L., Qu, J., Chen, L., Meng, Q., Zhang, L.-C., Qin, J., et al. (2015). Investigation of Deformation Mechanisms in β -Type Ti-35Nb-2Ta-3Zr Alloy via FSP leading to surface strengthening. *Metallurg. Mater. Trans. A* 46, 4813–4818. doi: 10.1007/s11661-015-3089-8
- Wang, Y., Yu, H., Chen, C., and Zhao, Z. (2015). Review of the biocompatibility of micro-arc oxidation coated titanium alloys. *Mater. Design* 85, 640–652. doi: 10.1016/j.matdes.2015.07.086
- Wang, L., Wang, C., Zhang, L. C., Chen, L., Lu, W., and Zhang, D. (2016). Phase transformation and deformation behavior of NiTi-Nb eutectic joined NiTi wires. *Sci. Rep.* 6:23905. doi: 10.1038/srep23905
- Wang, Q., Qiao, Y., Cheng, M., Jiang, G., He, G., Chen, Y., et al. (2016). Tantalum implanted entangled porous titanium promotes surface osseointegration and bone ingrowth. *Sci. Rep.* 6:26248. doi: 10.1038/srep26248
- Wang, L., Wang, Y., Huang, W., Liu, J., Tang, Y., Zhang, L., et al. (2020). Tensile and superelastic behaviors of Ti-35Nb-2Ta-3Zr with gradient structure. *Mater. Design* 194:108961. doi: 10.1016/j.matdes.2020.108961
- Wang, Q., Zhou, P., Liu, S., Attarilar, S., Ma, R. L., Zhong, Y., et al. (2020). Multi-scale surface treatments of titanium implants for rapid osseointegration: a review. *Nanomaterials* 10:1244. doi: 10.3390/nano10061244
- Wang, L., Xie, L., Lv, Y., Zhang, L.-C., Chen, L., Meng, Q., et al. (2017). Microstructure evolution and superelastic behavior in Ti-35Nb-2Ta-3Zr alloy processed by friction stir processing. *Acta Mater.* 131, 499–510. doi: 10.1016/j.actamat.2017.03.079
- Wang, L., Xie, L., Zhang, L.-C., Chen, L., Ding, Z., Lv, Y., et al. (2018). Microstructure evolution and superelasticity of layer-like NiTiNb porous metal prepared by eutectic reaction. *Acta Mater.* 143, 214–226. doi: 10.1016/j.actamat.2017.10.021
- Wang, S., Yang, C., Ren, L., Shen, M., and Yang, K. (2014). Study on antibacterial performance of Cu-bearing cobalt-based alloy. *Mater. Lett.* 129, 88–90. doi: 10.1016/j.matlet.2014.05.020
- Wu, W.-Y., Chan, M.-Y., Hsu, Y.-H., Chen, G.-Z., Liao, S.-C., Lee, C.-H., et al. (2019). Bioapplication of TiN thin films deposited using high power impulse magnetron sputtering. *Surf. Coat. Technol.* 362, 167–175. doi: 10.1016/j.surfcoat.2019.01.106
- Xia, C., Ma, X., Zhang, X., Li, K., Tan, J., Qiao, Y., et al. (2020). Enhanced physicochemical and biological properties of C/Cu dual ions implanted medical titanium. *Bioact. Mater.* 5, 377–386. doi: 10.1016/j.bioactmat.2020.02.017
- Xiao, M., Chen, Y. M., Biao, M. N., Zhang, X. D., and Yang, B. C. (2017). Bio-functionalization of biomedical metals. *Mater. Sci. Eng. C Mater. Biol. Appl.* 70(Pt 2), 1057–1070. doi: 10.1016/j.msec.2016.06.067
- Xu, J., Li, Y., Zhou, X., Li, Y., Gao, Z. D., Song, Y. Y., et al. (2016). Graphitic C3 N4 -Sensitized TiO2 nanotube layers: a visible-light activated efficient metal-free antimicrobial platform. *Chemistry* 22, 3947–3951. doi: 10.1002/chem.201505173
- Xu, R., Yang, X., Jiang, J., Li, P., Zhang, X., Wu, G., et al. (2015). Effects of silver plasma immersion ion implantation on the surface characteristics and cytocompatibility of titanium nitride films. *Surf. Coat. Technol.* 279, 166–170. doi: 10.1016/j.surfcoat.2015.08.033

- Yang, P., Huang, N., Leng, Y., Wan, G., Zhao, A., Chen, J., et al. (2007). Functional inorganic films fabricated by PIII(-D) for surface modification of blood contacting biomaterials: fabrication parameters, characteristics and antithrombotic properties. *Surf. Coat. Technol.* 201, 6828–6832. doi: 10.1016/j.surfcoat.2006.09.014
- Yetim, T. (2017). An investigation of the corrosion properties of Ag-doped TiO₂ -coated commercially pure titanium in different biological environments. *Surf. Coat. Technol.* 309, 790–794. doi: 10.1016/j.surfcoat.2016.10.084
- Youn, Y. H., Lee, S. J., Choi, G. R., Lee, H. R., Lee, D., Heo, D. N., et al. (2019). Simple and facile preparation of recombinant human bone morphogenetic protein-2 immobilized titanium implant via initiated chemical vapor deposition technique to promote osteogenesis for bone tissue engineering application. *Mater. Sci. Eng. C Mater. Biol. Appl.* 100, 949–958. doi: 10.1016/j.msec.2019.03.048
- Yousefi, M., Dadashpour, M., Hejazi, M., Hasanzadeh, M., Behnam, B., de la Guardia, M., et al. (2017). Anti-bacterial activity of graphene oxide as a new weapon nanomaterial to combat multidrug-resistance bacteria. *Mater. Sci. Eng. C Mater. Biol. Appl.* 74, 568–581. doi: 10.1016/j.msec.2016.12.125
- Yu, L., Jin, G., Ouyang, L., Wang, D., Qiao, Y., and Liu, X. (2016). Antibacterial activity, osteogenic and angiogenic behaviors of copper-bearing titanium synthesized by PIII&D. *J. Mater. Chem. B* 4, 1296–1309. doi: 10.1039/c5tb02300a
- Yu, L., Tian, Y., Qiao, Y., and Liu, X. (2017). Mn-containing titanium surface with favorable osteogenic and antimicrobial functions synthesized by PIII&D. *Colloids Surf. B Biointerfaces* 152, 376–384. doi: 10.1016/j.colsurf.2017.01.047
- Yu, Y., Jin, G., Xue, Y., Wang, D., Liu, X., and Sun, J. (2017). Multifunctions of dual Zn/Mg ion co-implanted titanium on osteogenesis, angiogenesis and bacteria inhibition for dental implants. *Acta Biomater.* 49, 590–603. doi: 10.1016/j.actbio.2016.11.067
- Zhang, C., Ding, Z., Xie, L., Zhang, L.-C., Wu, L., Fu, Y., et al. (2017). Electrochemical and in vitro behavior of the nanosized composites of Ti-6Al-4V and TiO₂ fabricated by friction stir process. *Appl. Surf. Sci.* 423, 331–339. doi: 10.1016/j.apsusc.2017.06.141
- Zhang, L. C., and Chen, L. Y. (2019). A review on biomedical titanium alloys: recent progress and prospect. *Adv. Eng. Mater.* 21:1215. doi: 10.1002/adem.201801215
- Zhang, L.-C., Chen, L.-Y., and Wang, L. (2020). Surface modification of titanium and titanium alloys: technologies, developments, and future interests. *Adv. Eng. Mater.* 22:1258. doi: 10.1002/adem.201901258
- Zhang, X., Peng, Z., Lu, X., Lv, Y., Cai, G., Yang, L., et al. (2020). Microstructural evolution and biological performance of Cu-incorporated TiO₂ coating fabricated through one-step micro-arc oxidation. *Appl. Surf. Sci.* 508:144766. doi: 10.1016/j.apsusc.2019.144766
- Zhang, M., Pu, X., Chen, X., and Yin, G. (2019). In-vivo performance of plasma-sprayed CaO-MgO-SiO₂-based bioactive glass-ceramic coating on Ti-6Al-4V alloy for bone regeneration. *Heliyon* 5:e02824. doi: 10.1016/j.heliyon.2019.e02824
- Zhang, X., Li, C., Yu, Y., Lu, X., Lv, Y., Jiang, D., et al. (2019). Characterization and property of bifunctional Zn-incorporated TiO₂ micro-arc oxidation coatings: the influence of different Zn sources. *Ceramics Int.* 45, 19747–19756. doi: 10.1016/j.ceramint.2019.06.228
- Zhao, J., Guo, Y., Lan, A., Luo, W., Wang, X., Fu, L., et al. (2018). The effect of amino plasma-enhanced chemical vapor deposition-treated titanium surface on Schwann cells. *J. Biomed. Mater. Res. A* 106, 265–271. doi: 10.1002/jbm.a.36167
- Zheng, L., Qian, S., and Liu, X. Y. (2020). Induced antibacterial capability of TiO₂ coatings in visible light via nitrogen ion implantation. *Trans. Nonferrous Metals Soc. China* 30, 171–180. doi: 10.1016/S1003-6326(19)65189-7
- Zhong, S.-P. (1999). *Method of Providing a Substrate with a Bio-Active/Biocompatible Coating*. U.S. Patent No: US5869127A. Washington, DC: U.S. Patent and Trademark Office.
- Zhong, S.-P. (2001). *Hybrid Coating for Medical Devices*. U.S. Patent No: US-6179817-B1. Washington, DC: U.S. Patent and Trademark Office.
- Zhu, C., Lv, Y., Qian, C., Qian, H., Jiao, T., Wang, L., et al. (2016). Proliferation and osteogenic differentiation of rat BMSCs on a novel Ti/SiC metal matrix nanocomposite modified by friction stir processing. *Sci. Rep.* 6:38875. doi: 10.1038/srep38875
- Zhu, J., Wang, X., Kou, L., Zheng, L., and Zhang, H. (2020). Prediction of control parameters corresponding to in-flight particles in atmospheric plasma spray employing convolutional neural networks. *Surf. Coat. Technol.* 394:125862. doi: 10.1016/j.surfcoat.2020.125862
- Ziabka, M., Kiszka, J., Trenczek-Zajac, A., Radecka, M., Cholewa-Kowalska, K., Bissenik, I., et al. (2020). Antibacterial composite hybrid coatings of veterinary medical implants. *Mater. Sci. Eng. C Mater. Biol. Appl.* 112:110968. doi: 10.1016/j.msec.2020.110968

Conflict of Interest: LL and BZ were employed by the company Chengsteel Group Co., Ltd., HBIS Group Co., Ltd.

The remaining authors declare that the research was conducted in the absence of any commercial or financial relationships that could be construed as a potential conflict of interest.

Copyright © 2020 Xue, Attarilar, Liu, Liu, Song, Li, Zhao and Tang. This is an open-access article distributed under the terms of the Creative Commons Attribution License (CC BY). The use, distribution or reproduction in other forums is permitted, provided the original author(s) and the copyright owner(s) are credited and that the original publication in this journal is cited, in accordance with accepted academic practice. No use, distribution or reproduction is permitted which does not comply with these terms.



Nano-Modified Titanium Implant Materials: A Way Toward Improved Antibacterial Properties

Jianqiao Liu^{1,2†}, Jia Liu^{1†}, Shokouh Attarilar^{3,4†}, Chong Wang⁵, Maryam Tamaddon⁶, Chengliang Yang¹, Kegong Xie¹, Jinguang Yao^{2*}, Liqiang Wang^{4*}, Chaozong Liu^{6*} and Yujin Tang^{1*}

¹ Department of Orthopaedics, Affiliated Hospital of Youjiang Medical University for Nationalities, Baise, China, ² Youjiang Medical University for Nationalities, Baise, China, ³ Department of Pediatric Orthopaedics, Xin Hua Hospital Affiliated to Shanghai Jiao Tong University School of Medicine, Shanghai, China, ⁴ State Key Laboratory of Metal Matrix Composites, School of Materials Science and Engineering, Shanghai Jiao Tong University, Shanghai, China, ⁵ College of Mechanical Engineering, Dongguan University of Technology, Dongguan, China, ⁶ Institute of Orthopaedic and Musculoskeletal Science, Division of Surgery & Orthopaedic Science, University College London, The Royal National Orthopaedic Hospital, Stanmore, United Kingdom

OPEN ACCESS

Edited by:

Jianxun Ding,
Changchun Institute of Applied
Chemistry, Chinese Academy
of Sciences, China

Reviewed by:

Ruslan Valiev,
Ufa State Aviation Technical
University, Russia
Pengfei Lei,
Central South University, China

*Correspondence:

Yujin Tang
tangyujin196709@163.com
Chaozong Liu
chaozong.liu@ucl.ac.uk
Liqiang Wang
wang_liqiang@sjtu.edu.cn
Jinguang Yao
yao7760698@126.com

[†] These authors have contributed
equally to this work

Specialty section:

This article was submitted to
Biomaterials,
a section of the journal
Frontiers in Bioengineering and
Biotechnology

Received: 27 June 2020

Accepted: 22 October 2020

Published: 23 November 2020

Citation:

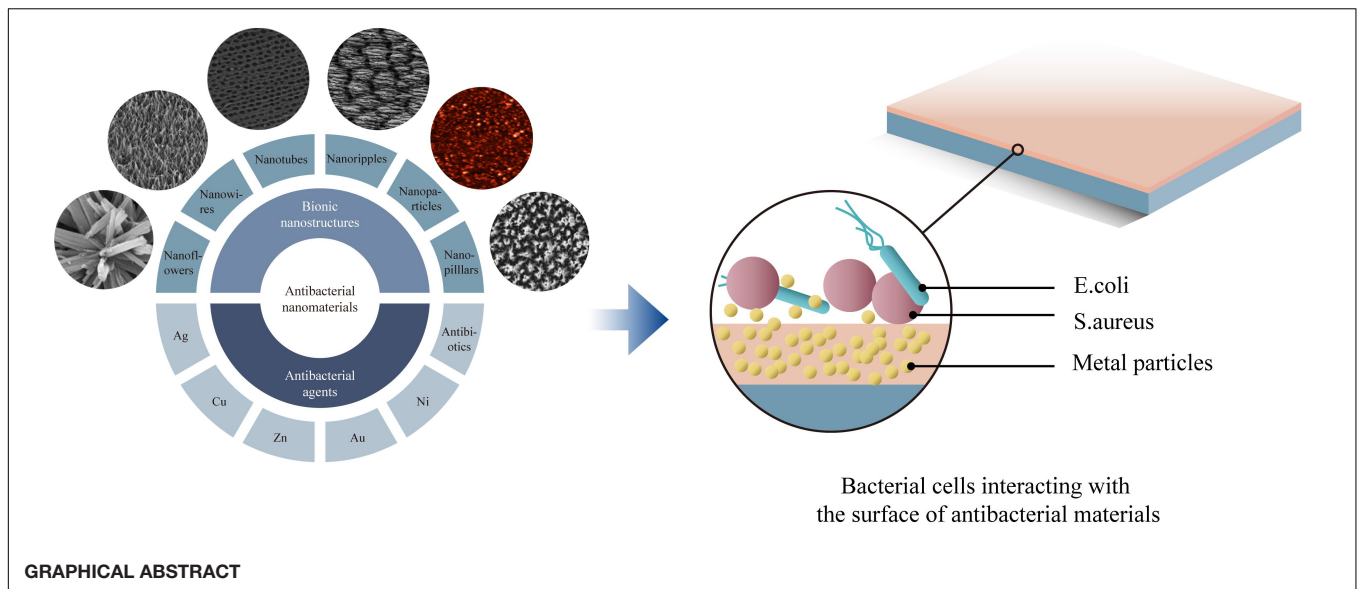
Liu J, Liu J, Attarilar S, Wang C, Tamaddon M, Yang C, Xie K, Yao J, Wang L, Liu C and Tang Y (2020) Nano-Modified Titanium Implant Materials: A Way Toward Improved Antibacterial Properties. *Front. Bioeng. Biotechnol.* 8:576969. doi: 10.3389/fbioe.2020.576969

Titanium and its alloys have superb biocompatibility, low elastic modulus, and favorable corrosion resistance. These exceptional properties lead to its wide use as a medical implant material. Titanium itself does not have antibacterial properties, so bacteria can gather and adhere to its surface resulting in infection issues. The infection is among the main reasons for implant failure in orthopedic surgeries. Nano-modification, as one of the good options, has the potential to induce different degrees of antibacterial effect on the surface of implant materials. At the same time, the nano-modification procedure and the produced nanostructures should not adversely affect the osteogenic activity, and it should simultaneously lead to favorable antibacterial properties on the surface of the implant. This article scrutinizes and deals with the surface nano-modification of titanium implant materials from three aspects: nanostructures formation procedures, nanomaterials loading, and nano-morphology. In this regard, the research progress on the antibacterial properties of various surface nano-modification of titanium implant materials and the related procedures are introduced, and the new trends will be discussed in order to improve the related materials and methods.

Keywords: bactericidal, nanostructure, antibacterial, nanoparticles, titanium-implants

INTRODUCTION

Currently, with the rapid development of materials science and biotechnology, titanium and its alloys as orthopedic implant materials (Sam Froes, 2018) have been widely used in applications such as skeleton structure fixation and joint function repair implants (Gode et al., 2015; Liang et al., 2016; Kaur and Singh, 2019). Many new types of titanium alloys with high-quality performance have been invented through in-depth research on titanium alloy preparation (Zhang C. et al., 2017; Wang et al., 2018; Attarilar et al., 2019a,b; Hafeez et al., 2019) and optimization of titanium alloy composition (Liu et al., 2015a; Wang et al., 2016; Rabadia et al., 2019a,b). These new titanium alloys show outstanding application value in mechanical properties (Guo et al., 2013; Wang et al., 2015; Jawed et al., 2019; Hafeez et al., 2020), corrosion resistance (Lee et al., 2015; Zhu W.Q. et al., 2019; Malhotra et al., 2020), and osteogenic action (Zhu et al., 2016; Li H.F. et al., 2019; Lei et al., 2020).



It is undeniable that the implant material plays a vital role in orthopedic diseases (Hanawa, 2018; Qian et al., 2020), and its infection risk which is directly related to the material condition cannot be ignored (Montanaro et al., 2011; Kumar and Misra, 2018; Li and Webster, 2018). The infection of the tissue in the periphery of implant material is one of the most severe complications in orthopedic surgery (Pfing et al., 2019). The occurrence of infection not only leads to the failure of the implant and the surgery but also increases the patients' recovery period and makes an economic burden on both patients and the medical system. The use of antibiotics is a common and effective way to control this issue, but it also has some disadvantages (Klein et al., 2016; Holleyman et al., 2019). Bacterial infection on the surface of the implanted material may eventually form a biofilm and reduce or completely inhibit the beneficial effects of the bactericidal drugs. Besides, the system-administered anti-infection method can also result in a low concentration of drugs in the surgical area due to scars or fibrosis of the surrounding tissues, which affects the antibacterial efficiency (Andersson and Hughes, 2012, 2014). For this reason, the preparation of titanium-based implant materials with antibacterial properties can effectively solve this problem. This infection issue can be solved by adding metallic bactericidal elements or the addition of antibacterial coatings on the surface of implants (Morones-Ramirez et al., 2005; Ben-Knaz Wakshlak et al., 2016; Pareek et al., 2018).

The emergence of nanotechnology has caused significant changes in many fields of science, such as physics, chemistry, materials science, biology, computer science. Compared with the conventional materials (Wang et al., 2008), nanoscale materials have many new and unique properties, including medical, mechanical, chemical, magnetic, optical (Whitesides, 2005; Dyakonov et al., 2017; Semenova et al., 2017). Some of the nanoscale materials have appeared as new antibacterial agents, and current studies have confirmed that antimicrobial nanoparticles (NPs) and nanocarriers that aimed to deliver antibiotics can effectively treat infectious

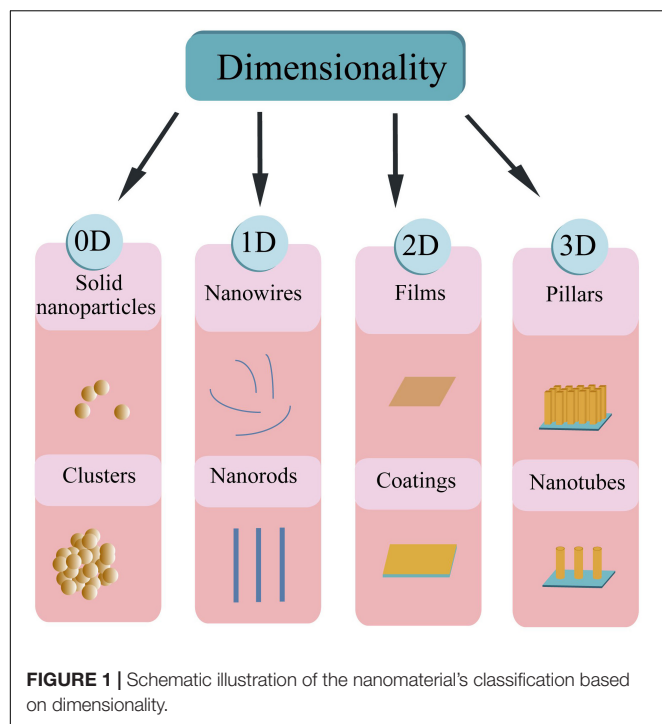
diseases (Huh and Kwon, 2011). Nanoscale materials have higher antibacterial properties compared to traditional antibacterial counterparts due to their high surface area to volume ratio. Therefore, it maintains more active area for biological interactions thus this subject seems to have outstanding research value in biomedical applications (Xia, 2008; Avila et al., 2018). This article summarizes and analyzes the advantages and disadvantages, procedures, antibacterial mechanisms, and possible improvement mechanisms for various nanoscale antibacterial materials, in order to provide a guideline for the modern nano-antibacterial materials with improved design and optimum properties for implant applications.

CLASSIFICATION OF NANOMATERIALS

Based on the dimension criteria, antibacterial nanomaterials can be divided into four categories: zero-dimensional—nanoparticles, one-dimensional—nanowires, two-dimensional—nanofilms, and three-dimensional—nanoblocks (Figure 1) (Saleh, 2020). Besides, antibacterial nanomaterials can also be classified according to the structural form or antibacterial active ingredients (Gleiter, 2000).

Classification by the Structural Form

Antibacterial nanomaterials based on the structural form can be classified into antibacterial NPs, antibacterial nanosolids, and antibacterial nano-assembled structures. NPs are known as tiny particles in the size range of 1~100 nm. Their specific structures induce some sort of surface and interface effects such as small size effect, macroscopic quantum tunneling and quantum size effect (Morris, 2018). As a result, nanomaterials with a series of excellent properties enhance the proficiency of nano-antibacterial agents. Compared with ordinary materials, nanomaterials have irreplaceable characteristics, especially in the antibacterial field. Hence it is worthwhile to expand



the scope of their applications. Antibacterial nanosolids can be formed by the aggregation of nano-sized antibacterial particles. They can be further divided into bulk, thin-film, and nanofibrous nanomaterials. Antibacterial nano-assembled structures refer to the artificially assembled and synthesized antibacterial nanomaterial systems. These systems are composed of antibacterial nanoparticles, nanofilaments, or tubes as the basic unit. These various nanostructures can be assembled and arranged in one dimensional, two or three-dimensional space to form the desired nanomaterial structures (Mageswari et al., 2016; Khan, 2020).

Nanomaterials can be synthesized through various methods such as construction and destruction (**Figure 2**) (Saleh, 2020). On the one hand, NPs can be obtained from the atomic level and then integrated into the desired materials. The methods of this kind of synthesis include self assembly (Zhang et al., 2019b; Deng et al., 2020), laser pyrolysis (Laurent et al., 2010; Dumitrache et al., 2019), condensation (Sano et al., 2020), CVD (Gutés et al., 2012; Tyurikova et al., 2020), sol-gel method (Gonçalves, 2018), soft lithography (Fu et al., 2018), hydrothermal methods (Zhen et al., 2019; Moreira et al., 2020), microwave methods (Henam et al., 2019), sonochemical (Gupta and Srivastava, 2019; Moreira et al., 2020), synthesis using plant extracts (Ogunyemi et al., 2019; Ranoszek-Soliwoda et al., 2019), and green synthesis (Gour and Jain, 2019; Irshad et al., 2020). On the other hand, macroscopic level materials can be trimmed down to NPs by different methods, including mechanical grinding (Sviridov et al., 2017; Haque et al., 2018), ball milling (Li Y. et al., 2020), lithography (Fu et al., 2018), vapor deposition (Choi et al., 2018), arc-plasma deposition (Ito et al., 2012; Takahashi et al., 2015), ion beam technique (Heo and Gwag, 2014; Yang J. et al., 2018), severe

plastic deformation (Cui et al., 2018; Sarkari Khorrami et al., 2019), chemical etching (Wareing et al., 2017; Pinna et al., 2020), sputtering (Pišlová et al., 2020), and laser ablation (Pandey et al., 2014; Abid et al., 2020).

Classification by Antibacterial Active Ingredients

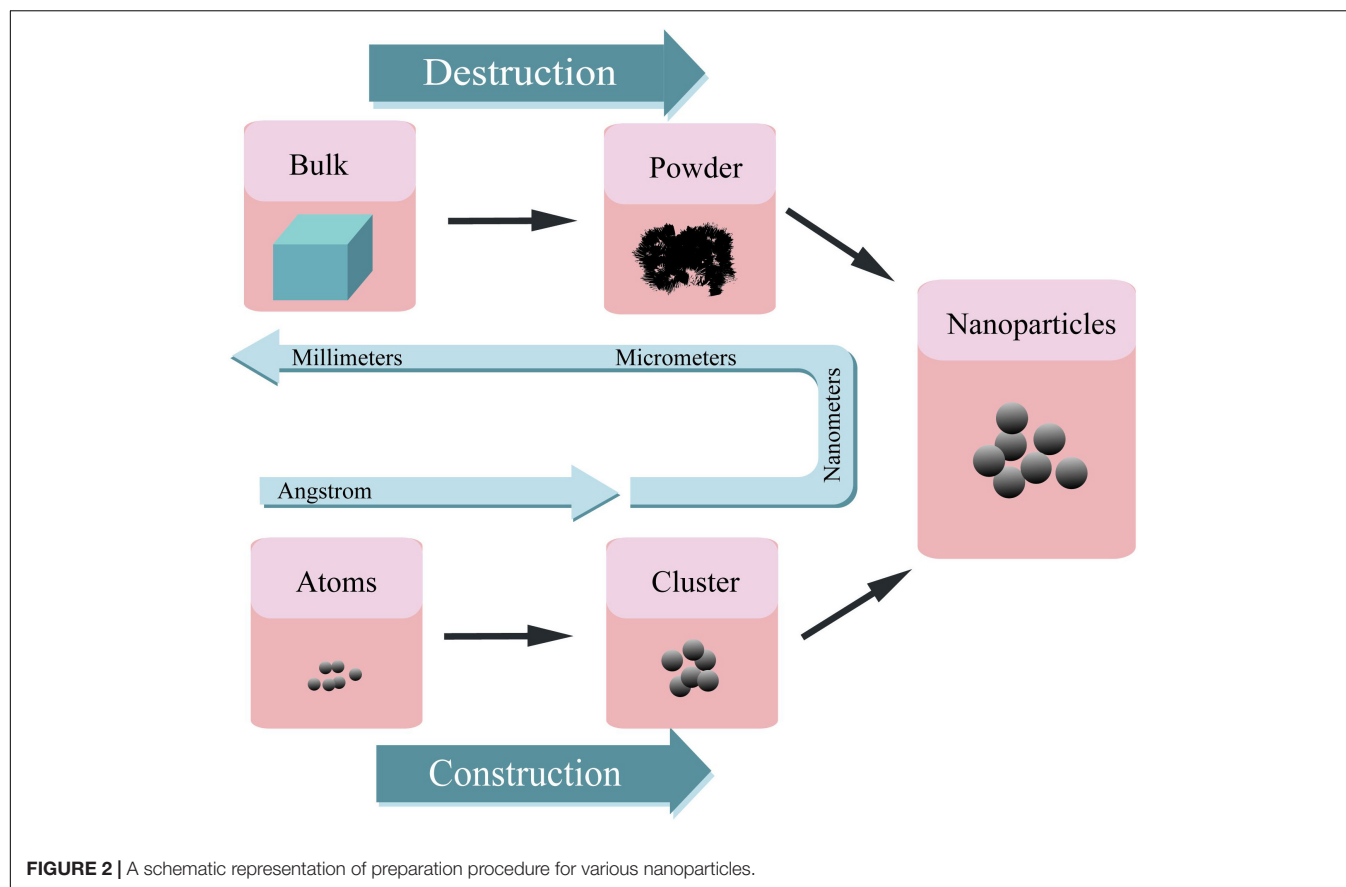
Antibacterial nanomaterials can be categorized into a metal ion and oxide photocatalytic type according to antibacterial active ingredients. Metal ion antibacterial nanomaterials are metallic ions with antibacterial functions (Ag, Cu, Zn, Ni, Co, Al) loaded in a variety of natural or synthetic substrates. They can slowly release the antibacterial ion components to periphery tissues in order to achieve the antibacterial and bactericidal effects. Oxide photocatalytic antimicrobial materials commonly are TiO₂, ZnO, MgO, CdS, etc. and act in the catalysis of photocatalyst in which OH⁻ and H₂O molecules oxidized to OH free radicals with strong oxidation capacity. Thus, these activated surfaces can inhibit and kill microorganisms that exists in the environment (Buzea and Pacheco, 2017).

PREPARATION OF NANOSTRUCTURE ON TITANIUM AND ITS ALLOYS

Titanium-based nanostructure (NS) materials have become the focus of current research because of their unique properties in optical, biological, and electrical fields (Miao et al., 2015; Gupta et al., 2018; Wei et al., 2020). Different preparation processes can be used to construct NS titanium surfaces, common nano-morphologies for titanium surfaces with antibacterial functions are nanotube and nano-coating forms. Titanium surfaces with different physical and chemical properties can influence the biological interactions and the adhesion of cells and bacteria (Zhou J. et al., 2018; Elbourne et al., 2019), which in turn affects the ability of early osseointegration and the risk of implant infection.

Preparation of Nanotubes

Titanium dioxide nanotubes have received extensive attention because of their controllable size and highly ordered surface arrangement. Nanotubes have a larger specific surface area and storage space than other NS forms such as nanorods, nanospikes, and nanowires. These characteristics make it a good candidate among the other NS morphologies for the storage and release of antibacterial agents. The preparation of nanotube structures on the surface of titanium is mainly achieved by three methods: template synthesis (Jung et al., 2002; Lee et al., 2005), electrochemical anodization (Jun et al., 2012; Roman et al., 2014; Cao S. et al., 2018; Shang et al., 2019; Zhang et al., 2019d), and hydrothermal treatment (Tsai and Teng, 2004, 2006), they have different advantages and disadvantages listed in **Table 1**.

**TABLE 1 |** Different nanotube formation processes.

Preparation technique	Shape and size	Characteristics	References
Template synthesis	(1) Tubular arrays or loose aggregates (2) Diameter: 10~500 nm (3) Length: Nanometer to micrometer	(1) Nanotubes with different diameters can be prepared (2) Removing the template may destroy the morphology of the nanotubes	Choi et al., 2017; Luo et al., 2018
Electrochemical anodization	(1) Highly ordered array of nanotubes (2) Diameter: 10~500 nm (3) Length: 100 nm~100 μ m	(1) Highly ordered (2) Low degree of aggregation	Fathy Fahim et al., 2009; Zhao et al., 2014
Hydrothermal treatment	(1) Single or loose block tube (2) Diameter: 2~20 nm (3) Length: nanometer to micrometer	(1) Simple process (2) It can prepare small diameter nanotubes (3) Difficult to form nanotube arrays	Wang L. et al., 2014; Aal et al., 2015

Template Synthesis

The template synthesis method can be categorized into a hard template and a soft template method according to the nature of templating agent. The hard template method uses columnar single-crystal anodized aluminum oxide (AAO) (Hoyer, 1996; Ma, 2007; Newland et al., 2018) as a template to prepare nanotube structures by electrochemical deposition. The preparation process for the hard template is complicated, and the shape and size of the nanotubes are dependent on the size and shape of the template hole. Besides, the nanotubes destruction is possible during the separation step from the matrix template so unfortunately, it has poor reproducibility. In the soft template procedure surfactants used as templates

(Bernal et al., 2012; Choi et al., 2017). Firstly, the surfactant should be mixed with water, titanium alkoxide, and other substances, then the polymerization takes place under certain conditions. After drying and calcination, the nanotube structure is prepared. The soft template method overcomes the shape and size dependence to the template holes, which is one of the big limitations of hard templates. However, due to the necessity of high temperatures in removing step of soft templates, the nanotubes may collapse.

Template synthesis can prepare nanomaterials upon design demands and obtain well-formed nanoarrays, but it still has some drawbacks. For example, the AAO template as a commonly used master plate is mechanically weak which makes it difficult to

prepare metal templates with large areas (Masuda and Fukuda, 1995). Moreover, when using solvents to remove the organic compound templates, the structure of the nanomaterials may encounter some damages. Therefore, this synthesis method has the potential to be further optimized to synthesize utility materials with the desired functions using a simple operation (Bera et al., 2004).

Electrochemical Anodization

Anodizing is one of the most commonly used methods for preparing TiO₂ nanotubes. The nanotube formation with a high aspect ratio and the excellent ordered condition can be attained by this method. The favorable nanotube size can be achieved by changing different factors (electrolyte composition, voltage, pH, anodizing time, etc.) (Gong et al., 2001; Ni et al., 2013; Wang L.N. et al., 2014; Khudhair et al., 2016; Song et al., 2017). Nanotube structures with tube dimensions in the range of 0.2–1000 µm length, 15–250 nm diameters and 10–70 nm thickness can be prepared with different anodic oxidation parameters. The main process of preparing titanium dioxide nanotubes by anodic oxidation are as follows: placing titanium foil or titanium sheet in a reaction cell (electrolytes are usually fluoride ions such as HF, NH₄F, Macak et al., 2005; Alivov et al., 2009; Minagar et al., 2014) of two- or three-electrode system, and then a constant voltage application. The titanium sheet or foil is oxidized by the combined action of the electric field and fluoride ions. After some time, arrays of titanium dioxide nanotubes with uniform distribution, ordered arrangement and perpendicular to the substrate would be formed. The diameter of the nanotube can be controlled by the oxidation voltage (Bozkurt Çırak et al., 2017); the length of the nanotube is controlled by the combination of the oxidation time (Bhadra et al., 2020), the oxidation temperature (Mohan et al., 2020), and the pH value of the electrolyte (Cipriano et al., 2014); the smoothness of the nanotube, and the cleanliness of the surface are respectively dependent on the type of electrolyte and the water content (Sivaprakash and Narayanan, 2020).

Hydrothermal Treatment

Hydrothermal treatment is among the momentous methods for nanotube production (Harsha et al., 2011). This method has the potential to produce titanium dioxide nanotubes with suitable crystalline structures (Swami et al., 2010). In this procedure, usually TiO₂ NPs were utilized as a titanium source to carry out a chemical reaction in a concentrated alkaline solution at high temperature. Subsequently, after ion exchange and calcination, the nanotube structure is reached (Wong et al., 2011). The hydrothermal method can synthesize nanotubes with different diameters and lengths by controlling the reaction conditions (Chi et al., 2007; Nakahira et al., 2010; Khoshnood et al., 2017; Mi et al., 2017). Hydrothermal synthesis is performed at high temperatures, and the rate of heating is a critical factor (Seo et al., 2001). Based on the rate of heating, the hydrothermal method can be divided into two categories: conventional and microwave hydrothermal procedures. In the traditional hydrothermal synthesis method, the sample is simply heated in a general

water bath. However, its heating rate is slow and the reaction cycle is long. Additionally, the heating of the reaction system is not uniform. The reaction system is exposed to microwave radiation during the microwave hydrothermal synthesis method. Since microwave heating is a rapid method of heating, the temperature of the reaction system very rapidly increases which results in a significantly reduced reaction period and the more uniform heating (Ribbens et al., 2008; Liu et al., 2014; Meng et al., 2016).

Titanium dioxide nanotubes can be synthesized by template synthesis, electrochemical anodization, and hydrothermal treatment. Additionally, there are some studies on the fabrication of nanotube structures by plasma electrolytic oxidation. Among the various possible methods, electrochemical anodization is the most commonly used method. By controlling the variables of the electrochemical anodization method, it is feasible to fabricate nanotube structures that satisfy the research needs. It is of great importance to delicately control the release of antibacterial agents in nanotubes and regulate the optimal size of nanotubes in order to promote cell adhesion, proliferation, and differentiation.

Preparation of Nano Coating

The formation of nano-scale coatings on the surface of titanium can endow new functionalities to the surface. There are various methods for nano-coatings preparation. the conventional surface coating technologies are chemical vapor deposition (CVD) and physical vapor deposition (PVD). Newly developed methods include sol-gel, spin coating, plasma spraying, layer-by-layer self-assembly, and electrophoretic deposition, these methods are listed in **Table 2**.

Chemical Vapor Deposition

In the CVD method a single substance or compound containing one or more gas phases of elements is utilized to perform a chemical reaction on the substrate surface and produce a coating. In recent decades, even inorganic coatings can be produced through CVD technologies. Moreover, these methods can be used to purify various substances and precipitates, single-crystal, polycrystalline, and other inorganic thin-film materials (Jin et al., 2013; Manawi et al., 2018). Based on the influential parameters and chemical interactions, CVD methods can be divided into ambient pressure (Jang et al., 2015), low-pressure (Gao et al., 2011; Umrao et al., 2017), thermal (Zeng et al., 2018), ultra-high vacuum (Multone et al., 2008), and organic metal CVD methods (Maury and Senocq, 2003; Gong et al., 2013). Various oxide coatings, nitrides, and metal nano-coatings can be prepared by CVD methods based on the material and the required properties through its varied techniques (Delfini et al., 2017).

Physical Vapor Deposition

In the PVD technology, a physical phenomenon is used to vaporize the surface of source material (solid or liquid) into gaseous atoms, molecules, or into ions by ionization under vacuum condition. After the vaporization step, a low-pressure gas (or plasma) is implemented and a functional thin film is

TABLE 2 | Various nano-coating preparation methods and the related characteristics.

Preparation technique	Characteristics	References
Chemical vapor deposition	(1) Lower equipment cost (2) Controllable coating density and purity (3) Coatings deposition on complex shapes (4) The coating is uniform and dense (5) Firmly combined with the base materials	Son et al., 2016
Physical vapor deposition	(1) Simple production process (2) No pollution, less consumables (3) The coating is uniform and dense (4) Firmly combined with the base materials	Hübsch et al., 2015
Spin-on deposition	(1) Simple production process (2) Low preparation cost and low pollution (3) Accurate and controllable coating thickness	Nguyen et al., 2020
Sol-gel method	(1) Simple production process and low equipment requirements (2) Can be prepared at room temperature (3) Large area coating (4) High purity and homogeneous coating	Hübsch et al., 2015
Plasma spraying	(1) Simple production process (2) Suitable for multiple materials (3) Coating with low porosity, high density and smooth feature	Mahade et al., 2019
Layer-by-layer self-assembly	(1) Simple production process without any need to special equipment (2) Suitable for multiple materials, including polymer materials (3) Can precisely control the coating structure and size	Elmi et al., 2019
Electrophoretic deposition	(1) Simple production process and convenient operation (2) Low preparation cost (3) Accurate thickness control, chemical composition, and porosity (4) Low temperature requirements	Pishbin et al., 2013

deposited on the substrate surface (Chouirfa et al., 2019). The PVD technology can deposit not only metallic and alloy films but also it is capable of depositing ceramics and polymers. The main PVD methods are vacuum evaporation, sputtering deposition, and ion plating.

Vacuum evaporation uses laser and electron beam heating to evaporate the material source into atoms or ions, and subsequently deposits atoms or ions onto the surface of the substrate to form a coating (Kumar et al., 2009; Garbacz et al., 2010). The resultant coating from this method has relatively large pores and poor adhesion to the substrate (Xingfang et al., 1988; Scott et al., 2003; Krysinina et al., 2020). Sputter plating uses the base material as the anode and the target material as the cathode. By using the sputtering deposition effect, the argon ions generated by argon ionization knocks out the target material atoms and deposits them on the surface of the base material. The characteristic of this kind of coating is the presence of a few pores, but it can combine with the substrate more efficiently (Ratova et al., 2017; Makówka et al., 2019; Zhang et al., 2019a). Ion plating is involved with the ionization of gasses or vaporized substances under vacuum conditions, during the bombardment of gas ions or vaporized material ions, evaporates, or other reaction products are deposited on the substrate. The coating prepared by this method is uniform and dense, basically free of pores with a strong binding with the substrate (Li et al., 2017c; Zhang et al., 2018a; Tian et al., 2019).

With the development of PVD methods, many advanced PVD-based technologies have been derived which facilitate the production of high-quality nano-coatings. These new developed technologies include activated reactive evaporation (Bulla et al., 2004; Biju et al., 2009; Yuvaraj et al., 2010), activated reactive sputtering (Alajlani et al., 2016, 2017), activated reactive ion plating (Xin et al., 2000), magnetron sputtering (Lelis et al., 2019; Avino et al., 2020; Vuchkov et al., 2020), magnetron sputtering pulsed laser deposition (MSPLD) (Endrino et al., 2002; Jones and Voevodin, 2004), ionized magnetron sputtering (Kusano et al., 1999; Tranchant et al., 2006), pulsed laser deposition (PLD) (Paneerselvam et al., 2020; Wang et al., 2020), and etc.

Sol-Gel Method

Sol-gel technology uses some compounds with high chemical activity as precursors. After the raw materials are uniformly mixed in the liquid phase, hydrolysis and condensation chemical reactions are carried out to form a stable sol. It reacts with water in a certain solvent and forms a sol through hydrolysis and polycondensation interactions. After the sol is aged, the colloidal particles slowly polymerize to form a gel with a three-dimensional grid structure. After the gel is dried, sintered, and solidified on the surface of the substrate, the NS coating would be achieved (Antonelli and Ying, 1995; Kim et al., 2004).

Spin-on Deposition

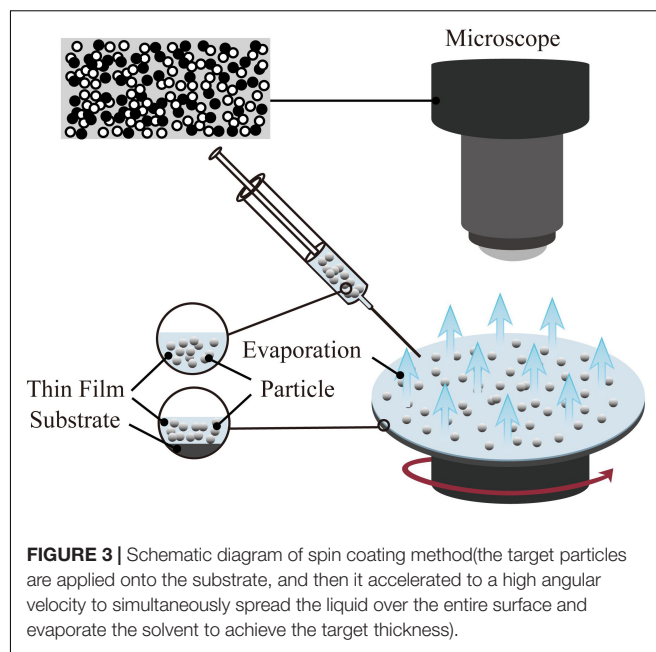
One of the coating preparation methods entitled as the spin coating is able to precisely control the thickness. However, the size of the substrate is limited by the size of the spinning device (Abu-Thabit and Makhoul, 2020). The thickness of the coating prepared by the spin coating method is in the range of 30 and 2000 nm. The typical spin coating method is mainly divided into three steps: glue dispensing, high-speed rotation, and drying. First, the spin-coating droplets are injected onto the surface of the substrate. Then, the spin coating solution is spread on the surface of the substrate through high-speed rotation to form a uniform film. Finally, the remaining solvent is removed by drying; hence the stable coating is obtained. In the process of preparing the coating by spin coating, high-speed rotation, and drying are the key steps to control the thickness, structure, and performance of the coating. The schematic of the spin coating method is shown in **Figure 3**.

Spin coating technology has been successfully applied in the fields of optics (Chtouki et al., 2017; Al-Douri et al., 2018) and electricity (Oytun and Basarir, 2019; Yildiz et al., 2019). Simultaneously, the spin coating method is also used in the preparation of functional thin films in the fields of biology and medicine. For example, a hydrophilic or hydrophobic film is produced on the surface of the base material to achieve the purpose of antibiosis (Kaviyarasu et al., 2017; Huang Y. et al., 2019; Li H. et al., 2020) and anti-corrosion (Kim et al., 2013; Akram et al., 2020).

Plasma Spraying

Plasma spraying technology uses a plasma arc that driven by direct current as a heat source to heat ceramics, alloys, metals, and other materials to a molten or semi-molten state (Fauchais and Montavon, 2007; Mostaghimi and Chandra, 2007). These materials are sprayed onto the surface of the base material at high speed, and a firmly attached surface coating is formed, this process is schematically presented in **Figure 4**. Plasma spraying is a fundamental nano-coating preparation process. This process has high stability and excellent controllability, and a variety of materials can be used to prepare the coating. At the same time, the prepared coating has low porosity and high deposition efficiency and it is suitable for preparing high melting point metal and ceramic coatings (Cheang and Khor, 1996; Huang et al., 2014; Goudarzi et al., 2018).

The plasma sprayed functional coatings can improve the thermal insulation, anti-oxidation, and surface optical performance of the base material. With further research on functional coatings prepared by plasma spraying, some advances have made in the biomedical field. For example, the preparation of silver-containing coatings with antibacterial effect on the surface of CoCr alloys using vacuum plasma spraying technique (Liang et al., 2020). Also, the HAp coating on the Ti6Al4V surface using the axial suspension plasma spraying method (Hameed et al., 2019), and the HAp coating prepared by the micro-plasma spray method (Wang et al., 2017), both presents enhanced biological performance than the traditional plasma spraying methods.



Layer-by-Layer Self-Assembly

Layer-by-layer self-assembly technology is a relatively new technology in recent years and is widely used in the biology, materials, and nanoscience fields. As shown in **Figure 5** (Zhang et al., 2018d), this technology can assemble a variety of materials (polyelectrolytes, small organic molecules, NPs, etc.) and can precisely control the surface structure and size of the coating. Nanomaterials with ordered structure prepared by self-assembly technology show unique properties. Self-assembly technology is currently a hotspot in the field of nanomaterial research.

Layer-by-layer self-assembly technology can be used to fabricate filtration membranes (Rajesh et al., 2016), sensors (Fernandes et al., 2011), and optoelectronic devices (Eom et al., 2017). Besides, it is able to produce antibacterial coatings (Wu et al., 2015; Huang J. et al., 2019; Li D. et al., 2019; Xia et al., 2019) or drug controlled release coatings (Cao M. et al., 2018; Silva et al., 2018; Zhou W. et al., 2018; Sun et al., 2020; Wu et al., 2020). Hence, this technology seems to would have broad application prospects in the biomedicine field.

Electrophoretic Deposition

Electrophoretic deposition is the directional movement of charged particles in the direction of the electrode under the action of an electric field. The outer layer of ions exerts pressure on the charged particles, forcing the particles to gather near the electrode and lead them to deposit (Besra and Liu, 2007). The method can prepare a coating with a thickness of 0.1–100 μm , which can meet the coating thickness requirements of various medical implant materials. Electrophoretic deposition techniques with many advantages can be used to prepare bioceramic coatings on metallic substrates (Boccaccini et al., 2010; Avcu et al., 2019; Alaei et al., 2020).

Mahlooji et al. (2019) prepared the chitosan-bioactive glass (CS-BG) nanocomposite coating on the surface of Ti-6Al-4V

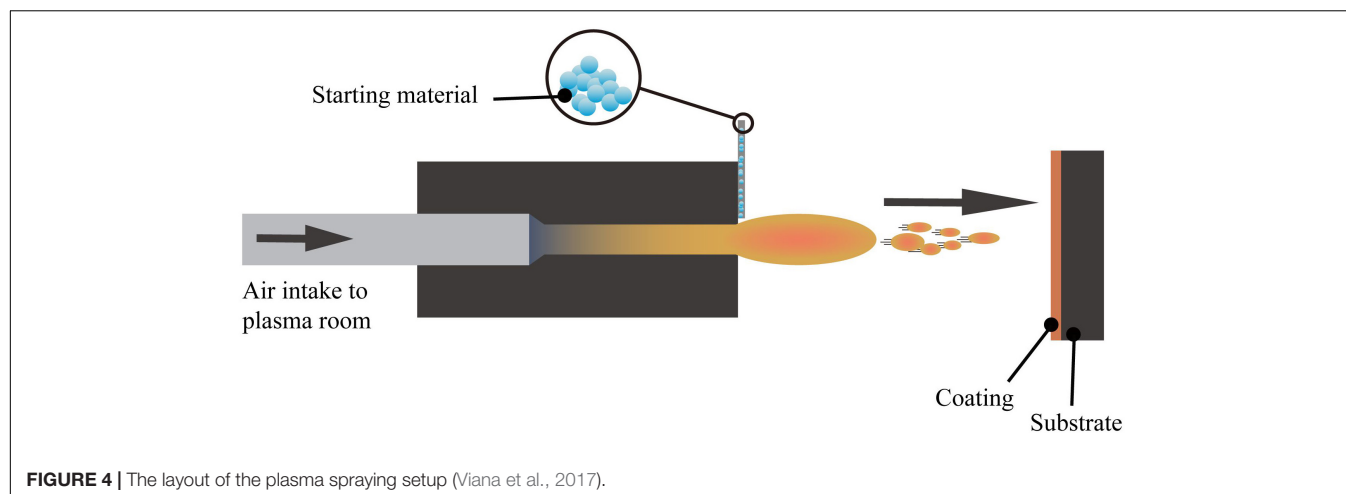


FIGURE 4 | The layout of the plasma spraying setup (Viana et al., 2017).

alloy by the electrophoretic deposition. The coating has excellent adhesive strength with the base material which can effectively promote the formation of apatite, and also it has a favorable biological activity. In addition, there are several related studies on the application of electrophoretic deposition technology to prepare bioactive glass coatings with various biological activities (Ur Rehman et al., 2018; Ghalayani Esfahani et al., 2019). There are also studies about the fabrication of antibacterial coatings by this method (Braem et al., 2017; Bakhshandeh and Amin Yavari, 2018; Ning et al., 2019; Thinakaran et al., 2020). A study used copper and chitosan to synthesize copper(II)-chitosan[Cu(II)-CS] complex coating, which has an excellent antibacterial effect on both Gram-positive and Gram-negative bacteria. In addition, Human osteoblast-like cells were cultured on the coating surface, which confirmed that the Cu (II) -CS coating had no cytotoxic effect (Akhtar et al., 2020). Furthermore, the results of a study about the chitosan hydrogel membrane (CHM) production by electrophoretic deposition show that the resultant coating can effectively promote the adhesion and growth of L-929 mouse fibroblast cells, and has good biocompatibility. It can also be loaded with suitable cells as a graft and is valuable from the application point of view (Li et al., 2017d).

Nanocoatings can be manufactured by various methods such as vapor deposition, different kinds of spraying, electrodeposition, etc. By considering the existing coating technologies, different manufacturing methods can be selected according to different needs. Adding the appropriate nanomaterials and precise adjustment of the coating parameters leads to manufacturing the desired nano-coatings. Compared with conventional coatings, nano-coatings have excellent mechanical properties, such as lower porosity, higher bond strength, higher hardness, oxidation resistance, corrosion resistance, etc. (Taylor and Sieradzki, 2003; Ranjbar and Rastegar, 2011; Lin et al., 2013). Therefore, the application of surface coatings in different fields will be very beneficial. In addition, the nanosurface coatings with antibacterial properties will be the great help in solving the implant-related infections and antibiotic resistance issues in clinical practice (Kose and Ayse Kose, 2015; Yilmaz and Yorgancioglu, 2018). There are

still many problems related to nanocoatings that need further research and discussion, such as the dispersion technique and stability of nanoparticles in the coating medium, the different properties of various types of nanoparticles, and their possible applications.

NANOMATERIALS LOADING

Nanomaterials can be used as antibacterial agents on the surface of titanium or titanium alloys and they have a potential to effectively improve the bactericidal properties (Chen et al., 2014; Xin et al., 2019; Xu J.W. et al., 2019). Most of the studies were focused on the metallic nano-antibacterial agents on the surface of titanium and its alloys (Liu et al., 2015b; Gunputh et al., 2018; Cheng et al., 2019). In this regard, the common metal particles are silver, zinc, copper, etc. (Vimbela et al., 2017). The NPs are tiny particles with a particle size in the range of 1–100 nm. The specific properties of NPs like large specific surface area, small size effect, and quantum size effect makes them an ideal option. Therefore, nanomaterials have a series of excellent properties, which improves the bactericidal effects of antibacterial agents in comparison to traditional antibacterial agents (Mi et al., 2018; Guo et al., 2020).

Metallic Antibacterial Agents

Metallic antibacterial agents have exceptional research value because of their strong antibacterial ability, good biocompatibility, and excellent stability (Ahmed et al., 2016). Inorganic antibacterial agents are usually present on the surface of titanium substrates in the form of NPs. They can be fixed on the surface of the titanium substrate by using a carrier or coated on the titanium substrate's surface to prepare a nano-coating (Kheiri et al., 2019).

Ag

Silver has many advantages in a broad-spectrum of antibacterial activity (Yang Z. et al., 2018; Wang L. et al., 2019). These advantages make it the most studied and widely used metal-based

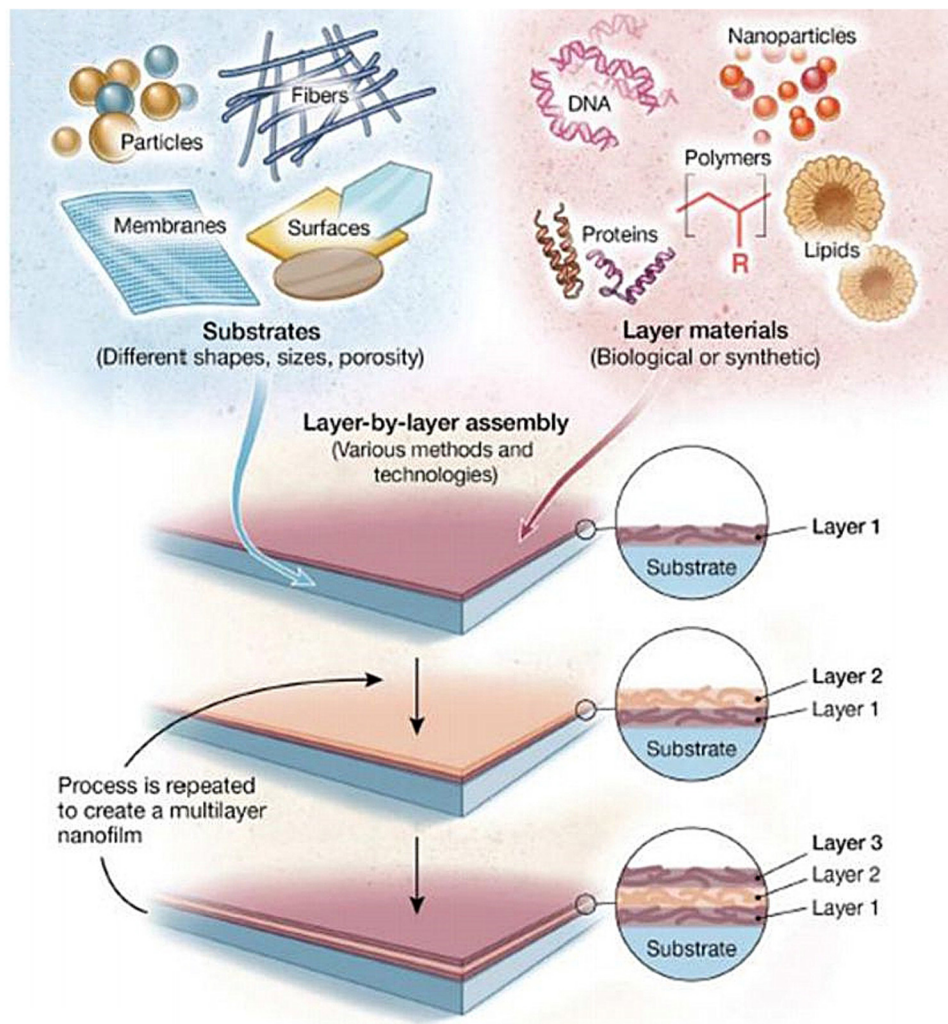


FIGURE 5 | Schematic illustration of LbL assembly technology, which can load different types of materials on different types of substrates (Zhang et al., 2018d).

antibacterial agent. Compared with traditional silver, silver NPs have a larger specific surface area, which significantly enhances their antibacterial ability. In the existing reports, the antibacterial mechanism of silver NPs mainly includes: destroying the structure of bacterial membranes, releasing silver ions and generating ROS to destroy enzymes in the oxidation respiratory chain, and regulating the signal transduction pathway of bacteria (Park et al., 2009; Tang and Zheng, 2018). Unfortunately, silver NPs can cause significant cytotoxicity above a specific dose range. The silver ions released by the silver NPs are highly mobile, and their entrance into living cells with high concentrations can kill healthy cells (AshaRani et al., 2009). The silver element forms which served as antibacterial are Ag₂O NPs (Chen et al., 2017; Sarraf et al., 2018a; Lv et al., 2019) and Ag NPs (Cheng et al., 2019; Pruchova et al., 2019; Surmeneva et al., 2019). The silver NPs that were loaded on the surface of the titanium substrate to produce NS, showing different antibacterial effects and performance that is listed in **Table 3**.

A large number of experiments have proved that silver NPs can effectively exert antibacterial properties. Silver NPs have a good killing effect on Gram-positive cocci represented by *Staphylococcus aureus* and Gram-negative bacilli represented by *Escherichia coli* (Deshmukh et al., 2018; Subramaniyan et al., 2019). Currently, the biggest challenge is to enable the stable release of silver at a suitable concentration on the surface of metal implants (Yang Z. et al., 2019; Zhu Y. et al., 2019; Lai et al., 2020). The nanotube structure, which is prepared on the surface of the titanium substrate and loaded with silver or Ag₂O NPs, is one of the solutions. Then, based on this structure, a controlled release coating (such as a polydopamine coating) is prepared, the controlled release phenomenon helps to achieve a long-term antibacterial effect (Gao et al., 2019). Compared with silver NPs, the amount of Ag⁺ released from Ag₂O NPs is lower, which may be due to the role of the oxide barrier. According to reports, Ag₂O NPs have a larger total surface-to-volume ratio, which increases their contact area with

TABLE 3 | Antibacterial effects and other related information about different silver-containing nanomaterials.

Materials	Base materials	Manufacturing technique	Nanostructure and Size	Antibacterial effect /Antibacterial rate	Cytotoxicity	Cells	References
Ag-CACS-Ti	Cp-Ti	<i>In situ</i> reduction	Nanoparticles	<i>E. coli</i> : 99.8% <i>S. aureus</i> : 99.9%	No	L929 cells	Cheng et al., 2019
Ag-TNTs	Ti-6Al-4V	Anodization+Chemical reduction	Nanoparticles: 102 ± 21 nm	<i>S. aureus</i> : 99.15%	–	–	Gunpath et al., 2018
Ag-HA	Ti-6Al-4V	Laser process	Nanoparticles: 20~30 nm	<i>S. aureus</i> : 77.59%	–	–	Liu and Man, 2017
Ag-HA-CS	Cp-Ti	Pulse electrochemical deposition	Nanoparticles: 303–321 nm	<i>E. coli</i> : 100% <i>S. aureus</i> : 100% <i>C. albicans</i> : 100% <i>P. aeruginosa</i> : 100%	No	BMSCs	Wang X. et al., 2019
Ag-PDA-TNTs	Cp-Ti	electrochemical anodization + <i>in situ</i> reduction	Nanoparticles: 13.5 ± 4.8 nm	<i>E. coli</i> : 54 ± 3.7%/14 days	–	–	Xu et al., 2017
Ag-PDA-TNTs	Ti-7.5Mo	Anodization + polydopamine assisted immobilization technique	Nanoparticles	<i>C. albicans</i> : 100%/48 h <i>S. aureus</i> : 100%/48 h	No	ADSCs	Rosifini Alves Claro et al., 2018
Ag-GO	Ti-67IMP	Physical vapor deposition magnetron sputtering + electrochemical anodization + spin coating	Nanoparticles	<i>E. coli</i> : 97.56%/24 h <i>S. aureus</i> : 98.15%/24 h	No	hFOB cells	Rafieerad et al., 2019
Ag-Ti	Cp-Ti	Target-ion induced plasma sputtering + Ag sputtering	Nanoparticles: 25 ± 5 nm	<i>E. coli</i> : 100%/12 h <i>S. aureus</i> : 100%/12 h	Yes	L929 fibroblast cells	Kim et al., 2018
TAN/TAP	Ti-Si	Vacuum arc remelting + sol-gel method	Nanoparticles: ~2 µm	<i>E. coli</i> : 98-100%/24 h <i>S. aureus</i> : 100%/24 h	No	L929 fibroblast cells; U-2OS human osteosarcoma cells	Horkavcová et al., 2017
Ag-Sr-HA coating	Cp-Ti	Hydrothermal method	Nanoparticles: ~100 nm	<i>E. coli</i> : 99%/24 h <i>S. aureus</i> : 95%/24 h	No	MG63 cells	Geng et al., 2016
Ag-HA coating	Cp-Ti	Electrostatic spraying	Nanorods: length: 50 nm, diameter: 20 nm	<i>E. coli</i> : 100%/24 h	No	Osteoblast	Gokcekaya et al., 2017
Ag film	Ti-6Al-4V	Thermal annealing + DC sputtering	Thickness: 20 nm	<i>E. coli</i> : 100%/24 h <i>S. aureus</i> : 100%/24 h	Yes	NIH3T3 fibroblast cells	Patil et al., 2019
Ag-TiN multilayers	Titanium alloy	Multi-arc ion plating	Thickness: 120 nm	<i>E. coli</i> : 99.88%/24h	Yes	MC3T3-E1 cells	Zhao et al., 2019
NiTiAg coating	Cp-Ti	Electrodeposition + anodization	–	<i>S. aureus</i> : 64.52% <i>S. epidermidis</i> : 92.35%	–	–	Huang et al., 2017

(Continued)

TABLE 3 | Continued

Materials	Base materials	Manufacturing technique	Nanostructure and Size	Antibacterial effect /Antibacterial rate	Cytotoxicity	Cells	References
Ag-DLC coating	Cp-Ti	Thermionic vacuum arc	Nanoparticles: 20 ± 3 nm	<i>S. aureus</i> : 94.2%/24 h	-	-	Mazare et al., 2018
Ag-CDHA	Ti-6Al-4V	Microwave assisted technique	Nanoparticles: 25.1–40.4 nm	<i>E. coli</i> : 83.68%/24 h <i>S. aureus</i> : 82.31%/24 h	No	MC3T3-E1 cells	Sikder et al., 2018
Ag-Pdop hybrid films	Ni-Ti	One-step immersion method	Nanoparticles: average 11.75 nm	<i>S. aureus</i> : >99%/24 h	No	hBMSCs	Yin et al., 2019
CS-Ag-MoS ₂ -Ti	Cp-Ti	Ultraviolet light induced reduction	-	<i>E. coli</i> : 99.77%/24 h <i>S. aureus</i> : 98.66%/24 h	No	NIH3T3-E1 cells	Zhu et al., 2020
Ag ₂ O-Ta ₂ O ₅ NTs	Ti-6Al-4V	Anodization + physical vapor deposition	-	<i>E. coli</i> : 100%/2 h	No	Osteoblast	Sarraf et al., 2018b
Ag ₂ O-TN ₂ S	Ti-6Al-4V	Anodization + physical vapor deposition	-	<i>E. coli</i> : 100%/2 h	No	Osteoblast	Sarraf et al., 2018a
Ag ₂ O-TiO ₂ coating	Cp-Ti	Micro-arc oxidation	-	<i>S. aureus</i> : 99%/24 h	No	NIH3T3-E1 cells	Lv et al., 2019
Ag ₂ O-TN ₂ S	Cp-Ti	Hydrothermal treatment	-	<i>S. aureus</i> : 100%/10 days; 84%/60 days	No	NIH3T3-E1 cells	Chen et al., 2017

TAN, Titania sol + AgNO₃; TAP, Titania sol + Ag₃PO₄; DLC, diamond-like carbon; CDHA, calcium deficient hydroxyapatite.

microorganisms (Morones-Ramirez et al., 2005). Compared with Ag NPs, Ag₂O NPs can also permeate or attach Ag⁺ ions to the bacterial membrane to achieve better killing of bacteria, while reducing the negative impact on mammalian cells (Sarraf et al., 2018b). In addition, the antibacterial effect of silver NPs *in vivo* is noteworthy. Guan et al. (2019). develop a novel surface strategy involving the formation of polydopamine (PDA) and silver (Ag) nanoparticle-loaded TiO₂ nanorods (NRDs) coatings on Ti alloy. *In vitro* antibacterial experiments showed that Ag-TiO₂@PDA NRDs coatings have antibacterial effects on Methicillin-resistant *Staphylococcus aureus* on days 7 and 14 according to the bacterial counting method. The efficiencies were 88.6 ± 1.5% and 80.1 ± 1.1%, respectively. The material was then implanted into the tibia of a rat model of osteomyelitis. After four weeks, the results of X-ray, micro-CT, and H&E staining showed that MRSA in the tibia of rats could be killed by Ag⁺, confirming that the material also had good antibacterial activity *in vivo*.

Moreover, with the release of silver NPs, the antibacterial properties of the implant material surface will gradually weaken hence it would be unable to have a long-term and stable antibacterial effect. Therefore, controlling the silver NPs release process and reducing the cytotoxic reactions caused by high concentrations of silver ions is one of the main research directions.

Cu

Copper is an essential trace element for the human body. Copper plays an important role in maintaining the normal hematopoietic function of the human body, promoting the formation of connective tissue and maintaining the health of the central nervous system. At the same time, copper has strong antibacterial properties and is not prone to drug resistance. Copper NPs can play an essential role in inhibiting infection and forming bone matrix by releasing copper ions (Liu et al., 2019; Mou et al., 2019; Anitha and Muthukumaran, 2020; Lv et al., 2020). As a redox metal (Tripathi and Gaur, 2004; Rauf et al., 2019), it can catalyze the formation of ROS, and at the same time, can destroy the permeability of bacterial membranes, resulting in the leakage of reducing sugars and proteins from cells. These mechanisms caused fatal damage to the bacteria. The antibacterial properties and characteristics of Cu NPs and NS containing Cu NPs are shown in Table 4.

Zn

Zinc is one of the important trace elements in the human body and plays a vital role in the growth and development of bones (Zhu et al., 2018). It was known that Zn can enhance the expression of M2 marker genes and proteins in macrophages. The adhesion, proliferation, and expression of osteoblast-related genes are increased by Zn (Zhang et al., 2018c; Chen et al., 2020). Zinc NPs are non-toxic and have a higher affinity to bacteria than ordinary zinc, which can lead to better antibacterial effect. In the current research on the antibacterial mechanism of zinc NPs, it has been found that zinc ions can destroy bacterial membranes and promote the production of ROS, thereby achieving antibacterial effects. Related research and results are shown in Table 5. To confirm the antibacterial effects and the

TABLE 4 | Antibacterial effects and other information of different copper-containing nanomaterials.

Materials	Base materials	Manufacturing technique	Nanostructure	Antibacterial effect/Antibacterial rate	Cytotoxicity	Cells	References
Cu NPs coating	Cp-Ti	Laser ablation	NPs: ~10nm	<i>S. aureus</i> : 83.21%/24 h		-	Fernández-Arias et al., 2020
Cu NPs coating	Cp-Ti	Plasma immersion ion implantation and deposition	Nanoparticles	<i>E. coli</i> : 50 ± 7%/24 h <i>S. aureus</i> : 90 ± 1%/24 h	No	rBMSC	Yu et al., 2016
CuO-TiO ₂ coating	Cp-Ti	Magnetron sputtering	NPs: ~100 nm	<i>S. aureus</i> : >99%/24 h	No	Osteoblasts	He et al., 2017
3Cu-HA coating	Ti-6Al-4V	Electrophoretic deposition	Nanoparticles: 50~100 nm	<i>E. coli</i> MIC: 700 µg*ml ⁻¹ /20 h <i>S. aureus</i> MIC: 1400 µg*ml ⁻¹ /20 h	No	MG63 cells	Hadidi et al., 2017
5Cu-HA coating	Ti-6Al-4V	Electrophoretic deposition	Nanoparticles: 50~100 nm	<i>E. coli</i> MIC: 300 µg*ml ⁻¹ /20 h <i>S. aureus</i> MIC: 700 µg*ml ⁻¹ /20 h	Yes	MG63 cells	Hadidi et al., 2017
2.5Cu-HA coating	Ti-6Al-4V	Laser deposition	Small aggregates: 200~1000 nm	<i>E. coli</i> : reduce growth to 42% /24 h <i>S. aureus</i> : reduce growth to 75% /24 h	No	NIH3T3-E1	Hidalgo-Robatto et al., 2018
Cu-TiO ₂ NTAS	Cp-Ti	Anodizing magnetron-sputtered	-	<i>S. aureus</i> : >90%/28 d	No	EA, hy926 cells	Zong et al., 2017

feasibility of clinical applications Zinc-containing nanocoatings were studied, the results have shown excellent antibacterial effects both in vitro and in vivo antimicrobial experiments. Li et al. (2017b) prepared hybrid ZnO/poly-dopamine/arginine-glycine-aspartate-cysteine nanorod arrays on the titanium surface using atomic layer deposition and hydrothermal methods. The material was implanted into the femur of the rabbit model infected with *S. aureus*. After four weeks, femurs from animal models were tested by H&E staining and Giemsa staining, the zinc-containing nanorod arrays were less infected than the control soft tissues and bones, demonstrating that the release of zinc ions can play an effective anti-infective role.

Au

Gold nanoparticles (Au NPs) as an antibacterial agent have been demonstrated in many researches (Grandi et al., 2011; Samanta et al., 2019). It has also some other surface functions such as photocatalysis, photothermal effect, and ROS-stimulating activity (Xia et al., 2015). Au NPs can also achieve antibacterial effects by destroying the cytoplasmic membrane of bacteria (Li et al., 2016). Au NPs are non-toxic and highly light stable, which can also be used as a probe to accurately locate biological macromolecules on the cell surface and within the cell, and can also be used for immunohistochemical localization.

Yang T. et al. (2019) prepared a gold nanorods (GNR) structure on the Ti surface by layer-by-layer self-assembly method. Also, they evaluate the photothermal antibacterial efficiency of Ti-GNR under near-infrared radiation (NIR) with a wavelength of 808 nm. The alamarBlueTM assay was used to detect the number of viable bacteria on different samples. The results showed that the antibacterial rates of Ti-GNR on *S. aureus*, *S. epidermidis*, *E. coli*, and *P. aeruginosa* were 45.72, 56.94, 14.61, and 20.24%, respectively. The NIR-treated Ti-GNR-NIR surface had antibacterial rates of 26.31, 31.84, 61.82, and 66.74%, respectively. The results show that the Ti-GNR surface after near-infrared radiation has high antibacterial activity against *E. coli* and *P. aeruginosa*. At the same time, the cell culture results showed that the Ti-GNR and Ti-GNR-NIR surfaces had lower cytotoxicity to MC3T3-E1 cells. Xu W. et al. (2019) prepared TiO₂ nanotube arrays (TNT) on Ti plates by anodizing, and then loaded gold NPs (Au NPs) into TNT. Under visible light, the antibacterial ability of nanotubes loaded with gold NPs against anaerobic bacteria was evaluated. The experimental results show that the average antibacterial efficiency of TNT materials loaded with Au NPs is above 85%, and the highest antibacterial rates for *F. nucleatum* and *P. gingivalis* can reach 92.13 and 97.34%.

Ni

Nickel is an indispensable element in the human body, and its content is in minimal range in the human body. Nickel maintains the structural stability and metabolism of biological macromolecules. Lack of nickel can cause diabetes, uremia, kidney failure, and other diseases. Studies have shown that Ni²⁺ can effectively kill bacteria (Yasuyuki et al., 2010), but excessive Ni²⁺ will cause cytotoxicity (Lü et al., 2009; Hang et al., 2012). A recent study showed that Ni²⁺ released from NiTi alloys could exhibit antibacterial properties (Ohtsu et al.,

TABLE 5 | Different antibacterial properties and biocompatibility of zinc-containing coatings.

Materials	Base materials	Manufacturing technique	Nanostructure	Antibacterial effect/Antibacterial rate	Cytotoxicity	Cells	References
ZnO-Sr-OPDA-TNTs	Cp-Ti	Anodization hydrothermal treatment + atomic layer deposition	ZnO film: thickness < 2 nm	<i>E. coli</i> : 87%/12 h <i>S. aureus</i> : 91%/24 h	No	MC3T3-E1 cells	Zhang K. et al., 2017
ZnO-CS-CNTs-Ti	Cp-Ti	Electrophoretic deposition atomic layer deposition	ZnO film thickness: < 10 nm	<i>E. coli</i> : 73%/24 h <i>S. aureus</i> : 98%/24 h	Yes	MC3T3-E1 cells	Zhu et al., 2017
ZnO-TiO ₂ coating	Cp-Ti	Hydrothermal low temperature liquid phase	Nanoparticle diameters: 50 ± 8~80 ± 9 nm	<i>E. coli</i> : 93.2%/12 h <i>S. aureus</i> : 97.5%/24 h	No	MC3T3-E1 cells	Pang et al., 2019
Zn-Ti nanowires	Cp-Ti	Sol-gel + alkali heat	–	<i>S. aureus</i> : 66.58%/3 days <i>P. gingivalis</i> : 45.02%/3 days <i>A. actinomycetemcomitans</i> : 53.42%/3 days	No	MC3T3-E1 cells	Shao et al., 2020
Zn-CHI-GEL multilayer films	Cp-Ti	LBL self-assembly	Film thickness: 14.91 ± 0.97~17.72 ± 0.63 nm	<i>E. coli</i> : 47.37%/24 h <i>S. aureus</i> : 52.94%/24 h	Yes	Osteoblasts	Karbowniczek et al., 2017
ZnO-TiO ₂ coating	Cp-Ti	Micro-arc oxidation	Nanoparticles: Average 30 nm	<i>S. aureus</i> : 51.4 ± 14.7%/24 h	No	MC3T3-E1 cells	Zhang et al., 2018b
ZnO-Ti coating	Cp-Ti	Micro-arc oxidation	–	<i>E. coli</i> : 48.08%/24h		–	Zhang et al., 2019c
ZnO-PPy-HA coating	Cp-Ti	Electrochemical deposition	Nanoparticle: Average 243 nm	<i>E. coli</i> : 63.5%/12h <i>S. aureus</i> : 72.8%/12h	No	BMSCs	Maimaiti et al., 2020
Zn-HA coating	Ti-6Al-4V	Co-precipitation + flame spraying	50–200 nm	<i>E. coli</i> : 99.9%/3 h	No	WST-1 cells	Yang et al., 2017
Zn-HA coating	Ti-6Al-4V	Plasma spraying	–	<i>E. coli</i> : 63.5%/7 days <i>S. aureus</i> : 36.6%/7 days	No	Saos-2 cells	Sergi et al., 2018

TABLE 6 | The antibiotics used in various NS titanium and its alloys.

Materials	Antibiotic	Manufacturing technique	Base materials	Antibacterial effect/Antibacterial rate	Cells	Cytotoxicity	References
PCL-HA-Rf coating	Rifampicin	Electrospinning	Cp-Ti	<i>S. aureus</i> : >99.9%/24 h <i>MRSA</i> : >99.9%/24 h <i>S. epidermidis</i> : >99.9%/24 h <i>P. aeruginosa</i> : >99%/24 h	hFOB	No	Kranthi Kiran et al., 2019
HA-GS coating	Gentamicin	Vacuum cold spraying	Ti-6Al-4V	<i>E. coli</i> : 96.4%/31 days	Osteoblasts	No	Fathi et al., 2019
GS-PAA coating	Gentamicin	Layer-by-layer assembly	Ti-6Al-4V	<i>E. coli</i> : 99.93%/16 h <i>S. aureus</i> : 99.86%/16 h	-	-	He et al., 2020
Van-Sr-HAP nanocomposite	Vancomycin	Co-precipitation	Cp-Ti	<i>MRSA</i> : 99.45%/12 h <i>MSSA</i> : 98.22%/12 h	MSCs	No	David and Nallaiyan, 2018
NFX-PLGA coating	Norfloracin	Nano spray drying	Cp-Ti	<i>E. coli</i> : 95.42~99.93%/24 h	L929	No	Baghdan et al., 2019

2017). However, due to slight Ni^{2+} release from the NiTi alloy, its antibacterial ability is relatively weak. Therefore, in nanometric range the specific surface area of the NiTi alloy is increased, and the release amount of Ni^{2+} is increased, thereby enhancing its antibacterial ability. Hang et al. (2018) produced Ni-Ti-O NPs with different lengths (0.55–114 μm) on NiTi alloys by anodization. The antibacterial effect of different samples to *S. aureus* was determined by the plate counting method. It was found that the antibacterial rate increased as the anodizing time increased. When the length of Ni-Ti-O NPs exceeds 11 μm , the antibacterial rate can reach 100% along with its excellent biocompatibility.

Liu et al. (2018) also used anodizing method to prepare Ni-Ti-O NPs on NiTi alloy and studied the effects of different annealing temperatures (200, 400, 600°C) on antibacterial properties and biocompatibility. The length of the NPs is 2.05–2.78 μm . The results show that the antibacterial rate of the smooth NiTi alloy surface is only 36%, and the antibacterial rate of the surface after anodizing reaches 84%. After annealing at 200°C, the antibacterial rate of Ni-Ti-O NPs was close to 100%. Ni-Ti-O NPs annealed at 200–400°C all showed good cell compatibility. Therefore, the preparation of NPs with different sizes on the surface of NiTi alloy can effectively enhance the antibacterial effect of the material by increasing the specific surface area.

An enormous number of studies on different inorganic nanoparticles (Ag, Cu, Zn, Au, Ni) indicate that Ag NPs as antibacterial agents have very efficient antibacterial performance compared to other antibacterial agents. At present, the mechanism of antibacterial actions of silver and silver ions is still under controversy. As mentioned previously, Ag NPs stimulate the generation of ROS and induce high oxidative stress, which is thought to be the foremost antibacterial mechanism (Park et al., 2009; Siritongsuk et al., 2016). Under normal circumstances, ROS generated in the cell receives a restriction that can be eliminated by antioxidants (Ramalingam et al., 2016). The antibacterial effect of Ag NPs stems from the dehydrogenase inactivation in the oxidative respiration chain along with excessive ROS generation. These circumstances inhibit oxidative respiration and the natural growth of the cells (Su et al., 2009; Quinteros et al., 2016). In addition, two antibacterial mechanisms, contact killing, and ion-mediated killing are widely accepted. Ag NPs can anchor to the bacterial cell wall and infiltrate it, which can cause physical changes to the bacterial membrane (bacterial membrane damage, leakage of bacterial contents) and ultimately lead to bacterial death (Khalandi et al., 2017; Seong and Lee, 2017). The primary antibacterial form of Ag NPs is the silver ion (Ag^+) (Liu and Hurt, 2010; Le Ouay and Stellacci, 2015), and the target of Ag^+ has been identified as a number of molecules [DNA, peptides (membrane-bound or inside the cell) or cofactors] (Le Ouay and Stellacci, 2015). The interaction of Ag NPs with cellular structures or biological molecules will result in impaired bacterial function and ultimately death. Antibiotics are usually used to attack particular molecules of certain bacteria, but silver ions react with all the nearby molecules, thus having a wide-spectrum antibacterial effect. Silver does not react with water, but can easily dissolve in water with the presence of an oxidizing agent

TABLE 7 | Antibacterial NS formation methods and the related properties.

Feature	Manufacturing technique	Base materials	Antibacterial effect and rate	Cells	Cytotoxicity	Wettability	Roughness	Morphology	References
Nanoflowers	Chemical etching + hydrothermal oxidation	Cp-Ti	<i>S. aureus</i> : 43.12%/24 h <i>MRSA</i> : 73.15%/24 h	hFOB	No	Hydrophilicity	Ra = 829 nm	A	Vishnu et al., 2019
Nanowires	Hydrothermal synthesis	Ti-6Al-4V	<i>S. aureus</i> : 74%/18 h	Osteoblasts	No	Hydrophilicity	–	B	Jaggessar et al., 2018
Regular nanotubes	Acid etching + anodic oxidation	Ti-6Al-4V	<i>E. coli</i> : 72.6%/2 h <i>S. aureus</i> : 68.2%/2 h	MG63	No	Hydrophilicity	Ra = 120 nm	C	Rahnamaee et al., 2020
Irregular nanotubes	Electrochemical anodization	Ti-6Al-4V	<i>E. coli</i> : 48.7%/2 h <i>S. aureus</i> : 50.8%/2 h	MG63	No	Superhydrophilicity	Ra = 360 nm	D	Rahnamaee et al., 2020
Nanotubes	Electrochemical anodization	Cp-Ti	<i>S. aureus</i> : 36.78%/16 h	–	–	Hydrophilicity	R_{rms} = 45.60 nm	E, F	Simi and Rajendran, 2017
Nano-ripples	Femtosecond laser direct writing	Cp-Ti	<i>E. coli</i> : 56%/24 h	MSCs	No	Superhydrophilicity	Ra = 274.6 nm	G	Luo et al., 2020
Nanoparticles	Aerosol flame synthesis	Aluminum alloy	<i>S. aureus</i> : 80%	–	–	Superhydrophilicity	–	H	De Falco et al., 2018
Nanopillars	Plasma etching	Cp-Ti	<i>P. aeruginosa</i> : 87 ± 2%/24 h <i>S. aureus</i> : 72.5 ± 13%/24 h	–	–	Hydrophobicity	–	I	Linklater et al., 2019

(oxygen), which is termed oxidative dissolution. The oxidative dissolution of silver is also an important mechanism for its antibacterial action (Molleman and Hiemstra, 2015), through the above mentioned multiple mechanisms, which directly or indirectly lead to the ability of Ag NPs to exert efficient antibacterial effects.

The issue of cytotoxicity of Ag NPs still needs further studies since it depends on lots of factors, including the shape of NPs, dimension, concentration, etc. (Attarilar et al., 2020), since high concentration of Ag NPs may be cytotoxic. Moreover, some other studies demonstrated the influence of NPs' size on cytotoxicity. Several studies have shown that Ag NPs with the small size range (<20 nm) may cause varying degrees of cytotoxic effects, while large or condensed particles (>100 nm) sometimes do not have any considerable adverse outcomes (Marambio-Jones and Hoek, 2010; Yang et al., 2012; Rizzello and Pompa, 2014; Foldbjerg et al., 2015). Traditionally, antibiotics targeting specific infections or classes of bacteria have been used for implant material infections. In this regard, Ag NPs have a substantial potential to replace with antibiotics due to their favorable antibacterial properties and broad antibacterial activity over other inorganic nanoparticles. Combining Ag NPs with implant materials for in vitro and in vivo studies makes them promising antibacterial implant materials. To reduce the toxicity of silver and to decrease the level of silver in the blood, future research should focus on developing effective techniques for combining silver nanoparticles with the implant materials that can release silver ions in a controlled and harmless way.

Antibiotics

In addition to using inorganic antibacterial agents to prepare materials with antibacterial properties, antibiotics can also be used on titanium or its alloys' surfaces to prepare nano-coatings or other NS to achieve antibacterial effects (Li et al., 2017a; Liu et al., 2017; Mohan Raj et al., 2018). The chosen antibiotics need to be able to kill Gram-positive cocci and Gram-positive bacillus effectively (Hickok and Shapiro, 2012). Available antibiotics include rifampicin, gentamicin, vancomycin, etc. (Simchi et al., 2011) (Table 6). Under ideal conditions, the antibiotics released by the prepared nanomaterials should reach the effective drug concentration and should maintain a long sufficient sterilization time (Salwiczek et al., 2014; Nguyen-Tri et al., 2019).

BIONIC NANOSTRUCTURES

In recent years, the wings of insects, such as dragonflies and cicadas, have attracted much attention as a model biological system because of their excellent antibacterial and antifungal properties (Ivanova et al., 2012; Diu et al., 2014; Kelleher et al., 2016). Some studies have shown the presence of physical nano-protrusions on the surface of insect wings. Their antibacterial properties may be due to the fact that when microbial cells come in contact with the protrusions, they possibility enhance the stress and deformation of the membrane structure of the microbial cells, leading to their

destruction. It eventually leads to the dissolution and death of the cells (Ivanova et al., 2013; Nowlin et al., 2014; Bandara et al., 2017). By investigating the surface structure of insect wings as a model and preparing bionic structures according to it, new ideas for preparing modern antibacterial titanium alloys have emerged.

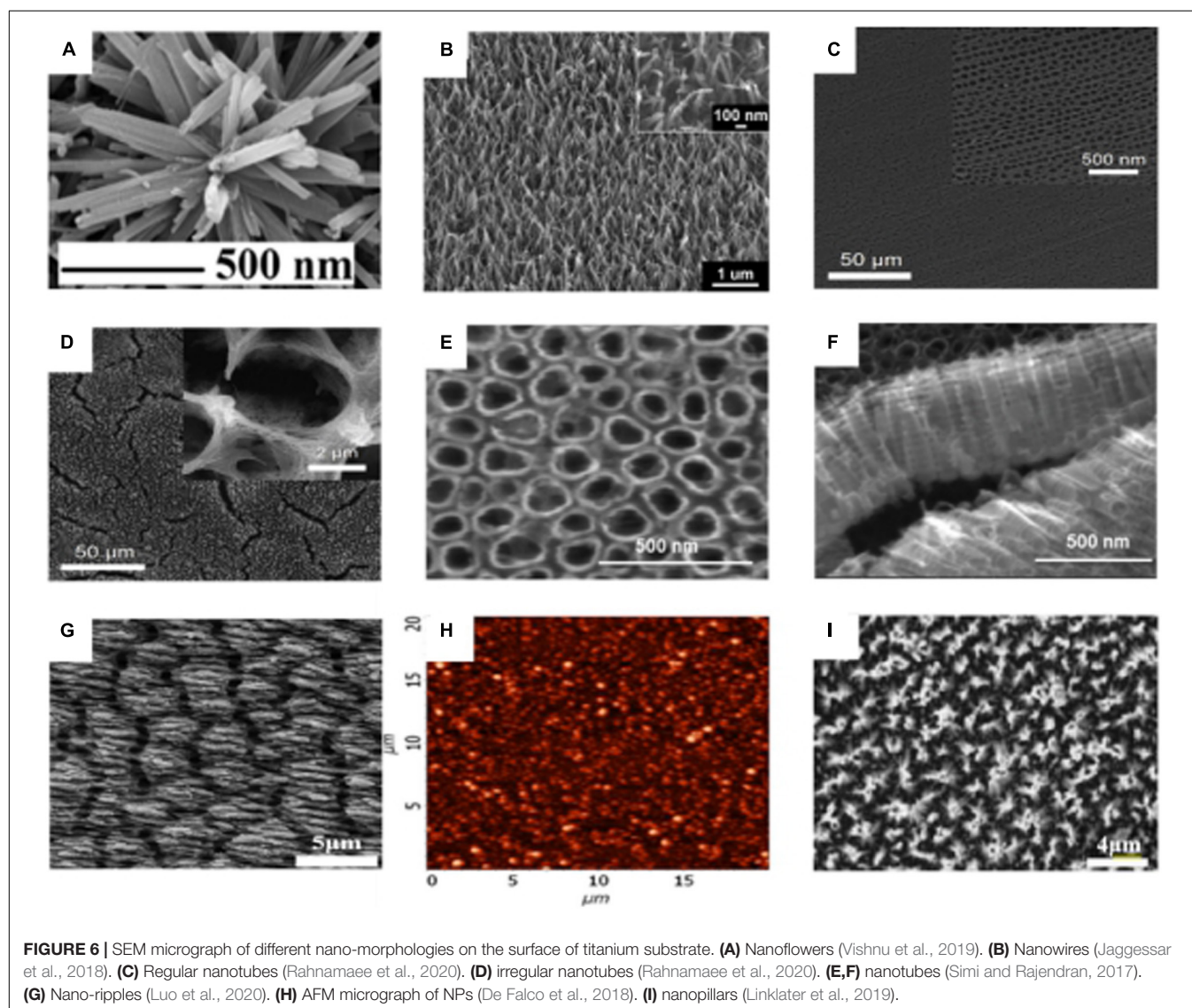
Antibacterial Nanopatterns and Fabrication Methods

It has been shown that modification of the surface morphology of materials can be used to achieve antibacterial effects and inhibition of biofilm formation (Modaresifar et al., 2019; Stratakis et al., 2020). By changing the surface morphology without adding other chemical reagents, the antibacterial and antibiofilm formation properties can also be achieved (Campoccia et al., 2013; Hasan et al., 2013). Moreover, it has a slight effect on the mechanical strength of the material.

Changing the surface morphology to prepare biomimetic structures with micron and nano-scale surface morphologies, and exploring the effect of surface morphology and size of titanium or its alloys that can effectively attack bacteria are the currently urgent problems to be solved. **Table 7** lists some of the antibacterial NS formation methods and their properties.

Different nano-morphologies can be prepared through different preparation processes: nanoflowers, nanowires, nanotubes, nano-ripples, NPs, and nanopillars are possible morphologies, **Figure 6**. Among these nano-topographies, nanopillars show good bactericidal effect, which may be related to its high aspect ratio (Linklater et al., 2018). In each nanotopography, cell activity was not significantly inhibited. Furthermore, in some nanotopographies, the cells' metabolic activity tends to increase (Jaggessar et al., 2018).

There are several methods to fabricate nanopatterns, and the commonly used methods are chemical etching (Heidarpour



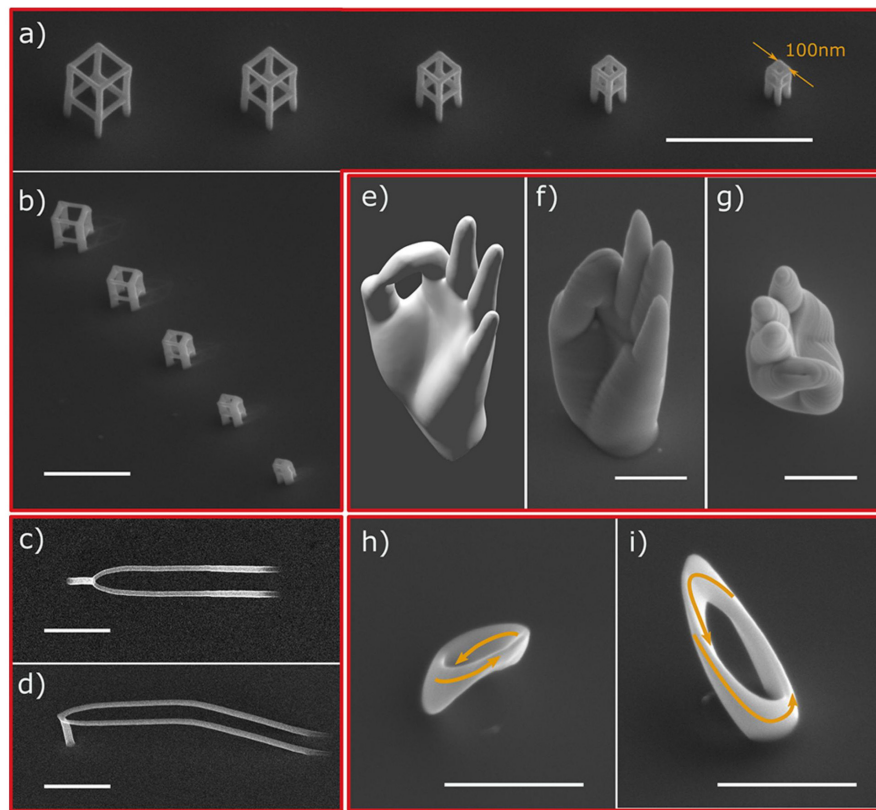


FIGURE 7 | SEM images of different 3D geometries prepared by the focused electronbeam-induced deposition (FEBID) method. **(a,b)** A series of cubes. **(c,d)** Smooth nanowires. **(e–g)** Nanoscale replica of a human hand. **(h,i)** Cobalt Mobius strip (Skoric et al., 2020).

et al., 2020), reactive ion etching (Ganjan et al., 2019), plasma etching (He et al., 2013), hydrothermal synthesis (Jaggessar and Yarlagaadda, 2020; Wategaonkar et al., 2020), and anodic oxidation (Mohan et al., 2020). The antibacterial nanopatterns with different antibacterial efficiencies have been prepared by these methods, but the antibacterial effect of these patterns is still not very satisfactory, which may be due to the fact that the production of antibacterial surfaces on titanium and its alloys are more difficult than other materials [silicon, polymethylmethacrylate (PMMA), etc.]. The development of nanopatterns with efficient antibacterial properties can enable the better clinical application of titanium-related medical materials and may address the bacterial resistance problem caused by antibiotic abuse. Currently, some novel methods for nanopatterning have been developed, such as two-photon polymerization (2PP) (Liao et al., 2020) and electron beam induced deposition (EBID) (Perentes et al., 2004; Skoric et al., 2020). Two-photon polymerization is a new 3D structure fabrication technology based on CAD/CAM, that precisely constructs 3D geometries with resolutions down to 100 nm. 2PP's high resolution, adaptability to a wide range of materials, and the ability to create true 3D structures make it a very promising technology for the fabrication of medical implants (Doraiswamy et al., 2006; Ovsianikov and Chichkov, 2012). EBID fabrication technology is also gaining much attention (Hirt et al., 2017),

enabling the fabrication of 3D structures in tens of nanometers and the deposition of a wide range of materials (metallic, organic, semiconducting, magnetic, superconducting, etc.) (Utke et al., 2008; Huth et al., 2018). EBID technology currently achieves vertical growth rates of hundreds of nanometers per second (Winkler et al., 2018) and can improve processing efficiency through several methods: optimizations of gas injection systems (GIS) (Friedli and Utke, 2009), deposition at low temperatures (Bresin et al., 2013), and simultaneous deposition of multiple beams (Riedesel et al., 2019). A variety of 3D geometries can be prepared by this method, as shown in **Figure 7**. In the future, the development of high-resolution, efficient, and controllable 3D nanomorphology methods will be a critical challenge to be overcome.

Antibacterial Mechanism of Nanopatterns

Nanoscale structures with specific dimensions are fabricated on the surface of the substrate material, and this nanoscale structure performs mechanocidal action through different mechanisms. The interactions between nanopatterns and bacteria are multifaceted, and the exact mechanism of bactericidal action and the role of various factors in regulating bactericidal behavior are still controversial (Bandara et al., 2017; Linklater et al.,

2017). Most researchers agree that nanopatterns with high aspect ratio are key factors in causing mechanical deformation of the bacterial cell walls, which in turn causes their rupture and death (Watson et al., 2015; Truong et al., 2017; Cao Y. et al., 2018). Xue et al. (2015) have developed mathematical models to explain the bactericidal properties of nanopatterns on the surface of cicada wings. Gravity as well as non-specific forces (such as van der Waals forces) have been demonstrated to play a role in bacterial cell wall rupture. In addition, extracellular polymeric substance (EPS) has been demonstrated to play an important role in regulating the bactericidal effects of nanopatterns, they are known as natural biopolymeric mixtures of proteins and polysaccharides which excreted by microorganisms. EPS plays an important role in the formation of biological membranes, also it promotes cell signaling and protects bacteria from the harmful effects of environmental factors (Limoli et al., 2015). Bandara et al. (2017) found that some bacteria under the influence of nanopillars secrete EPS with adhesion. Bacteria find the adherent surface unfit to survive and try to move away, and the anchoring action of EPS leads to rupture of the bacterial cell wall and bacterial death. Furthermore, the applied mechanical forces affect the metabolomics and bacterial genome and may also be the mechanism by which bacteria die on their surfaces (Rizzello et al., 2011; Belas, 2014; Persat, 2017; Velic et al., 2019). The mechanism of the antibacterial effect of nanopatterns is still not completely clarified, hence the research on the antibacterial mechanisms is crucial for the preparation of materials with excellent antibacterial effect.

Factors Affecting the Antibacterial Property of Nanopatterns

The design parameters (height, diameter, and spacing) of the nanopatterns have a significant influence on the antibacterial properties. Nanopatterns with different parameters (height from 100 nm to 900 nm, diameter from 10 nm to 300 nm, and spacing less than 500 nm) have been reported in the literature to exhibit bactericidal properties (Modaresifar et al., 2019). Velic et al. (2019) studied the effect of varied design parameters of nanopatterns on bacteria behavior by developing a two-dimensional finite element model and demonstrated that reducing the pillar diameter could effectively promote bactericidal efficiency. Additionally, preparing nanopillar structures with similar diameters but different densities and heights showed that extra stretched nanopillars with varying heights leads to rupture in the bacterial cell membranes (the membranes exceeded the threshold value of stretching) (Wu et al., 2018).

The occurrence of implant material-related infections often begins with bacterial adhesion to the implant surface subsequently the colonization of bacteria and biofilm formation happens. Biofilms are bacteria produced microbial communities formed by the EPS substrate to inhibit the damage of bacteria. Statistically, about 99% of bacteria could exist with biofilm status (Zimmerli and Sendi, 2017). Biofilms exist as reservoirs

for bacteria, often leading to chronic and systemic infections. Therefore, reducing the opportunity of bacteria to adhere to the surface of the implants is essential to prevent infection. The adhesion of bacteria to a material surface depends on the surface properties of the material, such as surface roughness, wettability, and topography. Bacteria are more likely to adhere to rough rather than smooth surfaces (Sarró et al., 2006; Fan et al., 2013) and more likely to adhere to hydrophobic rather than hydrophilic surfaces (Pagedar et al., 2010). At the same time, the nanoscale surface has a higher resistance to bacterial adhesion than the micron and macroscale surfaces (Singh et al., 2011; Spengler et al., 2019). The severe plastic deformation (SPD) process is a recently developed technique for the fabrication of nanostructures (Dyakonov et al., 2019; Shuitcev et al., 2020). It is noteworthy that by reducing the grain size to the sub-micron range (100–500 nm) through SPD processes, the mechanical properties of commercially pure titanium are comparable to those of conventional Ti-6Al-4V alloys (Singh et al., 2011). It was found that the increase in Ra of the pure titanium surface after SPD processing was followed by an increase in the adhesion density of *S. aureus*, which was independent to *P. aeruginosa*. The effect of surface hydrophilicity on bacterial adhesion can be explained by thermodynamics (Bruinsma et al., 2001), with a higher affinity of hydrophobic bacteria for hydrophobic surfaces and of hydrophilic bacteria for hydrophilic surfaces (Sabirov et al., 2015).

CONCLUSION

Nanomaterials have the characteristics of small size and large specific surface area which lead them to have more potent antibacterial activity and drug loading capacity than traditional materials, thus showing an excellent antibacterial effect. However, once the safe antimicrobial material exceeds its safe dose during the release process, it will produce cellular cytotoxicity and even affect the osteogenic performance of titanium implant materials' surfaces. Moreover, the antibacterial ability of the implant material surface will gradually weaken with the release of antibacterial substances. The nano-morphology on the surface of the titanium implant material can achieve a long-term antibacterial effect. However, the destructive effect of the nano-morphology surface on different bacteria is quite different, and the antibacterial range is limited. At present, the nanometer modification of implant materials is still in its infancy and lots of improvement must be done in order to make them an ideal option for medical applications both form cytotoxicity and functionality, this study aims to produce a guideline and achieve the as-mentioned goals. In this regard, nanostructure formation methods including template synthesis, electrochemical anodization, and hydrothermal treatment was discussed. In addition, nano coating methods such as CVD, PVD, sol-gel, spin coating, electrophoretic deposition, plasma spraying, and LBL technologies were introduced. Then different antibacterial agent loading on these nanostructured surfaces were analyzed. The loading substances can have metallic nature like Ag, Cu, Zn, Au,

and Ni, even some antibiotics including rifampicin, gentamicin, and vancomycin can be loaded on these nanostructures.

Although, there are many known involved parameters and methods, it seems that more research in this field is from crucial importance since it affect the health issues. Some modern, safe and economic methods and materials should be introduced by researchers. The accurate and complementary guidelines about the safe thresholds and stability of antibacterial agents and procedures must be prepared. The precise mechanisms both from bactericidal and functionality points of view should be understood. The effect of antibacterial schemes on biocompatibility, osteogenic activity, genotoxicity, and their possible influence on periphery tissues should be analyzed. In future, the direction of research shifts to improve the antibacterial properties of non-cytotoxic antibacterial nanoparticles and develop implant materials with stable and long-lasting antibacterial effects. In the study of cytotoxic nanoparticles with antibacterial properties (e.g., silver nanoparticles), further clarifying the factors and mechanisms leading to cytotoxicity and developing controllable and harmless antibacterial materials are the next research focuses. The possible bactericidal mechanisms, the design parameters to achieve the efficient antibacterial performance on different bacteria species, and the development of high-precision nanopattern processing technologies are still among the future problems to be solved in nanopattern antibacterial studies. This review paper can help the investigators to develop the new methods, procedures, and materials to attain a modern scheme in design of nanostructured antibacterial materials with long-last, safe, biocompatible, and effective on broad bacterial infections characteristics.

REFERENCES

- Aal, N. A., Al-Hazmi, F., Al-Ghamdi, A. A., Al-Ghamdi, A. A., El-Tantawy, F., and Yakuphanoglu, F. (2015). Novel rapid synthesis of zinc oxide nanotubes via hydrothermal technique and antibacterial properties. *Spectrochim. Acta Part A Mol. Biomol. Spectrosc.* 135, 871–877. doi: 10.1016/j.saa.2014.07.099
- Abid, S. A., Taha, A. A., Ismail, R. A., and Mohsin, M. H. (2020). Antibacterial and cytotoxic activities of cerium oxide nanoparticles prepared by laser ablation in liquid. *Environ. Sci. Pollut. Res.* 27, 30479–30489. doi: 10.1007/s11356-020-09332-9
- Abu-Thabit, N. Y., and Makhlof, A. S. H. (2020). *Fundamental of Smart Coatings and Thin Films: Synthesis, Deposition Methods, and Industrial Applications*. (Amsterdam: Elsevier Inc). doi: 10.1016/b978-0-12-849870-5.00001-x
- Ahmed, K. B. A., Raman, T., and Veerappan, A. (2016). Future prospects of antibacterial metal nanoparticles as enzyme inhibitor. *Mater. Sci. Eng. C* 68, 939–947. doi: 10.1016/j.msec.2016.06.034
- Akhtar, M. A., Ilyas, K., Siska, F., and Boccaccini, A. R. (2020). Electrophoretic deposition of copper(II)-chitosan complexes for antibacterial coatings. *Int. J. Mol. Sci.* 21:2637. doi: 10.3390/ijms21072637
- Akram, W., Rafique, A. F., Maqsood, N., Khan, A., Badshah, S., and Khan, R. U. (2020). Characterization of PTFE film on 316L stainless steel deposited through spin coating and its anticorrosion performance in multi acidic mediums. *Materials* 13:388. doi: 10.3390/ma13020388
- Alaei, M., Atapour, M., and Labbaf, S. (2020). Electrophoretic deposition of chitosan-bioactive glass nanocomposite coatings on AZ91 Mg alloy for biomedical applications. *Prog. Org. Coatings* 147:105803. doi: 10.1016/j.porgcoat.2020.105803
- Alajlani, Y., Placido, F., Barlow, A., Chu, H. O., Song, S., Ur Rahman, S., et al. (2017). Characterisation of Cu₂O, Cu₄O₃, and CuO mixed phase thin films produced by microwave-activated reactive sputtering. *Vacuum* 144, 217–228. doi: 10.1016/j.vacuum.2017.08.005
- Alajlani, Y., Placido, F., Gibson, D., Chu, H. O., Song, S., Porteous, L., et al. (2016). Nanostructured ZnO films prepared by hydro-thermal chemical deposition and microwave-activated reactive sputtering. *Surf. Coatings Technol.* 290, 16–20. doi: 10.1016/j.surfcoat.2016.01.036
- Al-Douri, Y., Fakhri, M. A., Badi, N., and Voon, C. H. (2018). Effect of stirring time on the structural parameters of nanophotonic LiNbO₃ deposited by spin-coating technique. *Optik* 156, 886–890. doi: 10.1016/j.ijleo.2017.12.059
- Alivov, Y., Pandikunta, M., Nikishin, S., and Fan, Z. Y. (2009). The anodization voltage influence on the properties of TiO₂ nanotubes grown by electrochemical oxidation. *Nanotechnology* 20:225602. doi: 10.1088/0957-4484/20/22/225602
- Andersson, D. I., and Hughes, D. (2012). Evolution of antibiotic resistance at non-lethal drug concentrations. *Drug Resist. Updat.* 15, 162–172. doi: 10.1016/j.drug.2012.03.005
- Andersson, D. I., and Hughes, D. (2014). Microbiological effects of sublethal levels of antibiotics. *Nat. Rev. Microbiol.* 12, 465–478. doi: 10.1038/nrmicro3270
- Anitha, S., and Muthukumaran, S. (2020). Structural, optical and antibacterial investigation of La, Cu dual doped ZnO nanoparticles prepared by co-precipitation method. *Mater. Sci. Eng. C. Mater. Biol. Appl.* 108:110387. doi: 10.1016/j.msec.2019.110387
- Antonelli, D. M., and Ying, J. Y. (1995). Synthesis of Hexagonally Packed Mesoporous TiO₂ by a Modified Sol–Gel Method. *Angew. Chem. Int. Ed. Engl.* 34, 2014–2017. doi: 10.1002/anie.199520141
- AshaRani, P. V., Low Kah, Mun, G., Hande, M. P., and Valiyaveetil, S. (2009). Cytotoxicity and genotoxicity of silver nanoparticles in human cells. *ACS Nano* 3, 279–290. doi: 10.1021/nn800596w
- Attarilar, S., Salehi, M. T., Al-Fadhalah, K. J., Djavanroodi, F., and Mozafari, M. (2019a). Functionally graded titanium implants: characteristic enhancement

AUTHOR CONTRIBUTIONS

JQL, JL, and SA contributed equally to the design, reorganize the figures, and writing the manuscript. CW, MT, KX, and CY collated the resource. JY, LW, CL, and YT helped with editing the manuscript. YT conceived and designed the outline of this review. All the authors read and approved the final manuscript.

FUNDING

This work was supported by Guangxi Key R&D Project (Guike AB18050008), Guangxi Science and Technology Program (2018GXNSFAA294116), Guangxi Science and Technology Program (2018GXNSFAA138074), Guangxi Science and Technology Program (2018GXNSAA294091), High-level Innovation Team and Outstanding Scholars Program of Colleges and Universities in Guangxi: Innovative Team of Basic and Clinical Comprehensive Research on Bone and Joint Degenerative Diseases, Scientific Research Project of High-level Talents in The Affiliated Hospital of Youjiang Medical University for Nationalities (R20196301), Scientific Research Project of High-level Talents in The Affiliated Hospital of Youjiang Medical University for Nationalities (R20196306), European Commission via H2020 MSCA RISE BAMOS Programme (734156), and Royal Society via International Exchange Programme (IEC\NSFC\191253).

- induced by combined severe plastic deformation. *PLoS One* 14:e0221491. doi: 10.1371/journal.pone.0221491
- Attarilar, S., Salehi, M.-T., and Djavanroodi, F. (2019b). Microhardness evolution of pure titanium deformed by equal channel angular extrusion. *Metall. Res. Technol.* 116:408. doi: 10.1051/metal/2018135
- Attarilar, S., Yang, J., Ebrahimi, M., Wang, Q., Liu, J., Tang, Y., et al. (2020). The toxicity phenomenon and the related occurrence in metal and metal oxide nanoparticles: a brief review from the biomedical perspective. *Front. Bioeng. Biotechnol.* 8:822. doi: 10.3389/fbioe.2020.00822
- Avcu, E., Baştan, F. E., Abdullah, H. Z., Rehman, M. A. U., Avcu, Y. Y., and Boccaccini, A. R. (2019). Electrophoretic deposition of chitosan-based composite coatings for biomedical applications: a review. *Prog. Mater. Sci.* 103, 69–108. doi: 10.1016/j.pmatsci.2019.01.001
- Avila, J. D., Bose, S., and Bandyopadhyay, A. (2018). "Additive manufacturing of titanium and titanium alloys for biomedical applications," in *Additive Manufacturing of Emerging Materials*, eds F. Froes and M. Qian (Amsterdam: Elsevier Inc), 325–343. doi: 10.1016/B978-0-12-812456-7.00015-9
- Avino, F., Fomesu, D., Koettig, T., Bonura, M., Senatore, C., Perez Fontenla, A. T., et al. (2020). Improved film density for coatings at grazing angle of incidence in high power impulse magnetron sputtering with positive pulse. *Thin Solid Films* 706:138058. doi: 10.1016/j.tsf.2020.138058
- Baghdan, E., Raschpichler, M., Lutfi, W., Pinnapireddy, S. R., Pourasghar, M., Schäfer, J., et al. (2019). Nano spray dried antibacterial coatings for dental implants. *Eur. J. Pharm. Biopharm.* 139, 59–67. doi: 10.1016/j.ejpb.2019.03.003
- Bakhshandeh, S., and Amin Yavari, S. (2018). Electrophoretic deposition: a versatile tool against biomaterial associated infections. *J. Mater. Chem. B* 6, 1128–1148. doi: 10.1039/c7tb02445b
- Bandara, C. D., Singh, S., Afara, I. O., Wolff, A., Tesfamichael, T., Ostrikov, K., et al. (2017). Bactericidal effects of natural nanotopography of dragonfly wing on *Escherichia coli*. *ACS Appl. Mater. Interfaces* 9, 6746–6760. doi: 10.1021/acsami.6b13666
- Belas, R. (2014). Biofilms, flagella, and mechanosensing of surfaces by bacteria. *Trends Microbiol.* 22, 517–527. doi: 10.1016/j.tim.2014.05.002
- Ben-Knaz Wakshlak, R., Pedahzur, R., Menagen, B., and Avnir, D. (2016). An antibacterial copper composite more bioactive than metallic silver. *J. Mater. Chem. B* 4, 4322–4329. doi: 10.1039/c6tb00719h
- Bera, D., Kuiri, S. C., and Seal, S. (2004). Synthesis of nanostructured materials using template-assisted Electrodeposition. *JOM* 56, 49–53. doi: 10.1007/s11837-004-0273-5
- Bernal, A., Tselev, A., Kalinin, S., and Bassiri-Gharb, N. (2012). Free-standing ferroelectric nanotubes processed via soft-template infiltration. *Adv. Mater.* 24, 1160–1165. doi: 10.1002/adma.201103993
- Besra, L., and Liu, M. (2007). A review on fundamentals and applications of electrophoretic deposition (EPD). *Prog. Mater. Sci.* 52, 1–61. doi: 10.1016/j.pmatsci.2006.07.001
- Bhadra, C. U., Jonas Davidson, D., and Henry Raja, D. (2020). Fabrication of titanium oxide nanotubes by varying the anodization time. *Mater. Today Proc.* doi: 10.1016/j.matpr.2020.01.455
- Biju, K. P., Subrahmanyam, A., and Jain, M. K. (2009). Growth of InN nanocrystalline films by activated reactive evaporation. *J. Nanosci. Nanotechnol.* 9, 5208–5213. doi: 10.1166/jnn.2009.1123
- Boccaccini, A. R., Cho, J., Subhani, T., Kaya, C., and Kaya, F. (2010). Electrophoretic deposition of carbon nanotube-ceramic nanocomposites. *J. Eur. Ceram. Soc.* 30, 1115–1129. doi: 10.1016/j.jeurceramsoc.2009.03.016
- Bozkurt Çırak, B., Karadeniz, S. M., Kılınç, T., Caglar, B., Ekinci, A. E., Yelgin, H., et al. (2017). Synthesis, surface properties, crystal structure and dye sensitized solar cell performance of TiO₂ nanotube arrays anodized under different voltages. *Vacuum* 144, 183–189. doi: 10.1016/j.vacuum.2017.07.037
- Braem, A., De Brucker, K., Delattin, N., Killian, M. S., Roeffaers, M. B. J., Yoshioka, T., et al. (2017). Alternating current electrophoretic deposition for the immobilization of antimicrobial agents on titanium implant surfaces. *ACS Appl. Mater. Interfaces* 9, 8533–8546. doi: 10.1021/acsami.6b16433
- Bresin, M., Toth, M., and Dunn, K. A. (2013). Direct-write 3D nanolithography at cryogenic temperatures. *Nanotechnology* 24:035301. doi: 10.1088/0957-4484/24/3/035301
- Bruinsma, G. M., Rustema-Abbing, M., Van Der Mei, H. C., and Busscher, H. J. (2001). Effects of cell surface damage on surface properties and adhesion of *Pseudomonas aeruginosa*. *J. Microbiol. Methods* 45, 95–101. doi: 10.1016/S0167-7012(01)00238-X
- Bulla, D. A. P., Li, W. T., Charles, C., Boswell, R., Ankiewicz, A., and Love, J. (2004). Deposition and characterization of silica-based films by helicon-activated reactive evaporation applied to optical waveguide fabrication. *Appl. Opt.* 43, 2978–2985. doi: 10.1364/AO.43.002978
- Buzea, C., and Pacheco, I. (2017). Nanomaterials and their classification. *Adv. Struct. Mater.* 62, 3–45. doi: 10.1007/978-81-322-3655-9_1
- Campoccia, D., Montanaro, L., and Arciola, C. R. (2013). A review of the biomaterials technologies for infection-resistant surfaces. *Biomaterials* 34, 8533–8554. doi: 10.1016/j.biomaterials.2013.07.089
- Cao, M., Zhao, W., Wang, L., Li, R., Gong, H., Zhang, Y., et al. (2018). Graphene oxide-assisted accumulation and layer-by-layer assembly of antibacterial peptide for sustained release applications. *ACS Appl. Mater. Interfaces* 10, 24937–24946. doi: 10.1021/acsami.8b07417
- Cao, S., Huang, W., Wu, L., Tian, M., and Song, Y. (2018). On the interfacial adhesion between TiO₂ nanotube array Layer and Ti Substrate. *Langmuir* 34, 13888–13896. doi: 10.1021/acs.langmuir.8b03408
- Cao, Y., Su, B., Chinnaraj, S., Jana, S., Bowen, L., Charlton, S., et al. (2018). Nanostructured titanium surfaces exhibit recalcitrance towards *Staphylococcus epidermidis* biofilm formation. *Sci. Rep.* 8:1071. doi: 10.1038/s41598-018-19484-x
- Cheang, P., and Khor, K. A. (1996). Addressing processing problems associated with plasma spraying of hydroxyapatite coatings. *Biomaterials* 17, 537–544. doi: 10.1016/0142-9612(96)82729-3
- Chen, B., You, Y., Ma, A., Song, Y., Jiao, J., Song, L., et al. (2020). Zn-Incorporated TiO₂ nanotube surface improves osteogenesis ability through influencing immunomodulatory function of macrophages. *Int. J. Nanomed.* 15, 2095–2118. doi: 10.2147/IJN.S244349
- Chen, J., Wang, F., Liu, Q., and Du, J. (2014). Antibacterial polymeric nanostructures for biomedical applications. *Chem. Commun.* 50, 14482–14493. doi: 10.1039/C4CC03001J
- Chen, Y., Gao, A., Bai, L., Wang, Y., Wang, X., Zhang, X., et al. (2017). Antibacterial, osteogenic, and angiogenic activities of SrTiO₃ nanotubes embedded with Ag₂O nanoparticles. *Mater. Sci. Eng. C* 75, 1049–1058. doi: 10.1016/j.msec.2017.03.014
- Cheng, Y. F., Zhang, J. Y., Wang, Y. B., Li, C. M., Lu, Z. S., Hu, X. F., et al. (2019). Deposition of catechol-functionalized chitosan and silver nanoparticles on biomedical titanium surfaces for antibacterial application. *Mater. Sci. Eng. C* 98, 649–656. doi: 10.1016/j.msec.2019.01.019
- Chi, B., Victorio, E. S., and Jin, T. (2007). Synthesis of TiO₂-based nanotube on Ti substrate by hydrothermal treatment. *J. Nanosci. Nanotechnol.* 7, 668–672. doi: 10.1166/jnn.2007.147
- Choi, D. S., Kim, C., Lim, J., Cho, S. H., Lee, G. Y., Lee, H. J., et al. (2018). Ultrastable graphene-encapsulated 3 nm nanoparticles by in situ chemical vapor deposition. *Adv. Mater.* 30:1805023. doi: 10.1002/adma.201805023
- Choi, H., Kim, J.-J., Mo, Y.-H., Reddy, B. M., and Park, S.-E. (2017). Novelty of dynamic process in the synthesis of biocompatible silica nanotubes by biomimetic glycidyldecylamide as a soft template. *Langmuir* 33, 10707–10714. doi: 10.1021/acs.langmuir.7b02881
- Chouirfa, H., Bouloussa, H., Migonney, V., and Falentin-Daudre, C. (2019). Review of titanium surface modification techniques and coatings for antibacterial applications. *Acta Biomater.* 83, 37–54. doi: 10.1016/j.actbio.2018.10.036
- Chetoui, T., Soumahoro, L., Kulyk, B., Bougharraf, H., Erguig, H., Ammous, K., et al. (2017). Comparative study on the structural, morphological, linear and nonlinear optical properties of CZTS thin films prepared by spin-coating and spray pyrolysis. *Mater. Today Proc.* 4, 5146–5153. doi: 10.1016/j.matpr.2017.05.020
- Cipriano, A. F., Miller, C., and Liu, H. (2014). Anodic growth and biomedical applications of TiO₂ nanotubes. *J. Biomed. Nanotechnol.* 10, 2977–3003. doi: 10.1166/jbn.2014.1927
- Cui, C., Cui, X., Li, X., Luo, K., Lu, J., Ren, X., et al. (2018). Plastic-deformation-driven SiC nanoparticle implantation in an Al surface by laser shock wave: mechanical properties, microstructure characteristics, and synergistic strengthening mechanisms. *Int. J. Plast.* 102, 83–100. doi: 10.1016/j.iijplas.2017.12.004

- David, N., and Nallaiyan, R. (2018). Biologically anchored chitosan/gelatin-SrHAP scaffold fabricated on Titanium against chronic osteomyelitis infection. *Int. J. Biol. Macromol.* 110, 206–214. doi: 10.1016/j.ijbiomac.2017.11.174
- De Falco, G., Ciardiello, R., Commiato, M., Del Gaudio, P., Minutolo, P., Porta, A., et al. (2018). TiO₂ nanoparticle coatings with advanced antibacterial and hydrophilic properties prepared by flame aerosol synthesis and thermophoretic deposition. *Surf. Coatings Technol.* 349, 830–837. doi: 10.1016/j.surfcoat.2018.06.083
- Delfini, A., Vricella, A., Morles, R. B., Pastore, R., Micheli, D., Gugliemetti, F., et al. (2017). CVD nano-coating of carbon composites for space materials atomic oxygen shielding. *Procedia Struct. Integr.* 3, 208–216. doi: 10.1016/j.prostr.2017.04.047
- Deng, K., Luo, Z., Tan, L., and Quan, Z. (2020). Self-assembly of anisotropic nanoparticles into functional superstructures. *Chem. Soc. Rev.* 49, 6002–6038. doi: 10.1039/d0cs00541j
- Deshmukh, S. P., Mullani, S. B., Koli, V. B., Patil, S. M., Kasabe, P. J., Dandge, P. B., et al. (2018). Ag Nanoparticles Connected to the Surface of TiO₂ Electrostatically for Antibacterial Photoinactivation Studies. *Photochem. Photobiol.* 94, 1249–1262. doi: 10.1111/php.12983
- Diu, T., Faruqi, N., Sjöström, T., Lamarre, B., Jenkinson, H. F., Su, B., et al. (2014). Cicada-inspired cell-instructive nanopatterned arrays. *Sci. Rep.* 4:7122. doi: 10.1038/srep07122
- Doraiswamy, A., Jin, C., Narayan, R. J., Mageswaran, P., Mente, P., Modi, R., et al. (2006). Two photon induced polymerization of organic-inorganic hybrid biomaterials for microstructured medical devices. *Acta Biomater.* 2, 267–275. doi: 10.1016/j.actbio.2006.01.004
- Dumitrache, F., Morjan, I. P., Dutu, E., Fleaca, C. T., Scarisoreanu, M., et al. (2019). Zn/F-doped tin oxide nanoparticles synthesized by laser pyrolysis: structural and optical properties. *Beilstein J. Nanotechnol.* 10, 9–21. doi: 10.3762/bjnano.10.2
- Dyakonov, G. S., Mironov, S., Semenova, I. P., Valiev, R. Z., and Semiatin, S. L. (2017). Microstructure evolution and strengthening mechanisms in commercial-purity titanium subjected to equal-channel angular pressing. *Mater. Sci. Eng. A* 701, 289–301. doi: 10.1016/j.msea.2017.06.079
- Dyakonov, G. S., Mironov, S., Semenova, I. P., Valiev, R. Z., and Semiatin, S. L. (2019). EBSD analysis of grain-refinement mechanisms operating during equal-channel angular pressing of commercial-purity titanium. *Acta Mater.* 173, 174–183. doi: 10.1016/j.actamat.2019.05.014
- Elbourne, A., Chapman, J., Gelmi, A., Cozzolino, D., Crawford, R. J., and Truong, V. K. (2019). Bacterial-nanostructure interactions: the role of cell elasticity and adhesion forces. *J. Colloid Interface Sci.* 546, 192–210. doi: 10.1016/j.jcis.2019.03.050
- Elmi, F., Valipour, E., and Ghasemi, S. (2019). Synthesis of anticorrosion nanohybrid films based on bioinspired dopamine, L-cys/CNT@PDA through self-assembly on 304 stainless steel in 3.5% NaCl. *Bioelectrochemistry* 126, 79–85. doi: 10.1016/j.bioelechem.2018.11.012
- Endrino, J. L., Nainparampil, J. J., and Krzanowski, E. (2002). Microstructure and vacuum tribology of TiC–Ag composite coatings deposited by magnetron sputtering-pulsed laser deposition.pdf. *Surf. Coatings Technol.* 157, 95–101.
- Eom, T., Woo, K., Cho, W., Heo, J. E., Jang, D., Shin, J. I., et al. (2017). Nanoarchitecturing of natural melanin nanospheres by layer-by-layer assembly: macroscale anti-inflammatory conductive coatings with optoelectronic tunability. *Biomacromolecules* 18, 1908–1917. doi: 10.1021/acs.biomac.7b00336
- Fan, A., Zhang, H., Ma, Y., Zhang, X., Zhang, J., and Tang, B. (2013). Bacteria adherence properties of nitrided layer on Ti6Al4V by the plasma nitriding technique. *J. Wuhan Univ. Technol. Mater. Sci. Ed.* 28, 1223–1226. doi: 10.1007/s11595-013-0849-4
- Fathi, M., Akbari, B., and Taheriazam, A. (2019). Antibiotics drug release controlling and osteoblast adhesion from Titania nanotubes arrays using silk fibroin coating. *Mater. Sci. Eng. C* 103:109743. doi: 10.1016/j.msec.2019.109743
- Fathy Fahim, N., Sekino, T., Farouk Morks, M., and Kusunose, T. (2009). Electrochemical growth of vertically-oriented high aspect ratio titania nanotubes by rapid anodization in fluoride-free media. *J. Nanosci. Nanotechnol.* 9, 1803–1818. doi: 10.1166/jnn.2009.440
- Fauchais, P., and Montavon, G. (2007). Plasma spraying: from plasma generation to coating structure. *Adv. Heat Transf.* 40, 205–344. doi: 10.1016/S0065-2717(07)40003-X
- Fernandes, E. G. R., Brazaca, L. C., Rodríguez-Mendez, M. L., de Saja, J. A., and Zucolotto, V. (2011). Immobilization of lutetium bisphthalocyanine in nanostructured biomimetic sensors using the LbL technique for phenol detection. *Biosens. Bioelectron.* 26, 4715–4719. doi: 10.1016/j.bios.2011.05.032
- Fernández-Arias, M., Boutinguiza, M., del Val, J., Riveiro, A., Rodríguez, D., Arias-González, F., et al. (2020). Fabrication and deposition of copper and copper oxide nanoparticles by laser ablation in open air. *Nanomaterials* 10:300. doi: 10.3390/nano10020300
- Foldbjerg, R., Jiang, X., Miclăuş, T., Chen, C., Autrup, H., and Beer, C. (2015). Silver nanoparticles - Wolves in sheep's clothing? *Toxicol. Res.* 4, 563–575. doi: 10.1039/c4tx00110a
- Friedli, V., and Utke, I. (2009). Optimized molecule supply from nozzle-based gas injection systems for focused electron- and ion-beam induced deposition and etching: simulation and experiment. *J. Phys. D Appl. Phys.* 42:125305. doi: 10.1088/0022-3727/42/12/125305
- Fu, X., Cai, J., Zhang, X., Li, W., Di, Ge, H., et al. (2018). Top-down fabrication of shape-controlled, monodisperse nanoparticles for biomedical applications. *Adv. Drug Deliv. Rev.* 132, 169–187. doi: 10.1016/j.addr.2018.07.006
- Ganjian, M., Modaresifar, K., Zhang, H., Hagedoorn, P. L., Fratila-Apachitei, L. E., and Zadpoor, A. A. (2019). Reactive ion etching for fabrication of biofunctional titanium nanostructures. *Sci. Rep.* 9:36857. doi: 10.1038/s41598-019-55093-y
- Gao, C., Cheng, H., Xu, N., Li, Y., Chen, Y., Wei, Y., et al. (2019). Poly(dopamine) and Ag nanoparticle-loaded TiO₂ nanotubes with optimized antibacterial and ROS-scavenging bioactivities. *Nanomedicine* 14, 803–818. doi: 10.2217/nnm-2018-0131
- Gao, Z. L., Zhang, K., and Yuen, M. M. F. (2011). Fabrication of carbon nanotube thermal interface material on aluminum alloy substrates with low pressure CVD. *Nanotechnology* 22:265611. doi: 10.1088/0957-4484/22/26/265611
- Garbacz, H., Wiciński, P., Adamczyk-Cieślak, B., Mizera, J., and Kurzydłowski, K. J. (2010). Studies of aluminium coatings deposited by vacuum evaporation and magnetron sputtering. *J. Microsc.* 237, 475–480. doi: 10.1111/j.1365-2818.2009.03297.x
- Geng, Z., Wang, R., Zhuo, X., Li, Z., Huang, Y.-C., Ma, L., et al. (2016). Incorporation of silver and strontium in hydroxyapatite coating on titanium surface for enhanced antibacterial and biological properties. *Mater. Sci. Eng. C* 71, 852–861. doi: 10.1016/j.msec.2016.10.079
- Ghalayani Esfahani, A., Soleimanzade, M., Campiglio, C. E., Federici, A., Altomare, L., Draghi, L., et al. (2019). Hierarchical microchannel architecture in chitosan/bioactive glass scaffolds via electrophoretic deposition positive-replica. *J. Biomed. Mater. Res. Part A* 107, 1455–1465. doi: 10.1002/jbm.a.36660
- Gleiter, H. (2000). Nanostructured materials: basic concepts and microstructure. *Acta Mater.* 48, 1–29. doi: 10.1016/S1359-6454(99)00285-2
- Gode, C., Attarilar, S., Eghbali, B., and Ebrahimi, M. (2015). Electrochemical behavior of equal channel angular pressed titanium for biomedical application. *AIP Conf. Proc.* 1653:020041. doi: 10.1063/1.4914232
- Gokcekaya, O., Webster, T., Ueda, K., Narushima, T., and Ergun, C. (2017). In vitro performance of Ag-incorporated hydroxyapatite and its adhesive porous coatings deposited by electrostatic spraying. *Mater. Sci. Eng. C* 77, 556–564. doi: 10.1016/j.msec.2017.03.233
- Gonçalves, M. C. (2018). Sol-gel silica nanoparticles in medicine: a natural choice. design, synthesis and products. *Molecules* 23:2021. doi: 10.3390/molecules23082021
- Gong, D., Grimes, C. A., Varghese, O. K., Hu, W., Singh, R. S., Chen, Z., et al. (2001). Titanium oxide nanotube arrays prepared by anodic oxidation. *J. Mater. Res.* 16, 3331–3334. doi: 10.1557/JMR.2001.0457
- Gong, Y., Tu, R., and Goto, T. (2013). High-speed deposition of titanium carbide coatings by laser-assisted metal-organic CVD. *Mater. Res. Bull.* 48, 2766–2770. doi: 10.1016/j.materresbull.2013.03.039
- Goudarzi, M., Saviz, S., Ghoranneviss, M., and Salar Elahi, A. (2018). Antibacterial characteristics of thermal plasma spray system. *J. Xray Sci. Technol.* 26, 509–521. doi: 10.3233/XST-17318
- Gour, A., and Jain, N. K. (2019). Advances in green synthesis of nanoparticles. *Artif. Cells Nanomed. Biotechnol.* 47, 844–851. doi: 10.1080/21691401.2019.1577878
- Grandi, S., Cassinelli, V., Bini, M., Saino, E., Mustarelli, P., Arciola, C. R., et al. (2011). Bone Reconstruction: Au Nanocomposite Bioglasses with Antibacterial Properties. *Int. J. Artif. Organs* 34, 920–928. doi: 10.5301/ijao.5000059

- Guan, M., Chen, Y., Wei, Y., Song, H., Gao, C., Cheng, H., et al. (2019). Long-lasting bactericidal activity through selective physical puncture and controlled ions release of polydopamine and silver nanoparticles-loaded TiO₂ nanorods *in vitro* and *in vivo*. *Int. J. Nanomed.* 14, 2903–2914. doi: 10.2147/IJN.S202625
- Gunpath, U. F., Le, H., Handy, R. D., and Tredwin, C. (2018). Anodised TiO₂ nanotubes as a scaffold for antibacterial silver nanoparticles on titanium implants. *Mater. Sci. Eng. C* 91, 638–644. doi: 10.1016/j.msec.2018.05.074
- Guo, Y., Chen, D., Cheng, M., Lu, W., Wang, L., and Zhang, X. (2013). The bone tissue compatibility of a new Ti35Nb2Ta3Zr alloy with a low Young's modulus. *Int. J. Mol. Med.* 31, 689–697. doi: 10.3892/ijmm.2013.1249
- Guo, Z., Chen, Y., Wang, Y., Jiang, H., and Wang, X. (2020). Advances and challenges in metallic nanomaterial synthesis and antibacterial applications. *J. Mater. Chem. B* 8, 4764–4777. doi: 10.1039/d0tb00099j
- Gupta, A., and Srivastava, R. (2019). Mini submersible pump assisted sonochemical reactors: large-scale synthesis of zinc oxide nanoparticles and nanoleaves for antibacterial and anti-counterfeiting applications. *Ultrason. Sonochem.* 52, 414–427. doi: 10.1016/j.ultrasonch.2018.12.020
- Gupta, M. C., Ungaro, C., Foley, J. J., and Gray, S. K. (2018). Optical nanostructures design, fabrication, and applications for solar/thermal energy conversion. *Sol. Energy* 165, 100–114. doi: 10.1016/j.solener.2018.01.010
- Gutés, A., Carraro, C., and Maboudian, R. (2012). Single-layer CVD-grown graphene decorated with metal nanoparticles as a promising biosensing platform. *Biosens. Bioelectron.* 33, 56–59. doi: 10.1016/j.bios.2011.12.018
- Hadidi, M., Bigham, A., Saebnoori, E., Hassanzadeh-Tabrizi, S. A., Rahmati, S., Alizadeh, Z. M., et al. (2017). Electrophoretic-deposited hydroxyapatite-copper nanocomposite as an antibacterial coating for biomedical applications. *Surf. Coatings Technol.* 321, 171–179. doi: 10.1016/j.surfcoat.2017.04.055
- Hafeez, N., Liu, J., Wang, L., Wei, D., Tang, Y., Lu, W., et al. (2020). Superelastic response of low-modulus porous beta-type Ti-35Nb-2Ta-3Zr alloy fabricated by laser powder bed fusion. *Addit. Manuf.* 34:101264. doi: 10.1016/j.addma.2020.101264
- Hafeez, N., Liu, S., Lu, E., Wang, L., Liu, R., Lu, W., et al. (2019). Mechanical behavior and phase transformation of β -type Ti-35Nb-2Ta-3Zr alloy fabricated by 3D-Printing. *J. Alloys Compd.* 790, 117–126. doi: 10.1016/j.jallcom.2019.03.138
- Hameed, P., Gopal, V., Bjorklund, S., Ganvir, A., Sen, D., Markocsan, N., et al. (2019). Axial Suspension Plasma Spraying: an ultimate technique to tailor Ti6Al4V surface with HAP for orthopaedic applications. *Colloids Surfaces B Biointerfaces* 173, 806–815. doi: 10.1016/j.colsurfb.2018.10.071
- Hanawa, T. (2018). *Transition of Surface Modification of Titanium for Medical and Dental Use*. Amsterdam: Elsevier Inc. doi: 10.1016/B978-0-12-812456-7.00005-6
- Hang, R., Liu, Y., Bai, L., Zhang, X., Huang, X., Jia, H., et al. (2018). Length-dependent corrosion behavior, Ni(2+) release, cytocompatibility, and antibacterial ability of Ni-Ti-O nanopores anodically grown on biomedical NiTi alloy. *Mater. Sci. Eng. C Mater. Biol. Appl.* 89, 1–7. doi: 10.1016/j.msec.2018.03.018
- Hang, R., Zhang, M., Ma, S., and Chu, P. (2012). Biological response of endothelial cells to diamond-like carbon-coated NiTi alloy. *J. Biomed. Mater. Res. A* 100, 496–506. doi: 10.1002/jbm.a.33295
- Haque, A. K. M. M., Kim, S., Kim, J., Noh, J., Huh, S., Choi, B., et al. (2018). Surface modification of graphene nanoparticles by acid treatment and grinding process. *J. Nanosci. Nanotechnol.* 18, 645–650. doi: 10.1166/jnn.2018.13928
- Harsha, N., Ranya, K. R., Babitha, K. B., Shukla, S., Biju, S., Reddy, M. L. P., et al. (2011). Hydrothermal processing of hydrogen titanate/anatase-titania nanotubes and their application as strong dye-adsorbents. *J. Nanosci. Nanotechnol.* 11, 1175–1187. doi: 10.1166/jnn.2011.3048
- Hasan, J., Crawford, R. J., and Ivanova, E. P. (2013). Antibacterial surfaces: the quest for a new generation of biomaterials. *Trends Biotechnol.* 31, 295–304. doi: 10.1016/j.tibtech.2013.01.017
- He, B., Yang, Y., Yuen, M. F., Chen, X. F., Lee, C. S., and Zhang, W. J. (2013). Vertical nanostructure arrays by plasma etching for applications in biology, energy, and electronics. *Nano Today* 8, 265–289. doi: 10.1016/j.nantod.2013.04.008
- He, L.-J., Hao, J.-C., Dai, L., Zeng, R.-C., and Li, S.-Q. (2020). Layer-by-layer assembly of gentamicin-based antibacterial multilayers on Ti alloy. *Mater. Lett.* 261:127001. doi: 10.1016/j.matlet.2019.127001
- He, X., Zhang, G., Wang, X., Hang, R., Huang, X., Qin, L., et al. (2017). Biocompatibility, corrosion resistance and antibacterial activity of TiO₂/CuO coating on titanium. *Ceram. Int.* 43, 16185–16195. doi: 10.1016/j.ceramint.2017.08.196
- Heidarpour, A., Aghamohammadi, H., and Ghasemi, S. (2020). Structural and morphological characterization of the layered carbide-derived-carbon nanostructures obtained by HF etching of Ti₂AlC. *Synth. Met.* 267:116478. doi: 10.1016/j.synthmet.2020.116478
- Henam, S. D., Ahmad, F., Shah, M. A., Parveen, S., and Wani, A. H. (2019). Microwave synthesis of nanoparticles and their antifungal activities. *Spectrochim. Acta Part A Mol. Biomol. Spectrosc.* 213, 337–341. doi: 10.1016/j.saa.2019.01.071
- Heo, K. C., and Gwag, J. S. (2014). Shape-modification of patterned nanoparticles by an ion beam treatment. *Sci. Rep.* 5:8523. doi: 10.1038/srep08523
- Hickok, N. J., and Shapiro, I. M. (2012). Immobilized antibiotics to prevent orthopaedic implant infections. *Adv. Drug Deliv. Rev.* 64, 1165–1176. doi: 10.1016/j.addr.2012.03.015
- Hidalgo-Robatto, B. M., López-Álvarez, M., Azevedo, A. S., Dorado, J., Serra, J., Azevedo, N. F., et al. (2018). Pulsed laser deposition of copper and zinc doped hydroxyapatite coatings for biomedical applications. *Surf. Coatings Technol.* 333, 168–177. doi: 10.1016/j.surfcoat.2017.11.006
- Hirt, L., Reiser, A., Spolenak, R., and Zambelli, T. (2017). Additive manufacturing of metal structures at the micrometer scale. *Adv. Mater.* 29:1604211. doi: 10.1002/adma.201604211
- Holleyman, R. J., Deehan, D. J., Walker, L., Charlett, A., Samuel, J., Shirley, M. D. F., et al. (2019). Staphylococcal resistance profiles in deep infection following primary hip and knee arthroplasty: a study using the NJR dataset. *Arch. Orthop. Trauma Surg.* 139, 1209–1215. doi: 10.1007/s00402-019-03155-1
- Horkavcová, D., Novák, P., Eerný, M., Jablonská, E., Lipov, J., et al. (2017). Titania sol-gel coatings containing silver on newly developed TiSi alloys and their antibacterial effect. *Mater. Sci. Eng. C* 76, 25–30. doi: 10.1016/j.msec.2017.02.137
- Hoyer, P. (1996). Formation of a titanium dioxide nanotube array. *Langmuir* 12, 1411–1413. doi: 10.1021/la9507803
- Huang, J., Cheng, Y., Wu, Y., Shi, X., Du, Y., and Deng, H. (2019). Chitosan/tannic acid bilayers layer-by-layer deposited cellulose nanofibrous mats for antibacterial application. *Int. J. Biol. Macromol.* 139, 191–198. doi: 10.1016/j.ijbiomac.2019.07.185
- Huang, Y., Dan, N., Dan, W., Zhao, W., Bai, Z., Chen, Y., et al. (2019). Facile fabrication of gelatin and polycaprolactone based bilayered membranes via spin coating method with antibacterial and cyto-compatible properties. *Int. J. Biol. Macromol.* 124, 699–707. doi: 10.1016/j.ijbiomac.2018.11.262
- Huang, Y., He, J., Gan, L., Liu, X., Wu, Y., Wu, F., et al. (2014). Osteoconductivity and osteoinductivity of porous hydroxyapatite coatings deposited by liquid precursor plasma spraying: *in vivo* biological response study. *Biomed. Mater.* 9:065007. doi: 10.1088/1748-6041/9/6/065007
- Huang, Y., Xu, Z., Zhang, X., Chang, X., Zhang, X., Li, Y., et al. (2017). Nanotube-formed Ti substrates coated with silicate/silver co-doped hydroxyapatite as prospective materials for bone implants. *J. Alloys Compd.* 697, 182–199. doi: 10.1016/j.jallcom.2016.12.139
- Hübsch, C., Dellinger, P., Maier, H. J., Stemme, F., Bruns, M., Stiesch, M., et al. (2015). Protection of yttria-stabilized zirconia for dental applications by oxidic PVD coating. *Acta Biomater.* 11, 488–493. doi: 10.1016/j.actbio.2014.09.042
- Huh, A. J., and Kwon, Y. J. (2011). “Nanoantibiotics”: a new paradigm for treating infectious diseases using nanomaterials in the antibiotics resistant era. *J. Control. Release* 156, 128–145. doi: 10.1016/j.jconrel.2011.07.002
- Huth, M., Porritt, F., and Dobrovolskiy, O. V. (2018). Focused electron beam induced deposition meets materials science. *Microelectron. Eng.* 185–186, 9–28. doi: 10.1016/j.mee.2017.10.012
- Irshad, M. A., Nawaz, R., Zia ur Rehman, M., Imran, M., Ahmad, J., Ahmad, S., et al. (2020). Synthesis and characterization of titanium dioxide nanoparticles by chemical and green methods and their antifungal activities against wheat rust. *Chemosphere* 258:127352. doi: 10.1016/j.chemosphere.2020.127352
- Ito, T., Kunimatsu, M., Kaneko, S., Hirabayashi, Y., Soga, M., Agawa, Y., et al. (2012). High performance of hydrogen peroxide detection using Pt nanoparticles-dispersed carbon electrode prepared by pulsed

- arc plasma deposition. *Talanta* 99, 865–870. doi: 10.1016/j.talanta.2012.07.048
- Ivanova, E. P., Hasan, J., Webb, H. K., Gervinskas, G., Juodkazis, S., Truong, V. K., et al. (2013). Bactericidal activity of black silicon. *Nat. Commun.* 4:2838. doi: 10.1038/ncomms3838
- Ivanova, E. P., Hasan, J., Webb, H. K., Truong, V. K., Watson, G. S., Watson, J. A., et al. (2012). Natural bactericidal surfaces: mechanical rupture of *Pseudomonas aeruginosa* cells by cicada wings. *Small* 8, 2489–2494. doi: 10.1002/smll.201200528
- Jaggessar, A., Mathew, A., Wang, H., Tesfamichael, T., Yan, C., and Yarlagaadda, P. K. D. V. (2018). Mechanical, bactericidal and osteogenic behaviours of hydrothermally synthesised TiO₂ nanowire arrays. *J. Mech. Behav. Biomed. Mater.* 80, 311–319. doi: 10.1016/j.jmbbm.2018.02.011
- Jaggessar, A., and Yarlagaadda, P. K. D. V. (2020). Modelling the growth of hydrothermally synthesised bactericidal nanostructures, as a function of processing conditions. *Mater. Sci. Eng. C* 108:110434. doi: 10.1016/j.msec.2019.110434
- Jang, J., Son, M., Chung, S., Kim, K., Cho, C., Lee, B. H., et al. (2015). Low-temperature-grown continuous graphene films from benzene by chemical vapor deposition at ambient pressure. *Sci. Rep.* 5:17955. doi: 10.1038/srep17955
- Jawed, S. F., Rabadia, C. D., Liu, Y. J., Wang, L. Q., Li, Y. H., Zhang, X. H., et al. (2019). Mechanical characterization and deformation behavior of β -stabilized Ti-Nb-Sn-Cr alloys. *J. Alloys Compd.* 792, 684–693. doi: 10.1016/j.jallcom.2019.04.079
- Jin, N., Yang, Y., Luo, X., and Xia, Z. (2013). Development of CVD Ti-containing films. *Prog. Mater. Sci.* 58, 1490–1533. doi: 10.1016/j.pmatsci.2013.07.001
- Jones, J. G., and Voevodin, A. A. (2004). Magnetron sputter pulsed laser deposition: technique and process control developments. *Surf. Coatings Technol.* 184, 1–5. doi: 10.1016/j.surfcoat.2003.10.016
- Jun, Y., Park, J. H., and Kang, M. G. (2012). The preparation of highly ordered TiO₂ nanotube arrays by an anodization method and their applications. *Chem. Commun.* 48, 6456–6471. doi: 10.1039/C2CC30733B
- Jung, J. H., Kobayashi, H., van Bommel, K. J. C., Shinkai, S., and Shimizu, T. (2002). Creation of novel helical ribbon and double-layered nanotube TiO₂ structures using an organogel template. *Chem. Mater.* 14, 1445–1447. doi: 10.1021/cm011625e
- Karbowiczek, J., Cordero-Arias, L., Virtanen, S., Misra, S. K., Valsami-Jones, E., Tuschscherr, L., et al. (2017). Electrophoretic deposition of organic/inorganic composite coatings containing ZnO nanoparticles exhibiting antibacterial properties. *Mater. Sci. Eng. C* 77, 780–789. doi: 10.1016/j.msec.2017.03.180
- Kaur, M., and Singh, K. (2019). Review on titanium and titanium based alloys as biomaterials for orthopaedic applications. *Mater. Sci. Eng. C* 102, 844–862. doi: 10.1016/j.msec.2019.04.064
- Kaviyasu, K., Maria Magdalane, C., Kanimozhi, K., Kennedy, J., Siddhardha, B., Subba Reddy, E., et al. (2017). Elucidation of photocatalysis, photoluminescence and antibacterial studies of ZnO thin films by spin coating method. *J. Photochem. Photobiol. B Biol.* 173, 466–475. doi: 10.1016/j.jphotobiol.2017.06.026
- Kelleher, S. M., Habimana, O., Lawler, J., O'reilly, B., Daniels, S., Casey, E., et al. (2016). Cicada wing surface topography: an investigation into the bactericidal properties of nanostructural features. *ACS Appl. Mater. Interfaces* 8, 14966–14974. doi: 10.1021/acsami.5b08309
- Khalandi, B., Asadi, N., Milani, M., Davaran, S., Abadi, A. J. N., Abasi, E., et al. (2017). A review on potential role of silver nanoparticles and possible mechanisms of their actions on bacteria. *Drug Res.* 67, 70–76. doi: 10.1055/s-0042-113383
- Khan, F. A. (2020). “Nanomaterials: types, classifications, and sources,” in *Applications of Nanomaterials in Human Health*, ed. F. Khan (Singapore: Springer), 1–13. doi: 10.1007/978-981-15-4802-4_1
- Kheiri, S., Liu, X., and Thompson, M. (2019). Nanoparticles at biointerfaces: antibacterial activity and nanotoxicology. *Colloids Surfaces B Biointerfaces* 184:110550. doi: 10.1016/j.colsurfb.2019.110550
- Khoshnood, N., Zamanian, A., and Massoudi, A. (2017). Mussel-inspired surface modification of titania nanotubes as a novel drug delivery system. *Mater. Sci. Eng. C* 77, 748–754. doi: 10.1016/j.msec.2017.03.293
- Khudhair, D., Bhatti, A., Li, Y., Hamedani, H. A., Garmestani, H., Hodgson, P., et al. (2016). Anodization parameters influencing the morphology and electrical properties of TiO₂ nanotubes for living cell interfacing and investigations. *Mater. Sci. Eng. C* 59, 1125–1142. doi: 10.1016/j.msec.2015.10.042
- Kim, H.-W., Koh, Y.-H., Li, L.-H., Lee, S., and Kim, H.-E. (2004). Hydroxyapatite coating on titanium substrate with titania buffer layer processed by sol-gel method. *Biomaterials* 25, 2533–2538. doi: 10.1016/j.biomaterials.2003.09.041
- Kim, S., Park, C., Cheon, K.-H., Jung, H.-D., Song, J., Kim, H.-E., et al. (2018). Antibacterial and bioactive properties of stabilized silver on titanium with a nanostructured surface for dental applications. *Appl. Surf. Sci.* 451, 232–240. doi: 10.1016/j.apsusc.2018.04.270
- Kim, S. B., Jo, J. H., Lee, S. M., Kim, H. E., Shin, K. H., and Koh, Y. H. (2013). Use of a poly(ether imide) coating to improve corrosion resistance and biocompatibility of magnesium (Mg) implant for orthopedic applications. *J. Biomed. Mater. Res. Part A* 101A, 1708–1715. doi: 10.1002/jbm.a.34474
- Klein, S., Nurjadi, D., Eigenbrod, T., and Bode, K. A. (2016). Evaluation of antibiotic resistance to orally administrable antibiotics in staphylococcal bone and joint infections in one of the largest university hospitals in Germany: Is there a role for fusidic acid? *Int. J. Antimicrob. Agents* 47, 155–157. doi: 10.1016/j.ijantimicag.2015.12.002
- Kose, N., and Ayse Kose, A. (2015). “Application of Nanomaterials in Prevention of Bone and Joint Infections,” in *Nanotechnology in Diagnosis, Treatment and Prophylaxis of Infectious Diseases*, eds M. Rai and K. Kon (Cambridge, MA: Academic Press), 107–117. doi: 10.1016/B978-0-12-801317-5.00007-4
- Kranthi Kiran, A. S., Kizhakeyil, A., Ramalingam, R., Verma, N. K., Lakshminarayanan, R., Kumar, T. S. S., et al. (2019). Drug loaded electrospun polymer/ceramic composite nanofibrous coatings on titanium for implant related infections. *Ceram. Int.* 45, 18710–18720. doi: 10.1016/j.ceramint.2019.06.097
- Krysin, O. V., Prokopenko, N. A., Ivanov, Y. F., Tolkachev, O. S., Shugurov, V. V., and Petrikova, E. A. (2020). Multi-layered gradient (Zr,Nb)N coatings deposited by the vacuum-arc method. *Surf. Coatings Technol.* 393, 125759. doi: 10.1016/j.surfcoat.2020.125759
- Kumar, A., and Misra, R. D. K. (2018). *3D-Printed Titanium Alloys for Orthopedic Applications*. (Amsterdam: Elsevier Inc). doi: 10.1016/B978-0-12-812456-7.00012-3
- Kumar, S., Kumar, P., and Shan, H. S. (2009). Characterization of the refractory coating material used in vacuum assisted evaporative pattern casting process. *J. Mater. Process. Technol.* 209, 2699–2706. doi: 10.1016/j.jmatprotec.2008.06.010
- Kusano, Y., Christou, C., Barber, Z. H., Evetts, J. E., and Hutchings, I. M. (1999). Deposition of carbon nitride films by ionized magnetron sputtering. *Thin Solid Films* 355, 117–121. doi: 10.1016/S0040-6090(99)00510-6
- Lai, Y., Dong, L., Zhou, H., Yan, B., Chen, Y., Cai, Y., et al. (2020). Coexposed nanoparticulate Ag alleviates the acute toxicity induced by ionic Ag⁺ in vivo. *Sci. Total Environ.* 723:138050. doi: 10.1016/j.scitotenv.2020.138050
- Laurent, S., Bridot, J. L., Elst, L., Vander, and Muller, R. N. (2010). Magnetic iron oxide nanoparticles for biomedical applications. *Future Med. Chem.* 2, 427–449. doi: 10.4155/fmc.09.164
- Le Ouay, B., and Stellacci, F. (2015). Antibacterial activity of silver nanoparticles: a surface science insight. *Nano Today* 10, 339–354. doi: 10.1016/j.nantod.2015.04.002
- Lee, J.-H., Leu, I.-C., Hsu, M.-C., Chung, Y.-W., and Hon, M.-H. (2005). Fabrication of Aligned TiO₂ one-dimensional nanostructured arrays using a one-step templating solution approach. *J. Phys. Chem. B* 109, 13056–13059. doi: 10.1021/jp052203l
- Lee, T., Mathew, E., Rajaraman, S., Manivasagam, G., Singh, A. K., and Lee, C. S. (2015). Tribological and corrosion behaviors of warm- and hot-rolled Ti-13Nb-13zr alloys in simulated body fluid conditions. *Int. J. Nanomed.* 10, 207–212. doi: 10.2147/IJN.S79996
- Lei, T., Zhang, W., Qian, H., Lim, P. N., Thian, E. S., Lei, P., et al. (2020). Silicon-incorporated nanohydroxyapatite-reinforced poly(ϵ -caprolactone) film to enhance osteogenesis for bone tissue engineering applications. *Colloids Surfaces B Biointerfaces* 187:110714. doi: 10.1016/j.colsurfb.2019.110714
- Lelis, M., Tuckute, S., Varnagiris, S., Urbonavicius, M., Laukaitis, G., and Bockute, K. (2019). Tailoring of TiO₂ film microstructure by pulsed-DC and RF magnetron co-sputtering. *Surf. Coatings Technol.* 377:124906. doi: 10.1016/j.surfcoat.2019.124906

- Li, B., and Webster, T. J. (2018). Bacteria antibiotic resistance: new clant-associated orthopedic infehalenges and opportunities for impctions. *J. Orthop. Res.* 36, 22–32. doi: 10.1002/jor.23656
- Li, D., Cheng, Y., Jiang, G., Yi, Y., Shi, X., et al. (2019). Egg source natural proteins LBL modified cellulose nanofibrous mats and their cellular compatibility. *Carbohydr. Polym.* 213, 329–337. doi: 10.1016/j.carbpol.2019.02.096
- Li, D., Lv, P., Fan, L., Huang, Y., Yang, F., Mei, X., et al. (2017a). The immobilization of antibiotic-loaded polymeric coatings on osteoarticular Ti implants for the prevention of bone infections. *Biomater. Sci.* 5, 2337–2346. doi: 10.1039/c7bm00693d
- Li, H., Feng, X., Peng, Y., and Zeng, R. (2020). Durable lubricant-infused coating on a magnesium alloy substrate with anti-biofouling and anti-corrosion properties and excellent thermally assisted healing ability. *Nanoscale* 12, 7700–7711. doi: 10.1039/c9nr10699e
- Li, H. F., Nie, F. L., Zheng, Y. F., Cheng, Y., Wei, S. C., and Valiev, R. Z. (2019). Nanocrystalline Ti49.2Ni50.8 shape memory alloy as orthopaedic implant material with better performance. *J. Mater. Sci. Technol.* 35, 2156–2162. doi: 10.1016/j.jmst.2019.04.026
- Li, J., Li, Q., Ma, X., Tian, B., Li, T., Yu, J., et al. (2016). Biosynthesis of gold nanoparticles by the extreme bacterium *Deinococcus radiodurans* and an evaluation of their antibacterial properties. *Int. J. Nanomed.* 11, 5931–5944. doi: 10.2147/IJN.S119618
- Li, J., Tan, L., Liu, X., Cui, Z., Yang, X., Yeung, K. W. K., et al. (2017b). Balancing Bacteria-Osteoblast Competition through Selective Physical Puncture and Biofunctionalization of ZnO/Polydopamine/Arginine-Glycine-Aspartic Acid-Cysteine Nanorods. *ACS Nano* 11, 11250–11263. doi: 10.1021/acsnano.7b05620
- Li, J., Wang, Y., Yao, Y., Wang, Y., and Wang, L. (2017c). Structure and tribological properties of TiSiCN coating on Ti6Al4V by arc ion plating. *Thin Solid Films* 644, 115–119. doi: 10.1016/j.tsf.2017.09.053
- Li, W. W., Wang, H. Y., and Zhang, Y. Q. (2017d). A novel chitosan hydrogel membrane by an improved electrophoretic deposition and its characteristics *in vitro* and *in vivo*. *Mater. Sci. Eng. C* 74, 287–297. doi: 10.1016/j.msec.2016.12.005
- Li, Y., Zimmerman, A. R., He, F., Chen, J., Han, L., Chen, H., et al. (2020). Solvent-free synthesis of magnetic biochar and activated carbon through ball-mill extrusion with Fe3O4 nanoparticles for enhancing adsorption of methylene blue. *Sci. Total Environ.* 722:137972. doi: 10.1016/j.scitotenv.2020.137972
- Liang, R., Xu, Y., Zhao, M., Han, G., Li, J., Wu, W., et al. (2020). Properties of silver contained coatings on CoCr alloys prepared by vacuum plasma spraying. *Mater. Sci. Eng. C* 106:110156. doi: 10.1016/j.msec.2019.110156
- Liang, S. X., Feng, X. J., Yin, L. X., Liu, X. Y., Ma, M. Z., and Liu, R. P. (2016). Development of a new β Ti alloy with low modulus and favorable plasticity for implant material. *Mater. Sci. Eng. C* 61, 338–343. doi: 10.1016/j.msec.2015.12.076
- Liao, C., Wuethrich, A., and Trau, M. (2020). A material odyssey for 3D nano/microstructures: two photon polymerization based nanolithography in bioapplications. *Appl. Mater. Today* 19:100635. doi: 10.1016/j.apmt.2020.100635
- Limoli, D. H., Jones, C. J., and Wozniak, D. J. (2015). Bacterial extracellular polysaccharides in biofilm formation and function. *Microb. Biofilms* 223–247. doi: 10.1128/9781555817466.ch11
- Lin, J., Chen, H., Fei, T., and Zhang, J. (2013). Highly transparent superhydrophobic organic-inorganic nanocoating from the aggregation of silica nanoparticles. *Colloids Surfaces A Physicochem. Eng. Asp.* 421, 51–62. doi: 10.1016/j.colsurfa.2012.12.049
- Linklater, D. P., De Volder, M., Baulin, V. A., Werner, M., Jessl, S., Golozar, M., et al. (2018). High aspect ratio nanostructures kill bacteria via storage and release of mechanical energy. *ACS Nano* 12, 6657–6667. doi: 10.1021/acsnano.8b01665
- Linklater, D. P., Juodkazis, S., Crawford, R. J., and Ivanova, E. P. (2019). Mechanical inactivation of *Staphylococcus aureus* and *Pseudomonas aeruginosa* by titanium substrata with hierarchical surface structures. *Materialia* 5:100197. doi: 10.1016/j.mtl.2018.100197
- Linklater, D. P., Juodkazis, S., Rubanov, S., and Ivanova, E. P. (2017). Comment on “bactericidal Effects of Natural Nanotopography of Dragonfly Wing on *Escherichia coli*.”. *ACS Appl. Mater. Interfaces* 9, 29387–29393. doi: 10.1021/acsaami.7b05707
- Liu, D., He, C., Liu, Z., and Xu, W. (2017). Gentamicin coating of nanotubular anodized titanium implant reduces implant-related osteomyelitis and enhances bone biocompatibility in rabbits. *Int. J. Nanomed.* 12, 5461–5471. doi: 10.2147/IJN.S137137
- Liu, J., and Hurt, R. H. (2010). Ion release kinetics and particle persistence in aqueous nano-silver colloids. *Environ. Sci. Technol.* 44, 2169–2175. doi: 10.1021/es9035557
- Liu, N., Chen, X., Zhang, J., and Schwank, J. W. (2014). A review on TiO₂-based nanotubes synthesized via hydrothermal method: formation mechanism, structure modification, and photocatalytic applications. *Catal. Today* 225, 34–51. doi: 10.1016/j.cattod.2013.10.090
- Liu, R., Ma, Z., Kolawole, S., Zeng, L., Zhao, Y., Ren, L., et al. (2019). *In vitro* study on cytocompatibility and osteogenesis ability of Ti–Cu alloy. *J. Mater. Sci. Mater. Med.* 30:75. doi: 10.1007/s10856-019-6277-z
- Liu, W., Cheng, M., Wahafu, T., Zhao, Y., Qin, H., Wang, J., et al. (2015a). The *in vitro* and *in vivo* performance of a strontium-containing coating on the low-modulus Ti35Nb2Ta3Zr alloy formed by micro-arc oxidation. *J. Mater. Sci. Mater. Med.* 26:203. doi: 10.1007/s10856-015-5533-0
- Liu, W., Su, P., Gonzales, A., Chen, S., Wang, N., Wang, J., et al. (2015b). Optimizing stem cell functions and antibacterial properties of TiO₂ nanotubes incorporated with ZnO nanoparticles: experiments and modeling. *Int. J. Nanomed.* 10, 1997–2019. doi: 10.2147/IJN.S74418
- Liu, X., and Man, H. C. (2017). Laser fabrication of Ag-HA nanocomposites on Ti6Al4V implant for enhancing bioactivity and antibacterial capability. *Mater. Sci. Eng. C* 70, 1–8. doi: 10.1016/j.msec.2016.08.059
- Liu, Y., Hang, R., Zhao, Y., Bai, L., Sun, Y., Yao, X., et al. (2018). The effects of annealing temperature on corrosion behavior, Ni²⁺ release, cytocompatibility, and antibacterial ability of Ni-Ti-O nanopores on NiTi alloy. *Surf. Coatings Technol.* 352, 175–181. doi: 10.1016/j.surfcoat.2018.08.016
- Lü, X., Bao, X., Huang, Y., Qu, Y., Lu, H., and Lu, Z. (2009). Mechanisms of cytotoxicity of nickel ions based on gene expression profiles. *Biomaterials* 30, 141–148. doi: 10.1016/j.biomaterials.2008.09.011
- Luo, X., Yao, S., Zhang, H., Cai, M., Liu, W., Pan, R., et al. (2020). Biocompatible nano-ripples structured surfaces induced by femtosecond laser to rebel bacterial colonization and biofilm formation. *Opt. Laser Technol.* 124:105973. doi: 10.1016/j.optlastec.2019.105973
- Luo, Z. M., Wang, J. W., Tan, J. B., Zhang, Z. M., and Lu, T. B. (2018). Self-Template Synthesis of Co-Se-S-O Hierarchical Nanotubes as Efficient Electrocatalysts for Oxygen Evolution under Alkaline and Neutral Conditions. *ACS Appl. Mater. Interfaces* 10, 8231–8237. doi: 10.1021/acsaami.8b00986
- Lv, P., Zhu, L., Yu, Y., Wang, W., Liu, G., and Lu, H. (2020). Effect of NaOH concentration on antibacterial activities of Cu nanoparticles and the antibacterial mechanism. *Mater. Sci. Eng. C* 110:110669. doi: 10.1016/j.msec.2020.110669
- Lv, Y., Lu, X., Wu, Y., Yu, Y., Fu, S., Yang, L., et al. (2019). Microstructure, bio-corrosion and biological property of Ag-incorporated TiO₂ coatings: influence of Ag₂O contents. *Ceram. Int.* 45, 22357–22367. doi: 10.1016/j.ceramint.2019.07.265
- Ma, B. (2007). *Porous Structured Titania by Chemical Methods*. Ph.D. thesis, Nanyang Technological University, Singapore. doi: 10.32657/10356/5088
- Macak, J. M., Tsuchiya, H., Taveira, L., Ghicov, A., and Schmuki, P. (2005). Self-organized nanotubular oxide layers on Ti-6Al-7Nb and Ti-6Al-4V formed by anodization in NH₄F solutions. *J. Biomed. Mater. Res. Part A* 75, 928–933. doi: 10.1002/jbm.a.30501
- Mageswari, A., Srinivasan, R., Subramanian, P., Ramesh, N., and Gothandam, K. M. (2016). Nanomaterials: classification, biological synthesis and characterization. *Nanosci. Food Agric.* 3, 31–71. doi: 10.1007/978-3-319-48009-1_2
- Mahade, S., Narayan, K., Govindarajan, S., Björklund, S., Curry, N., and Joshi, S. (2019). Exploiting suspension plasma spraying to deposit wear-resistant carbide coatings. *Materials* 12:2344. doi: 10.3390/ma12152344
- Mahlooji, E., Atapour, M., and Labbaf, S. (2019). Electrophoretic deposition of Bioactive glass – Chitosan nanocomposite coatings on Ti-6Al-4V for orthopedic applications. *Carbohydr. Polym.* 226:115299. doi: 10.1016/j.carbpol.2019.115299
- Maimaiti, B., Zhang, N., Yan, L., Luo, J., Xie, C., Wang, Y., et al. (2020). Stable ZnO-doped hydroxyapatite nanocoating for anti-infection and osteogenic on

- titanium. *Colloids Surfaces B Biointerfaces* 186:110731. doi: 10.1016/j.colsurfb.2019.110731
- Makowska, M., Pawlak, W., Konarski, P., Wendler, B., and Szymanowski, H. (2019). Modification of magnetron sputter deposition of nc-WC/a-C(H) coatings with an additional RF discharge. *Diam. Relat. Mater.* 98:107509. doi: 10.1016/j.diamond.2019.107509
- Malhotra, R., Han, Y. M., Morin, J. L. P., Luong-Van, E. K., Chew, R. J. J., Castro Neto, A. H., et al. (2020). Inhibiting corrosion of biomedical-grade Ti-6Al-4V alloys with graphene nanocoating. *J. Dent. Res.* 99, 285–292. doi: 10.1177/0022034519897003
- Manawi, Y. M., Samara, A., Al-Ansari, T., and Atieh, M. A. (2018). A Review of Carbon Nanomaterials' Synthesis via the Chemical Vapor Deposition (CVD) Method. *Materials* 11:822. doi: 10.3390/ma11050822
- Maramba-Jones, C., and Hoek, E. M. V. (2010). A review of the antibacterial effects of silver nanomaterials and potential implications for human health and the environment. *J. Nanoparticle Res.* 12, 1531–1551. doi: 10.1007/s11051-010-9900-y
- Masuda, H., and Fukuda, K. (1995). Ordered metal nanohole arrays made by a two-step replication of honeycomb structures of anodic alumina. *Science* 268, 1466–1468. doi: 10.1126/science.268.5216.1466
- Maury, F., and Senocq, F. (2003). Iridium coatings grown by metal-organic chemical vapor deposition hot-wall CVD reactor. *Surf. Coatings Technol.* 163–164, 208–213. doi: 10.1016/S0257-8972(02)00485-1
- Mazare, A., Anghel, A., Carmen, S.-B., Totea, G., and Ionita, D. (2018). Silver doped diamond-like carbon antibacterial and corrosion resistance coatings on titanium. *Thin Solid Films* 657, 16–23. doi: 10.1016/j.tsf.2018.04.036
- Meng, L. Y., Wang, B., Ma, M. G., and Lin, K. L. (2016). The progress of microwave-assisted hydrothermal method in the synthesis of functional nanomaterials. *Mater. Today Chem.* 1, 63–83. doi: 10.1016/j.mtchem.2016.11.003
- Mi, B., Xiong, W., Xu, N., Guan, H., Fang, Z., Liao, H., et al. (2017). Strontium-loaded titania nanotube arrays repress osteoclast differentiation through multiple signalling pathways: *in vitro* and *in vivo* studies. *Sci. Rep.* 7:2328. doi: 10.1038/s41598-017-02491-9
- Mi, G., Shi, D., Wang, M., and Webster, T. J. (2018). Reducing bacterial infections and biofilm formation using nanoparticles and nanostructured antibacterial surfaces. *Adv. Healthc. Mater.* 7, 1–23. doi: 10.1002/adhm.201800103
- Miao, H., Hu, X., Fan, J., Li, C., Sun, Q., Hao, Y., et al. (2015). Hydrothermal synthesis of TiO₂ 2 nanostructure films and their photoelectrochemical properties. *Appl. Surf. Sci.* 358, 418–424. doi: 10.1016/j.apsusc.2015.08.212
- Minagar, S., Berndt, C. C., Gengenbach, T., and Wen, C. (2014). Fabrication and characterization of TiO₂-ZrO₂-ZrTiO₄ nanotubes on TiZr alloy manufactured via anodization. *J. Mater. Chem. B* 2, 71–83. doi: 10.1039/c3tb21204a
- Modaresifar, K., Azizian, S., Ganjian, M., Fratila-Apachitei, L. E., and Zadpoor, A. A. (2019). Bactericidal effects of nanopatterns: a systematic review. *Acta Biomater.* 83, 29–36. doi: 10.1016/j.actbio.2018.09.059
- Mohan, L., Dennis, C., Padmapriya, N., Anandan, C., and Rajendran, N. (2020). Effect of electrolyte temperature and anodization time on formation of TiO₂ nanotubes for biomedical applications. *Mater. Today Commun.* 23:101103. doi: 10.1016/j.mtcomm.2020.101103
- Mohan Raj, R., Priya, P., and Raj, V. (2018). Gentamicin-loaded ceramic-biopolymer dual layer coatings on the Ti with improved bioactive and corrosion resistance properties for orthopedic applications. *J. Mech. Behav. Biomed. Mater.* 82, 299–309. doi: 10.1016/j.jmbbm.2017.12.033
- Molleman, B., and Hiemstra, T. (2015). Surface structure of silver nanoparticles as a model for understanding the oxidative dissolution of silver ions. *Langmuir* 31, 13361–13372. doi: 10.1021/acs.langmuir.5b03686
- Montanaro, L., Speciale, P., Campoccia, D., Ravaoli, S., Pietrocola, G., et al. (2011). Scenery of Staphylococcus implant infections in orthopedics. *Future Microbiol.* 6, 1329–1349. doi: 10.2217/fmb.11.117
- Moreira, A. J., Campos, L. O., Maldi, C. P., Dias, J. A., Paris, E. C., Giralaldi, T. R., et al. (2020). Photocatalytic degradation of Prozac® mediated by TiO₂ nanoparticles obtained via three synthesis methods: sonochemical, microwave hydrothermal, and polymeric precursor. *Environ. Sci. Pollut. Res.* 27, 27032–27047. doi: 10.1007/s11356-020-08798-x
- Morones-Ramirez, J., Elechiguerra, J., Camacho, A., Holt, K., Kouri, J., Tapia, J., et al. (2005). The bactericidal effect of silver nanoparticles. *Nanotechnology* 16, 2346–2353. doi: 10.1088/0957-4484/16/10/059
- Morris, J. E. (2018). “Nanoparticle properties,” in *Nanopackaging*, 2nd Edn, ed. J. E. Morris (Cham: Springer), 201–217. doi: 10.1007/978-3-319-90362-0_6
- Mostaghimi, J., and Chandra, S. (2007). Heat transfer in plasma spray coating processes. *Adv. Heat Transf.* 40, 143–204. doi: 10.1016/S0065-2717(07)40002-8
- Mou, P., Peng, H., Zhou, L., Li, L., Li, H., and Huang, Q. (2019). A novel composite scaffold of Cu-doped nano calcium-deficient hydroxyapatite/multi-(amino acid) copolymer for bone tissue regeneration. *Int. J. Nanomed.* 14, 3331–3343. doi: 10.2147/IJN.S195316
- Multone, X., Luo, Y., and Hoffmann, P. (2008). Er-doped Al₂O₃ thin films deposited by high-vacuum chemical vapor deposition (HV-CVD). *Mater. Sci. Eng. B Solid State Mater. Adv. Technol.* 146, 35–40. doi: 10.1016/j.mseb.2007.07.086
- Nakahira, A., Kubo, T., and Numako, C. (2010). Formation mechanism of TiO₂-derived titanate nanotubes prepared by the hydrothermal process. *Inorg. Chem.* 49, 5845–5852. doi: 10.1021/ic9025816
- Newland, B., Taplan, C., Pette, D., Friedrichs, J., Steinhart, M., Wang, W., et al. (2018). Soft and flexible poly(ethylene glycol) nanotubes for local drug delivery. *Nanoscale* 10, 8413–8421. doi: 10.1039/C8NR00603B
- Nguyen, A. N., Solard, J., Nong, H. T. T., Osman, C., Ben, Gomez, A., et al. (2020). Spin coating and micro-patterning optimization of composite thin films based on PVDF. *Materials* 13:1342. doi: 10.3390/ma13061342
- Nguyen-Tri, P., Tran, H. N., Plamondon, C. O., Tuduri, L., Vo, D. V. N., Nanda, S., et al. (2019). Recent progress in the preparation, properties and applications of superhydrophobic nano-based coatings and surfaces: a review. *Prog. Org. Coatings* 132, 235–256. doi: 10.1016/j.porgcoat.2019.03.042
- Ni, J., Frandsen, C. J., Noh, K., Johnston, G. W., He, G., Tang, T., et al. (2013). Fabrication of thin film TiO₂ nanotube arrays on Co-28Cr-6Mo alloy by anodization. *Mater. Sci. Eng. C* 33, 1460–1466. doi: 10.1016/j.msec.2012.12.068
- Ning, C., Jiajia, J., Meng, L., Hongfei, Q., Xianglong, W., and Tingli, L. (2019). Electrophoretic deposition of GHK-Cu loaded MSN-chitosan coatings with pH-responsive release of copper and its bioactivity. *Mater. Sci. Eng. C* 104:109746. doi: 10.1016/j.msec.2019.109746
- Nowlin, K., Boseman, A., Covell, A., and Lajeunesse, D. (2014). Adhesion-dependent rupturing of Saccharomyces cerevisiae on biological antimicrobial nanostructured surfaces. *J. R. Soc. Interface* 12:20140999. doi: 10.1098/rsif.2014.0999
- Ogunyemi, S. O., Abdallah, Y., Zhang, M., Fouad, H., Hong, X., Ibrahim, E., et al. (2019). Green synthesis of zinc oxide nanoparticles using different plant extracts and their antibacterial activity against *Xanthomonas oryzae* pv. *oryzae*. *Artif. Cells Nanomed. Biotechnol.* 47, 341–352. doi: 10.1080/21691401.2018.1557671
- Ohtsu, N., Suginishi, S., and Hirano, M. (2017). Antibacterial effect of nickel-titanium alloy owing to nickel ion release. *Appl. Surf. Sci.* 405, 215–219. doi: 10.1016/j.apsusc.2017.02.037
- Ovsianikov, A., and Chichkov, B. N. (2012). Three-dimensional microfabrication by two-photon polymerization technique. *Methods Mol. Biol.* 868, 311–325. doi: 10.1007/978-1-61779-764-4_19
- Oytun, F., and Basarir, F. (2019). Spin-assisted layer-by-layer assembled oppositely charged reduced graphene oxide films. *Mater. Lett.* 257:126756. doi: 10.1016/j.matlet.2019.126756
- Pagedar, A., Singh, J., and Batish, V. K. (2010). Surface hydrophobicity, nutritional contents affect Staphylococcus aureus biofilms and temperature influences its survival in preformed biofilms. *J. Basic Microbiol.* 50, S98–S106. doi: 10.1002/jobm.201000034
- Pandey, J. K., Swarnkar, R. K., Soumya, K. K., Dwivedi, P., Singh, M. K., Sundaram, S., et al. (2014). Silver nanoparticles synthesized by pulsed laser ablation: as a potent antibacterial agent for human enteropathogenic gram-positive and gram-negative bacterial strains. *Appl. Biochem. Biotechnol.* 174, 1021–1031. doi: 10.1007/s12010-014-0934-y
- Paneerselvam, E., Vasa, N. J., Nakamura, D., Palani, I. A., Higashihata, M., Ramachandra Rao, M. S., et al. (2020). Pulsed laser deposition of SiC thin films and influence of laser-assisted annealing. *Mater. Today Proc.* doi: 10.1016/j.matpr.2020.01.535
- Pang, S., He, Y., Zhong, R., Guo, Z., He, P., Zhou, C., et al. (2019). Multifunctional ZnO/TiO₂ 2 nanoarray composite coating with antibacterial activity, cytocompatibility and piezoelectricity. *Ceram. Int.* 45, 12663–12671. doi: 10.1016/j.ceramint.2019.03.076

- Pareek, V., Gupta, R., and Panwar, J. (2018). Do physico-chemical properties of silver nanoparticles decide their interaction with biological media and bactericidal action? A review. *Mater. Sci. Eng. C* 90, 739–749. doi: 10.1016/j.msec.2018.04.093
- Park, H.-J., Kim, J. Y., Kim, J., Lee, J.-H., Hahn, J.-S., Gu, M. B., et al. (2009). Silver-ion-mediated reactive oxygen species generation affecting bactericidal activity. *Water Res.* 43, 1027–1032. doi: 10.1016/j.watres.2008.12.002
- Patil, D., Wasson, M. K., Aravindan, S., Vivekanandan, P., and Rao, P. V. (2019). Antibacterial and cytocompatibility study of modified Ti6Al4V surfaces through thermal annealing. *Mater. Sci. Eng. C* 99, 1007–1020. doi: 10.1016/j.msec.2019.02.058
- Perentes, A., Bachmann, A., Leutenegger, M., and Sandu, C. (2004). Focused electron beam induced deposition of a periodic transparent nano-optic pattern. *Microelectron. Eng.* 73–74, 412–416. doi: 10.1016/j.mee.2004.02.079
- Persat, A. (2017). Bacterial mechanotransduction. *Curr. Opin. Microbiol.* 36, 1–6. doi: 10.1016/j.mib.2016.12.002
- Pfäng, B. G., García-Cañete, J., García-Lasheras, J., Blanco, A., Auñón, Á., Parron-Cambero, R., et al. (2019). Orthopedic implant-associated infection by multidrug resistant *Enterobacteriaceae*. *J. Clin. Med.* 8:220. doi: 10.3390/jcm8020220
- Pinna, E., Le Gall, S., Torralba, E., Mula, G., Cachet-Vivier, C., and Bastide, S. (2020). Mesopore formation and silicon surface nanostructuring by metal-assisted chemical etching with silver nanoparticles. *Front. Chem.* 8:658. doi: 10.3389/fchem.2020.00658
- Pishbin, F., Mourinho, V., Gilchrist, J. B., McComb, D. W., Kreppel, S., Salih, V., et al. (2013). Single-step electrochemical deposition of antimicrobial orthopaedic coatings based on a bioactive glass/chitosan/nano-silver composite system. *Acta Biomater.* 9, 7469–7479. doi: 10.1016/j.actbio.2013.03.006
- Pišlová, M., Kolářová, K., Vokatá, B., Brož, A., Ulbrich, P., Bačáková, L., et al. (2020). A new way to prepare gold nanoparticles by sputtering – Sterilization, stability and other properties. *Mater. Sci. Eng. C* 115:111087. doi: 10.1016/j.msec.2020.111087
- Pruchova, E., Kosova, M., Fojt, J., Jarolimova, P., Jablonska, E., Hybasek, V., et al. (2019). A two-phase gradual silver release mechanism from a nanostructured TiAlV surface as a possible antibacterial modification in implants. *Bioelectrochemistry* 127, 26–34. doi: 10.1016/j.bioelechem.2019.01.003
- Qian, H., Lei, T., Lei, P. E., and Hu, Y. (2020). Additively manufactured Tantalum implants for repairing bone defects: a systematic review. *Tissue Eng. Part B Rev.* doi: 10.1089/ten.teb.2020.0134 [Epub ahead of print].
- Quinteros, M. A., Cano Aristizábal, V., Dalmasso, P. R., Paraje, M. G., and Pérez, P. L. (2016). Oxidative stress generation of silver nanoparticles in three bacterial genera and its relationship with the antimicrobial activity. *Toxicol. In Vitro* 36, 216–223. doi: 10.1016/j.tiv.2016.08.007
- Rabadia, C. D., Liu, Y. J., Chen, L. Y., Jawed, S. F., Wang, L. Q., Sun, H., et al. (2019a). Deformation and strength characteristics of Laves phases in titanium alloys. *Mater. Des.* 179:107891. doi: 10.1016/j.matdes.2019.107891
- Rabadia, C. D., Liu, Y. J., Zhao, C. H., Wang, J. C., Jawed, S. F., Wang, L. Q., et al. (2019b). Improved trade-off between strength and plasticity in titanium based metastable beta type Ti-Zr-Fe-Sn alloys. *Mater. Sci. Eng. A* 766:138340. doi: 10.1016/j.msea.2019.138340
- Rafeerad, A. R., Bushroa, A. R., Nasiri-Tabrizi, B., Baradaran, S., Amiri, A., Saber-Samandari, S., et al. (2019). Simultaneous enhanced antibacterial and osteoblast cytocompatibility performance of Ti6Al7Nb implant by nano-silver/graphene oxide decorated mixed oxide nanotube composite. *Surf. Coatings Technol.* 360, 181–195. doi: 10.1016/j.surfcoat.2018.12.119
- Rahnamaee, S. Y., Bagheri, R., Vossoughi, M., Ahmadi Seyedkhani, S., and Samadikuchaksaraei, A. (2020). Bioinspired multifunctional TiO₂ hierarchical micro/nanostructures with tunable improved bone cell growth and inhibited bacteria adhesion. *Ceram. Int.* 46, 9669–9679. doi: 10.1016/j.ceramint.2019.12.234
- Rajesh, S., Zhao, Y., Fong, H., and Menkhaus, T. J. (2016). Polyacrylonitrile nanofiber membranes modified with ionically crosslinked polyelectrolyte multilayers for the separation of ionic impurities. *Nanoscale* 8, 18376–18389. doi: 10.1039/c6nr06295d
- Ramalingam, B., Parandhaman, T., and Das, S. K. (2016). Antibacterial Effects of Biosynthesized Silver Nanoparticles on Surface Ultrastructure and Nanomechanical Properties of Gram-Negative Bacteria viz. *Escherichia coli* and *Pseudomonas aeruginosa*. *ACS Appl. Mater. Interfaces* 8, 4963–4976. doi: 10.1021/acsami.6b00161
- Ranjbar, Z., and Rastegar, S. (2011). Nano mechanical properties of an automotive clear-coats containing nano silica particles with different surface chemistries. *Prog. Org. Coatings* 72, 40–43. doi: 10.1016/j.porgcoat.2010.11.001
- Ranoszek-Soliwoda, K., Tomaszewska, E., Małek, K., Celichowski, G., Orlowski, P., Krzyzowska, M., et al. (2019). The synthesis of monodisperse silver nanoparticles with plant extracts. *Colloids Surfaces B Biointerfaces* 177, 19–24. doi: 10.1016/j.colsurfb.2019.01.037
- Ratova, M., Klaysri, R., Praserttham, P., and Kelly, P. J. (2017). Pulsed DC magnetron sputtering deposition of crystalline photocatalytic titania coatings at elevated process pressures. *Mater. Sci. Semicond. Process.* 71, 188–196. doi: 10.1016/j.mssp.2017.07.028
- Rauf, A., Ye, J., Zhang, S., Qi, Y., Wang, G., Che, Y., et al. (2019). Copper(ii)-based coordination polymer nanofibers as a highly effective antibacterial material with a synergistic mechanism. *Dalt. Trans.* 48, 17810–17817. doi: 10.1039/C9DT03649K
- Ribbens, S., Meynen, V., Tendeloo, G., Van, Ke, X., Mertens, M., et al. (2008). Development of photocatalytic efficient Ti-based nanotubes and nanoribbons by conventional and microwave assisted synthesis strategies. *Microporous Mesoporous Mater.* 114, 401–409. doi: 10.1016/j.micromeso.2008.01.028
- Riedesel, C., Kaufmann, N., Adolf, A., Kaemmer, N., Fritz, H., et al. (2019). “First demonstration of a 331-beam SEM,” in *Proceedings of the SPIE 10959, Metrology, Inspection, and Process Control for Microlithography XXXIII*, San Jose, CA. doi: 10.1117/12.2528795
- Rizzello, L., and Pompa, P. P. (2014). Nanosilver-based antibacterial drugs and devices: mechanisms, methodological drawbacks, and guidelines. *Chem. Soc. Rev.* 43, 1501–1518. doi: 10.1039/c3cs60218d
- Rizzello, L., Sorce, B., Sabella, S., Vecchio, G., Galeone, A., Brunetti, V., et al. (2011). Impact of nanoscale topography on genomics and proteomics of adherent bacteria. *ACS Nano* 5, 1865–1876. doi: 10.1021/nn102692m
- Roman, I., Trusca, R. D., Soare, M.-L., Fratila, C., Krasicka-Cydzik, E., Stan, M., et al. (2014). Titanium dioxide nanotube films: preparation, characterization and electrochemical biosensitivity towards alkaline phosphatase. *Mater. Sci. Eng. C* 37, 374–382. doi: 10.1016/j.msec.2014.01.036
- Rosifini Alves Claro, A. P., Konatu, R. T., do Amaral Escada, A. L., de Souza Nunes, M. C., Maurer-Morelli, C. V., Dias-Netipany, M. F., et al. (2018). Incorporation of silver nanoparticles on Ti7.5Mo alloy surface containing TiO₂ nanotubes arrays for promoting antibacterial coating – *in vitro* and *in vivo* study. *Appl. Surf. Sci.* 455, 780–788.
- Sabirov, I., Enikeev, N. A., Murashkin, M. Y., and Valiev, R. Z. (2015). *Nanostructures in Materials Subjected to Severe Plastic Deformation*. (Cham: Springer), 11–26. doi: 10.1007/978-3-319-19599-5_2
- Saleh, T. A. (2020). Nanomaterials: classification, properties, and environmental toxicities. *Environ. Technol. Innov.* 20:101067. doi: 10.1016/j.eti.2020.101067
- Salwiczek, M., Qu, Y., Gardiner, J., Strugnell, R. A., Lithgow, T., McLean, K. M., et al. (2014). Emerging rules for effective antimicrobial coatings. *Trends Biotechnol.* 32, 82–90. doi: 10.1016/j.tibtech.2013.09.008
- Sam Froes, F. H. (2018). Titanium for medical and dental applications-An introduction. *Titan. Med. Dent. Appl.* 3–21. doi: 10.1016/B978-0-12-812456-7.00001-9
- Samanta, A., Podder, S., Kumarasamy, M., Ghosh, C. K., Lahiri, D., Roy, P., et al. (2019). Au nanoparticle-decorated aragonite microdumbbells for enhanced antibacterial and anticancer activities. *Mater. Sci. Eng. C Mater. Biol. Appl.* 103:109734. doi: 10.1016/j.msec.2019.05.019
- Sano, K., Kuttassery, F., Shimada, T., Ishida, T., Takagi, S., Ohtani, B., et al. (2020). Optically Transparent Colloidal Dispersion of TiO₂ Nanoparticles Storable for longer than One year Prepared by Sol/Gel Progressive Hydrolysis/Condensation. *ACS Appl. Mater. Interfaces* 12, 44743–44753. doi: 10.1021/acsami.0c12951
- Sarkari Khorrami, M., Saito, N., Miyashita, Y., and Kondo, M. (2019). Texture variations and mechanical properties of aluminum during severe plastic deformation and friction stir processing with SiC nanoparticles. *Mater. Sci. Eng. A* 744, 349–364. doi: 10.1016/j.msea.2018.12.031

- Sarraf, M., Dabbagh, A., Abdul Razak, B., Mahmoodian, R., Nasiri-Tabrizi, B., Hosseini, H. R. M., et al. (2018a). Highly-ordered TiO₂ nanotubes decorated with Ag₂O nanoparticles for improved biofunctionality of Ti6Al4V. *Surf. Coatings Technol.* 349, 1008–1017. doi: 10.1016/j.surfcoat.2018.06.054
- Sarraf, M., Dabbagh, A., Abdul Razak, B., Nasiri-Tabrizi, B., Hosseini, H. R. M., Saber-Samandari, S., et al. (2018b). Silver oxide nanoparticles-decorated tantalum nanotubes for enhanced antibacterial activity and osseointegration of Ti6Al4V. *Mater. Des.* 154, 28–40. doi: 10.1016/j.matdes.2018.05.025
- Sarró, M. I., Moreno, D. A., Ranninger, C., King, E., and Ruiz, J. (2006). Influence of gas nitriding of Ti6Al4V alloy at high temperature on the adhesion of *Staphylococcus aureus*. *Surf. Coatings Technol.* 201, 2807–2812. doi: 10.1016/j.surfcoat.2006.05.023
- Scott, C., Olier, C., Lamandé, A., Choquet, P., and Chaleix, D. (2003). Structural evolution of co-deposited Zn-Cr coatings produced by vacuum evaporation. *Thin Solid Films* 436, 232–237. doi: 10.1016/S0040-6090(03)00597-2
- Semenova, I. P., Polyakov, A. V., Polyakova, V. V., Grishina, Y. F., Huang, Y., Valiev, R. Z., et al. (2017). Mechanical behavior and impact toughness of the ultrafine-grained Grade 5 Ti alloy processed by ECAP. *Mater. Sci. Eng. A* 696, 166–173. doi: 10.1016/j.msea.2017.04.073
- Seo, D. S., Lee, J. K., and Kim, H. (2001). Preparation of nanotube-shaped TiO₂ powder. *J. Cryst. Growth* 229, 428–432. doi: 10.1016/S0022-0248(01)0196-4
- Seong, M., and Lee, D. G. (2017). Silver nanoparticles against *Salmonella enterica* Serotype typhimurium: role of inner membrane dysfunction. *Curr. Microbiol.* 74, 661–670. doi: 10.1007/s00284-017-1235-9
- Sergi, R., Bellucci, D., Candidato, R. T., Lusvarghi, L., Bolelli, G., Pawlowski, L., et al. (2018). Bioactive Zn-doped hydroxyapatite coatings and their antibacterial efficacy against *Escherichia coli* and *Staphylococcus aureus*. *Surf. Coatings Technol.* 352, 84–91. doi: 10.1016/j.surfcoat.2018.08.017
- Shang, F., Chen, S., Liang, J., and Liu, C. (2019). Preparation and Photocatalytic Properties of ZnO Deposited TiO₂ Nanotube Arrays by Anodization. *J. Nanosci. Nanotechnol.* 19, 2070–2077. doi: 10.1166/jnn.2019.15797
- Shao, S. Y., Chen, J. X., Tang, H. Y., Ming, P. P., Yang, J., Zhu, W. Q., et al. (2020). A titanium surface modified with zinc-containing nanowires: enhancing biocompatibility and antibacterial property *in vitro*. *Appl. Surf. Sci.* 515:146107. doi: 10.1016/j.apsusc.2020.146107
- Shuitcev, A., Gunderov, D. V., Sun, B., Li, L., Valiev, R. Z., and Tong, Y. X. (2020). Nanostructured Ti₂₉Ni_{50.3}Hf₂₀ high temperature shape memory alloy processed by high-pressure torsion. *J. Mater. Sci. Technol.* 52, 218–225. doi: 10.1016/j.jmst.2020.01.065
- Sikder, P., Koju, N., Ren, Y., Phares, T., Lin, B., and Bhaduri, S. (2018). Development of single-phase silver-doped antibacterial CDHA coatings on Ti6Al4V with sustained release. *Surf. Coatings Technol.* 342, 105–116. doi: 10.1016/j.surfcoat.2018.02.100
- Silva, D., Sousa, H. C. D., Gil, M. H., Santos, L. F., Moutinho, G. M., Serro, A. P., et al. (2018). Antibacterial layer-by-layer coatings to control drug release from soft contact lenses material. *Int. J. Pharm.* 553, 186–200. doi: 10.1016/j.ijpharm.2018.10.041
- Simchi, A., Tamjid, E., Pishbin, F., and Boccacini, A. R. (2011). Recent progress in inorganic and composite coatings with bactericidal capability for orthopaedic applications. *Nanomed. Nanotechnol. Biol. Med.* 7, 22–39. doi: 10.1016/j.nano.2010.10.005
- Simi, V. S., and Rajendran, N. (2017). Influence of tunable diameter on the electrochemical behavior and antibacterial activity of titania nanotube arrays for biomedical applications. *Mater. Charact.* 129, 67–79. doi: 10.1016/j.matchar.2017.04.019
- Singh, A. V., Vyas, V., Patil, R., Sharma, V., Scopelliti, P. E., Bongiorno, G., et al. (2011). Quantitative characterization of the influence of the nanoscale morphology of nanostructured surfaces on bacterial adhesion and biofilm formation. *PLoS One* 6:e25029. doi: 10.1371/journal.pone.0025029
- Siritongsuk, P., Hongsing, N., Thammawithan, S., Daduang, S., Klaynongsruang, S., Tuanyok, A., et al. (2016). Two-phase bactericidal mechanism of silver nanoparticles against *Burkholderia pseudomallei*. *PLoS One* 11:e0168098. doi: 10.1371/journal.pone.0168098
- Sivaprakash, V., and Narayanan, R. (2020). Synthesis of TiO₂ nanotubes via electrochemical anodization with different water content. *Mater. Today Proc.* doi: 10.1016/j.matpr.2020.04.657
- Skoric, L., Sanz-Hernández, D., Meng, F., Donnelly, C., Merino-Aceituno, S., and Fernández-Pacheco, A. (2020). Layer-by-layer growth of complex-shaped three-dimensional nanostructures with focused electron beams. *Nano Lett.* 20, 184–191. doi: 10.1021/acs.nanolett.9b03565
- Son, I. H., Park, J. H., Kwon, S., Choi, J. W., and Rummeli, M. H. (2016). Graphene coating of silicon nanoparticles with CO₂-enhanced chemical vapor deposition. *Small* 12, 658–667. doi: 10.1002/smll.201502880
- Song, J., Zheng, M., Zhang, B., Li, Q., Wang, F., Ma, L., et al. (2017). Fast Growth of Highly Ordered TiO₂ Nanotube Arrays on Si Substrate under High-Field Anodization. *Nano Micro Lett.* 9:13. doi: 10.1007/s40820-016-0114-4
- Spengler, C., Nolle, F., Mischo, J., Faidt, T., Grandthyll, S., Thewes, N., et al. (2019). Strength of bacterial adhesion on nanostructured surfaces quantified by substrate morphometry. *Nanoscale* 11, 19713–19722. doi: 10.1039/c9nr04375f
- Stratakis, E., Bonse, J., Heitz, J., Siegel, J., Tsididis, G. D., Skoulas, E., et al. (2020). Laser engineering of biomimetic surfaces. *Mater. Sci. Eng. R Rep.* 141:100562. doi: 10.1016/j.mser.2020.100562
- Su, H. L., Chou, C. C., Hung, D. J., Lin, S. H., Pao, I. C., Lin, J. H., et al. (2009). The disruption of bacterial membrane integrity through ROS generation induced by nanohybrids of silver and clay. *Biomaterials* 30, 5979–5987. doi: 10.1016/j.biomaterials.2009.07.030
- Subramaniam, S. B., Megarajan, S., Vijayakumar, S., Mariappan, M., and Anbazhagan, V. (2019). Evaluation of the toxicities of silver and silver sulfide nanoparticles against Gram-positive and Gram-negative bacteria. *IET Nanobiotechnol.* 13, 326–331. doi: 10.1049/iet-nbt.2018.5221
- Sun, H., Choi, D., Heo, J., Jung, S. Y., and Hong, J. (2020). Studies on the drug loading and release profiles of degradable chitosan-based multilayer films for anticancer treatment. *Cancers* 12:593. doi: 10.3390/cancers12030593
- Surmeneva, M., Lapanje, A., Chudinova, E., Ivanova, A., Koptug, A., Loza, K., et al. (2019). Decreased bacterial colonization of additively manufactured Ti6Al4V metallic scaffolds with immobilized silver and calcium phosphate nanoparticles. *Appl. Surf. Sci.* 480, 822–829. doi: 10.1016/j.apsusc.2019.03.003
- Sviridov, A. P., Osminkina, L. A., Kharin, A. Y., Gongansky, M. B., Kargina, J. V., Kudryavtsev, A. A., et al. (2017). Cytotoxicity control of silicon nanoparticles by biopolymer coating and ultrasound irradiation for cancer theranostic applications. *Nanotechnology* 28:105102. doi: 10.1088/1361-6528/aa5b7c
- Swami, N., Cui, Z., and Nair, L. S. (2010). Titania nanotubes: novel nanostructures for improved osseointegration. *J. Heat Transfer* 133:034002. doi: 10.1115/1.4002465
- Takahashi, S., Chiba, H., Kato, T., Endo, S., Hayashi, T., Todoroki, N., et al. (2015). Oxygen reduction reaction activity and structural stability of Pt-Au nanoparticles prepared by arc-plasma deposition. *Phys. Chem. Chem. Phys.* 17, 18638–18644. doi: 10.1039/c5cp2048d
- Tang, S., and Zheng, J. (2018). Antibacterial activity of silver nanoparticles: structural effects. *Adv. Healthc. Mater.* 7:1701503. doi: 10.1002/adhm.201701503
- Taylor, S. R., and Sieradzki, K. (2003). The development of a multi-functional aerospace coating: considerations in the use of nano-dimensional materials. *Prog. Org. Coatings* 47, 169–173. doi: 10.1016/S0300-9440(03)00136-X
- Thinakaran, S., Loordhuswamy, A. M., and Venkateshwaram Rengaswami, G. D. (2020). Electrophoretic deposition of chitosan/nano silver embedded micro sphere on centrifugal spun fibrous matrices – A facile biofilm resistant biocompatible material. *Int. J. Biol. Macromol.* 148, 68–78. doi: 10.1016/j.ijbiomac.2020.01.086
- Tian, C. X., Wang, Z. S., Zou, C. W., Tang, X. S., Xie, X., Li, S. Q., et al. (2019). Ternary and quaternary TiBN and TiBCN nanocomposite coatings deposited by arc ion plating. *Surf. Coatings Technol.* 359, 445–450. doi: 10.1016/j.surfcoat.2018.12.081
- Tranchant, J., Angleraud, B., Tessier, P. Y., Besland, M. P., Landesman, J. P., and Djouadi, M. A. (2006). Residual stress control in MoCr thin films deposited by ionized magnetron sputtering. *Surf. Coatings Technol.* 200, 6549–6553. doi: 10.1016/j.surfcoat.2005.11.104
- Tripathi, B. N., and Gaur, J. P. (2004). Relationship between copper- and zinc-induced oxidative stress and proline accumulation in *Scenedesmus* sp. *Planta* 219, 397–404. doi: 10.1007/s00425-004-1237-2
- Truong, V. K., Geeganagamage, N. M., Baulin, V. A., Vongsvivut, J., Tobin, M. J., Luque, P., et al. (2017). The susceptibility of *Staphylococcus aureus* CIP 65.8 and *Pseudomonas aeruginosa* ATCC 9721 cells to the bactericidal action

- of nanostructured *Calopteryx haemorrhoidalis* damselfly wing surfaces. *Appl. Microbiol. Biotechnol.* 101, 4683–4690. doi: 10.1007/s00253-017-8205-9
- Tsai, C.-C., and Teng, H. (2004). Regulation of the physical characteristics of Titania Nanotube Aggregates Synthesized from Hydrothermal Treatment. *Chem. Mater.* 16, 4352–4358. doi: 10.1021/cm049643u
- Tsai, C.-C., and Teng, H. (2006). Structural Features of Nanotubes Synthesized from NaOH Treatment on TiO₂ with Different Post-Treatments. *Chem. Mater.* 18, 367–373. doi: 10.1021/cm0518527
- Tyurikova, I. A., Alexandrov, S. E., Tyurikov, K. S., Kirilenko, D. A., Sheshilova, A. B., and Shakhmin, A. L. (2020). Fast and Controllable Synthesis of Core-Shell Fe₃O₄-C Nanoparticles by Aerosol CVD. *ACS Omega* 5, 8146–8150. doi: 10.1021/acsomega.0c00392
- Umrao, S., Jeon, J., Jeon, S. M., Choi, Y. J., and Lee, S. (2017). A homogeneous atomic layer MoS₂(1-*X*)Se₂ alloy prepared by low-pressure chemical vapor deposition, and its properties. *Nanoscale* 9, 594–603. doi: 10.1039/c6nr07240b
- Ur Rehman, M. A., Bastan, F. E., Nawaz, Q., Goldmann, W. H., Maqbool, M., Virtanen, S., et al. (2018). Electrophoretic deposition of lawsone loaded bioactive glass (BG)/chitosan composite on polyetheretherketone (PEEK)/BG layers as antibacterial and bioactive coating. *J. Biomed. Mater. Res. Part A* 106, 3111–3122. doi: 10.1002/jbm.a.36506
- Utke, I., Hoffmann, P., and Melngailis, J. (2008). Gas-assisted focused electron beam and ion beam processing and fabrication. *J. Vac. Sci. Technol. B Microelectron. Nanom. Struct.* 26:1197. doi: 10.1116/1.2955728
- Velic, A., Tesfamichael, T., Li, Z., and Yarlaga, P. K. D. V. (2019). Parametric study on nanopattern bactericidal activity. *Procedia Manuf.* 30, 514–521. doi: 10.1016/j.promfg.2019.02.072
- Viana, M., Fonseca, A. S., Querol, X., López-Lilao, A., Carpio, P., Salmatidis, A., et al. (2017). Workplace exposure and release of ultrafine particles during atmospheric plasma spraying in the ceramic industry. *Sci. Total Environ.* 599–600, 2065–2073. doi: 10.1016/j.scitotenv.2017.05.132
- Vimbela, G. V., Ngo, S. M., Frazee, C., Yang, L., and Stout, D. A. (2017). Antibacterial properties and toxicity from metallic nanomaterials. *Int. J. Nanomed.* 12, 3941–3965. doi: 10.2147/IJN.S134526
- Vishnu, J., Manivasagam, V., Gopal, V., Bartomeu Garcia, C., Hameed, P., Manivasagam, G., et al. (2019). Hydrothermal treatment of etched titanium: a potential surface nano-modification technique for enhanced biocompatibility. *Nanomed. Nanotechnol. Biol. Med.* 20:102016. doi: 10.1016/j.nano.2019.102016
- Vuchkov, T., Evaristo, M., Yaqub, T., Bin, Polcar, T., and Cavaleiro, A. (2020). Synthesis, microstructure and mechanical properties of W–S–C self-lubricant thin films deposited by magnetron sputtering. *Tribol. Int.* 150:106363. doi: 10.1016/j.triboint.2020.106363
- Wang, D. G., Xiao, F. H., Li, Y., Ming, X. C., Zhai, J. Q., and Chen, C. Z. (2020). Properties of HA-based composite films fabricated by pulsed laser deposition with an in-situ heat treatment. *Surf. Coatings Technol.* 394. doi: 10.1016/j.surfcoat.2020.125863
- Wang, L., Deng, X., Li, J., Liao, X., Zhang, G., Wang, C., et al. (2014). Hydrothermal synthesis of tetragonal BaTiO₃ nanotube arrays with high dielectric performance. *J. Nanosci. Nanotechnol.* 14, 4224–4228. doi: 10.1166/jnn.2014.7782
- Wang, L., Lu, W., Qin, J., Zhang, F., and Zhang, D. (2008). Microstructure and mechanical properties of cold-rolled TiNbTaZr biomedical β titanium alloy. *Mater. Sci. Eng. A* 490, 421–426. doi: 10.1016/j.msea.2008.03.003
- Wang, L., Wang, C., and Dunand, D. C. (2015). Microstructure and Strength of NiTi-Nb Eutectic Braze Joining NiTi Wires. *Metall. Mater. Trans. A Phys. Metall. Mater. Sci.* 46, 1433–1436. doi: 10.1007/s11661-015-2781-z
- Wang, L., Wang, C., Zhang, L. C., Chen, L., Lu, W., and Zhang, D. (2016). Phase transformation and deformation behavior of NiTi-Nb eutectic joined NiTi wires. *Sci. Rep.* 6:23905. doi: 10.1038/srep23905
- Wang, L., Xie, L., Shen, P., Fan, Q., Wang, W., Wang, K., et al. (2019). Surface microstructure and mechanical properties of Ti-6Al-4V/Ag nanocomposite prepared by FSP. *Mater. Charact.* 153, 175–183. doi: 10.1016/j.matchar.2019.05.002
- Wang, L., Xie, L., Zhang, L. C., Chen, L., Ding, Z., Lv, Y., et al. (2018). Microstructure evolution and superelasticity of layer-like NiTiNb porous metal prepared by eutectic reaction. *Acta Mater.* 143, 214–226. doi: 10.1016/j.actamat.2017.10.021
- Wang, L. N., Jin, M., Zheng, Y., Guan, Y., Lu, X., and Luo, J. L. (2014). Nanotubular surface modification of metallic implants via electrochemical anodization technique. *Int. J. Nanomed.* 9, 4421–4435. doi: 10.2147/IJN.S65866
- Wang, X., Yan, L., Ye, T., Cheng, R., Tian, J., Ma, C., et al. (2019). Osteogenic and antiseptic nanocoating by in situ chitosan regulated electrochemical deposition for promoting osseointegration. *Mater. Sci. Eng. C* 102, 415–426. doi: 10.1016/j.msec.2019.04.060
- Wang, Y., Liu, X., Fan, T., Tan, Z., Zhou, Z., and He, D. (2017). *In vitro* evaluation of hydroxyapatite coatings with (002) crystallographic texture deposited by micro-plasma spraying. *Mater. Sci. Eng. C* 75, 596–601. doi: 10.1016/j.msec.2017.02.119
- Wareing, N., Szymanski, K., Akkaraju, G. R., Loni, A., Canham, L. T., Gonzalez-Rodriguez, R., et al. (2017). *In vitro* gene delivery with large porous silicon nanoparticles fabricated using cost-effective, metal-assisted chemical etching. *Small* 13:1602739. doi: 10.1002/smll.201602739
- Wategaonkar, S. B., Pawar, R. P., Parale, V. G., Nade, D. P., Sargar, B. M., and Mane, R. K. (2020). Synthesis of rutile TiO₂ nanostructures by single step hydrothermal route and its characterization. *Mater. Today Proc.* 23, 444–451. doi: 10.1016/j.matpr.2020.02.065
- Watson, G. S., Green, D. W., Schwarzkopf, L., Li, X., Cribb, B. W., Myhra, S., et al. (2015). A gecko skin micro/nano structure - A low adhesion, superhydrophobic, anti-wetting, self-cleaning, biocompatible, antibacterial surface. *Acta Biomater.* 21, 109–122. doi: 10.1016/j.actbio.2015.03.007
- Wei, W., Liu, Y., Yao, X., and Hang, R. (2020). Na-Ti-O nanostructured film anodically grown on titanium surface have the potential to improve osteogenesis. *Surf. Coatings Technol.* 397. doi: 10.1016/j.surfcoat.2020.125907
- Whitesides, G. M. (2005). Nanoscience, Nanotechnology, and Chemistry. *Small* 1, 172–179. doi: 10.1002/smll.200400130
- Winkler, R., Lewis, B. B., Fowlkes, J. D., Rack, P. D., and Plank, H. (2018). High-Fidelity 3D-nanoprinting via focused electron beams: growth fundamentals. *ACS Appl. Nano Mater.* 1, 1014–1027. doi: 10.1021/acsanm.8b00158
- Wong, C. L., Tan, Y. N., and Mohamed, A. R. (2011). A review on the formation of Titania nanotube photocatalysts by hydrothermal treatment. *J. Environ. Manage.* 92, 1669–1680. doi: 10.1016/j.jenvman.2011.03.006
- Wu, J., Wang, X., Zhu, B., He, Q., Ren, F., Tong, F., et al. (2020). pH-sensitive magnetic drug delivery system via layer-by-layer self-assembly of CS/PEG and its controlled release of DOX. *J. Biomater. Sci. Polym. Ed.* 31, 1057–1070. doi: 10.1080/09205063.2020.1740963
- Wu, S., Zuber, F., Maniura-Weber, K., Brugger, J., and Ren, Q. (2018). Nanostructured surface topographies have an effect on bactericidal activity. *J. Nanobiotechnol.* 16:20. doi: 10.1186/s12951-018-0347-0
- Wu, Y., Long, Y., Li, Q. L., Han, S., Ma, J., Yang, Y. W., et al. (2015). Layer-by-Layer (LBL) self-assembled biohybrid nanomaterials for efficient antibacterial applications. *ACS Appl. Mater. Interfaces* 7, 17255–17263. doi: 10.1021/acsami.5b04216
- Xia, K., Zhang, L., Huang, Y., and Lu, Z. (2015). Preparation of gold nanorods and their applications in photothermal therapy. *J. Nanosci. Nanotechnol.* 15, 63–73. doi: 10.1166/jnn.2015.9586
- Xia, L., Long, Y., Li, D., Huang, L., Wang, Y., Dai, F., et al. (2019). LBL deposition of chitosan and silk fibroin on nanofibers for improving physical and biological performance of patches. *Int. J. Biol. Macromol.* 130, 348–356. doi: 10.1016/j.ijbiomac.2019.02.147
- Xia, Y. (2008). Nanomaterials at work in biomedical research. *Nat. Mater.* 7, 758–760. doi: 10.1038/nmat2277
- Xin, H. W., Tian, L. H., Pan, J., De, He, Q., Xu, Z., et al. (2000). Synthesis of aluminum nitride films by activated reactive ion plating with a cathodic arc source. *Surf. Coatings Technol.* 131, 167–170. doi: 10.1016/S0257-8972(00)00756-8
- Xin, Q., Shah, H., Nawaz, A., Xie, W., Akram, M. Z., Batool, A., et al. (2019). Antibacterial carbon-based nanomaterials. *Adv. Mater.* 31, 1–15. doi: 10.1002/adma.201804838
- Xingfang, H. U., Shuyin, Q. I. N., Jingfen, T., and Miefeng, H. (1988). Selectively absorbing black aluminium coating deposited by vacuum evaporation. *Solar. Energy Mater.* 17, 207–215.
- Xu, J., Xu, N., Zhou, T., Xiao, X., Gao, B., Fu, J., et al. (2017). Polydopamine coatings embedded with silver nanoparticles on nanostructured

- titania for long-lasting antibacterial effect. *Surf. Coat. Technol.* 320, 608–613.
- Xu, J. W., Yao, K., and Xu, Z. K. (2019). Nanomaterials with a photothermal effect for antibacterial activities: an overview. *Nanoscale* 11, 8680–8691. doi: 10.1039/c9nr01833f
- Xu, W., Qi, M., Li, X., Liu, X., Wang, L., Yu, W., et al. (2019). TiO₂ nanotubes modified with Au nanoparticles for visible-light enhanced antibacterial and anti-inflammatory capabilities. *J. Electroanal. Chem.* 842, 66–73. doi: 10.1016/j.jelechem.2019.04.062
- Xue, F., Liu, J., Guo, L., Zhang, L., and Li, Q. (2015). Theoretical study on the bactericidal nature of nanopatterned surfaces. *J. Theor. Biol.* 385, 1–7. doi: 10.1016/j.jtbi.2015.08.011
- Yang, E. J., Kim, S., Kim, J. S., and Choi, I. H. (2012). Inflammasome formation and IL-1 β release by human blood monocytes in response to silver nanoparticles. *Biomaterials* 33, 6858–6867. doi: 10.1016/j.biomaterials.2012.06.016
- Yang, J., Zhang, M., Lan, X., Weng, X., Shu, Q., Wang, R., et al. (2018). Controllable fabrication of non-close-packed colloidal nanoparticle arrays by ion beam etching. *Nanoscale Res. Lett.* 13:177. doi: 10.1186/s11671-018-2586-2
- Yang, T., Wang, D., and Liu, X. (2019). Assembled gold nanorods for the photothermal killing of bacteria. *Colloids Surfaces B Biointerfaces* 173, 833–841. doi: 10.1016/j.colsurfb.2018.10.060
- Yang, Y. C., Chen, C. C., Wang, J. B., Wang, Y. C., and Lin, F. H. (2017). Flame sprayed zinc doped hydroxyapatite coating with antibacterial and biocompatible properties. *Ceram. Int.* 43, S829–S835. doi: 10.1016/j.ceramint.2017.05.318
- Yang, Z., Gu, H., Sha, G., Lu, W., Yu, W., Zhang, W., et al. (2018). TC4/Ag metal matrix nanocomposites modified by friction stir processing: surface characterization, antibacterial property, and cytotoxicity *in Vitro*. *ACS Appl. Mater. Interfaces* 10, 41155–41166. doi: 10.1021/acsami.8b16343
- Yang, Z., Ma, C., Wang, W., Zhang, M., Hao, X., and Chen, S. (2019). Fabrication of Cu₂O-Ag nanocomposites with enhanced durability and bactericidal activity. *J. Colloid Interface Sci.* 557, 156–167. doi: 10.1016/j.jcis.2019.09.015
- Yasuyuki, M., Kunihiro, K., Kurissey, S., Kanavillil, N., Sato, Y., and Kikuchi, Y. (2010). Antibacterial properties of nine pure metals: a laboratory study using *Staphylococcus aureus* and *Escherichia coli*. *Biofouling* 26, 851–858. doi: 10.1080/08927014.2010.527000
- Yildiz, Z. K., Atilgan, A., Atli, A., Özel, K., Altinkaya, C., and Yildiz, A. (2019). Enhancement of efficiency of natural and organic dye sensitized solar cells using thin film TiO₂ photoanodes fabricated by spin-coating. *J. Photochem. Photobiol. A Chem.* 368, 23–29. doi: 10.1016/j.jphotochem.2018.09.018
- Yilmaz, O., and Yorgancıoğlu, A. (2018). “Nanocoatings: preparation, properties, and biomedical applications,” in *Polyme Nanomaterials in Nanotherapeutics*, ed. C. Vasile (Amsterdam: Elsevier Inc), 299–331. doi: 10.1016/B978-0-12-813932-5.00008-X
- Yin, Y., Li, Y., Cai, W., and Sui, J. (2019). One-step deposition of antibacterial Ag@Pdop hybrid films on an NiTi alloy. *RSC Adv.* 9, 29263–29272. doi: 10.1039/C9RA05764A
- Yu, L., Jin, G., Ouyang, L., Wang, D., Qiao, Y., and Liu, X. (2016). Antibacterial activity, osteogenic and angiogenic behaviors of copper-bearing titanium synthesized by PIII&D. *J. Mater. Chem. B* 4, 1296–1309. doi: 10.1039/C5TB02300A
- Yuvaraj, D., Kaushik, R., and Narasimha Rao, K. (2010). Optical, field-emission, and antimicrobial properties of ZnO nanostructured films deposited at room temperature by activated reactive evaporation. *ACS Appl. Mater. Interfaces* 2, 1019–1024. doi: 10.1021/am900792k
- Zeng, J., Ji, X., Ma, Y., Zhang, Z., Wang, S., Ren, Z., et al. (2018). 3D graphene fibers grown by thermal chemical vapor deposition. *Adv. Mater.* 30:e1705380. doi: 10.1002/adma.201705380
- Zhang, C., Ding, Z., Xie, L., Zhang, L. C., Wu, L., Fu, Y., et al. (2017). Electrochemical and *in vitro* behavior of the nanosized composites of Ti-6Al-4V and TiO₂ fabricated by friction stir process. *Appl. Surf. Sci.* 423, 331–339. doi: 10.1016/j.apsusc.2017.06.141
- Zhang, K., Zhu, Y., Liu, X., Cui, Z., Xianjin, Y., Yeung, K. W. K., et al. (2017). Sr/ZnO doped titania nanotube array: an effective surface system with excellent osteoinductivity and self-antibacterial activity. *Mater. Des.* 130, 403–412. doi: 10.1016/j.matdes.2017.05.085
- Zhang, Q., Wu, Z., Xu, Y. X., Wang, Q., Chen, L., and Kim, K. H. (2019a). Improving the mechanical and anti-wear properties of AlTiN coatings by the hybrid arc and sputtering deposition. *Surf. Coatings Technol.* 378:125022. doi: 10.1016/j.surfcoat.2019.125022
- Zhang, Q., Xu, Y., Zhang, T., Wu, Z., and Wang, Q. (2018a). Tribological properties, oxidation resistance and turning performance of AlTiN/AlCrSiN multilayer coatings by arc ion plating. *Surf. Coatings Technol.* 356, 1–10. doi: 10.1016/j.surfcoat.2018.09.027
- Zhang, R., Liu, X., Xiong, Z., Huang, Q., Yang, X., Yan, H., et al. (2018b). Novel micro/nanostructured TiO₂/ZnO coating with antibacterial capacity and cytocompatibility. *Ceram. Int.* 44, 9711–9719. doi: 10.1016/j.ceramint.2018.02.202
- Zhang, R., Liu, X., Xiong, Z., Huang, Q., Yang, X., Yan, H., et al. (2018c). The immunomodulatory effects of Zn-incorporated micro/nanostructured coating in inducing osteogenesis. *Artif. Cells Nanomed. Biotechnol.* 46, 1123–1130. doi: 10.1080/21691401.2018.1446442
- Zhang, S., Xing, M., and Li, B. (2018d). Biomimetic layer-by-layer self-assembly of nanofilms, nanocoatings, and 3D scaffolds for tissue engineering. *Int. J. Mol. Sci.* 19:1641. doi: 10.3390/ijms19061641
- Zhang, W. J., Hong, C. Y., and Pan, C. Y. (2019b). Polymerization-Induced Self-Assembly of Functionalized Block Copolymer Nanoparticles and Their Application in Drug Delivery. *Macromol. Rapid Commun.* 40:e1800279. doi: 10.1002/marc.201800279
- Zhang, X., Li, C., Yu, Y., Lu, X., Lv, Y., Jiang, D., et al. (2019c). Characterization and property of bifunctional Zn-incorporated TiO₂ micro-arc oxidation coatings: the influence of different Zn sources. *Ceram. Int.* 45, 19747–19756. doi: 10.1016/j.ceramint.2019.06.228
- Zhang, X., Zhang, D., Peng, Q., Lin, J., and Wen, C. (2019d). Biocompatibility of nanoscale hydroxyapatite coating on TiO(2) nanotubes. *Materials* 12:1979. doi: 10.3390/ma12121979
- Zhao, M., Gong, H., Ma, M., Dong, L., Huang, M., Wan, R., et al. (2019). A comparative antibacterial activity and cytocompatibility for different top layers of TiN, Ag or TiN-Ag on nanoscale TiN/Ag multilayers. *Appl. Surf. Sci.* 473, 334–342. doi: 10.1016/j.apsusc.2018.12.159
- Zhao, Y., Xing, Q., Janjanam, J., He, K., Long, F., Low, K., et al. (2014). Facile electrochemical synthesis of antimicrobial TiO₂ nanotube arrays. *Int. J. Nanomed.* 9, 5177–5187. doi: 10.2147/IJN.S65386
- Zhen, W., An, S., Wang, W., Liu, Y., Jia, X., Wang, C., et al. (2019). Gram-scale fabrication of Bi@C nanoparticles through one-step hydrothermal method for dual-model imaging-guided NIR-II photothermal therapy. *Nanoscale* 11, 9906–9911. doi: 10.1039/c9nr01557d
- Zhou, J., Zhang, X., Sun, J., Dang, Z., Li, J., Li, X., et al. (2018). The effects of surface topography of nanostructure arrays on cell adhesion. *Phys. Chem. Chem. Phys.* 20, 22946–22951. doi: 10.1039/C8CP03538E
- Zhou, W., Jia, Z., Xiong, P., Yan, J., Li, M., Cheng, Y., et al. (2018). Novel pH-responsive tobramycin-embedded micelles in nanostructured multilayer-coatings of chitosan/heparin with efficient and sustained antibacterial properties. *Mater. Sci. Eng. C* 90, 693–705. doi: 10.1016/j.msec.2018.04.069
- Zhu, C., Lv, Y., Qian, C., Ding, Z., Jiao, T., Gu, X., et al. (2018). Microstructures, mechanical, and biological properties of a novel Ti-6V-4V/zinc surface nanocomposite prepared by friction stir processing. *Int. J. Nanomed.* 13, 1881–1898. doi: 10.2147/IJN.S154260
- Zhu, C., Lv, Y., Qian, C., Qian, H., Jiao, T., Wang, L., et al. (2016). Proliferation and osteogenic differentiation of rat BMSCs on a novel Ti/SiC metal matrix nanocomposite modified by friction stir processing. *Sci. Rep.* 6:38875. doi: 10.1038/srep38875
- Zhu, M., Liu, X., Tan, L., Cui, Z., Liang, Y., Li, Z., et al. (2020). Photo-responsive chitosan/Ag/MoS₂ for rapid bacteria-killing. *J. Hazard. Mater.* 383:121122. doi: 10.1016/j.jhazmat.2019.121122
- Zhu, W. Q., Shao, S. Y., Xu, L. N., Chen, W. Q., Yu, X. Y., Tang, K. M., et al. (2019). Enhanced corrosion resistance of zinc-containing nanowires-modified titanium surface under exposure to oxidizing microenvironment. *J. Nanobiotechnol.* 17:55. doi: 10.1186/s12951-019-0488-9
- Zhu, Y., Dong, M., Chang, K., Li, J., and Wang, L. (2019). Prolonged antibacterial action by sluggish release of Ag from TiSiN/Ag multilayer coating. *J. Alloys Compd.* 783, 164–172. doi: 10.1016/j.jallcom.2018.12.295

- Zhu, Y., Liu, X., Yeung, K. W. K., Chu, P. K., and Wu, S. (2017). Biofunctionalization of carbon nanotubes/chitosan hybrids on Ti implants by atom layer deposited ZnO nanostructures. *Appl. Surf. Sci.* 400, 14–23. doi: 10.1016/j.apsusc.2016.12.158
- Zimmerli, W., and Sendi, P. (2017). Orthopaedic biofilm infections. *APMIS* 125, 353–364. doi: 10.1111/apm.12687
- Zong, M., Bai, L., Liu, Y., Wang, X., Zhang, X., Huang, X., et al. (2017). Antibacterial ability and angiogenic activity of Cu-Ti-O nanotube arrays. *Mater. Sci. Eng. C* 71, 93–99. doi: 10.1016/j.msec.2016.09.077

Conflict of Interest: The authors declare that the research was conducted in the absence of any commercial or financial relationships that could be construed as a potential conflict of interest.

Copyright © 2020 Liu, Liu, Attarilar, Wang, Tamaddon, Yang, Xie, Yao, Wang, Liu and Tang. This is an open-access article distributed under the terms of the Creative Commons Attribution License (CC BY). The use, distribution or reproduction in other forums is permitted, provided the original author(s) and the copyright owner(s) are credited and that the original publication in this journal is cited, in accordance with accepted academic practice. No use, distribution or reproduction is permitted which does not comply with these terms.



Copper-Containing Alloy as Immunoregulatory Material in Bone Regeneration via Mitochondrial Oxidative Stress

Daorong Xu^{1,2†}, Jikun Qian^{1,2†}, Xin Guan^{1,2†}, Ling Ren³, Kaifan Yang^{1,2}, Xuan Huang⁴, Shuyuan Zhang³, Yu Chai^{1,2}, Xiaohu Wu^{1,2}, Hangtian Wu^{1,2}, Xianrong Zhang^{1,2*}, Ke Yang^{3*} and Bin Yu^{1,2*}

¹ Division of Orthopedic Surgery, Department of Orthopedics, Nanfang Hospital, Southern Medical University, Guangzhou, China, ² Guangdong Provincial Key Laboratory of Bone and Cartilage Regenerative Medicine, Nanfang Hospital, Southern Medical University, Guangzhou, China, ³ Institute of Metal Research, Chinese Academy of Sciences, Shenyang, China, ⁴ State Key Laboratory of Organ Failure Research, Guangdong Provincial Key Laboratory of Viral Hepatitis Research, Department of Infectious Diseases, Nanfang Hospital, Southern Medical University, Guangzhou, China

OPEN ACCESS

Edited by:

Liqiang Wang,
Shanghai Jiao Tong University, China

Reviewed by:

Jian Wang,
Xihua University, China
Ahmed El-Fiqi,
Dankook University, South Korea

*Correspondence:

Bin Yu
yubin@smu.edu.cn
Ke Yang
kyang@imr.ac.cn
Xianrong Zhang
xianrongzh@smu.edu.cn

[†]These authors have contributed
equally to this work

Specialty section:

This article was submitted to
Biomaterials,
a section of the journal
Frontiers in Bioengineering and
Biotechnology

Received: 23 October 2020

Accepted: 08 December 2020

Published: 14 January 2021

Citation:

Xu D, Qian J, Guan X, Ren L, Yang K,
Huang X, Zhang S, Chai Y, Wu X,
Wu H, Zhang X, Yang K and Yu B
(2021) Copper-Containing Alloy as
Immunoregulatory Material in Bone
Regeneration via Mitochondrial
Oxidative Stress.
Front. Bioeng. Biotechnol. 8:620629.
doi: 10.3389/fbioe.2020.620629

In the mammalian skeletal system, osteogenesis and angiogenesis are closely linked by type H vessels during bone regeneration and repair. Our previous studies confirmed the promotion of these processes by copper-containing metal (CCM) *in vitro* and *in vivo*. However, whether and how the coupling of angiogenesis and osteogenesis participates in the promotion of bone regeneration by CCM *in vivo* is unknown. In this study, M2a macrophages but not M2c macrophages were shown to be immunoregulated by CCM. A CCM, 316L–5Cu, was applied to drilling hole injuries of the tibia of C57/6 mice for comparison. We observed advanced formation of cortical bone and type H vessels beneath the new bone in the 316L–5Cu group 14 and 21 days postinjury. Moreover, the recruitment of CD206-positive M2a macrophages, which are regarded as the primary source of platelet-derived growth factor type BB (PDGF-BB), was significantly promoted at the injury site at days 14 and 21. Under the stimulation of CCM, mitochondria-derived reactive oxygen species were also found to be upregulated in CD206^{hi} M2a macrophages *in vitro*, and this upregulation was correlated with the expression of PDGF-BB. In conclusion, our results indicate that CCM promotes the evolution of callus through the generation of type H vessels during the process of bone repair by upregulating the expression of PDGF-BB derived from M2a macrophages.

Keywords: 316-5Cu stainless steel, type H vessel, M2a macrophage, PDGF-BB, immunoregulation

HIGHLIGHTS:

- Copper-containing metal promoted the evolution of callus through the generation of type H vessels in the process of bone repair.
- CD206⁺ M2a macrophage-derived PDGF-BB were elevated by copper-containing metal in callus beneath the newly formed cortical bone.
- The coupling of osteogenesis and angiogenesis was linked by immunoregulation of copper-containing biomaterials.

INTRODUCTION

Bone fracture is an increasingly common medical incident that results from both traumatic injury and disease-related bone fragility. Even when adequate bone repair is achieved within the expected time frame, treating fractures is costly and can be protracted in the 10–20% of cases in which healing is delayed or fails (Parker et al., 2007; Hernandez et al., 2012). The limited treatment options for accelerating fracture repair and sustaining peak bone mass throughout life represent a growing clinical problem. Current biological treatments (for example, teriparatide and strontium ranelate) are modestly effective or not broadly applicable, creating a treatment gap in the management of fractures and osteoporosis (Wu et al., 2013).

The intimate spatial and temporal link between osteogenesis and angiogenesis, termed angiogenic–osteogenic coupling, can recruit both endothelial and osteoblast precursor cells to the locus (Zheng et al., 2018; Peng et al., 2020). A recent study by Romeo et al. (2019) reported that type H vessels play a crucial part in promoting the conversion of cartilage matrix to bone tissue during bone development and regeneration. Platelet-derived growth factor type BB (PDGF-BB), which is derived from macrophages, contributes to the generation of type H vessels in the first stages of these processes. It was also noted in a recent study that *emcn*^{hi}*CD31*^{hi} endothelium was present during endochondral bone formation in the osteotomy gap (Stefanowski et al., 2019). Moreover, administration of recombinant SLIT3, which is derived from osteoblasts and promotes formation of type H vessels, effectively accelerated bone fracture healing in a mouse bone fracture model (Xu et al., 2018). Thus, it was proposed that fracture healing could be enhanced by promoting type H vessel angiogenesis, providing a potential therapeutic approach, particularly for cases of delayed union or non-union.

The most popular biomaterials used in managing bone fractures are metals including titanium alloy and stainless steel, which promote bone repair and have specific effects depending on their components (Spiller et al., 2014; Inzana et al., 2016). Magnesium, a transition metal element that contributes to the biological activity regulated by neurotransmitters in bone,

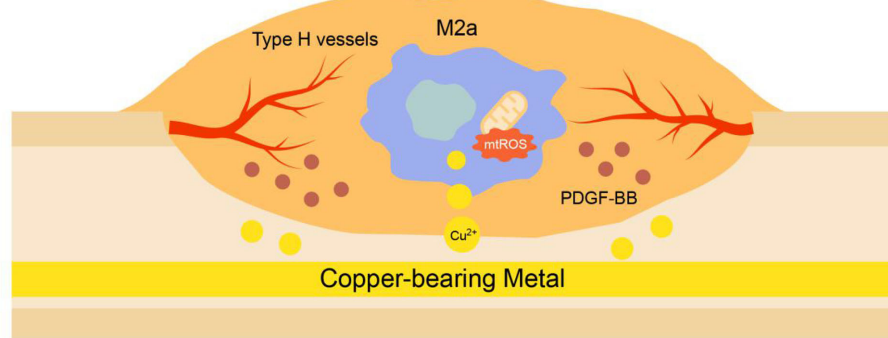
is favored for modification of the composition of orthopedic medical metals (Zhang et al., 2016). Another transition metal, copper, which is known to be an antibacterial agent, is noted for its promotion of osteogenesis and angiogenesis (Ren et al., 2012, 2015; Ryan et al., 2019). Our previous studies showed that copper-containing stainless steel promoted fracture healing by accelerating the process of callus evolution in a fracture model (Wang et al., 2015). In the research by Chen et al. (2020), focusing on the underlying mechanism, copper promoted the migration of bone marrow mesenchymal stem cells via Rnd3-dependent cytoskeleton remodeling; however, there was no involvement of angiogenesis. Hence, exploring whether copper participates in the coupling of osteogenesis and angiogenesis in bone regeneration could enhance our understanding of this mechanism.

The immune system protects the body by eradicating pathogenic microorganisms; however, its additional physiological and pathological roles in a variety of biological systems, including the musculoskeletal system, are being gradually discovered. Xie et al. (2014) demonstrated that PDGF-BB enhanced the formation of type H vessels and bone during bone modeling and remodeling. They showed that macrophages/non-resorbing osteoclast lineage cells are the main sources of PDGF-BB in bone marrow, which further recruits both endothelial and osteoblast precursor cells, thereby coupling angiogenesis with osteogenesis. More specifically, Spiller et al. (2014) found that M2a macrophages marked with *CD206*^{high} secreted the most PDGF-BB *in vitro*, compared with M1 and M2c macrophages. The present study shows that copper-containing metal (CCM) promotes bone repair in a drilling hole injury model through enhancing the generation of type H vessels via recruiting and activating infiltrating M2a macrophages in callus.

METHODS AND MATERIALS

Copper-Containing Stainless Steel

Copper-containing stainless steel was designed and fabricated by the addition of the appropriate amount of copper to medical



GRAPHICAL ABSTRACT | 316L–5Cu stainless steel promoted the evolution of callus through the generation of type H vessels in the process of bone repair by upregulating the expression of PDGF-BB derived from M2a macrophages, which contributes to the expression of mitochondria-derived reactive oxygen species due to copper stress.

stainless steel. The experimental materials used in this study included a previously reported 316L–5Cu stainless steel with a nominal chemical composition (wt%) of Cr 19, Ni 13, Mo 3.5, Cu 4.5, and Fe in balance, which was obtained by vacuum induction melting. Purchased medical-grade 316L stainless steel was used for comparison (Ren et al., 2012, 2015). Samples were cut from forged bars into disks of 1 mm thickness and small disks of 5 mm diameter and 1 mm thickness for use in the *in vitro* experiments. Intramedullary nails, which were used to create tibia injury in C57 mice *in vivo*, were processed by cold-drawing 316L–5Cu stainless steel to 0.45 mm diameter and then cut into 9-mm lengths. All the experimental steels with single austenitic structures were solution treated at 1,050°C for 0.5 h, followed by water quenching, and then aged at 700°C for 6 h to achieve Cu-rich precipitation in the 316L–5Cu stainless steel; this was expected to promote the release of Cu ions from the surface of the steel. All the samples were ground with SiC sand papers up to grade 2000#, soaked in absolute ethanol, cleaned with ultrasonic and deionized water, and finally sterilized at 121°C prior to use in experiments.

Preparation of Extracted Medium and Polarized Macrophage Culture

Each steel sample was placed in one well of a 24-well culture plate. Sugar-rich Dulbecco's modified Eagle's medium (DMEM) was dropped onto the samples (1 ml medium per 3 cm² surface area of experimental material), followed by incubation at 4°C for 72 h. The media cocultured with the steel samples were extracted and collected.

RAW264.7 cells were purchased from Cyagen Biosciences (China). High-glucose DMEM (Life Technologies, USA) containing 1% (v/v) penicillin/streptomycin (Thermo, USA) and 10% fetal bovine serum (Thermo, USA) was used for culture of RAW cells. RAW cells were incubated at 37°C with 5% CO₂. Additional drugs, namely, Mito-TEMPO (a mitochondria-targeted ROS antagonist, 50 nM, Sigma), were added to the culture medium for 60 min before polarization.

Polarization was started by changing the culture medium for complete medium, 316L–5Cu extracted medium, or 316L extracted medium, supplemented with the following cytokines: 40 ng/ml recombinant murine interleukin (IL)-4 (PeproTech, 214-14) and 20 ng/ml recombinant murine IL-13 (PeproTech, 210-13) for M2a; and 40 ng/ml recombinant murine IL-10 (PeproTech, 210-10) for M2c. After 48 h of polarization, cells and culture supernatants were collected for further experiments.

Western Blotting

Total protein was extracted from RAW 264.7 cells using the same procedures as described in detail elsewhere (Santa et al., 2016). Briefly, raw cells were lysed using radioimmunoprecipitation assay (RIPA) lysis buffer (Thermo, 89901) containing proteinase inhibitors and phosphatase inhibitors (KeyGEN BioTECH, KGP250). The protein concentrations were determined using a bicinchoninic acid (BCA) protein assay kit (Thermo Fisher Scientific, 23,225). Subsequently, the phenol-ethanol supernatant was mixed with isopropanol to isolate proteins.

Equal amounts of protein and supernatants were separated by 12.5 or 15% sodium dodecyl sulfate polyacrylamide gel electrophoresis and transferred to 0.45 or 0.20 μm-pore polyvinylidene fluoride membranes (Merck Millipore, IPVH00010 or ISEQ00005). Membranes were incubated overnight with antibodies against CD163 (Abcam, ab182422), CD206 (Abcam, ab64693), PDGF-BB (Santa Cruz, sc365805), MMP9 (Abcam, ab38898), and β-actin (Cell Signaling technology, 2118). The membranes were then incubated with peroxidase-conjugated goat antirabbit immunoglobulin G (IgG) (h + l) secondary antibody (1:5,000) for 1 h. Protein signals were detected using an enhanced chemiluminescence kit (Cat. WBKLS0500, Millipore), and Western blot bands were examined and analyzed with a chemiluminescence instrument (Guangzhou Ewell Bio Technology Co. Ltd., China).

Animals and Surgical Procedure

Male C57BL/6 mice (10–12 weeks old) were housed at a controlled temperature (22 ± 1°C) with a light–dark cycle (7:00 am to 7:00 pm) and allowed food and water *ad libitum*. They were randomly divided into two evenly sized groups: a control (316L) group and a 316L–5Cu group. Mice were anesthetized, and hair was removed from the left hind limb. An incision was made on the skin over the medial aspect of the proximal tibia. Soft tissue was cleared from the distal end of the tibial crest, and a hole (0.8 mm in diameter) that penetrated through both the medial cortices and the intervening medulla was created in the bone using a 21-gauge needle. A stainless steel pin (316L or 316L–5Cu) with length of 8 mm and diameter of 0.45 mm was inserted into the tibial medullary cavity from the proximal tibia following skin closure.

The study design and procedures were entirely in accordance with the US National Research Council (2011). This study was approved by the Animal Ethics Committee of Nanfang Hospital, Southern Medical University.

Microcomputed Tomography

After being fixed in 10% formalin solution for 12 h at 4°C, microcomputed tomography (μCT) scanning was performed (Scanco Medical, AG, Switzerland) with X-ray energy of 55 kVp and a current of 145 mA, voxel size of 9 μm, and an integration time of 400 ms. The scanned images were reconstructed with NRecon (v1.6), and the data were analyzed using CTAn (v1.9) and three-dimensional model visualization software (μCTVol v2.0). A sequence of images within the bone defect were chosen for analysis. Three-dimensional histomorphometric analysis was performed using longitudinal images of the tibia. The region of interest was set as the cylindrical region bordered by the defect edge. The three-dimensional structural parameter of bone volume to tissue volume ratio was analyzed.

Histological, Immunohistochemistry, and Immunofluorescence Analysis

Mice (*n* = 12 per group) were sacrificed, and tibia specimens were harvested at days 7, 14, and 21 postinjury for observation of the histological and histochemical alterations after injury.

After being fixed in 10% formalin solution for 12 h at 4°C, the specimens were decalcified in 10% ethylenediaminetetraacetic acid (EDTA) (Sigma) solution for 4.5 days. Two incisions, parallel with the major axis of the drilling hole, were made on the ventral and dorsal sides of the tibia, respectively. At the crevice of the incisions, the bone tissue surrounding the implant was carefully divided into two parts and forced apart from the implant surface, minimizing the damage to the interface tissues.

Samples were immersed in 30% (w/v) sucrose in 0.1 M phosphate buffer (pH 7.3) overnight at 4°C, embedded in paraffin ($n = 6$) and optimal cutting temperature compound ($n = 6$, Sakura Finetek), and then cut into 6 μm thick sections longitudinally for hematoxylin and eosin (H&E) and immunohistochemical staining, and 10 μm thick sections in a cryostat (Leica CM1800; Heidelberg, Germany) for immunofluorescence staining.

For H&E staining, some of the sections obtained previously were preheated in an air oven at 60°C, followed by deparaffinization and rehydration in xylene and ethanol solutions (reducing concentrations of 100 to 70%). The sections were then successively soaked in H&E dyes. After dehydration with graded alcohol, histological observation was performed using a microscope (BX63, Olympus, Tokyo, Japan), and the fracture healing process was evaluated.

Immunohistochemical staining was performed on the deparaffinized and rehydrated sections as described previously, with specific primary antibody (rabbit anti-CD206; ab64693, Abcam 1:200, UK). All the sections were counterstained using Mayer's hematoxylin (Sigma-Aldrich) and mounted using a permanent mounting medium (Thermo Fisher Scientific, Waltham, MA, USA). Quantification of positive cell numbers within the injury site was carried out on 4 μm serial sections stained for CD206 expression. Three representative images ($\times 40$ magnification) were taken within the intramedullary injury zone for each sample at two sectional depths at least 50 μm apart. The number of CD206+ cells was quantified by counting each positively stained cell in each field of view.

Frozen sections embedded in optimal cutting temperature (OCT) were processed for immunofluorescence staining of Emcn, CD31, F4/80, CD163, CD206, and PDGF-BB. Sections were incubated in blocking buffer (10% goat serum in phosphate-buffered saline; PBS) for 1 h at room temperature and incubated with primary antibodies overnight at 4°C. The following primary antibodies were used for immunostaining: rat anti-CD206 (Emcn, SC-65495, Santa Cruz, 1:50, US), rabbit anti-CD31 (ab222783, Abcam, 1:50, UK), rat anti-F4/80 (71299, Cell Signaling Technology, 1:500, USA), rabbit anti-CD206 (ab64693, Abcam 1:200, UK), rabbit anti-CD163 (ab182422, Abcam, 1:200, UK), and mouse anti-PDGF-BB (sc-365805, Santa Cruz, 1:50, USA). Sections were washed three times in PBS and then incubated with secondary antibodies at room temperature for 1 h. The following secondary antibodies were used for immunostaining: Alexa Fluor 594-conjugated goat anti-rabbit IgG (8889, Cell Signaling Technology, USA), Alexa Fluor 488-conjugated goat anti-rat IgG (4416, Cell Signaling Technology, USA), and 594-conjugated goat anti-mouse

(HA1112, HuaBio, China). Nuclei were counterstained with 4',6-diamidino-2-phenylindole (DAPI) (S2110, Solarbio, China). All the sections were observed under a BX63 microscope (Olympus, Tokyo, Japan).

Quantitative analysis was carried out using three representative images ($\times 40$ magnification) taken within the intramedullary injury zone for each specimen at three sectional depths at least 50 μm apart. The number of positive cells was quantified by counting each positively stained cell in each field of view.

Mitochondrial Potential Detection Using Mitotracker Green and Mitotracker Orange

By combining both Mitotracker Green (MTG) and Mitotracker Orange (MTO) (Invitrogen, CA, USA), the relative mitochondrial potential with its mitochondrial mass as baseline can be obtained (Agnello et al., 2008). Polarized and pretreated RAW264.7 cells were seeded in six-well chamber slides and grown to 50–70% confluence. After washing twice with warm $1\times$ PBS, cells were stained with 100 μM MTG, 500 μM MTO, and Hoechst 33324 (HuaBio, China) in DPBS + Ca/Mg/glucose to maintain their normal metabolic state. Cells were then incubated for 45 min at 37°C under standard culture conditions. The u-slide was then transferred to a confocal microscopic station with a 37°C heated chamber supplied with 5% CO_2 for live cell imaging. Tile scan images were captured randomly using the same TCS-SP2 confocal microscopy system (Leica Microsystem, Nussloch GmbH, Germany) with sequential detection for both stains. The fluorescence intensities of MTO (excitation/emission, 554/576 nm) and MTG (excitation/emission, 490/516 nm) were measured. For five samples from each group, a total of 20 different microscopic fields per sample, containing comparable numbers of cells, were integrated to obtain fluorescence mean pixel intensity values. The ratio of MTO/MTG intensities was then calculated and denoted the mean index of MTO/MTG, reflecting the relative mitochondrial potential.

Mitochondrial ROS Assay

To determine mitochondrial superoxide production, polarized and pretreated RAW 264.7 cells were incubated for 30 min with 100 μM MitoSOX dye (Thermo Fisher Scientific, M36008) and Hoechst 33324 diluted in cell imaging solution (10 mM HEPES, 1 mg/ml bovine serum albumin, 1 mg/ml glucose, 1 mM MgCl_2 , and 1.8 mM CaCl_2 in PBS) at 37°C in a humidified atmosphere containing 5% CO_2 . Then, cells were washed with PBS. The fluorescence was read using a SpectraMax i3x microplate reader at 510/580 nm, and the cell number in each well was determined using a SpectraMax MiniMax 300 imaging cytometer. Fluorescence values were first normalized to the cell number in each well; then, all the conditions for each genotype were normalized to the non-treated control group.

Statistical Analysis

Statistically significant differences were determined using unpaired *t*-tests with one- or two-tailed distributions using

PRISM 7 (GraphPad software, La Jolla, CA, USA). A value of $p < 0.05$ was deemed statistically significant. In all cases, data are represented as mean \pm standard error of the mean (SEM).

RESULTS

CCM Promotes the Expression of PDGF-BB in M2a Macrophages

M2a and M2c, two subtypes of macrophages, are known to be closely associated with angiogenesis, linked by IL4, IL13, and IL10 (Wu et al., 2013; Spiller et al., 2014). To identify the subtype with the major role under CCM stimulation, Western blotting was performed on M2 macrophages *in vitro*. Upon copper stimulation, M2a cells with high expression of

CD206 and M2c cells with higher CD163 expression were detected. The expression levels of PDGF-BB and CD206 were higher in M2a macrophages stimulated by 316L–5Cu extract (Figure 1A), and CD206 and CD163 were identified in this distinct type of macrophage (Figures 1A,B). Notably, the expression levels of MMP9 and CD163 showed no difference between the 316L and 316L–5Cu groups (Figure 1B), indicating that M2a macrophages predominantly promoted the expression of PDGF-BB under the stimulation of 316L–Cu extract.

The Callus Formation Process of Bone Repair Is Accelerated by CCM

To determine the role of M2a macrophages in bone regeneration, a tibia drilling hole injury model in C57BL/6 mice was

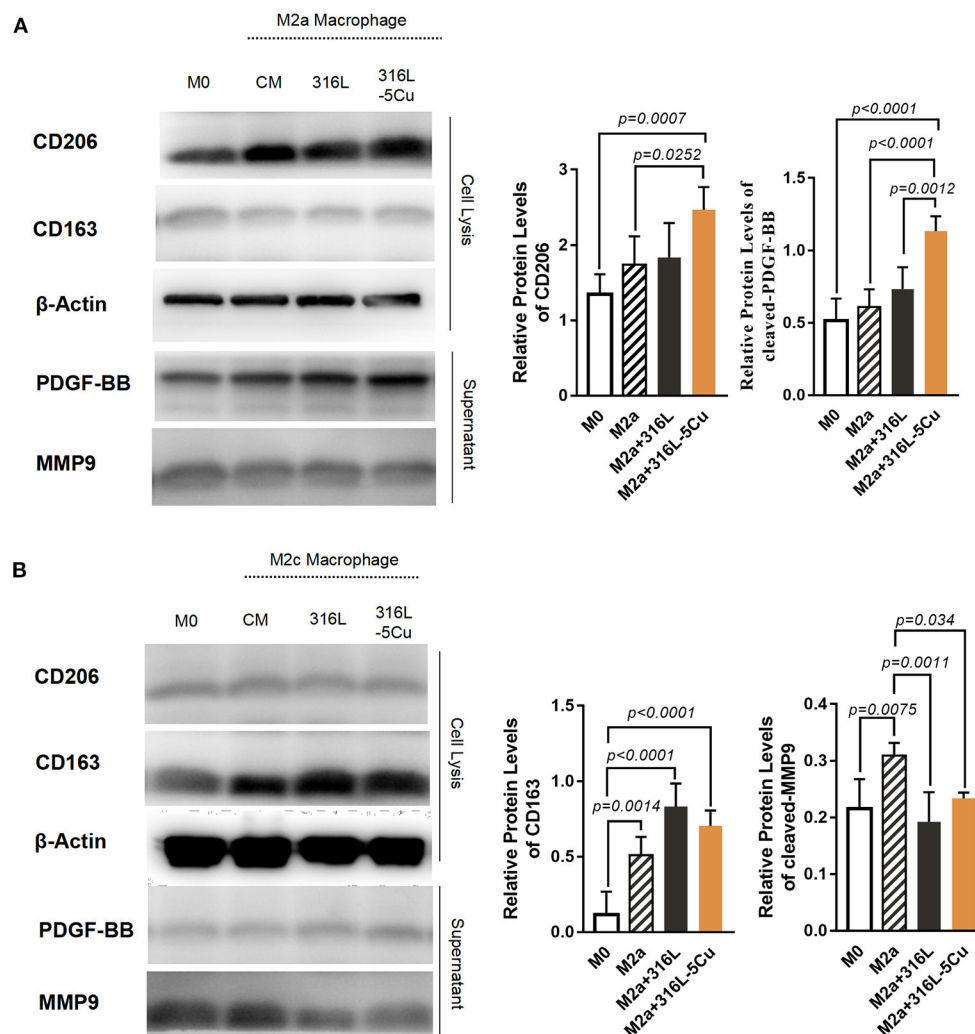


FIGURE 1 | Copper-containing metal (CCM) promoted the expression of platelet-derived growth factor type BB (PDGF-BB) in M2a macrophages. Western blotting was performed to examine the expression levels of CD206, CD163, PDGF-BB, and MMP9 in the following macrophages: M0, M2a, M2c, M2a with 316L, M2c with 316L, M2a with 316L–5Cu, and M2c with 316L–5Cu. β-Actin from cell lysis was used as a loading control. **(A)** Representative images of Western blots and quantification of relative protein levels of CD206 and PDGF-BB in M2a macrophages. **(B)** Representative images of Western blots and quantification of relative protein levels of CD163 and MMP9 in M2c macrophages. Data were statistically analyzed by Student's *t*-test. Results are presented as mean \pm SEM. $n = 5$.

established, and the closure degree of the drilling hole was measured and assessed by μ CT and histomorphological procedures. The model was established by inserting 316L–5Cu/316L pins into the bone marrow cavity of the injured tibia as intramedullary nails. Formation of new cortical bone in the drilling hole was faster in the 316L–5Cu group than in the 316L group at days 14 and 21 (**Figure 2A**). The bone mineral content within the drill hole was almost 2-fold higher in the 316L–5Cu group compared with the 316L group at day 21 (**Figure 2B**). Using H&E staining, no difference was observed in the callus between the two groups at day 7, whereas the formation of cortical bone callus in the 316L–5Cu group was accelerated at the later stage. New and integral cortical bones were observed in the 316L–5Cu group, covering the top of the drilling hole on day 21 (**Figure 2A**).

Type H vessels have been reported to participate in bone fracture healing (Stefanowski et al., 2019). In the drilling hole injury model, expression levels of Emcn and CD31 were examined; these are markers of generation of type H vessels

in immunofluorescence-stained tissue slices. Emcn+CD31+ immunofluorescence staining was observed on the bone callus; this was more intense from days 7 to 21 in the 316L–5Cu group, indicating the generation of type H vessels (**Figures 3A,B**). These signals were located particularly beneath the new cortical bone at day 21. These results show that 316L–5Cu significantly accelerated the formation of callus, accompanied by promotion of the generation of type H vessels.

CCM Promotes Infiltration of CD206+M2a Macrophages into Callus During Bone Repair

Macrophages have been shown to infiltrate into the callus and periosteum during the healing of bone fractures; in particular, CD206+ M2 macrophages were primarily assembled in the periosteum, with very few present in the fracture gap at day 14 in a bone fracture model (Stefanowski et al., 2019). According to our results, CD206+ cells in both groups were located in the callus around the newly formed bone between the hole

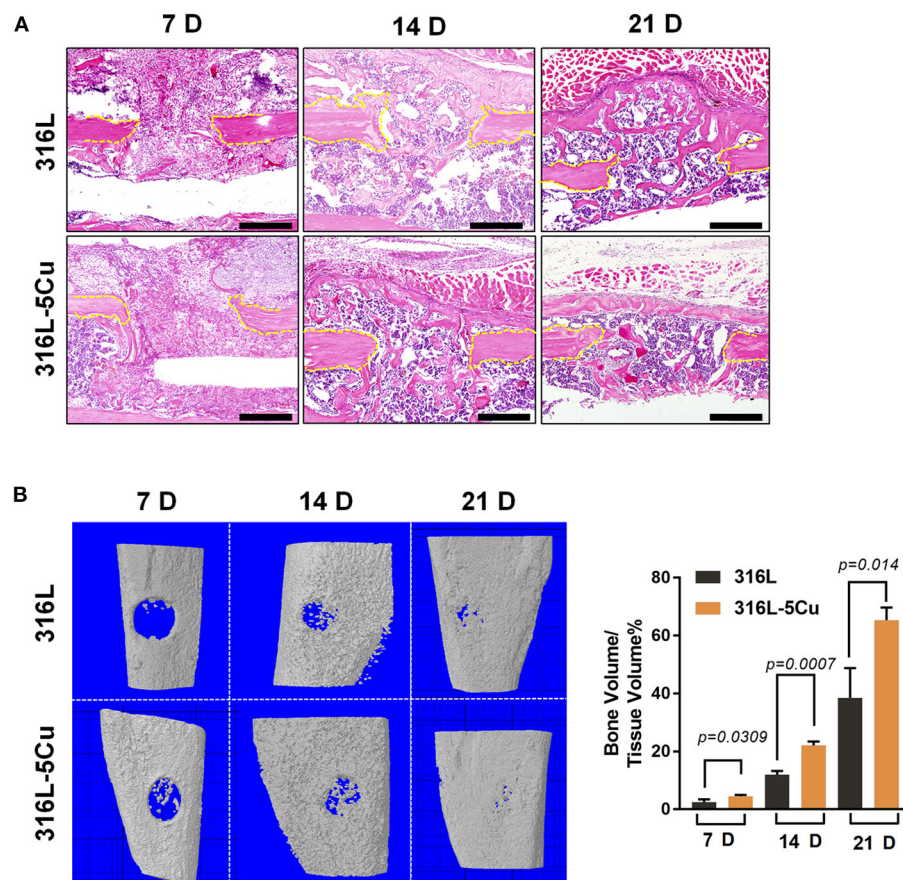
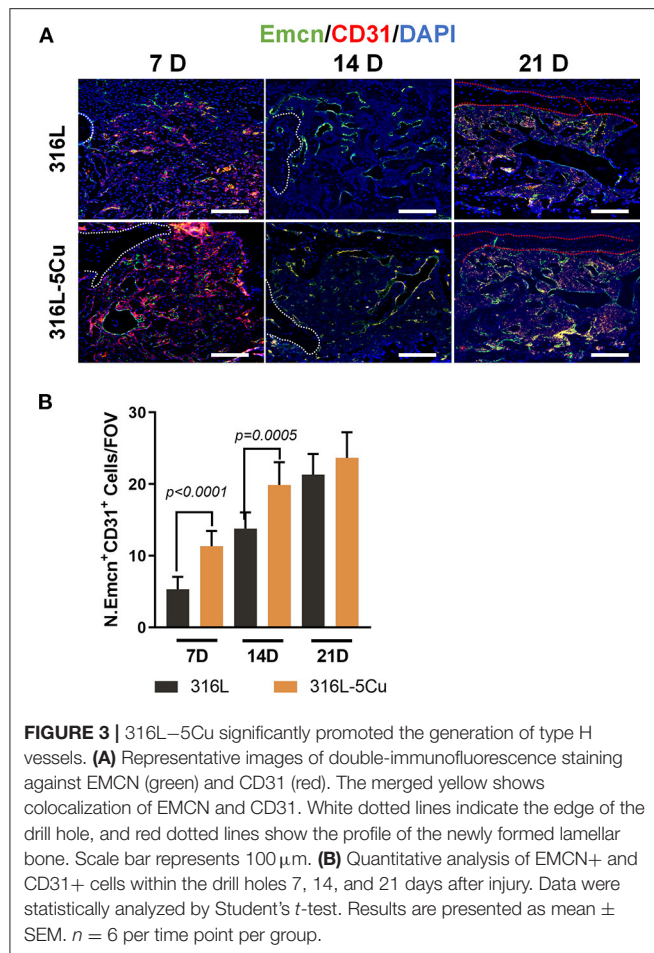


FIGURE 2 | Copper-containing metal (CCM) accelerated callus formation in bone repair. **(A)** HandE-stained histological images of the tibia of 316L/316L–5Cu-inserted mice 7, 14, and 21 days after injury. Yellow dotted lines indicate the edge of the drill hole. Scale bar represents 200 μ m.

(B) Three-dimensional microcomputed tomography (μ CT) images of the drill holes in 316L/316L–5Cu-inserted mice 7, 14, and 21 days after injury. The ratio of bone volume to tissue volume (BV/TV), representing bone formation in the drill holes, was calculated. Data were statistically analyzed by Student's *t*-test. Results are presented as mean \pm SEM. *n* = 6 per time point per group.



gaps. Furthermore, a significant increase in CD206+ cells was observed in the callus of the 316L-5Cu group (Figure 4A). We further detected CD163+ cells (also known as M2c macrophages) with an association with angiogenesis by immunohistochemistry and immunofluorescence. Few CD163+ cells were found during the process of bone regeneration by immunohistochemistry (data not published), but it was notable that a few 163+ (M2c) macrophages were located in hole gaps and in the bone marrow cavity, especially near the endosteum. There was no difference between the two groups (Figure 4C). We further detected the relationship between the CD206 and F4/80 immunofluorescence signals; coexpression of CD206 and F4/80 indicates M2a macrophages. From days 7 to 21, coexpression of CD206 and F4/80 exceeded 70% of the whole CD206 signal in the 316L-5Cu group and was significantly higher than 316L at days 7 and 14 (Figure 4E). The coexpression of the above two signals was also higher in the 316L-5Cu group compared with the 316L group during the bone regeneration process (Figure 4D). CD206+ M2a macrophages were found mainly in the callus of the drilling hole in the early stage (day 7) and around the surface of the newly formed bone (day 14). In the later stage, cells were observed beneath the new cortical bone (day 21), indicating a close relationship between M2a macrophages and newly formed cortical bone (Figure 4B).

Copper Induced the Formation of Type H Vessels Activated by M2a-Macrophage-derived PDGF-BB

PDGF-BB, which is secreted by M2a macrophages and TRAP+ preosteoclasts, is critical for enhancing the formation of type H vessels and bone during bone modeling and remodeling (Xu et al., 2018). We examined PDGF-BB in callus (Figure 5A) and found that it showed significantly higher expression in the 316-5Cu group than in the 316L group at days 14 and 21 and that it was located in the F4/80+ macrophages beneath the new cortical bone (Figures 5A,B). At day 7, no difference in PDGF-BB expression in callus was found between the 316L-5Cu and 316L groups. These results indicate that the M2a macrophages secreted PDGF-BB in the revolution process of bone regeneration, which was promoted by 316-5Cu.

High Levels of Mitochondrial-Derived Reactive Oxygen Species Might Enhance CCM-Promoted Expression of PDGF-BB by M2a Macrophages

Low-concentration copper preparations have been reported to have promising immunomodulatory potential and to contribute to oxidative stress in macrophages (Videla et al., 2003; Steinborn et al., 2017; Zhao and Zhao, 2019). Mitochondrial-derived reactive oxygen species (mtROS) are believed to derive mainly from NADH dehydrogenase when there is a high NADH/NAD+ ratio in the mitochondrial matrix. The inhibitory effect of copper on NADH dehydrogenase has been demonstrated in adenine-copper complexes and chelating 2-valent copper complexes (Hammud et al., 2008; Roy et al., 2015). To determine the role of CCM in inducing PDGF-BB expression by M2a macrophages, the oxidative stress caused by copper in macrophages was detected. According to our results, inhibition of NADH dehydrogenase activity occurred in M2a macrophages in the 316L-5Cu group, compared with 316L and control group (Figure 6D). In addition, levels of mitochondrial potential (Figures 6A,E) and mtROS (Figures 6B,F) were significantly elevated in IL4- and IL13-induced M2a macrophages by 316L-5Cu. Furthermore, the elevation of PDGF-BB expression in M2a macrophages induced by 316L-5Cu was found to be inhibited by a selective mtROS inhibitor (Mito-TEMPO) (Figures 6C,G).

DISCUSSION

Bone injury disrupts vessels, leading to reduced nutrient supply at the injury site. Vascularization is pivotal to the success of complete and scar-free bone regeneration (Lienau et al., 2009). After bone injury, type H vessels evolve in the bone formation region and persist throughout the entire bone regeneration process. The phenotype of type H endothelial cell structure, which has been described in endochondral long bone growth, is also reflected in bone regeneration (Kusumbe et al., 2014; Ramasamy et al., 2014; Filipowska et al., 2017; Stefanowski et al., 2019). Our findings showed that CCM inserted into the bone marrow resulted in a significant acceleration of callus formation by promoting the generation of type H vessels. Thus,

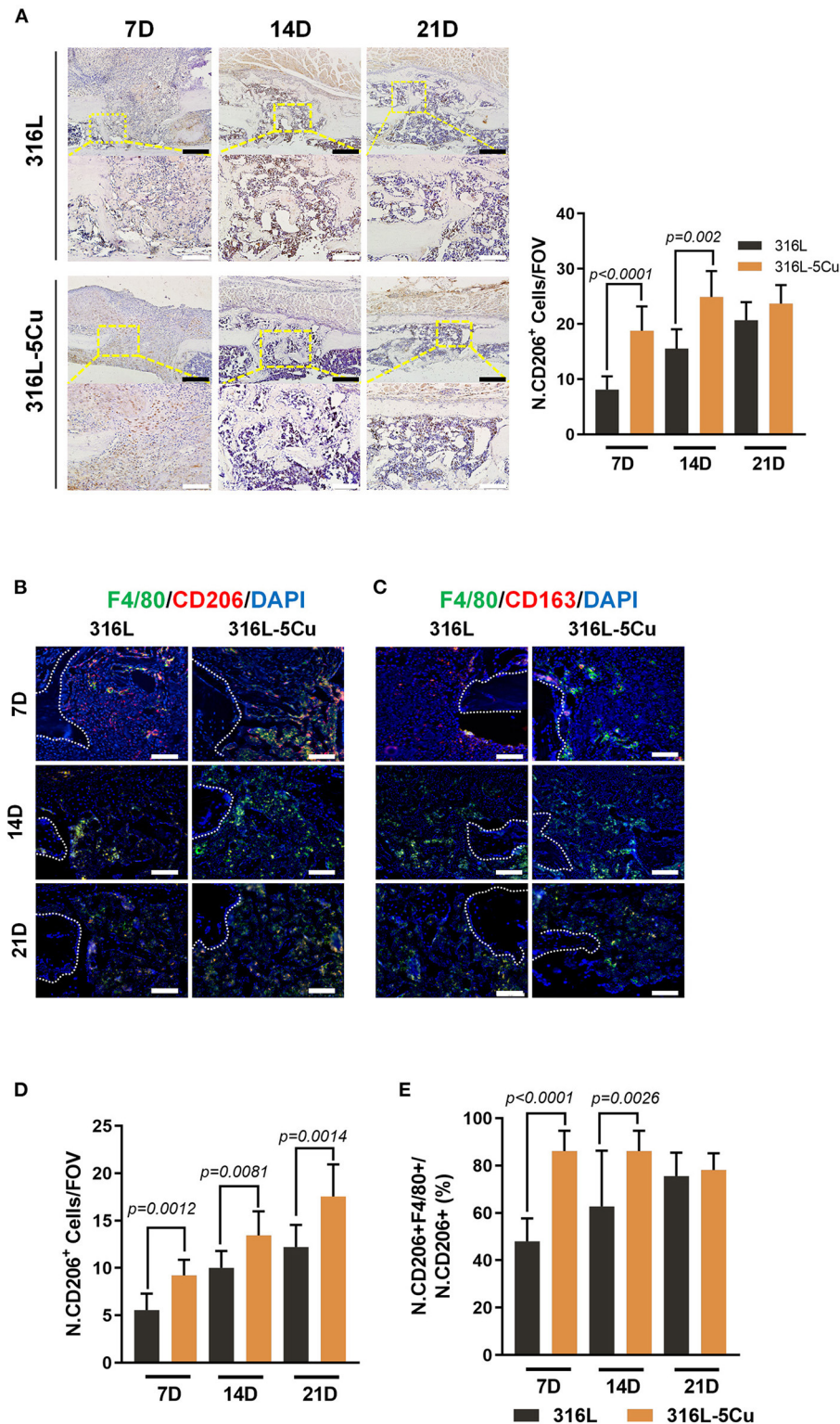
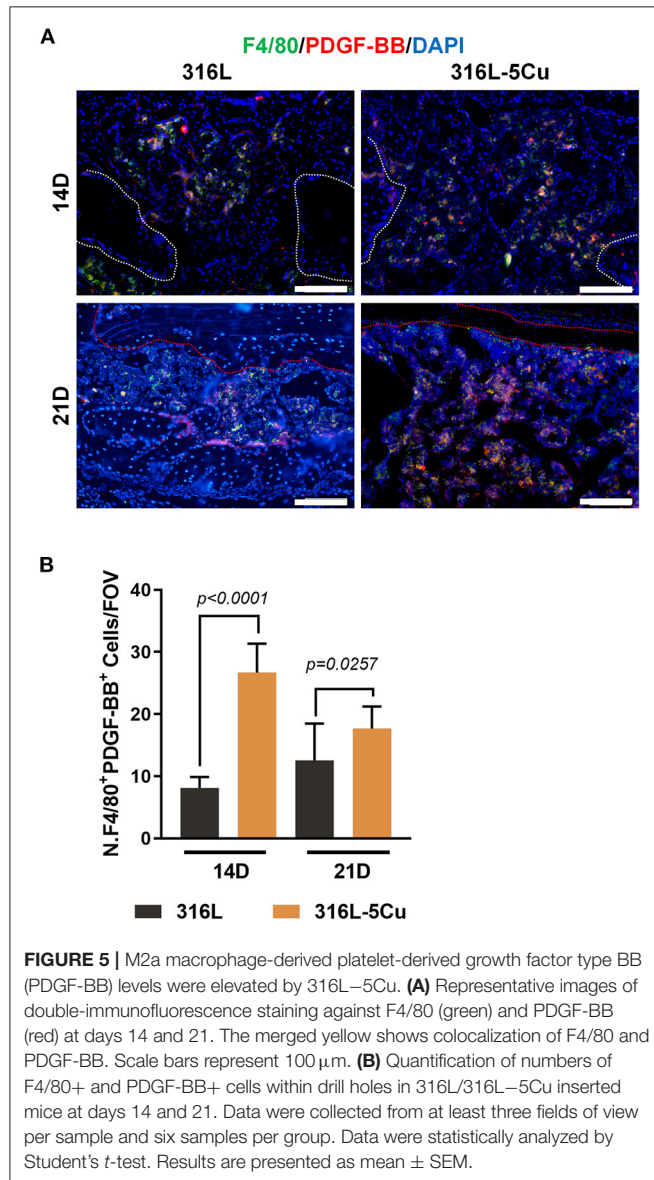


FIGURE 4 | Copper-containing metal (CCM) promoted infiltration of CD206⁺M2a macrophages into callus during bone repair. **(A)** Representative images of immunohistochemical staining and quantification of numbers of CD206⁺ cells within the drill holes in 316L/316L–5Cu-inserted mice at days 7, 14, and 21. Black and white scale bars represent 100 and 50 μ m. **(B)** Representative images of double-immunofluorescence staining against F4/80 (green) and CD206 (red). The merged yellow shows colocalization of F4/80 and CD206. **(C)** Representative images of immunofluorescence staining against F4/80 (green) and CD163 (red). The merged yellow shows colocalization of F4/80 and CD163. **(D)** Quantification of the number of CD206⁺ cells within the drill holes in 316L/316L–5Cu-inserted mice at days 7, 14, and 21. **(E)** Quantification of the ratio of CD206⁺ to F4/80⁺ cells within the drill holes in 316L/316L–5Cu-inserted mice at days 7, 14, and 21. *(Continued)*

FIGURE 4 | yellow shows colocalization of F4/80 and CD163. White dotted lines indicate the edges of the drill holes, and red dotted lines show the profile of the newly formed lamellar bone. White scale bar represents 100 μm . **(D)** Quantification of number of F4/80+ and CD206+ cells within the drill holes in 316L/316L–5Cu-inserted mice at days 7, 14, and 21. **(E)** Quantitative analysis of the fractions of F4/80+ and CD206+ cells within the drill holes in 316L/316L–5Cu-inserted mice at days 7, 14, and 21. All data were collected from at least three fields of view per sample and six samples per group. Data were statistically analyzed by Student's *t*-test. Results are presented as mean \pm SEM.



it appeared that copper also took advantage of angiogenesis in bone regeneration.

Macrophages are a heterogeneous group of cells that carry out distinct functions in different tissues; they also lie on, or close to, the outer (abluminal) surface of blood vessels and perform several crucial activities at this interface between the tissue and blood. In addition to adaptive immunity, the inflammatory innate immune response is a major regulator of vascularization through the activity of different types of macrophages and the cytokines secreted (Lapenna et al., 2018). Macrophages exist on

a spectrum of diverse phenotypes, from “classically activated” M1 to “alternatively activated” M2 macrophages (Murray et al., 2014). The M2a and M2c subsets that constitute M2 macrophages are typically considered to promote angiogenesis and tissue regeneration (Wang et al., 2017; Stefanowski et al., 2019). Lin’s research on the incorporation of Cu^{2+} into bioactive glass ceramics showed that copper ions considerably induced the transition to M2 polarization of macrophages *in vitro*, possibly via activating the hypoxia-inducible factor (HIF) signaling pathway. However, M2 polarization was only verified *in vitro*, and its mechanism was unclear. Among the M2 macrophages involved in angiogenesis, CD206+M2a macrophages are known to specifically secrete high levels of PDGF-BB, whereas M2c macrophages secrete high levels of MMP9, an important protease involved in vascular remodeling (Wu et al., 2013; Spiller et al., 2014). In the present study, the subset of CD206+ macrophages was proved to infiltrate into the callus and was located beneath the newly formed type H vessels in the 316L–5Cu group, whereas few CD206+ macrophages were found in the 316L group. These results were consistent with those reported by Stefanowski et al. (2019). CD163+ macrophages have been proven to play a part in angiogenesis in the liver and brain but have not been reported to have a role in bone injury (Etzerodt and Moestrup, 2013; Nielsen et al., 2020). Few CD163+ macrophages were found to be involved in the process of fracture healing in either group, suggesting that the association between CD163+ and angiogenesis in bone injury is not strong. Our findings indicate that CCM accelerated the formation of callus in bone regeneration via activating the expression of PDGF-BB derived from M2a macrophages.

The immunoregulatory effect of intracellular copper metabolism has been examined in several studies (Videla et al., 2003; Steinborn et al., 2017; Zhao and Zhao, 2019). Deigendesch et al. (2018) found that depriving intracellular copper transporters of copper ions inhibited inflammasome activation in macrophages, thereby regulating the immune phenotype of macrophages. The present study found that mtROS were pivotal to the beneficial effect of CCM on bone repair. mt-ROS are believed to originate from proton leakage, which occurs mostly in complexes I and III (Angajala et al., 2018). Two copper-containing complexes were proved to inhibit the activity of mitochondrial complex I (NADH-UQ-reductase). In other work (not published), we found that bone infections treated with CCM also showed inhibition of NADH, resulting in an increase in mtROS. In this study, we found a similar upregulation of mtROS induced by copper in M2a macrophages, which promoted the expression of PDGF-BB. The increased PDGF-BB expression induced by copper was reduced by Mito-TEMPO, further confirming our results.

In our previous studies, the copper-containing stainless steel, 316L–5Cu, possessed a typical austenitic microstructure, have

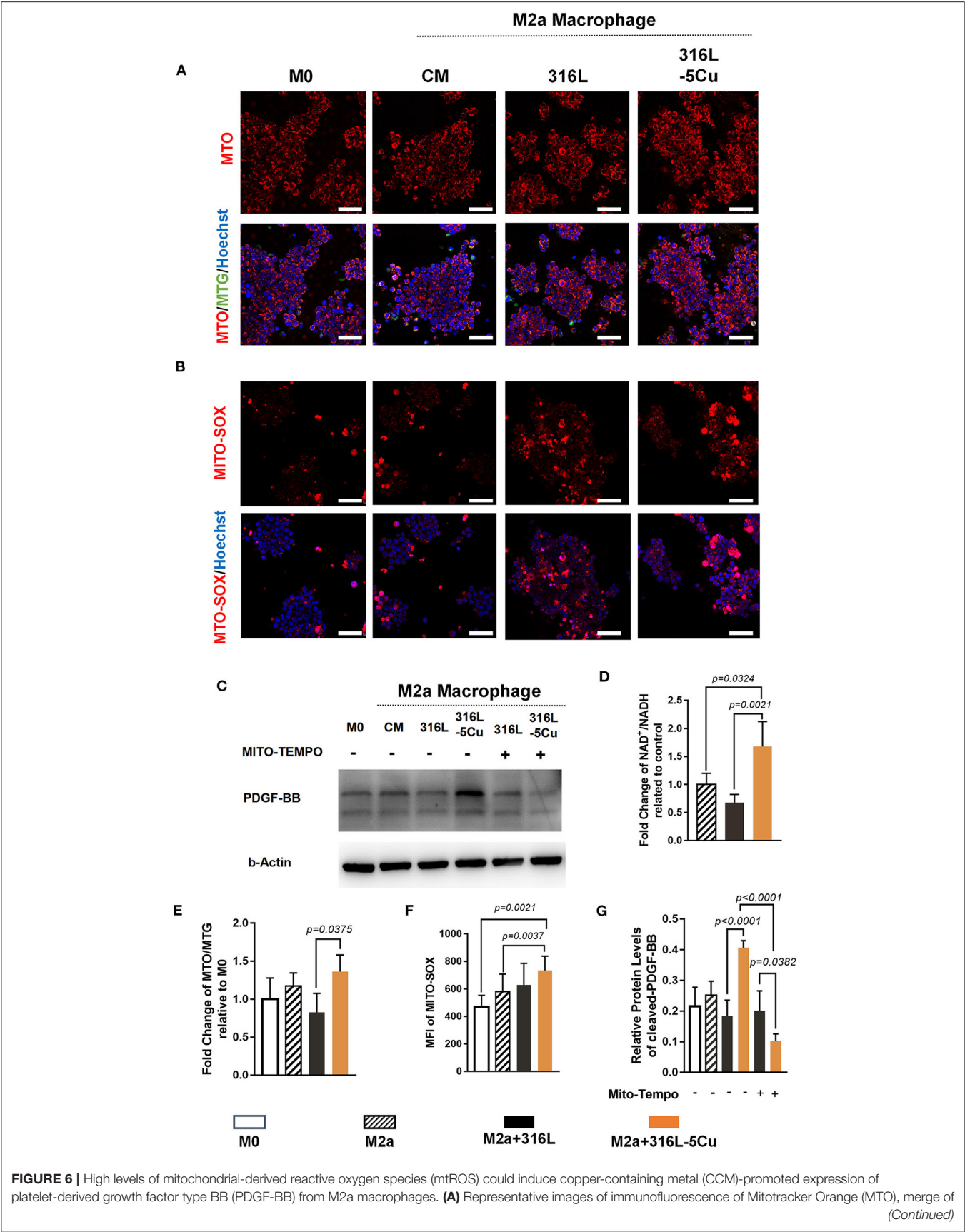


FIGURE 6 | MTO/Mitotracker Green (MTG)/Hoechst 33324 of M0 macrophages and M2a macrophages pretreated with vehicle (complete medium), 316L, and 316L–5Cu extract, respectively. **(B)** Representative images of immunofluorescence of MitoSOX, merge of MitoSOX/Hoechst 33324 of M0 and M2a macrophages pretreated with vehicle (complete medium), 316L, and 316L–5Cu extract, respectively. Scale bars in **(A,B)** represent 50 μm . **(C)** Western blotting was performed to examine levels of PDGF-BB in medium of M0 and M2a macrophages pretreated with vehicle, 316L, and 316L–5Cu. In addition, M2a macrophages pretreated with 316L and 316L–5Cu were further prestimulated with 50 nM Mito-TEMPO for 60 min before macrophage polarization. **(D)** Quantitative analysis of NADH/NAD⁺ in M2a macrophages pretreated with vehicle, 316L, and 316L–5Cu extract, respectively. Data were statistically analyzed by Student's *t* test. Results are presented as mean \pm SEM. *n* = 5. **(E)** Quantification of fluorescence intensity of MTO/MTG based on the cell count, representing mitochondrial potential. **(F)** Quantification of mean fluorescence intensity (MFI) of MitoSOX based on the cell count, which was represented by mtROS. **(G)** Data were statistically analyzed by Student's *t*-test. Results are presented as mean \pm SEM. *n* = 5.

been proven to have the stable precipitating behavior *in vitro*, the release rate of copper ions was 5.079 ng/cm²/day over 28 days *in vitro* (Sun et al., 2016; Yang et al., 2017). Our other study showed that there was a significant increase in Cu²⁺ content in the bone calluses of the copper-containing stainless steel at 3, 6, and 9 weeks, but in serum. Over all, the Cu ions release from the steel was measured to be very tiny, <10 ppb/day (Wang et al., 2017).

Like the study of biochemical reagents, immunoregulation of copper-containing metal has become an important target in research on the use of biomaterials in bone disease (Dukhinova et al., 2019). In the past few years, the development direction of biomaterials engineering has shifted from “immune evasive” to “immune interactive,” with a focus on modulating the inflammatory response and promoting tissue regeneration (Taraballi et al., 2018). The effects on angiogenesis and osteogenesis of copper-containing biomaterials are continuously followed in bone diseases. Recently, the immunoregulatory effect of copper was reported in several studies (Lin et al., 2019; Liu et al., 2019). This study was the first to establish the links among immunoregulation, angiogenesis, and osteogenesis induced by copper-containing biomaterials in bone repair.

Taken together, these results demonstrate that formation of type H vessels was promoted during bone regeneration by the application of 316L–5Cu to drilling hole models in mice. CD206+ M2a macrophages in callus beneath the newly formed cortical bone were elevated by 316L–5Cu. The important crosstalk between M2a macrophages and vascularization was confirmed to be mediated by PDGF-BB. In addition, the promotion of PDGF-BB expression in M2a macrophages by CCM might have been induced by high levels of mtROS resulting

from the inhibition of NADH dehydrogenase. Our findings underline the importance of CCM in the bone regeneration process by linking the innate immune response in bone repair to local angiogenesis.

DATA AVAILABILITY STATEMENT

The datasets presented in this study can be found in online repositories. The names of the repository/repositories and accession number(s) can be found in the article/supplementary material.

ETHICS STATEMENT

The animal study was reviewed and approved by Ethics Committee of Nanfang Hospital of Southern Medical University.

AUTHOR CONTRIBUTIONS

BY, KY, and XZ designed the research. DX analyzed the data. LR and SZ prepared the materials. DX, JQ, XG, XH, XW, and HW performed the research. DX, XG, and KY wrote the paper. BY and XZ supervised the experiments and revised the manuscript. All authors contributed to the article and approved the submitted version.

FUNDING

This work was supported by The Major Program of National Natural Science Foundation of China (81830079) and the National Natural Science Foundation of China (31870954 and 81702009).

REFERENCES

- Agnello, M., Morici, G., and Rinaldi, A. M. (2008). A method for measuring mitochondrial mass and activity. *Cytotechnology* 56, 145–149. doi: 10.1007/s10616-008-9143-2
- Angajala, A., Lim, S., Phillips, J. B., Kim, J. H., Yates, C., and You, Z., et al. (2018). Diverse roles of mitochondria in immune responses: novel insights into immuno-metabolism. *Front Immunol.* 9:1605. doi: 10.3389/fimmu.2018.01605
- Chen, X., Hu, J. G., Huang, Y. Z., Li, S., Li, S. F., and Wang, M., et al. (2020). Copper promotes the migration of bone marrow mesenchymal stem cells via Rnd3-dependent cytoskeleton remodeling. *J. Cell. Physiol.* 235, 221–231. doi: 10.1002/jcp.28961
- Deigendesch, N., Zychlinsky, A., and Meissner, F. (2018). Copper regulates the canonical NLRP3 inflammasome. *J. Immunol.* 200, 1607–1617. doi: 10.4049/jimmunol.1700712
- Dukhinova, M. S., Prilepskii, A. Y., Shtil, A. A., and Vinogradov, V. V. (2019). Metal oxide nanoparticles in therapeutic regulation of macrophage functions. *Nanomaterials* 9:1631. doi: 10.3390/nano9111631
- Etzerodt, A., and Moestrup, S. K. (2013). CD163 and inflammation: biological, diagnostic, and therapeutic aspects. *Antioxid. Redox Signal* 18, 2352–2363. doi: 10.1089/ars.2012.4834
- Filipowska, J., Tomaszewski, K. A., Niedzwiedzki, L., Walocha, J. A., and Niedzwiedzki, T. (2017). The role of vasculature in bone development, regeneration and proper systemic functioning. *Angiogenesis* 20, 291–302. doi: 10.1007/s10456-017-9541-1

- Hammud, H. H., Nemer, G., Sawma, W., Touma, J., Barnabe, P., and Bou-Mouglabey, Y., et al. (2008). Copper-adenine complex, a compound, with multi-biochemical targets and potential anti-cancer effect. *Chem. Biol. Interact.* 173, 84–96. doi: 10.1016/j.cbi.2008.03.005
- Hernandez, R. K., Do, T. P., Critchlow, C. W., Dent, R. E., and Jick, S. S. (2012). Patient-related risk factors for fracture-healing complications in the United Kingdom General Practice Research Database. *Acta Orthop.* 83, 653–660. doi: 10.3109/17453674.2012.747054
- Inzana, J. A., Schwarz, E. M., Kates, S. L., and Awad, H. A. (2016). Biomaterials approaches to treating implant-associated osteomyelitis. *Biomaterials* 81, 58–71. doi: 10.1016/j.biomaterials.2015.12.012
- Kusumbe, A. P., Ramasamy, S. K., and Adams, R. H. (2014). Coupling of angiogenesis and osteogenesis by a specific vessel subtype in bone. *Nature* 507, 323–328. doi: 10.1038/nature13145
- Lapenna, A., De Palma, M., and Lewis, C. E. (2018). Perivascular macrophages in health and disease. *Nat. Rev. Immunol.* 18, 689–702. doi: 10.1038/s41577-018-0056-9
- Lienau, J., Schmidt-Bleek, K., Peters, A., Haschke, F., Duda, G. N., and Perka, C., et al. (2009). Differential regulation of blood vessel formation between standard and delayed bone healing. *J. Orthop. Res.* 27, 1133–1140. doi: 10.1002/jor.20870
- Lin, R., Deng, C., Li, X., Liu, Y., Zhang, M., Qin, C., et al. (2019). Copper-incorporated bioactive glass-ceramics inducing anti-inflammatory phenotype and regeneration of cartilage/bone interface. *Theranostics* 9, 6300–6313. doi: 10.7150/thno.36120
- Liu, W., Li, J., Cheng, M., Wang, Q., Qian, Y., Yeung, K. W. K., et al. (2019). A surface-engineered polyetheretherketone biomaterial implant with direct and immunoregulatory antibacterial activity against methicillin-resistant *Staphylococcus aureus*. *Biomaterials* 208, 8–20. doi: 10.1016/j.biomaterials.2019.04.008
- Murray, P. J., Allen, J. E., Biswas, S. K., Fisher, E. A., Gilroy, D. W., and Goerdts, S., et al. (2014). Macrophage activation and polarization: nomenclature and experimental guidelines. *Immunity* 41, 14–20. doi: 10.1016/j.immuni.2014.06.008
- Nielsen, M. C., Hvidbjerg, G. R., Claria, J., Trebicka, J., Moller, H. J., and Gronbaek, H. (2020). Macrophage activation markers, CD163 and CD206, in acute-on-chronic liver failure. *Cells* 9:1175. doi: 10.3390/cells9051175
- Parker, M. J., Raghavan, R., and Gurusamy, K. (2007). Incidence of fracture-healing complications after femoral neck fractures. *Clin. Orthop. Relat. Res.* 458, 175–179. doi: 10.1097/BLO.0b013e3180325a42
- Peng, Y., Wu, S., Li, Y., and Crane, J. L. (2020). Type H blood vessels in bone modeling and remodeling. *Theranostics* 10, 426–436. doi: 10.7150/thno.34126
- Ramasamy, S. K., Kusumbe, A. P., Wang, L., and Adams, R. H. (2014). Endothelial Notch activity promotes angiogenesis and osteogenesis in bone. *Nature* 507, 376–380. doi: 10.1038/nature13146
- Ren, L., Wong, H. M., Yan, C. H., Yeung, K. W., and Yang, K. (2015). Osteogenic ability of Cu-containing stainless steel. *J. Biomed. Mater. Res. Part B Appl. Biomater.* 103, 1433–1444. doi: 10.1002/jbm.b.33318
- Ren, L., Xu, L., Feng, J., Zhang, Y., and Yang, K. (2012). *In vitro* study of role of trace amount of Cu release from Cu-containing stainless steel targeting for reduction of in-stent restenosis. *J. Mater. Sci. Mater. Med.* 23, 1235–1245. doi: 10.1007/s10856-012-4584-8
- Romeo, S. G., Alawi, K. M., Rodrigues, J., Singh, A., Kusumbe, A. P., and Ramasamy, S. K. (2019). Endothelial proteolytic activity and interaction with non-resorbing osteoclasts mediate bone elongation. *Nat. Cell Biol.* 21, 430–441. doi: 10.1038/s41556-019-0304-7
- Roy, S., Mondal, P., Sengupta, P. S., Dhak, D., Santra, R. C., and Das, S., et al. (2015). Spectroscopic, computational and electrochemical studies on the formation of the copper complex of 1-amino-4-hydroxy-9,10-anthraquinone and effect of it on superoxide formation by NADH dehydrogenase. *Dalton Trans.* 44, 5428–5440. doi: 10.1039/C4DT03635B
- Ryan, E. J., Ryan, A. J., Gonzalez-Vazquez, A., Philippart, A., Ciraldo, F. E., and Hobbs, C., et al. (2019). Collagen scaffolds functionalised with copper-eluting bioactive glass reduce infection and enhance osteogenesis and angiogenesis both *in vitro* and *in vivo*. *Biomaterials* 197, 405–416. doi: 10.1016/j.biomaterials.2019.01.031
- Santa, C., Anjo, S. I., and Manadas, B. (2016). Protein precipitation of diluted samples in SDS-containing buffer with acetone leads to higher protein recovery and reproducibility in comparison with TCA/acetone approach. *Proteomics* 16, 1847–1851. doi: 10.1002/pmic.201600024
- Spiller, K. L., Anfang, R. R., Spiller, K. J., Ng, J., Nakazawa, K. R., and Daulton, J. W., et al. (2014). The role of macrophage phenotype in vascularization of tissue engineering scaffolds. *Biomaterials* 35, 4477–4488. doi: 10.1016/j.biomaterials.2014.02.012
- Stefanowski, J., Lang, A., Rauch, A., Aulich, L., Kohler, M., and Fiedler, A. F., et al. (2019). Spatial distribution of macrophages during callus formation and maturation reveals close crosstalk between macrophages and newly forming vessels. *Front. Immunol.* 10:2588. doi: 10.3389/fimmu.2019.02588
- Steinborn, C., Diegel, C., Garcia-Kaufer, M., Grundemann, C., and Huber, R. (2017). Immunomodulatory effects of metal salts at sub-toxic concentrations. *J. Appl. Toxicol.* 37, 563–572. doi: 10.1002/jat.3390
- Sun, D., Xu, D., Yang, C., Shahzad, M. B., Xia, J., Zhao, J., et al. (2016). An investigation of the antibacterial ability and cytotoxicity of a novel Cu-containing 317L stainless steel. *Sci. Rep.* 6:29244. doi: 10.1038/srep29244
- Taraballi, F., Sushnitha, M., Tsao, C., Bauza, G., Liverani, C., and Shi, A., et al. (2018). Biomimetic tissue engineering: tuning the immune and inflammatory response to implantable biomaterials. *Adv. Healthc. Mater.* 7:e1800490. doi: 10.1002/adhm.201800490
- Videla, L. A., Fernandez, V., Tapia, G., and Varela, P. (2003). Oxidative stress-mediated hepatotoxicity of iron and copper: role of Kupffer cells. *Biomaterials* 16, 103–111. doi: 10.1023/A:1020707811707
- Wang, L., Li, G., Ren, L., Kong, X., Wang, Y., Han, X., et al. (2017). Nano-copper-containing stainless steel promotes fracture healing by accelerating the callus evolution process. *Int. J. Nanomed.* 12, 8443–8457. doi: 10.2147/IJN.S146866
- Wang, L., Ren, L., Tang, T., Dai, K., Yang, K., and Hao, Y. (2015). A novel nano-copper-containing stainless steel with reduced Cu(2+) release only inducing transient foreign body reaction via affecting the activity of NF-kappaB and Caspase-3. *Int. J. Nanomed.* 10, 6725–6739. doi: 10.2147/IJN.S90249
- Wu, A. C., Raggatt, L. J., Alexander, K. A., and Pettit, A. R. (2013). Unraveling macrophage contributions to bone repair. *Bonekey Rep.* 2:373. doi: 10.1038/bonekey.2013.107
- Xie, H., Cui, Z., Wang, L., Xia, Z., Hu, Y., and Xian, L., et al. (2014). PDGF-BB secreted by preosteoclasts induces angiogenesis during coupling with osteogenesis. *Nat. Med.* 20, 1270–1278. doi: 10.1038/nm.3668
- Xu, R., Yallowitz, A., Qin, A., Wu, Z., Shin, D. Y., and Kim, J. M., et al. (2018). Targeting skeletal endothelium to ameliorate bone loss. *Nat. Med.* 24, 823–833. doi: 10.1038/s41591-018-0020-z
- Yang, K., Zhou, C., Fan, H., Fan, Y., Jiang, Q., Song, P., et al. (2017). Bio-functional design, application and trends in metallic biomaterials. *Int. J. Mol. Sci.* 19:24. doi: 10.3390/ijms19010024
- Zhang, Y., Xu, J., Ruan, Y. C., Yu, M. K., O'Laughlin, M., Wise, H., et al. (2016). Implant-derived magnesium induces local neuronal production of CGRP to improve bone-fracture healing in rats. *Nat. Med.* 22, 1160–1169. doi: 10.1038/nm.4162
- Zhao, H. J., and Zhao, X. H. (2019). Modulatory effect of the supplemented copper ion on *in vitro* activity of bovine lactoferrin to murine splenocytes and raw264.7 macrophages. *Biol. Trace Elem. Res.* 189, 519–528. doi: 10.1007/s12011-018-1472-1
- Zheng, Z. W., Chen, Y. H., Wu, D. Y., Wang, J. B., Lv, M. M., Wang, X. S., et al. (2018). Development of an accurate and proactive immunomodulatory strategy to improve bone substitute material-mediated osteogenesis and angiogenesis. *Theranostics* 8, 5482–5500. doi: 10.7150/thno.28315

Conflict of Interest: The authors declare that the research was conducted in the absence of any commercial or financial relationships that could be construed as a potential conflict of interest.

Copyright © 2021 Xu, Qian, Guan, Ren, Yang, Huang, Zhang, Chai, Wu, Wu, Zhang, Yang and Yu. This is an open-access article distributed under the terms of the Creative Commons Attribution License (CC BY). The use, distribution or reproduction in other forums is permitted, provided the original author(s) and the copyright owner(s) are credited and that the original publication in this journal is cited, in accordance with accepted academic practice. No use, distribution or reproduction is permitted which does not comply with these terms.



Functional Gradient Metallic Biomaterials: Techniques, Current Scenery, and Future Prospects in the Biomedical Field

Hongyuan Shi¹, Peng Zhou^{1*}, Jie Li¹, Chaozong Liu^{2*} and Liqiang Wang³

¹ School of Aeronautical Materials Engineering, Xi'an Aeronautical Polytechnic Institute, Xi'an, China, ² Institute of Orthopaedic & Musculoskeletal Science, University College London, Royal National Orthopaedic Hospital, London, United Kingdom,

³ State Key Laboratory of Metal Matrix Composites, Shanghai Jiao Tong University, Shanghai, China

OPEN ACCESS

Edited by:

Michel Assad,
Charles River Laboratories, Canada

Reviewed by:

Sergey V. Dorozhkin,
Independent Researcher,
Moscow, Russia
Joanna Mystkowska,
Bialystok University of
Technology, Poland

*Correspondence:

Peng Zhou
pzhou1975@163.com
Chaozong Liu
chaozong.liu@ucl.ac.uk

Specialty section:

This article was submitted to
Biomaterials,
a section of the journal
Frontiers in Bioengineering and
Biotechnology

Received: 13 October 2020

Accepted: 10 December 2020

Published: 18 January 2021

Citation:

Shi H, Zhou P, Li J, Liu C and Wang L
(2021) Functional Gradient Metallic
Biomaterials: Techniques, Current
Scenery, and Future Prospects in the
Biomedical Field.
Front. Bioeng. Biotechnol. 8:616845.
doi: 10.3389/fbioe.2020.616845

Functional gradient materials (FGMs), as a modern group of materials, can provide multiple functions and are able to well mimic the hierarchical and gradient structure of natural systems. Because biomedical implants usually substitute the bone tissues and bone is an organic, natural FGM material, it seems quite reasonable to use the FGM concept in these applications. These FGMs have numerous advantages, including the ability to tailor the desired mechanical and biological response by producing various gradations, such as composition, porosity, and size; mitigating some limitations, such as stress-shielding effects; improving osseointegration; and enhancing electrochemical behavior and wear resistance. Although these are beneficial aspects, there is still a notable lack of comprehensive guidelines and standards. This paper aims to comprehensively review the current scenery of FGM metallic materials in the biomedical field, specifically its dental and orthopedic applications. It also introduces various processing methods, especially additive manufacturing methods that have a substantial impact on FGM production, mentioning its prospects and how FGMs can change the direction of both industry and biomedicine. Any improvement in FGM knowledge and technology can lead to big steps toward its industrialization and most notably for much better implant designs with more biocompatibility and similarity to natural tissues that enhance the quality of life for human beings.

Keywords: implants, biomedicine, functional gradient material, additive manufacturing, graded structures

INTRODUCTION

Today's medicine desperately needs modern materials and methods that have multiple applications meeting different goals. In this regard, the biomedical field deals with technology development that helps to enhance the quality of human life; hence, each parameter is of crucial importance. The success of biomedical devices mostly depends on the materials used to make them; a variety of materials, including metals and their alloys, ceramics, composites (Zhu et al., 2018; Wang L. et al., 2019), and polymers, are used in the biomedical field. Moreover, implant design is the other significant factor; currently, there are many types of implant designs, and most of them are in an attempt to mimic the function of natural organs. Generally, each device consists of only one component with a unified structure. However, medical devices should meet some requirements,

such as biocompatibility, osseointegration, strength, corrosion, and abrasion resistance, low elastic modulus, fatigue durability, and chemical similarity with biological tissues, and the traditional designs may not satisfy these varied requirements (Ehtemam-Haghighi et al., 2016; Okulov et al., 2017; Wang S. et al., 2019). For instance, some devices can cause premature failure or failure after long-term use in the human body (Niinomi and Nakai, 2011; Liu et al., 2016); these issues stem from the fact that one or more basic mechanical or biological requirements are not fully met. Bone structure is always in a remodeling procedure, which makes it possible to react with its environment and stressors in this regard. According to Wolff's law, bone tissue is produced and strengthens in the direction of mechanical stress lines. Wolff's law clinically has been proven by the apparent fabrication of osteophytes around an arthritic joint and also by the occurrence of osteoporosis due to the stress-shielding effect (Burke and Goodman, 2008). The stress-shielding effect is the bone density reduction (osteopenia) that happens as a result of stress removal from the bone by an implant, specifically orthopedic implants, and it is a major problem leading to failure of the implant and increasing the cost of surgery (Zhang B. et al., 2018). Taking this information into account, the necessity to find modern solutions is urgent and leads to the development of functional graded materials (FGMs). This FGM concept is a promising method to control the stress-shielding effect. For example, both radial and axial FGM dental implants considerably reduced the stress-shielding effect in the periphery of bone tissue (Asgharzadeh Shirazi et al., 2017), and FGM utilization can also prevent this phenomena in femoral prostheses (Oshkour et al., 2013) and other biomedical implants. In this regard, Hedia and Fouda (2013) show that FGM material with vertical gradation of hydroxyapatite (HA) at the end of the stem tibia to collagen at the upper layers of the tibia plate can reduce the stress-shielding effect by 78%. Moreover, FGM materials can also withstand high sliding and contact forces (Suresh, 2001) and have better and stronger adhesion, shear bond strength, and fatigue properties (Matsuo et al., 2001; Henriques et al., 2012).

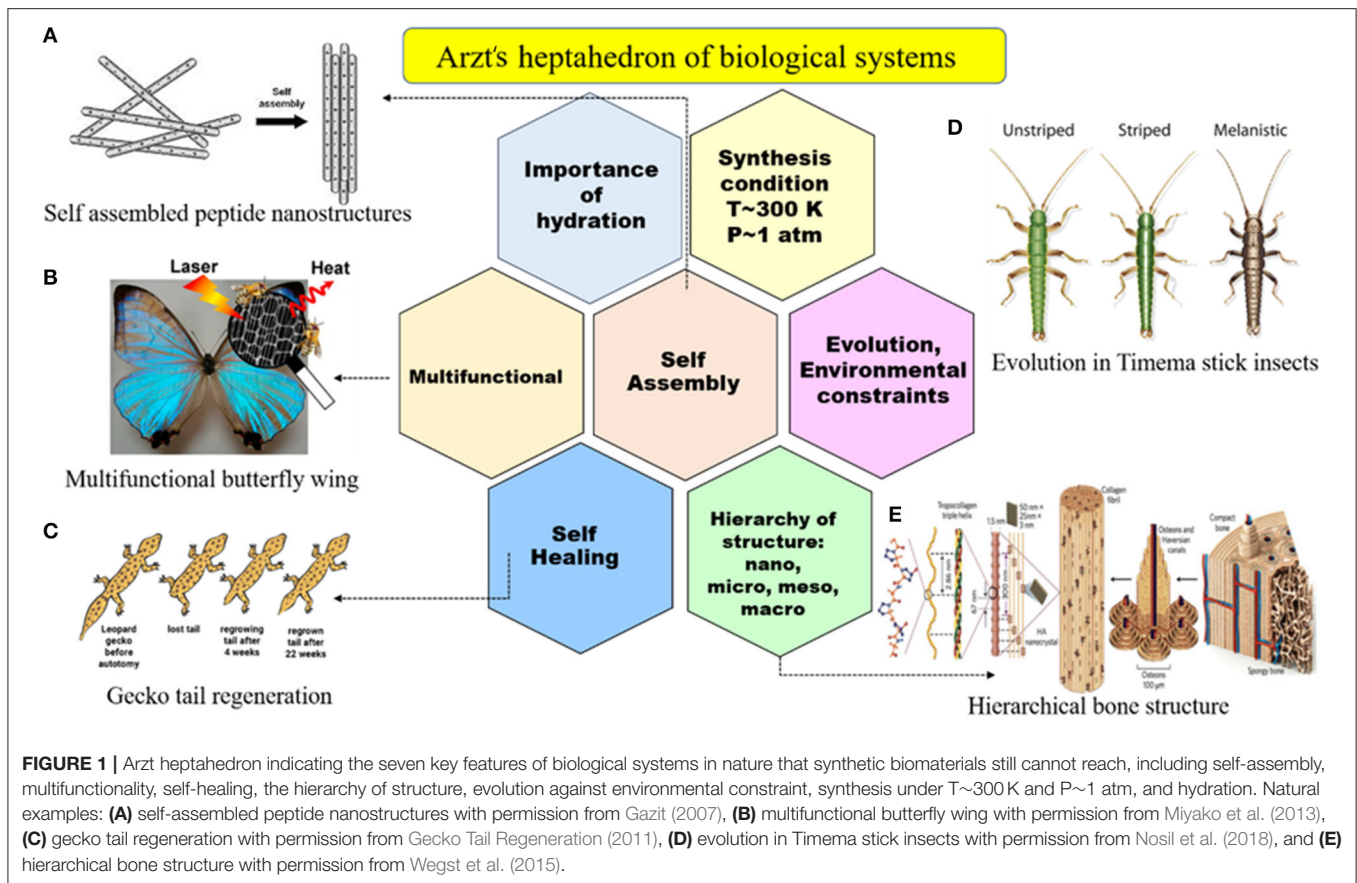
The FGM concept was first introduced during the 1980s by Japanese scholars, whose main goal was the reduction of thermal stresses in metallic-composite materials utilized in reusable rocket engines (Koizumi and Niino, 1995). Nowadays, there are lots of studies devoted to FGM design (Mohd Ali et al., 2020). Over time, the benefits of this concept were realized in the modern biomedical and tissue engineering field because one of the characteristics of living tissues and natural structures is their functional gradation that can be seen in bone (Wegst et al., 2015), the wings of various insects (Appel et al., 2015), fish armor (Zimmermann et al., 2013), gecko skin (Arzt, 2006; Jagnandan et al., 2014), etc. (Liu et al., 2017).

The main objective of tissue engineering is to fabricate biological substitutes that well mimic the structure and properties of the live organ and structure in order to treat the injured regions of the body (Vacanti, 2006). Nature is full of various structures known as spatially heterogeneous composites with customizable properties. Biological systems have seven key characteristics, known as the Arzt heptahedron, based on which all bioinspired conceptions must be designed, and it is shown in **Figure 1**.

These seven key characteristics of biological systems are (1) self-assembly, (2) multifunctionality, (3) self-healing, (4) hierarchy of structure, (5) evolution against environmental constraint, (6) synthesis under $T \sim 300$ K and $P \sim 1$ atm conditions, and (7) hydration necessity. FGM biomaterials try to obey these criteria to fully mimic the natural structures because these natural components have excellent proficiency, and manmade parts still have a long way to go to reach them. There are lots of successful biomimetic FGM designs with promising properties that show the ability of utilizing this concept in biomedical implants (Chavara et al., 2009; Bin Qasim et al., 2020). One of the commercially used examples in this field is superelastic nickel titanium (Ni-Ti) orthodontic arch wires with graded functionality (Braz Fernandes et al., 2019).

In this regard, FGM design in tissue engineering is considered an innovative scheme for improving biomedical device performance and aims to reach specified multifunctional characteristics through spatial, structural, or compositional gradation, leading to tailored properties (Kawasaki and Watanabe, 1997). The most important advantage of FGMs is their capability in providing tailored morphological features that lead to the occurrence of graded physical and mechanical properties in a specific direction. FGMs have gradual transitions from composition, constituents, microstructure, grain size, texture, porosity, etc., along with one or more directions that lead to functional property changes. Also, according to interface condition, FGMs are classified into continuous and discontinues types. **Figure 2** schematically represents the FGM structure and types. Moreover, to produce biomimetic FGM parts, it is better to use seven common biological structure parts found in nature, such as fibers, helical, layered, tubular, gradient, cellular, suture, and overlapped components (Liu et al., 2017).

Metallic implant materials, including titanium (Ti) and its alloys, stainless steel, Co-Cr alloys, and NiTi shape memory alloys, are utilized commonly in cases in which high mechanical properties are required. Among these metallic materials, Ti attracted much attention because of its supreme biocompatibility, excellent corrosion resistance, low density, good mechanical properties, etc. (Rack and Qazi, 2006; Gode et al., 2015; Wang et al., 2017a; Attarilar et al., 2019a,b, 2020). For the case of Ti utilized in dental and orthopedic surgeries, the main goal of functionalization is to improve the osseointegration of the implant by surface engineering (Yang et al., 2006; Wang et al., 2015; Zhu et al., 2016; Ding et al., 2019; Wang Q. et al., 2020). Nowadays, additive manufacturing is also used in order to mitigate the stress-shielding effect by the production of Ti structures with gradation in pore size and shape from the surface to the center of the part (Yuan et al., 2019). Metallic FGMs have lots of applications as biomaterials utilized in various parts of the body. Finite element analysis by Enab (2012) indicates that the FGM tibia tray has superb biomechanical performance, mitigating stress-shielding and shear stress issues. It is shown that downward gradual elastic modulus variation of the tibia tray from 40 to 110 GPa in the vertical direction reduces the stresses. Also, the metallic FGMs have numerous applications in orthopedic surgery (Sola et al., 2016) and dentistry (Senan and Madfa, 2017). Metallic implants are very suitable to maintain the



requirements for bone implant application, load-bearing parts, and scaffolds, and this review paper especially focuses on the materials utilized in dental and bone applications. Due to the growing number of older populations in the world, the need for *de novo* multifunctional implants grows rapidly day by day; hence, this subject is of crucial importance and may open new horizons in the aspect of metallic FGMs.

FGM MANUFACTURING METHODS

The manufacturing technique is of key importance to attain high-quality FGMs with the desired gradation and properties; therefore, numerous methods have been proposed and used so far; each of which has its own pros and cons, and these methods are listed in **Figure 3**. The FGM production techniques can be categorized into four main processes: gas-based methods, liquid phase (Chen et al., 2000), solid phase (Tripathy et al., 2018), and additive manufacturing processes. Also, there are some other methods, such as ion beam-assisted deposition. Recently, additive manufacturing (AM) techniques have become a very popular method for the production of FGMs because these methods have the capability to manufacture complex porous structures with even nanometric resolution (Zhang et al., 2019). These AM techniques are among the best options for biomedical and implant applications because they are fast and economic, and

most importantly, they can be precisely adjusted to meet patient-specific needs, such as shape, dimension, and even texture of the related live tissues (Javaid and Haleem, 2018; Culmone et al., 2019).

Gas-Based Techniques

Chemical Vapor Deposition

One of the most common ways to produce FGMs is to produce surface coatings and induce surface gradation. Gas-based processes are among these coating-based methods, and chemical vapor deposition (CVD) is a popular method in this group. In the CVD method, various energy sources can be used, including light, heat, and plasma, to deposit materials on a surface. The used gases are usually in the form of hydride, bromide, and chloride. The gradation of deposited material can be tailored by temperature, gas ratio, gas type, flow rate, etc. (Hirai, 1995). The beneficial aspects of the CVD method in FGM fabrication are the potential to control the continuous variation of the composition, its low-temperature condition, and the resultant near-net designated shape of samples (Naebe and Shirvanimoghaddam, 2016). In the CVD technique, a carbon source in the gas phase and a kind of energy source (light, plasma, or a resistively heated coil) is utilized to transfer energy to a gaseous carbon molecule. In this process, hydrocarbons, including methane, carbon monoxide, and acetylene, etc., are used as carbon sources. These hydrocarbons flow in a quartz

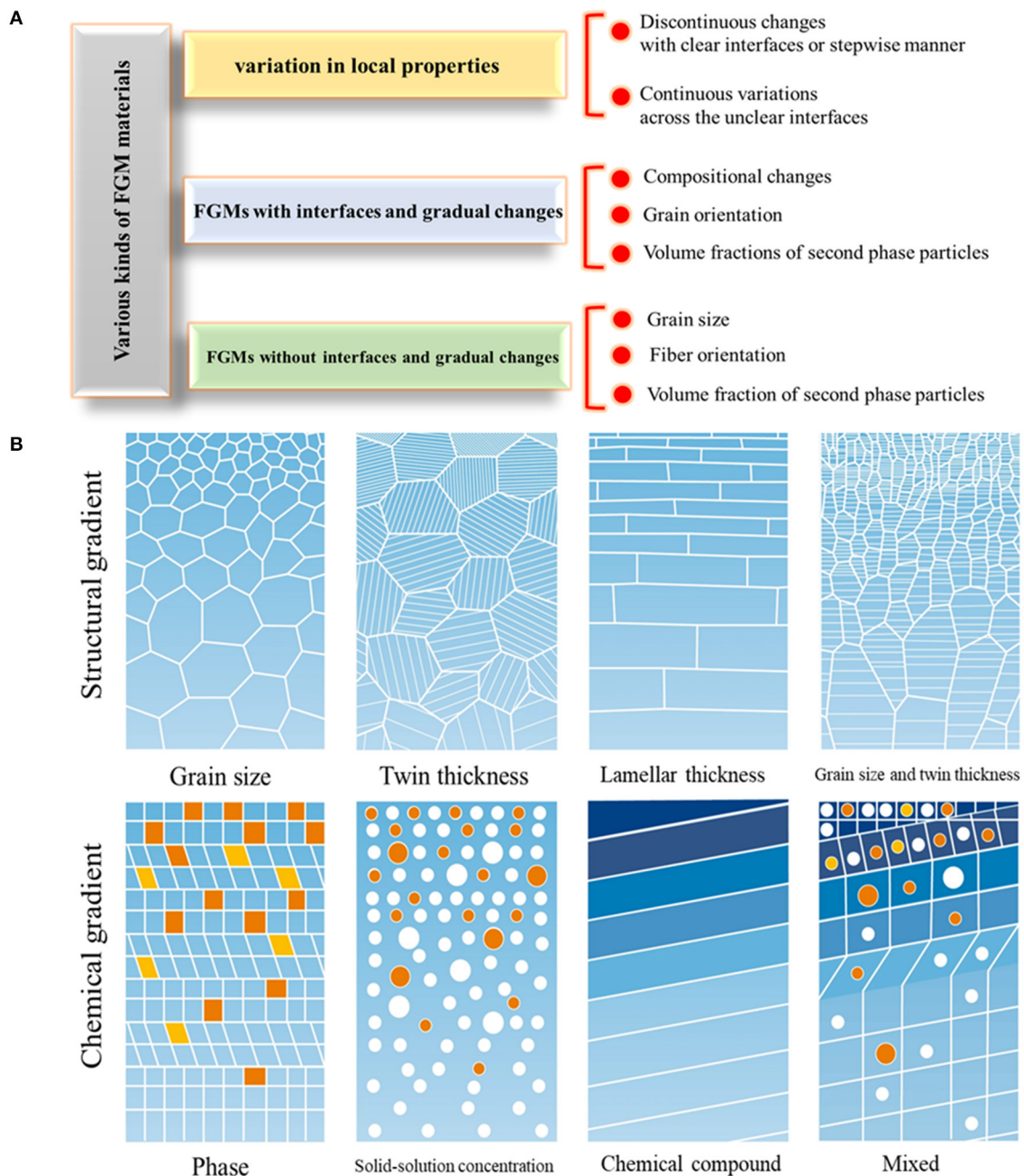


FIGURE 2 | The various kinds of FGM materials. **(A)** The categorization, **(B)** schematic representing the various kinds of structural and chemical gradients in FGMs with permission from Li X. et al. (2020).

tube while heating in an oven ($\sim 720^{\circ}\text{C}$); a schematic of the CVD technique can be found in **Figure 4A**. Due to energy application, the hydrocarbon chains are broken, and this leads to the production of pure carbon molecules; hence, the carbon can diffuse toward the heated substrate that is coated with a catalyst species (usually transition metals, such as Ni, Fe, or Co), where it binds. The CVD process has several advantages, such as low power input, lower temperature range, relatively

high purity, and most importantly, the possibility to scale up the process (Endo et al., 1993). Liu et al. (2006) show the effectiveness of the plasma-enhanced CVD process in the development of an anticorrosion diamond-like carbon (DLC) FGM coating deposition on a Nitinol (NiTi) substrate. The produced DLC coating has a 150-nm-thick graded layer with excellent adhesivity to the substrate and effective corrosion protection in simulated body fluids.

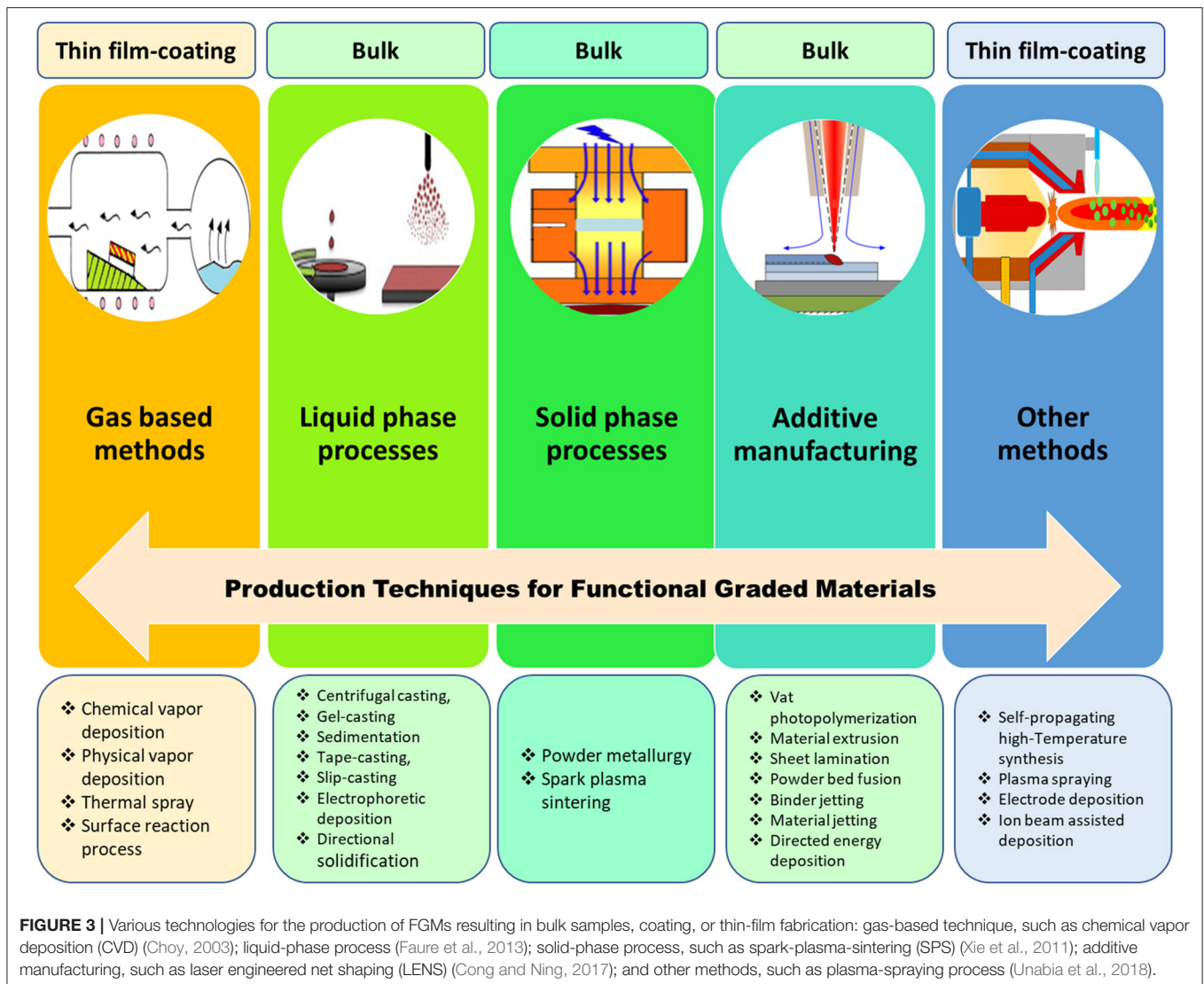


FIGURE 3 | Various technologies for the production of FGMs resulting in bulk samples, coating, or thin-film fabrication: gas-based technique, such as chemical vapor deposition (CVD) (Choy, 2003); liquid-phase process (Faure et al., 2013); solid-phase process, such as spark-plasma-sintering (SPS) (Xie et al., 2011); additive manufacturing, such as laser engineered net shaping (LENS) (Cong and Ning, 2017); and other methods, such as plasma-spraying process (Unabia et al., 2018).

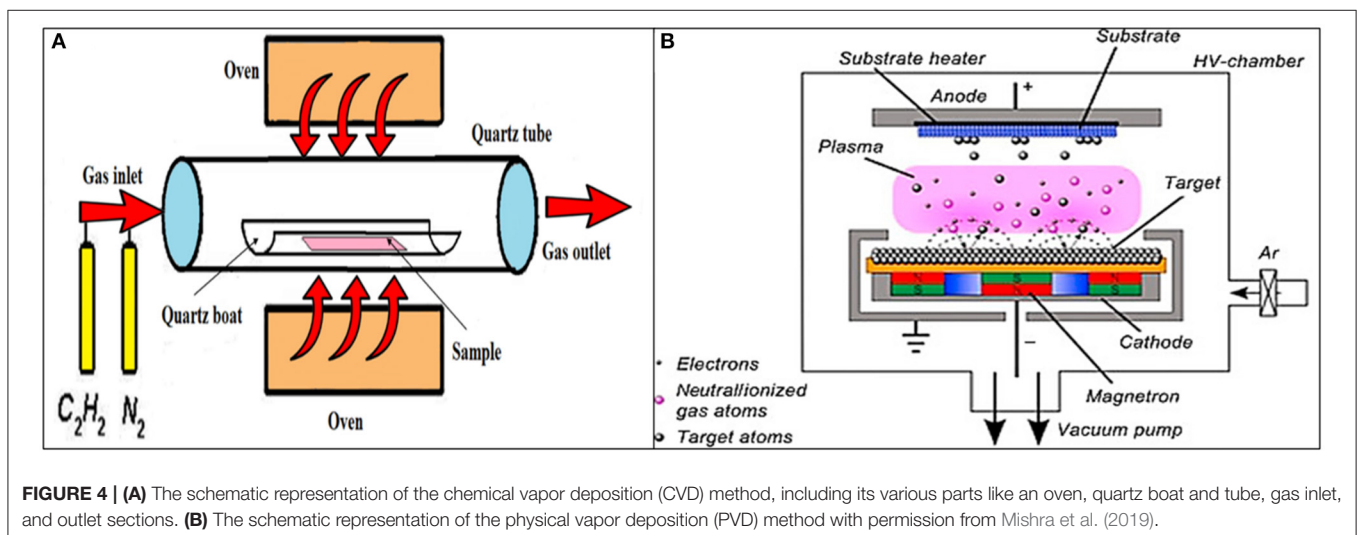


FIGURE 4 | (A) The schematic representation of the chemical vapor deposition (CVD) method, including its various parts like an oven, quartz boat and tube, gas inlet, and outlet sections. **(B)** The schematic representation of the physical vapor deposition (PVD) method with permission from Mishra et al. (2019).

Physical Vapor Deposition

The gas-based physical vapor deposition (PVD) technique is among the well-known approaches to produce various thin films and coatings. In this process, the material transforms from the condensed phase to a vapor phase and subsequently rearranges to the condensed phase as a thin film or coating on the substrate. **Figure 4B** shows a schematic of the PVD device. The PVD method has numerous applications, including optics, electronic, chemical, semiconductors, solar panels, food packaging, TiN coatings in cutting tools, etc. The advantages of the PVD process are its ability to produce various kinds of coatings (organic and inorganic), environmentally friendliness, and achieving durable coatings with favorable properties, but unfortunately, it is operating under high temperatures and vacuum conditions. The magnetron sputtering PVD systems can be used to produce ion-substituted Ca-P-based coatings on the surface of an implant, and these coatings, such as hydroxyapatite (HA) show significant influence on cell interactions, including cell proliferation, adhesion, and differentiation (Qadir et al., 2019). The PVD method is a proper candidate to develop a reproducible preparation of nano rough titanium thin films with biological properties (Lüdecke et al., 2013). Also, a new kind of gradient DLC coating is produced by the plasma source ion PVD system, and it can have some applications on artificial mechanical heart valves (Yin et al., 1999).

The plasma spray technique, as one of the PVD methods, can be used to produce three-layered-FGM hydroxyapatite (HA)/Ti-6Al-4V coatings with progressive variation of microhardness, Young's modulus, microstructure, and porosity between layers (Khor et al., 2003). The excellent tensile adhesion strength of these coatings, fracture toughness, microhardness, etc., of this FGM makes it a suitable choice for biomedical applications. The beneficial properties of compositionally graded doped (HA)/Ti-6Al-4V FGM produced by the plasma spray technique are also confirmed by Ke et al. (2019). Moreover, the *in vitro* human experiments by osteoblast cell culture and tests against *E. coli* and *S. aureus* bacterial species prove its superb biological performance. This FGM shows favorable interfacial mechanical and antibacterial properties (due to an MgO and Ag₂O mixture with HA) for possible use in load-bearing orthopedic and dental implants (Ke et al., 2019).

Liquid Phase Processes

Electrophoretic Deposition

In the electrophoretic deposition (EPD) technique, a stable colloidal suspension is used in which, due to the existence of an electric field, the charged particles are moved and deposited on a conductive substrate with the oppositely charged condition. As observed in **Figure 5A**, the colloidal particles are randomly dispersed and are able to move freely in the solvent suspension. In **Figure 5B**, the surface of the particles are charged due to electrochemical equilibrium, and in **Figure 5C**, the external electrical field causes the preferential movement of charged particles toward the oppositely charged electrode, which is the substrate. Finally, in **Figure 5D**, the adsorbed charged particles get some electrons and transform into the firmly deposited layer of particles on the surface of the substrate (Amrollahi et al.,

2016). EPD has the potential to fabricate a variety of materials from traditional to advanced materials from nanometric thin films and coatings to a thick film, and from porous scaffold parts to highly compact coatings and FGMs. In EPD, both AC and DC electrical fields can be used, but DC is more common (Amrollahi et al., 2016). This method has lots of advantages with versatile application: some of its pros include simple device and utilization, short processing time, economic, facile modification, desirable dense packing of particles, high-quality microstructure, fabrication of geometrically complicated shapes, and simple control of the thickness and morphology (Sarkar et al., 2012). Sun et al. (2009) utilize a cathodic EPD method in order to fabricate multilayered HA-chitosan FGM coatings with HA particles, and this method has the potential to produce layers with different thicknesses ranging between 2 to 200 μm . The resultant composite chitosan-heparin layers can be used for surface modification of HA-chitosan coatings and improving blood compatibility.

Solid Phase Processes

Powder Metallurgy

Powder metallurgy (PM) is one of the well-known solid-phase processes to produce FGMs in which a graded powder material is mixed with a specific proportion stacked together in a continuous manner or *via* step-by-step stages. Then, the stacked material is compacted by pressing to achieve a dense condition, and the resultant compact part is sintered in a specified range of temperature to reach a 100% dense part (Madan and Bhowmick, 2020). The most significant stages of the PM process, respectively, are powder weighing, powder mixing, compaction, and sintering. Compaction is usually performed under a controlled atmosphere with low temperatures, and sintering should be done at a high temperature range. To improve the quality of the PM part, it is common to do some postprocessing, such as coining, repressing, and resintering. PM methods are widely used in the production of FGM parts, specifically ceramic FGMs. One of the important advantages of these methods is their ability to produce intricate and complicated shapes out of any metallic or ceramic powders, and it is the best method to produce FGMs out of solid constituents (Tripathy et al., 2017). Shahrjerdi et al. (2011) produce metal-ceramic composite FGM by a pressureless sintering method using pure Ti and HA; the compositional gradation was from the metallic (Ti) end to the ceramic (HA) end. In order to optimize biocompatibility and mechanical properties, Watari et al. (2004) fabricate a Ti/HA FGM by PM method, and this specimen shows the better maturation of freshly formed bone cells in the HA-rich region than the Ti-rich zone. The produced graded structure causes proper osteogenesis and mechanical and stress relaxation properties. Overall, these studies indicate that FGM fabrication and the resultant gradation affect the tissue reaction in a graded manner; hence, it is possible to tailor the biological response of tissues by the development of FGM biomaterials.

Spark Plasma Sintering

The spark plasma sintering (SPS) method is a compressive, solid-state method in which a pulsed electric current energizing

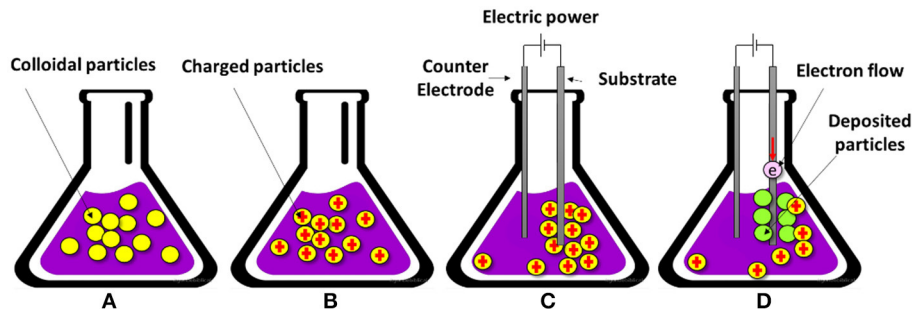


FIGURE 5 | The schematic of four stages of the electrophoretic deposition (EPD) technique: **(A)** colloidal particle dispersion, **(B)** charged particles due to electrochemical interactions, **(C)** electrophoresis, and **(D)** deposition of a firm layer of particles on the substrate.

sintering is used (Tokita, 2010) and can be efficiently utilized to produce FGM parts. Kondo et al. (2004) use the SPS method to fabricate titanium nitride/apatite functionally graded implants with acceptable mechanical properties and new bone formation around the femur of a rat model. In the SPS method, electric current is utilized in the densification step, in which a pulsed DC current is directly transferred to a graphite die and the powder compact; this process is schematically shown in **Figure 6**. In the SPS method, the compact part is heated internally; hence, high heating rates ($\sim 1,000$ K/min) are possible, and also, it leads to a very fast sintering process (a few minutes). The characteristics of this method include short holding times, fast heating, fast cooling, and the potential to achieve completely dense parts at relatively low temperatures. Using the SPS method in the fabrication of HAp/zirconia composites with biomedical applications helps to inhibit undesirable chemical reactions that lead to reduction in the biocompatibility and mechanical properties of the part. The SPS process with a proper temperature range and high pressing loads ensures the proper characteristics of HA ceramic composites without the accuracy of decomposition reactions; hence, the resultant HAp/zirconia composites are five to seven times stronger and seven times tougher with the suitable biological response (Shen et al., 2001).

Additive Manufacturing Methods

Additive manufacturing (AM) technologies, also known as 3-D printing methods, are among the most recent FGM fabrication procedures (Zhang B. et al., 2016), and some of them are shown in **Figure 7**. They have the potential to fabricate very complex and intricate porous parts with high resolution. They are simple and direct methods that do not need any dies, tooling, joining, sintering, or assembling steps. AM technology has numerous advantages and is a unique procedure to produce different structural and industrial parts. In particular, it has a big impact on the biomedical field. Some of its advantages that can be mentioned are its economic nature, ability to mass produce, potential to produce very complex parts, repeatability, shorter time to market, ability to use various materials (organic or inorganic), etc. (Attaran, 2017). One of the significant benefits of 3-D printing technology is the possibility to use a computer-aided design (CAD) technique that enables fabricating completely patient-specific implants (Jardini et al., 2014; Mobbs et al.,

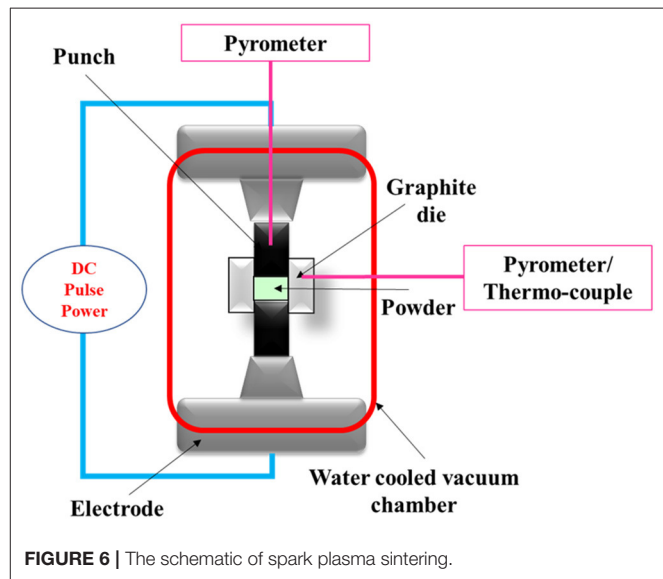
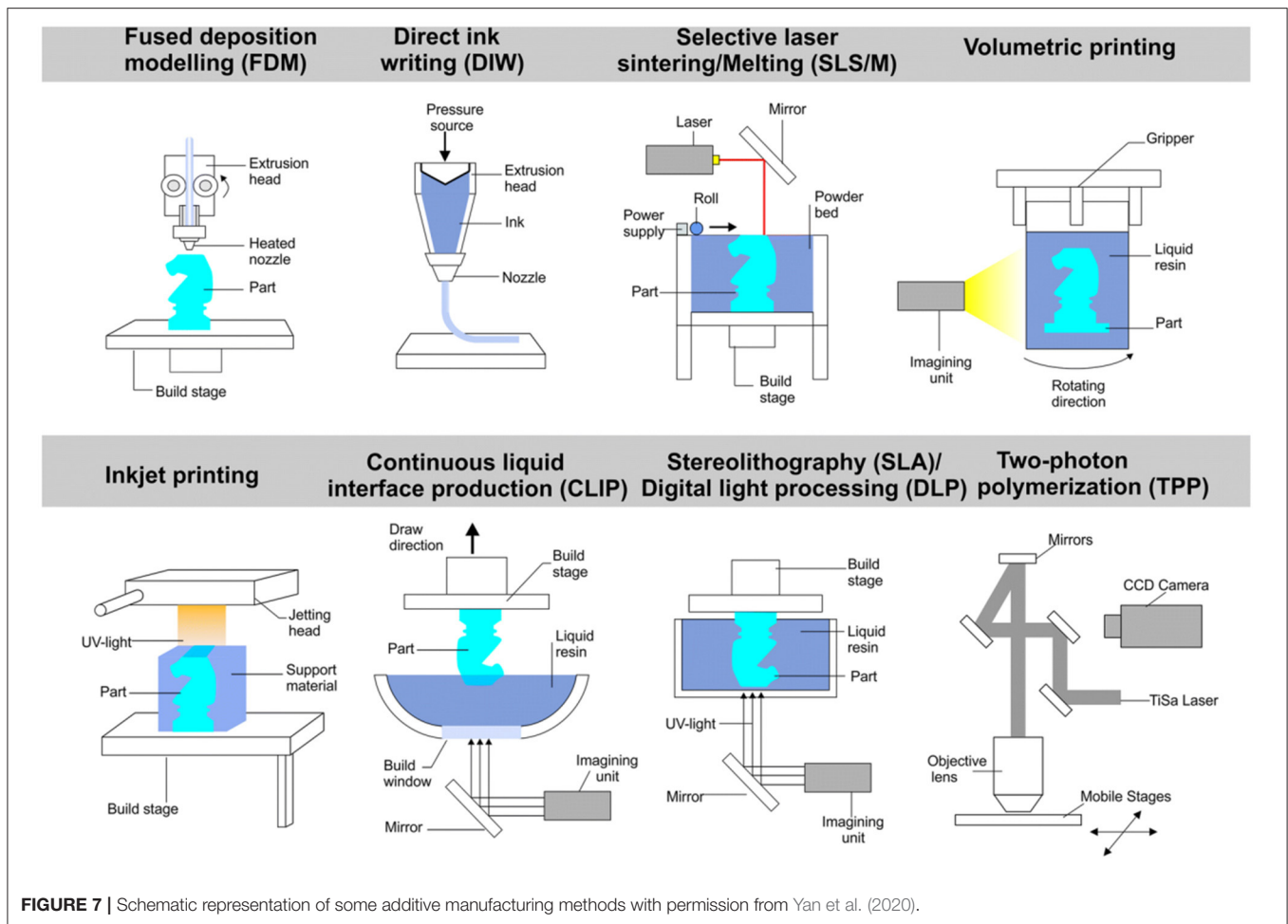


FIGURE 6 | The schematic of spark plasma sintering.

2017). During AM processing, first, the 3-D CAD model is converted to a printable digital files (such as STL files), and then the processed data are grouped as thin, 2-D slices using slicing software. Subsequently, the developed slices are fed to the 3-D printer device to build the final parts in a layer-by-layer manner (Zhang L. et al., 2016). There are numerous AM methods, each of which has its benefits and limitations. The most important methods in the fabrication of metallic FGM structures are selective laser melting (SLM) and electron beam melting (EBM) methods, and more information about the AM methods can be found in (Bikas et al., 2016; Awad et al., 2018; Ngo et al., 2018). AM manufacturing techniques have a sizeable impact on the biomedical field. **Table 1** summarizes some of the studies that have been done on the biomedical application of AM-manufactured FGMs.

Selective Laser Melting (SLM) and Electron Beam Melting (EBM)

The SLM method, also known as direct metal laser melting (DMLM) or laser powder bed fusion (LPBF), is among the most



famous rapid prototyping techniques, and it uses a high power-density laser to melt and fuse metallic powders together. The SLM process has several successive steps from digital data preparation to the ejection of the produced part from the building platform. At the first step, stereolithography (.STL) files are utilized to generate the slice data for each layer, and then the CAD data are transferred to the SLM machine. Initially, the first thin layer of metal powder lies on a tray, and then a laser beam with a high energy-density beam melts and fuses the preferred regions of the powder layer according to the CAD data. After that, the building platform is lowered, and the next layer of powder is deposited on the previous layer. Then, the laser beam begins to scan a new layer. This cycle is repeated numerous times until the 3-D part is completely produced. Finally, the completed 3-D part can be removed from the platform manually or by special devices, and also, the loose powder is removed from the surface of the part (Yap et al., 2015). The SLM process has numerous benefits that make it one of the most used 3-D printing methods, including the short time to market-, no restriction in geometry and ability to produce very complex and porous parts, relatively low cost, no need for assembly steps, etc. (Yap et al., 2015).

The SLM technique is able to produce complex porous FGM scaffolds; for example, the gradient porosity variation strategy

is suitable for orthopedic implants to mimic the natural bone structure. Xiong et al. (2020) studied the production of porous Ti6Al4V FGM parts for orthopedic applications by utilization of the SLM method. The gradient porous cellular structures have two kinds of unit cells (honeycomb and diamond-like unit cells). The porosity of samples was in the range of 52–67% with the approximate pore size between 420 and 630 μm , and then the mechanical and physical properties as well as their deformation behavior was studied. The resultant Young's modulus was comparable with the cortical bone (Xiong et al., 2020). In another study, Onal et al. (2018) use the SLM technique to produce Ti6Al4V porous scaffolds with three strut diameters (0.4, 0.6, and 0.8 mm), two gradations (dense-in, dense-out), and BCC structure. The obtained mechanical properties of all designed scaffolds fall in the cortical bone range. Also, the results indicate that dense-in scaffolds with small pores located in the core region and large pores on the outer surface are the best condition for load-bearing implants (Onal et al., 2018).

The EBM method is one of the famous layer-by-layer techniques. It has great potential in the fabrication of high-resolution metallic components (Chern et al., 2020; Tan et al., 2020) and the near net shape parts with intricate geometries (Wang et al., 2016). The process begins with the selective

TABLE 1 | The application and the biological and mechanical properties of mostly AM-fabricated metallic FGMs.

Method	Material	Mechanical properties	Biological properties	Application	References
SLM	Ti6Al4V	Young's modulus in the range of cortical bone. The highest strength and toughness in honeycomb structures with supporting structure in the outer layer.	–	Orthopedic	Xiong et al., 2020
SLM	Ti6Al4V	Mechanical properties in the range of cortical bone. Small pores with ~900 μm in core regions increase mechanical strength.	Large pores, about 1,100 μm in the outer surface, enhances cell penetration and proliferation.	Load-bearing implants	Onal et al., 2018
SLM	Ti6Al4V	The variation in unit cell orientation affects the mechanical properties; this change is a function of the geometrical dimension of the unit cell size. There is a functional relationship between elastic modulus and compressive strength.	–	Bone implant	Weißmann et al., 2016
SLM	Ti6Al4V	AM-produced porous FGM can decrease the elastic modulus up to 80% and enhance the biomechanical performance.	–	Bone scaffolds and orthopedic implants	Wang et al., 2017b
SLM	Ti6Al4V	Porosity variation strategy (diamond lattice structures) results in an elastic modulus of 3.7–5.7 GPa and yield strength of 27.1–84.7 MPa, which lie in the range of the corresponding mechanical properties of cancellous bone and cortical bone.	–	Bone scaffolds	Zhang X.-Y. et al., 2018
SLM	Pure Ti	Diamond porous FGM scaffold production with a good geometric reproduction, possessing a wide range of graded volume fraction. The elastic modulus is comparable to cancellous bone and can be tailored by tuning the graded volume fraction.	–	Bone implant	Han et al., 2018a
SLM	CoCr	Pillar-octahedral-shape CoCr cellular structures with a porosity range of 41–67% indicate stiffness, strength, and energy absorption values that are similar to natural bone.	–	Metallic orthopedic implants	Limhakhun et al., 2017
SLM	CoCrMo	FGM design (square pore cellular structures) decrease the stiffness and weight up to 48% compared to the traditional fully dense stem.	–	Femoral stem implant	Hazlehurst et al., 2014a
SLM	CoCrMo	FGM structure (square pore) reduced the stress-shielding effect without compromising the bone strength. The most effective design is the full porous stems with an axially graded stiffness.	–	Hip implant	Hazlehurst et al., 2014b
EBM	Ti6Al4V	The deformation response of graded meshes is the weighted percentage of stress-strain response of each uniform mesh constituent. By tailoring the relative density and volume fraction, the graded meshes can achieve high strength and energy absorption values.	–	Implants that can withstand abrupt impact fractures.	Li et al., 2016
EBM	Ti6Al4V	–	AM manufactured interconnected gradient porous architecture enhances cellular functions, including adhesion, proliferation, mineralization, and synthesis of actin and vinculin proteins.	Medication of segmental bone defects and bone remodeling	Nune et al., 2016
EBM	Ti6Al4V	Aimed to inhibit the stress-shielding effect by decreasing the elastic modulus mismatch between the bone tissue and titanium alloy implant.	3-D printed interconnected porous FGM is conducive to osteoblast cell functions, including proliferation, adhesion, calcium deposition, and synthesis of proteins, such as actin, vinculin, and fibronectin.	Bone implants	Nune et al., 2017
EBM	Ti6Al4V	The weighted average gradient porosities of 65–21% show high compressive strength and hardness and suitable elastic modulus for bone implant application.	–	Treatment of segmental bone defect	Surmeneva et al., 2017

(Continued)

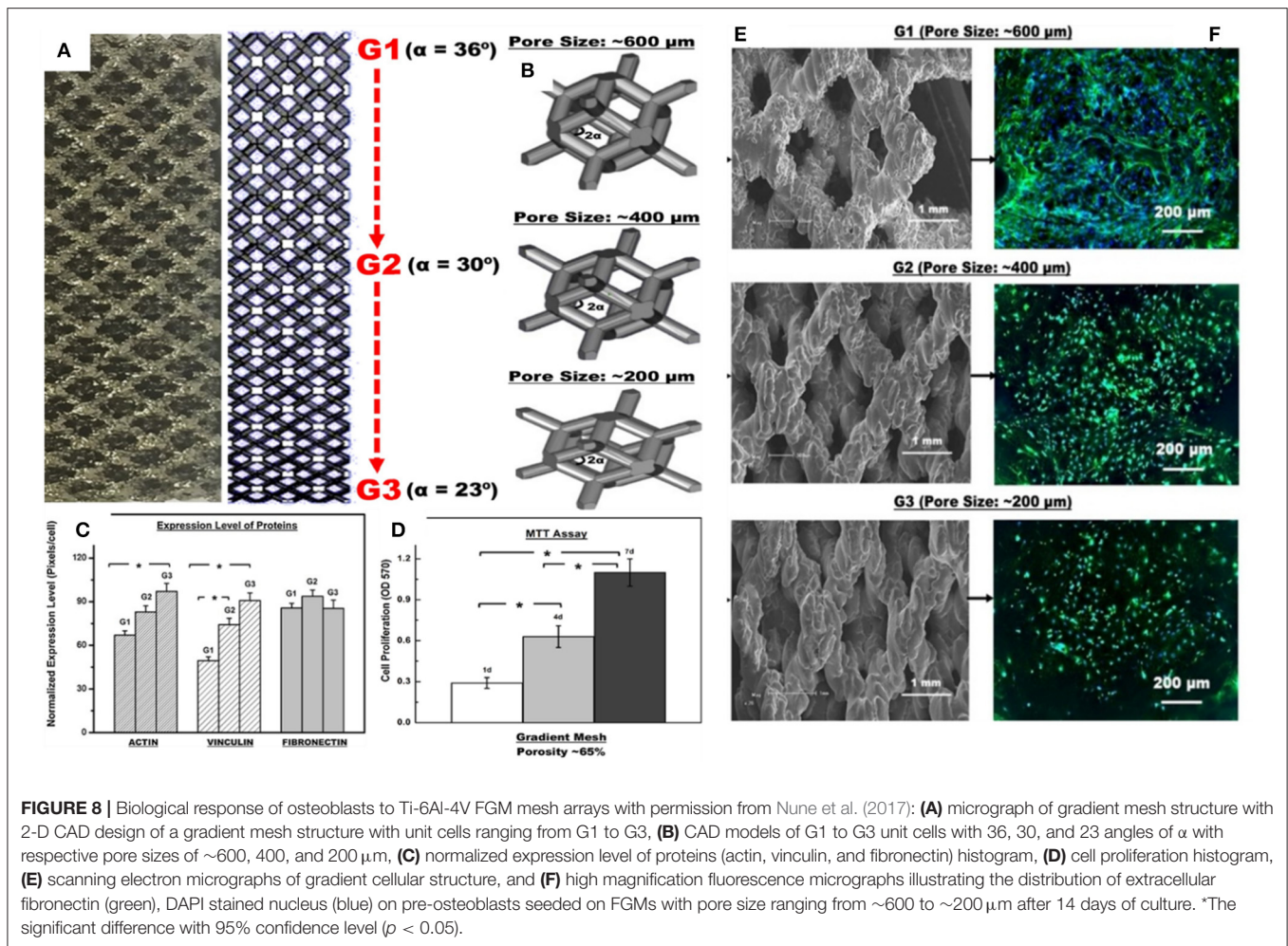
TABLE 1 | Continued

Method	Material	Mechanical properties	Biological properties	Application	References
EBM	Ti6Al4V	Regular diamond lattice indicates suitable compression strength and elastic modulus to implant application. Uniaxial compression behavior along the direction of gradation can be well-predicted by a simple rule of mixtures approach.	–	Orthopedic implant applications	van Grunsven et al., 2014
EBM	Ti6Al4V	Periodic cellular structures with a 49%–70% porosity range with mechanical properties (effective stiffness, compressive strength values) suitable for loading conditions.	–	Hip and mandible implants	Parthasarathy et al., 2011
EBM	Ti6Al4V	The porous FGM (open-cell cubic structure) has a compressive strength with a transition region between 4 and 8 mm and is superior to a sharp interface.	–	Biomedical implants	Wu et al., 2018
SLM	316L stainless steel	High density of subgrain boundaries and dislocations is responsible for good plasticity, and the considerable number of voids induces premature instability and fracture.	Higher biocompatibility and good biological performance.	Medical implant applications.	Kong et al., 2018
Laser metal deposition	Stainless steel, HS6-5-2	Low porosity and no delamination occurrence were seen. According to microhardness tests, gradient materials sintered in the N ₂ -10% H ₂ atmosphere and reinforced with the VC carbide have the maximum hardness.	–	Possible biomedical application.	Matula and Dobrzański, 2006
Laser cladding	Dissimilar stainless steel (SS)-zirconium (Zr)	Functionally graded deposition in dissimilar materials resulted in production of disintegrated structure and numerous longitudinal and horizontal cracks. Possibly micro-cracks are the result of large thermal stress build-up during the layer-by-layer AM process.	–	–	Khodabakhshi et al., 2019

melting of discrete powder layers *via* an electron-beam gun under the vacuum condition, and this melting stage is accomplished by the energy emission *via* the electron beam of a tungsten filament, which can be effectively controlled by two magnetic coils (Galarraga et al., 2016). In the EBM process, each slice is separated into two prescribed zones, including contours and squares. Initially, the contour zone known as an interface between the sample and the surrounding powders is 3-D printed. After that, the square zone acting as the inner zone between these boundary and contour zones is 3-D printed by EBM. One of the advantages of EBM is the use of a vacuum chamber that restrains any impurity and contamination accumulation and leads to the fabrication of high-quality specimens possessing good mechanical properties (Wang et al., 2018; Wang P. et al., 2020).

A multiple-layered, gradient cellular Ti6Al4V scaffold was produced by the EBM technique, and the mechanical properties were studied by uniaxial compression testing (Surmeneva et al., 2017). Five types of structures with various designs (two layers, three-layered structures, BCC and diamond-like structures with different unit cell sizes) and with weighted average gradient porosities of 65–21% resulted in compressive strength and Young's modulus in the range of 31–212 MPa and 0.9–3.6 GPa, respectively. Also, the results indicate that the lattice cell design significantly affects the failure mechanism. Nune et al. (2017) investigate the biological response of osteoblasts to Ti-6Al-4V

FGM mesh arrays fabricated by the EBM method. The gradient structure is composed of different unit cells from G1 to G3 (rhombic dodecahedrons) because it is reported that these types of unit cells have more production flexibility (Li et al., 2014). They are shown in **Figure 8A**. The CAD models of unit cells ranging from G1 to G3 with 36, 30, and 23 α angles with respective pore sizes of about 600, 400, and 200 μm are shown in **Figure 8B**. Also, the scanning electron micrographs (SEM) of these gradient mesh structures are, respectively, shown in **Figure 8E**. It is worth mentioning that the strut thickness was fixed at $\sim 500 \mu\text{m}$. **Figure 8C** shows a histogram of the normalized expression level of proteins (actin, vinculin, and fibronectin). There is not any significant difference in the normalized expression level of fibronectin protein on the struts of the FGM with respect to different regions, but overall, the cellular structure is conducive to the synthesis of proteins. In addition, the cell proliferation histogram in **Figure 8D** shows that the proliferation of osteoblast cells repeatedly increased with time such that the proliferation rate was about 47%/day on the seventh day. The G1 to G3 regions of FGM demonstrated substantial variations in the distribution of cell nuclei (**Figure 8F**), and it declined from G1 to G3 with higher density on G1. This reduction in the distribution of nuclei can be related to the topography of the strut surface. In general, this EBM-produced FGM improved the osteoblasts response, including protein synthesis, cell adhesion, proliferation, and calcium deposition (Nune et al., 2017).



THE FUNCTIONAL DESIGN OF FGMS IN BIOMEDICAL APPLICATIONS

Metallic implants are usually designed to serve as load-bearing implants and are not aimed at being temporary used. They usually have a permanent nature except for some magnesium-based ones for specific applications in which the corrosion rate is of significant importance. Although they have excellent mechanical strength and uniaxial tensile and compression strength, the metallic implants have one major limitation because of their Young's modulus, which is much larger than natural human bone and leads to stress shielding issues and early failure of the implant. The cortical bone has a Young's modulus value between 5 and 23 GPa, and these values are, respectively, about 114, 190, 45, 44, and 120 for Ti-6Al-4V, 316L stainless steel, pure Mg, WE43 Mg alloy, and pure Ti (Haghshenas, 2017). Because of this big difference, the FGM design in metallic implants aim to solve this issue. Satisfactorily good mechanical gradation can be achieved by FGM design and controlling the related variants. Also, by smart hierarchical surface design and fabrication of biomechanical and chemical bonding in surface layers of FGMS, the bone cells can attach and differentiate easily on them and facilitate the treatment procedure (Liu et al., 2017; Bahraminasab

and Edwards, 2019; Bai et al., 2019). This kind of gradation is also seen in natural systems and can lead to variations in the mechanical properties of the part; one of the good examples is the bone shown in **Figure 1E** that can be used in load-bearing applications (Wegst et al., 2015). There are lots of examples in nature, including fish scales and shark teeth, where their unique structure can resist contact and impact forces (Chen et al., 2012). This concept can be used in metallic parts in order to enhance mechanical strength against contact deformation and damage (Suresh, 2001), cracking (Bao and Wang, 1995), and improvement of other mechanical properties (Islam et al., 2020). Sedighi et al. (2017) produce a five-layered Ti/HA composite FGM for dental implant applications. In this study, Ti and HA powders were mixed with different Ti-to-HA ratios (100, 90:10, 80:20, 70:30, and 60:40), and then samples were sintered by the SPS method, the results confirm the graded microhardness values and microstructure differences. Also, some other researchers studied the effect of these gradual changes using AM methods (Lima et al., 2017; Han et al., 2018b).

FGM Dental Implants

The primary idea behind the utilization of FGMS in dental implants is that the characteristics of the implant can be

accurately designed and adjusted to ensure the complete mimicking of the periphery bone tissue and provide the biomechanical necessities according to a specific region of the host bone. Hence, the utilization of FGM dental implants is very beneficial and can enhance integration and implant stability (Lin et al., 2009a). The main advantages of using FGM parts in dental applications are reducing the stress-shielding effect (Hedia, 2005), improving biocompatibility (Watari et al., 2004), inhibition of thermal-mechanical failure (Wang et al., 2007), and providing biomechanical requirements (Yang and Xiang, 2007). Moreover, these modern FGM implants can help to solve the mechanical properties' mismatch issues between implants and native biomaterials, and this is an important problem because it can reduce osseointegration and bone remodeling. In FGM dental implant applications, usually a cylindrical shape is utilized in which the composition varies in the axial direction (Mehrali et al., 2013). The FGM dental implants are designed with varied properties in a certain pattern to match the biomechanical characteristics in a specified region (Lin et al., 2009b). These FGMs are usually composed of collagen HA and Ti as it is known that collagen HA is a key constituent of human bones and other related tissues, and this material can enhance the biocompatibility (Watari et al., 2004). Lin et al. (2009b) studied the effect of FGM design on bone remodeling in a computational remodeling scheme [finite element modeling (FEM)]. In this study, 8 FE models were used, seven of them with varying m values ($m = 10, 8, 5, 2, 1, 0.5$, and 0.1) plus a model of full Ti for comparison. The m value indicates the ratio in the volumetric fraction of the Ti to HAP/Col compositions, $m = 10$ shows the richest content of Ti, and $m = 0.1$ indicates the highest ratio of collagen HAP. **Figure 9** shows the results of this investigation. It clearly indicates that reducing the FGM gradient leads to better bone remodeling performance, but unfortunately, the low m values at the same time can reduce the stiffness of implantation. It is suggested that this problem can be solved by a multi-objective optimization scheme.

Yang and Xiang (2007) investigate a biomechanical response of a dental FGM implant under static and harmonic occlusal forces by the 3-D FEM concept. The implant material was a combination of a bioceramic and a biometal with a smooth composition and properties gradient in the longitudinal direction. In this study, the interaction of the implant and the periphery bone tissues was studied. The samples were produced by the dry method and electric furnace heating (similar to Watari et al., 1998), and varied ratios of Ti to HAP were used (composition varying between pure Ti to 100% HAP) in the longitudinal direction. The dental implant, along with the supporting bone system, is shown in **Figure 10A**, and other properties of the implant can be seen in **Figures 10B–F**. The occlusal forces are directly applied to the upper part of the abutment, and then it is directed down to the implant by the screw connection. These occlusal forces mostly are supported by the cortical bone; the large volume percentage of Ti in the upper region of the implant and higher HAP amount in the lower region is favorable because it maintains a satisfactory load-bearing capacity, and also, it can effectively reduce the material mismatch between the implant and the surrounding bone tissues.

Figures 10G–J illustrates the von-Mises stress and displacement distributions in FGM under various conditions and confirms that produced stresses are much lower in the middle and lower regions of the implant. Moreover, in **Figure 10K**, the maximum Von-Mises stress values at various osseointegration phases (zones A = initial, B = mid, and C = complete osseointegration) are compared, and the maximum stresses decrease by increasing the Young's modulus, and the osseointegration condition improves. The condition of the surrounding bone system largely affects the natural frequencies, the variations of frequencies upon the elastic modulus can be used to analyze dental implant performance and its osseointegration. **Figure 10L** shows that the fundamental frequency considerably enhanced in improved osseointegration conditions. Overall, this study suggests that the utilization of the FGM scheme is a very beneficial procedure for improving the biomechanical response of dental implants (Yang and Xiang, 2007).

The FGM surface coatings can also be used to improve dental implant function (He and Swain, 2009; He et al., 2014), Aldousari et al. (2018) compare three various dental implant models, including (1) a homogenous dental implant with a homogenous coating, (2) a homogenous dental implant with an FGM coating, and (3) a functionally graded implant with a homogenous coating material. It is seen that the third model with the FGM structure and homogenous coating is the most suitable to reduce the stress-shielding effect. Also, the porous FGMs can be used in orthodontic or maxillofacial implants (Becker and Bolton, 1997; Suk et al., 2003). In this regard, Becker et al. (1995) studied various porous biomedical alloys, including 316L stainless-steel, Co-29Cr-6Mo alloy, and Ti-6Al-4V alloy, and confirmed their possible use. Subsequently, Oh et al. (2007) investigated the effect of various pore size in both *in vitro* and *in vivo* biological experiments and showed that the optimum pore size range for fibroblast ingrowth is 5–15 μm , for chondrocyte ingrowth is about 70–120 μm , and for bone regeneration is in the range of 100–400 μm . There are lots of investigations about the porous FGMs. Matsuno et al. (1998) studied the laminated HA/Zr composite with the gradient composition, and its promising properties, such as osteoconductivity and high mechanical strength, show its potential for use in dental and orthopedic implants. Another successful porous FGM Ti dental implant was produced by Traini et al. (2008) *via* direct laser metal sintering with satisfactorily elastic properties, minimum stress shielding effects, and improved long-term performance. Additionally, there are lots of finite element modeling about FGM dental implants showing the effectiveness of the FGM concept in reduction of stresses in periphery tissues (Sadollah and Bahreininejad, 2011; Ichim et al., 2016).

FGM Orthopedic Implants

Bone tissue is a popular natural FGM structure; hence, it seems very rational to use FGM parts in the treatment of various bone-related issues, such as orthopedic implants. In this regard, biomimetic FGM designs seems to be a prospective solution for implant applications (Boughton et al., 2006, 2013). One example is the BioFITM arthroplasty design, which emulates

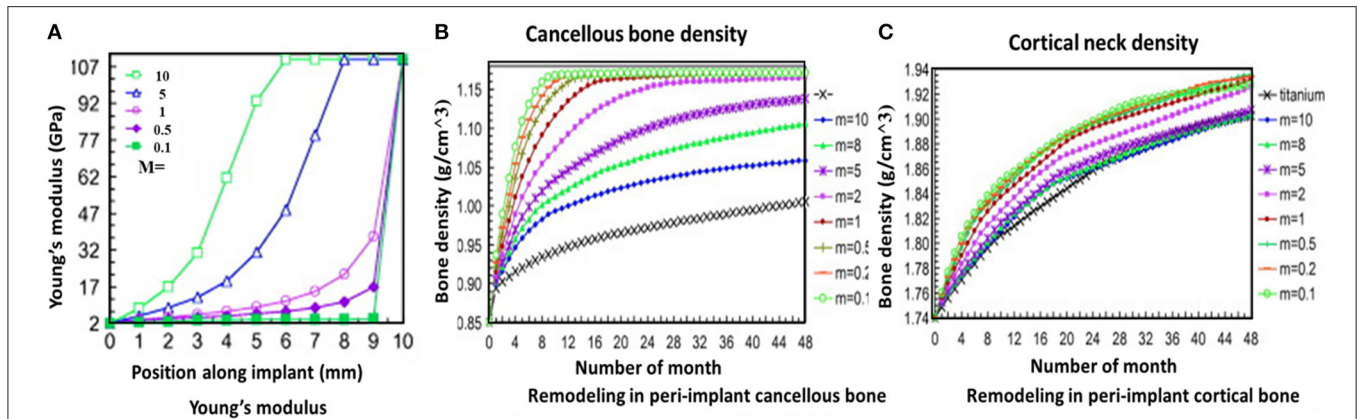


FIGURE 9 | Variation of FGM properties in accordance with FGM characteristics: **(A)** Young's modulus, **(B)** peri-implant bone remodeling against cancellous bone density, and **(C)** peri-implant bone remodeling against cortical neck density with permission from Lin et al. (2009b).

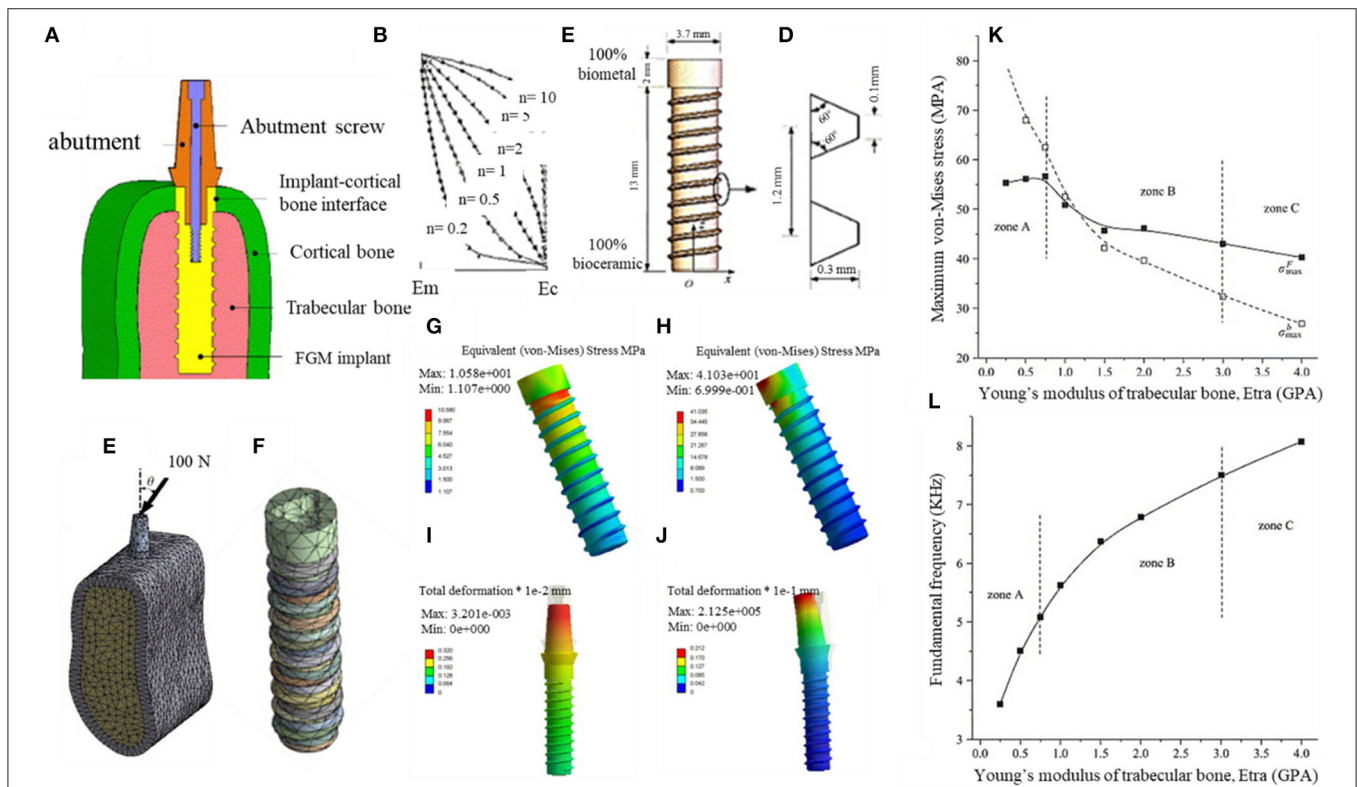


FIGURE 10 | The biomechanical response of three-dimensional FEM designed FGM dental implant in the surrounding bone with permission from Yang and Xiang (2007): **(A)** FGM dental implant to bone condition, **(B)** longitudinal fluctuations in material properties of FGM implant, **(C)** FGM configuration, **(D)** the thread details, **(E)** the implant-bone system, **(F)** FGM implant; the von-Mises stress and displacement distributions in FGM under various conditions: **(G)** vertical occlusal force, **(H)** inclined occlusal force, **(I)** vertical occlusal force, **(J)** inclined occlusal force. Influence of elastic modulus of the peri-implant bones **(K)** on maximum Von-Mises stresses and **(L)** on the FGM fundamental frequency.

bone characteristics of vertebral bone; it successfully mimics the connective intervertebral disk function (Boughton et al., 2010).

AM technologies have a great potential to fabricate various orthopedic implants from lattice structures and FGMs (Mahmoud and Elbestawi, 2017). The FGM parts can be

designed in order to exactly mimic the features of the desired region and maintain the necessities, such as inhibition of the stress-shielding effect and preventing the harmful shear stresses that may be produced in the bone-implant interface regions. There are numerous studies about FGM orthopedic

implants, but this review briefly discusses metallic orthopedic FGM implants. Batin and Popa (2011) fabricates a Ti/HA-based implant by powder metallurgy with compositional changes in various layers. It is concluded that, by increasing the HA content, the elastic modulus and compressive strength show the decreasing trend. Akmal et al. (2016) investigate the bioactivity and electrochemical properties of various FGMs produced from stainless steel 316L (SS) reinforced with HA by the powder metallurgy technique. The HA concentration was varied between 0 and 20 wt.% with 5 wt.% increments in each layer; a montage micrograph of successive layers of the mix-FGM in the unetched condition is shown in **Figure 11a**, and it can be seen that HA has a homogenous distribution in various layers of mix-FGM. Also, an increasing trend of HA from the top to bottom layers is clear, and there is not any crack formation inside the layers or even at the interfaces. To further analyze the interlocking between the matrix and the reinforcement phases, the cross-section of mix-FGM was etched, and its montage micrograph is shown in **Figure 11b**. The grayish phase demonstrates the SS matrix, and the dull phases are the discontinuous HA phase. Moreover, the microstructure shows the existence of pores, and the porosity has an increasing manner, and grain size reduces in HA content increments. This means that HA content can hinder grain growth by the pinning effect. The electrochemical observations confirm the great performance of these FGMs against corrosion attack in 0.9% NaCl solution.

As discussed earlier, AM manufacturing has a great impact on the biomedical implant industry, and this is also true of orthopedic implants. Lots of new concepts have been introduced. Xiong et al. (2020) investigate the mechanical properties of SLM-produced Ti6Al4V FGMs with orthopedic implant applications. The rational design in which a radial gradient porous architecture with the potential to mimic the gradient structure of bone is proposed and can be seen in **Figure 12**. The SLM-produced samples have a linear varying porosity along the radial direction with two porous regions. A high-porosity region is similar to cancellous bone in the inside part for maintaining favorable regeneration and growth of cells and a low-porosity region is similar to cortical bone in the outer areas of the implant with a high load-bearing potential. This design leads to mechanical properties (Young's modulus and yield strength) in the range of natural human bone. It is confirmed that the addition of structural support can substantially improve its compressive strength and toughness along with the preservation of the appropriate elastic modulus. It can also improve the stability of the scaffold and maintain solid energy absorption ability (Xiong et al., 2020). Overall, AM methods are among the best candidates for FGM production in the biomedical field.

The mechanical property gradation (Young's modulus and hardness) was developed by Jung et al. (2009) *via* local heating of a groove rolled (Ti-35Nb)-4%Sn rod for artificial hip joint application with high strength value at one side and low Young's modulus at the other side; this design can be used for novel orthopedic implants. Hedia et al. (2014) design a cemented stem scheme through an FGM concept, and the result is that the most optimized approach is to use a cemented stem with gradation of Ti and collagen in which the upper stem layer is from Ti and the lower stem layer is composed of collagen. This novel cemented

stem design has the potential to eliminate the stress-shielding issue, especially at the nearby medial femoral region.

METALLIC FGMs FOR BIOMEDICAL APPLICATIONS

In previous sections, the importance and many applications of FGM Ti alloys are discussed, especially the AM manufactured ones. This section aims to analyze other types of FGM manufacturing methods in various metallic and multi-metallic systems. Metal and metal-ceramic composites are one of the most important classes of metallic FGMs, and most of them are designed especially for biomedical applications (Mortensen and Suresh, 1995; Suresh and Mortensen, 1997; Petit et al., 2018). In one study (Matuła et al., 2020), gradient porosities were produced by the powder metallurgy method on titanium/zirconium samples for biomedical applications, and this is shown in **Figure 13**. It is observed that the sintering process led to fabrication of a non-stoichiometric Zr (Ti) phase due to diffusion along the transition area. Also, gradual microstructural changes are seen in the transition zones, which lead to improved microhardness values. Moreover, the Rietveld refinement results confirm that pressure application during cold isostatic pressing had no significant influence on the unit cells.

Wilson et al. (2013) fabricate a functionally gradient bio-coating containing Co-Cr-Mo material (0–100%) on Ti-6Al-4V substrate *via* laser deposition (**Figure 14A**). Also, the SEM images of gradient Ti-6Al-4V/Co-Cr-Mo composite structure is shown in **Figures 14B–G**. This FGM material is aimed at reducing the influence of thermal expansion differences between two biomaterials through insulation cover. The results show the successful formation of a composite with excellent microscopic integrity without gross crack formation (**Figure 14H**) and favorable bonding strength between Co-Cr-Mo-alloy coatings and Ti-6Al-4V substrates. The gradual microhardness improvement by more than 83% was seen from Ti-6Al-4V substrate to the 50:50 composition layer. The average bonding strength was about 63.4 MPa; it was seen that the particles of Co-Cr-Mo coating were removed from the Ti-6Al-4V substrate through the adhesive mechanism. Also, the tensile strength was about 34.5 MPa and was much greater than the required minimum coating strength according to the ASTM standards. Overall, functionally gradient Ti-6Al-4V/Co-Cr-Mo material has a great potential to reduce the effects of thermal expansion differences between two biomaterials and, according to favorable microhardness, tensile, bonding strength, and biocompatibility, can be considered as a good FGM candidate for biomedical applications.

One of the approaches to produce various metallic FGMs is sedimentation and flotation because gravity is a phenomenon that is active everywhere on the earth. By exploiting this method, particles with varied size, density, and mass can move differently in liquid metals and alloys, leading to formation of graded structures, and this can be done by thermal controlling of die cooling (Drenchev et al., 2002). It is believed that sedimentation and flotation is one of the best available concepts to fabricate large-scale FGMs with very smooth and gradual variations in

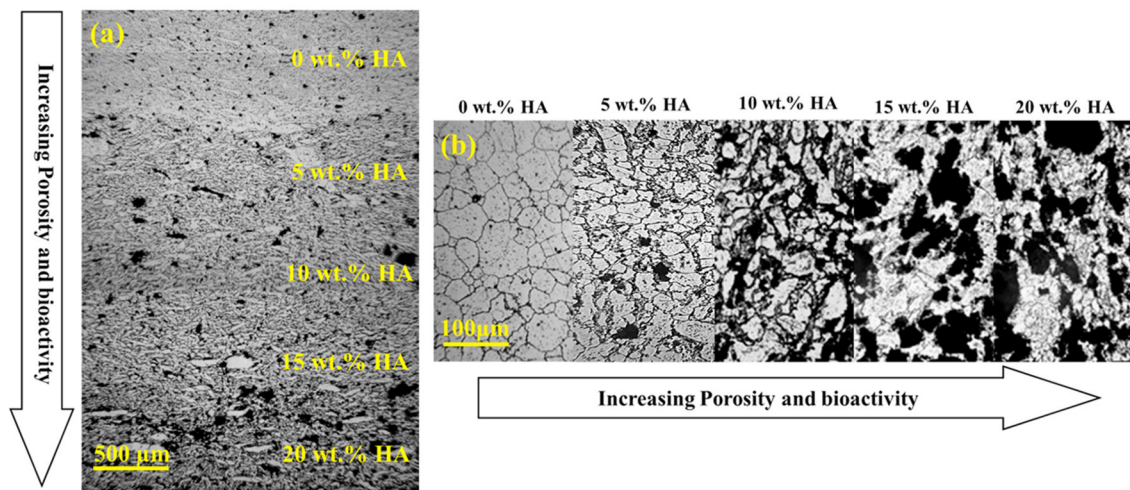


FIGURE 11 | (a) A montage micrograph without etching condition of mix-FGMs and (b) Montage image after etching with permission from Akmal et al. (2016).

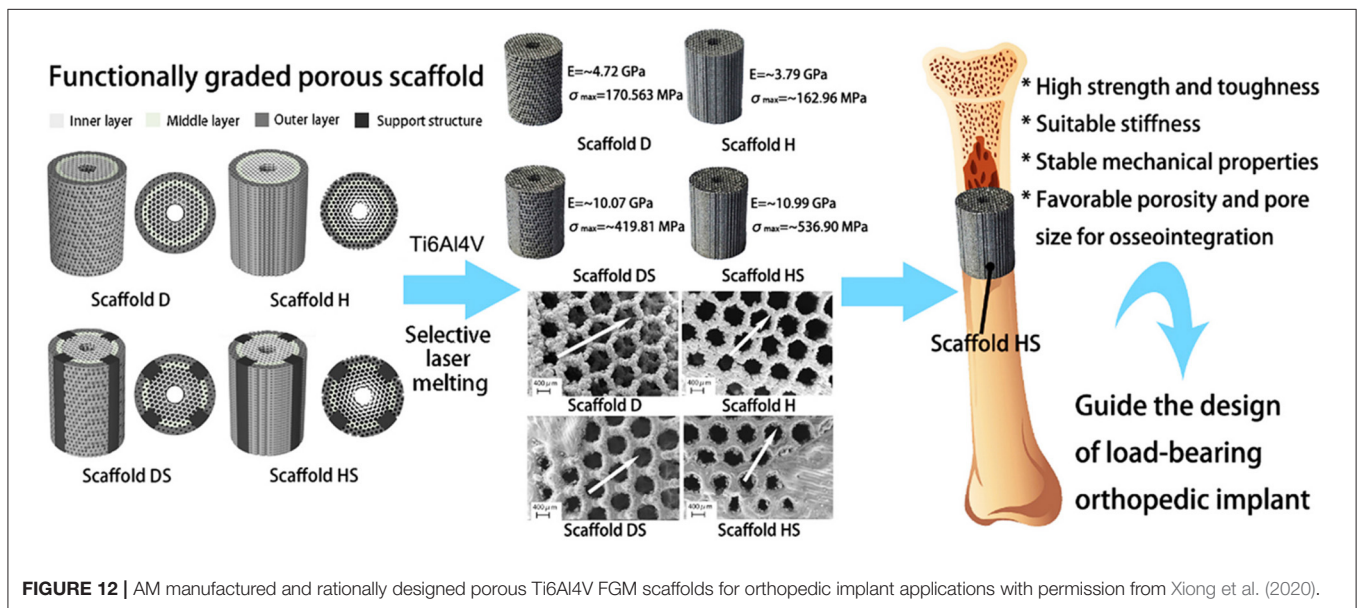


FIGURE 12 | AM manufactured and rationally designed porous Ti6Al4V FGM scaffolds for orthopedic implant applications with permission from Xiong et al. (2020).

composition and microstructure. Yu et al. (2003) produce a sort of W–Mo–Ti FGM with density gradients *via* a co-sedimentation method, and the samples were deposited after layer-by-layer settlement of the corresponding powders. First, the pure Ti layer is settled; second, the Ti–Mo graded layer; third, the Mo–W graded layer, and finally, the pure W layer has been settled. Also, a minor amount of Ni and Cu powders were used as sintering activators. After powder treatment, a set of suspensions was prepared and poured successively into a sedimentation container. After attaining full particle sedimentation, the deposit body compacted and sintered at 1,200°C under a pressure of 30 MPa in a vacuum furnace; **Figure 15** shows the electron micrograph and linear distributions of elements along the cross-section of W–Mo–Ti FGM.

The structural, physical, and mechanical properties of stainless steel (SS-316L)/HA and SS-316L/calcium silicate (CS) FGMs that were produced by powder metallurgical solid-state sintering were studied by Ataollahi et al. (2015). It is shown that high-temperature sintering led to the reaction between compounds of the SS-316L and HA although it has no considerable effect in the SS-316L/CS composite. Uniaxial compressive mechanical experiments show sharp reduction in SS-316L/HA with increasing HA content up to 20 wt.% and gradual variations in SS-316L/CS composites with CS content up to 50 wt.%. Also, the mechanical properties of SS-316L/HA FGM decreased with temperature increment although it showed improvement for the case of SS-316L/CS FGM. It is concluded that the SS-316L/CS composites and their

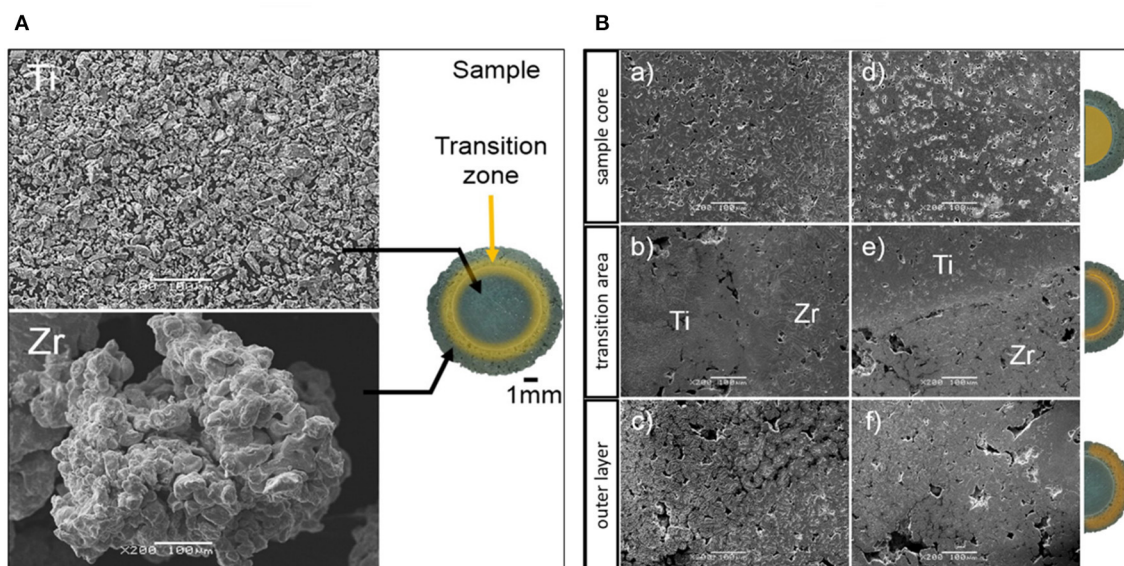


FIGURE 13 | (A) The SEM micrographs of initial powders and photo of the sample, including various zones across the sample; **(B)** the SEM micrographs of various zones: (a–c) Ti/Zr(–) produced under the pressure of 500 MPa; and (d–f) Ti/Zr(+) that was produced under 1,000 MPa pressure, reproduced with permission of (Matula et al., 2020).

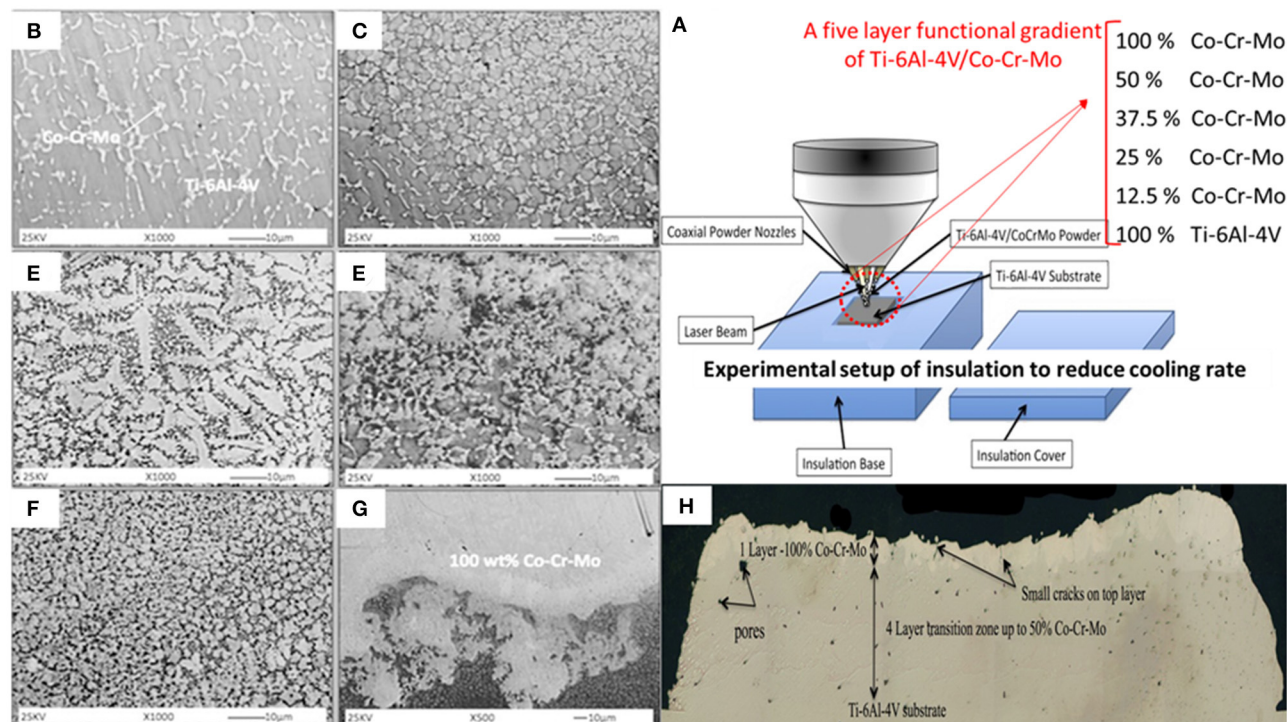


FIGURE 14 | (A) The experimental setup of laser deposition, including the insulation cover and the composition of five-layer functional gradient of Ti-6Al-4V/Co-Cr-Mo samples; **(B–G)** Corresponding SEM images of gradient Ti-6Al-4V/Co-Cr-Mo composite structure 1000 \times , **(B)** 10 wt.%, **(C)** ~20 wt.%, **(D)** ~30 wt.%, **(E)** ~35 wt.%, and **(F)** ~40 wt.% Co-Cr-Mo material, **(G)** the interface zone between 50/50 wt.% Ti-6Al-4V/Co-Cr-Mo and 100 wt.% Co-Cr-Mo; **(H)** Cross-section of the sample showing the Co-Cr-Mo gradient coating and some crack and pore formation on Ti-6Al-4V with up to 100% coating on the top layer; images were reproduced from Wilson et al. (2013) with permission.

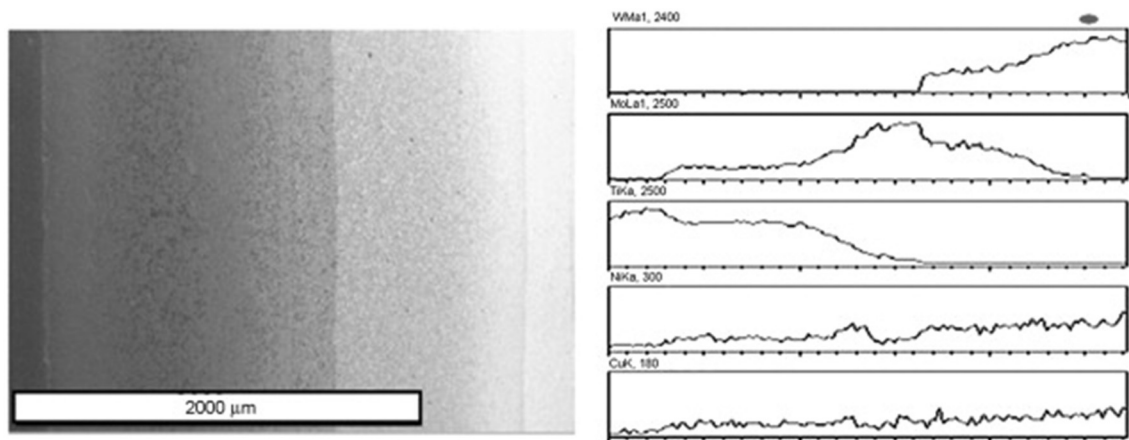


FIGURE 15 | The electron micrograph and linear distributions of elements along the cross-section of W-Mo-Ti FGM with permission from Yu et al. (2003).

FGMs have much better compressive mechanical properties compared to the SS-316L/HA composites and their FGMs. Moreover, the SS-316L/CS FGMs with better mechanical and enhanced gradation in physical and structural properties are among the suitable candidates for potential use in the load-bearing application (Ataollahi et al., 2015). A novel FGM by introduction of aluminum oxide and an yttria stabilized zirconia (YSZ) cushion layer was produced *via* the SPS process for potential bone implant applications (Afzal et al., 2012). The main goal of this FGM design was to attain a smooth gradation of functionality, including improved toughness of the bulk, and retained biocompatibility of the surface. In this regard, HA and YSZ with, respectively, ~ 1.5 and ~ 6.2 MPa.m^{1/2} fracture toughness were attached to a transition layer of Al₂O₃, inducing the minimum gradient of mechanical properties with fracture toughness of ~ 3.5 MPa.m^{1/2} (Figure 16). Measurement of hardness, fracture toughness, and cellular activities across the FGM cross-section illustrates the successful achievement to smooth transition in the HAp-Al₂O₃-YSZ FGM composite. Also, L929 fibroblast and Saos-2 osteoblast cell culturing showed the promising cell proliferation and adhesion on the FGM surface. It seems that this HAp-Al₂O₃-YSZ FGM has favorable properties for its possible utilization in bone implants.

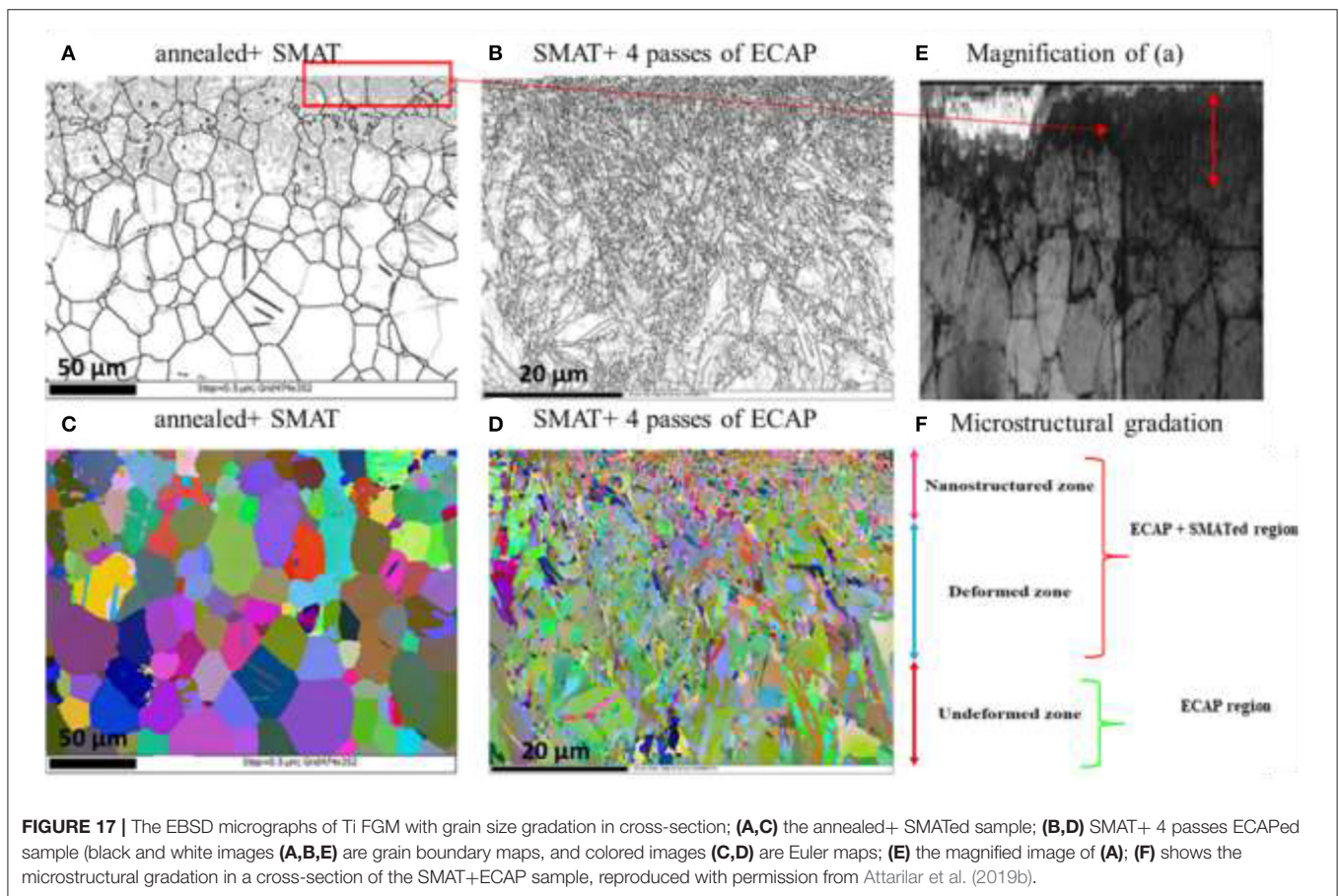
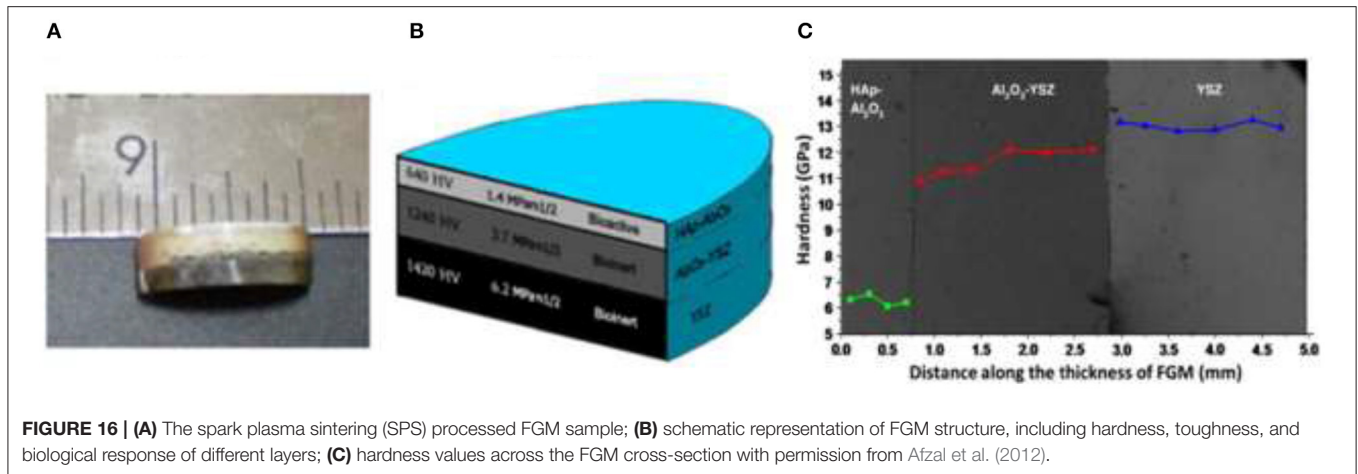
Another interesting study (Attarilar et al., 2019b), uses the grain size variation concept to fabricate pure Ti FGM material for biomedical applications with enhanced mechanical and biocompatibility properties. For this aim, a combined severe plastic deformation method was used. First, an ultrafine-grained (UFG) structure in the bulk of a material was produced by equal channel angular pressing (ECAP) in order to strengthen the bulk. Subsequently, the surface of the material reached a nanosized (NS) microstructure *via* surface mechanical attrition treatment (SMAT) (Figure 17). The surface nanostructures were considerably beneficial because they enhanced roughness, wettability, and TiO₂ oxide formation and led to better biomechanical bonding of cells and, finally, improved biological response. Moreover, nanoindentation experiments showed the gradual microhardness improvement values from the UFG

substrate to the NS surface layer, and the osteosarcoma G292 cell culturing confirmed the improved biological response through cell viability, alkaline phosphatase (ALP) activity, and cell attachment experiments (Attarilar et al., 2019b). A very interesting aspect of this research is that the successful FGM structure was achieved without the need to create composites and additional materials, so the bonding and separation issues encountered between different layers was completely mitigated.

A magnesium-based FGM composite for temporary orthopedic implant applications was produced by the SPS method due to its exceptional biodegradation behavior and mechanical characteristics similar to natural bone, which reduces the unfavorable stress-shielding effect (Dubey et al., 2020). The major drawback of Mg is its high *in vivo* corrosion rate, so the Mg-HA FGM production aimed to overcome this limitation. The FGM consisted of Mg at the core area with gradual increments of HA toward the outer layers (Figure 18). It is confirmed that this FGM has the potential to successfully attain a high corrosion-resistant property (about 154% improvement) in the surface along with uniform mechanical integrity distribution across the FGM structure. Moreover, it improved biocompatibility, osteoconductivity, and excellent osteogenic differentiation confirmed by MG63 cell culturing (Dubey et al., 2020). It seems that utilization of Mg-based FGM is a promising candidate with favorable properties for temporary orthopedic implant applications.

Gradient Nanostructured (GNS) Metals and Alloys

One of the important classes of FGMs is called gradient nanostructures (GNS), including gradient nanograined, nano-twinned, and nano-laminated metals and alloys. Sometimes, these GNS materials can exhibit extraordinary mechanical properties, such as strain hardening, strength-ductility synergy, enhanced fracture and fatigue resistance, and significant corrosion and wear resistance, that are not easily found in materials with homogeneous or random structures. Usually



GNS metals and alloys are fabricated with a gradation in the microstructure (grain size, twin thickness, and/or lamellar thickness) from the surface to the depth of the sample as illustrated in **Figure 2B** (Li X. et al., 2020).

One of the good examples of GNS materials is the nano-twin structure. Wang et al. (2013) produced an architected surface layer with a gradient decrease in twin density in a Fe-Mn austenitic steel *via* the surface mechanical grinding treatment

(SMGT) technique. This gradation in twin density corresponds to a gradient hardness reduction from 5.3 GPa in the top layer to about 2.2 GPa in the coarse-grained core. Also, the hardness dependence to twin thickness and superior strength-ductility synergy was observed in these samples; **Figure 19** shows the TEM cross-sectional micrographs of the SMGT Fe-Mn sample at different depths from the top surface. In the topmost layer ($\sim 10 \mu\text{m}$ thick, **Figure 19A**), the existence of nanosized

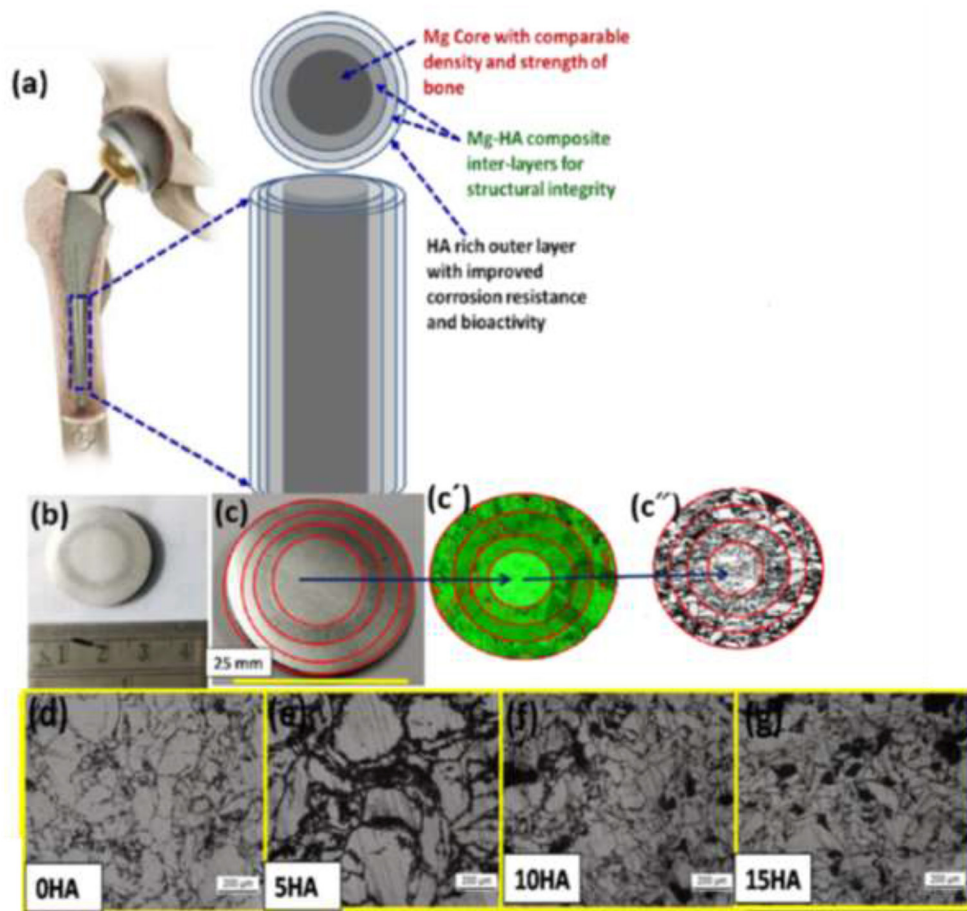


FIGURE 18 | (a) The schematic of Mg-based co-centric FGM composite, (b,c) image of FGM sample with different co-centric layers, (c',c'') the corresponding EDS and optical morphology images in various FGM layers, (d–g) optical micrographs of individual layers with various HA constituent with permission from Dubey et al. (2020).

grains with random orientations is clear. In the underneath layer ($45\text{ }\mu\text{m}$), a mixed microstructure of nanosized grains and nanoscale twin bundles are seen. Then, as we get closer to the depths of the sample, it can be seen that, gradually, the twin density and nano-twin bundle volume fraction increases while the volume fraction of nanograins drops.

As another example of GNS, the gradient nano-grained (GND) Cu with almost twice the yield stress of conventional Cu samples, significant strain softening, and excellent plasticity, was fabricated by the SMGT process (Chen et al., 2017) (Figure 20A). It was seen that the GND Cu layer could accommodate massive plastic strains. Liu et al. (2015) use the SMGT process to fabricate a nano-laminated structure in nickel by utilization of varied gradation of strain and strain rates in the subsurface layer with about $10\text{--}80\text{ }\mu\text{m}$ depth from surface; the existence of 2-D laminated structures with low angle boundaries and strong deformation textures with an average thickness of about 20 nm were observed (Figure 20B). It was confirmed that deformation of these nano-laminated structures happened due to dislocation slip and deformation twinning at the nanoscale, finally leading to

formation of nano-sized equiaxed grain structure. Another GND Cu structure was fabricated by direct-current electrodeposition with a controllable, homogeneous nano-twinned component (Cheng et al., 2018). It was seen that the structure includes a large number of preferentially oriented nanometer-scale twin boundaries enclosed within the micrometer-scale columnar-shaped grains (Figure 20C).

THE 4-D PRINTING IN METALLIC FGMs

Four-dimensional (4D) printing methods have the same principles as 3-D printing and are very similar to it; the main difference is the layer-by-layer formation of smart materials in which one more dimension is added to the material. Therefore, the 4-D printed part can transform its shape with respect to other physical and chemical parameters, such as temperature, pressure, humidity, light, magnetic and electric fields, and even time. These 4-D printed parts have a programmable nature that is a very favorable property; they can easily be controlled and

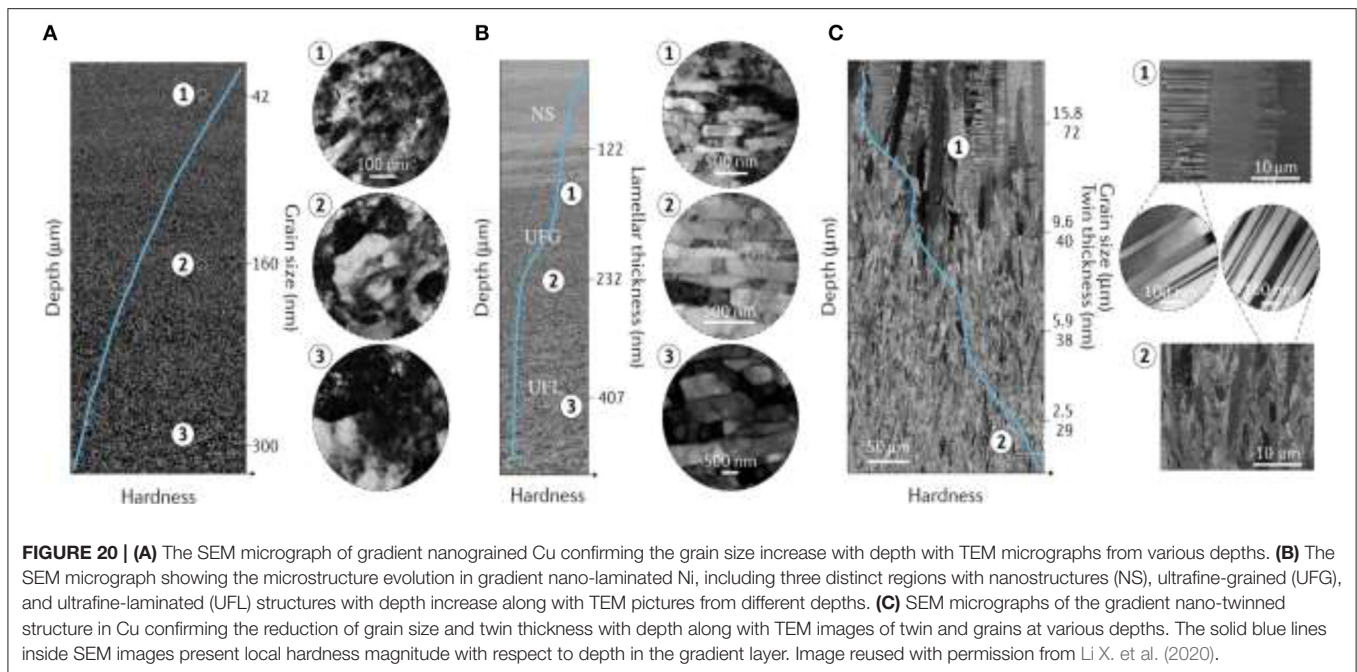


FIGURE 20 | (A) The SEM micrograph of gradient nanograined Cu confirming the grain size increase with depth with TEM micrographs from various depths. **(B)** The SEM micrograph showing the microstructure evolution in gradient nano-laminated Ni, including three distinct regions with nanostructures (NS), ultrafine-grained (UFG), and ultrafine-laminated (UFL) structures with depth increase along with TEM pictures from different depths. **(C)** SEM micrographs of the gradient nano-twinned structure in Cu confirming the reduction of grain size and twin thickness with depth along with TEM images of twin and grains at various depths. The solid blue lines inside SEM images present local hardness magnitude with respect to depth in the gradient layer. Image reused with permission from Li X. et al. (2020).

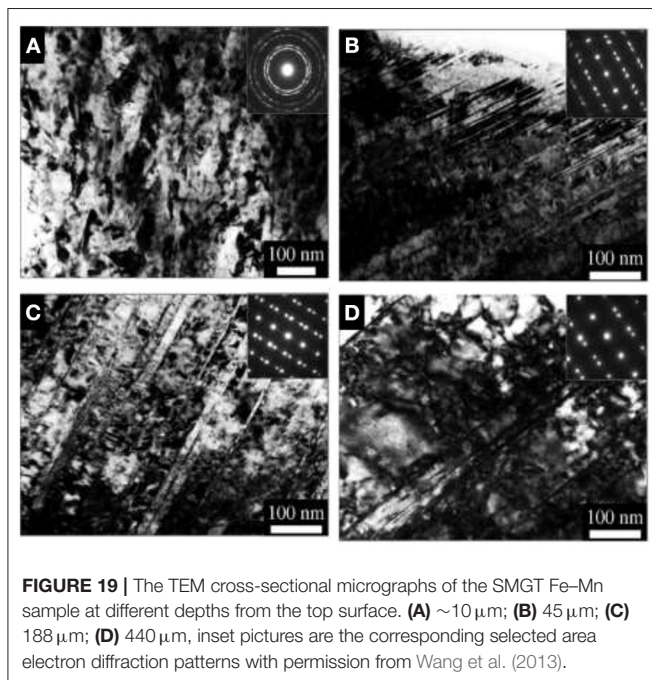


FIGURE 19 | The TEM cross-sectional micrographs of the SMGT Fe-Mn sample at different depths from the top surface. **(A)** ~10 μm; **(B)** 45 μm; **(C)** 188 μm; **(D)** 440 μm, inset pictures are the corresponding selected area electron diffraction patterns with permission from Wang et al. (2013).

respond according to the environmental condition and design requirements. This technology has many promising applications especially in customized implants and smart biomaterials (Javaid and Haleem, 2020). There are very limited studies about 4-D printing of metallic parts, most of the studies are about the 4-D printing of polymeric materials. Chen et al. (2019) introduces an innovative procedure capable of 3-D printed multimetal *via* an electrochemical 3-D printer system. This modern technology can

produce bimetallic structures through the selective deposition of various metals; hence, a temperature-responsive reaction can be programmed into the 4-D printed metallic parts. Although the studies in this area are very rare, due to the favorable and controllable properties of 4-D printing technologies, it seems that they have a very bright future in the production of smart metallic biomaterials.

FUTURE SCENERY

The FGM concept was an evolutionary pathway toward the design of multifunctional systems with lots of advantages, including smart design, potential to mimic natural biological systems, rapid and integrated designs, utilization of CAD systems and FEM-based schemes, enhanced properties, and conquering limitations such as the stress-shielding effect, etc. Although these are valuable advantages, numerous issues should still be solved, such as lack of systematic and detailed guidelines for various applications, design principles, involved mechanisms, widely accepted standards, and new technologies. Hence, future investigations should focus on overcoming these issues and providing comprehensive databases; improving techniques and related computer models, software, etc.; fabrication of modern devices; enhancing the compatibility of these parts with the entire system both biologically and mechanically; improving the fabrication resolution with the capacity to produce slight gradations; finding new methods to carefully tailor the distribution of phases, pores, and other constituents; upgrading the utilized materials; application of new concepts such as 4-D designs (Javaid and Haleem, 2019); bioprinting (Dwivedi and Mehrotra, 2020); metamaterials (Zhu et al., 2019; Sepehri et al., 2020); and so on. In this regard, considering the great impact of

AM technology, it should be further developed because it still is not applicable in real industrial conditions.

FGMs can be utilized in various areas, including biomedicine, structural parts, aviation, thermal management, energy-absorbing systems, optoelectronic, electromagnetic interference shielding (EMI), and even geological models that can analyze earthquakes and natural landslide disasters (Li Y. et al., 2020). The FGM concept can also be used in 4-D printing by the functionally graded additive manufacturing (FGAM) concept in which a single AM process incorporates the gradational mixing of materials in order to construct freeform geometries with changing properties within one component (Sudarmadji et al., 2011; Pei et al., 2017). Unfortunately, the existing AM technologies only have prototyping advantages with very limited functionality, so extensive research progress should be devoted to this field. The FGM designs profiting from the 4-D concept (Javaid and Haleem, 2020) can lead to the fabrication of *de novo* and smart parts that can completely change our lives; these intelligent, multifunctional systems can be used in the treatment of various diseases and hazardous tasks for humans. In brief, it can be said that FGMs have a great potential to influence the future of biomedicine and industry through their intricate gradients and multifunctional nature, and they demonstrate great prospects in the future of our technologies. In particular, it would open new horizons in biomedicine.

CONCLUSIONS

FGMs as a modern concept of materials attract much attention from academicians, the medical field, and industry. Because of the graded nature of bone and other natural systems, utilization of FGMs are very beneficial in biomedicine, and they can improve the overall performance of implants both biologically and biomechanically. This review paper comprehensively discusses the design criteria, techniques, applications, pros, and cons of FGMs, especially in biomaterials. In this regard, different FGM production methods are studied, especially additive manufacturing methods that are very capable in the production of complex FGM structures with high resolution and with multifunctional characteristics. Also, other methods, such as powder metallurgy, gas-based, liquid-based, and solid-phase processes, are introduced. The biological concept of FGM design

and the functional design of FGMs in biomedical applications are discussed thoroughly. The utilization of FGM design in dental and orthopedic implants is specifically considered in which the FEM-based designs are used to simulate natural tissues. The effect of FEM design in biological and biomechanical performance of implants is the focus of research because the main aim of these graded designs is to affect these properties. Subsequently, the future scenery of FGM, its applications, and the limitations that should be overcome were briefly mentioned. The modern concepts that can assist the more rapid development of FGM and its applications were introduced, including bioprinting, 4-D designs, metamaterials, etc. Finally, it can be said that FGMs, as a modern scheme, can substantially influence the future of biomedicine and its application, but still, it needs to be further developed from both a technological point of view and scientific aspect, and it has a long way to go to reach its optimum condition and vast industrialization. Hence, this review paper aimed to illuminate the way toward the modern, smart, and advantageous FGM biomaterials.

AUTHOR CONTRIBUTIONS

HS wrote the main part of the manuscript. PZ and JL contributed to the writing FGMs techniques section, biomedical applications, prepared, and formulated the references. PZ made major contributions particularly in choosing the figures. PZ, JL, CL, and LW made significant contribution to the revision stage. All authors contributed to the article and approved the submitted version.

FUNDING

The authors would like to acknowledge the financial supports provided by the Youth Innovation Team of Shaanxi Universities of Education Department of Shaanxi Provincial Government under Grant No. 2019-73. Royal Society via an International Exchange programme (Grant No. IEC/NSFC\191253), National Natural Science Foundation, a collaboration between Shanghai Jiao Tong University, and UCL under Grant No. 52011530181. CL would like to acknowledge the financial support from Engineering and Physical Science Research Council (EPSRC) via DTP CASE programme (Grant No. EP/T517793/1).

REFERENCES

- Afzal, M. A. F., Kesarwani, P., Reddy, K. M., Kalmodia, S., Basu, B., and Balani, K. (2012). Functionally graded hydroxyapatite-alumina-zirconia biocomposite: synergy of toughness and biocompatibility. *Mater. Sci. Eng. C* 32, 1164–1173. doi: 10.1016/j.msec.2012.03.003
- Akmal, M., Hussain, M. A., Ikram, H., Sattar, T., Jameel, S., Kim, J. Y., et al. (2016). In-vitro electrochemical and bioactivity evaluation of SS316L reinforced hydroxyapatite functionally graded materials fabricated for biomedical implants. *Ceram. Int.* 42, 3855–3863. doi: 10.1016/j.ceramint.2015.11.050
- Aldousari, S. M., Fouda, N., Hedia, H. S., and AlThobiani, F. W. H. (2018). Comparison of titanium and FGM dental implants with different coating types. *Mater. Test.* 60, 142–148. doi: 10.3139/120.111133
- Amrollahi, P., Krasinski, J. S., Vaidyanathan, R., Tayebi, L., and Vashae, D. (2016). “Electrophoretic Deposition (EPD): fundamentals and applications from nano- to microscale structures,” in *Handbook Nanoelectrochemistry*, eds M. Aliofkhaezraei and A. S. Hamdy Makhlof (Cham: Springer International Publishing), 561–591.
- Appel, E., Heepe, L., Lin, C.-P., and Gorb, S. N. (2015). Ultrastructure of dragonfly wing veins: composite structure of fibrous material supplemented by resilin. *J. Anat.* 227, 561–582. doi: 10.1111/joa.12362
- Arzt, E. (2006). Biological and artificial attachment devices: lessons for materials scientists from flies and geckos. *Mater. Sci. Eng. C* 26, 1245–1250. doi: 10.1016/j.msec.2005.08.033
- Asgharzadeh Shirazi, H., Ayatollahi, M. R., and Asnafi, A. (2017). To reduce the maximum stress and the stress shielding effect around a dental implant–bone interface using radial functionally graded biomaterials. *Comput. Methods Biomech. Biomed. Eng.* 20, 750–759. doi: 10.1080/10255842.2017.1299142
- Ataollahi, O., Pramanik, S., Mehrali, M., Yau, Y. H., Tarlochan, F., and Abu Osman, N. A. (2015). Mechanical and physical behavior of newly developed

- functionally graded materials and composites of stainless steel 316L with calcium silicate and hydroxyapatite. *J. Mech. Behav. Biomed. Mater.* 49, 321–331. doi: 10.1016/j.jmbbm.2015.05.020
- Attaran, M. (2017). The rise of 3-D printing: the advantages of additive manufacturing over traditional manufacturing. *Bus. Horiz.* 60, 677–688. doi: 10.1016/j.bushor.2017.05.011
- Attarilar, S., Djavanroodi, F., Irfan, O. M., Al-Mufadi, F. A., Ebrahimi, M., and Wang, Q. D. (2020). Strain uniformity footprint on mechanical performance and erosion-corrosion behavior of equal channel angular pressed pure titanium. *Results Phys.* 17:103141. doi: 10.1016/j.rinp.2020.103141
- Attarilar, S., Salehi, M. T., Al-Fadhalah, K. J., Djavanroodi, F., and Mozafari, M. (2019a). Functionally graded titanium implants: characteristic enhancement induced by combined severe plastic deformation. *PLoS ONE* 14:e0221491. doi: 10.1371/journal.pone.0221491
- Attarilar, S., Salehi, M. T., and Djavanroodi, F. (2019b). Microhardness evolution of pure titanium deformed by equal channel angular extrusion. *Metall. Res. Technol.* 116:408. doi: 10.1051/metal/2018135
- Awad, R. H., Habash, S. A., and Hansen, C. J. (2018). “3D printing methods,” in *3D Printing Applications in Cardiovascular Medicine*, eds J. Min, B. Mosadegh, S. Dunham, and S. Al'Aref (London: Elsevier), 11–32.
- Bahraminasab, M., and Edwards, K. L. (2019). “Computational tailoring of orthopaedic biomaterials: design principles and aiding tools,” in *BT - Biomaterials in Orthopaedics and Bone Regeneration: Design and Synthesis*, eds P. S. Bains, S. S. Sidhu, M. Bahraminasab, and C. Prakash (Singapore: Springer), 15–31.
- Bai, L., Gong, C., Chen, X., Sun, Y., Zhang, J., Cai, L., et al. (2019). Additive manufacturing of customized metallic orthopedic implants: materials, structures, surface modifications. *Metals* 9:1004. doi: 10.3390/met9091004
- Bao, G., and Wang, L. (1995). Multiple cracking in functionally graded ceramic/metal coatings. *Int. J. Solids Struct.* 32, 2853–2871. doi: 10.1016/0020-7683(94)00267-Z
- Batin, G., and Popa, C. (2011). Mechanical properties of Ti / HA functionally graded materials for hard tissue replacement. *Powder Metall. Prog.* 11, 206–209.
- Becker, B. S., and Bolton, J. D. (1997). Corrosion behaviour and mechanical properties of functionally gradient materials developed for possible hard-tissue applications. *J. Mater. Sci. Mater. Med.* 8, 793–797. doi: 10.1023/A:1018525015421
- Becker, B. S., Bolton, J. D., and Youseffi, M. (1995). Production of porous sintered Co–Cr–Mo alloys for possible surgical implant applications: part 1: compaction sintering behaviour, and properties. *Powder Metall.* 38, 201–208. doi: 10.1179/pom.1995.38.3.201
- Bikas, H., Stavropoulos, P., and Chrysosolouris, G. (2016). Additive manufacturing methods and modelling approaches: a critical review. *Int. J. Adv. Manuf. Technol.* 83, 389–405. doi: 10.1007/s00170-015-7576-2
- Bin Qasim, S. S., Zafar, M. S., Niazi, F. H., Alshahwan, M., Omar, H., and Daood, U. (2020). Functionally graded biomimetic biomaterials in dentistry: an evidence-based update. *J. Biomater. Sci. Polym. Ed.* 31, 1144–1162. doi: 10.1080/09205063.2020.1744289
- Boughton, P., Merhebi, J., Kim, C., Roger, G., Diwan, A. D., Clarke, E., et al. (2010). An interlocking ligamentous spinal disk arthroplasty with neural network infrastructure. *Biomimetics J. Biomater. Tissue Eng.* 7, 55–79. doi: 10.4028/www.scientific.net/JBBTE.7.55
- Boughton, P., Roger, G., Rohanizadeh, R., Mason, R. S., and Ruys, A. (2013). Functional gradients in natural and biomimetic spinal disk structures. *Biomim. Biomater.* 2013, 127–150. doi: 10.1533/9780857098887.1.127
- Boughton, P., Ruys, A., Roger, G., Rohanizadeh, R., Fisher, S., and Kolos, E. (2006). Functionally graded material for a spinal disk prosthesis. *Australas. Phys. Eng. Sci. Med.* 29:107.
- Braz Fernandes, F. M., Rodrigues, P. F., Magalhães, R., Camacho, E., Inácio, P., Santos, T., et al. (2019). “Functionally graded orthodontic archwires - production and characterization,” in *International Conference on Shape Memory and Superelastic Technologies, SMST 2019* (Konstanz).
- Burke, M., and Goodman, S. (2008). “Failure mechanisms in joint replacement,” in *Woodhead Publishing Series, Biomater*, ed P. A. Revell (Cambridge: Woodhead Publishing), 264–285.
- Chavara, D. T., Wang, C. X., and Ruys, A. (2009). Biomimetic functionally graded materials: synthesis by impeller-dry-blending. *Biomimetics J. Biomater. Tissue Eng.* 3, 37–49. doi: 10.4028/www.scientific.net/JBBTE.3.37
- Chen, L., Lengauer, W., Ettmayer, P., Dreyer, K., Daub, H. W., and Kassel, D. (2000). Fundamentals of liquid phase sintering for modern cermets and functionally graded cemented carbonitrides (FGCC). *Int. J. Refract. Met. Hard Mater.* 18, 307–322. doi: 10.1016/S0263-4368(00)00041-X
- Chen, P.-Y., Schirer, J., Simpson, A., Nay, R., Lin, Y.-S., Yang, W., et al. (2012). Predation versus protection: fish teeth and scales evaluated by nanoindentation. *J. Mater. Res.* 27, 100–112. doi: 10.1557/jmr.2011.332
- Chen, W., You, Z. S., Tao, N. R., Jin, Z. H., and Lu, L. (2017). Mechanically-induced grain coarsening in gradient nano-grained copper. *Acta Mater.* 125, 255–264. doi: 10.1016/j.actamat.2016.12.006
- Chen, X., Liu, X., Ouyang, M., Chen, J., Taiwo, O., Xia, Y., et al. (2019). Multi-metal 4D printing with a desktop electrochemical 3D printer. *Sci. Rep.* 9:3973. doi: 10.1038/s41598-019-40774-5
- Cheng, Z., Zhou, H., Lu, Q., Gao, H., and Lu, L. (2018). Extra strengthening and work hardening in gradient nanotwinned metals. *Science* 362:eaau1925. doi: 10.1126/science.aau1925
- Chern, A. H., Nandwana, P., Mcdaniels, R., Dehoff, R. R., Liaw, P. K., Tryon, R., et al. (2020). Build orientation, surface roughness, and scan path influence on the microstructure, mechanical properties, and flexural fatigue behavior of Ti–6Al–4V fabricated by electron beam melting. *Mater. Sci. Eng. A* 772:138740. doi: 10.1016/j.msea.2019.138740
- Choy, K. (2003). Chemical vapour deposition of coatings. *Prog. Mater. Sci.* 48, 57–170. doi: 10.1016/S0079-6425(01)00009-3
- Cong, W., and Ning, F. (2017). A fundamental investigation on ultrasonic vibration-assisted laser engineered net shaping of stainless steel. *Int. J. Mach. Tools Manuf.* 121, 61–69. doi: 10.1016/j.ijmactools.2017.04.008
- Culmone, C., Smit, G., and Breedveld, P. (2019). Additive manufacturing of medical instruments: a state-of-the-art review. *Addit. Manuf.* 27, 461–473. doi: 10.1016/j.addma.2019.03.015
- Ding, Z., Fan, Q., and Wang, L. (2019). A review on friction stir processing of titanium alloy: characterization, method, microstructure, properties. *Metall. Mater. Trans. B* 50, 2134–2162. doi: 10.1007/s11663-019-01634-9
- Drenchev, L., Sobczak, J., and Sobczak, N. (2002). Sedimentation phenomenon and viscosity of water–SiC suspension under gravity conditions—a water model study for composites synthesis. *Colloids Surf. A Physicochem. Eng. Asp.* 197, 203–211. doi: 10.1016/S0927-7757(01)00893-7
- Dubey, A., Jaiswal, S., Haldar, S., Roy, P., and Lahiri, D. (2020). Functionally gradient magnesium based composite for temporary orthopedic implant with improved corrosion resistance and osteogenic properties. *Biomed. Mater.* 16:015017. doi: 10.1088/1748-605X/abb721
- Dwivedi, R., and Mehrotra, D. (2020). 3D bioprinting and craniofacial regeneration. *J. Oral Biol. Craniofacial Res.* 10, 650–659. doi: 10.1016/j.jobcr.2020.08.011
- Ehtemam-Haghighi, S., Prashanth, K. G., Attar, H., Chaubey, A. K., Cao, G. H., and Zhang, L. C. (2016). Evaluation of mechanical and wear properties of Ti xNb 7Fe alloys designed for biomedical applications. *Mater. Des.* 111, 592–599. doi: 10.1016/j.matdes.2016.09.029
- Enab, T. A. (2012). A comparative study of the performance of metallic and FGM tibia tray components in total knee replacement joints. *Comput. Mater. Sci.* 53, 94–100. doi: 10.1016/j.commatsci.2011.09.032
- Endo, M., Takeuchi, K., Igarashi, S., Kobori, K., Shiraishi, M., and Kroto, H. W. (1993). The production and structure of pyrolytic carbon nanotubes (PCNTs). *J. Phys. Chem. Solids* 54, 1841–1848. doi: 10.1016/0022-3697(93)90297-5
- Faure, B., Salazar-Alvarez, G., Ahnizay, A., Villaluenga, I., Berriozabal, G., and De Miguel, Y. R. (2013). Bergström L, dispersion and surface functionalization of oxide nanoparticles for transparent photocatalytic and UV-protecting coatings and sunscreens. *Sci. Technol. Adv. Mater.* 14:023001. doi: 10.1088/1468-6996/14/2/023001
- Galarraga, H., Lados, D. A., Dehoff, R. R., Kirka, M. M., and Nandwana, P. (2016). Effects of the microstructure and porosity on properties of Ti–6Al–4V ELI alloy fabricated by electron beam melting (EBM). *Addit. Manuf.* 10, 47–57. doi: 10.1016/j.addma.2016.02.003
- Gazit, E. (2007). Self-assembled peptide nanostructures: the design of molecular building blocks and their technological utilization. *Chem. Soc. Rev.* 36, 1263–1269. doi: 10.1039/b605536m
- Gecko Tail Regeneration (2011). Available online at: <https://www.toppr.com/content/story/amp/asexual-reproduction-regeneration-16733/>

- Gode, C., Attarilar, S., Eghbali, B., and Ebrahimi, M. (2015). Electrochemical behavior of equal channel angular pressed titanium for biomedical application. *AIIP Conf. Proc.* 1653:020041. doi: 10.1063/1.4914232
- Haghshenas, M. (2017). Mechanical characteristics of biodegradable magnesium matrix composites: a review. *J. Magnes. Alloy* 5, 189–201. doi: 10.1016/j.jma.2017.05.001
- Han, C., Li, Y., Wang, Q., Cai, D., Wei, Q., Yang, L., et al. (2018a). Titanium/hydroxyapatite (Ti/HA) gradient materials with quasi-continuous ratios fabricated by SLM: material interface and fracture toughness. *Mater. Des.* 141, 256–266. doi: 10.1016/j.matdes.2017.12.037
- Han, C., Li, Y., Wang, Q., Wen, S., Wei, Q., Yan, C., et al. (2018b). Continuous functionally graded porous titanium scaffolds manufactured by selective laser melting for bone implants. *J. Mech. Behav. Biomed. Mater.* 80, 119–127. doi: 10.1016/j.jmbbm.2018.01.013
- Hazlehurst, K. B., Wang, C. J., and Stanford, M. (2014a). A numerical investigation into the influence of the properties of cobalt chrome cellular structures on the load transfer to the periprosthetic femur following total hip arthroplasty. *Med. Eng. Phys.* 36, 458–466. doi: 10.1016/j.medengphys.2014.02.008
- Hazlehurst, K. B., Wang, C. J., and Stanford, M. (2014b). An investigation into the flexural characteristics of functionally graded cobalt chrome femoral stems manufactured using selective laser melting. *Mater. Des.* 60, 177–183. doi: 10.1016/j.matdes.2014.03.068
- He, G., Guo, B., Wang, H., Liang, C., Ye, L., Lin, Y., et al. (2014). Surface characterization and osteoblast response to a functionally graded hydroxyapatite/fluoro-hydroxyapatite/titanium oxide coating on titanium surface by sol-gel method. *Cell Prolif.* 47, 258–266. doi: 10.1111/cpr.12105
- He, L.-H., and Swain, M. V. (2009). Enamel—a functionally graded natural coating. *J. Dent.* 37, 596–603. doi: 10.1016/j.jdent.2009.03.019
- Hedia, H. S. (2005). Design of functionally graded dental implant in the presence of cancellous bone. *J. Biomed. Mater. Res. B Appl. Biomater.* 75B, 74–80. doi: 10.1002/jbm.b.30275
- Hedia, H. S., Aldousari, S. M., Abdellatif, A. K., and Fouda, N. (2014). A new design of cemented stem using functionally graded materials (FGM). *Biomed. Mater. Eng.* 24, 1575–1588. doi: 10.3233/BME-140962
- Hedia, H. S., and Fouda, N. (2013). Improved stress shielding on a cementless tibia tray using functionally graded material. *Mater. Test.* 55, 845–851. doi: 10.3139/120.110507
- Henriques, B., Gonçalves, S., Soares, D., and Silva, F. S. (2012). Shear bond strength comparison between conventional porcelain fused to metal and new functionally graded dental restorations after thermal-mechanical cycling. *J. Mech. Behav. Biomed. Mater.* 13, 194–205. doi: 10.1016/j.jmbbm.2012.06.002
- Hirai, T. (1995). CVD processing. *MRS Bull.* 20, 45–47. doi: 10.1557/S0883769400048946
- Ichim, P. I., Hu, X., Bazen, J. J., and Yi, W. (2016). Design optimization of a radial functionally graded dental implant. *J. Biomed. Mater. Res. B Appl. Biomater.* 104, 58–66. doi: 10.1002/jbm.b.33345
- Islam, M., Thakur, M. S. H., Mojumder, S., Al Amin, A., and Islam, M. M. (2020). Mechanical and vibrational characteristics of functionally graded Cu–Ni nanowire: a molecular dynamics study. *Compos. B Eng.* 198:108212. doi: 10.1016/j.compositesb.2020.108212
- Jagnandan, K., Russell, A. P., and Higham, T. E. (2014). Tail autotomy and subsequent regeneration alter the mechanics of locomotion in lizards. *J. Exp. Biol.* 217, 3891–3897. doi: 10.1242/jeb.110916
- Jardini, A. L., Larosa, M. A., Filho, R. M., de Zavaglia, C. A., Bernardes, L. F., Lambert, C. S., et al. (2014). Cranial reconstruction: 3D biomodel and custom-built implant created using additive manufacturing. *J. Cranio Maxillofacial Surg.* 42, 1877–1884. doi: 10.1016/j.jcms.2014.07.006
- Javadi, M., and Haleem, A. (2018). Additive manufacturing applications in medical cases: a literature based review. *Alexandria J. Med.* 54, 411–422. doi: 10.1016/j.ajme.2017.09.003
- Javadi, M., and Haleem, A. (2019). 4D printing applications in medical field: a brief review. *Clin. Epidemiol. Glob. Heal.* 7, 317–321. doi: 10.1016/j.cegh.2018.09.007
- Javadi, M., and Haleem, A. (2020). Significant advancements of 4D printing in the field of orthopaedics. *J. Clin. Orthop. Trauma* 11, S485–S490. doi: 10.1016/j.jcot.2020.04.021
- Jung, T. K., Matsumoto, H., Abumiya, T., Masahashi, N., Kim, M. S., and Hanada, S. (2009). Mechanical properties-graded Ti alloy implants for orthopedic applications. *Mater. Sci. Forum.* 631–632, 205–210. doi: 10.4028/www.scientific.net/MSF.631-632.205
- Kawasaki, A., and Watanabe, R. (1997). Concept and P/M fabrication of functionally gradient materials. *Ceram. Int.* 23, 73–83. doi: 10.1016/0272-8842(95)00143-3
- Ke, D., Vu, A. A., Bandyopadhyay, A., and Bose, S. (2019). Compositionally graded doped hydroxyapatite coating on titanium using laser and plasma spray deposition for bone implants. *Acta Biomater.* 84, 414–423. doi: 10.1016/j.actbio.2018.11.041
- Khodabakhshi, F., Farshidianfar, M. H., Bakhshivash, S., Gerlich, A. P., and Khajepour, A. (2019). Dissimilar metals deposition by directed energy based on powder-fed laser additive manufacturing. *J. Manuf. Process.* 43, 83–97. doi: 10.1016/j.jmapro.2019.05.018
- Khor, K., Gu, Y., Quek, C., and Cheang, P. (2003). Plasma spraying of functionally graded hydroxyapatite/Ti–6Al–4V coatings. *Surf. Coatings Technol.* 168, 195–201. doi: 10.1016/S0257-8972(03)00238-X
- Koizumi, M., and Niino, M. (1995). Overview of FGM research in Japan. *MRS Bull.* 20, 19–21. doi: 10.1557/S0883769400048867
- Kondo, H., Yokoyama, A., Omori, M., Ohkubo, A., Hirai, T., Watari, F., et al. (2004). Fabrication of titanium nitride/apatite functionally graded implants by spark plasma sintering. *Mater. Trans.* 45, 3156–3162. doi: 10.2320/matertrans.45.3156
- Kong, D., Ni, X., Dong, C., Lei, X., Zhang, L., Man, C., et al. (2018). Bio-functional and anti-corrosive 3D printing 316L stainless steel fabricated by selective laser melting. *Mater. Des.* 152, 88–101. doi: 10.1016/j.matdes.2018.04.058
- Li, S., Zhao, S., Hou, W., Teng, C., Hao, Y., Li, Y., et al. (2016). Functionally graded Ti–6Al–4V meshes with high strength and energy absorption. *Adv. Eng. Mater.* 18, 34–38. doi: 10.1002/adem.201500086
- Li, S. J., Xu, Q. S., Wang, Z., Hou, W. T., Hao, Y. L., Yang, R., et al. (2014). Influence of cell shape on mechanical properties of Ti–6Al–4V meshes fabricated by electron beam melting method. *Acta Biomater.* 10, 4537–4547. doi: 10.1016/j.actbio.2014.06.010
- Li, X., Lu, L., Li, J., Zhang, X., and Gao, H. (2020). Mechanical properties and deformation mechanisms of gradient nanostructured metals and alloys. *Nat. Rev. Mater.* 5, 706–723. doi: 10.1038/s41578-020-0212-2
- Li, Y., Feng, Z., Hao, L., Huang, L., Xin, C., Wang, Y., et al. (2020). Review on functionally graded materials and structures via additive manufacturing: from multi-scale design to versatile functional properties. *Adv. Mater. Technol.* 5:1900981. doi: 10.1002/admt.201900981
- Lima, D. D., Mantri, S. A., Mikler, C. V., Contieri, R., Yannetta, C. J., Campo, K. N., et al. (2017). Laser additive processing of a functionally graded internal fracture fixation plate. *Mater. Des.* 130, 8–15. doi: 10.1016/j.matdes.2017.05.034
- Limmahakun, S., Oloyede, A., Sitthiseripratip, K., Xiao, Y., and Yan, C. (2017). Stiffness and strength tailoring of cobalt chromium graded cellular structures for stress-shielding reduction. *Mater. Des.* 114, 633–641. doi: 10.1016/j.matdes.2016.11.090
- Lin, D., Li, Q., Li, W., and Swain, M. (2009a). Bone remodeling induced by dental implants of functionally graded materials. *J. Biomed. Mater. Res. B Appl. Biomater.* 92, 430–438. doi: 10.1002/jbm.b.31531
- Lin, D., Li, Q., Li, W., Zhou, S., and Swain, M. V. (2009b). Design optimization of functionally graded dental implant for bone remodeling. *Compos. B Eng.* 40, 668–675. doi: 10.1016/j.compositesb.2009.04.015
- Liu, C., Hu, D., Xu, J., Yang, D., and Qi, M. (2006). *In vitro* electrochemical corrosion behavior of functionally graded diamond-like carbon coatings on biomedical Nitinol alloy. *Thin Solid Films* 496, 457–462. doi: 10.1016/j.tsf.2005.09.109
- Liu, X. C., Zhang, H. W., and Lu, K. (2015). Formation of nano-laminated structure in nickel by means of surface mechanical grinding treatment. *Acta Mater.* 96, 24–36. doi: 10.1016/j.actamat.2015.06.014
- Liu, Y. J., Li, S. J., Wang, H. L., Hou, W. T., Hao, Y. L., Yang, R., et al. (2016). Microstructure, defects and mechanical behavior of beta-type titanium porous structures manufactured by electron beam melting and selective laser melting. *Acta Mater.* 113, 56–67. doi: 10.1016/j.actamat.2016.04.029
- Liu, Z., Meyers, M. A., Zhang, Z., and Ritchie, R. O. (2017). Functional gradients and heterogeneities in biological materials: design principles, functions, bioinspired applications. *Prog. Mater. Sci.* 88, 467–498. doi: 10.1016/j.pmatsci.2017.04.013
- Lüdecke, C., Bossert, J., Roth, M., and Jandt, K. D. (2013). Physical vapor deposited titanium thin films for biomedical applications: reproducibility of nanoscale surface roughness and microbial adhesion properties. *Appl. Surf. Sci.* 280, 578–589. doi: 10.1016/j.apsusc.2013.05.030

- Madan, R., and Bhowmick, S. (2020). A review on application of FGM fabricated using solid-state processes. *Adv. Mater. Process. Technol.* 6, 608–619. doi: 10.1080/2374068X.2020.1731153
- Mahmoud, D., and Elbestawi, M. (2017). Lattice structures and functionally graded materials applications in additive manufacturing of orthopedic implants: a review. *J. Manuf. Mater. Process.* 1:13. doi: 10.3390/jmmp1020013
- Matsuno, T., Watanabe, K., Ono, K., and Koishi, M. (1998). Preparation of laminated hydroxyapatite/zirconia sintered composite with the gradient composition. *J. Mater. Sci. Lett.* 17, 1349–1351. doi: 10.1023/A:1026487222287
- Matsuo, S., Watari, F., and Ohata, N. (2001). Fabrication of a functionally graded dental composite resin post and core by laser lithography and finite element analysis of its stress relaxation effect on tooth root. *Dent. Mater. J.* 20, 257–274. doi: 10.4012/dmj.20.257
- Matula, G., and Dobrzański, L. A. (2006). Structure and properties of FGM manufactured on the basis of HS6-5-2. *J. Achiev. Mater. Manuf. Eng.* 17, 101–104.
- Matula, I., Dercz, G., and Barczyk, J. (2020). Titanium/Zirconium functionally graded materials with porosity gradients for potential biomedical applications. *Mater. Sci. Technol.* 36, 972–977. doi: 10.1080/02670836.2019.1593603
- Mehrali, M., Shirazi, F. S., Mehrali, M., Metselaar, H. S. C., Bin Kadri, N. A., and Osman, N. A. A. (2013). Dental implants from functionally graded materials. *J. Biomed. Mater. Res. A* 101, 3046–3057. doi: 10.1002/jbm.a.34588
- Mishra, A., Bhatt, N., and Bajpai, A. K. (2019). Nanostructured superhydrophobic coatings for solar panel applications. *Nanomater. Based Coat.* 2019, 397–424. doi: 10.1016/B978-0-12-815884-5.00012-0
- Miyako, E., Sugino, T., Okazaki, T., Bianco, A., Yudasaka, M., and Iijima, S. (2013). Self-assembled carbon nanotube honeycomb networks using a butterfly wing template as a multifunctional nanobiohybrid. *ACS Nano* 7, 8736–8742. doi: 10.1021/nn403083v
- Mobbs, R. J., Coughlan, M., Thompson, R., Sutterlin, C. E., and Phan, K. (2017). The utility of 3D printing for surgical planning and patient-specific implant design for complex spinal pathologies: case report. *J. Neurosurg. Spine.* 26, 513–518. doi: 10.3171/2016.9.SPINE16371
- Mohd Ali, M., Yang, R., Zhang, B., Furini, F., Rai, R., Otte, J. N., et al. (2020). Enriching the functionally graded materials (FGM) ontology for digital manufacturing. *Int. J. Prod. Res.* 1–18. doi: 10.1080/00207543.2020.1787534
- Mortensen, A., and Suresh, S. (1995). Functionally graded metals and metal-ceramic composites: part 1 processing. *Int. Mater. Rev.* 40, 239–265. doi: 10.1179/imr.1995.40.6.239
- Naebe, M., and Shirvanimoghaddam, K. (2016). Functionally graded materials: a review of fabrication and properties. *Appl. Mater. Today* 5, 223–245. doi: 10.1016/j.apmt.2016.10.001
- Ngo, T. D., Kashani, A., Imbalzano, G., Nguyen, K. T. Q., and Hui, D. (2018). Additive manufacturing (3D printing): a review of materials, methods, applications and challenges. *Compos. B Eng.* 143, 172–196. doi: 10.1016/j.compositesb.2018.02.012
- Niinomi, M., and Nakai, M. (2011). Titanium-based biomaterials for preventing stress shielding between implant devices and bone. *Int. J. Biomater.* 2011:836587. doi: 10.1155/2011/836587
- Nosil, P., Villoutreix, R., de Carvalho, C. F., Farkas, T. E., Soria-Carrasco, V., Feder, J. L., et al. (2018). Natural selection and the predictability of evolution in Timema stick insects. *Science* 359, 765–770. doi: 10.1126/science.aap9125
- Nune, K., Kumar, A., Misra, R., Li, S., Hao, Y., and Yang, R. (2016). Osteoblast functions in functionally graded Ti-6Al-4V mesh structures. *J. Biomater. Appl.* 30, 1182–1204. doi: 10.1177/0885328215617868
- Nune, K. C., Kumar, A., Misra, R. D. K., Li, S. J., Hao, Y. L., and Yang, R. (2017). Functional response of osteoblasts in functionally gradient titanium alloy mesh arrays processed by 3D additive manufacturing. *Colloids Surf. B Biointerfaces* 150, 78–88. doi: 10.1016/j.colsurfb.2016.09.050
- Oh, S. H., Park, I. K., Kim, J. M., and Lee, J. H. (2007). *In vitro* and *in vivo* characteristics of PCL scaffolds with pore size gradient fabricated by a centrifugation method. *Biomaterials* 28, 1664–1671. doi: 10.1016/j.biomaterials.2006.11.024
- Okulov, I. V., Volegov, A. S., Attar, H., Bönisch, M., Ehtemam-Haghighi, S., Calin, M., et al. (2017). Composition optimization of low modulus and high-strength TiNb-based alloys for biomedical applications. *J. Mech. Behav. Biomed. Mater.* 65, 866–871. doi: 10.1016/j.jmbbm.2016.10.013
- Onal, E., Frith, J., Jurg, M., Wu, X., and Molotnikov, A. (2018). Mechanical properties and *in vitro* behavior of additively manufactured and functionally graded Ti6Al4V porous scaffolds. *Metals* 8:200. doi: 10.3390/met8040200
- Oshkour, A., Abu Osman, N., Yau, Y., Tarlochan, F., and Wan Abas, W. (2013). Design of new generation femoral prostheses using functionally graded materials: a finite element analysis. *Proc. Inst. Mech. Eng. H J. Eng. Med.* 227, 3–17. doi: 10.1177/0954411912459421
- Parthasarathy, J., Starly, B., and Raman, S. (2011). A design for the additive manufacture of functionally graded porous structures with tailored mechanical properties for biomedical applications. *J. Manuf. Process.* 13, 160–170. doi: 10.1016/j.jmapro.2011.01.004
- Pei, E., Loh, G. H., Harrison, D., de Almeida, H. A., Monzón Verona, M. D., and Paz, R. (2017). A study of 4D printing and functionally graded additive manufacturing. *Assem. Autom.* 37, 147–153. doi: 10.1108/AA-01-2017-012
- Petit, C., Montanaro, L., and Palmero, P. (2018). Functionally graded ceramics for biomedical application: concept, manufacturing, and properties. *Int. J. Appl. Ceram. Technol.* 15, 820–840. doi: 10.1111/ijac.12878
- Qadir, M., Li, Y., and Wen, C. (2019). Ion-substituted calcium phosphate coatings by physical vapor deposition magnetron sputtering for biomedical applications: a review. *Acta Biomater.* 89, 14–32. doi: 10.1016/j.actbio.2019.03.006
- Rack, H. J., and Qazi, J. I. (2006). Titanium alloys for biomedical applications. *Mater. Sci. Eng. C* 26, 1269–1277. doi: 10.1016/j.msec.2005.08.032
- Sadollah, A., and Bahreininejad, A. (2011). Optimum gradient material for a functionally graded dental implant using metaheuristic algorithms. *J. Mech. Behav. Biomed. Mater.* 4, 1384–1395. doi: 10.1016/j.jmbbm.2011.05.009
- Sarkar, P., De, D., Uchikochi, T., and Besra, L. (2012). “Electrophoretic Deposition (EPD): fundamentals and novel applications in fabrication of advanced ceramic microstructures,” in *Electrophoretic Deposition of Nanomaterials*, eds J. Dickerson, and A. Boccaccini (New York, NY: Nanostructure Science and Technology; Springer). doi: 10.1007/978-1-4419-9730-2_5
- Sedighi, M., Omid, N., and Jabbari, A. (2017). Experimental investigation of FGM dental implant properties made from Ti/HA composite. *Mech. Adv. Compos. Struct.* 4, 233–237. doi: 10.22075/macs.2017.1819.1096
- Senan, E. M., and Madfa, A. A. (2017). “Functional biomimetic dental restoration,” in *Insights Into Various Aspects of Oral Health* (IntTech). Available online at: <https://www.intechopen.com/books/insights-into-various-aspects-of-oral-health/functional-biomimetic-dental-restoration>
- Sepehri, S., Jafari, H., Mosavi Mashhadi, M., Hairi Yazdi, M. R., and Seyyed Fakhraabadi, M. M. (2020). Tunable elastic wave propagation in planar functionally graded metamaterials. *Acta Mech.* 231, 3363–3385. doi: 10.1007/s00707-020-02705-8
- Shahrjerdi, A., Mustapha, F., Bayat, M., Sapuan, S. M., and Majid, D. L. A. (2011). Fabrication of functionally graded hydroxyapatite-titanium by applying optimal sintering procedure and powder metallurgy. *Int. J. Phys. Sci.* 6, 2258–2267. doi: 10.5897/IJPS11.223
- Shen, Z. J., Adolfsson, E., Nygren, M., Gao, L., Kawaoka, H., and Niihara, K. (2001). Dense hydroxyapatite-zirconia ceramic composites with high strength for biological applications. *Adv. Mater.* 13, 214–216. doi: 10.1002/1521-4095(200102)13:3<214::AID-ADMA214>3.0.CO;2-5
- Sola, A., Bellucci, D., and Cannillo, V. (2016). Functionally graded materials for orthopedic applications – an update on design and manufacturing. *Biotechnol. Adv.* 34, 504–531. doi: 10.1016/j.biotechadv.2015.12.013
- Sudarmadji, N., Tan, J. Y., Leong, K. F., Chua, C. K., and Loh, Y. T. (2011). Investigation of the mechanical properties and porosity relationships in selective laser-sintered polyhedral for functionally graded scaffolds. *Acta Biomater.* 7, 530–537. doi: 10.1016/j.actbio.2010.09.024
- Suk, M.-J., Choi, S.-I., Kim, J.-S., Do Kim, Y., and Kwon, Y.-S. (2003). Fabrication of a porous material with a porosity gradient by a pulsed electric current sintering process. *Met. Mater. Int.* 9, 599–603. doi: 10.1007/BF03027261
- Sun, F., Pang, X., and Zhitomirsky, I. (2009). Electrophoretic deposition of composite hydroxyapatite–chitosan–heparin coatings. *J. Mater. Process. Technol.* 209, 1597–1606. doi: 10.1016/j.jmatprotec.2008.04.007
- Suresh, S. (2001). Graded materials for resistance to contact deformation and damage. *Science* 292, 2447–2451. doi: 10.1126/science.1059716
- Suresh, S., and Mortensen, A. (1997). Functionally graded metals and metal-ceramic composites: part 2 thermomechanical behaviour. *Int. Mater. Rev.* 42, 85–116. doi: 10.1179/imr.1997.42.3.85

- Surmeneva, M. A., Surmenev, R. A., Chudinova, E. A., Koptioug, A., Tkachev, M. S., Gorodzha, S. N., et al. (2017). Fabrication of multiple-layered gradient cellular metal scaffold via electron beam melting for segmental bone reconstruction. *Mater. Des.* 133, 195–204. doi: 10.1016/j.matdes.2017.07.059
- Tan, J. H. K., Sing, S. L., and Yeong, W. Y. (2020). Microstructure modelling for metallic additive manufacturing: a review. *Virtual Phys. Prototyp.* 15, 87–105. doi: 10.1080/17452759.2019.1677345
- Tokita, M. (2010). The potential of Spark Plasma Sintering (SPS) method for the fabrication on an industrial scale of functionally graded materials. *Adv. Sci. Technol.* 63, 322–331. doi: 10.4028/www.scientific.net/AST.63.322
- Traini, T., Mangano, C., Sammons, R. L., Mangano, F., Macchi, A., and Piattelli, A. (2008). Direct laser metal sintering as a new approach to fabrication of an isoelastic functionally graded material for manufacture of porous titanium dental implants. *Dent. Mater.* 24, 1525–1533. doi: 10.1016/j.dental.2008.03.029
- Tripathy, A., Sarangi, S. K., and Chaubey, A. K. (2018). A review of solid state processes in manufacture of functionally graded materials. *Int. J. Eng. Technol.* 7, 1–5. doi: 10.14419/ijet.v7i4.39.23686
- Tripathy, A., Sarangi, S. K., and Panda, R. (2017). Fabrication of functionally graded composite material using powder metallurgy route: an overview. *Int. J. Mech. Prod. Eng. Res. Dev.* 7, 135–145. doi: 10.24247/ijmperdec201714
- Unabia, R., Candidato, R., and Pawlowski, L. (2018). Current progress in solution precursor plasma spraying of cermets: a review. *Metals* 8:420. doi: 10.3390/met8060420
- Vacanti, C. A. (2006). History of tissue engineering and a glimpse into its future. *Tissue Eng.* 12, 1137–1142. doi: 10.1089/ten.2006.12.1137
- van Grunsven, W., Hernandez-Nava, E., Reilly, G., and Goodall, R. (2014). Fabrication and mechanical characterisation of titanium lattices with graded porosity. *Metals* 4, 401–409. doi: 10.3390/met4030401
- Wang, F., Lee, H. P., and Lu, C. (2007). Thermal-mechanical study of functionally graded dental implants with the finite element method. *J. Biomed. Mater. Res. A* 80A, 146–158. doi: 10.1002/jbm.a.30855
- Wang, H. T., Tao, N. R., and Lu, K. (2013). Architected surface layer with a gradient nanotwinned structure in a Fe–Mn austenitic steel. *Scr. Mater.* 68, 22–27. doi: 10.1016/j.scriptamat.2012.05.041
- Wang, L., Kang, J., Sun, C., Li, D., Cao, Y., and Jin, Z. (2017a). Mapping porous microstructures to yield desired mechanical properties for application in 3D printed bone scaffolds and orthopaedic implants. *Mater. Des.* 133, 62–68. doi: 10.1016/j.matdes.2017.07.021
- Wang, L., Qu, J., Chen, L., Meng, Q., Zhang, L.-C., Qin, J., et al. (2015). Investigation of deformation mechanisms in β -type Ti-35Nb-2Ta-3Zr Alloy via FSP leading to surface strengthening. *Metall. Mater. Trans. A* 46, 4813–4818. doi: 10.1007/s11661-015-3089-8
- Wang, L., Xie, L., Lv, Y., Zhang, L.-C., Chen, L., Meng, Q., et al. (2017b). Microstructure evolution and superelastic behavior in Ti-35Nb-2Ta-3Zr alloy processed by friction stir processing. *Acta Mater.* 131, 499–510. doi: 10.1016/j.actamat.2017.03.079
- Wang, L., Xie, L., Shen, P., Fan, Q., Wang, W., Wang, K., et al. (2019). Surface microstructure and mechanical properties of Ti-6Al-4V/Ag nanocomposite prepared by FSP. *Mater. Charact.* 153, 175–183. doi: 10.1016/j.matchar.2019.05.002
- Wang, P., Goh, M. H., Li, Q., Nai, M. L. S., and Wei, J. (2020). Effect of defects and specimen size with rectangular cross-section on the tensile properties of additively manufactured components. *Virtual Phys. Prototyp.* 15, 251–264. doi: 10.1080/17452759.2020.1733430
- Wang, P., Nai, M. L. S., Sin, W. J., Lu, S., Zhang, B., Bai, J., et al. (2018). Realizing a full volume component by *in-situ* welding during electron beam melting process. *Addit. Manuf.* 22, 375–380. doi: 10.1016/j.addma.2018.05.022
- Wang, P., Tan, X., Nai, M. L. S., Tor, S. B., and Wei, J. (2016). Spatial and geometrical-based characterization of microstructure and microhardness for an electron beam melted Ti-6Al-4V component. *Mater. Des.* 95, 287–295. doi: 10.1016/j.matdes.2016.01.093
- Wang, Q., Zhou, P., Liu, S., Attarilar, S. R., Ma, L.-W., et al. (2020). Multi-scale surface treatments of titanium implants for rapid osseointegration: a review. *Nanomaterials* 10:1244. doi: 10.3390/nano10061244
- Wang, S., Liu, L., Li, K., Zhu, L., Chen, J., and Hao, Y. (2019). Pore functionally graded Ti6Al4V scaffolds for bone tissue engineering application. *Mater. Des.* 168:107643. doi: 10.1016/j.matdes.2019.107643
- Watari, F., Yokoyama, A., Otori, M., Hirai, T., Kondo, H., Uo, M., et al. (2004). Biocompatibility of materials and development to functionally graded implant for bio-medical application. *Compos. Sci. Technol.* 64, 893–908. doi: 10.1016/j.compscitech.2003.09.005
- Watari, F., Yokoyama, A., Saso, F., Uo, M., Matsuno, H., and Kawasaki, T. (1998). Imaging of gradient structure of titanium/apatite functionally graded dental implant. *Nippon Kinzoku Gakkaishi J. Japan Instit. Metals* 62, 1095–1101.
- Wegst, U. G. K., Bai, H., Saiz, E., Tomsia, A. P., and Ritchie, R. O. (2015). Bioinspired structural materials. *Nat. Mater.* 14, 23–36. doi: 10.1038/nmat4089
- Weißmann, V., Bader, R., Hansmann, H., and Laufer, N. (2016). Influence of the structural orientation on the mechanical properties of selective laser melted Ti6Al4V open-porous scaffolds. *Mater. Des.* 95, 188–197. doi: 10.1016/j.matdes.2016.01.095
- Wilson, J. M., Jones, N., Jin, L., and Shin, Y. C. (2013). Laser deposited coatings of Co-Cr-Mo onto Ti-6Al-4V and SS316L substrates for biomedical applications. *J. Biomed. Mater. Res. B Appl. Biomater.* 101, 1124–1132. doi: 10.1002/jbm.b.32921
- Wu, Y. C., Kuo, C. N., Shie, M. Y., Su, Y. L., Wei, L. J., Chen, S. Y., et al. (2018). Structural design and mechanical response of gradient porous Ti-6Al-4V fabricated by electron beam additive manufacturing. *Mater. Des.* 158, 256–265. doi: 10.1016/j.matdes.2018.08.027
- Xie, W., He, J., Zhu, S., Holgate, T., Wang, S., Tang, X., et al. (2011). Investigation of the sintering pressure and thermal conductivity anisotropy of melt-spun spark-plasma-sintered (Bi,Sb) 2 Te 3 thermoelectric materials. *J. Mater. Res.* 26, 1791–1799. doi: 10.1557/jmr.2011.170
- Xiong, Y.-Z., Gao, R.-N., Zhang, H., Dong, L.-L., Li, J.-T., and Li, X. (2020). Rationally designed functionally graded porous Ti6Al4V scaffolds with high strength and toughness built via selective laser melting for load-bearing orthopedic applications. *J. Mech. Behav. Biomed. Mater.* 104:103673. doi: 10.1016/j.jmbbm.2020.103673
- Yan, C., Jiang, P., Jia, X., and Wang, X. (2020). 3D printing of bioinspired textured surfaces with superamphiphobicity. *Nanoscale* 12, 2924–2938. doi: 10.1039/C9NR09620E
- Yang, J., and Xiang, H.-J. (2007). A three-dimensional finite element study on the biomechanical behavior of an FGBM dental implant in surrounding bone. *J. Biomech.* 40, 2377–2385. doi: 10.1016/j.jbiomech.2006.11.019
- Yang, Y., Oh, N., Liu, Y., Chen, W., Oh, S., Appleford, M., et al. (2006). Enhancing osseointegration using surface-modified titanium implants. *JOM* 58, 71–76. doi: 10.1007/s11837-006-0146-1
- Yap, C. Y., Chua, C. K., Dong, Z. L., Liu, Z. H., Zhang, D. Q., Loh, L. E., et al. (2015). Review of selective laser melting: materials and applications. *Appl. Phys. Rev.* 2:041101. doi: 10.1063/1.4935926
- Yin, G. F., Luo, J. M., Zheng, C. Q., Tong, H. H., Huo, Y. F., and Mu, L. L. (1999). Preparation of DLC gradient biomaterials by means of plasma source ion implant-ion beam enhanced deposition. *Thin Solid Films* 345, 67–70. doi: 10.1016/S.0040-6090(99)00076-0
- Yu, L. C., Gong, D. R., Bin Wang, C., Yang, Z. M., and Zhang, L. M. (2003). Microstructure analysis of W-Mo-Ti functionally graded materials fabricated by co-sedimentation. *Key Eng. Mater.* 249, 299–302. doi: 10.4028/www.scientific.net/KEM.249.299
- Yuan, L., Ding, S., and Wen, C. (2019). Additive manufacturing technology for porous metal implant applications and triple minimal surface structures: a review. *Bioact. Mater.* 4, 56–70. doi: 10.1016/j.bioactmat.2018.12.003
- Zhang, B., Jaiswal, P., Rai, R., and Nelaturi, S. (2016). “Additive manufacturing of functionally graded objects: a review,” in *Proceedings of the ASME 2016 International Design Engineering Technical Conferences and Computers and Information in Engineering Conference. Volume 1A: 36th Computers and Information in Engineering Conference* (Charlotte, NC).
- Zhang, B., Pei, X., Zhou, C., Fan, Y., Jiang, Q., Ronca, A., et al. (2018). The biomimetic design and 3D printing of customized mechanical properties porous Ti6Al4V scaffold for load-bearing bone reconstruction. *Mater. Des.* 152, 30–39. doi: 10.1016/j.matdes.2018.04.065
- Zhang, C., Chen, F., Huang, Z., Jia, M., Chen, G., Ye, Y., et al. (2019). Additive manufacturing of functionally graded materials: a review. *Mater. Sci. Eng. A* 764:138209. doi: 10.1016/j.msea.2019.138209
- Zhang, L., Dong, H., and El Saddik, A. (2016). From 3D sensing to printing. *ACM Trans. Multimed. Comput. Commun. Appl.* 12, 1–23. doi: 10.1145/2818710

- Zhang, X.-Y., Fang, G., Xing, L.-L., Liu, W., and Zhou, J. (2018). Effect of porosity variation strategy on the performance of functionally graded Ti-6Al-4V scaffolds for bone tissue engineering. *Mater. Des.* 157, 523–538. doi: 10.1016/j.matdes.2018.07.064
- Zhu, C., Lv, Y., Qian, C., Ding, Z., Jiao, T., Gu, X., et al. (2018). Microstructures, mechanical, and biological properties of a novel Ti-6V-4V / zinc surface nanocomposite prepared by friction stir processing. *Int. J. Nanomed.* 13, 1881–1898. doi: 10.2147/IJN.S154260
- Zhu, C., Lv, Y., Qian, C., Qian, H., Jiao, T., and Wang, L. (2016). Proliferation and osteogenic differentiation of rat BMSCs on a novel Ti / SiC metal matrix nanocomposite modified by friction stir processing. *Sci. Rep.* 6:38875. doi: 10.1038/srep38875
- Zhu, S., Tan, X., Wang, B., Chen, S., Hu, J., Ma, L., et al. (2019). Bio-inspired multistable metamaterials with reusable large deformation and ultra-high mechanical performance. *Extrem. Mech. Lett.* 32:100548. doi: 10.1016/j.eml.2019.100548
- Zimmermann, E. A., Gludovatz, B., Schaible, E., Dave, N. K. N., Yang, W., Meyers, M. A., et al. (2013). Mechanical adaptability of the Bouligand-type structure in natural dermal armour. *Nat. Commun.* 4:2634. doi: 10.1038/ncomms3634

Conflict of Interest: The authors declare that the research was conducted in the absence of any commercial or financial relationships that could be construed as a potential conflict of interest.

Copyright © 2021 Shi, Zhou, Li, Liu and Wang. This is an open-access article distributed under the terms of the Creative Commons Attribution License (CC BY). The use, distribution or reproduction in other forums is permitted, provided the original author(s) and the copyright owner(s) are credited and that the original publication in this journal is cited, in accordance with accepted academic practice. No use, distribution or reproduction is permitted which does not comply with these terms.



Influence of Isothermal ω Transitional Phase-Assisted Phase Transition From β to α on Room-Temperature Mechanical Performance of a Meta-Stable β Titanium Alloy Ti–10Mo–6Zr–4Sn–3Nb (Ti-B12) for Medical Application

OPEN ACCESS

Edited by:

Liqiang Wang,
Shanghai Jiao Tong University, China

Reviewed by:

PaYaM ZarrinTaj,
Oklahoma State University,
United States
Fei Zhao,
Guizhou University, China
Ruifeng Dong,
North University of China, China

*Correspondence:

Jun Cheng
524161386@qq.com
Jinshan Li
ljsh@nwpu.edu.cn

Specialty section:

This article was submitted to
Biomaterials,
a section of the journal
Frontiers in Bioengineering and
Biotechnology

Received: 06 November 2020

Accepted: 11 December 2020

Published: 20 January 2021

Citation:

Cheng J, Li J, Yu S, Du Z, Zhang X,
Zhang W, Gai J, Wang H, Song H and
Yu Z (2021) Influence of Isothermal ω
Transitional Phase-Assisted Phase
Transition From β to α on
Room-Temperature Mechanical
Performance of a Meta-Stable β
Titanium Alloy
Ti–10Mo–6Zr–4Sn–3Nb (Ti-B12) for
Medical Application.
Front. Bioeng. Biotechnol. 8:626665.
doi: 10.3389/fbioe.2020.626665

Jun Cheng^{1,2*}, Jinshan Li^{1*}, Sen Yu², Zhaoxin Du³, Xiaoyong Zhang⁴, Wen Zhang²,
Jinyang Gai⁴, Hongchuan Wang⁵, Hongjie Song² and Zhentao Yu⁶

¹ State Key Laboratory of Solidification Processing, Northwestern Polytechnical University, Xi'an, China, ² Shaanxi Key Laboratory of Biomedical Metal Materials, Northwest Institute for Nonferrous Metal Research, Xi'an, China, ³ School of Materials Science and Engineering, Inner Mongolia University of Technology, Hohhot, China, ⁴ State Key Laboratory of Powder Metallurgy, Central South University, Changsha, China, ⁵ School of Material Science and Engineering, Northeastern University, Shenyang, China, ⁶ Institute of Advanced Wear and Corrosion Resistant and Functional Materials, Jinan University, Guangzhou, China

The microstructural evolution and tensile performance of a meta-stable β -type biomedical Ti–10Mo–6Zr–4Sn–3Nb (Ti-B12) alloy subjected to one-stage aging (OSA) and two-stage aging (TSA) are investigated in this work. The OSA treatment is performed at 510°C for 8 h. The TSA treatments are composed of low-temperature aging and high-temperature aging. In the first step, low-temperature aging is conducted at 325°C for 2 h. In the second step, the aging temperature is the same as that in the OSA. The result of the microstructure evolution shows that the precipitated secondary phase after aging is mainly influenced by the process of phase transition. There is a marked difference in the microstructure of the Ti-B12 alloy subjected to the OSA and TSA treatments. The needle-shaped α phases are precipitated in the parent β phase after the OSA treatment. Conversely, the short shuttle-like α phases precipitated after the TSA treatment are formed in the β matrix with the aid of the role of the isothermal ω transitional phase-assisted phase transition. The electron backscattered diffraction results indicate that the crystallographic orientation relationship of the α phases precipitated during the TSA treatment is basically analogous to those in the OSA treatment. The relatively higher tensile strength of 1,275 MPa is achieved by strengthening the effect of the short shuttle-like α precipitation with a size of 0.123 μ m in length during the TSA treatment, associating with a suitable elongation of 12% at room temperature simultaneously. The fracture surfaces of the samples after the OSA and TSA treatments indicate that preventing the coarsening of the α layers in the grain boundaries is favorable for the enhancement of strength of Ti-B12 at room temperature. MTT test was carried out to evaluate the acute

cytotoxicity and biocompatibility of the implanted material using L929 cells. The relative proliferation rates of cytotoxicity levels 0, 1, 2, 3, and 4 are ≥ 100 , 80–99, 50–79, 30–49, and 0–29%, respectively. The cytotoxicity of the Ti-B12 alloy is slightly better than that of the Ti–6Al–4V alloy, which can meet the requirements of medical materials for biomedical materials.

Keywords: phase transition, aging treatment, α precipitated phases, tensile properties, biomedical Ti alloy

INTRODUCTION

In comparison to α and ($\alpha + \beta$) Ti alloys, meta-stable β -type Ti alloys possess outstanding comprehensive mechanical performance (Weiss and Semiatin, 1998; Banerjee and Williams, 2013; Zhu et al., 2016; Zhang et al., 2017; Kaur and Singh, 2019). They have been successfully applied in the aerospace, biomedical, marine, and weapon industries for several decades, owing to their superior biocompatibility, low modulus, corrosion resistance, specific strength, and processability (Cui et al., 2011; Niinomi et al., 2012; Guo et al., 2013; Zhang and Chen, 2019). The higher tensile strength at room temperature could be achieved through the use of aging with a lower temperature due to the finer-scale secondary phases precipitated in the parent β phase for β -type titanium alloys. Moreover, a microstructural configuration with finer, dispersive, and more uniformly distributed α precipitates at the prior β grain boundaries is considered to optimize and enhance the mechanical performance and microstructure stability for the vast majority of β -type titanium alloys (Tang et al., 2000; Qazi et al., 2005; Chen et al., 2020; Vishnu et al., 2020; Zhang et al., 2020). Compared with the conventional one-stage aging treatment, the two-stage aging (TSA) treatment is considered to be a valid approach to optimize the mechanical performance of most meta-stable β -type Ti alloys. Schmidt et al. (2011) discussed the influence of duplex aging treatment on the fatigue behavior of a typical meta-stable Ti–3Al–8V–6Cr–4Mo–4Zr (wt%). They found that, compared with the one-stage aged specimen, the two-stage aging treatment was employed to improve the fatigue limit value and reduce the rate of fatigue crack growth. The primary reason was that the plenty dispersive ω_{iso} phases result in the uniform precipitation of α phases after the TSA treatment. Cui and Guo (2009) reported the microstructural evolution and tensile performances of a meta-stable Ti–28Nb–13Zr–0.5Fe under various aging conditions. They found that, when the alloy was aged at 350°C, the formation of precipitated α phases would lead to a dramatic increase in the number density of nucleation sites within the β matrix. The isothermal ω transitional phase was transformed into the α phase step by step with the increase in the temperature or the duration of aging, resulting in the refinement of precipitates and the improvement in the strength of alloy at room temperature. Santhosh et al. (2014) proved that the objective of the refinement and the increase in the amount of α phase could be achieved using low-temperature aging. A method of TSA was used to enhance the comprehensive mechanical performances at room temperature. For instance, higher tensile strength and favorable elongation can be achieved using this

method. Ivasishin et al. (2008) studied the microstructure control using the different thermo-mechanical working methods in a typical β -type Ti–15V–3Cr–3Sn–3Al alloy. They reported that this alloy with the slowest kinetics in precipitation of the secondary phase could be prepared through the use of duplex aging in order to obtain a relatively higher strength within a limited time for industrial-scale applications.

The Ti–10Mo–6Zr–4Sn–3Nb (Ti-B12) alloy is a newly developed β -Ti alloy used in surgical implants, such as dental archwires and catheter guide wires. It is considered to be an excellent candidate alloy for Ti–6Al–4V, CP-Ti applied in orthopedic surgery and dentistry, owing to its relatively higher tensile strength, lower modulus, and non-toxic alloying elements (Guo et al., 2019; Du et al., 2020; Rabadia et al., 2019). The Ti-B12 alloy is developed by Shaanxi Key Laboratory of Biomedical Metal Materials based on the d -electron theoretical approach (Cheng et al., 2020). The room-temperature mechanical performance for the meta-stable β -type Ti-B12 alloy can be controlled and optimized through the use of different solution treatments plus aging treatments. The Ti-B12 alloy subjected to solution treatment followed by aging treatment would possess an attractive combination of room-temperature tensile strength and ductility. Moreover, the molybdenum equivalent of the Ti-B12 alloy is calculated to be about 10.9. Generally, a higher molybdenum equivalent value is one of the necessary conditions for the continuous phase transformation of $\beta \rightarrow \omega \rightarrow \alpha$ in meta-stable β -Ti alloys (Li et al., 2015, 2016, 2018). Microstructure and micro-texture evolution in the process of aging treatment can result in a significant change in the mechanical performance of the alloy. Therefore, it is necessary to understand the evolution law of microstructure and texture components during the OSA and TSA treatments. The objective is to clarify the phase transformation mechanism of $\beta \rightarrow \alpha$ and $\beta \rightarrow \omega \rightarrow \alpha$ under various aging conditions.

The room-temperature and elevated-temperature mechanical performances of meta-stable β -type Ti alloys can be improved by the formation of a large number of finer α precipitates uniformly distributed in the β matrix. The meta-stable ω transitional phase can be considered as a type of effective nucleation site for the precipitation of the α phase during the TSA treatment. The isothermal ω transitional phase can be induced by the diffusion of solute atoms during aging at a relatively lower temperature (300–400°C). To clarify the formation mechanism of the ω phase, the crystal structure, and the elemental diffusion during the phase transformation from an unsymmetrical ω embryo to a symmetrical isothermal ω phase is very important.

TABLE 1 | Chemical composition of Ti-B12 alloy ingot used in the present work (wt%).

Ti	Mo	Zr	Sn	Nb	C	N	O	H	Fe
Bal.	10.11	5.71	4.32	2.83	0.024	0.017	0.11	0.0037	0.02

Nevertheless, almost no investigations have been conducted on the above-mentioned scientific questions, and no research efforts have been made to clarify the atomic-scale structure evolution and elemental diffusion of isothermal ω phase after the low-temperature aging treatment. Consequently, the mechanism of phase transformation from β to ω during the low-temperature aging has not been explained yet.

This research work is carried out to investigate the microstructural evolution of Ti-B12 alloy after the OSA and TSA treatments and its influence on room-temperature mechanical performance. Furthermore, the influence of TSA treatment on the precipitation and the transformation mechanism of the α phase is discussed as well. Cytotoxicity evaluation for Ti-B12 alloy is also carried out using the MTT method.

EXPERIMENTAL MATERIALS AND METHODS

The Ti-B12 alloy ingot was produced using a vacuum arc remelting furnace (VAR, 50 kg). The ingot was remelted three times to ensure homogeneity and prevent segregation. In this work, the raw materials for VAR included sponge titanium with small particles (particle size: 0.83–12.7 mm; grade 0), Ti-32Mo master alloy with thin sheet-like, industrial zirconium sponge (Zr-1; particle size: 3–8 mm), and Ti-80Sn and Nb-47Ti master alloy with chips-like. The chemical composition of the Ti-B12 alloy ingot is provided in **Table 1**. The Ti-B12 cast ingot was homogenized at 1,180°C to improve the metallurgical quality. A 6.3 MN rapid forging press and a GFM (Austria) radial forging machine were used to carry out billet forging and final forging in the temperature range of the β and ($\alpha + \beta$) phase regions, respectively. Finally, a 250-type bar rolling mill was employed to manufacture hot-rolled round bars (diameter: 9 mm). Several bars were cut using an electric discharge machine and lathe.

Based on the Ti-Mo phase diagram and ITT diagram, it can be deduced that the isothermal ω transitional phase will precipitate within the parent β phase after low-temperature aging. The low-temperature aging treatment is usually carried out below 400°C. Moreover, the α phase is prone to precipitate in the temperature ranging from 500 to 600°C. In our previous work, the finer α phase tends to precipitate after aging at 510°C for 8 h, which is beneficial for the significant improvement in strength at room temperature. First of all, the Ti-B12 alloy bars were subjected to a solution treatment at 790°C for 1 h, followed by water cooling. Subsequently, two types of aging treatments were carried out by electric furnace in air. One-stage aging was carried out at 510°C for 1, 2, 4, and 8 h, respectively. TSA was firstly performed at 325°C for 2 h and then conducted at 510°C for 0.2, 1, 2, 4, and 8 h, respectively.

The microstructure of each specimen was observed using optical microscopy (OM, OLYMPUS BX61), scanning electron microscopy (SEM, FEI Quanta 650F) equipped with electron backscattered diffraction (EBSD, Oxford Instruments + HKL Channel 5 software package), and transmission electron microscopy (TEM) (FEI Tecnai G2 F20). EBSD and X-ray diffraction (XRD, Bruker D8 Focus) techniques were used to characterize the evolution of microstructure and crystallographic orientation. The polished bulk specimen was examined by XRD to analyze the phase constituent and phase transformation. The measurements of XRD were carried out in the range of 30–80°, with a constant step of 0.02° and a scanning speed of 6°/min. The accelerating voltage and current are 40 kV and 40 mA, respectively.

Uniaxial tensile testing was conducted using an INSTRON 598X system (maximum load: 250 kN) at room temperature. The strain rate was ~ 0.006 mm/min. Tensile specimens were machined following the GB/T 228-2007 standard. The diameter and the gauge length of the tensile samples were 3 and 15 mm, respectively. The specimens were etched using Kroll reagent (8% HNO₃ + 2% HF + 90% H₂O, vol%) for 5–10 s. The fracture surface and the microstructure of the specimen were characterized by SEM in secondary electron mode. TEM observation was conducted by a FEI Tecnai G2 F20 operated at an accelerating voltage of 300 kV. TEM specimen was mechanically ground to a foil with a thickness of 40 μ m using SiC paper until 2000 grade. The foil was punched into several discs of 3 mm in diameter, which would be thinned by the ion milling technique (Gatan 691) for the TEM characterization.

MTT test was carried out to evaluate the cytotoxicity and biocompatibility of the implanted material using L929 cells. GB/T 16886.5-2017 biological evaluation of medical devices—part 5: tests for *in vitro* cytotoxicity was used in this work. The L929 cells in the logarithmic growth phase were selected to be digested with trypsin. The cell culture medium was diluted to a L929 cell suspension with a concentration of 1×10^4 /ml. They were inoculated on four 96-well culture plates (0.20 ml cell suspension per well). The cells were cultured for 24 h at 37°C. The original culture medium was discarded after the cells adhered to the wall. After rinsing with physiological saline three times, two kinds of extracts for Ti-B12 and Ti-6Al-4V alloy and RPMI1640 cell culture medium were added to a 48-well plate (0.20 ml cell suspension per well). They were incubated at 5% CO₂ atmosphere at a constant temperature (37°C). The respective culture solution was carefully replaced after 72 and 120 h. A culture plate was taken out, and the original culture medium was carefully aspirated after 24, 72, 120, and 168 h. The 0.20 ml fresh RPMI1640 culture medium and 20 μ l MTT (5 mg/ml, thiazolyl blue) solution were added to the culture plate and continued to be cultured for 4 h. The solution in wells was carefully removed and washed twice with physiological saline; 0.20 ml dimethyl sulfoxide (DMSO) was added into each well. The culture plate was gently shaken for 10 min, and the absorbance value (OD value) of each well with an enzyme-linked immunoassay at 490-nm wavelength was measured using 0.20 ml DMSO as a reference.

RESULTS AND DISCUSSION

Microstructure for Solution-Treated, One-Stage-Aged, and Two-Stage-Aged Specimens

Figure 1 displays OM and SEM images for Ti-B12 alloy subjected to solution-treated, one-stage aging, and two-stage aging treatments. Based on previous investigations (Rack et al., 1970; Laheurte et al., 2006; Cai et al., 2012, 2013), the Ti-B12 alloy subjected to an appropriate solution treatment in conjunction with aging treatment could achieve outstanding comprehensive mechanical properties. Therefore, in this work, based on β transus temperature ($T_\beta = 760^\circ\text{C}$) measured using the conventional metallographic procedure, the solution heat treatment is determined to be 790°C/h and air cooling (AC). As shown in **Figure 1A**, the specimen subjected to solution treatment followed by air cooling is mainly composed of equiaxed β grains. Based on the analysis by Image pro-plus 6.0 software, the average grain size is about $88\text{ }\mu\text{m}$. Some deformation streamlines also exist in the microstructure. **Figure 1B** displays the SEM image for the Ti-B12 alloy bar subjected to the OSA. Cluster-like α phase with micron-scale was precipitated in the β grains of the sample subjected to the OSA for 4 h. The SEM image for the Ti-B12 alloy subjected to solution treatment in conjunction with low-temperature aging at 325°C for 2 h followed by high-temperature aging at 510°C for 4 h is presented in **Figure 1C**. It can be clearly seen that the α phase continuously precipitates at the grain boundary triple junctions of β grains. Meanwhile, a large amount of fine and dispersive α phases with “needle-like” shape are generated within the β equiaxed grains. Compared with **Figures 1B,C** shows that the size of the α phase precipitating in the sample subjected to TSA is significantly finer than that subjected to OSA. It is noteworthy that there are some differences between the nucleation site and the growth rate of grains under various heat treatments.

The TEM bright-field (BF) images and the corresponding selected area diffraction (SAD) patterns of Ti-B12 alloys subjected to OSA at 510°C for 1 h and TSA at 325°C for 2 h followed by 510°C for 1 h are presented in **Figure 2**. In general, BF and dark-field (DF) images are employed to characterize the morphology and distribution of secondary phase in the metallic materials. Meanwhile, SAD patterns are often used to illustrate the phase transition mechanism and orientation relationship after various aging treatments. **Figure 2C** presents a SAD pattern of $[001]\beta$ zone axis for Ti-B12 alloy subjected to solution treatment followed by OSA. It can be found that the reflection spots are presented at $1/2\{211\}\beta$ positions, which reveals that the α phase precipitates from the parent β phase after aging. As presented in **Figures 2A,B**, the α precipitates in the OSA specimen are needle-shaped. The length is $\sim 0.675\text{ }\mu\text{m}$, and the width is about $0.087\text{ }\mu\text{m}$. The morphologies of the α phases precipitated from the β matrix after low-temperature aging at 325°C for 2 h followed by high-temperature aging at 510°C for 1 h are shown in **Figure 2D**. It can be found that the refining effect of the α phase in the TSA specimen is obvious compared to the OSA one. The morphology of the α phases precipitated from the β matrix after TSA is short shuttle-like. The length and

width are about 0.123 and $0.0228\text{ }\mu\text{m}$, respectively. As seen in the difference between **Figures 2A,D**, it can be noticed that the α phase has been refined obviously after the TSA treatment, owing to the effect of the isothermal ω transitional phase-assisted phase transition. Furthermore, as seen in **Figure 2E**, the SAD pattern of the Ti-B12 alloy does not display any additional reflection spots because a large number of isothermal ω transitional phases precipitated from the parent β phase during the low-temperature aging treatment have completely transformed into α precipitates after the high-temperature aging at 510°C for 1 h. As can be observed in **Figures 2B,D**, it is necessary to note that the isothermal ω transitional phase-assisted nucleation mechanism plays a significant role in the precipitation and growth of the precipitated α phase within the β grains. However, the accurate nucleation positions of the α precipitates are too difficult to be confirmed only by TEM dark-field images (Nag et al., 2009; Zheng et al., 2016a,b; Chen et al., 2018; Shi et al., 2019).

Phase Transition in Ti-B12 Alloy After the Two-Stage Aging Treatment

The XRD patterns for the Ti-B12 alloy subjected to solution treatment at 790°C in conjunction with low-temperature aging at 325°C followed by high-temperature aging at 510°C are shown in **Figure 3**. The XRD spectra for the Ti-B12 specimen solution-treated at 790°C for 1 h followed by water quenching are shown in **Figure 3A**. The experimental result indicates that there are some diffraction peaks of the β phase with a body-centered cubic structure because the solution temperature is located in the temperature range of the β phase zone. As can be seen in **Figure 3B**, the diffraction peaks of the ω phase begin to emerge in (111) and (112) planes during low-temperature aging at 325°C for 2 h. The co-existence of the diffraction peaks for β and ω phases indicates that the phase transition from ω phase to α phase has not yet taken place after low-temperature aging. Furthermore, the SAD pattern for the low-temperature aged specimen is presented in **Figure 4B**. It can be deduced that there are no α precipitates which are transformed from the β parent phase or isothermal ω transitional phase under this condition. When the Ti-B12 alloy was subjected to low-temperature aging at 325°C for 2 h followed by high-temperature aging at 510°C for 0.2 h, the (101) α diffraction peak is presented. This phase transformation is also accompanied by the appearance of isothermal (111) ω and (112) ω diffraction peaks. Moreover, when the Ti-B12 alloy is subjected to low-temperature aging at 325°C for 2 h followed by high-temperature aging at 510°C for 0.2 h, the precipitated α phase with finer scale would be transformed from isothermal ω transitional phase or β parent phase. Previous investigations showed that the phase transition from ω phase to α phase would be induced in some biomedical β Ti alloys (Chaves et al., 2015; Wang et al., 2018). As can be seen in **Figure 3C**, the XRD results for the TSA specimen (low-temperature aging at 325°C for 2 h followed by high-temperature aging at 510°C for 1 h) show that there is no isothermal ω transitional phase retained after the high-temperature aging at 510°C for 1 h. The result of the XRD is identical to that of the SAD pattern for the Ti-B12 alloy in **Figure 2E**. Moreover, it can

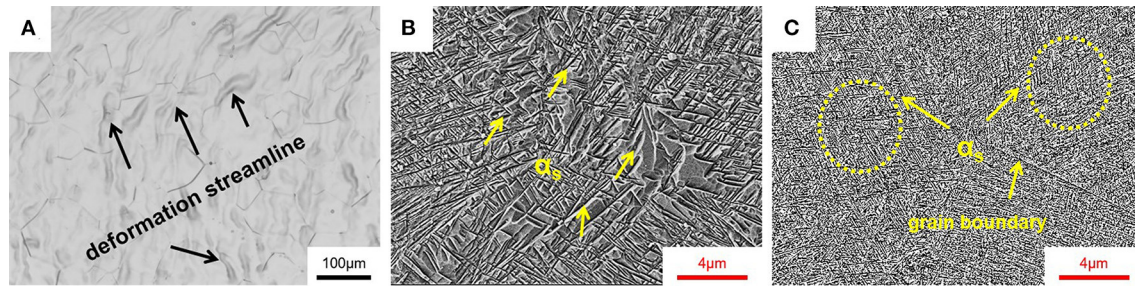


FIGURE 1 | Microstructures of Ti-B12 alloy subjected to (A) solution treatment at 790°C for 1 h followed by air cooling (optical microscopy), (B) one-stage aging at 510°C for 4 h after solution treatment (scanning electron microscopy, SEM), and (C) two-stage aging (TSA) at 325°C for 2 h followed by 510°C for 4 h after solution treatment (SEM).

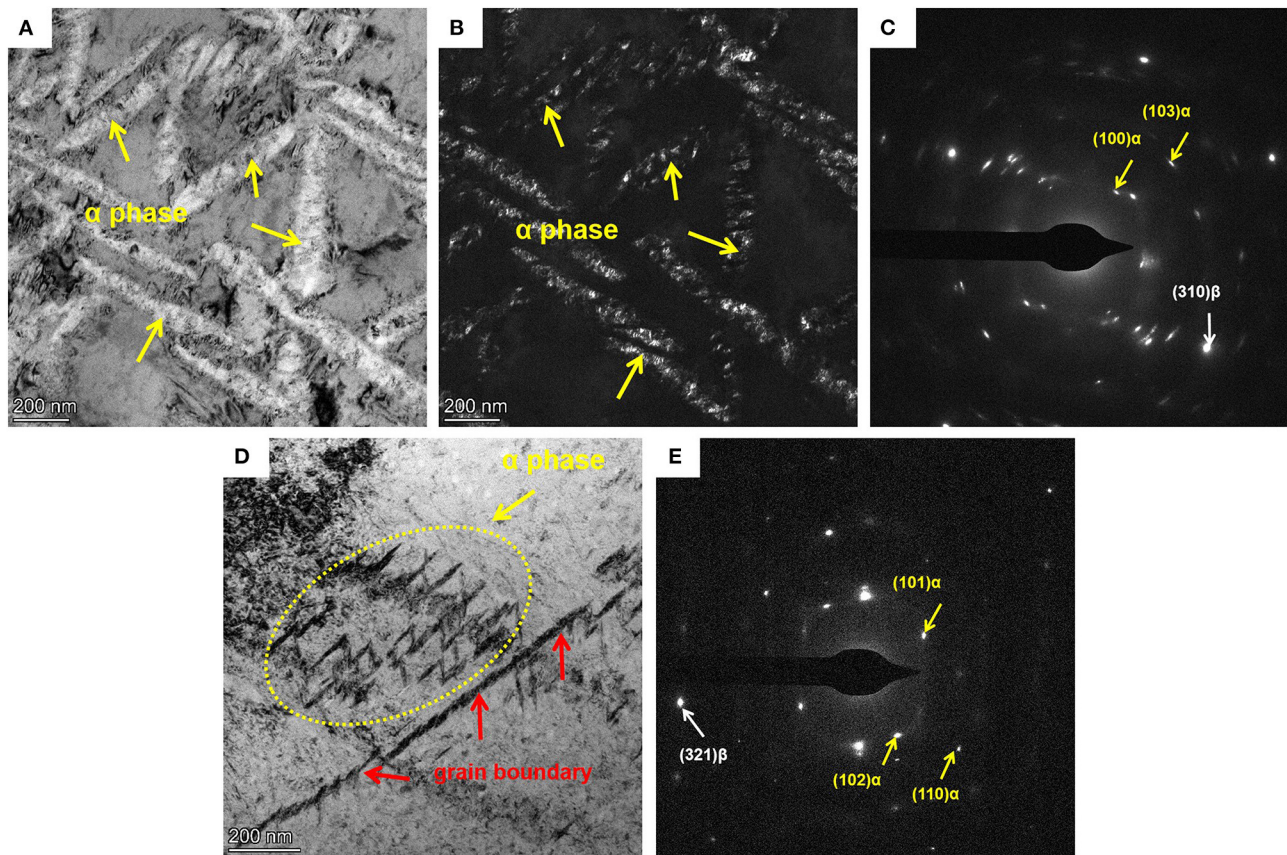
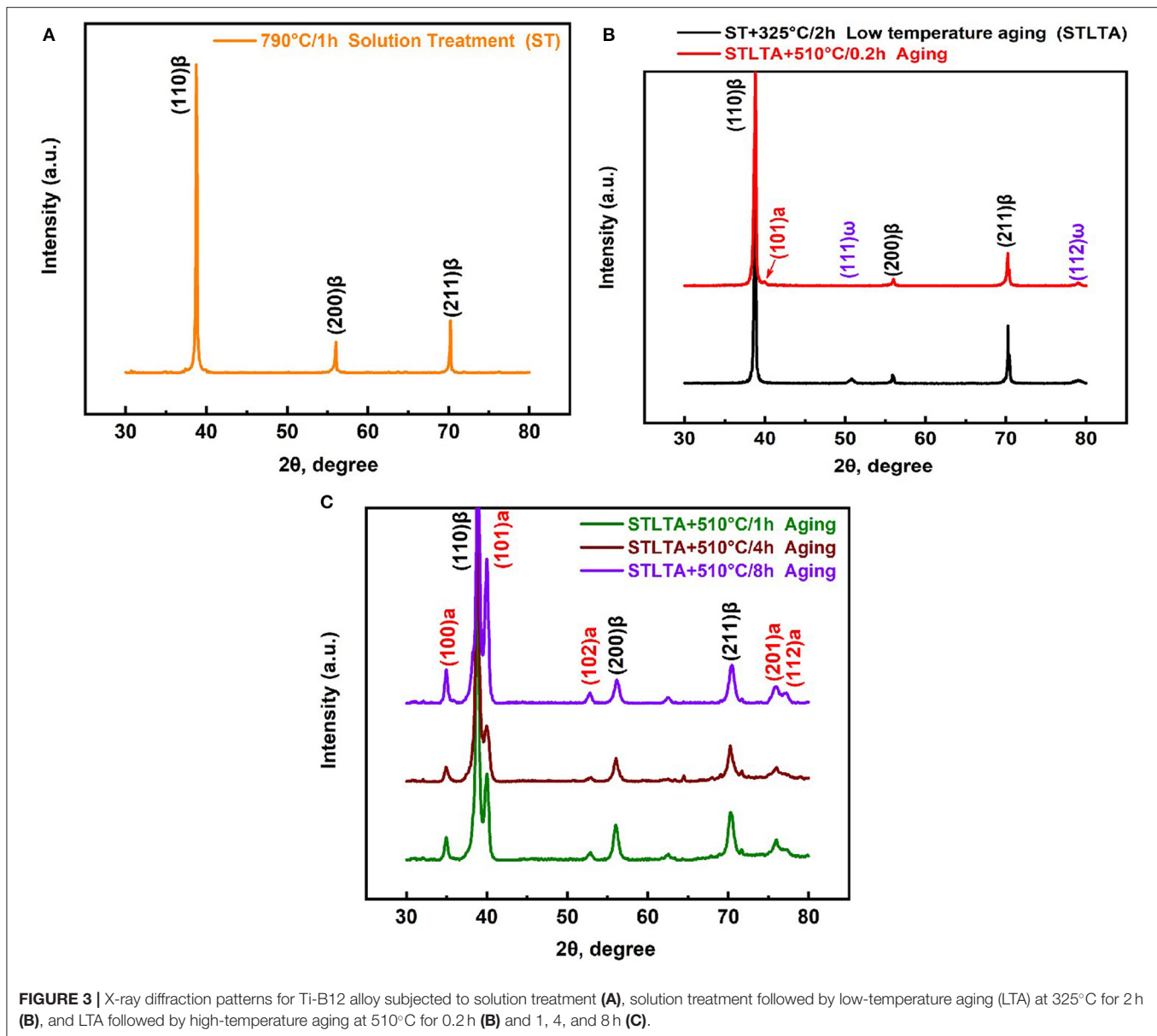


FIGURE 2 | Transmission electron microscopy (TEM) pictures for Ti-B12 alloy subjected to one-stage aging (OSA) and two-stage aging (TSA) (B,C) OSA at 510°C for 1 h (D,E) and TSA at 325°C for 2 h followed by 510°C for 1 h. (A,D) TEM bright-field images, (B) TEM dark-field images, and (C,E) selected area diffraction patterns.

be seen in **Figure 3C** that extending the aging time will result in the enhancement of (100) α , (101) α , and (102) α diffraction peak intensity in the XRD spectrum. Compared with the XRD spectra of the Ti-B12 alloy subjected to aging at 510°C for 0.2 and 1 h, the results of the XRD spectra for the Ti-B12 specimens subjected to aging at 510°C for 4 and 8 h indicate that the quantity of α precipitates obviously increases with the prolongation of aging time. Meanwhile, the intensity of (100) α , (101) α , and (102) α

diffraction peaks also increases under the above-mentioned heat treatment conditions.

Figures 4A,B present the DF image and SAD pattern of the Ti-B12 alloy subjected to low-temperature aging at 325°C for 2 h. As can be observed in **Figure 4A**, a lot of ellipsoid-like isothermal ω transitional phases with the size of ~ 57 nm are precipitated from the parent β phases. As shown in **Figure 4B**, reflection spots are presented at $1/3$ and $2/3$ $\{211\}\beta$ positions of



the Ti-B12 alloy subjected to solution heat treatment at 790°C for 1 h plus low-temperature aging at 325°C for 2 h, owing to the precipitation of ω phases. The result of **Figure 4B** will coincide with the specific orientation relationship of $[210](002)\beta // [-1011](-11-1)\omega_1 // [-2111](-101)\omega_2$ (Qazi et al., 2005; Cui and Guo, 2009; Nag et al., 2009; Wang et al., 2009). As can be seen in **Figure 4C**, there is evidence that the short shuttle-like α phases precipitate with the assistance of the isothermal ω phase during aging treatment. The enlarged image provides a strong evidence for the evolution of the ω transitional phase transformed into α phase. It can be reasonably deduced that the potential nucleation and growth of a new phase may emerge at the boundaries between parent β phase and ω_{iso} phase. Previous research work has been carried out for the investigation of phase transformation in Ti-5Al-5Mo-5V-3Cr-0.5Fe (Ti-5553) alloy (Nag et al., 2009). A SAD pattern of the Ti-B12 alloy

subjected to solution treatment followed by low-temperature aging at 325°C for 2 h and high-temperature aging at 510°C for 0.2 h is presented in **Figure 4D**. Reflection spots are presented at 1/3 and 2/3 $\{110\}\beta$ positions because of the existence of a residual isothermal ω transitional phase during the low-aging treatment. Moreover, the emergence of newly generated reflection spots corresponding to the α phase demonstrates that these α precipitates are transformed from the isothermal ω transitional phase or the parent β phase during high-temperature aging treatment at 510°C for 0.2 h.

Texture Evolution of Ti-B12 Alloy Subjected to OSA and TSA

EBSD maps of Ti-B12 alloys subjected to one-stage aging and two-stage aging are shown in **Figure 5**. It can be seen from the inverse pole figure (IPF) maps (**Figures 5A,B**)

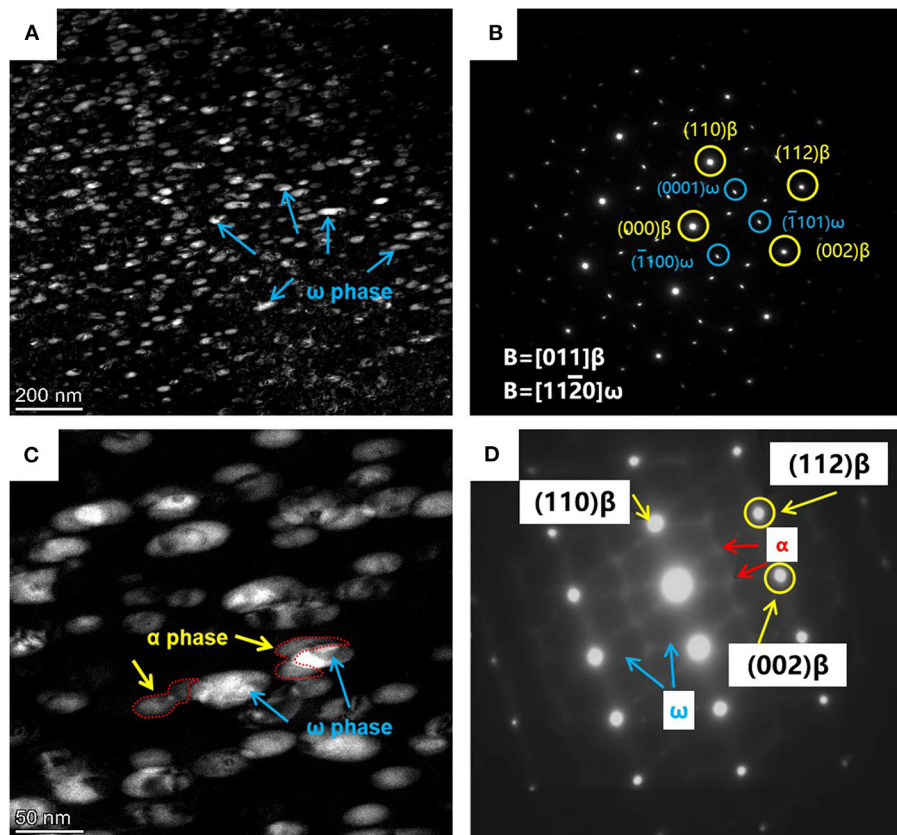


FIGURE 4 | Transmission electron microscopy (TEM) pictures for Ti-B12 alloy solution treated at 790°C for 1 h plus **(A,B)** low temperature aging at 325°C for 2 h and **(C,D)** low-temperature aging at 325°C for 2 h followed by high-temperature aging at 510°C for 0.2 h. **(A,C)** TEM dark-field images. **(B,D)** Selected area diffraction patterns.

that complete recrystallization can be obtained in the alloy after solution treatment followed by aging. Meanwhile, the β grain size of the TSA sample is slightly larger than that of the OSA sample. As can be observed in **Figures 5C,D**, the β grain orientation of the Ti-B12 alloys subjected to OSA and TSA presents a random distribution. The maximum values of pole density are 3.63 and 3.93, respectively.

A small step (20 nm) is applied to collect the crystal orientation information on the α and β phases in order to clearly characterize the orientation relationship between the parent phase and the precipitated phase. The results of the orientation relationship between the α and β phases are displayed in **Figure 6**. **Figure 6A** presents the IPF map of the OSA sample, which contains one β grain and two α grains (α_1 and α_2). **Figures 6B,C** are the pole figures of the β grains and the α phases, respectively. It can be clearly seen that the α_1 , α_2 , and β_1 grains satisfy the following orientation relationship: $\{0001\}\alpha // \{110\}\beta$ and $\langle 11-20 \rangle \alpha // \langle 111 \rangle \beta$, that is to say, the $\beta \rightarrow \alpha$ in the OSA specimen follows the typical Burgers orientation relationship (BOR) (Chai et al., 2017, 2018). Similarly, **Figure 6D** shows the IPF map of the TSA specimen. As can be seen in **Figures 6E,F**, both α and β phases follow the BOR as well.

Previous investigations have indicated that the finer α precipitates are formed by contact with the surface of the isothermal ω phase. The habit plane is usually defined as $(11-20) \omega // (11-20) \alpha$. It is proved that the α phase tends to nucleate at the interface between the ω and β phases. The reason is that this interface is regarded as the minimum misfit low-index habit plane between ω and β phases, resulting in a significant reduction of apparent activation energy for the nucleation and growth of α precipitates (Ohmori et al., 2001; Cremasco et al., 2011; Chen et al., 2019; Dong et al., 2020; Xiang et al., 2020). Hence, α phases with the aid of the isothermal ω phase-assisted nucleation will possess a basically similar BOR with those formed under the OSA condition. It can also be reasonably deduced that, although the size of the secondary phase has become obviously smaller, the phase transition from β to α phase with the aid of isothermal ω phase cannot change the crystallographic orientation of the precipitated phase.

Mechanical Properties at Room Temperature and Fracture Behavior for OSA and TSA Ti-B12 Alloy

The most outstanding mechanical properties for the Ti-B12 alloy can be achieved after TSA (low-temperature aging followed

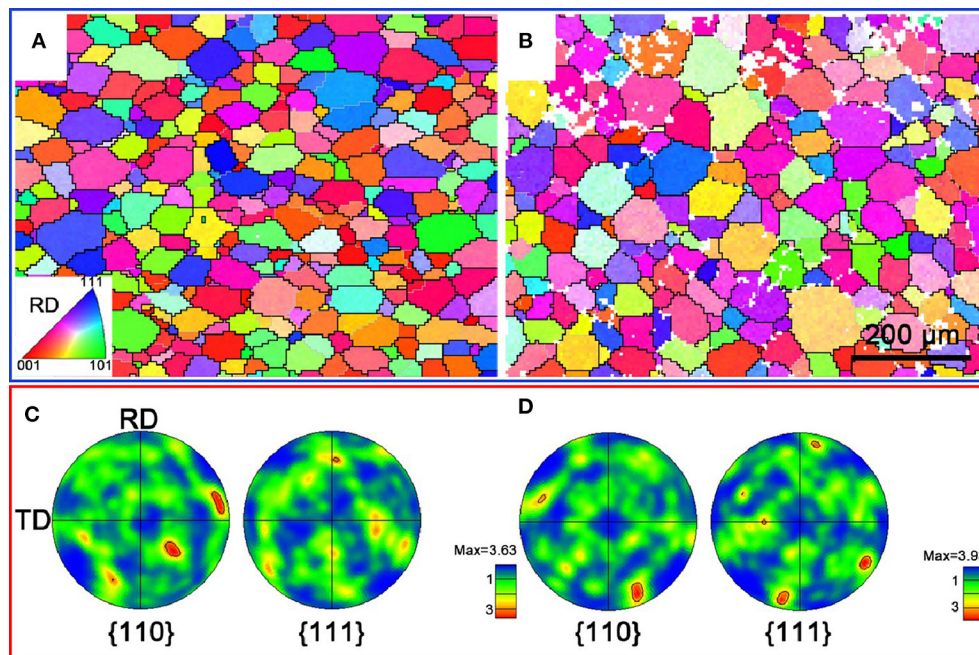


FIGURE 5 | Electron backscattered diffraction maps of Ti-B12 alloys subjected to one-stage aging (790°C/h, AC + 510°C/8 h, AC) and two-stage aging (790°C/h, AC + 325°C/2 h, AC + 510°C/8 h, AC). **(A,B)** Inverse pole figure maps. **(C,D)** Pole figure maps.

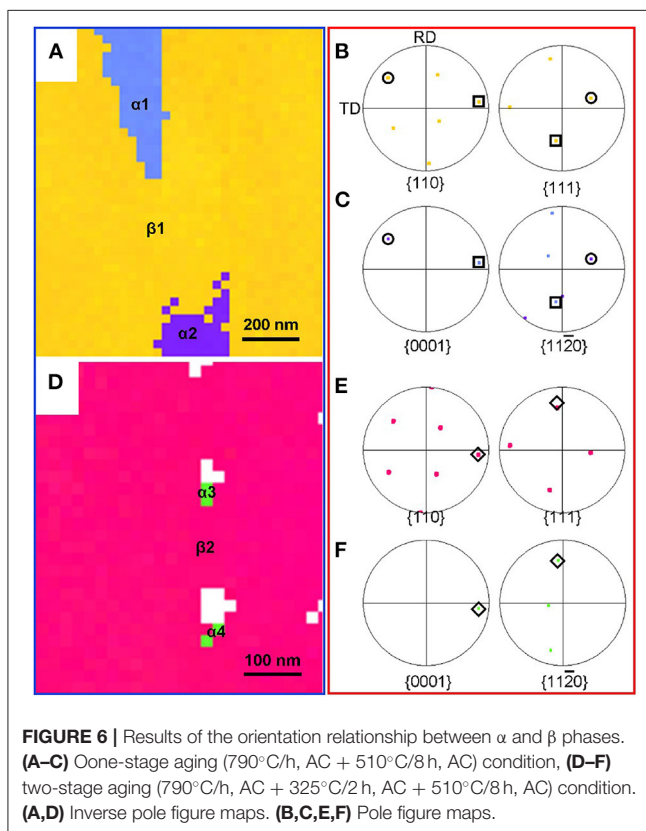


FIGURE 6 | Results of the orientation relationship between α and β phases. **(A–C)** One-stage aging (790°C/h, AC + 510°C/8 h, AC) condition, **(D–F)** two-stage aging (790°C/h, AC + 325°C/2 h, AC + 510°C/8 h, AC) condition. **(A,D)** Inverse pole figure maps. **(B,C,E,F)** Pole figure maps.

by high-temperature aging). An attractive matching degree of strength and elongation can be obtained through the use of low-temperature aging at 325°C for 2 h followed by high-temperature aging at 510°C for 8 h. In this case, the influence of low-temperature aging at 325°C on the microstructural evolution is favorable for the refinement of α precipitates. The reason for this phenomenon is that the isothermal ω transitional phase precipitated during low-temperature aging will result in the increase in the density of nucleation sites for the phase transformation from β phase to α phase. Therefore, the adoption of TSA is beneficial to form a significant number of dispersed α precipitates with a significantly small size in the β matrix. A schematic drawing of isothermal ω transitional phase-assisted phase transformation from β to α is presented in **Figure 7**. In general, the process of isothermal ω transitional phase-assisted α precipitates predominantly includes the nucleation, multiplication, growth of ω embryo in conjunction with precipitation and, near *in situ* growth of α phase as well as the consumption of ω precipitates during the whole aging process. Both the precipitation of the ω phase and the parent β phase satisfy a given crystallographic orientation relationship, that is, the habit plane. The growth orientation of the isothermal ω phase is considered to be in the invariant direction of the habit plane. Moreover, there is a Burgers vector whose constant normal is perpendicular to the habit plane. The crystallographic orientation relationship of constant normal is maintained unchanged during the whole phase transformation process. Assuming that the constant normal in the real space and the one in the reciprocal

space are all determined, the growth direction of the precipitated phase can be deduced based on the orientation relationship between the ω and β phases. The ω phase possesses a $\{111\}\beta$ habit plane, and the growth direction of the precipitated phase is usually $\langle 14\ 14\ 15 \rangle_\beta$. The migration interface between the ω and α phases is extremely close to the habit plane of the α phase, and the deviation angle of the two planes is about 5.1° . Since the Ti-B12 alloy is subjected to low-temperature aging, the morphological characteristics of the ω phase are strongly influenced by the role of the secondary α phase nucleation and growth, owing to the intimate contact between the isothermal ω precipitated phase and the parent β phase as well as the anisotropy of the α precipitates. The α precipitates are prone to nucleate at the ω/β interface. In the initial stage of low-temperature aging, the isothermal ω phase is quickly exhausted by the secondary α phase, and it finally disappeared under the influence of ω -assisted α phase precipitates. Consequently, the initial ellipsoid-like ω phase will be decomposed along the direction of the ω/α interface migration, leading to the formation of a short shuttle-like precipitated phase during TSA.

The tensile curves of the Ti-B12 alloy subjected to OSA (510°C for 8 h) and TSA (low-temperature aging at 325°C for 2 h followed by high-temperature aging at 510°C for 8 h) after solution treatment are presented in **Figure 8**. In contrast to the OSA specimen, a relatively higher strength and an acceptable elongation at room temperature can be obtained through the TSA process. As can be seen in **Figure 8**, the tensile strength of the OSA specimen subjected to aging at 510°C for 8 h is about 982 MPa. However, the most outstanding mechanical properties (tensile strength: 1,275 MPa, elongation: 12%) can be achieved in the TSA Ti-B12 alloy, owing to its peculiar microstructure. In addition, a serration phenomenon can be observed in the stress-strain curve. Such a serration phenomenon is attributed to the effect of stress relaxation during tensile testing at room temperature. Therefore, this phenomenon is inevitable. The microstructure and fracture behavior for the alloy will be described in detail in the following paragraphs.

The mechanical properties for some β -type Ti alloys are greatly affected by the precipitation of secondary phases after aging treatment because the mechanical properties, including strength and ductility, strongly depend on the density (ρ) and volume fraction (vol.%) of the precipitated phases within the parent phase (Gao et al., 2019; Yang et al., 2019; Li et al., 2020; Tang et al., 2020; Xiao et al., 2020; Lai et al., 2021). Hence, optical microscopy can be employed to analyze and evaluate the peculiar microstructure for various aged specimens and the plastic deformation behavior. The optical images for the microstructures for OSA ($790^\circ\text{C}/\text{h}$, AC + $510^\circ\text{C}/8\text{ h}$, AC) and TSA (low-temperature aging at 325°C for 2 h followed by high-temperature aging at 510°C for 8 h) specimens are presented in **Figures 9A,D**. It can be seen in **Figure 9A** that there are some precipitate-free zones existing in the microstructure and continuously thick α layers covering a portion of grain boundaries entirely in the OSA sample. Therefore, we can suppose that low-temperature aging is critical to increase the number of α precipitates and inhibit the coarsening of α layers. In contrast, as can be observed in **Figure 9D**, the α layers and

the size of α phases within the β grains for the TSA specimen are obviously smaller than those of the OSA one. Meanwhile, as can be seen in **Figure 1C**, the region around triple grain boundaries displays the morphology of the α phase precipitated within the β grains and continuous α layers in the boundaries at high magnification. A large number of isothermal ω transitional phases can be regarded as effective obstacles that prevent the emergence of α layers in the boundaries and the growth of secondary phase within the β grains. **Figures 9B,C,E,F** show the morphologies of the fracture surfaces at low and high magnification in the OSA and TSA samples. It can be seen from the fracture surfaces of the OSA and TSA samples that the predominant mechanism is the ductile fracture with a certain degree of cleavage fracture feature after tensile deformation at room temperature. As can be seen in **Figure 9B**, transgranular fracture and some deep dimples are observed on the fracture surface of the Ti-B12 alloy after OSA. As shown in **Figure 9C**, some evidence of predominantly ductile and slightly brittle fracture is detected on the fracture surface using secondary electron mode. Therefore, it can be deduced that a mixed fracture behavior is exhibited in the Ti-B12 alloy subjected to OSA at 510°C for 8 h after solution treatment in the temperature range of the β phase region. In particular, a transgranular fracture mode plays a more dominant role in the alloy after tensile deformation to some extent. Moreover, **Figures 9E,F** indicate that intergranular fracture plays a pivotal role during tensile deformation. The numbers of dimples decrease sharply and become shallow. The overall number of cleavage facets in the fracture surface increases obviously after tensile deformation at room temperature. The scale of dimples is $\sim 40\text{--}90\ \mu\text{m}$. This characteristic is associated with the shape of the α phase, owing to the refinement of the secondary phase and the absence of thick α layers in the boundaries. This comparative study on the fracture behavior of the Ti-B12 alloy can demonstrate the negative influence of the thick α layers in the grain boundaries on the elongation and the positive role of TSA on the fracture behavior at room temperature. Hence, one can conclude that the employment of TSA can effectively prevent the coarsening of the α layers in the boundaries to achieve an attractive combination of higher room-temperature tensile strength and reasonable ductility.

Cytotoxicity Evaluation for Ti-B12 Alloy Using the MTT Method

The relative number of L929 cells in each well (indicated by the OD value) is determined using the MTT method after 24, 72, 120, and 168 h. The measured OD values are displayed in **Table 2**; relative rate of cell proliferation = (OD value of experimental group / OD value of blank control group) $\times 100\%$. The relative cell proliferation rate is calculated. The evaluation criteria are obtained for the cytotoxicity of implanted material. The relative proliferation rate of cytotoxicity levels 0, 1, 2, 3, and 4 is ≥ 100 , 80–99, 50–79, 30–49, and 0–29%, respectively. The results of the cytotoxicity test indicate that, compared with the cell culture medium, neither the Ti-B12 nor the Ti-6Al-4V alloy showed obvious cytotoxicity. The Ti-6Al-4V alloy has been widely used

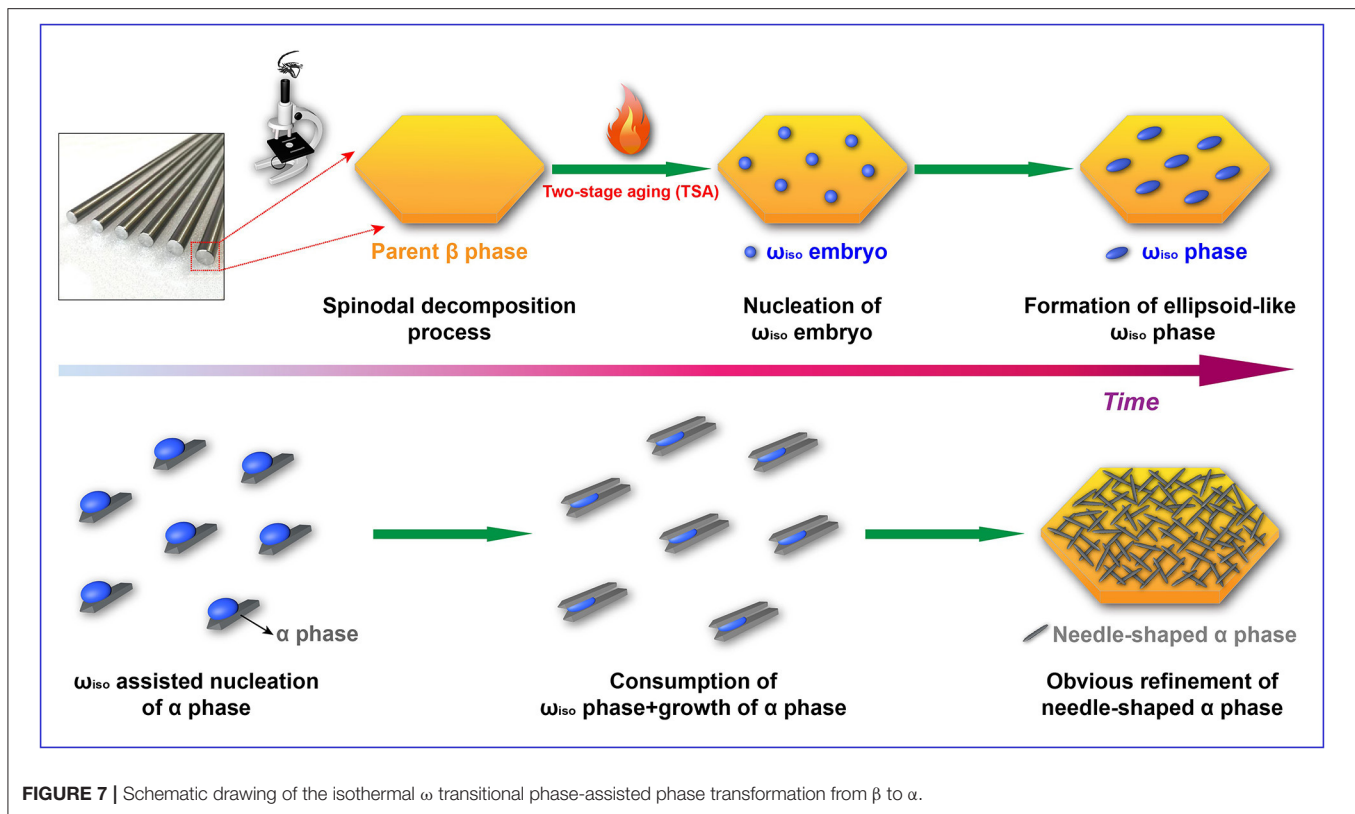


FIGURE 7 | Schematic drawing of the isothermal ω transitional phase-assisted phase transformation from β to α .

as an implanted material. In addition, it can be seen that the cytotoxicity of the Ti-B12 alloy is slightly better than that of the Ti-6Al-4V alloy, which can meet the requirements of medical materials for material cytotoxicity. Thus, it is evident that the Ti-B12 alloy has excellent biocompatibility.

CONCLUSIONS

The influence of isothermal ω transitional phase-assisted phase transition for the Ti-10Mo-6Zr-4Sn-3Nb (Ti-B12) alloy is investigated in this work. The microstructural evolution and mechanical performance at room temperature of the Ti-B12 alloy subjected to OSA and TSA treatment are investigated using OM, SEM, TEM (SAD), XRD, and EBSD. MTT test was carried out to evaluate the acute cytotoxicity and biocompatibility of the implanted material. The main conclusions can be summarized as follows:

- (1) The small ellipsoid-like isothermal ω transitional phases with the size of ~ 57 nm precipitated from the parent β phase when the Ti-B12 alloy is subjected to solution treatment at 790°C for 1 h and air cooling in conjunction with low-temperature aging at 325°C for 2 h. A definite orientation relationship (OR) is presented between the ω phase and the β matrix. While the alloy is subjected to high-temperature aging treatment at 510°C , a large number of short shuttle-like α phases precipitate at positions of the isothermal ω transitional phases. Such a microstructure is considered to be

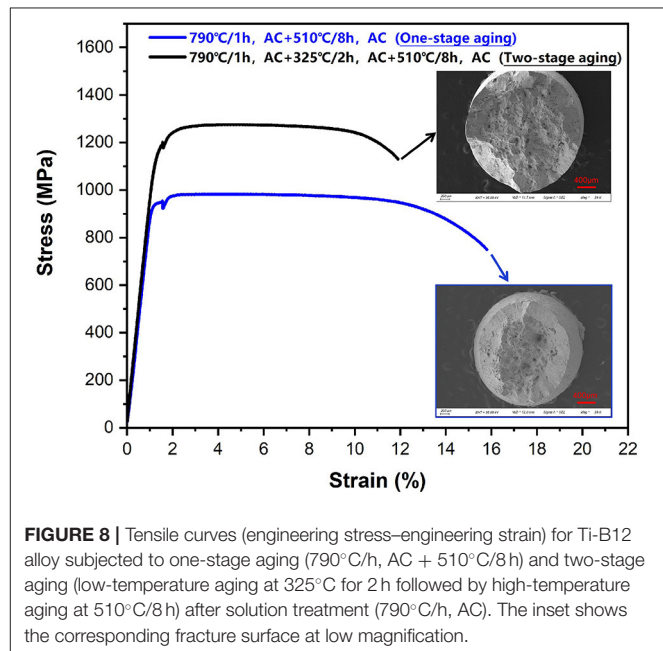


FIGURE 8 | Tensile curves (engineering stress–engineering strain) for Ti-B12 alloy subjected to one-stage aging ($790^\circ\text{C}/\text{h}$, AC + $510^\circ\text{C}/8\text{h}$) and two-stage aging (low-temperature aging at 325°C for 2 h followed by high-temperature aging at $510^\circ\text{C}/8\text{h}$) after solution treatment ($790^\circ\text{C}/\text{h}$, AC). The inset shows the corresponding fracture surface at low magnification.

favorable for the room-temperature mechanical properties of the Ti-B12 alloy.

- (2) The Ti-B12 alloy subjected to OSA at 510°C for 8 h possesses a relatively lower tensile strength, owing to the

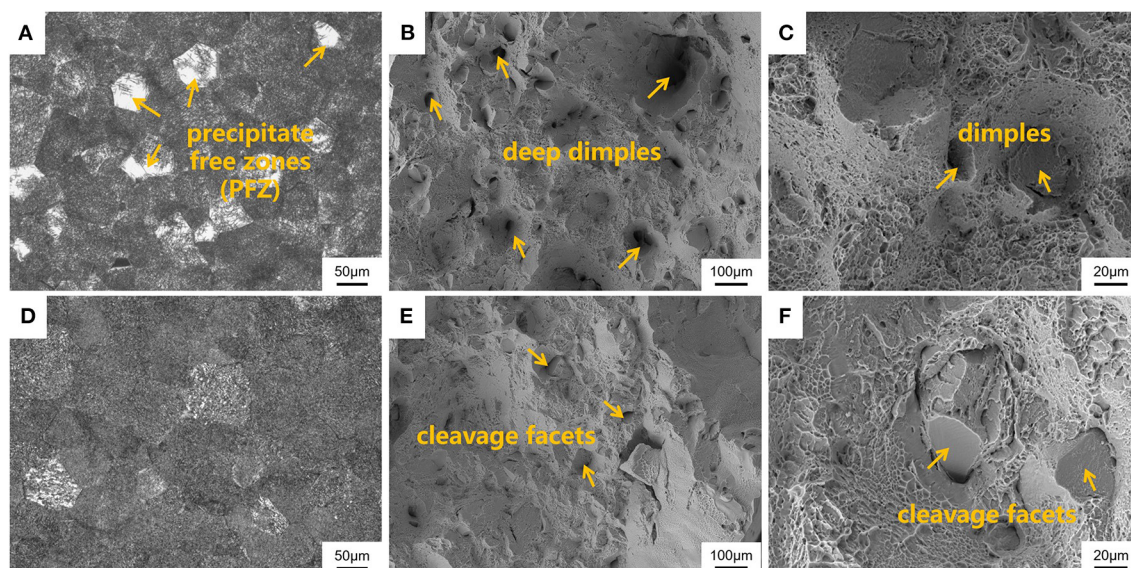


FIGURE 9 | Scanning electron microscopy images of the microstructures and fracture surfaces for Ti-B12 alloy subjected to (A–C) solution treatment (790°C/h, AC) plus one-stage aging treatment at 510°C for 8 h and (D–F) solution treatment (790°C/h, AC) in conjunction with two-stage aging treatment at 325°C for 2 h followed by 510°C for 8 h. (A,D) Optical microstructures. (B,C,E,F) Magnified images of fracture surfaces.

TABLE 2 | The result of cytotoxicity measured by MTT assay (OD values) ($n = 24$).

Time (h)	OD values		
	RPMI1640	Ti-B12 (relative proliferation rate, %)	TC4 (relative proliferation rate, %)
24	0.235 ± 0.021	0.240 ± 0.018 (102)	0.230 ± 0.027 (98)
72	0.532 ± 0.026	0.528 ± 0.025 (99)	0.515 ± 0.028 (97)
120	0.894 ± 0.035	0.887 ± 0.032 (99)	0.850 ± 0.042 (95)
168	1.15 ± 0.042	1.12 ± 0.038 (97)	1.10 ± 0.051 (96)

coarsening of the α phases on the β grain boundaries and in the β grains. The precipitated α phases in the OSA alloy are directly generated in the parent β phase, which fulfills the BOR of $(0001)\alpha // (110)\beta$. In addition, the crystallographic orientation of the α phases in the TSA alloy subjected to low-temperature aging at 325°C for 2 h followed by high-temperature aging at 510°C for 8 h is basically analogous to those in the OSA due to the existence of $(10\text{--}20)\omega // (10\text{--}20)\alpha$ orientation relationship after the high-temperature aging.

- (3) The Ti-B12 alloy subjected to TSA (low-temperature aging at 325°C for 2 h followed by high-temperature aging at 510°C for 8 h) possesses outstanding comprehensive mechanical properties (tensile strength: 1,275 MPa, elongation: 12%) at room temperature. A large number of isothermal ω transitional phases can be regarded as effective obstacles that prevent the emergence of thick α layers in boundaries and the rapid growth of secondary phases in the β grains for the Ti-B12 alloy subjected to low-temperature aging at 325°C. The

morphologies of the fracture surfaces in the TSA specimen show that the number of dimples tends to decrease and become shallow; the intergranular fracture mechanism plays a major role during tensile deformation.

- (4) The relative proliferation rate of cytotoxicity levels 0, 1, 2, 3, and 4 is ≥ 100 , 80–99, 50–79, 30–49, and 0–29%, respectively, for the Ti-B12 alloy. The cytotoxicity of the Ti-B12 alloy is slightly better than that of the Ti–6Al–4V alloy, which can meet the requirements of biomedical materials.

DATA AVAILABILITY STATEMENT

The original contributions presented in the study are included in the article/supplementary materials, further inquiries can be directed to the corresponding author/s.

AUTHOR CONTRIBUTIONS

JC took charge of the paper writing and data analysis. JL took charge of the technical guidance and supervision. SY took charge of literature research and providing research idea. ZD and XZ took charge of the microstructure characterization. WZ took charge of the room-temperature mechanical properties testing. JG and HW took charge of the preparation of samples. HS took charge of the hot rolling of alloy bars. ZY took charge of the texture evolution analysis.

FUNDING

This work was financially supported by the National Natural Science Foundation of China (nos. 51901193, 51861029,

51801162, and 32071327), the Key Research and Development Program of Shaanxi (program Nos. 2019GY-151, 2019GY-178, and 2020GY-251), the Science and Technology Plan Project of

Weiyang District in Xi'an City (201905), and the Xi'an Science and Technology Project (2020KJRC0141). JC was the leader of the funding.

REFERENCES

- Banerjee, D., and Williams, J. C. (2013). Perspectives on titanium science and technology. *Acta Mater.* 61, 844–879. doi: 10.1016/j.actamat.2012.10.043
- Cai, S., Bailey, D. M., and Kay, L. E. (2012). Effect of annealing and cold work on mechanical properties of β III titanium. *J. Mater. Eng. Performance* 21, 2559–2565. doi: 10.1007/s11665-012-0302-4
- Cai, S., Daymond, M. R., Ren, Y., Bailey, D. M., and Kay, L. E. (2013). Influence of short time anneal on recoverable strain of β III titanium alloy. *Mater. Sci. Eng. A* 562, 172–179. doi: 10.1016/j.msea.2012.11.005
- Chai, L., Chen, K., Zhi, Y., Murty, K. L., Chen, L. Y., and Yang, Z. (2018). Nanotwins induced by pulsed laser and their hardening effect in a Zr alloy. *J. Alloys Compounds* 748, 163–170. doi: 10.1016/j.jallcom.2018.03.126
- Chai, L. J., Wang, S. Y., Wu, H., Guo, N., Pan, H. C., Chen, L. Y., et al. (2017). $\alpha \rightarrow \beta$ Transformation characteristics revealed by pulsed laser-induced non-equilibrium microstructures in duplex-phase Zr alloy. *Sci. China Technol. Sci.* 60, 1255–1262. doi: 10.1007/s11431-016-9038-y
- Chaves, J. M., Florêncio, O., Silva, P. S., Marques, P. W. B., and Afonso, C. R. M. (2015). Influence of phase transformations on dynamical elastic modulus and anelasticity of β Ti–Nb–Fe alloys for biomedical applications. *J. Mech. Behav. Biomed. Mater.* 46, 184–196. doi: 10.1016/j.jmbbm.2015.02.030
- Chen, L., Shen, P., Zhang, L., Lu, S., Chai, L., Yang, Z., et al. (2018). Corrosion behavior of non-equilibrium Zr–Sn–Nb–Fe–Cu–O alloys in high-temperature 0.01 M LiOH aqueous solution and degradation of the surface oxide films. *Corrosion Sci.* 136, 221–230. doi: 10.1016/j.corsci.2018.03.012
- Chen, L., Xu, T., Wang, H., Sang, P., Lu, S., Wang, Z.-X., et al. (2019). Phase interaction induced texture in a plasma sprayed-remelted NiCrBSi coating during solidification: an electron backscatter diffraction study. *Surf. Coat. Technol.* 358, 467–480. doi: 10.1016/j.surfcoat.2018.11.019
- Chen, L.-Y., Cui, Y.-W., and Zhang, L.-C. (2020). Recent development in β titanium alloys for biomedical applications. *Metals* 10:1139. doi: 10.3390/met10091139
- Cheng, J., Wang, H., Li, J., Gai, J., Ru, J., Du, Z., et al. (2020). The effect of cold swaging deformation on the microstructures and mechanical properties of a novel metastable β type Ti–10Mo–6Zr–4Sn–3Nb alloy for biomedical devices. *Front. Mater.* 7:228. doi: 10.3389/fmats.2020.00228
- Cremasco, A., Andrade, P. N., Contieri, R. J., Lopes, E. S. N., Afonso, C. R. M., and Caram, R. (2011). Correlations between aging heat treatment, ω phase precipitation and mechanical properties of a cast Ti–Nb alloy. *Mater. Design* 32, 2387–2390. doi: 10.1016/j.matdes.2010.11.012
- Cui, C., Hu, B., Zhao, L., and Liu, S. (2011). Titanium alloy production technology, market prospects and industry development. *Mater. Design* 32, 1684–1691. doi: 10.1016/j.matdes.2010.09.011
- Cui, W. F., and Guo, A. H. (2009). Microstructures and properties of biomedical TiNbZrFe β -titanium alloy under aging conditions. *Mater. Sci. Eng. A* 527, 258–262. doi: 10.1016/j.msea.2009.08.057
- Dong, R., Li, J., Kou, H., Fan, J., Zhao, Y., Hou, H., et al. (2020). ω -Assisted refinement of α phase and its effect on the tensile properties of a near β titanium alloy. *J. Mater. Sci. Technol.* 44, 24–30. doi: 10.1016/j.jmst.2019.10.031
- Du, Z., Guo, H., Liu, J., Cheng, J., Zhao, X., Wang, X., et al. (2020). Microstructure evolution during aging heat treatment and its effects on tensile properties and dynamic Young's modulus of a biomedical β titanium alloy. *Mater. Sci. Eng. A* 791:139677. doi: 10.1016/j.msea.2020.139677
- Gao, J., Knowles, A. J., Guan, D., and Rainforth, W. M. (2019). ω phase strengthened 1.2GPa metastable β titanium alloy with high ductility. *Scripta Mater.* 162, 77–81. doi: 10.1016/j.scriptamat.2018.10.043
- Guo, H., Du, Z., Wang, X., Cheng, J., Liu, F., Cui, X., et al. (2019). Flowing and dynamic recrystallization behavior of new biomedical metastable β titanium alloy. *Mater. Res. Express* 6:0865d2. doi: 10.1088/2053-1591/ab2421
- Guo, Y., Chen, D., Cheng, M., Lu, W., Wang, L., and Zhang, X. (2013). The bone tissue compatibility of a new Ti35Nb2Ta3Zr alloy with a low Young's modulus. *Int. J. Mol. Med.* 31, 689–697. doi: 10.3892/ijmm.2013.1249
- Ivasishin, O. M., Markovsky, P. E., Matviychuk, Y. V., Semiatin, S. L., Ward, C. H., and Fox, S. (2008). A comparative study of the mechanical properties of high-strength β -titanium alloys. *J. Alloys Compounds* 457, 296–309. doi: 10.1016/j.jallcom.2007.03.070
- Kaur, M., and Singh, K. (2019). Review on titanium and titanium based alloys as biomaterials for orthopaedic applications. *Mater. Sci. Eng. C* 102, 844–862. doi: 10.1016/j.msec.2019.04.064
- Laheurte, P., Eberhardt, A., Philippe, M., and Deblock, L. (2006). Improvement of pseudoelasticity and ductility of β III titanium alloy—application to orthodontic wires. *Eur. J. Orthodontics* 29, 8–13. doi: 10.1093/ejo/cj038
- Lai, M. J., Li, T., Yan, F. K., Li, J. S., and Raabe, D. (2021). Revisiting ω phase embrittlement in metastable β titanium alloys: role of elemental partitioning. *Scripta Mater.* 193, 38–42. doi: 10.1016/j.scriptamat.2020.10.031
- Li, H.-B., Chen, M.-S., Tian, Y.-Q., Chen, L.-S., and Chen, L.-Q. (2020). Ultra-fine-grained ferrite prepared from dynamic reversal austenite during warm deformation. *Acta Metallurgica Sinica* 33, 290–298. doi: 10.1007/s40195-019-00973-5
- Li, T., Kent, D., Sha, G., Cairney, J. M., and Dargusch, M. S. (2016). The role of ω in the precipitation of α in near- β Ti alloys. *Scripta Mater.* 117, 92–95. doi: 10.1016/j.scriptamat.2016.02.026
- Li, T., Kent, D., Sha, G., Dargusch, M. S., and Cairney, J. M. (2015). The mechanism of ω -assisted α phase formation in near β -Ti alloys. *Scripta Mater.* 104, 75–78. doi: 10.1016/j.scriptamat.2015.04.007
- Li, T., Kent, D., Sha, G., Liu, H., Fries, S. G., Ceguerra, A. V., et al. (2018). Nucleation driving force for ω -assisted formation of α and associated ω morphology in β -Ti alloys. *Scripta Mater.* 155, 149–154. doi: 10.1016/j.scriptamat.2018.06.039
- Nag, S., Banerjee, R., Srinivasan, R., Hwang, J. Y., Harper, M., and Fraser, H. L. (2009). ω -Assisted nucleation and growth of α precipitates in the Ti–5Al–5Mo–5V–3Cr–0.5Fe β titanium alloy. *Acta Mater.* 57, 2136–2147. doi: 10.1016/j.actamat.2009.01.007
- Niinomi, M., Nakai, M., and Hieda, J. (2012). Development of new metallic alloys for biomedical applications. *Acta Biomater.* 8, 3888–3903. doi: 10.1016/j.actbio.2012.06.037
- Ohmori, Y., Ogo, T., Nakai, K., and Kobayashi, S. (2001). Effects of ω -phase precipitation on $\beta \rightarrow \alpha$, α' transformations in a metastable β titanium alloy. *Mater. Sci. Eng. A* 312, 182–188. doi: 10.1016/S0921-5093(00)01891-8
- Qazi, J. I., Marquardt, B., Allard, L. F., and Rack, H. J. (2005). Phase transformations in Ti–35Nb–7Zr–5Ta–(0.06–0.68)O alloys. *Mater. Sci. Eng. C* 25, 389–397. doi: 10.1016/j.msec.2005.01.022
- Rabadia, C. D., Liu, Y. J., Zhao, C. H., Wang, J. C., Jawed, S. F., Wang, L. Q., et al. (2019). Improved trade-off between strength and plasticity in titanium based metastable β type Ti–Zr–Fe–Sn alloys. *Mater. Sci. Eng. A* 766:138340. doi: 10.1016/j.msea.2019.138340
- Rack, H. J., Kalish, D., and Fike, K. D. (1970). Stability of as-quenched β -III titanium alloy. *Mater. Sci. Eng.* 6, 181–198. doi: 10.1016/0025-5416(70)90048-0
- Santhosh, R., Geetha, M., Saxena, V. K., and Nageswararao, M. (2014). Studies on single and duplex aging of metastable β titanium alloy Ti–15V–3Cr–3Al–3Sn. *J. Alloys Compounds* 605, 222–229. doi: 10.1016/j.jallcom.2014.03.183
- Schmidt, P., El-Chaikh, A., and Christ, H. J. (2011). Effect of duplex aging on the initiation and propagation of fatigue cracks in the solute-rich metastable β titanium alloy Ti 38-644. *Metall Mater. Trans. A* 42, 2652–2667. doi: 10.1007/s11661-011-0662-7
- Shi, R., Zheng, Y., Banerjee, R., Fraser, H. L., and Wang, Y. (2019). ω -Assisted α nucleation in a metastable β titanium alloy. *Scripta Mater.* 171, 62–66. doi: 10.1016/j.scriptamat.2019.06.020

- Tang, B., Chu, Y., Zhang, M., Meng, C., Fan, J., Kou, H., et al. (2020). The ω phase transformation during the low temperature aging and low rate heating process of metastable β titanium alloys. *Mater. Chem. Phys.* 239:122125. doi: 10.1016/j.matchemphys.2019.122125
- Tang, X., Ahmed, T., and Rack, H. J. (2000). Phase transformations in Ti-Nb-Ta and Ti-Nb-Ta-Zr alloys. *J. Mater. Sci.* 35, 1805–1811. doi: 10.1023/A:1004792922155
- Vishnu, J., Sankar, M., Rack, H. J., Rao, N., Singh, A. K., and Manivasagam, G. (2020). Effect of phase transformations during aging on tensile strength and ductility of metastable β titanium alloy Ti–35Nb–7Zr–5Ta–0.35O for orthopedic applications. *Mater. Sci. Eng. A* 779:139127. doi: 10.1016/j.msea.2020.139127
- Wang, L., Lu, W., Qin, J., Zhang, F., and Zhang, D. (2009). Effect of precipitation phase on microstructure and superelasticity of cold-rolled β titanium alloy during heat treatment. *Mater. Design* 30, 3873–3878. doi: 10.1016/j.matdes.2009.03.042
- Wang, P., Todai, M., and Nakano, T. (2018). ω -phase transformation and lattice modulation in biomedical β -phase Ti-Nb-Al alloys. *J. Alloys Compounds* 766, 511–516. doi: 10.1016/j.jallcom.2018.06.266
- Weiss, I., and Semiatin, S. L. (1998). Thermomechanical processing of β titanium alloys—an overview. *Mater. Sci. Eng. A* 243, 46–65. doi: 10.1016/S0921-5093(97)00783-1
- Xiang, K., Chen, L.-Y., Chai, L., Guo, N., and Wang, H. (2020). Microstructural characteristics and properties of CoCrFeNiNb_x high-entropy alloy coatings on pure titanium substrate by pulsed laser cladding. *Appl. Surf. Sci.* 517:146214. doi: 10.1016/j.apsusc.2020.146214
- Xiao, J. F., Nie, Z. H., Ma, Z. W., Liu, G. F., Hao, F., and Tan, C. W. (2020). ω precipitation: deformation regulator in metastable titanium alloys. *Mater. Sci. Eng. A* 772:138687. doi: 10.1016/j.msea.2019.138687
- Yang, Z. N., Wang, X. B., Liu, F., Zhang, F. C., Chai, L. J., Qiu, R. S., et al. (2019). Effect of intercritical annealing temperature on microstructure and mechanical properties of duplex Zr-2.5Nb alloy. *J. Alloys Compounds* 776, 242–249. doi: 10.1016/j.jallcom.2018.10.320
- Zhang, C., Ding, Z., Xie, L., Zhang, L.-C., Wu, L., Fu, Y., et al. (2017). Electrochemical and in vitro behavior of the nanosized composites of Ti-6Al-4V and TiO₂ fabricated by friction stir process. *Appl. Surf. Sci.* 423, 331–339. doi: 10.1016/j.apsusc.2017.06.141
- Zhang, L.-C., and Chen, L.-Y. (2019). A review on biomedical titanium alloys: recent progress and prospect. *Adv. Eng. Mater.* 21:1801215. doi: 10.1002/adem.201801215
- Zhang, L.-C., Chen, L.-Y., and Wang, L. (2020). Surface modification of titanium and titanium alloys: technologies, developments and future interests. *Adv. Eng. Mater.* 22:1901258. doi: 10.1002/adem.201901258
- Zheng, Y., Choudhuri, D., Alam, T., Williams, R. E. A., Banerjee, R., and Fraser, H. L. (2016a). The role of cuboidal ω precipitates on α precipitation in a Ti-20V alloy. *Scripta Mater.* 123, 81–85. doi: 10.1016/j.scriptamat.2016.06.004
- Zheng, Y., Williams, R. E. A., Wang, D., Shi, R., Nag, S., Kami, P., et al. (2016b). Role of ω phase in the formation of extremely refined intragranular α precipitates in metastable β -titanium alloys. *Acta Mater.* 103, 850–858. doi: 10.1016/j.actamat.2015.11.020
- Zhu, C., Lv, Y., Qian, C., Qian, H., Jiao, T., Wang, L., et al. (2016). Proliferation and osteogenic differentiation of rat BMSCs on a novel Ti/SiC metal matrix nanocomposite modified by friction stir processing. *Sci. Rep.* 6:38875. doi: 10.1038/srep38875

Conflict of Interest: The authors declare that the research was conducted in the absence of any commercial or financial relationships that could be construed as a potential conflict of interest.

Copyright © 2021 Cheng, Li, Yu, Du, Zhang, Zhang, Gai, Wang, Song and Yu. This is an open-access article distributed under the terms of the Creative Commons Attribution License (CC BY). The use, distribution or reproduction in other forums is permitted, provided the original author(s) and the copyright owner(s) are credited and that the original publication in this journal is cited, in accordance with accepted academic practice. No use, distribution or reproduction is permitted which does not comply with these terms.



A Novel Design of Temporomandibular Joint Prosthesis for Lateral Pterygoid Muscle Attachment: A Preliminary Study

Luxiang Zou^{1,2,3†}, Yingqian Zhong^{1,2,3†}, Yinze Xiong^{4†}, Dongmei He^{1,2,3*}, Xiang Li⁴, Chuan Lu^{1,2,3} and Huimin Zhu^{1,2,3}

OPEN ACCESS

Edited by:

Chaozong Liu,
University College London,
United Kingdom

Reviewed by:

Hongyu Zhang,
Tsinghua University, China
Zhongmin Jin,
Southwest Jiaotong University, China
Hui Peng,
Beihang University, China
Zikai Hua,
Orthotek Laboratory, China

*Correspondence:

Dongmei He
lucyhe119@163.com

[†]These authors have contributed
equally to this work

Specialty section:

This article was submitted to
Biomaterials,
a section of the journal
Frontiers in Bioengineering and
Biotechnology

Received: 18 November 2020

Accepted: 28 December 2020

Published: 21 January 2021

Citation:

Zou L, Zhong Y, Xiong Y, He D, Li X,
Lu C and Zhu H (2021) A Novel
Design of Temporomandibular Joint
Prosthesis for Lateral Pterygoid
Muscle Attachment: A Preliminary
Study.
Front. Bioeng. Biotechnol. 8:630983.
doi: 10.3389/fbioe.2020.630983

¹ Department of Oral Surgery, Ninth People's Hospital, Shanghai Jiao Tong University School of Medicine, Shanghai, China, ² Shanghai Key Laboratory of Stomatology & Shanghai Research Institute of Stomatology, Shanghai, China, ³ National Clinical Research Center of Stomatology, Shanghai, China, ⁴ State Key Laboratory of Mechanical System and Vibration, School of Mechanical Engineering, Shanghai Jiao Tong University, Shanghai, China

Introduction: In temporomandibular joint (TMJ) replacement operation, due to the condylectomy, the lateral pterygoid muscle (LPM) lost attachment and had impact on the mandible kinematic function. This study aimed to design a novel TMJ replacement prosthesis for LPM attachment and to verify its feasibility by preliminary *in vitro* and *in vivo* experiments.

Materials and Methods: An artificial TMJ prosthesis designed with a porous structure on the condylar neck region for LPM attachment was fabricated by a 3D printed titanium (Ti) alloy. A rat myoblast cell line (L6) was tested for adhesion and biocompatibility with porous titanium scaffolds *in vitro* by cell counting Kit-8 (CCK-8), scanning electron microscope (SEM), flow cytometry (FCM), real-time quantitative polymerase chain reaction (RT-qPCR), immunocytofluorescence, western blotting, etc. The porous titanium scaffolds were further embedded in the rat intervertebral muscle to analyze muscle growth and biomechanical strength *in vivo*. The novel artificial TMJ prosthesis was implanted to reconstruct the goat's condyle and LPM reattachment was analyzed by hard tissue section and avulsion force test.

Results: L6 muscle cells showed good proliferation potential on the porous Ti scaffold under SEM scanning and FCM test. In RT-qPCR, immunocytofluorescence and western blotting tests, the L6 cell lines had good myogenic capacity when cultured on the scaffold with high expression of factors such as Myod1 and myoglobin, etc. In the *in vivo* experiment, muscles penetrated into the porous scaffold in both rats and goats. In rat's intervertebral muscle implantation, the avulsion force was 0.716 N/mm² in 4 weeks after operation and was significantly increased to 0.801 N/mm² at 8 weeks ($p < 0.05$). In goat condylar reconstruction with the porous scaffold prosthesis, muscles attached to the prosthesis with the avulsion force of 0.436 N/mm² at 8 weeks, but was smaller than the biological muscle-bone attachment force.

Conclusion: The novel designed TMJ prosthesis can help LPM attach to its porous titanium scaffold structure area for future function.

Keywords: temporomandibular joint, prosthesis, lateral pterygoid muscle, porous titanium scaffold, muscle attachment

INTRODUCTION

The temporomandibular joint (TMJ) plays a key role in mouth opening, speech, chewing, and swallowing. TMJ disease is common in clinical settings. At present, artificial total joint replacement has become a mainstay treatment modality for advanced osteoarthritis, condylar tumors, TMJ ankylosis, autologous bone graft failure, and other conditions (Mercuri et al., 2007; Guarda-Nardini et al., 2008). However, removal of the condyle also leads to the detachment of the lateral pterygoid muscle (LPM) which participates in the movement of mandibular laterotrusion and protrusion (Westermarck, 2010; Celebi et al., 2011; Zheng et al., 2019). Although it has been reported that muscle can reattach to an autologous bone graft (Wang et al., 2018), it has not been found to form a reattachment with the metal of the artificial joint. The loss of attachment of the pterygoid muscle results in lateral and forward movement limitation and serves as an obstacle in fine chewing functions. Studies have shown that the natural condylar translational movement range is about 16 mm, whereas the artificial joint can only make a rotation movement <6 mm (Sonnenburg and Sonnenburg, 1985; Mercuri et al., 1995; Wojczyńska et al., 2016). This increases the burden on other muscles and the contralateral natural joint, leading to discomfort and/or internal derangement of the contralateral joint (Ramos and Mesnard, 2015). Our previous study also found out that more than 30% of patients with unilateral joint replacement complained about discomfort in their contralateral joints, including clicking, soreness, muscle tension, etc. (Zou et al., 2019).

Based on the above, we propose a hypothesis that if the LPM can reattach to the artificial joint, it will promote the function of the joint (Figure 1A). In this study, we used 3D printing technology to establish a porous structure in the TMJ prosthesis for LPM reattachment. We then tested its feasibility through an *in vitro* cell experiment and *in vivo* in rat intramuscular implantation and goat condyle reconstruction to test its biocompatibility.

MATERIALS AND METHODS

This study was approved by the local ethics board of the hospital (Jiuyuan Lunshen, No. 73, 2015).

Design and Manufacture of 3D Printed Porous Titanium Scaffold and TMJ Prosthesis

A porous titanium structure with a diameter of 5 mm, a thickness of 2 mm, a pore diameter of 500 μ m, and a porosity of 75% was designed for cell adhesion experiments *in vitro*. In addition, a porous titanium scaffold with a diameter of 10 mm, a thickness of 5 mm, and same pore diameter and porosity as the first

structure was designed for the use of intervertebral muscles in the rat's back implantation. Based on the Computed Tomography (CT) dicom data of goat mandibles, a prosthesis for condyle replacement was designed with a porous structure in the neck for LPM reattachment (Figures 1B–E). The scanning electron microscopy (SEM) and energy dispersive spectrometer (EDS) scanning were used to confirm the element consist of the printed scaffold (Figures 1F–J). All the above scaffolds and prosthesis were produced using 3D printing by Ti6Al4V (Sunshine Co Ltd, Shanghai, China). Ultrasonic cleaning and disinfection under high temperature and high pressure conditions were also performed.

Cytology Evaluation of 3D Printed Porous Titanium Scaffold for Myogenic Cell Adhesion and Bioactivity

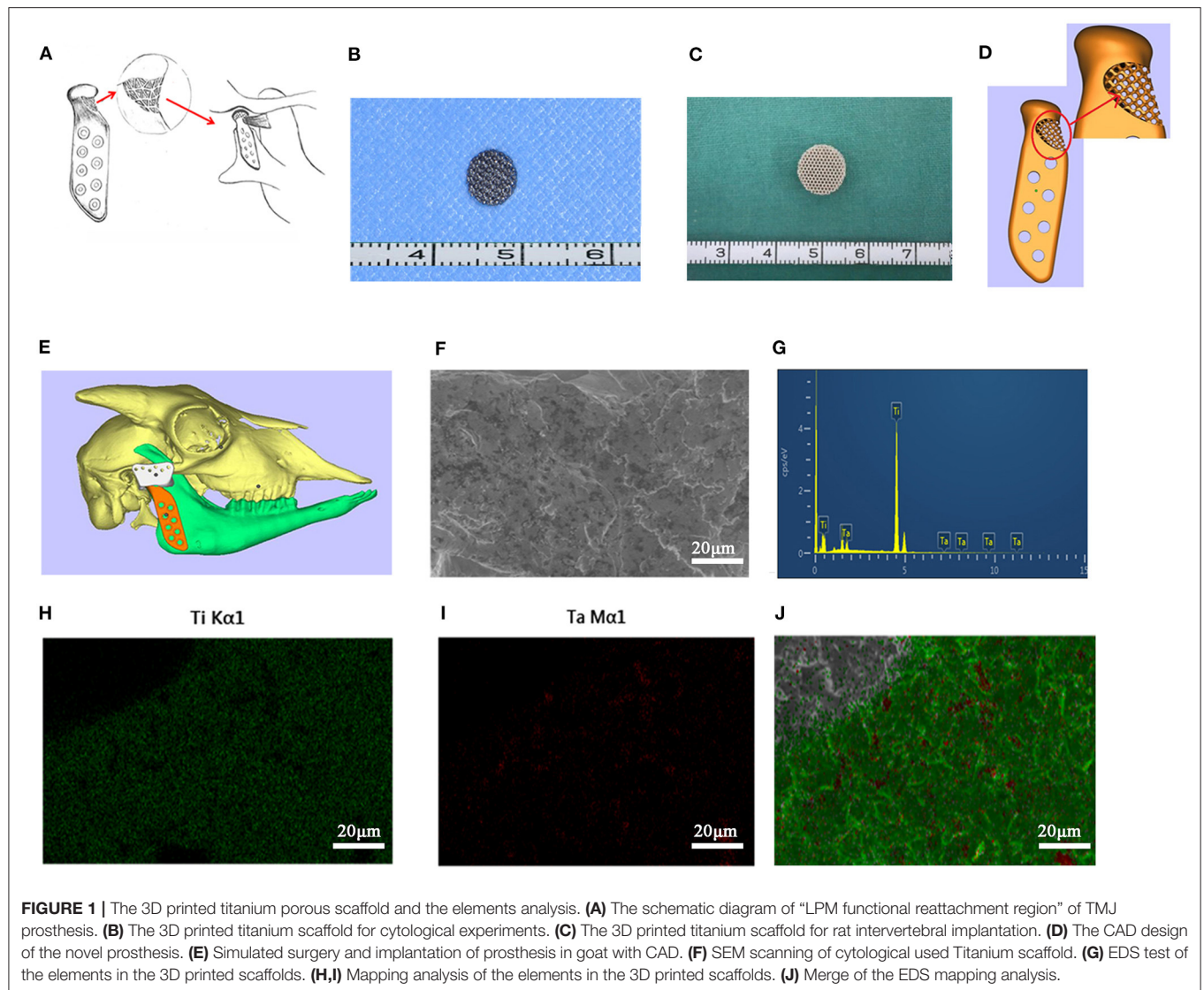
The porous titanium scaffold materials were fully immersed in α -MEM medium containing 10% fetal bovine serum (FBS) and cultured at 37°C in a 5% CO₂ incubator for 72 h. The material leaching liquid was collected and stored in a refrigerator at 4°C.

The L6 rat myoblast cell line (purchased from the Chinese Academy of Biology Cell Bank, Shanghai) was inoculated into a 96-well plate at a density of 2×10^3 cells per well. The material leaching liquid and a 10% FBS α -MEM complete medium were also added. The observation period was every 24 h and lasted for 5 days, with five replicate wells set in each group. The proliferation of cells in the two groups was determined by a cell counting kit-8 (CCK-8) test in order to study the biological toxicity impact of porous titanium material on L6 cells.

The L6 cells were inoculated on the surface of the porous titanium scaffold at a concentration of 1×10^6 /ml and cultured in a 37°C 5% CO₂ incubator for 4 h to allow the cells to adhere to the material. They were then cultured in a complete medium containing of 10% serum, which was changed every other day. After days 1, 3, and 5 of incubation, the cells were fixed with 2.5% glutaraldehyde for 4 h at room temperature, and the morphology, adhesion, as well as proliferation of the cells were observed by SEM.

Flow cytometric analysis was carried out to verify the apoptosis which was led by the L6 cells co-cultured with scaffolds due to impact of metal material after 1, 3, and 5 days. Furthermore, after co-culturing with scaffolds, the L6 cells were stained by Calcein-AM and propidium iodide (PI) to label living cells and dead cells, respectively. In the fluorescence scan, the Calcein-AM stained living cells showed green fluorescence and PI stained dead cells showed red fluorescence.

Total RNA was obtained from the L6 cells cultured on the scaffold for 3 days by using RNA Express Total RNA Kit (Ncambio, Suzhou, China) according to the manufacturer's instructions.



NanoDrop 2000/2000C spectrophotometer was used to tested the purity and concentration of RNA at wavelengths of 260/280 nm. PrimeScript™ RT Reagent Kit (TaKaRa Biotechnology) was then used to reverse transcribe 1 µg of extracted RNA into cDNA. The resultant cDNA was used as template in the TB Green® Premix ExTaq™ Kit (TaKaRa Biotechnology) master mix and real-time quantitative polymerase chain reaction (RT-qPCR) reactions was performed on the Light Cycler96 Real-Time PCR System (Roche, Ltd, Switzerland). And the rat primer sets used were displayed in **Table 1**.

After 3 days of co-cultured with scaffold incubation, the scaffold material combined with the cells was fixed with 4% paraformaldehyde and permeabilized with 0.5% Triton X-100 (Sigma Aldrich) for 10 min at room temperature. It was then blocked with 5% bovine serum albumin (BSA) for 30 min and incubated with the primary antibodies for the cell adhesion and myogenic-related proteins (integrin-β₁, 1:200; myoD, 1:200; Desmin, 1:200, Myoglobin, 1:100)

overnight at 4°C. After that, the secondary anti-bodies and the Fluorescein isothiocyanate-labeled (FITC) phalloidin for cytoskeleton staining were incubated for 1 h at 37°C. The results were tested using immunofluorescence detection to confirm adhesion and biological activity of the L6 myoblasts on the 3D printed porous titanium scaffolds.

To define the biological activity potential of the L6 myoblasts on the Titanium scaffold, total cellular proteins (TCPs) were extracted from both the L6 cells cultivated on the scaffold and the common culture dish to be used as a control, after 3 days of inoculation for western blotting. The membranes were kept in 5% skim milk in 1 × TBST (Tris-buffered saline with 0.1% Tween 20) at room temperature for 1 h and then incubated with the primary antibodies (Gapdh, HuaxingBio, 1:3000; Desmin, Zenbio, 1:1000; MyoD, HuaxingBio, 1:1000; Myoglobin, Zenbio, 1:1000; Integrin-β₁, HuaxingBio, 1:2000, TNNT1, HuaxingBio, 1:1000; VCL, HuaxingBio, 1:1000) overnight shaking at 4°C. Thereafter, the secondary anti-bodies were incubated for 1 h at

TABLE 1 | Primers for the target gene.

Gene name		5'-3' sequence (forward; reverse)
Integrin- β 1	Forward	5'-CTGGTTCTATTTACCTACTCAG-3'
	Reverse	5'-CCAGTAGGACAGTCTGGAG-3'
VCL	Forward	5'-CTACAACTCCCATCAAGCTG-3'
	Reverse	5'-TCTCGTCAAATACCTCTTCCC-3'
Desmin	Forward	5'-TCTCAACTTCCGAGAAACCA-3'
	Reverse	5'-TCAATGGTCTTGATCATCACTG-3'
MYH4	Forward	5'-TCATCTGGTAACACAAGAGGTGC-3'
	Reverse	5'-ACTTCCGGAGGTAAGGAGCA-3'
MyoD1	Forward	5'-ATGGCATGATGGATTACAGC-3'
	Reverse	5'-GACGCCTCACTGTAGTAGG-3'
TNN1	Forward	5'-GATGGAGAAATTGAAGCAACAG-3'
	Reverse	5'-CCCTTTCGGAATTTCTGGG-3'
Myoglobin	Forward	5'-GCAGGCTCAAGAAAGTGAATGA-3'
	Reverse	5'-TAGGCGCTCAATGTAAGGAT-3'
GAPDH	Forward	5'-AACTCCATTCTTCCACCT-3'
	Reverse	5'-TTGTCATACCAGGAAATGAGC-3'

room temperature and the antibody reactivity was visualized by using Bio-rad Gel Doc XR+ image scanning (Bio-rad, Inc., CA, USA).

Rat Intramuscular Implantation of 3D Printed Porous Titanium Scaffold for Muscle Attachment Evaluation

After chloral hydrate injection anesthesia, the porous titanium scaffold with a diameter of 10 mm and a thickness of 5 mm was implanted into the intervertebral muscles of both sides of six male Sprague-Dawley rats (6 weeks), with one scaffold on each side (**Figures 2A,B**). The rats were then overdosed with an excess of anesthetic on weeks 4 and 8. Each time 3 rats were sacrificed and one side of the fresh samples were then tested for the maximum peeling off force of the porous titanium scaffold-muscle using a tensile tester (Instron 3345, Shanghai, China); while the other side specimens were fixed in 4% paraformaldehyde for 24 h and embedded in resin for hard tissue slicing. The distribution of muscle and collagen fibers was distinguished by Van Gieson (V-G) staining. The microscopy scans mainly focused on the integration of tissue-scaffold interface integration and angiogenesis in slice. Three fields from the upper, middle and lower part of the complete image acquisition were selected randomly for each sample, which were analyzed by Image J software (NIH, USA) to quantify the percentage of tissue ingrowth area of the total pore area and to demonstrate the integration of the muscle-metal interface as well as the muscle and collagen distribution.

Goat Condylar Replacement by Novel Designed Prosthesis for LPM Attachment

Six male 12-month-old goats were used for right condyle removal and reconstruction with a novel designed prosthesis under general anesthesia (**Figure 2C**). Their left TMJ was untouched

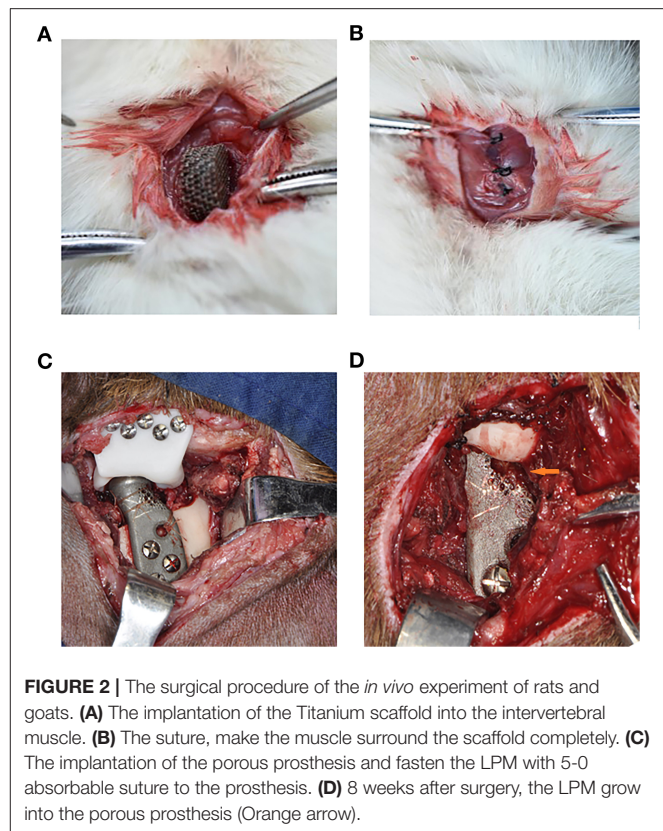


FIGURE 2 | The surgical procedure of the *in vivo* experiment of rats and goats. **(A)** The implantation of the Titanium scaffold into the intervertebral muscle. **(B)** The suture, make the muscle surround the scaffold completely. **(C)** The implantation of the porous prosthesis and fasten the LPM with 5-0 absorbable suture to the prosthesis. **(D)** 8 weeks after surgery, the LPM grow into the porous prosthesis (Orange arrow).

as a control method. Eight weeks after their operations, the goats were euthanized in order to enable mandible removal. Three of the prosthesis specimens was used to test the avulsion force of the LPM from the prosthesis with the tensile tester. The other three prostheses along with the LPM was fixed with 4% paraformaldehyde and prepared for hard tissue slicing with hematoxylin-eosin (HE) staining and V-G staining. The six normal condyles were resected with LPM attachment for avulsion force for use as a control base. The passive maximum incision opening (MIO) of the goats pre- and post-operation were also recorded as a biological function test of the prosthesis.

Statistical Analysis

All statistical analyses were performed with SPSS software (version 19.0). The results of measurement were displayed as mean \pm standard deviation (SD). The independent-sample *t*-test was used for RT-qPCR, western blotting measurement, histological analysis and avulsion force comparison, and one-way ANOVA test was used for CCK-8 proliferation rate. A *p*-value of 0.05 was considered statistically significant.

RESULTS

The results of CCK-8 cell proliferation test experiment showed that there was no significant difference in cell proliferation between the material leaching solution culture group and the normal medium group, indicating that the porous titanium

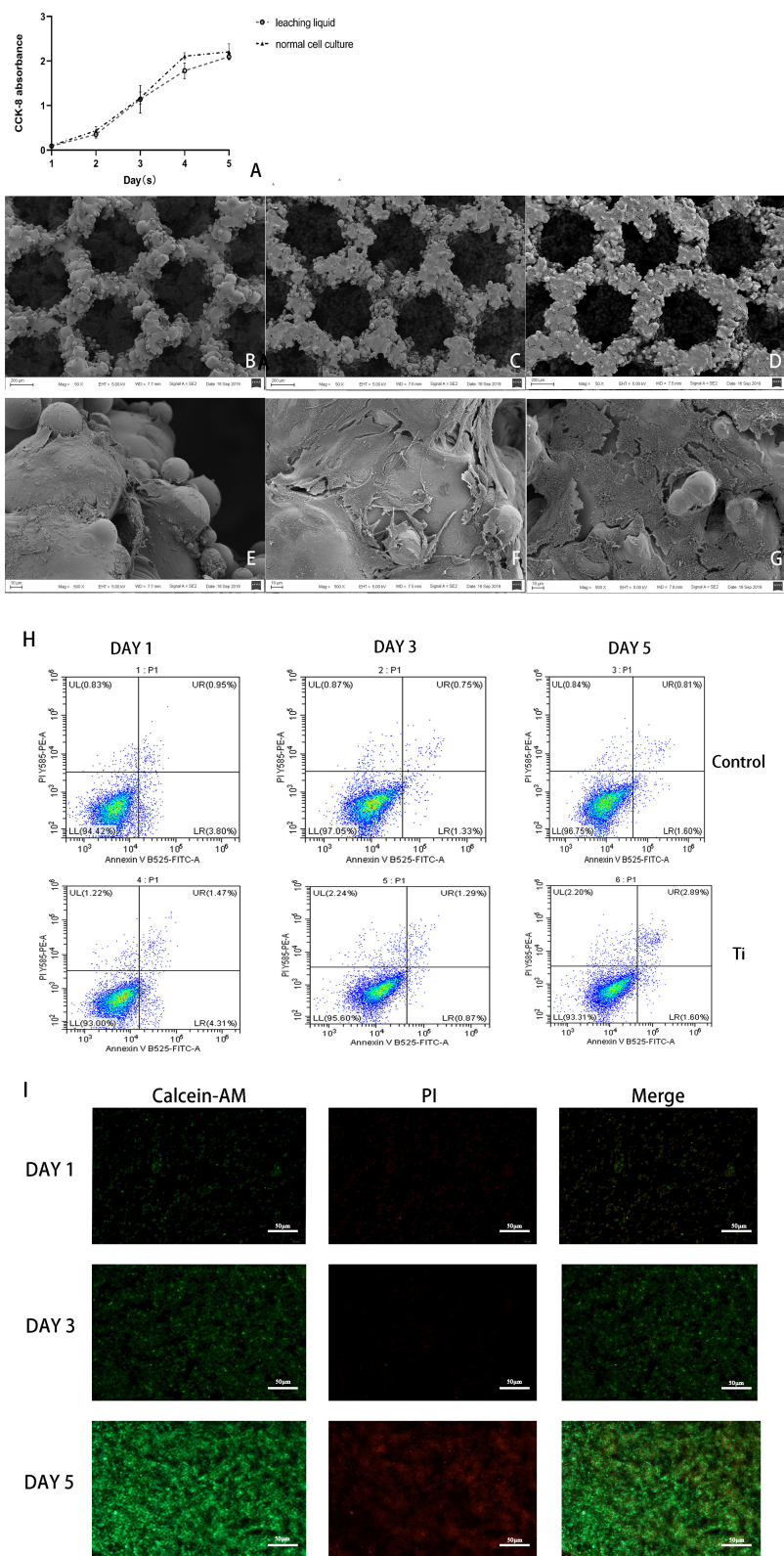


FIGURE 3 | The biosafety of the scaffold were verified after co-cultivation with the scaffold. **(A)** CCK-8 test of cell proliferation in leaching liquid and ordinary culture medium, and in both situations, cells proliferate actively with no statistical difference ($p > 0.05$). **(B–G)** SEM scanning of L6 myoblast cultivated on the Titanium
(Continued)

FIGURE 3 | scaffold, (B,E) showed in 1 day, (C,F) showed in 3 days, (D,G) showed in 5 days, could see significant cell proliferation in 5 days, (B–D) 50 x, (E–G) 500 x. (H) Flow cytometry detection analysis of the cells cultured in dishes and on the Ti scaffold; and both the cells cultured in dishes or on the scaffold showed high activity with low apoptosis rate. (I) The cells on the scaffolds were taken by laser confocal microscopy (Green are living cells, and red are dead cells) in 1, 3, and 5 days. Significant proliferation with low cell death rate can be observed.

material had no obvious toxicity to L6 cell proliferation (Figure 3A).

SEM observation showed that the L6 cells adhered tightly to the porous titanium scaffold material, with continuous cell proliferation and the number of cells increasing significantly. Under the 50-fold microscope, a large number of cells can be seen sticking to the scaffold material. Furthermore, under the 500-fold microscope, the cells can be seen to be stretched, and reveal pseudopods. The pseudopods allow the cells to connect to each other and across the pores of the material, which can be seen from adjacent cells. Moreover, some cells even merged to form a sheet, and a large amount of secretory matrix is visible covering the surface of the material (Figures 3B–G). Flow cytometric analysis of L6 co-cultured with scaffolds revealed that the co-cultured on the scaffold did not cause an obvious increase in apoptosis due to the metal ion release or scaffold structure compared with dishes (Figure 3H). Moreover, after co-culturing with scaffolds, the Calcein-AM and PI staining results revealed that the L6 cells exhibited good biocompatibility and proliferation capacity cultured on the scaffold (Figure 3I).

The RT-qPCR results showed that when co-cultured on the scaffold, the L6 cells showed even stronger myogenic bioactivity compared with cultured in the dishes (Figure 4A). The results of confocal microscopy scanning showed that the FITC labeled cytoskeleton and integrin- β 1 were abundantly expressed after the L6 cells were co-cultured with porous titanium scaffolds. The myogenic-related factors as MyoD, Myoglobin, Desmin were significantly expressed, indicating that the myoblasts and porous titanium scaffold have strong biocompatibility *in vitro* (Figure 4B). The western blot results of cell culture on scaffold and the control group showed that the L6 myoblast showed greater myogenic differentiation factor expression on the 3D printed titanium scaffold, and the expression of MyoD, myoglobin and TNNT1 were significantly higher than the control group, with no difference in Desmin. However, the expression of integrin- β 1 factor in the scaffold group was lower than that in control group ($p < 0.05$, Figures 4C,D).

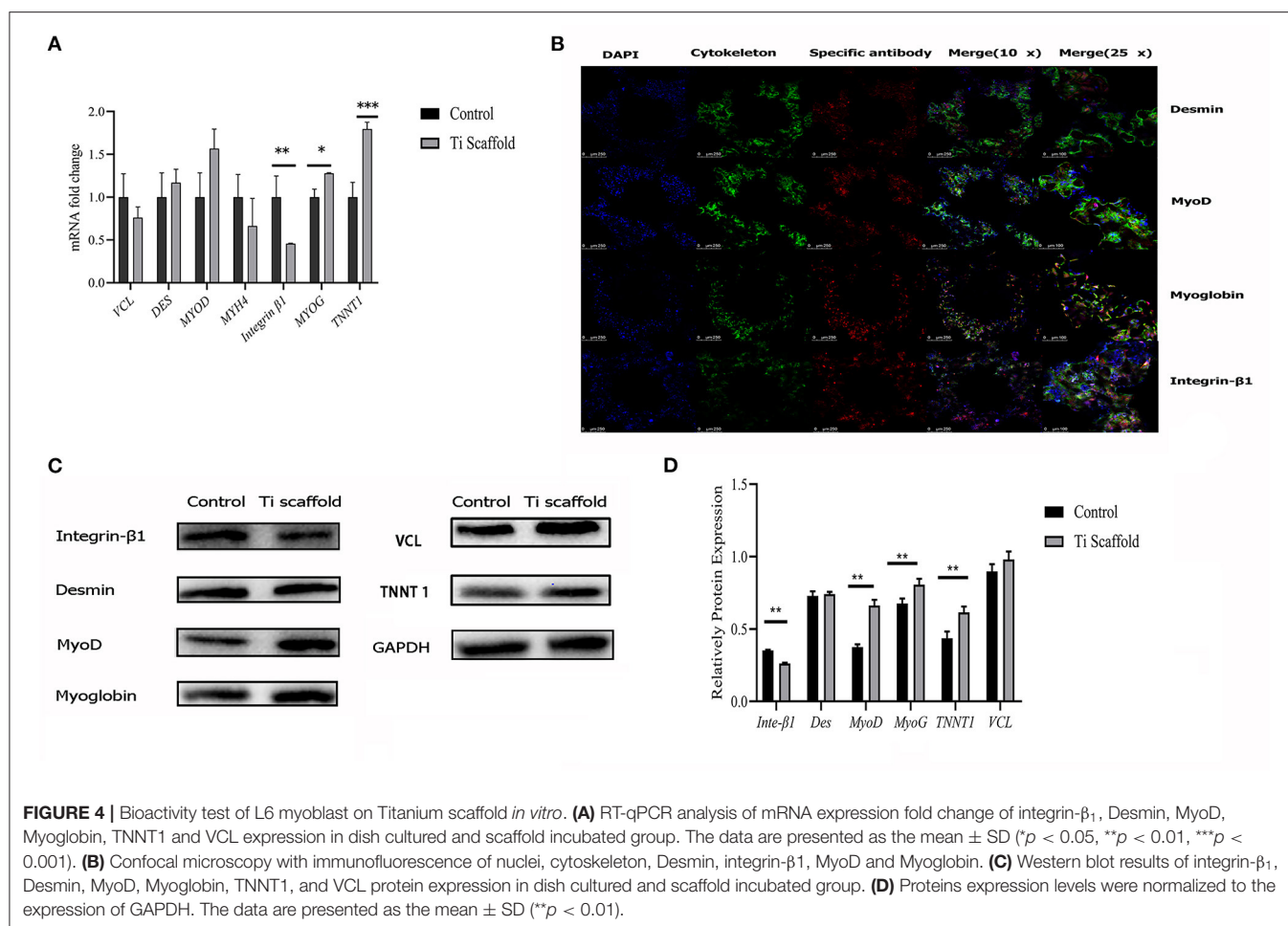
For the *in vivo* experiment, the rat intervertebral muscle porous titanium scaffold was implanted for 4 and 8 week-periods. After drawing materials, the gross overview showed that the muscles and materials of the two groups were both well-combined, the color was red-pink and soft to the touch, with no ectopic bone formation (Figures 5A,E). Additionally, the V-G staining of the slice showed that the muscle cells and collagen fibers grew into the porous titanium scaffold together, and some porous titanium scaffolds had blank areas at the edges of the scaffold and the tissue, which means that they were not fully integrated. The newly formed red stained tube-like structure is visible in the pores, which is more common in the week 8 samples and demonstrates a new capillary (Figures 5B–D,F–H). The

muscle tissue can grow into majority of the pores of in the cross-section view of the specimen of 8 week, but the distribution was not uniform (Figure 5I). The avulsion force for the 4 weeks group was 0.716 N/mm^2 and increased to 0.801 N/mm^2 at 8 weeks (Figure 5J). And in the histological analysis, the average rate of integration was 88.36% at 4 weeks, which further increased to 93.27% ($p < 0.05$) at 8 weeks, at which the proportion of collagen fibers increased from 27.37% to 35.98% ($p < 0.05$) and the proportion of muscle fibers decreased accordingly (Figure 5K).

The average passive MIO of the six goats under general anesthesia was $57.38 \pm 2.83 \text{ mm}$ pre-operatively, and the average passive MIO was $56.47 \pm 3.97 \text{ mm}$ at 8 weeks after the operation, with no significant difference ($p > 0.05$). A gross view of the six prosthesis specimens showed that muscle grew into the porous area of the prosthesis (Figure 2D). There was no ectopic bone formation either in or outside the muscle attachment. The average maximum avulsion pressure of the LPM from the condyle in the goat was $0.989 \pm 0.036 \text{ N/mm}^2$, and $0.436 \pm 0.038 \text{ N/mm}^2$ of the LPM from the novel designed prosthesis at 8 weeks ($p < 0.05$, Figures 6A–C). The hard tissue slice with HE staining and V-G staining showed that the biomimetic prosthesis formed increasingly good biological integration with the tissue. It is showed that until the 8th week, the tissue penetrated into the muscle function zone and almost formed complete integration with obvious vessel generated (Figures 6D–I). The prosthesis-tissue junction was mainly collagen fiber binding, and the neonatal vessel structure was visible. And according to the HE staining and histological analysis, the tissue ingrowth percentage increase from 73.28 ± 5.86 to 93.65 ± 3.78 ($p < 0.01$, Figure 6J), and the number of capillaries and vessels increased to 7.29 ± 1.48 per field as well at 8 weeks specimens ($p < 0.05$, Figure 6K). Also, it has to be admitted that there were still some small blank gaps between the edge of the prosthesis and the tissue.

DISCUSSION

TMJ is the only movable joint of the cranial and maxillofacial region, which dominates the mandibular movement and participates in important functions such as speech and chewing. Artificial TMJ replacement is an effective method for end-stage TMJ diseases. It has been widely used in European and North America. However, the main problem of artificial TMJ prosthesis is limited joint function, especially in laterotrusion and protrusion movement, which is caused by the loss of LPM attachment and functioning (Wojczyńska et al., 2016). Although there have been many modifications based on mechanical changes, few considered muscle reattachment, until one sutured muscle to a porous structure filled with bone marrow in a designed TMJ prosthesis (Mommaerts, 2019). In this study, we



proposed a novel design for LPM attachment to prostheses by using 3D printed porous scaffold and test the possibility of only muscle attachment and ingrowth by *in vitro* and *in vivo* experiments.

It is confirmed that titanium and titanium alloys have good biological compatibility with bone tissue and, as such, have been widely employed in surgical internal rigid fixation, implants, and prostheses (Li et al., 2013; Dai et al., 2016; Bosshardt et al., 2017; Ghanaati et al., 2019). The modification of titanium alloy can be benefit to the tissue integration as more elements has been added to the mixture, which can increase the bone growth and integration (Guo et al., 2013; Liu et al., 2015). The development of 3D printing technology has helped to realize advances in porous scaffold manufacture, which provides a favorable environment for the transportation of cells, blood vessels, tissue metabolites products and nutrients. It is reported that a pore size of about 400 μm is beneficial for the growth of bone tissue (Bobyn et al., 1999), and a large pore size is conducive to the penetration and regeneration of blood vessels (Thorson et al., 2019). Porous titanium also has good osteo-conductivity and can achieve biological fixation with bone. The studies above gave us a clue that the Ti porous structure

scaffold may also have the potential for soft tissue reconstruction, thus in this study, we tried to use porous Ti scaffold for muscle attachment.

Research on the adhesion between titanium alloys and soft tissues has gained more and more attention in recent years. In the previous studies, researchers found that the fibroblast can form a dense biological integration with the implants and can reach better results with surface modifications as roughed surface (Lee et al., 2015; Rieger et al., 2015). Furthermore, it was also discovered in the craniofacial surgery that after 1 year implantation, the surface of the titanium plate was generally covered with dense, fibrous connective tissue (Armencea et al., 2019). Janseen et al. found the porous titanium is suitable for the soft tissue ingrowth and combination (Janssen et al., 2009). He used a porous titanium mesh to reconstruct a tracheal support placed under the mucosa of rabbit trachea. After 6 weeks, HE staining revealed that the fibrous connective tissue grew into the titanium mesh and that the porous titanium mesh formed a tight integration with the tracheal cartilage. Additionally, Zhao et al. (2008) implanted the porous titanium mesh into the intervertebral muscle of rats. After 8 weeks, the maximum muscle avulsion force from the porous titanium mesh reached to 2.46 N,

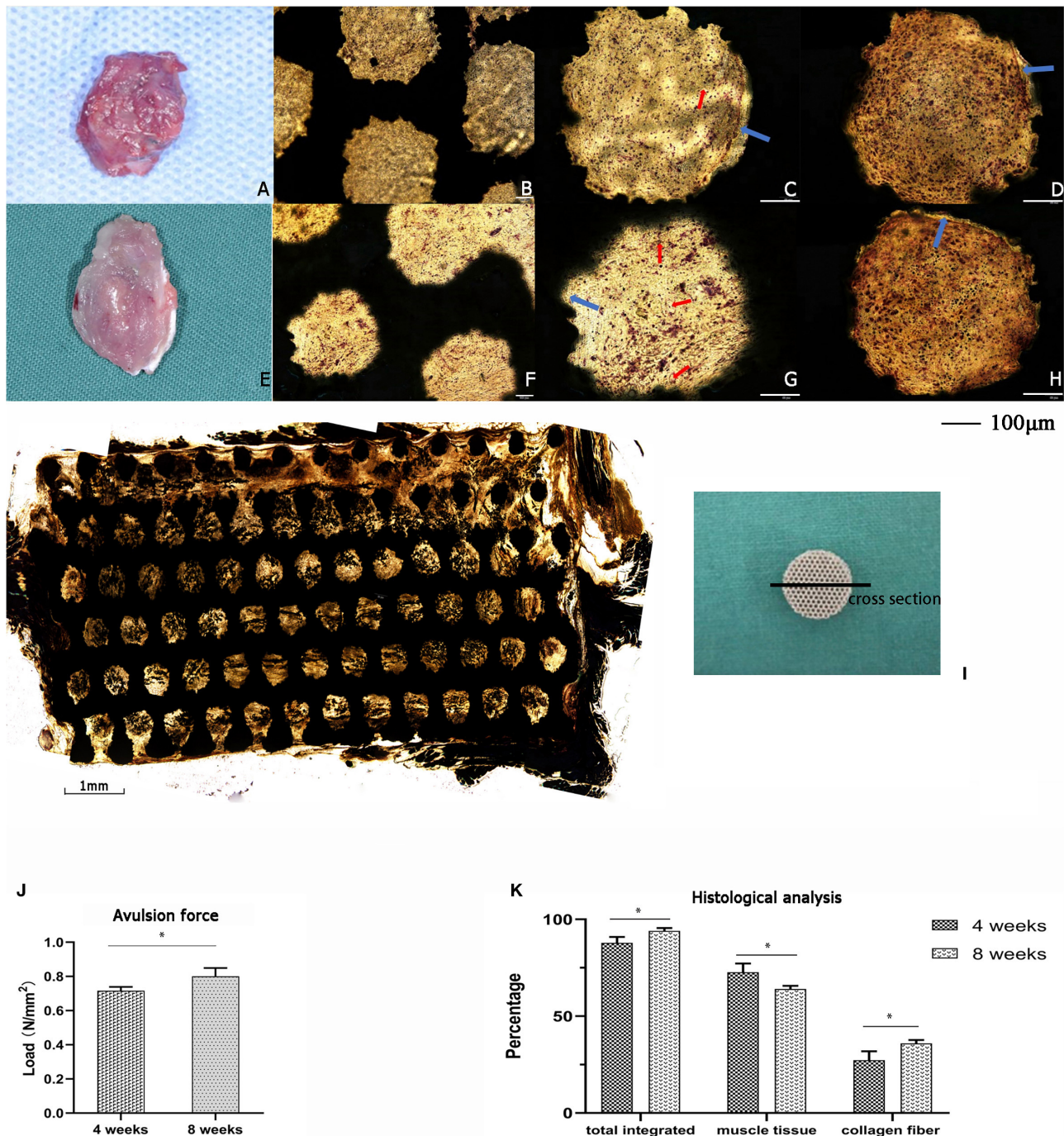


FIGURE 5 | The implantation of titanium scaffold into the intervertebral muscle of rats. **(A–D)** The specimen of 4 weeks, **(A)** Gross specimen, **(B)** hard slicing with V-G staining, 10 x, **(C,D)** hard slicing with V-G staining, 20 x; **(E–H)** The specimen of 8 weeks, **(E)** Gross specimen, **(F)** hard slicing with V-G staining, 10 x, **(G,H)** hard slicing with V-G staining, 20 x. Blue arrow: the blank gap between tissue and pore, red arrow: the newly formed capillary. **(I)** Histologic cross-section at 8 weeks showing the ingrowth of muscle tissue into the scaffold, 4 x. **(J)** The avulsion force of titanium scaffold implanted in rats for 4 and 8 weeks; with a significant increase in 8 weeks ($p < 0.05$). **(K)** The histological analysis of the tissue integrated percentage and distribution in rats. The data are presented as the mean \pm SD ($p < 0.05$).

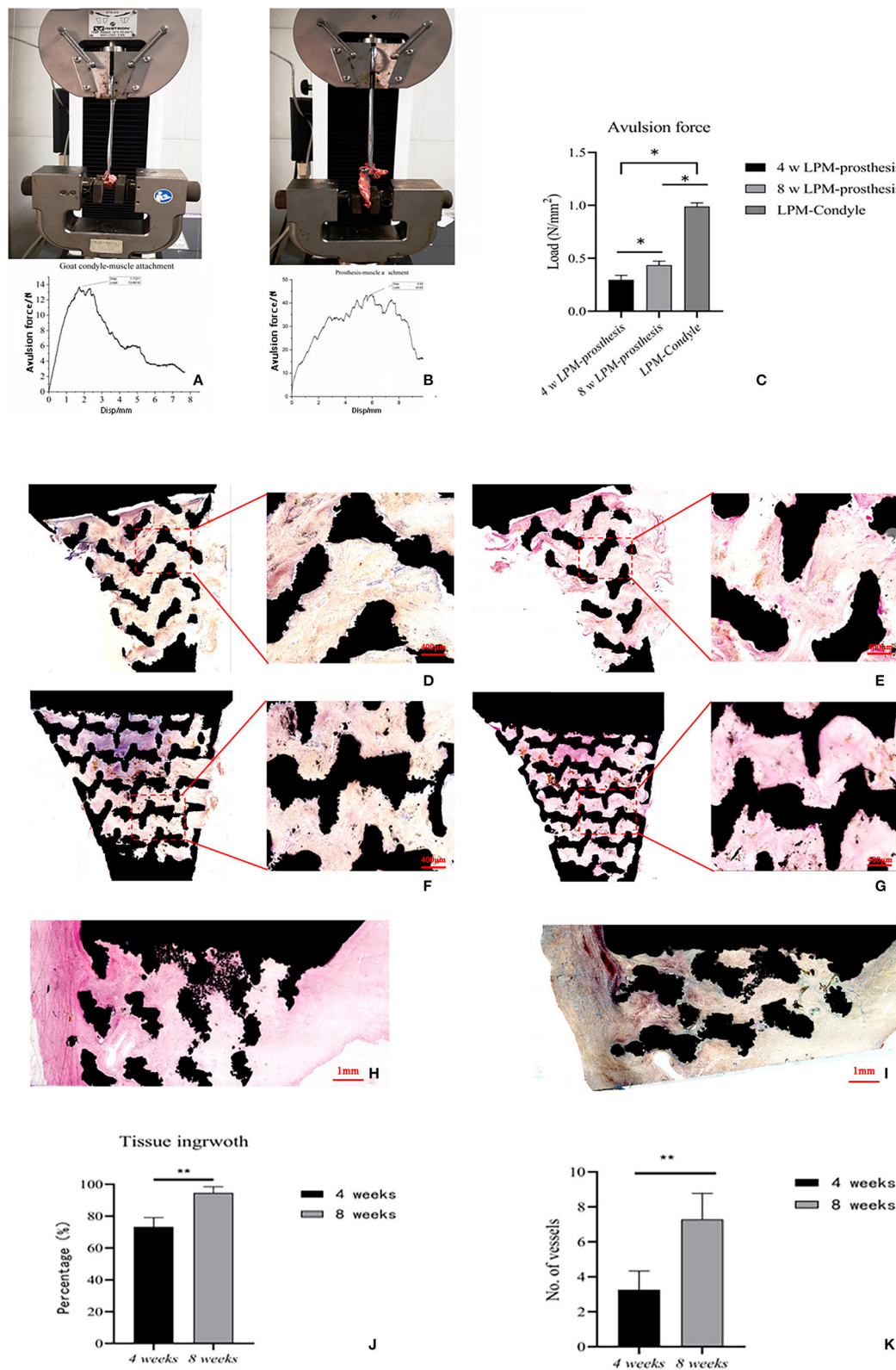


FIGURE 6 | data are presented as the mean \pm SD (* $p < 0.05$). **(D–I)** The hard slicing of prosthesis-LPM specimen. **(D)** The V-G staining of hard slice of muscle-reattachment functional prosthesis at 4 weeks, 4x–10x. **(E)** The HE staining of hard slice of muscle-reattachment functional prosthesis at 4 weeks, 4x–10x. **(F)** The V-G staining of hard slice of muscle-reattachment functional prosthesis at 8 weeks, 4x–10x. **(G)** The HE staining of hard slice of muscle-reattachment functional prosthesis at 8 weeks, higher percentage of space were occupied with new ingrowth tissue with vessels compared with 4 weeks specimen, 4x–10x. **(H)** The V-G staining of hard slice of muscle-reattachment functional prosthesis through cross-section at 8 weeks, 4x. **(I)** The HE staining of hard slice of muscle-reattachment functional prosthesis through cross-section at 8 weeks; and the muscle tissue with new generated vessel can be observed, 4x. **(J)** The histological analysis of the tissue ingrowth percentage in the *in-situ* replaced prosthesis based on HE staining. The data are presented as the mean \pm SD (** $p < 0.01$). **(K)** The number of capillaries and vessels in optical microscope scanning filed. The data are presented as the mean \pm SD (** $p < 0.01$).

and the pressure reached to 0.56 ± 0.23 N/mm², which is smaller than that (0.801 N/mm²) in our study.

In tendon reconstruction, Reach et al. (2007) showed that the tendon can heal directly with the porous titanium material and reached 90% of the mechanical strength of the control side 6 weeks after fixation with titanium nails and spacers in the achilles tendon reconstruction of beagles, and good kinematic function as walking and running was also acquired. As it was shown in our study, the bio-connection of porous structure and the soft tissue is mainly formed with collagen fibers, thus how to form a prosthesis-tendon-muscle reconstruction and its function may need further research to meet higher requirement.

In this study, we first proposed the hypothesis that muscle can attach to the prosthesis with porous scaffold, then tested the possibility by muscle cells with the porous scaffold *in vitro*. After positive result, we moved to rat muscle implantation and later on condyle reconstruction in goat. The results showed that both myoblast cells and muscle tissues had good biocompatibility with the porous titanium scaffolds. According to the PCR and western blot experiment, the L6 myoblast cells cultured on the scaffold showed better myogenic capability when compared with the common culture group, but less integrin- β_1 expression because of the culture dish surface treatment. This serves as an important reminder that future improvement of the scaffold design could consider enhancing the muscle adhesion through material modification, which plays a vital important role in the tissue integration and the metal material scaffold. More irons or structure modifications may be tested for cell adhesion improvement. The implantation of a porous titanium scaffold in rat muscle further confirmed that muscle can grow into the pores of the scaffold *in vivo*, and the integration percentage between muscle and the porous titanium scaffold increased along with the implantation time. Our novel prosthesis for goat condyle reconstruction likewise showed the feasibility of muscle attachment to a prosthesis. Muscles with new blood vessels could be observed in the porous titanium scaffold. In the pore, collagen fibers were integrated with the titanium at the edge, while muscle fibers were integrated in the middle of the pore. This being the case, more time and observation are needed to understand whether muscle fibers will change to collagen fibers like muscle tendons after biomechanical movement. Whereas, the tracking force of the muscle from the prosthesis 8 weeks after implantation reached to 0.436 N/mm², which is still insufficient compared with the one of condyle-LPM attachment (0.989 N/mm²). Thus, further research is needed to optimize the material structure and improve the force of muscle attachment to the porous scaffold. In the future study, it may be concerned that the promising

myogenic iron could be added into the metal materials to promote the cell adhesion and tissue integration as what has been done in the bone research.

In conclusion, our novel TMJ prosthetic provides the possibility of muscle ingrowth and attachment which may improve mandibular movement in the future.

DATA AVAILABILITY STATEMENT

The original contributions presented in the study are included in the article/supplementary material, further inquiries can be directed to the corresponding author/s.

ETHICS STATEMENT

The animal study was reviewed and approved by the Shanghai Ninth People's Hospital Human Research Ethics Committee.

AUTHOR CONTRIBUTIONS

LZ was involved in the processed experiments, acquisition of data, and drafting the manuscript. YZ helped with the molecular biology experiments. YX helped with the prosthesis design and collecting data of the avulsion force. DH contributed to the study protocol design and the surgery of the goats. XL helped with 3D printing technical details. CL helped with *in vivo* experiments. HZ helped draw the novel prosthesis picture. All authors read and approved the final manuscript.

FUNDING

This study was supported by grants from the National Natural Science Foundation of China (32071313), the Science and Technology Commission of Shanghai Municipality Science Research Project (17441900300, 20S31902500, and 20Y11903900), Clinical plus project of Shanghai 9th People's Hospital (JYLJ201805), Seed Founding of Shanghai Ninth People's Hospital, Shanghai Jiao Tong University School of Medicine (JYZZ041).

ACKNOWLEDGMENTS

Authors thank Mr. Ruining Gao and Hang Zhang (School of Mechanical Engineering, Shanghai Jiao Tong University, State Key Laboratory of Mechanical System and Vibration, China) for help with the avulsion force test.

REFERENCES

- Armencea, G., Gheban, D., Onisor, F., Mitre, I., Manea, A., Trombitas, V., et al. (2019). Histological change in soft tissue surrounding titanium plates after jaw surgery. *Materials* 12:3205. doi: 10.3390/ma12193205
- Bobyn, J. D., Stackpool, G. J., Hacking, S. A., Tanzer, M., and Krygier, J. J. (1999). Characteristics of bone ingrowth and interface mechanics of a new porous tantalum biomaterial. *J. Bone Joint Surg. Br.* 81, 907–914. doi: 10.1302/0301-620X.81B5.0810907
- Bosshardt, D. D., Chappuis, V., and Buser, D. (2017). Osseointegration of titanium, titanium alloy and zirconia dental implants: current knowledge and open questions. *Periodontol.* 2000 73, 22–40. doi: 10.1111/prd.12179
- Celebi, N., Rohner, E. C., Gateno, J., Noble, P. C., Ismaily, S. K., Teichgraber, J. F., et al. (2011). Development of a mandibular motion simulator for total joint replacement. *J. Oral. Maxil. Surg.* 69, 66–79. doi: 10.1016/j.joms.2010.05.085
- Dai, J., Shen, G., Yuan, H., Zhang, W., Shen, S., and Shi, J. (2016). Titanium mesh shaping and fixation for the treatment of comminuted mandibular fractures. *J. Oral. Maxillofac. Surg.* 74, 331–337. doi: 10.1016/j.joms.2015.10.003
- Ghanaati, S., Al-Maawi, S., Conrad, T., Lorenz, J., Rössler, R., and Sader, R. (2019). Biomaterial-based bone regeneration and soft tissue management of the individualized 3D-titanium mesh: an alternative concept to autologous transplantation and flap mobilization. *J. Cranio. Maxill. Surg.* 47, 1633–1644. doi: 10.1016/j.jcms.2019.07.020
- Guarda-Nardini, L., Manfredini, D., and Ferronato, G. (2008). Temporomandibular joint total replacement prosthesis: current knowledge and considerations for the future. *Int. J. Oral. Max. Surg.* 37, 103–110. doi: 10.1016/j.ijom.2007.09.175
- Guo, Y., Chen, D., Cheng, M., Lu, W., Wang, L., and Zhang, X. (2013). The bone tissue compatibility of a new Ti35Nb2Ta3Zr alloy with a low young's modulus. *Int. J. Mol. Med.* 31, 689–697. doi: 10.3892/ijmm.2013.1249
- Janssen, L. M., van Osch, G. J., Li, J. P., Kops, N., de Groot, K., Von den Hoff, J. W., et al. (2009). Tracheal reconstruction: mucosal survival on porous titanium. *Arch. Otolaryngol. Head Neck Surg.* 135, 472–478. doi: 10.1001/archoto.2009.29
- Lee, H. J., Lee, J., Lee, J. T., Hong, J. S., Lim, B. S., Park, H. J., et al. (2015). Microgrooves on titanium surface affect peri-implant cell adhesion and soft tissue sealing; an *in vitro* and *in vivo* study. *J. Periodontol. Implant. Sci.* 45, 120–126. doi: 10.5051/jpis.2015.45.3.120
- Li, X., Wang, L., Yu, X., Feng, Y., Wang, C., Yang, K., et al. (2013). Tantalum coating on porous Ti6Al4V scaffold using chemical vapor deposition and preliminary biological evaluation. *Mater. Sci. Eng. C Mater. Biol. Appl.* 33, 2987–2994. doi: 10.1016/j.msec.2013.03.027
- Liu, W., Cheng, M., Wahafu, T., Zhao, Y., Qin, H., Wang, J., et al. (2015). The *in vitro* and *in vivo* performance of a strontium-containing coating on the low-modulus Ti35Nb2Ta3Zr alloy formed by micro-arc oxidation. *J. Mater. Sci. Mater. Med.* 26:203. doi: 10.1007/s10856-015-5533-0
- Mercuri, L. G., Edibam, N. R., and Giobbie-Hurder, A. (2007). Fourteen-year follow-up of a patient-fitted total temporomandibular joint reconstruction system. *J. Oral. Maxil. Surg.* 65, 1140–1148. doi: 10.1016/j.joms.2006.10.006
- Mercuri, L. G., Wolford, L. M., Sanders, B., White, R. D., Hurder, A., and Henderson, W. (1995). Custom CAD/CAM total temporomandibular joint reconstruction system: preliminary multicenter report. *J. Oral. Maxillofac. Surg.* 53, 106–115, 115–116. doi: 10.1016/0278-2391(95)90381-X
- Mommaerts, M. Y. (2019). On the reinsertion of the lateral pterygoid tendon in total temporomandibular joint replacement surgery. *J. Craniomaxillofac. Surg.* 47, 1913–1917. doi: 10.1016/j.jcms.2019.11.018
- Ramos, A. M., and Mesnard, M. (2015). The stock alloplastic temporomandibular joint implant can influence the behavior of the opposite native joint: a numerical study. *J. Cranio. Maxill. Surg.* 43, 1384–1391. doi: 10.1016/j.jcms.2015.06.042
- Reach, J. J., Dickey, I. D., Zobitz, M. E., Adams, J. E., Scully, S. P., and Lewallen, D. G. (2007). Direct tendon attachment and healing to porous tantalum: an experimental animal study. *J. Bone Joint Surg. Am.* 89, 1000–1009. doi: 10.2106/JBJS.E.00886
- Rieger, E., Dupret-Bories, A., Salou, L., Metz-Boutigue, M. H., Layrolle, P., Debry, C., et al. (2015). Controlled implant/soft tissue interaction by nanoscale surface modifications of 3D porous titanium implants. *Nanoscale* 7, 9908–9918. doi: 10.1039/C5NR01237F
- Sonnenburg, I., and Sonnenburg, M. (1985). Total condylar prosthesis for alloplastic jaw articulation replacement. *J. Maxillofac. Surg.* 13, 131–135. doi: 10.1016/S0301-0503(85)80033-3
- Thorson, T. J., Gurlin, R. E., Botvinick, E. L., and Mohraz, A. (2019). Bijel-templated implantable biomaterials for enhancing tissue integration and vascularization. *Acta Biomater.* 94, 173–182. doi: 10.1016/j.actbio.2019.06.031
- Wang, X., Bai, G., Dong, M., Huo, L., Zheng, J., Chen, M., et al. (2018). Effect of modified costochondral graft in temporomandibular joint reconstruction with lateral pterygoid muscle preservation technique. *China J. Oral. Maxillofac. Surg.* 16, 420–424. doi: 10.19438/j.cjoms.2018.05.007
- Westermarck, A. (2010). Total reconstruction of the temporomandibular joint. Up to 8 years of follow-up of patients treated with biomet((R)) total joint prostheses. *Int. J. Oral. Maxillofac. Surg.* 39, 951–955. doi: 10.1016/j.ijom.2010.05.010
- Wojczyńska, A., Leiggener, C. S., Bredell, M., Ettlin, D. A., Erni, S., Gallo, L. M., et al. (2016). Alloplastic total temporomandibular joint replacements: do they perform like natural joints? Prospective cohort study with a historical control. *Int. J. Oral. Max. Surg.* 45, 1213–1221. doi: 10.1016/j.ijom.2016.04.022
- Zhao, D., Moritz, N., Vedel, E., Hupa, L., and Aro, H. T. (2008). Mechanical verification of soft-tissue attachment on bioactive glasses and titanium implants. *Acta Biomater.* 4, 1118–1122. doi: 10.1016/j.actbio.2008.02.012
- Zheng, J., Chen, X., Jiang, W., Zhang, S., Chen, M., and Yang, C. (2019). An innovative total temporomandibular joint prosthesis with customized design and 3D printing additive fabrication: a prospective clinical study. *J. Transl. Med.* 17:4. doi: 10.1186/s12967-018-1759-1
- Zou, L., Zhao, J., and He, D. (2019). Preliminary clinical study of Chinese standard alloplastic temporomandibular joint prosthesis. *J. Craniomaxillofac. Surg.* 47, 602–606. doi: 10.1016/j.jcms.2019.01.045

Conflict of Interest: The authors declare that the research was conducted in the absence of any commercial or financial relationships that could be construed as a potential conflict of interest.

Copyright © 2021 Zou, Zhong, Xiong, He, Li, Lu and Zhu. This is an open-access article distributed under the terms of the Creative Commons Attribution License (CC BY). The use, distribution or reproduction in other forums is permitted, provided the original author(s) and the copyright owner(s) are credited and that the original publication in this journal is cited, in accordance with accepted academic practice. No use, distribution or reproduction is permitted which does not comply with these terms.



Characteristics of Passive Films Formed on As-Cast Ti-6Al-4V in Hank's Solution Before and After Transpassivation

Guo Yi¹, Xinxin Liu², Chuanbo Zheng^{1,3*}, Hongyue Zhang¹, Cheng Xu¹, Yu-Wei Cui² and Shuan Liu³

¹School of Materials Science and Engineering, Jiangsu University of Science and Technology, Zhenjiang, China, ²School of Science, Jiangsu University of Science and Technology, Zhenjiang, China, ³Key Laboratory of Marine Materials and Related Technologies, Zhejiang Key Laboratory of Marine Materials and Protective Technologies, Ningbo Institute of Materials Technologies and Engineering, Chinese Academy of Sciences, Ningbo, China

OPEN ACCESS

Edited by:

Liqiang Wang,
Shanghai Jiao Tong University, China

Reviewed by:

Jun Cheng,
Northwest Institute For Non-Ferrous
Metal Research, China
Linjiang Chai,
Chongqing University of Technology,
China

*Correspondence:

Chuanbo Zheng
15952802516@139.com

Specialty section:

This article was submitted to
Biomaterials,
a section of the journal
Frontiers in Materials.

Received: 10 December 2020

Accepted: 23 December 2020

Published: 05 February 2021

Citation:

Yi G, Liu X, Zheng C, Zhang H, Xu C,
Cui Y-W and Liu S (2021)
Characteristics of Passive Films
Formed on As-Cast Ti-6Al-4V in
Hank's Solution Before and
After Transpassivation.
Front. Mater. 7:640081.
doi: 10.3389/fmats.2020.640081

In this work, the characteristics of passive films formed on as-cast Ti-6Al-4V before and after transpassivation by electrochemical methods will be studied. A simulated body fluid of Hank's solution was used as the electrolyte in this work. According to the potentiodynamic polarization test, the passivation range, transpassive range, and repassivation range of as-cast Ti-6Al-4V were obtained. Afterward, the potentiostatic polarization was employed to passivate the Ti-6Al-4V in both passivation and repassivation ranges. Electrochemical impedance spectroscopy (EIS) was used to analyze the characteristics of formed passive films. Different electrochemical behavior of as-cast Ti-6Al-4V is found in passivation and repassivation ranges. The passivation current density of the sample in the repassivation range is significantly larger than that in the passivation range. Meanwhile, the growth rate of passive film in the repassivation range is also greater than that in the passivation range. Although the sample shows a higher charge transfer impedance in the repassivation range, metastable pitting corrosion is also observed, indicating the formation of the unstable passive film. Such results advance the understanding of as-cast Ti-6Al-4V polarized under different potentials for potential biomedical applications.

Keywords: Ti-6Al-4V, corrosion, passive film, transpassivation, electrochemical measurement, Mott-Schottky

INTRODUCTION

Titanium (Ti) and its alloys are widely used in a wide variety of industrial applications, such as biomedical, marine, and chemical industries, due to their fascinating properties, including high specific strength, excellent corrosion resistance, and good biocompatibility (Lu et al., 2009; Rabadia et al., 2019a; Zhang and Chen, 2019; Chen et al., 2020a; Liu et al., 2020). Primarily, Ti alloys can be classified as α -type Ti alloys (Zhang and Attar, 2016; Chen et al., 2017b; Zheng et al., 2019; Chen et al., 2020b), ($\alpha+\beta$)-type Ti alloys (Kang and Yang, 2019; Montiel et al., 2020; Semenova et al., 2020), β -type Ti alloys (Zhang et al., 2011; Wang et al., 2016; Wang et al., 2018a; Rabadia et al., 2019b; S. Liu et al., 2020), and Ti-based composites (Zhang and Xu, 2004; Zhang et al., 2006; Lu et al., 2009; Yang et al., 2020a; Yang et al., 2020b). Among the commercial Ti materials, Ti-6Al-4V alloy has received considerable attention owing to good fatigue resistance, strength, and corrosion resistance (Bai et al., 2017; Dai et al., 2017; Zhao et al., 2018). However, Ti-6Al-4V still has some intrinsic disadvantages.

For example, Ti-6Al-4V exhibits a relatively low hardness of 290–375 HV (Zhang et al., 2020b). The low wear resistance of Ti-6Al-4V may easily cause the seizure in service (Stolyarov et al., 2004). Furthermore, although Ti-6Al-4V exhibits good corrosion resistance in the corrosive environment, a complex corrosive environment always degrades the corrosion resistance of Ti-6Al-4V due to the presence of halogen ions, hydrogen ions, hydroxyl ions, and also other functional groups (Hanawa, 2004; Chen and Thouas, 2015; Yu et al., 2015; Qin et al., 2019). Such species degrade the passive film formed on Ti-6Al-4V and thereby the corrosion resistance. Therefore, surface modifications are frequently employed to produce the barrier layer on Ti-6Al-4V before it is applied.

So far, there are a variety of surface modification methods for improving the surface properties of metallic materials, such as laser processing (Balla et al., 2010; Chai et al., 2017; Chai et al., 2018; Xiang et al., 2020), microarc oxidation (Wang et al., 2018b; Dehghanghadikolaei et al., 2019; Yang et al., 2020b), thermal spraying (Jaeggi et al., 2011; Chen et al., 2019a; Chen et al., 2019b), friction stir processing (Wang et al., 2015; Wang et al., 2017; Zhang et al., 2019c), ion implantation (Rautray et al., 2011; Qin et al., 2017), and so on. Among these methods, anodic oxidation is a costly method that applies an anodic potential on the metallic sample in the solution. Afterward, a compact and protective oxide film can be produced after the anodic oxidation process (Liu et al., 2004). Such a protective oxide film enhances the surface properties of Ti and Ti alloys. Therefore, anodic oxidation is a good method to synthesize different types of oxide films on metallic materials. The primary advantage of anodic oxidation is the good adhesion and bonding between the oxide film and Ti substrate. Hence, the anodic oxidized Ti and Ti alloys can be well-employed in the aerospace and biomedical industry (Aladjem, 1973; Babilas et al., 2016; Yang et al., 2020c).

The thickness of the produced oxide film on Ti and Ti alloys is determined by the applied anodic potential (Liu et al., 2004). Generally, the thickness of oxide film is almost linearly dependent on the applied potential, obeying the relationship of $d = \alpha U$, where d is the thickness of produced oxide film and U is the applied potential. α is a constant, which is within a range of 1.5–3 nm V⁻¹, depending on the chemical compositions of Ti electrodes and solution (Liu et al., 2004). However, such an empirical formula may be not accurate since the transpassive behavior and the repassivation are always found in the potentiodynamic polarization curve of Ti and Ti alloys above the applied potential of about 1–1.5 V (Narayanan and Seshadri, 2008; Qin et al., 2019; Seo and Lee, 2019). The transpassive behavior of Ti and Ti alloys results from the oxygen evolution reaction (Kong and Wu, 2007). Water is decomposed into H₂ and O₂ during this reaction, leading to the imperfection of the passive films formed on Ti and Ti alloys. Therefore, is this equation appropriate for Ti and Ti alloys in all passivation range? Or is the passivation film produced at the higher potential certainly better than that produced at lower potential? Such questions are still unclear. However, the information regarding the passive films produced before and after transpassive behavior is significantly important to the further understanding of the passivation behavior of Ti and Ti alloys and their wider applications.

Therefore, in this work, as-cast Ti-6Al-4V is selected as the experimental alloy. According to the potentiodynamic polarization curve, the first passivation range and the repassivation range can be obtained. Subsequently, the oxide films are produced at the different passivation range and are investigated based on their semiconductive properties and impedances. Hence, electrochemical measurements are primarily used and the formation mechanism of oxide film on Ti-6Al-4V.

EXPERIMENTAL

Material Preparation and Microstructural Characterization

As-cast Ti-6Al-4V alloy was prepared via vacuum arc remelting three times to ensure uniformity. The compositions of the experimental alloy were 5.94 wt% Al, 4.28 wt% V, and the balance of Ti. The sample was ground and polished to a mirror surface finish. Afterward, the polished sample was etched in a mixed solution of HF, HNO₃, and H₂O for about 15 s (1:2:7 in vol%). The microstructure of the etched sample was examined by an optical microscope (OM, OLYMPUS PMG3). The phase constituent of the polished sample was analyzed by an X-ray diffraction (XRD) diffractometer (Empyrean, PANalytical) with Co-K_α radiation. During the XRD test, the following parameters were used: the scanning range was between 30° and 100°, and the scanning rate was 0.03°/s. Jade 6.5 software was used to analyze the obtained XRD data.

Electrochemical Measurements

The specimens with a size of 10 × 10 × 10 mm³ were employed for electrochemical measurements. The exposure area of the specimen was about 100 mm². Hank's solution is used as the electrolyte and composed of 0.35 g/L NaHCO₃, 0.140 gL⁻¹ CaCl₂, 0.098 gL⁻¹ MgSO₄, 0.4 gL⁻¹ KCl, 0.06 gL⁻¹ KH₂PO₄, 8 gL⁻¹ NaCl, 0.048 gL⁻¹ Na₂HPO₄, 1 gL⁻¹ C₆H₁₂O₆, and 0.011 gL⁻¹ C₁₉H₁₄O₅Na. The pH of Hank's solution is adjusted to 7.35 by diluted HCl and NaOH. A three-electrode-system electrochemical workstation (CHI660E, Chenhua) was employed for characterizing the corrosion behavior of as-cast Ti-6Al-4V. Ti-6Al-4V was employed as the working electrode, a platinum sheet was used as the counter electrode, and a saturated calomel electrode (SCE) was used as the reference electrode. The open-circuit potential (OCP) test for 1800 s was conducted before the electrochemical impedance spectroscopy (EIS) test and potentiodynamic polarization test. Subsequently, a potentiodynamic polarization test was conducted in a sweeping range of -0.25–+2 V (vs. OCP) at a sweeping step of 0.2 mV/s. According to the potentiodynamic polarization test, the passivation range, transpassive range, and repassivation range were obtained. Therefore, the potentiostatic polarization was employed to passivate the Ti-6Al-4V samples at the potentials of 0.1 V_{SCE}, 0.3 V_{SCE}, 0.5 V_{SCE}, 0.7 V_{SCE}, 0.9 V_{SCE}, 2.1 V_{SCE}, 2.3 V_{SCE}, 2.5 V_{SCE}, 2.7 V_{SCE}, and 2.9 V_{SCE}. Then, EIS was conducted to acquire effective capacitance at 1 kHz (Guan et al., 2018). Subsequently, Mott-Schottky tests were done at the frequency of 1 kHz, sweeping the potential from film formation potential to –

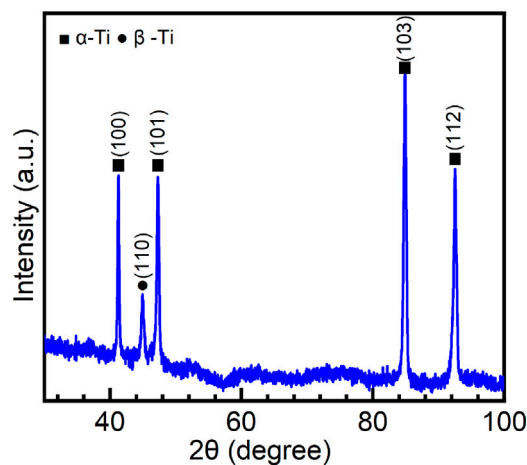


FIGURE 1 | X-ray diffraction pattern of as-cast Ti-6Al-4V used in this work.

1.0 V (vs. OCP) with a step of 10 mV/s. All potentials reported were against SCE in this work. Each test was repeated three times to ensure the data reproducibility. The software ZsimpWin 3.30 was used to analyze the EIS data and the software Cview 2.6 was used to analyze the potentiodynamic polarization data.

RESULTS AND DISCUSSION

Microstructural Features

Figure 1 shows the XRD pattern of the Ti-6Al-4V sample. Since Ti-6Al-4V is a dual-phase Ti alloy ((α + β)-type Ti alloy), the peaks of both α -Ti and β -Ti are observed. V is a β -stabilizer for Ti alloys (Chen et al., 2020a). Due to the small content of V in the sample, only a weak peak of β -Ti is observed in the XRD pattern. According to the integrated area method (Zhang et al., 2003; Chen et al., 2018a; Sang et al., 2019), the volume fraction of α -Ti is calculated to be 95% and β -Ti is 5%. Generally, (α + β)-type Ti alloys contain a certain fraction of β phase (about 5–30 vol%) (Lei et al., 2017). Therefore, (α + β)-type Ti alloys are heat treatable due to the second phase in the

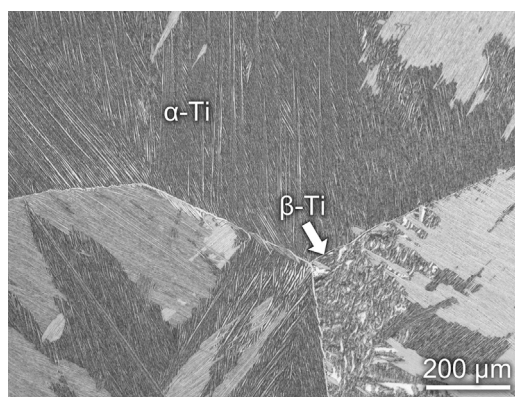


FIGURE 2 | Optical image of the microstructure of as-cast Ti-6Al-4V.

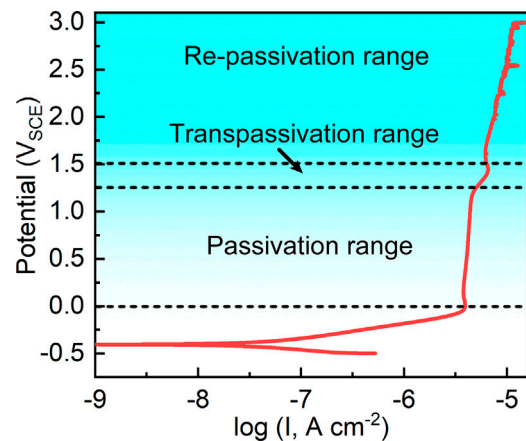


FIGURE 3 | Potentiodynamic polarization curve of as-cast Ti-6Al-4V in Hank's solution at 37°C.

metal matrix (Chen et al., 2015b; Zhang et al., 2017; Sabban et al., 2019). **Figure 2** is the optical image of the microstructure of Ti-6Al-4V. It can be observed that the primary β grains have a size over several hundred microns. β -Ti is distributed on the boundaries of primary β grains. In the inner part of primary β grains, a considerable number of α -Ti laths are found. Such a Widmanstätten microstructure is produced due to the transformation of $\beta \rightarrow \alpha$ at a relatively low speed. Similar microstructures can be frequently found in the hexagonal close-packed metallic materials, such as Zr alloys and other Ti alloys (Chen et al., 2018b; Chen et al., 2018c; Yang et al., 2019; Yang et al., 2020a).

Potentiodynamic Polarization Test

Figure 3 shows the potentiodynamic polarization curve of the sample in Hank's solution at 37°C. Typically, the sample is passivated after the anodic activation zone as an indication of nearly constant passivation current density. Such a typical electrochemical behavior is frequently observed in valve metals (Qin et al., 2019). After fitting the potentiodynamic polarization curve, it shows that the corrosion potential of as-cast Ti-6Al-4V in Hank's solution at 37°C is -0.405 ± 0.027 V_{SCE}. The corrosion potential indicates the energy needed for corrosion reaction of a specific alloy in a specific corrosive environment (Chen et al., 2017a). The corrosion current density of as-cast Ti-6Al-4V is 0.031 ± 0.008 $\mu\text{A cm}^{-2}$. The corrosion current density illustrates the spontaneous corrosion rate of a specific alloy at the corrosion potential (Chen et al., 2017a). The data of both corrosion potential and corrosion current density fall in the outcomes in the literature, indicating the reliability of the potentiodynamic polarization test in this work. As seen from **Figure 3**, when the applied anodic potential exceeds a certain value, the passivation current density keeps almost constant as the applied anodic potential increases (Qin et al., 2017; Zhang et al., 2019a; Zhang et al., 2019b). The passivation current density is nearly constant from the potential of 0 V_{SCE} to 1.2 V_{SCE}. For Ti and Ti alloys, transpassive behavior is often observed (Narayanan and Seshadri, 2008; Qin et al., 2019; Seo and Lee, 2019). In this work, the transpassivation range is observed from 1.2 V_{SCE} to 1.5 V_{SCE}. The

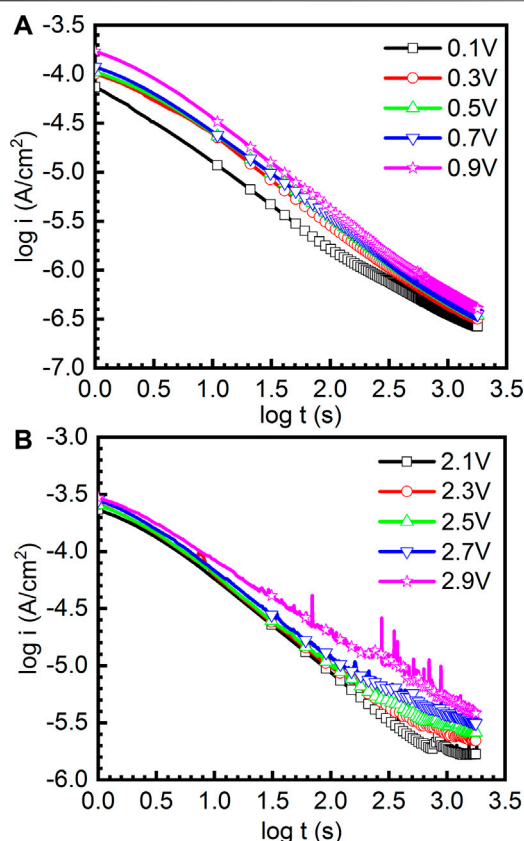


FIGURE 4 | Double-log plots of current-time of as-cast Ti-6Al-4V in the potentiostatic polarization tests under different film formation potentials in Hank's solution at 37°C, (A) the curves obtained under 0.1–0.9 V and (B) the curves obtained under 2.1–2.9 V.

current density rapidly increases with increasing the applied potential. When the applied potential reaches $1.5 V_{\text{SCE}}$, the repassivation behavior of Ti-6Al-4V takes place. The passivation current density of Ti-6Al-4V slowly increases with increasing the applied potential in the repassivation range. Meanwhile, another feature can be observed. In the passivation range, the potentiodynamic polarization curve is significantly smooth. However, in the repassivation range, the potentiodynamic polarization curve is not smooth but has several stabs. Such stabs are indicative of metastable pitting corrosion (Frankel, 1998). Such a finding indicates the passivation of Ti-6Al-4V is imperfect in the repassivation range. According to the results of potentiodynamic polarization tests, the film formation potentials for potentiostatic polarization tests are selected at 0.1–0.9 V_{SCE} and 2.1–2.9 V_{SCE} in the following.

Potentiostatic Polarization Tests

It has been widely reported that the current density of the sample decreases quickly within the first 30 s and then slowly decreases to a nearly stable value due to the formation of the passive film (Gai et al., 2018). Therefore, the growth kinetics of passive film follows the Macdonald model (Lakatos-Varsányi et al., 1998), which can be expressed as the following equation:

$$\log i = \log A - n \log t, \quad (1)$$

where i is the current density, t is the passive time, and A and n are constants. The value of n can be used to indicate the growth rate of the passive film. Figure 4 reveals the double-log plots of current-time of as-cast Ti-6Al-4V in the potentiostatic polarization tests in the passivation range and repassivation range in Hank's solution at 37°C, respectively. It can be found that the double-log plots of current-time are basically linear and the current density of the sample at high potential is always greater than that at low potential. Basically, n in Eq. (1) tending to be -1 illustrates that the growth process is primarily determined by the electrical field to generate a compact and protective passive film (Galvele et al., 1990). In Figure 4A, the values of n are -0.857 , -0.912 , -0.877 , -0.859 , and -0.935 for the double-log plots of current-time obtained at 0.1 V_{SCE} , 0.3 V_{SCE} , 0.5 V_{SCE} , 0.7 V_{SCE} , and 0.9 V_{SCE} . In Figure 4B, the values of n are -0.816 , -0.834 , -0.835 , -0.788 , and -0.713 for the double-log plots of current-time obtained at 2.1 V_{SCE} , 2.3 V_{SCE} , 2.5 V_{SCE} , 2.7 V_{SCE} , and 2.9 V_{SCE} . Based on these results, the passive films formed at the passivation range have higher quality than those formed at the repassivation range. Meanwhile, similar to the results presented in Figure 3, the curves obtained at the passivation range (0.1–0.9 V_{SCE}) are smooth. By contrast, the curves obtained at the repassivation range are not smooth. Some features of metastable pitting corrosion are found. In particular, at the applied potential of 2.9 V_{SCE} , the metastable pitting corrosion is significantly obvious. The pitting corrosion results from the rupture of passive films form on the Ti and Ti alloys. If the rupture of passive films is healed by the passivation ability of alloys, the pitting corrosion is defined as the metastable pitting corrosion. If the rupture of passive films is not healed, the pitting corrosion is stable pitting corrosion. Generally, such stabs in the curves of current density (including Figures 3, 4) indicate the rupture and healing of passive film (Dai et al., 2016a; Dai et al., 2016b; Qin et al., 2018). The higher applied anodic potential provides a higher capability to adsorb the anions, including halide ions (Basame and White, 2000). The halide ions are well known as one of the factors to trigger the metastable pitting corrosion, even stable pitting corrosion for the passive metals. Therefore, lots of metastable pitting corrosion phenomena are

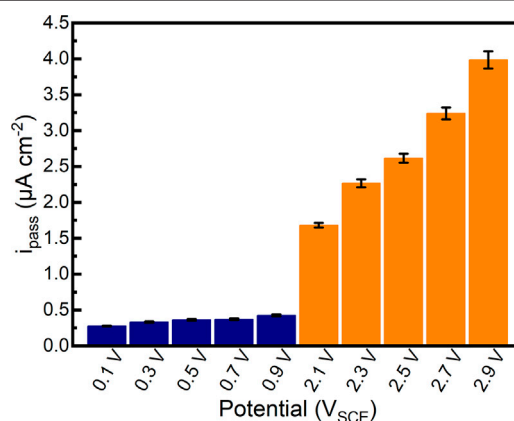


FIGURE 5 | Quasi-steady passivation current densities of as-cast Ti-6Al-4V in potentiostatic polarization tests under different applied potentials in Hank's solution at 37°C.

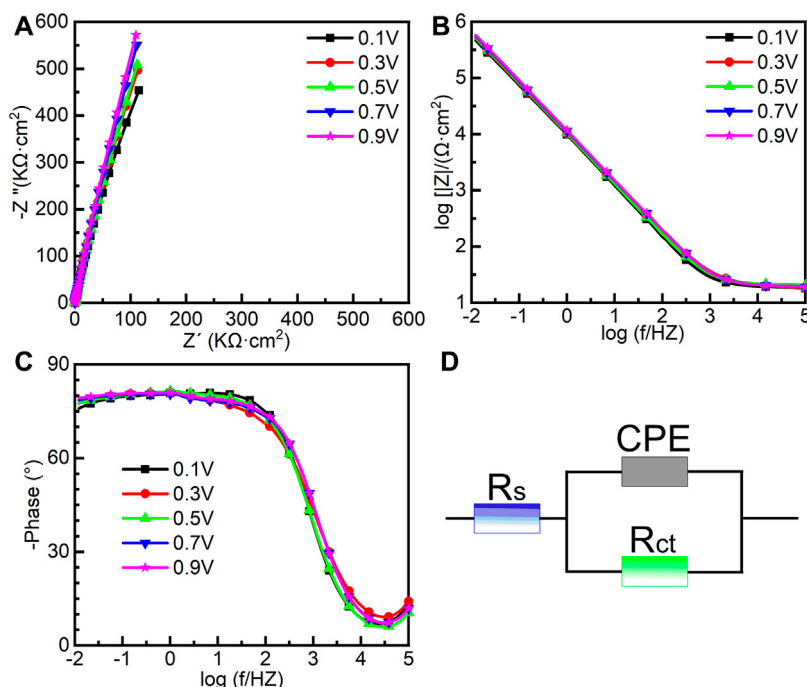


FIGURE 6 | Electrochemical impedance spectroscopy of as-cast Ti-6Al-4V under different film formation potentials in passivation range in Hank's solution at 37°C, (A) Nyquist plots, (B) Bode impedance plots, (C) Bode phase diagram and (D) equivalent circuit.

observed under high potential. Such a phenomenon is always associated with the sudden increase and subsequent decrease in the current density. This finding reflects the low quality of passive film formed on the sample at the applied potential of $2.9 V_{SCE}$.

After 1800 s potentiostatic polarization tests in Hank's solution at 37°C, the passivation current densities of the samples almost reach stability. The quasi-steady passivation current densities of samples are shown in **Figure 5**. It can be found that the quasi-steady passivation current densities of samples gradually increase from $0.276 \mu A cm^{-2}$ to $0.425 \mu A cm^{-2}$ in the passivation range. In comparison, the quasi-steady passivation current densities of samples significantly increase to $1.682 \mu A cm^{-2}$ – $3.985 \mu A cm^{-2}$ in the repassivation range, which is increased by an order of magnitude. The quasi-steady passivation current densities could elucidate the migration of ions at a specific potential (Chen et al., 2017b; Guan et al., 2018). Although the alloy can be regarded as the stable passivation state in the current situation, the quasi-steady passivation current density illustrates the balance of the formation and dissolution of the passive film. According to Faraday's law, higher quasi-steady passivation current density is related to the smaller impedance of passive film (Vautrin-Ul et al., 2007). Therefore, such a finding may specify that the quality of passive films formed on as-cast Ti-6Al-4V in the repassivation range is not as good as that formed on as-cast Ti-6Al-4V in the passivation range.

Electrochemical Impedance Spectroscopy

To further investigate the electrochemical system at the metal/solution interfaces, EIS was conducted on the samples polarized under different potentials in Hank's solution at 37°C. **Figure 6** shows the EIS results of the samples on which the potentiostatic polarization tests were conducted at 0.1–0.9 V_{SCE} , including the

Nyquist diagram, Bode plot, and equivalent circuit diagram. **Figure 6A** is the Nyquist plots. All Nyquist plots have only one capacitor arc, which has a very large radius. The radius of the capacitor arc increases with increasing the film formation potential. From the Bode plots (**Figures 6B, C**), it is hard to distinguish the difference among the five samples. By fitting the EIS data using the equivalent circuit diagram in **Figure 6D**, the impedance information of passive films formed on the samples at different potentials can be obtained. In this equivalent circuit diagram (**Figure 6D**), R_s and R_{ct} correspond to the solution resistance and charge transfer resistance, respectively. Because of the influence of the surface roughness, the constant phase element (CPE) is used (Chen et al., 2018d; Liang et al., 2018; Yang et al., 2018). n is the parameter of CPE. For $n = 1$, CPE is regarded as an ideal capacitor, whereas CPE is nonideal when $0.5 < n < 1$ (Zhang et al., 2020a). The fitted results of EIS are listed in **Table 1**. χ^2 is the sum of the square of the difference between theoretical and experimental points, which is lower than 0.007, indicating a good quality of the fitting in this experiment. These results show that the values of R_s for all tests are almost the same. However, there is a significant distinction in the values of R_{ct} . For the sample on which the potentiostatic polarization test was conducted at 0.1 V_{SCE} , the value of R_{ct} is $1.86 \pm 0.10 M\Omega cm^2$. The values of R_{ct} increase with the increasing film formation potential. When the film formation potential is 0.9 V_{SCE} , the value of R_{ct} reaches $4.35 \pm 1.21 M\Omega cm^2$. R_{ct} indicates the impedance of electrons from the metal to the solution. Therefore, the higher value of R_{ct} illustrates the higher protectiveness of passive film. Such a result is consistent with the outcome in the other works (Shibata and Zhu, 1994).

TABLE 1 | Fitting results of electrochemical impedance spectra for as-cast Ti-6Al-4V after OCP tests in Hank's solutions at 37°C. R_s means solution resistance, R_{ct} indicates charge transfer resistance, CPE describes charge transfer capacitance, n is the exponent of CPE, and χ^2 is the sum of the square of the difference between theoretical and experimental points.

Potential (V_{SCE})	R_s ($\Omega \cdot \text{cm}^2$)	n	R_{ct} ($M\Omega \cdot \text{cm}^2$)	CPE $\times 10^{-5}$ ($F \cdot \text{cm}^{-2}$)	χ^2
0.1	18.01 ± 0.89	0.8654 ± 0.072	1.86 ± 0.10	2.24 ± 0.12	3.03×10^{-3}
0.3	17.64 ± 0.72	0.8601 ± 0.090	2.76 ± 0.30	1.87 ± 0.57	1.14×10^{-3}
0.5	16.70 ± 0.86	0.9049 ± 0.008	3.34 ± 0.03	1.92 ± 0.02	6.37×10^{-3}
0.7	19.18 ± 0.80	0.9081 ± 0.003	3.26 ± 1.10	2.12 ± 0.43	1.53×10^{-3}
0.9	18.94 ± 1.20	0.8997 ± 0.005	4.35 ± 1.21	2.01 ± 0.05	2.75×10^{-3}

EIS was also conducted in the repassivation range in order to understand the electrochemical system at the metal/solution interfaces after transpassivation. **Figure 7** shows the Nyquist diagram, Bode plot, and the equivalent circuit diagram used for the samples on which the potentiostatic polarization tests were conducted at 2.1–2.9 V_{SCE} . The impedance of passive film formed in the range of 2.1–2.9 V_{SCE} (**Figure 7A**) is significantly larger than that in the range of 0.1–0.9 V_{SCE} (**Figure 6A**). Such a result is in line with the outcomes in the literature that the thickness of the passive film formed on Ti and Ti alloys increases with increasing the applied anodic potential (Al-Mayouf et al., 2004; Guan et al., 2018). The Bode phase angle plot in **Figure 7C** is also different from that in **Figure 6C**. In **Figure 6C**, the curve from 10^2 Hz to 10^{-2} Hz is a wide plateau. In comparison, the curve from 10^2 Hz to 10^{-2} Hz has dual dumps in **Figure 7C**. Such a finding illustrates that the passive film formed on the samples in the repassivation range may have a bilayer structure, namely, the inner barrier layer and outer porous layer

(Aziz-Kerrzo et al., 2001). **Table 2** lists the fitting results of EIS in **Figure 7**. Different equivalent circuits are used for fitting EIS of different-structured passive films. Therefore, for this EIS, a $R(Q(R(QR)))$ equivalent circuit diagram is used to highlight the outer porous layer on the polarized sample. R_s , R_{ct} , and CPE have the same meaning as **Figure 6**. R_f is the film resistance, which illustrates the diffusion resistance in the defects of the outer porous layer (Zhang et al., 2020a). χ^2 is lower than 0.0007, which also indicates a good quality of the fitting. Apparently, R_f is significantly lower than R_{ct} . Therefore, the corrosion resistance (as well as the impedance of passive film) of the polarized sample strongly depends on the value of R_{ct} . The value of R_{ct} for the sample polarized at 2.1 V_{SCE} is $7.691 \pm 1.203 M\Omega \cdot \text{cm}^2$, which is nearly two times that for the sample polarized at 0.9 V_{SCE} . Such a finding demonstrates that the impedance of passive film formed on the as-cast Ti-6Al-4V increases with increasing the applied potential regardless of the occurrence of transpassive behavior. With the continuous

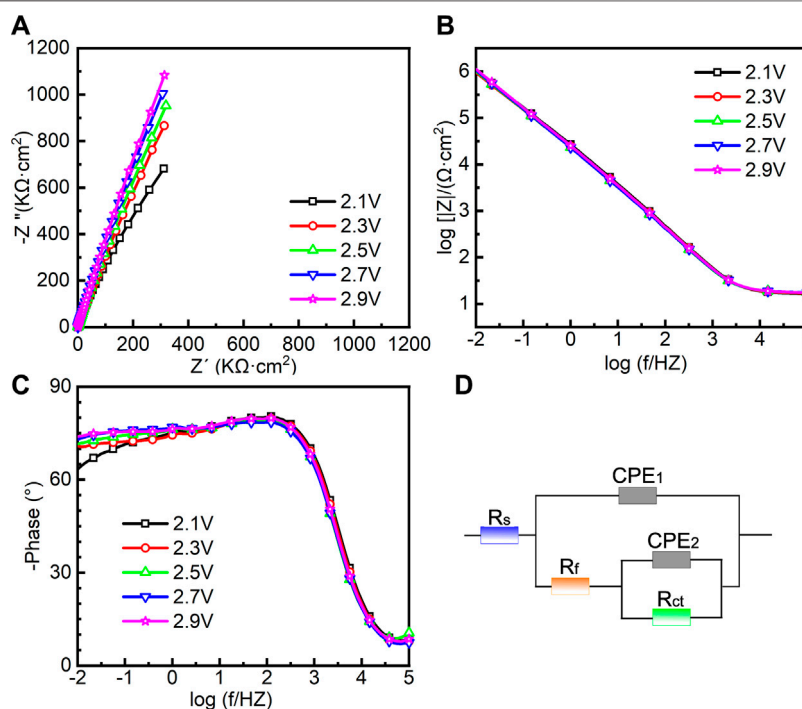


FIGURE 7 | Electrochemical impedance spectroscopy of as-cast Ti-6Al-4V under different film formation potentials in the repassivation range in Hank's solution at 37°C, (A) Nyquist plots, (B) Bode impedance plots, (C) Bode phase diagram and (D) equivalent circuit.

TABLE 2 | Fitting results of electrochemical impedance spectra for as-cast Ti-6Al-4V after OCP tests in Hank's solutions at 37°C. R_s means solution resistance, R_f is film resistance, R_{ct} indicates charge transfer resistance, CPE_1 and CPE_2 describe film capacitance and charge transfer capacitance, n_1 and n_2 are the exponents of CPE_1 and CPE_2 , and χ^2 is the sum of the square of the difference between theoretical and experimental points.

Potential (V _{SCE})	R_s ($\Omega \cdot \text{cm}^2$)	R_f ($\text{k}\Omega \cdot \text{cm}^2$)	n_1	$CPE_1 \times 10^{-6}$ ($\text{F} \cdot \text{cm}^{-2}$)	R_{ct} ($\text{M}\Omega \cdot \text{cm}^2$)	$CPE_2 \times 10^{-5}$ ($\text{F} \cdot \text{cm}^{-2}$)	n_2	χ^2
2.1	15.05 ± 1.28	6.191 ± 0.50	0.8018 ± 0.050	7.19 ± 0.84	7.691 ± 1.20	2.109 ± 0.08	0.9266 ± 0.052	5.71 × 10 ⁻⁴
2.3	16.03 ± 1.12	6.728 ± 0.02	0.8306 ± 0.061	7.15 ± 0.52	14.587 ± 1.11	2.425 ± 0.65	0.8316 ± 0.104	3.47 × 10 ⁻⁴
2.5	13.26 ± 2.55	7.495 ± 0.52	0.7919 ± 0.098	5.66 ± 0.32	18.337 ± 1.72	2.972 ± 0.04	0.9409 ± 0.060	4.08 × 10 ⁻⁴
2.7	15.66 ± 1.83	7.570 ± 0.20	0.8608 ± 0.088	6.30 ± 0.69	24.580 ± 2.86	3.449 ± 0.86	0.9084 ± 0.037	6.11 × 10 ⁻⁴
2.9	14.19 ± 0.20	8.027 ± 0.06	0.7717 ± 0.006	7.33 ± 0.05	27.143 ± 2.74	2.226 ± 0.08	0.9805 ± 0.012	3.73 × 10 ⁻⁴

increase in the applied potential, the value of R_{ct} reaches 27.143 ± 2.74 MΩ cm² for the sample polarized at 2.9 V_{SCE}. Therefore, the passive film formed on the sample polarized at 2.9 V_{SCE} has the best protectiveness in all samples used in this work.

Growth of Passive Films

According to the anodic oxidation theory, the thickness of the passive film is almost linearly dependent on the applied potential (Liu et al., 2004). Therefore, the thicknesses of passive films (L_{ss}) formed on samples polarized at different passivation ranges were calculated by the following equation:

$$L_{ss} = \frac{\varepsilon \varepsilon_0 A}{C_{eff}}, \quad (2)$$

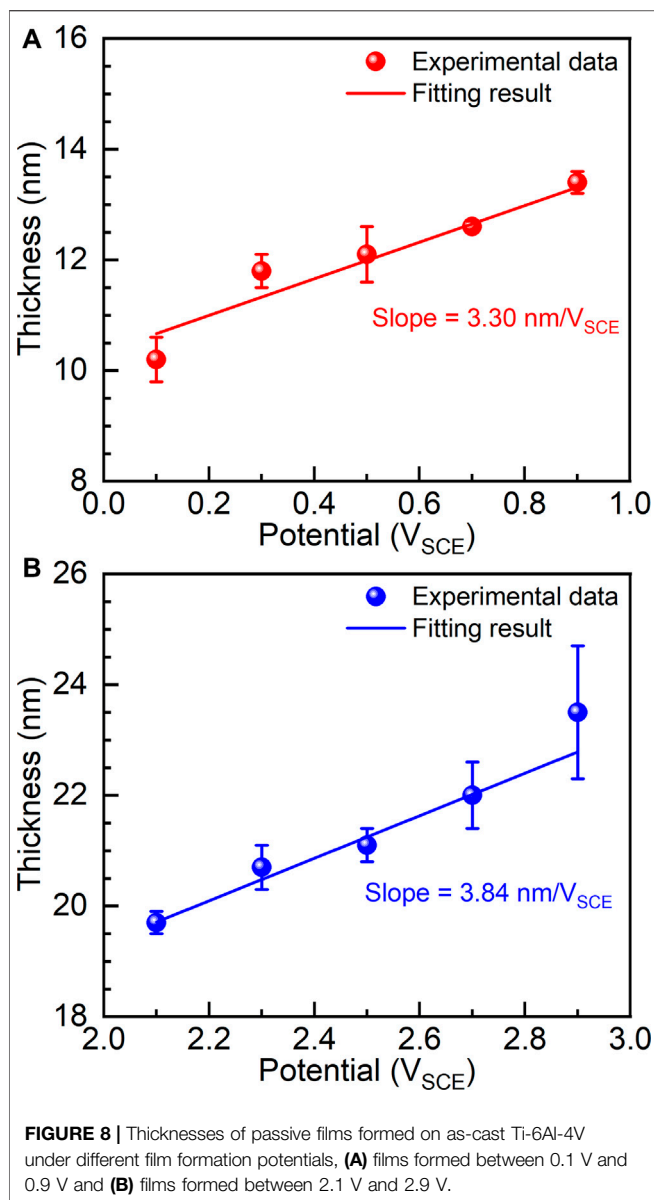
where ε is the relative dielectric constant (60 for TiO₂ (Gai et al., 2018)), ε_0 is the vacuum dielectric constant (8.85×10^{-14} F cm⁻¹), A is the area of Ti electrode, and C_{eff} is the effective capacitance. By processing the EIS data using ZsimpWin software, the capacitance vs. frequency curves of the polarized samples could be obtained. The capacitance at 1 kHz was selected as effective capacitance (Guan et al., 2018). Based on the calculation using Eq. 1, the thicknesses of passive films formed on samples polarized at different passivation ranges are shown in Figure 8. Figure 8A shows the thicknesses of passive films formed on samples polarized in the passivation range. The thicknesses of passive films basically obey the linear relationship with the film formation potential, which is consistent with the anodic oxidation theory. As seen from the fitting result, the slope of the fitted line is 3.30 nm/V_{SCE}. This result means that the passive film has an increase of 3.30 nm per V_{SCE}. The thicknesses of passive films also obey the linear relationship with the film formation potential in the repassivation range. However, the slope of the fitted line in Figure 8B is different from that in Figure 8A. The passive film grows at a growth rate of 3.84 nm/V_{SCE} in the repassivation range, which is higher than that in the passivation range. Therefore, one can conclude that the as-cast Ti-6Al-4V has distinct passive film growth rates in different passivation range.

Possible Film Formation Mechanism Before and After Transpassivation

As is well known, the quality of formed passive films determines the corrosion resistance of passive metals in corrosive environments (Chen et al., 2015a; Chen et al., 2016). The criterion for the quality of passive films may be varied in line with different purposes (Lu et al., 2008; Zhang et al., 2019b). In this work, an apparent transpassivation

range is found before the passivation range and repassivation range. Both passivation current densities and quasi-steady passivation current densities of the samples in the potentiodynamic polarization and potentiostatic polarization significantly increase in the repassivation range as compared to those in the passivation range (Figures 3, 5). The passivation current densities illustrate the ionic migration in the passive films formed on the samples at the given potentials, namely, the exchange of substances between the sample and corrosive environment (Huang and Blackwood, 2005). Therefore, it can be confirmed that the higher film formation potential results in a higher film growth rate and a higher film dissolution rate (Figure 5). Although the passive films formed under higher applied potentials show a higher impedance, the higher passivation current densities of the samples also indicate the higher corrosion rates under the given applied potentials. Therefore, two questions can be divided hereafter. The as-cast Ti-6Al-4V may have a higher corrosion rate at a higher applied potential, hence it can not be applied as an electrode (or other equivalents) under a high potential. However, the passive film formed under the high potential has high impedance. Therefore, the polarized as-cast Ti-6Al-4V can be used as the workpiece (or part) in a corrosive environment without applied potential (such as the human body). Such a polarized as-cast Ti-6Al-4V would possess superior corrosion resistance due to the high-impedance passive film.

The applied potential provides the higher driving force to adsorb the negative ions in the electrolyte and also increases the electric field in the passive film (Despić et al., 1988). Within the adsorbed negative ions, OH⁻ or O²⁻ forms TiO₂ (Zhang et al., 2020b). As such, the thickness of passive film always increases with increasing applied potential. However, the higher applied potential also would adsorb more ingress ions (such as halide ions). Such ingress ions would trigger the localized breakdown of passive film (Zhang et al., 2018), which is observed in the samples polarized at 2.9 V_{SCE} (Figure 5). According to the point defect model, the pitting corrosion or metastable pitting corrosion results from the condensation of cation vacancies catalyzed by aggressive ions (Macdonald, 2011). Based on the existing data, the density of oxygen vacancies in the passive films formed on Ti-6Al-4V decreases with increasing applied potential (Jia et al., 2016; Gai et al., 2018). Hence, to achieve the condensation of oxygen vacancies, a high electric field in the passive film is required. As discussed above, the sample polarized under higher applied potential shows higher steady-state passivation current density. Such a phenomenon also demonstrates a higher electric field in the passive film. The higher electric field directly results in the high



diffusion coefficient of oxygen vacancies (Lu et al., 2009; Guan et al., 2018). The flux of oxygen vacancies is the function of the density of oxygen vacancies and their diffusion coefficient. A high flux of oxygen vacancies could result in the condensation of cation vacancies. Due to observed high possibility of metastable pitting corrosion under high applied potential (repassivation range), one can conclude that the applied potential is decisive for the localized destruction of the passive film.

CONCLUSION

In this work, the electrochemical behavior of as-cast Ti-6Al-4V in Hank's solution at 37 °C before and after transpassivation was investigated. After carefully analyzing the microstructure of as-cast Ti-6Al-4V, the potentiodynamic polarization test was

conducted to confirm the passivation and repassivation ranges. By investigating the electrochemical impedance spectroscopy of the samples polarized in passivation and repassivation ranges, characteristics of passive films formed on as-cast Ti-6Al-4V are further understood. Some key conclusions are drawn as follows.

- (1) In the potentiodynamic polarization test, the passivation range is observed from 0 V_{SCE} to 1.2 V_{SCE} for the sample. Subsequently, the transpassivation behavior of the sample is found from 1.2 V_{SCE} to 1.5 V_{SCE} . Afterward, the repassivation range is observed from 1.5 V_{SCE} to the end of the test.
- (2) Potentiostatic polarization tests were conducted at 0.1~0.9 V_{SCE} and 2.1~2.9 V_{SCE} to produce passive films on the samples. The growth kinetics of the passive film follows the Macdonald model. With increasing the film formation potential, the quasi-steady passivation current densities of as-cast Ti-6Al-4V increase. Metastable pitting corrosion is observed under the applied potentials of 2.7 V_{SCE} and 2.9 V_{SCE} .
- (3) Electrochemical impedance spectroscopy examinations were carried out on the potentiostatic polarized samples. The results show that the thickness of the passive film as well as the charge transfer of the samples increases with increasing the applied potential. The formed passive films before and after transpassivation have different growth rates, which are calculated as 3.30 nm/ V_{SCE} and 3.84 nm/ V_{SCE} in the passivation range and repassivation range.
- (4) Based on the result of this work, one can conclude that the passive film formed under high applied potential has better protectiveness. Therefore, although the transpassivation behavior may destroy the passive film to some extent, the passive film formed under higher applied potential still has higher impedance. However, the higher applied potential also provides the higher driving force to adsorb the aggressive ions in the electrolyte and also increases the electric field in the passive film. Therefore, metastable pitting corrosion is observed at the high applied potential.

DATA AVAILABILITY STATEMENT

The original contributions presented in the study are included in the article/Supplementary Material, further inquiries can be directed to the corresponding author.

AUTHOR CONTRIBUTIONS

GY and XL conceived and designed the experiments; HZ performed experiments; CH and Y-WC analyzed the data; GY, CZ, and SL wrote the paper.

FUNDING

The study was funded by Postgraduate Research & Practice Innovation Program of Jiangsu Province.

REFERENCES

- Al-Mayouf, A. M., Al-Swayih, A. A., and Al-Mobarak, N. A. (2004). Effect of potential on the corrosion behavior of a new titanium alloy for dental implant applications in fluoride media. *Mater. Corros.* 55 (2), 88–94. doi:10.1002/maco.200303697
- Aladjem, A. (1973). Anodic oxidation of titanium and its alloys. *J. Mater. Sci.* 8 (5), 688–704. doi:10.1007/bf00561225
- Aziz-Kerrzo, M., Conroy, K. G., Fenelon, A. M., Farrell, S. T., and Breslin, C. B. (2001). Electrochemical studies on the stability and corrosion resistance of titanium-based implant materials. *Biomaterials* 22 (12), 1531–1539. doi:10.1016/s0142-9612(00)00309-4
- Babilas, D., Urbańczyk, E., Sowa, M., Maciej, A., Korotin, D. M., Zhidkov, I. S., et al. (2016). On the electropolishing and anodic oxidation of Ti-15Mo alloy. *Electrochim. Acta.* 205, 256–265. doi:10.1016/j.electacta.2016.01.218
- Bai, Y., Gai, X., Li, S., Zhang, L.-C., Liu, Y., Hao, Y., et al. (2017). Improved corrosion behaviour of electron beam melted Ti-6Al-4V alloy in phosphate buffered saline. *Corrosion Sci.* 123, 289–296. doi:10.1016/j.corsci.2017.05.003
- Balla, V. K., Banerjee, S., Bose, S., and Bandyopadhyay, A. (2010). Direct laser processing of a tantalum coating on titanium for bone replacement structures. *Acta Biomater.* 6 (6), 2329–2334. doi:10.1016/j.actbio.2009.11.021
- Basame, S. B., and White, H. S. (2000). Pitting corrosion of titanium the relationship between pitting potential and competitive anion adsorption at the oxide film/electrolyte interface. *J. Electrochem. Soc.* 147 (4), 1376. doi:10.1149/1.1393364
- Chai, L., Chen, K., Zhi, Y., Murty, K. L., Chen, L. Y., and Yang, Z. (2018). Nanotwins induced by pulsed laser and their hardening effect in a Zr alloy. *J. Alloys Compd.* 748, 163–170. doi:10.1016/j.jallcom.2018.03.126
- Chai, L. J., Wang, S. Y., Wu, H., Guo, N., Pan, H. C., Chen, L. Y., et al. (2017). $\alpha \rightarrow \beta$ transformation characteristics revealed by pulsed laser-induced non-equilibrium microstructures in duplex-phase Zr alloy. *Sci. China Technol. Sci.* 60 (8), 1255–1262. doi:10.1007/s11431-016-9038-y
- Chen, L.-Y., Cui, Y.-W., and Zhang, L.-C. (2020a). Recent development in beta titanium alloys for biomedical applications. *Metals* 10 (9), 1139. doi:10.3390/met10091139
- Chen, L.-Y., Wang, H., Zhao, C., Lu, S., Wang, Z.-X., Sha, J., et al. (2019a). Automatic remelting and enhanced mechanical performance of a plasma sprayed NiCrBSi coating. *Surf. Coating. Technol.* 369, 31–43. doi:10.1016/j.surfcoat.2019.04.052
- Chen, L.-Y., Xu, T., Lu, S., Wang, Z.-X., Chen, S., and Zhang, L.-C. (2018a). Improved hardness and wear resistance of plasma sprayed nanostructured NiCrBSi coating via short-time heat treatment. *Surf. Coating. Technol.* 350, 436–444. doi:10.1016/j.surfcoat.2018.07.037
- Chen, L.-Y., Xu, T., Wang, H., Sang, P., Lu, S., Wang, Z.-X., et al. (2019b). Phase interaction induced texture in a plasma sprayed-remelted NiCrBSi coating during solidification: an electron backscatter diffraction study. *Surf. Coating. Technol.* 358, 467–480. doi:10.1016/j.surfcoat.2018.11.019
- Chen, L., Huang, J., Lin, C., Pan, C., Chen, S., Yang, T., et al. (2017a). Anisotropic response of Ti-6Al-4V alloy fabricated by 3D printing selective laser melting. *Mater. Sci. Eng. A* 682, 389–395. doi:10.1016/j.msea.2016.11.061
- Chen, L., Li, J., Zhang, Y., Zhang, L. C., Lu, W., Wang, L., et al. (2015a). Zr-Sn-Nb-Fe-Si-O alloy for fuel cladding candidate: processing, microstructure, corrosion resistance and tensile behavior. *Corrosion Sci.* 100, 332–340. doi:10.1016/j.corsci.2015.08.005
- Chen, L., Li, J., Zhang, Y., Zhang, L. C., Lu, W., Zhang, L., et al. (2015b). Effects of alloyed Si on the autoclave corrosion performance and periodic corrosion kinetics in Zr-Sn-Nb-Fe-O alloys. *Corrosion Sci.* 100, 651–662. doi:10.1016/j.corsci.2015.08.043
- Chen, L. Y., Sang, P., Zhang, L., Song, D., Chu, Y. Q., Chai, L., et al. (2018b). Homogenization and growth behavior of second-phase particles in a deformed Zr-Sn-Nb-Fe-Cu-Si-O alloy. *Metals* 8 (10), 759. doi:10.3390/met8100759
- Chen, L. Y., Shen, P., Zhang, L., Lu, S., Chai, L., Yang, Z., et al. (2018c). Corrosion behavior of non-equilibrium Zr-Sn-Nb-Fe-Cu-O alloys in high-temperature 0.01 M LiOH aqueous solution and degradation of the surface oxide films. *Corrosion Sci.* 136, 221–230. doi:10.1016/j.corsci.2018.03.012
- Chen, L., Zeng, Q., Li, J., Lu, J., Zhang, Y., Zhang, L.-C., et al. (2016). Effect of microstructure on corrosion behavior of a Zr-Sn-Nb-Fe-Cu-O alloy. *Mater. Des.* 92, 888–896. doi:10.1016/j.matdes.2015.12.067
- Chen, Q., and Thouas, G. A. (2015). Metallic implant biomaterials. *Mater. Sci. Eng. R Rep.* 87, 1–57. doi:10.1016/j.mser.2014.10.001
- Chen, W., Xu, J., Liu, D., Bao, J., Sabbaghianrad, S., Shan, D., et al. (2020b). Microstructural evolution and microhardness variations in pure titanium processed by high-pressure torsion. *Adv. Eng. Mater.* 22 (6), 1901462. doi:10.1002/adem.201901462
- Chen, Y., Zhang, J., Dai, N., Qin, P., Attar, H., and Zhang, L.-C. (2017b). Corrosion behaviour of selective laser melted Ti-TiB biocomposite in simulated body fluid. *Electrochim. Acta.* 232, 89–97. doi:10.1016/j.electacta.2017.02.112
- Chen, Y., Zhang, J., Gu, X., Dai, N., Qin, P., and Zhang, L. C. (2018d). Distinction of corrosion resistance of selective laser melted Al-12Si alloy on different planes. *J. Alloys Compd.* 747, 648–658. doi:10.1016/j.jallcom.2018.03.062
- Dai, N., Zhang, J., Chen, Y., and Zhang, L.-C. (2017). Heat treatment degrading the corrosion resistance of selective laser melted Ti-6Al-4V alloy. *J. Electrochem. Soc.* 164 (7), C428–C434. doi:10.1149/2.1481707jes
- Dai, N., Zhang, L.-C., Zhang, J., Chen, Q., and Wu, M. (2016a). Corrosion behavior of selective laser melted Ti-6Al-4V alloy in NaCl solution. *Corrosion Sci.* 102, 484–489. doi:10.1016/j.corsci.2015.10.041
- Dai, N., Zhang, L.-C., Zhang, J., Zhang, X., Ni, Q., Chen, Y., et al. (2016b). Distinction in corrosion resistance of selective laser melted Ti-6Al-4V alloy on different planes. *Corrosion Sci.* 111, 703–710. doi:10.1016/j.corsci.2016.06.009
- Dehghanghadikolaei, A., Ibrahim, H., Amerinatanzi, A., Hashemi, M., Moghaddam, N. S., and Elahinia, M. (2019). Improving corrosion resistance of additively manufactured nickel–titanium biomedical devices by micro-arc oxidation process. *J. Mater. Sci.* 54 (9), 7333–7355. doi:10.1007/s10853-019-03375-1
- Despić, A. R., Dražić, D. M., and Gajić-Krstajić, U. (1988). Effect of the addition of chloride on the anodic dissolution of aluminium through barrier films. *J. Electroanal. Chem. Interfacial Electrochem.* 242 (1–2), 303–315. doi:10.1016/0022-0728(88)80259-6
- Frankel, G. S. (1998). Pitting corrosion of metals a review of the critical factors. *J. Electrochem. Soc.* 145, 2186–2198.
- Gai, X., Bai, Y., Li, J., Li, S., Hou, W., Hao, Y., et al. (2018). Electrochemical behaviour of passive film formed on the surface of Ti-6Al-4V alloys fabricated by electron beam melting. *Corrosion Sci.* 145, 80–89. doi:10.1016/j.corsci.2018.09.010
- Galvele, J., Torresi, R., and Carranza, R. (1990). Passivity breakdown, its relation to pitting and stress-corrosion-cracking processes. *Corrosion Sci.* 31, 563–571. doi:10.1016/0010-938x(90)90163-y
- Guan, L., Li, Y., Wang, G., Zhang, Y., and Zhang, L.-C. (2018). pH dependent passivation behavior of niobium in acid fluoride-containing solutions. *Electrochim. Acta.* 285, 172–184. doi:10.1016/j.electacta.2018.07.221
- Hanawa, T. (2004). Metal ion release from metal implants. *Mater. Sci. Eng. C* 24 (6–8), 745–752. doi:10.1016/j.msec.2004.08.018
- Huang, Y. Z., and Blackwood, D. J. (2005). Characterisation of titanium oxide film grown in 0.9% NaCl at different sweep rates. *Electrochim. Acta.* 51 (6), 1099–1107. doi:10.1016/j.electacta.2005.05.051
- Jaeggi, C., Frauchiger, V., Eitel, F., Stiefel, M., Schmotzer, H., and Siegmund, S. (2011). The effect of surface alloying of Ti powder for vacuum plasma spraying of open porous titanium coatings. *Acta Mater.* 59 (2), 717–725. doi:10.1016/j.actamat.2010.10.010
- Jia, Z., Duan, X., Zhang, W., Wang, W., Sun, H., Wang, S., et al. (2016). Ultra-sustainable Fe₇₈Si₀B₁₃ metallic glass as a catalyst for activation of persulfate on methylene blue degradation under UV-Vis light. *Sci. Rep.* 6 (1), 38520. doi:10.1038/srep38520
- Kang, L., and Yang, C. (2019). A review on high-strength titanium alloys: microstructure, strengthening, and properties. *Adv. Eng. Mater.* 21 (8), 1801359. doi:10.1002/adem.201801359
- Kong, D.-S., and Wu, J.-X. (2007). An electrochemical study on the anodic oxygen evolution on oxide film covered titanium. *J. Electrochem. Soc.* 155 (1), C32. doi:10.1149/1.2799731
- Lakatos-Varsányi, M., Falkenberg, F., and Olefjord, I. (1998). The influence of phosphate on repassivation of 304 stainless steel in neutral chloride solution. *Electrochim. Acta.* 43 (1–2), 187–197. doi:10.1016/s0013-4686(97)00224-7

- Lei, X., Dong, L., Zhang, Z., Liu, Y., Hao, Y., Yang, R., et al. (2017). Microstructure, texture evolution and mechanical properties of VT3-1 titanium alloy processed by multi-pass drawing and subsequent isothermal annealing. *Metals* 7 (4), 131. doi:10.3390/met7040131
- Liang, S. X., Jia, Z., Liu, Y. J., Zhang, W., Wang, W., Lu, J., et al. (2018). Compelling rejuvenated catalytic performance in metallic glasses. *Adv. Mater.* 30 (45), e1802764. doi:10.1002/adma.201802764
- Liu, S., Han, S., Zhang, L., Chen, L.-Y., Wang, L., Zhang, L., et al. (2020a). Strengthening mechanism and micropillar analysis of high-strength NiTi-Nb eutectic-type alloy prepared by laser powder bed fusion. *Compos. B. Eng.* 200, 108358. doi:10.1016/j.compositesb.2020.108358
- Liu, S., Liu, J., Wang, L., Ma, R. L. W., Zhong, Y., Lu, W., et al. (2020b). Superelastic behavior of in-situ eutectic-reaction manufactured high strength 3D porous NiTi-Nb scaffold. *Scripta Mater.* 181, 121–126. doi:10.1016/j.scriptamat.2020.02.025
- Liu, X., Chu, P. K., and Ding, C. (2004). Surface modification of titanium, titanium alloys, and related materials for biomedical applications. *Mater. Sci. Eng. R* 47 (3–4), 49–121. doi:10.1016/j.mser.2004.11.001
- Lu, H.-B., Poh, C.-K., Zhang, L. C., Guo, Z. P., Yu, X. B., and Liu, H.-K. (2009). Dehydrogenation characteristics of Ti- and Ni/Ti-catalyzed Mg hydrides. *J. Alloys Compd.* 481 (1–2), 152–155. doi:10.1016/j.jallcom.2009.02.125
- Lu, H., Zhang, L., Gebert, A., and Schultz, L. (2008). Pitting corrosion of Cu-Zr metallic glasses in hydrochloric acid solutions. *J. Alloys Compd.* 462 (1–2), 60–67. doi:10.1016/j.jallcom.2007.08.023
- Macdonald, D. D. (2011). The history of the point defect model for the passive state: a brief review of film growth aspects. *Electrochim. Acta.* 56 (4), 1761–1772. doi:10.1016/j.electacta.2010.11.005
- Montiel, A., Onofre, E., and Escudero, M. L. (2020). Synthesis and electrochemical characterisation of magnetite coatings on Ti6Al4V-ELI. *Metals* 10 (12), 1640. doi:10.3390/met10121640
- Narayanan, R., and Seshadri, S. K. (2008). Point defect model and corrosion of anodic oxide coatings on Ti-6Al-4V. *Corrosion Sci.* 50 (6), 1521–1529. doi:10.1016/j.corsci.2008.02.023
- Qin, P., Chen, Y., Liu, Y.-J., Zhang, J., Chen, L.-Y., Li, Y., et al. (2019). Resemblance in corrosion behavior of selective laser melted and traditional monolithic β Ti-24Nb-4Zr-8Sn alloy. *ACS Biomater. Sci. Eng.* 5 (2), 1141–1149. doi:10.1021/acsbomaterials.8b01341
- Qin, P., Liu, Y., Sercombe, T. B., Li, Y., Zhang, C., Cao, C., et al. (2018). Improved corrosion resistance on selective laser melting produced Ti-5Cu alloy after heat treatment. *ACS Biomater. Sci. Eng.* 4 (7), 2633–2642. doi:10.1021/acsbomaterials.8b00319
- Qin, X., Guo, X., Lu, J., Chen, L., Qin, J., and Lu, W. (2017). Erosion-wear and intergranular corrosion resistance properties of AISI 304L austenitic stainless steel after low-temperature plasma nitriding. *J. Alloys Compd.* 698, 1094–1101. doi:10.1016/j.jallcom.2016.12.164
- Rabadia, C. D., Liu, Y. J., Chen, L. Y., Jawed, S. F., Wang, L. Q., Sun, H., et al. (2019a). Deformation and strength characteristics of Laves phases in titanium alloys. *Mater. Des.* 179, 107891. doi:10.1016/j.matdes.2019.107891
- Rabadia, C. D., Liu, Y. J., Zhao, C. H., Wang, J. C., Jawed, S. F., Wang, L. Q., et al. (2019b). Improved trade-off between strength and plasticity in titanium based metastable beta type Ti-Zr-Fe-Sn alloys. *Mater. Sci. Eng. A* 766, 138340. doi:10.1016/j.msea.2019.138340
- Rautray, T. R., Narayanan, R., and Kim, K. H. (2011). Ion implantation of titanium based biomaterials. *Prog. Mater. Sci.* 56 (8), 1137–1177. doi:10.1016/j.pmatsci.2011.03.002
- Sabban, R., Bahl, S., Chatterjee, K., and Suwas, S. (2019). Globularization using heat treatment in additively manufactured Ti-6Al-4V for high strength and toughness. *Acta Mater.* 162, 239–254. doi:10.1016/j.actamat.2018.09.064
- Sang, P., Chen, L.-Y., Zhao, C., Wang, Z.-X., Wang, H., Lu, S., et al. (2019). Particle size-dependent microstructure, hardness and electrochemical corrosion behavior of atmospheric plasma sprayed NiCrBSi coatings. *Metals* 9 (12), 1342. doi:10.3390/met9121342
- Semenova, I. P., Polyakova, V. V., Dyakonov, G. S., and Polyakov, A. V. (2020). Ultrafine-Grained titanium-based alloys: structure and service properties for engineering applications. *Adv. Eng. Mater.* 22 (1), 1900651. doi:10.1002/adem.201900651
- Seo, D.-I., and Lee, J.-B. (2019). Corrosion characteristics of additive-manufactured Ti-6Al-4V using microdroplet cell and critical pitting temperature techniques. *J. Electrochem. Soc.* 166 (13), C428–C433. doi:10.1149/2.0571913jes
- Shibata, T., and Zhu, Y.-C. (1994). The effect of film formation potential on the stochastic processes of pit generation on anodized titanium. *Corrosion Sci.* 36 (1), 153–163. doi:10.1016/0010-938x(94)90116-3
- Stolyarov, V. V., Shuster, L. S., Miganov, M. S., Valiev, R. Z., and Zhu, Y. T. (2004). Reduction of friction coefficient of ultrafine-grained CP titanium. *Mater. Sci. Eng. A* 371 (1–2), 313–317. doi:10.1016/j.msea.2003.12.026
- Vautrin-Ul, C., Taleb, A., Stafiej, J., Chaussé, A., and Badiali, J. P. (2007). Mesoscopic modelling of corrosion phenomena: coupling between electrochemical and mechanical processes, analysis of the deviation from the Faraday law. *Electrochim. Acta.* 52 (17), 5368–5376. doi:10.1016/j.electacta.2007.02.051
- Wang, L., Wang, C., Zhang, L. C., Chen, L., Lu, W., and Zhang, D. (2016). Phase transformation and deformation behavior of NiTi-Nb eutectic joined NiTi wires. *Sci. Rep.* 6 (1), 23905. doi:10.1038/srep23905
- Wang, L., Qu, J., Chen, L., Meng, Q., Zhang, L. C., Qin, J., et al. (2015). Investigation of deformation mechanisms in β -type Ti-35Nb-2Ta-3Zr alloy via FSP leading to surface strengthening. *Metall. Mater. Trans.* 46 (11), 4813–4818. doi:10.1007/s11661-015-3089-8
- Wang, L., Xie, L., Lv, Y., Zhang, L.-C., Chen, L., Meng, Q., et al. (2017). Microstructure evolution and superelastic behavior in Ti-35Nb-2Ta-3Zr alloy processed by friction stir processing. *Acta Mater.* 131, 499–510. doi:10.1016/j.actamat.2017.03.079
- Wang, L., Xie, L., Zhang, L.-C., Chen, L., Ding, Z., Lv, Y., et al. (2018a). Microstructure evolution and superelasticity of layer-like NiTiNb porous metal prepared by eutectic reaction. *Acta Mater.* 143, 214–226. doi:10.1016/j.actamat.2017.10.021
- Wang, Z.-X., Chen, G.-Q., Chen, L.-Y., Xu, L., and Lu, S. (2018b). Degradation behavior of micro-arc oxidized ZK60 magnesium alloy in a simulated body fluid. *Metals* 8 (9), 724. doi:10.3390/met8090724
- Xiang, K., Chen, L.-Y., Chai, L., Guo, N., and Wang, H. (2020). Microstructural characteristics and properties of CoCrFeNiNb_x high-entropy alloy coatings on pure titanium substrate by pulsed laser cladding. *Appl. Surf. Sci.* 517, 146214. doi:10.1016/j.apusuc.2020.146214
- Yang, H.-Y., Wang, Z., Shu, S.-L., and Lu, J.-B. (2020a). Effect of Ta addition on the microstructures and mechanical properties of in situ bi-phase (TiB₂-TiC_xNy)/(Ni-Ta) cermet. *Ceram. Int.* 45 (4), 4408–4417. doi:10.1016/j.ceramint.2018.11.118
- Yang, H.-Y., Wang, Z., Yue, X., Ji, P.-J., and Shu, S.-L. (2020b). Simultaneously improved strength and toughness of in situ bi-phased TiB₂-Ti(C,N)-Ni cermet by Mo addition. *J. Alloys Compd.* 820, 153068. doi:10.1016/j.jallcom.2019.153068
- Yang, H., Yue, X., Wang, Z., Shao, Y., and Shu, S. (2020c). Strengthening mechanism of TiC/Al composites using Al-Ti-C/CNTs with doping alloying elements (Mg, Zn and Cu). *J. Mater. Res. Tech.* 9 (3), 6475–6487. doi:10.1016/j.jmrt.2020.04.033
- Yang, Y., Chen, Y., Zhang, J., Gu, X., Qin, P., Dai, N., et al. (2018). Improved corrosion behavior of ultrafine-grained eutectic Al-12Si alloy produced by selective laser melting. *Mater. Des.* 146, 239–248. doi:10.1016/j.matdes.2018.03.025
- Yang, Z. N., Wang, X. B., Liu, F., Zhang, F. C., Chai, L. J., Qiu, R. S., et al. (2019). Effect of intercritical annealing temperature on microstructure and mechanical properties of duplex Zr-2.5Nb alloy. *J. Alloys Compd.* 776, 242–249. doi:10.1016/j.jallcom.2018.10.320
- Yu, F., Addison, O., and Davenport, A. J. (2015). A synergistic effect of albumin and H₂O₂ accelerates corrosion of Ti₆Al₄V. *Acta Biomater.* 26, 355–365. doi:10.1016/j.actbio.2015.07.046
- Zhang, B., Wang, J., Wu, B., Guo, X. W., Wang, Y. J., Chen, D., et al. (2018). Unmasking chloride attack on the passive film of metals. *Nat. Commun.* 9 (1), 2559. doi:10.1038/s41467-018-04942-x
- Zhang, H., Man, C., Wang, L., Dong, C., Wang, L., Kong, D., et al. (2020a). Different corrosion behaviors between α and β phases of Ti6Al4V in fluoride-containing solutions: influence of alloying element Al. *Corrosion Sci.* 169, 108605. doi:10.1016/j.corsci.2020.108605

- Zhang, L.-C., and Attar, H. (2016). Selective laser melting of titanium alloys and titanium matrix composites for biomedical applications: a review. *Adv. Eng. Mater.* 18 (4), 463–475. doi:10.1002/adem.201500419
- Zhang, L.-C., Chen, L.-Y., and Wang, L. (2020b). Surface modification of titanium and titanium alloys: technologies, developments and future interests. *Adv. Eng. Mater.* 22 (5), 1901258. doi:10.1002/adem.201901258
- Zhang, L.-C., Xu, J., and Eckert, J. (2006). Thermal stability and crystallization kinetics of mechanically alloyed TiC/Ti-based metallic glass matrix composite. *J. Appl. Phys.* 100 (3), 033514. doi:10.1063/1.2234535
- Zhang, L. C., and Chen, L. Y. (2019). A review on biomedical titanium alloys: recent progress and prospect. *Adv. Eng. Mater.* 21 (4), 1801215. doi:10.1002/adem.201801215
- Zhang, L., Chen, L.-Y., Zhao, C., Liu, Y., and Zhang, L.-C. (2019a). Calculation of oxygen diffusion coefficients in oxide films formed on low-temperature annealed Zr alloys and their related corrosion behavior. *Metals* 9 (8), 850. doi:10.3390/met9080850
- Zhang, L. C., Jia, Z., Lyu, F., Liang, S. X., and Lu, J. (2019b). A review of catalytic performance of metallic glasses in wastewater treatment: recent progress and prospects. *Prog. Mater. Sci.* 105, 100576. doi:10.1016/j.pmatsci.2019.100576
- Zhang, L. C., Klemm, D., Eckert, J., Hao, Y. L., and Sercombe, T. B. (2011). Manufacture by selective laser melting and mechanical behavior of a biomedical Ti-24Nb-4Zr-8Sn alloy. *Scripta Mater.* 65 (1), 21–24. doi:10.1016/j.scriptamat.2011.03.024
- Zhang, L. C., Shen, Z. Q., and Xu, J. (2003). Glass formation in a (Ti, Zr, Hf)–(Cu, Ni, Ag)–Al high-order alloy system by mechanical alloying. *J. Mater. Res.* 18 (9), 2141–2149. doi:10.1557/jmr.2003.0300
- Zhang, L. C., and Xu, J. (2004). Glass-forming ability of melt-spun multicomponent (Ti, Zr, Hf)–(Cu, Ni, Co)–Al alloys with equiatomic substitution. *J. Non-cryst. Solids* 347 (1–3), 166–172. doi:10.1016/j.jnoncrystol.2004.09.007
- Zhang, M., Li, Y. N., Zhang, F. C., Wang, X. B., Chen, L. Y., and Yang, Z. N. (2017). Effect of annealing treatment on the microstructure and mechanical properties of a duplex Zr-2.5 Nb alloy. *Mater. Sci. Eng. A* 706, 236–241. doi:10.1016/j.msea.2017.08.107
- Zhang, Y.-M., Chen, L.-Y., Lu, S., Zhao, C., and Wang, Y.-H. (2019c). Refined microstructure and enhanced hardness in friction stir-welded AZ31 magnesium alloy induced by heat pipe with different cooling liquid. *Metals* 9 (11), 1227. doi:10.3390/met9111227
- Zhao, S., Li, S. J., Wang, S. G., Hou, W. T., Li, Y., Zhang, L. C., et al. (2018). Compressive and fatigue behavior of functionally graded Ti-6Al-4V meshes fabricated by electron beam melting. *Acta Mater.* 150, 1–15. doi:10.1016/j.actamat.2018.02.060
- Zheng, X., Gong, M., Xiong, T., Ge, H., Yang, L., Zhou, Y., et al. (2019). Deformation induced FCC lamellae and their interaction in commercial pure Ti. *Scripta Mater.* 162, 326–330. doi:10.1016/j.scriptamat.2018.11.037

Conflict of Interest: The authors declare that the research was conducted in the absence of any commercial or financial relationships that could be construed as a potential conflict of interest.

Copyright © 2021 Yi, Liu, Zheng, Zhang, Xu, Cui and Liu. This is an open-access article distributed under the terms of the Creative Commons Attribution License (CC BY). The use, distribution or reproduction in other forums is permitted, provided the original author(s) and the copyright owner(s) are credited and that the original publication in this journal is cited, in accordance with accepted academic practice. No use, distribution or reproduction is permitted which does not comply with these terms.



Elastically Graded Titanium Alloy Produced by Mechanical Surface Deformation

Stéphanie Delannoy^{1,2*}, Sarah Baiz³, Pascal Laheurte⁴, Laurence Jordan^{1,5,6} and Frédéric Prima¹

¹ PSL Research University, Chimie ParisTech—CNRS, Institut de Recherche de Chimie Paris UMR CNRS 8247, Paris, France, ² Biotech Dental, Salon-de-Provence, France, ³ Laboratoire Procédés et Ingénierie en Mécanique et Matériaux, PIMM, ENSAM, UMR 8006, CNRS, CNAM, Paris, France, ⁴ Laboratoire d'Etude des Microstructures et de Mécanique des Matériaux, LEM3 UMR CNRS 7239, Université de Lorraine, Metz, France, ⁵ Dental Faculty, Université de Paris, Paris, France, ⁶ Hospital Rothschild, AP-HP, Paris, France

OPEN ACCESS

Edited by:

Chaozong Liu,
University College London,
United Kingdom

Reviewed by:

Carlos Roberto Grandini,
São Paulo State University, Brazil
Lai-Chang Zhang,
Edith Cowan University, Australia

*Correspondence:

Stéphanie Delannoy
stephanie.delannoy@chimieparistech.psl.eu

Specialty section:

This article was submitted to
Biomaterials,
a section of the journal
Frontiers in Materials

Received: 27 November 2020

Accepted: 23 February 2021

Published: 16 March 2021

Citation:

Delannoy S, Baiz S, Laheurte P,
Jordan L and Prima F (2021)
Elastically Graded Titanium Alloy
Produced by Mechanical Surface
Deformation. *Front. Mater.* 8:634236.
doi: 10.3389/fmats.2021.634236

The objective of this study was to develop a thermo-mechanical strategy to create a radial elasticity gradient in a β metastable Ti-Nb-Zr alloy, and to characterize it in terms of microstructural and mechanical properties. A first investigation was conducted on thin samples of Ti-20Nb-6Zr (at.%) submitted to various thermo-mechanical treatments. Microstructure-properties relationships and elastic variability of this alloy were determined performing uniaxial tensile tests, X-ray diffraction and scanning and transmission electron microscopies. Based on these preliminary results, mechanical deformation was identified as a potential way to lower the elastic modulus of the alloy. In order to create elastically graded pieces, shot-peening was therefore carried out on thicker samples to engender surface deformation. In this second part of the work, local mechanical properties were evaluated by instrumented micro-indentation. Experimental observations demonstrated that shot-peening enabled to locally induce martensitic transformation on surface, and a decrease in indentation elastic modulus from 85 to 65 GPa over 400 μm was highlighted. Surface deformation proved to be an efficient way of creating an elasticity gradient in β metastable titanium alloys. This combination of material and process could be suitable to produce dental implants with mechanically enhanced biocompatibility.

Keywords: titanium alloys, elasticity gradient, elastic modulus, surface deformation, instrumented indentation, stress-induced martensite

INTRODUCTION

In the field of implanted medical devices, the notion of biocompatibility has evolved steadily over time and is no longer only synonymous with bio-inertness. Nowadays, an active biocompatibility is being sought, giving a greater focus on the integration of biomaterials and the responses of the human body (Williams, 1987, 2003; Doherty et al., 1992). In the case of dental implants, this means to promote bone remodeling in order to achieve good osseointegration. Aside from biological and chemical considerations, mechanical aspects are therefore equally critical to the development of highly performant biomaterials. Indeed, the bone remodeling is physiologically driven by mechanical stimuli and under- or overloading of bone tissue could engender resorption or necrosis issues (Rieger et al., 2011; Laheurte et al., 2014). The difficulty relies on the fact that the use of dental implants can affect this bone density regulation in various ways. First, the absence

of periodontal ligament no longer allows to provide a damping effect, which can create load peaks in the surrounding bone (Kitamura et al., 2004; Mariani et al., 2008; Consolaro et al., 2010). And several studies have shown that the elastic mismatch observed at the bone/implant interface could give rise to stress shielding and poor stress distribution around the device (Kroger et al., 1998; Niinomi and Nakai, 2011). As a matter of fact, although lower than those of previously used 316L steel or Co-Cr-Mo alloys, Young's moduli of current standard biomedical titanium alloys (CP Ti or TA6V) still remain about 5–10 times higher than the one of bone (Geetha et al., 2009). This calls for further efforts to minimize this modulus gap.

In recent years, various research works have been carried out to reduce the originally quite high elastic modulus of titanium alloys, classically around 100 GPa for conventional α or $\alpha + \beta$ alloys (Kuroda et al., 1998; Geetha et al., 2009; Zhang and Chen, 2019). One of the most advanced track concerns the development of new low-modulus compositions, mainly belonging to β -type alloys, which started in the 90's and enabled to reach moduli down to about 60 GPa (Zheng et al., 2012; Shi et al., 2013; Laheurte et al., 2014; Piotrowski et al., 2014; Brizuela et al., 2019). It should be noted, however, that these alloys generally exhibit a limited mechanical strength. Alongside this research of adapted formulations and thermo-mechanical treatments, the creation of porous structures (Li et al., 2014; Liu et al., 2015; Wally et al., 2015; Okulov et al., 2017) or the use of low-modulus coatings (Koshy and Philip, 2015) have also proven to be effective in lowering the stiffness of investigated materials. Nevertheless, these methods, based on complex processes which can be difficult to control, have often led to a deterioration of other properties, including drops in mechanical resistance (Yue et al., 1984; Bandyopadhyay et al., 2010; Oldani and Dominguez, 2012) or additional weaknesses related to the multi-material interfaces (Mimura et al., 2004; Oshida et al., 2010; Xue et al., 2020). To face these issues, and since iso-elasticity is essentially required at the bone/implant interface, structures displaying gradients in porosity or in chemical compositions were also studied. Once again, even after having overcome the obstacle of producing such complex structures, a compromise between promoting bone remodeling and maintaining a sufficient level of mechanical resistance was difficult to achieve (Lin et al., 2010; Mehrali et al., 2013).

The original concept developed in this work tries to exploit the advantages of some of the previously mentioned research axes, based on the diversity offered by titanium alloys. Indeed, in addition to intrinsic reasons, related to their chemical composition, some titanium alloys can present changes in modulus due to specific elastic behaviors linked to martensitic transformations. The innovative idea investigated here, which has recently been patented (Prima and Nowak, 2012), consists in using the elastic variability displayed by this kind of alloys and creating an elastic gradient resulting from a microstructural gradient, thus preserving a monolithic material with a homogeneous chemical composition. The elastic softening should be localized on surface, to enhance the load transfer to the bone, and the initial stiffer microstructure should be kept in the core material to ensure the stability and durability of the

medical implanted device. In order to induce only a superficial transformation, shot-peening has emerged as a suitable option. This technical process is commonly used to superficially treat medical implants and, as well as creating a rough surface with beneficial effect on bone growth, the resulting residual stress layer seems to enhance fatigue performance of the materials (Javier Gil et al., 2007).

Therefore the aim of this study is to assess the feasibility of creating an elasticity gradient through this strategy of surface deformation by shot-peening on a β -metastable titanium alloy, and thus consider this approach for the production of dental implants.

MATERIALS AND METHODS

Material Selection

Among titanium alloys, Ti-20Nb-6Zr (at.%), also referred as TNZ, was selected as a candidate for this project for several motives. Already studied for its superelastic behavior (Sun et al., 2010, 2011; Zhang et al., 2013), this alloy only contains biocompatible chemical elements and avoids, in particular, species such as aluminum or vanadium, considered likely to contribute to cytotoxicity or neurodegenerative troubles, thus compromising the extensive use of TA6V (Laing et al., 1967; Steinemann, 1980; Walker et al., 1989; Rao et al., 1996; Riley et al., 2003; Gomes et al., 2011; US Food and Drug Administration, 2019). This material also displays interesting mechanical properties, namely strength-elongation combination comparable to the one of grade 4 CP Ti in a quenched state (full β phase). Moreover, its martensitic start temperature is situated just below room temperature, which provides the alloy the possibility to easily undergo stress-induced martensitic (SIM) transformation at room temperature. As previously said, this enables to further reduce its originally already low intrinsic modulus.

Elaboration and Thermo-Mechanical Processing Route

A Ti-20Nb-6Zr (at.%) ingot was prepared by vacuum arc melting and hot forged down to a 50-mm-diameter billet. Plate-shaped parts, cut from this billet, were solution treated under air at 1,173 K for 900s, water quenched and mechanically polished to remove the outer oxidized part. From this step, cold-rolled state with controlled thickness reduction was obtained differently, depending on the part of the considered work, as follows: for the preliminary work, performed on thin samples, polished pieces were cold-rolled (CR) at room temperature down to about 0.5 mm of thickness (reduction ratio $\approx 90\%$), whereas for the work on thicker samples, cold-rolling was stopped at about 5 mm of thickness (reduction ratio $\approx 70\%$). To produce quenched state, both thin and thick samples were then thermally treated at 1,173 K during 1,800s under controlled atmosphere and finally water quenched.

Additional surface mechanical treatment was applied on some of the 5 mm-thick samples by shot-peening. This was done on a Wheelabrator industrial prototype (IRT-M2P, Metz), using s130 steel balls at an intensity of 32A on Almen scale, which

represents severe conditions. Both static and dynamic tests were performed. Static experiments were defined by the exposure time to shot-peening during which the nozzle was kept in front of the treated area, whereas dynamic experiments used the coverage percentage of the surface. In that later case, for which the shot-peening nozzle moved parallel to the surface, a number of passes necessary to cover 100% of the surface was determined and, as an example, a coverage of 300% was done reproducing three times this number of passes.

Microstructural Characterization

Phase constitution was analyzed by X-ray diffraction (XRD) using a copper anticathode (Panalytical X'Pert PRO, 45 kV, 40 mA). All the samples were mechanically polished prior to XRD analyses except shot-peened samples, which were kept without any further surface alteration. Microstructural observations were done on an EBSD-equipped scanning electron microscope (SEM—Zeiss LEO-1530). For that purpose, thick samples were cut in half to reveal the cross-section of the shot-peened surface—for concerned sample—, mounted in conductive resin (Struers Polyfast) and mechanically polished on 800, 1,200, 2,500, and 4,000 silicon carbide abrasive papers. Further polishing was done using a mixture of colloidal silica suspension (Struers OP-S) and hydrogen peroxide until mirror-like finish, and a final step was performed on a vibratory polisher (Buehler VibroMet) for 12 h with silica suspension (Struers OP-S) to remove slight deformations and damages remaining from mechanical polishing. Observations were also done using a transmission electron microscope (TEM—JEOL 2000FX). Sections of thin samples were cut, mechanically rounded and polished on silicon carbide abrasive papers to get pre-thinned 3-mm-diameter disks, typically between 100 and 200 μm thick. They were then prepared using twin-jet electrochemical polishing (Struers TenuPol with a solution of methanol, 2-butoxyethanol, perchloric and hydrochloric acids at around 263 K).

Mechanical Properties

Uniaxial tensile tests were conducted to measure the mechanical properties of flat samples. Dogbone tensile specimens were taken along the rolling direction and tested at a strain rate of 10^{-3}s^{-1} on a MTS Criterion (Model 43) machine equipped with a 25 mm gauge length extensometer. Regarding thicker samples, local properties were estimated by carrying out indentation profiles on mirror-polished samples prepared as previously mentioned for SEM observations. Micro-hardness values and elasticity moduli were extracted from instrumented indentation experiments performed on an Anton Paar Micro Hardness Tester (ENSAM, Paris) using Vickers indent and 500 mN load with 5 s holding. Experimental parameters were determined on the basis of a previous design of experiments, done on pure titanium, in order to maximize the measurement accuracy. Oliver-Pharr method was used and indentation moduli E_{IT} were calculated from the unloading curves through the following relation:

$$E_{IT} = \frac{1 - (\nu_s)^2}{\frac{1}{E_r} - \frac{1 - (\nu_i)^2}{E_i}}$$

where E_r is the reduced elastic modulus, E_i is the indenter modulus, and ν_s and ν_i represent, respectively the specimen and the indenter Poisson coefficients (Oliver and Pharr, 1992, 2004).

RESULTS AND DISCUSSION

Assessment of Elastic Variability on Thermo-Mechanically Treated TNZ Samples

The first part of the work aimed at studying the behavior of the TNZ alloy and assessing the potential variability of its microstructure and properties, and particularly its elastic modulus, after various thermo-mechanical treatments. For this purpose, thin samples (0.5 mm) were prepared as mentioned in the previous section. Mechanical tests and observations were performed in the as-obtained cold-rolled state, referred as CR, and after an additional solution treatment in the β phase field followed by water quenching, referred as ST or quenched state. This rapid cooling was done to avoid the precipitation of alpha or isothermal omega phases, which would cause a chemical partition of β -stabilizing elements in the matrix and therefore the inhibition of subsequently desired stress-induced martensitic transformation.

XRD profiles of deformed and quenched states are presented in **Figure 1**. ST state is mainly constituted of β phase, and its lattice parameter is estimated based on experimentally observed peak positions as follows: $a_\beta = 3.299\text{\AA}$ for this bcc structure belonging to $Im\bar{3}m$ space group. No α phase is detected, thus assessing the efficiency of rapid quenching. Regarding the CR state, formation of a large amount of α'' martensite during cold-rolling process can be clearly evidenced by the appearance of several additional peaks on the corresponding diffractogram. Compared to quenched state, a broadening of the XRD peaks can be noticed. This accounts for the important grain refinement—decrease of the coherent domain sizes—and high level of distortion generated by the deformation process, as well as the near-continuous diffraction rings obtained for this microstructure and visible on the SAED pattern in **Figure 2**. In addition, in the bright-field image, dark areas linked to dislocation tangles are also indicators of the severity of the cold-rolling deformation.

Tensile stress-strain curves of ST and CR specimens are presented in **Figure 3**. The quenched specimen exhibits large ductility ($>40\%$) and moderate strength ($R_m = 530\text{ MPa}$). A double-yielding phenomenon can be seen at the beginning of the ST curve. The first yielding, located in the elastic part (“plateau” at about 250 MPa), is the signature of the stress-induced martensitic transformation, whereas the second yielding (around 375 MPa) can be attributed to the transition to the plastic range.

Tensile curve of deformed state shows that severe cold-rolling up to 90% reduction ratio enabled to drastically increase the mechanical resistance of the alloy up to 1,050 MPa, but at the expense of the ductility which drops to only a few percent. The presence, at the initial stage of the tensile test, of a fine martensitic microstructure and a high dislocation density can be responsible

for this impressive strengthening. In addition, a classical linear elastic behavior can be noticed here, suggesting that any further martensitic transformation or martensite variants reorientation takes place in the material and a saturation state has been reached (Schneider et al., 2005).

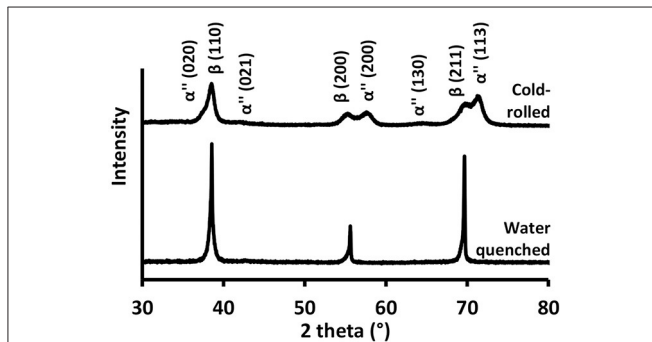


FIGURE 1 | XRD profiles of cold-rolled (CR– 90% thickness reduction) and water quenched (ST) TNZ specimens.

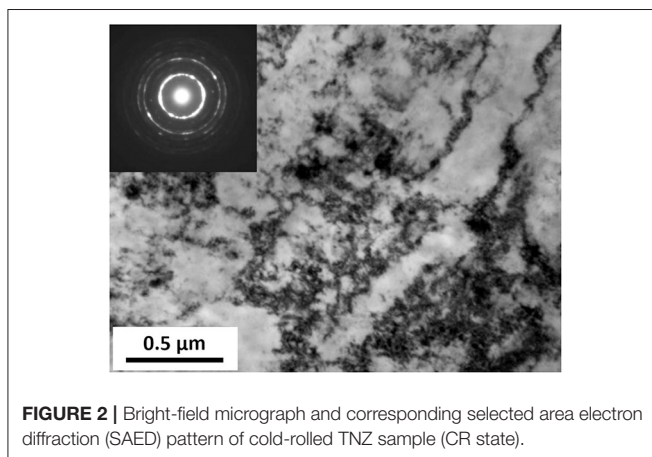


FIGURE 2 | Bright-field micrograph and corresponding selected area electron diffraction (SAED) pattern of cold-rolled TNZ sample (CR state).

Incipient Young's moduli were extracted from the early stage of the curves for both microstructural states, 66 and 55 GPa were obtained for ST and CR specimens, respectively. Bearing in mind that cold-rolling was performed on a solution-treated state, these results indicate that stress-induced martensitic transformation and variants rearrangement that occur when deforming single phase β TNZ alloy can lead to an elastic softening exceeding 15%. This result is consistent with the gradual lowering of elastic modulus which was already observed in previous works during incremental loading-unloading tensile tests performed on this alloy (Sun et al., 2010; Zhang et al., 2013). This information is of great relevance since it enables to develop a practical strategy to create an elasticity gradient in TNZ, by applying a local deformation on surface of thicker samples in β phase.

Creation of Elasticity Gradient

As the creation of a gradient was now being sought, thin samples could no longer be used from a practical point of view. To put into action the strategy described just above, thicker water-quenched TNZ samples were produced. The thickness of 5 mm was chosen in order to be close to the diameter of current commercial dental implants. Shot-peening mechanical treatment was then applied on one side of the pieces. Various experimental conditions were used: 100%, 300% and 1s as defined in section Elaboration and Thermo-Mechanical Processing Route.

XRD analyses were performed on samples before and after shot-peening as illustrated by **Figure 4**. For the initial ST state, only surface XRD profile is displayed but mid-thickness was also analyzed to ensure that the whole sample was in single β phase. After shot-peening, additional peaks ascribed to α'' martensite were detected for all treated samples. (020) (021), and (130) peaks were the easier to identify although they are quite small. This low intensity may reflect that only a moderate quantity of martensite is actually trapped after this mechanical process, compared to previous heavy cold-rolling. The fact that no other potential peaks associated with martensite were revealed can be attributed to the broadening of β peaks, due to residual stress in the material after the mechanical treatment, or is simply linked to the strong

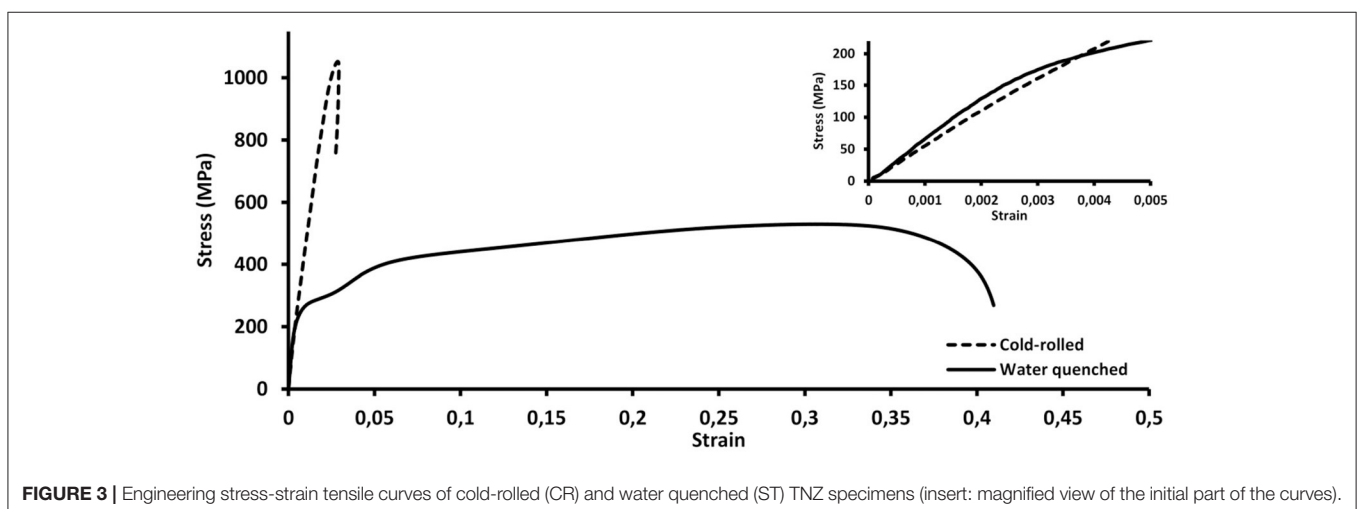


FIGURE 3 | Engineering stress-strain tensile curves of cold-rolled (CR) and water quenched (ST) TNZ specimens (insert: magnified view of the initial part of the curves).

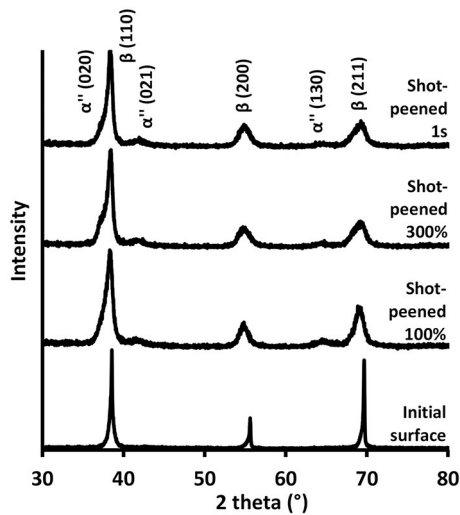


FIGURE 4 | XRD profiles obtained on surface of TNZ samples before (initial surface-ST state) and after shot-peening (at various coverage percentages).

crystallographic variant selection which operates during stress-induced martensitic transformation. Nevertheless, based on the observation of $(020)_{\alpha''}$ peak, which is more pronounced for samples shot-peened at 300% or during 1s, it can be suggested that these tougher conditions led to the creation of a higher amount of martensite, compared to shot-peening at 100%.

Cross-sectional observations carried out before and after mechanical surface treatment are gathered in **Figure 5**. EBSD analysis revealed equiaxed β grains in the initial ST state and additional bands were found for all the samples which were submitted to shot-peening. The density of these bands is very high on extreme surface and is decreasing gradually toward the depth. Furthermore, it may be noted that the size of the affected area seems to correlate with the severity of the shot-peening. Indeed, as can be seen from the bottom part of **Figure 5**, a larger dark saturated zone is observable for the sample submitted to the 1s treatment, which can be regarded as the tougher mechanical process, compared to 300 and 100% coverages. Due to important residual stresses and the fine scale of these new microstructural features, and despite the use of a small step size of $0.2 \mu\text{m}$, EBSD indexation of the bands was difficult to achieve

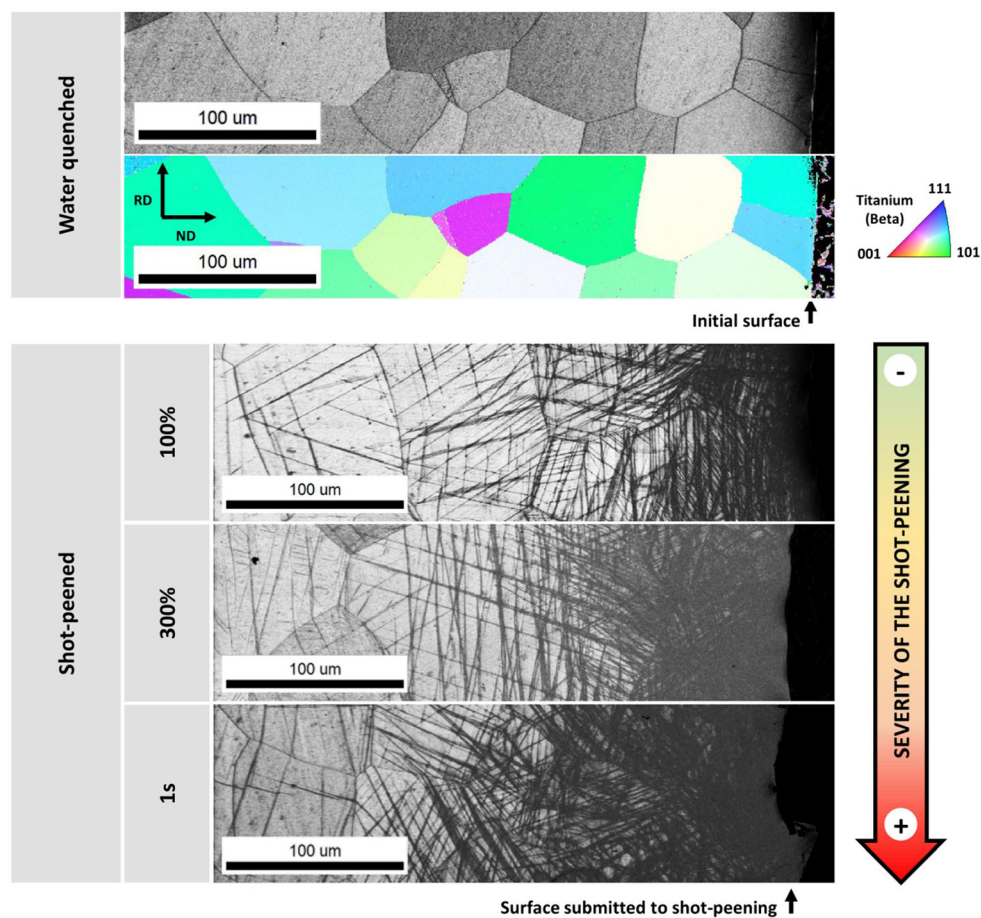


FIGURE 5 | Cross-sectional microstructural observations by scanning electron microscopy of TNZ samples before (top) and after various shot-peening conditions (bottom). Gray scale images correspond to EBSD IQ (Image Quality) maps and the colored one is a crystallographic orientation cartography of the β phase, color coding is given by the standard triangle on the right.

for shot-peened samples. However, based on the shape of these bands, their size, and information from previous XRD analyses, it seems quite obvious to associate them with the presence of α'' martensite. In addition, some features appeared as potential β twins. As a matter of fact, and as illustrated by **Figure 6**, misorientation profiles made across the β matrix and some of the bands revealed misorientation angles of about 50.5° which are typical of $\{332\}\langle 113 \rangle_\beta$ twins. The origin of these twins is not yet clear and investigations did not allow us to determine whether they have been induced during the shot-peening process or whether they have resulted from the reversion of α'' phase, itself created during the deformation process. This second assumption is based on the fact that the reversion of parent $\{130\}\langle 310 \rangle_{\alpha''}$ twins to $\{332\}\langle 113 \rangle_\beta$ twins has already been reported in the literature during unloading of a α'' martensitic titanium alloy (Bertrand et al., 2016; Castany et al., 2016).

Previous elements are all indicators showing that shot-peening was efficient to trigger martensitic transformation in surface of TNZ samples. To evaluate the associated local changes in terms of mechanical properties and highlight the desired elasticity gradient, instrumented micro-indentation tests were conducted. Hardness and modulus profiles obtained from the surface toward the depth of samples shot-peened at a coverage percentage of 300% are given in **Figure 7**. Whereas the mechanical treatment increased the surface hardness, as expected from the literature (Schulze, 2006), mainly because of the residual stresses and the introduction of numerous dislocations into the material, a decrease in indentation modulus (E_{IT}) was also evidenced. Its value falls from about 87 GPa at mid-thickness to 67 GPa on the shot-peened surface of the piece.

It is important to point out that indentation modulus values, computed from indentation experiments using Oliver-Pharr method, are higher than Young's modulus values extracted from tensile curves. This overestimation at nano- or micro-scale compared to macro-scale has already been reported in previous works (Fizanne-Michel et al., 2014). Nonetheless, despite the shift that might exist, the two moduli remain comparable as they

follow the same evolution, making it possible to bring to light the presence of an elasticity gradient. It can be observed that data points are slightly scattered. In addition to experimental uncertainty, which was estimated to be around ± 2 GPa in a preliminary work, this dispersion could be attributed to the large grain size of our material (up to about $100\ \mu\text{m}$). As a matter of fact, recent study showed a significant influence of crystal orientation on indentation modulus in a superelastic titanium alloy, highlighting the strong elastic anisotropy of the β phase (Jabir et al., 2019). Yet, in our tested range, diagonals of the indentation prints are only about $20\ \mu\text{m}$ long and reflect, therefore, the contribution of only one single grain in most cases.

As can be seen from the bottom part of **Figure 7**, the evolution of the mechanical properties is well correlated with the evolution of the microstructure. From the depth to the surface, a clear relationship can be established between the decrease in the elastic modulus and the increase in the band density, both related to a higher amount of martensite near the surface. Concerning the depth affected by the mechanical treatment, it is worth noting that changes in properties extend over $\sim 400\ \mu\text{m}$ for these shot-peening conditions. This gradient depth would be particularly appropriate to the current common size of dental implants (diameter from 3 to 5 mm).

These results validate the strategy we developed and establish a proof of concept that mechanical surface treatment of a biocompatible β -metastable titanium alloy can induce martensitic transformation on surface, and that this microstructural gradient can lead to an elasticity gradient. This turns out to be promising for dental implantology, as the resulting decrease in modulus obtained in surface should help avoid stress-shielding issues and thus promote osseointegration of the implant. In other words, it should mechanically improve the biocompatibility of implanted devices.

Furthermore, the method that was chosen in our study, namely shot-peening, is particularly relevant because it creates a rough surface which could certainly enhance not only bone remodeling but also fatigue performance of the implant. Further

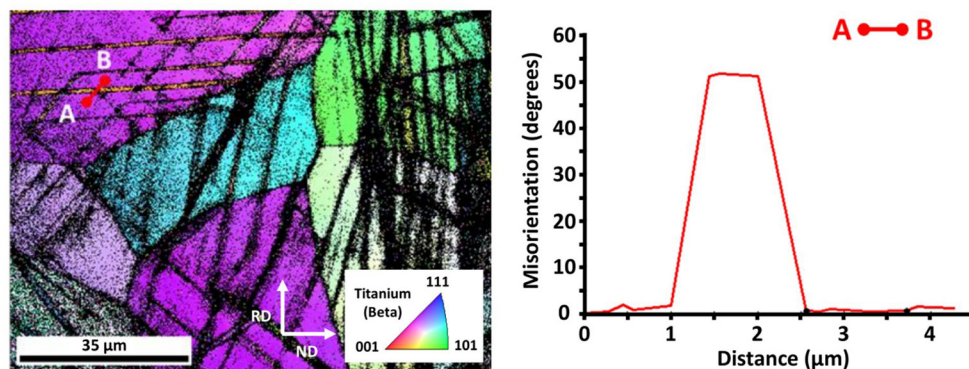


FIGURE 6 | EBSD crystallographic orientation cartography of β phase obtained on a TNZ sample submitted to shot-peening at a coverage percentage of 100% (left). Acquisition was made about $150\ \mu\text{m}$ away from the surface to get better confidence index. Misorientation profile between A and B points indicated on the orientation map (right).

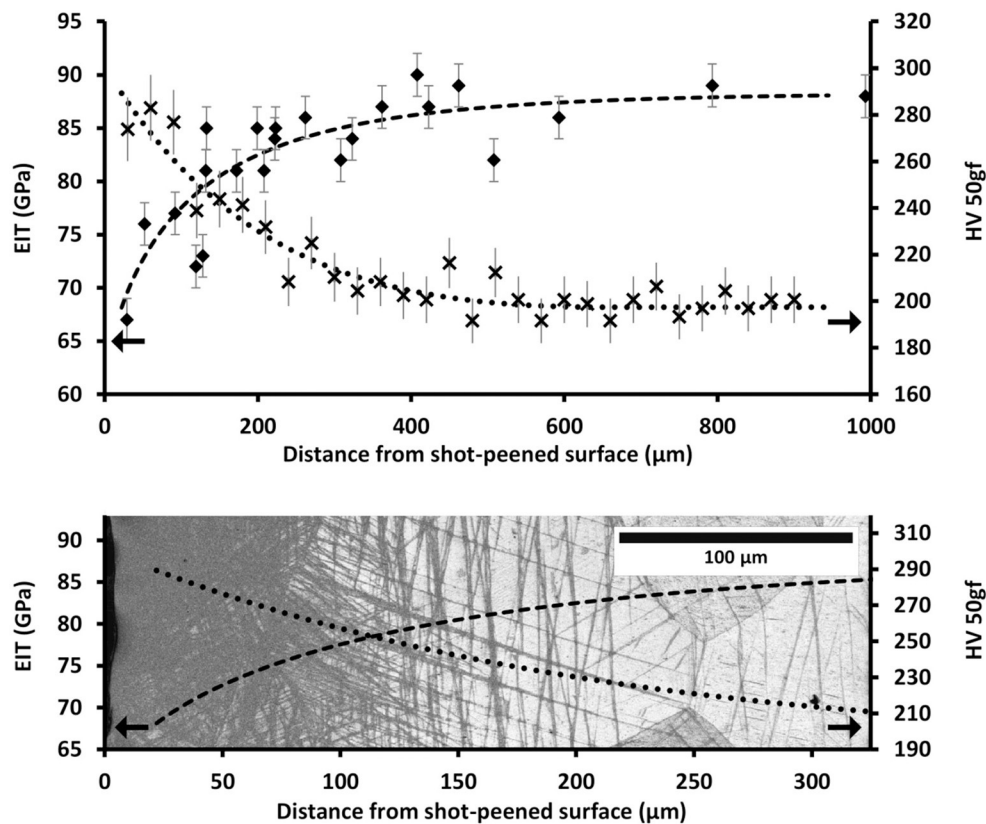


FIGURE 7 | Hardness and modulus profiles obtained from instrumented micro-indentation measurements conducted on a TNZ sample submitted to shot-peening at a coverage percentage of 300% (top). First part of the curves (surface) superimposed on the EBSD Image Quality map corresponding to this sample (bottom).

specific mechanical and biological tests should be conducted to check these properties. The impact of the shot-peening process on a threading should also be assessed to ensure it does not damage this important part of the device. In case of deterioration, thread-rolling could be considered as an attractive alternative in the production of dental implants, since it could be a suitable process to create the threaded part and induce the desired surface deformation at the same time (Domblesky and Feng, 2002).

Although the depth of created gradient, of about 400 μm , seems convenient for the intended application, the mechanical strength of the core material or the amplitude of modulus change could be optimized. Regarding TNZ alloy, future work could concern the modification of the solution treatment parameters in order to reduce the grain size. This would strengthen the material due to Hall-Petch effect and would also be more desirable for indentation measurements. In addition, it may be relevant to try applying the strategy we built to other β -metastable alloys or, even, to develop new strategies suitable for other types of titanium alloys. This could be done by investigating other microstructural states and identifying those which can also cause changes in the elastic modulus.

CONCLUSION

According to the results presented in this study, the following conclusions can be drawn:

- (1) Stress-induced martensitic transformation in a β metastable biocompatible Ti-20Nb-6Zr (at.%) alloy led to a decrease in elastic modulus. This has given rise to a novel strategy consisting in applying a surface mechanical treatment on a β phase titanium alloy in order to create an elasticity gradient.
- (2) Shot-peening turned out to be efficient to induce local deformation, microstructural gradient based on martensitic transformation, and thus to create an elasticity gradient.
- (3) Local evolution of elastic modulus was measured by instrumented micro-indentation and a gradient in indentation modulus from 87 GPa in the core material to 67 GPa on surface, over 400 μm , was revealed after shot-peening at a coverage percentage of 300%.
- (4) Creation of elasticity gradient is a promising way to avoid stress-shielding issues, promote osseointegration and produce implanted devices with mechanically enhanced biocompatibility.

DATA AVAILABILITY STATEMENT

The raw data supporting the conclusions of this article will be made available by the authors, without undue reservation.

AUTHOR CONTRIBUTIONS

SD collected the experimental data, performed the data analysis, produced the figures, and wrote the manuscript. SB and PL were involved in planning and supervising, respectively, instrumented indentation measurements, and shot-peening experiments. FP conceived the original idea, directed this research project and contributed to the interpretation of the results. LJ helped

supervise the project. All authors contributed to the article and approved the submitted version.

FUNDING

BIOTECH DENTAL company is gratefully acknowledged for its financial support on SD grant.

ACKNOWLEDGMENTS

The authors would like to thank Yulin Hao for the supply of TNZ alloy. They are also grateful to PIMM laboratory (ENSAM, CNAM, CNRS) for access to their instrumented indentation equipment.

REFERENCES

- Bandyopadhyay, A., Espana, F., Balla, V. K., Bose, S., and Davies, N. M. (2010). Influence of porosity on mechanical properties and in vivo response of Ti-6Al-4V implants. *Acta Biomater.* 6, 1640–1648. doi: 10.1016/j.actbio.2009.11.011
- Bertrand, E., Castany, P., Yang, Y., Menou, E., and Gloriant, T. (2016). Deformation twinning in the full- α' martensitic Ti-25Ta-20Nb shape memory alloy. *Acta Mater.* 105, 94–103. doi: 10.1016/j.actamat.2015.12.001
- Brizuela, A., Herrero-Climent, M., Rios-Carrasco, E., Rios-Santos, J. V., Pérez, R. A., Manero, J. M., et al. (2019). Influence of the elastic modulus on the osseointegration of dental implants. *Materials (Basel)*. 12, 1–7. doi: 10.3390/ma12060980
- Castany, P., Yang, Y., Bertrand, E., and Gloriant, T. (2016). Reversion of a parent {130}<310> α' martensitic twinning system at the origin of {332}<113> β twins observed in metastable β titanium alloys. *Phys. Rev. Lett.* 117:245501. doi: 10.1103/PhysRevLett.117.245501
- Consolaro, A., Carvalho, R. S., de Francischone, C. E. J., Consolaro, M. F. M. O., and Francischone, C. E. (2010). Saucerization of osseointegrated implants and planning of simultaneous orthodontic clinical cases. *Dental. Press J. Orthod.* 15, 19–30. doi: 10.1590/S2176-94512010000300003
- Doherty, P. J., Williams, R. L., Williams, D. F., and Lee, A. J. C. (1992). *Biomaterial-Tissue Interfaces: Proceedings of the Ninth European Conference on Biomaterials, Chester, U.K., September 9–11, 1991*. Amsterdam: Elsevier.
- Domblesky, J. P., and Feng, F. (2002). Two-dimensional and three-dimensional finite element models of external thread rolling. *Proc. Inst. Mech. Eng. Part B J. Eng. Manuf.* 216, 507–517. doi: 10.1243/0954405021520201
- Fizanne-Michel, C., Cornen, M., Castany, P., Péron, I., and Gloriant, T. (2014). Determination of hardness and elastic modulus inverse pole figures of a polycrystalline commercially pure titanium by coupling nanoindentation and EBSD techniques. *Mater. Sci. Eng. A* 613, 159–162. doi: 10.1016/j.msea.2014.06.098
- Geetha, M., Singh, A. K., Asokamani, R., and Gogia, A. K. (2009). Ti based biomaterials, the ultimate choice for orthopaedic implants—a review. *Prog. Mater. Sci.* 54, 397–425. doi: 10.1016/j.pmatsci.2008.06.004
- Gomes, C. C., Moreira, L. M., Santos, V. J. S. V., Ramos, A. S., Lyon, J. P., Soares, C. P., et al. (2011). Assessment of the genetic risks of a metallic alloy used in medical implants. *Genet. Mol. Biol.* 34, 116–121. doi: 10.1590/S1415-47572010005000118
- Jabir, H., Fillon, A., Castany, P., and Gloriant, T. (2019). Crystallographic orientation dependence of mechanical properties in the superelastic Ti-24Nb-4Zr-8Sn alloy. *Phys. Rev. Mater.* 3, 1–11. doi: 10.1103/PhysRevMaterials.3.063608
- Javier Gil, F., Planell, J. A., Padrós, A., and Aparicio, C. (2007). The effect of shot blasting and heat treatment on the fatigue behavior of titanium for dental implant applications. *Dent. Mater.* 23, 486–491. doi: 10.1016/j.dental.2006.03.003
- Kitamura, E., Stegaroiu, R., Nomura, S., and Miyakawa, O. (2004). Biomechanical aspects of marginal bone resorption around osseointegrated implants: considerations based on a three-dimensional finite element analysis. *Clin. Oral Implants Res.* 15, 401–412. doi: 10.1111/j.1600-0501.2004.01022.x
- Koshy, E., and Philip, S. R. (2015). Dental implant surfaces: an overview. *Int. J. Clin. Implant Dent.* 1, 14–22. doi: 10.5005/jp-journals-10004-1028
- Kroger, H., Venesmaa, P., Jurvelin, J., Miettinen, H., Suomalainen, O., and Alhava, E. (1998). Bone density at the proximal femur after total hip arthroplasty. *Clin. Orthop. Relat. Res.* 352, 66–74. doi: 10.1097/00003086-199807000-00009
- Kuroda, D., Niinomi, M., Morinaga, M., Kato, Y., and Yashiro, T. (1998). Design and mechanical properties of new β type titanium alloys for implant materials. *Mater. Sci. Eng. A* 243, 244–249. doi: 10.1016/S0921-5093(97)00808-3
- Laheurte, P., Elmay, W., Prima, F., and Gloriant, T. (2014). “Titane et alliages: Des matériaux de choix pour les applications médicales,” in *Techniques de l'ingénieur (M4781)*. Available online at: <https://www.techniques-ingenieur.fr/base-documentaire/materiaux-th11/metaux-et-alliages-non-ferreux-42357210/titane-et-alliages-m4781/> (accessed March 03, 2021).
- Laing, P. G., Ferguson, A. B., and Hodge, E. S. (1967). Tissue reaction in rabbit muscle exposed to metallic implants. *J. Biomed. Mater. Res.* 1, 135–149. doi: 10.1002/jbm.820010113
- Li, S. J., Xu, Q. S., Wang, Z., Hou, W. T., Hao, Y. L., Yang, R., et al. (2014). Influence of cell shape on mechanical properties of Ti-6Al-4V meshes fabricated by electron beam melting method. *Acta Biomater.* 10, 4537–4547. doi: 10.1016/j.actbio.2014.06.010
- Lin, D., Li, Q., Li, W., and Swain, M. (2010). Bone remodeling induced by dental implants of functionally graded materials. *J. Biomed. Mater. Res. B. Appl. Biomater.* 92, 430–438. doi: 10.1002/jbm.b.31531
- Liu, Y., Bao, C., Wismeijer, D., and Wu, G. (2015). The physicochemical/biological properties of porous tantalum and the potential surface modification techniques to improve its clinical application in dental implantology. *Mater. Sci. Eng. C* 49, 323–329. doi: 10.1016/j.msec.2015.01.007
- Mariani, P., Margossian, P., and Laborde, G. (2008). Choix d'un concept occlusal en implantologie—1ère partie : données fondamentales. *Strat. prothétique* 8, 145–153. Available online at: https://www.idweblogs.com/wp-content/uploads/2013/06/10588_spvol8n1p5-13.pdf (accessed March 03, 2021).
- Mehrali, M., Shirazi, F. S., Mehrali, M., Metselaar, H. S. C., Kadri, N. A. B., and Osman, N. A. A. (2013). Dental implants from functionally graded materials. *J. Biomed. Mater. Res. A* 101A, 3046–3057. doi: 10.1002/jbm.a.34588
- Mimura, K., Watanabe, K., Okawa, S., Kobayashi, M., and Miyakawa, O. (2004). Morphological and chemical implant characterizations of the interface of a hydroxyapatite-coated implant. *Dent. Mater. J.* 23, 353–360. doi: 10.4012/dmj.23.353
- Niinomi, M., and Nakai, M. (2011). Titanium-based biomaterials for preventing stress shielding between implant devices and bone. *Int. J. Biomater.* 2011:836587. doi: 10.1155/2011/836587
- Okulov, I. V., Weissmüller, J., and Markmann, J. (2017). Dealloying-based interpenetrating-phase nanocomposites matching the elastic behavior of human bone. *Sci. Rep.* 7, 1–7. doi: 10.1038/s41598-017-00048-4
- Oldani, C., and Dominguez, A. (2012). “Titanium as a biomaterial for implants,” in *Recent Advances in Arthroplasty (InTech)*. doi: 10.5772/27413

- Available online at: <http://www.intechopen.com/books/recent-advances-in-arthroplasty/titanium-as-a-biomaterial-for-implants>. (accessed March 03, 2021).
- Oliver, W. C., and Pharr, G. M. (1992). An improved technique for determining hardness and elastic modulus using load and displacement sensing indentation experiments. *J. Mater. Res.* 7, 1564–1583. doi: 10.1557/JMR.1992.1564
- Oliver, W. C., and Pharr, G. M. (2004). Measurement of hardness and elastic modulus by instrumented indentation: advances in understanding and refinements to methodology. *J. Mater. Res.* 19, 3–20. doi: 10.1557/jmr.2004.19.1.3
- Oshida, Y., Tuna, E. B., Aktören, O., and Gençay, K. (2010). Dental implant systems. *Int. J. Mol. Sci.* 11, 1580–1678. doi: 10.3390/ijms11041580
- Piotrowski, B., Baptista, A. A., Patoor, E., Bravetti, P., Eberhardt, A., and Laheurte, P. (2014). Interaction of bone-dental implant with new ultra low modulus alloy using a numerical approach. *Mater. Sci. Eng. C* 38, 151–160. doi: 10.1016/j.msec.2014.01.048
- Prima, F., and Nowak, S. (2012). *Metallic Material With an Elasticity Gradient*. Patent WO 2012/059895 A1. World Intellectual Property Organization (WIPO), Geneva. Available online at: <https://patentscope.wipo.int/search/en/detail.jsf?docId=WO2012059895> (accessed March 03, 2021).
- Rao, S., Ushida, T., Tateishi, T., Okazaki, Y., and Asao, S. (1996). Effect of Ti, Al, and V ions on the relative growth rate of fibroblasts (L929) and osteoblasts (MC3T3-E1) cells. *Biomed. Mater. Eng.* 6, 79–86. doi: 10.3233/BME-1996-6202
- Rieger, R., Hambl, R., and Jennane, R. (2011). Modeling of biological doses and mechanical effects on bone transduction. *J. Theor. Biol.* 274, 36–42. doi: 10.1016/j.jtbi.2011.01.003
- Riley, M. R., Boesewetter, D. E., Kim, A. M., and Sirvent, F. P. (2003). Effects of metals Cu, Fe, Ni, V, and Zn on rat lung epithelial cells. *Toxicology* 190, 171–184. doi: 10.1016/S0300-483X(03)00162-8
- Schneider, S., Schneider, S. G., Da Silva, H., and de Moura Neto, C. (2005). Study of the non-linear stress-strain behavior in Ti-Nb-Zr alloys. *Mater. Res.* 8, 435–438. doi: 10.1590/S1516-14392005000400013
- Schulze, V. (ed.). (2006). *Modern Mechanical Surface Treatment: States, Stability, Effects*. Weinheim: Wiley-VCH. doi: 10.1002/3527607811
- Shi, L., Wang, L., Duan, Y., Lei, W., Wang, Z., Li, J., et al. (2013). The improved biological performance of a novel low elastic modulus implant. *PLoS ONE* 8:e55015. doi: 10.1371/journal.pone.0055015
- Steinemann, S. G. (1980). “Corrosion of surgical implants—in vivo and in vitro tests,” in *Evaluation of Biomaterials*, eds G. D. Winter, J. L. Leray, and K. de Groot (Chichester: Wiley), 1–34.
- Sun, F., Hao, Y. L., Nowak, S., Gloriant, T., Laheurte, P., and Prima, F. (2011). A thermo-mechanical treatment to improve the superelastic performances of biomedical Ti-26Nb and Ti-20Nb-6Zr (at.%) alloys. *J. Mech. Behav. Biomed. Mater.* 4, 1864–1872. doi: 10.1016/j.jmbbm.2011.06.003
- Sun, F., Nowak, S., Gloriant, T., Laheurte, P., Eberhardt, A., and Prima, F. (2010). Influence of a short thermal treatment on the superelastic properties of a titanium-based alloy. *Scr. Mater.* 63, 1053–1056. doi: 10.1016/j.scriptamat.2010.07.042
- US Food and Drug Administration (2019). *Biological Responses to Metal Implants*. Available online at: <https://www.fda.gov/media/131150/download> (accessed March 03, 2021).
- Walker, P. R., LeBlanc, J., and Sikorska, M. (1989). Effects of aluminum and other cations on the structure of brain and liver chromatin. *Biochemistry* 28, 3911–3915. doi: 10.1021/bi00435a043
- Wally, Z., van Grunsven, W., Claeysens, F., Goodall, R., and Reilly, G. (2015). Porous titanium for dental implant applications. *Metals (Basel)* 5, 1902–1920. doi: 10.3390/met5041902
- Williams, D. F. (1987). *Definitions in Biomaterials: Proceedings of a Consensus Conference of the European Society for Biomaterials (ESB)*, Chester, England, March 3–5, 1986. Amsterdam: Elsevier.
- Williams, D. F. (2003). Revisiting the definition of biocompatibility. *Med. Device Technol.* 14, 10–13. doi: 10.1016/S1369-7021(03)01019-8
- Xue, T., Attarilar, S., Liu, S., Liu, J., Song, X., Li, L., et al. (2020). Surface modification techniques of titanium and its alloys to functionally optimize their biomedical properties: thematic review. *Front. Bioeng. Biotechnol.* 8:603072. doi: 10.3389/fbioe.2020.603072
- Yue, S., Pilliar, R. M., and Weatherly, G. C. (1984). The fatigue strength of porous-coated Ti-6%Al-4%V implant alloy. *J. Biomed. Mater. Res.* 18, 1043–1058. doi: 10.1002/jbm.820180908
- Zhang, J. Y., Sun, F., Hao, Y. L., Gozdecki, N., Lebrun, E., Vermaut, P., et al. (2013). Influence of equiatomic Zr/Nb substitution on superelastic behavior of Ti-Nb-Zr alloy. *Mater. Sci. Eng. A* 563, 78–85. doi: 10.1016/j.msea.2012.11.045
- Zhang, L. C., and Chen, L. Y. (2019). A review on biomedical titanium alloys: recent progress and prospect. *Adv. Eng. Mater.* 21:1801215. doi: 10.1002/adem.201801215
- Zheng, Y., Zhang, B., Wang, B., and Li, L. (2012). “New kind of titanium alloys for biomedical application,” in *Integrated Biomaterials for Biomedical Technology*, eds M. Ramalingam, A. Tiwari, S. Ramakrishna, and H. Kobayashi (Salem, MA: Scrivener Publishing LLC), 253–272. doi: 10.1002/9781118482513.ch6

Conflict of Interest: SD is employed by the company BIOTECH DENTAL.

The remaining authors declare that the research was conducted in the absence of any commercial or financial relationships that could be construed as a potential conflict of interest.

Copyright © 2021 Delannoy, Baiz, Laheurte, Jordan and Prima. This is an open-access article distributed under the terms of the Creative Commons Attribution License (CC BY). The use, distribution or reproduction in other forums is permitted, provided the original author(s) and the copyright owner(s) are credited and that the original publication in this journal is cited, in accordance with accepted academic practice. No use, distribution or reproduction is permitted which does not comply with these terms.



Mg/ZrO₂ Metal Matrix Nanocomposites Fabricated by Friction Stir Processing: Microstructure, Mechanical Properties, and Corrosion Behavior

Ke Qiao^{1*}, Ting Zhang¹, Kuaishe Wang¹, Shengnan Yuan¹, Shengyi Zhang¹, Liqiang Wang², Zhi Wang¹, Pai Peng¹, Jun Cai¹, Chaozong Liu^{3*} and Wen Wang^{1*}

OPEN ACCESS

Edited by:

David K. Mills,
Louisiana Tech University,
United States

Reviewed by:

Joanna Mystkowska,
Bialystok University of Technology,
Poland
K. K. Deng,
Taiyuan University of Technology,
China

*Correspondence:

Ke Qiao
qiaoke_2020@126.com
Chaozong Liu
chaozong.liu@ucl.ac.uk
Wen Wang
wangwen2016@126.com

Specialty section:

This article was submitted to
Biomaterials,
a section of the journal
Frontiers in Bioengineering and
Biotechnology

Received: 11 September 2020

Accepted: 24 February 2021

Published: 25 March 2021

Citation:

Qiao K, Zhang T, Wang K, Yuan S,
Zhang S, Wang L, Wang Z, Peng P,
Cai J, Liu C and Wang W (2021)
Mg/ZrO₂ Metal Matrix
Nanocomposites Fabricated by
Friction Stir Processing:
Microstructure, Mechanical
Properties, and Corrosion Behavior.
Front. Bioeng. Biotechnol. 9:605171.
doi: 10.3389/fbioe.2021.605171

¹ School of Metallurgical Engineering, National and Local Joint Engineering Research Center for Functional Materials Processing, Xi'an University of Architecture and Technology, Xi'an, China, ² State Key Laboratory of Metal Matrix Composites, School of Materials Science and Engineering, Shanghai Jiao Tong University, Shanghai, China, ³ Institute of Orthopaedics and Musculoskeletal Science, University College London, Royal National Orthopaedic Hospital, Stanmore, United Kingdom

Magnesium (Mg) and its alloys have attracted more and more attention because of their potential as a new type of biodegradable metal materials. In this work, AZ31/ZrO₂ nanocomposites with good uniformity were prepared successfully by friction stir processing (FSP). The scanning electron microscope (SEM) and transmission electron microscope (TEM) were used to characterize the microstructure of the composites. The mechanical properties, electrochemical corrosion properties and biological properties were evaluated. In addition, the effect of reinforced particles (ZrO₂) on the microstructure and properties of the composite was studied comparing with FSP AZ31 Mg alloy. The results show that compared with the base metal (BM), the AZ31/ZrO₂ composite material achieves homogenization, densification, and grain refinement after FSP. The combination of dynamic recrystallization and ZrO₂ particles leads to grain refinement of Mg alloy, and the average grain size of AZ31/ZrO₂ composites is 3.2 μm. After FSP, the c-axis of grain is deflected under the compression stress of shoulder and the shear stress of pin. The ultimate tensile strength (UTS) and yield strength (YS) of BM were 283 and 137 MPa, respectively, the UTS and YS of AZ31/ZrO₂ composites were 427 and 217 MPa, respectively. The grain refinement and Orowan strengthening are the major strengthening mechanisms. Moreover, the corrosion resistance in simulated body fluid of Mg alloy is improved by grain refinement and the barrier effect of ZrO₂.

Keywords: Friction stir processing, microstructure, mechanical properties, corrosion properties, texture

INTRODUCTION

Magnesium (Mg) and its alloys are considered to have great potential in biomedical application due to the high strength-to-weight ratio, good biocompatibility and promotion of bone cell healing (Staiger et al., 2006; Castellani et al., 2011; Henderson et al., 2014). However, the high corrosion and degradation rates *in vivo*, and the low strength limit their application development

(Morisada et al., 2006a). Previous studies have shown that the Mg matrix composites prepared by adding secondary particles to Mg can significantly reduce the corrosion and degradation rates, thus improve strength, corrosion resistance, and biocompatibility (Lan et al., 2004; Wang et al., 2004; Ugandhar et al., 2006).

At present, powder metallurgy (Davis and Ward, 1993), in-situ fabrication (Daniel et al., 1997), spray deposition (Lavernia and Grant, 1988), and stir casting (Hashim et al., 1999) are commonly used to fabricate composites. However, the composites fabricated by the above methods have many defects such as voids, which is eliminated by severe plastic deformation methods such as extrusion and rolling, leading to a longer process and higher cost. Therefore, it is necessary to develop an effective technique to prepare high-quality composites.

Friction stir processing (FSP) is an alternative solid-state processing technology for producing Mg matrix composites, based on the principles of friction stir welding (FSW), potentially addressing the above-mentioned limitations (Mishra and Ma, 2005). Specifically, FSP can achieve the homogenization, densification, and grain refinement of microstructure simultaneously (Ammouri et al., 2015; Ni et al., 2016; Xu and Bao, 2016), thus improve the mechanical properties and corrosion properties of materials. In 2006, Morisada et al. (2006b) first prepared AZ31/MWCNTs (multi-walled carbon nanotubes) surface composites by FSP. It was reported that the low temperature could avoid the interfacial reaction between reinforced particles and Mg matrix during FSP. Furthermore, severe plastic deformation contributed to the fragment and uniform mixing of reinforced particles. This work has attracted many research interests in the preparation of Mg matrix composites by FSP.

So far, a lot of reinforced particles, such as TiC (Balakrishnan et al., 2015; Navazani and Dehghani, 2015), TiAlC (Gobara et al., 2015), Al₂O₃ (Azizieh et al., 2018), B₄C (Vedabouriswaran and Aravindan, 2018), MWCNT (Morisada et al., 2006b; Arab et al., 2017), and SiC (Morisada et al., 2006a) have been added in Mg matrix by FSP, improving the mechanical properties of the alloys. For example, Navazani and Dehghani (2015) and Balakrishnan et al. (2015) studied the microstructure and mechanical properties of AZ31/TiC composites fabricated by FSP. The results showed that TiC particles distributed uniformly in AZ31 Mg matrix after FSP, which promoted the grain refinement and improved the microhardness. According to the research of Azizieh et al. (2018), adding Al₂O₃ to AZ31 Mg alloy with FSP effectively increased the wear resistance of the material. It has been reported (Vedabouriswaran and Aravindan, 2018) that after adding B₄C particles to RZ 5 Mg alloy, the coarse grains in base metal (BM) become the fine grains in composites due to the pinning effect of reinforced particles. The microhardness and tensile strength from 81 HV and 200 MPa (BM) increased to 403 HV and 320 MPa (composites), respectively. This phenomenon also be founded in AZ31/SiC composites fabricated by FSP (Morisada et al., 2006a). However, there are few reports on the above-mentioned reinforcing particles for improving biocompatibility of Mg alloys, it is vital to find other materials to address the above problem.

Studies have shown that the addition of ZrO₂ particles in Mg matrix contributes to the mechanical properties and biocompatibility of materials (Navazani and Dehghani, 2016; Vignesh et al., 2019). For example, Navazani and Dehghani (2016) added ZrO₂ particles to AZ31 Mg plate through FSP, then observed that the particles promote the grain refinement and improve the mechanical properties of composites. Vignesh et al. (2019) prepared AZ91D-ZrO₂ surface composites by FSP. It was reported that the combination of FSP and ZrO₂ reduced the grain size, and broke and disperse the secondary particles. The dispersion of ZrO₂ particles can increase the accumulated surface potential, thereby improving the corrosion resistance of composites. However, only simply characterize and evaluate the microstructure and performance of ZrO₂/Mg matrix composites in previous researches, the influence mechanism of microstructure on mechanical properties and corrosion resistance has not been thoroughly and comprehensively analyzed and discussed.

In view of the above problems, AZ31/ZrO₂ nanocomposites are prepared in this work by FSP. The microstructure, mechanical properties, and corrosion resistance of AZ31 Mg alloy and AZ31/ZrO₂ nanocomposites are analyzed in detail to clarify the influence of FSP and ZrO₂ particles on the Mg alloy, respectively. The present work intends to provide a new insight for the preparation of biomedical Mg matrix composites.

MATERIALS AND EXPERIMENTAL METHODS

Materials Preparation

A rolled AZ31 Mg plate with a dimension of 100 mm × 80 mm × 3 mm was used as Base metal (BM) in this work. ZrO₂ powder with a diameter ranging from 50 to 150 nm and an average diameter of 80 nm was used as reinforcement as shown in **Figure 1**. The volume fraction of the ZrO₂ particles added to the plate is about 17.6%. Holes with diameter of 3 mm, depth of 1 mm and hole spacing of 10 mm were drilled by a drilling machine on the surface of the AZ31 Mg alloy plates. After filling the prefabricated holes with ZrO₂ particles, these plates were processed by FSP. The AZ31 Mg alloy plates with and without ZrO₂ particles were processed on a FSP machine (LM-BM16), respectively. The stir tool consisting of cylindrical shoulder of 20 mm in diameter, pin of 2 mm in length and 4 mm in diameter. The tool rotation speed was 1180 rpm, the processing speed was 23.5 mm/min, the tilt angle was 2° and the plunge depth was 0.5 mm. All samples were processed six passes. The schematic of the FSP is shown in **Figure 2**. Here into, AZ31 Mg alloy sample without ZrO₂ particles by FSP is marked as FSP, and the AZ31 Mg alloy sample with ZrO₂ particles is marked as FSP-ZrO₂.

Microstructural Characterization

Metallographic specimens were taken along the perpendicular PD with a dimension of 20 mm × 5 mm × 3 mm, which were grinded, polished, and etched by picric acid etching

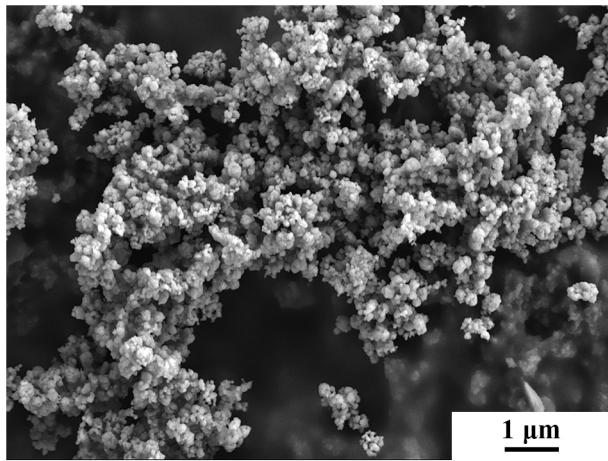


FIGURE 1 | SEM micrograph of ZrO₂ powder.

solution (10 mL acetic acid + 10 mL water + 4.2 g picric acid dissolved in 100 mL alcohol) for 10 s. The microstructures were observed using scanning electron microscope (SEM, Gemini SEM 300) with electron backscatter diffraction (EBSD) at a voltage of ~ 5 kv. The samples were electrolytically polished in a 10 vol.% of perchloric acid solution at a voltage of ~ 10 V and a temperature of -20°C . TEM samples with a dimension of $10\text{ mm} \times 10\text{ mm} \times 1\text{ mm}$ were cut from stir zone (SZ) in FSP-ZrO₂, and ground to a thickness of approximately to $40\text{ }\mu\text{m}$ with sandpaper, and

then the twin-jet electropolishing was conducted using 6% perchloric acid ethanol solution at -30°C . TEM observations were performed on JEM-200CX equipment at a voltage of ~ 120 kv.

Mechanical Properties

The hardness sample with the dimension of $20\text{ mm} \times 5\text{ mm} \times 3\text{ mm}$ were cut along the vertical PD. The hardness testing was carried on the TD \times ND plane using a 401MVD microhardness tester with a loading of 100 g and a dwell time of 10 s. Indentations spacing were 0.5 mm in this work. The tensile specimens with a gauge section dimension of $34\text{ mm} \times 8\text{ mm} \times 3\text{ mm}$ were cut along PD, ground and polished, then tested on an Instron 8,801 equipment at room temperature. The strain rate was $1.0 \times 10^{-3}\text{ s}^{-1}$. Each testing was repeated at least three times to ensure the accuracy of data. The fracture surfaces of tensile specimens were characterized by SEM.

Electrochemical Corrosion Performance

The electrochemical corrosion samples with a dimension of $8\text{ mm} \times 8\text{ mm} \times 3\text{ mm}$ were cut from BM, FSP (SZ), and FSP-ZrO₂ (SZ). After grinding and polishing the sample, the electrochemical test was performed on the Gamry Reference 600 + instrument. The corrosion solution was simulated body fluid (8.035 g/L). NaCl, 0.355 g/L NaHCO₃, 0.225 g/L KCl, 0.231 g/L K₂HPO₄·3H₂O, 0.311 g/L MgCl₂·6H₂O, 39 mL/L HCl (1 mol/L), 0.292 g/L CaCl₂, 0.072 g/L NaSO₄, 6.118 g/L Tris, 1 mol/L HCl) (Kokubo and Takadama, 2006). The samples

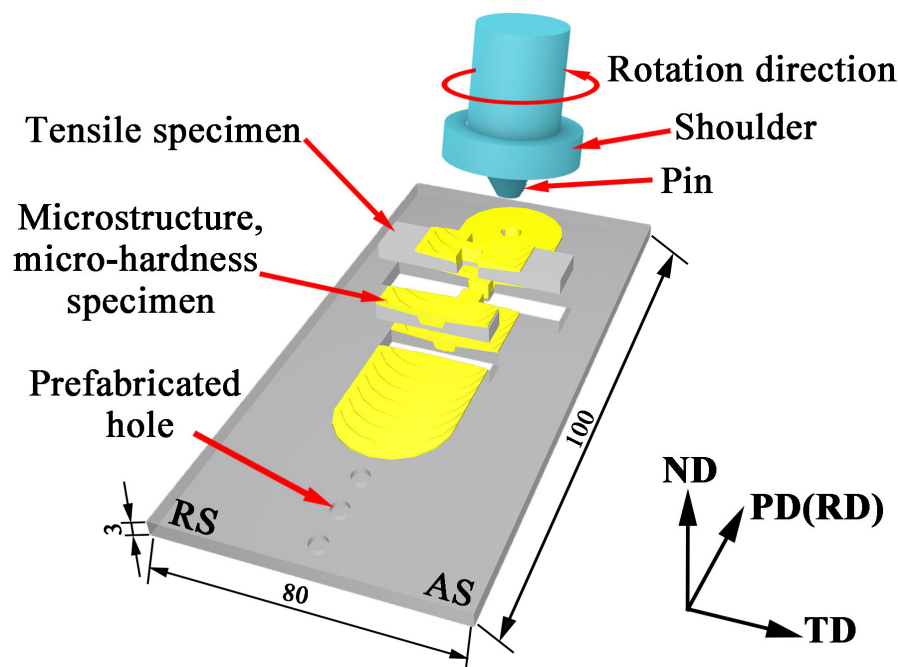


FIGURE 2 | Schematic of the FSP. (AS and RS represent the advancing and retreating sides, respectively. PD, TD, and ND represent processing, transverse, and normal directions, respectively. Unit: mm).

were used as the working electrodes, Ag/AgCl (saturated KCl) and platinum strip were used as the reference and counter electrodes, respectively. Before recording the potentiodynamic polarization curves, the samples were soaked in the simulated body fluid (SBF) solution for 300 s to get the steady reaction condition. The impedance measurement scan frequency ranges from 100,000 Hz to 0.1 Hz with an excitation signal amplitude is 10 mV. The impedance data were analyzed using the ZSimpWin software. The initial potential is reduced by 500 mV relative to the open circuit potential (OCP), and the termination potential is increased by 1.5 V relative to the

OCP. The scan rate is 1 mV/s, and the test temperature is room temperature.

Scanning Vibrating Electrode Technique (SVET) Measurement

The SVET samples were cut from BM, and SZ of the FSP and FSP-ZrO₂ samples with a dimension of 8 μm \times 8 μm . After grinding and polishing, they were tested on the Princeton VersaSCAN instrument. The measurements were performed in SBF and at an OCP. The scanning range was 600 μm \times 600 μm , the scanning

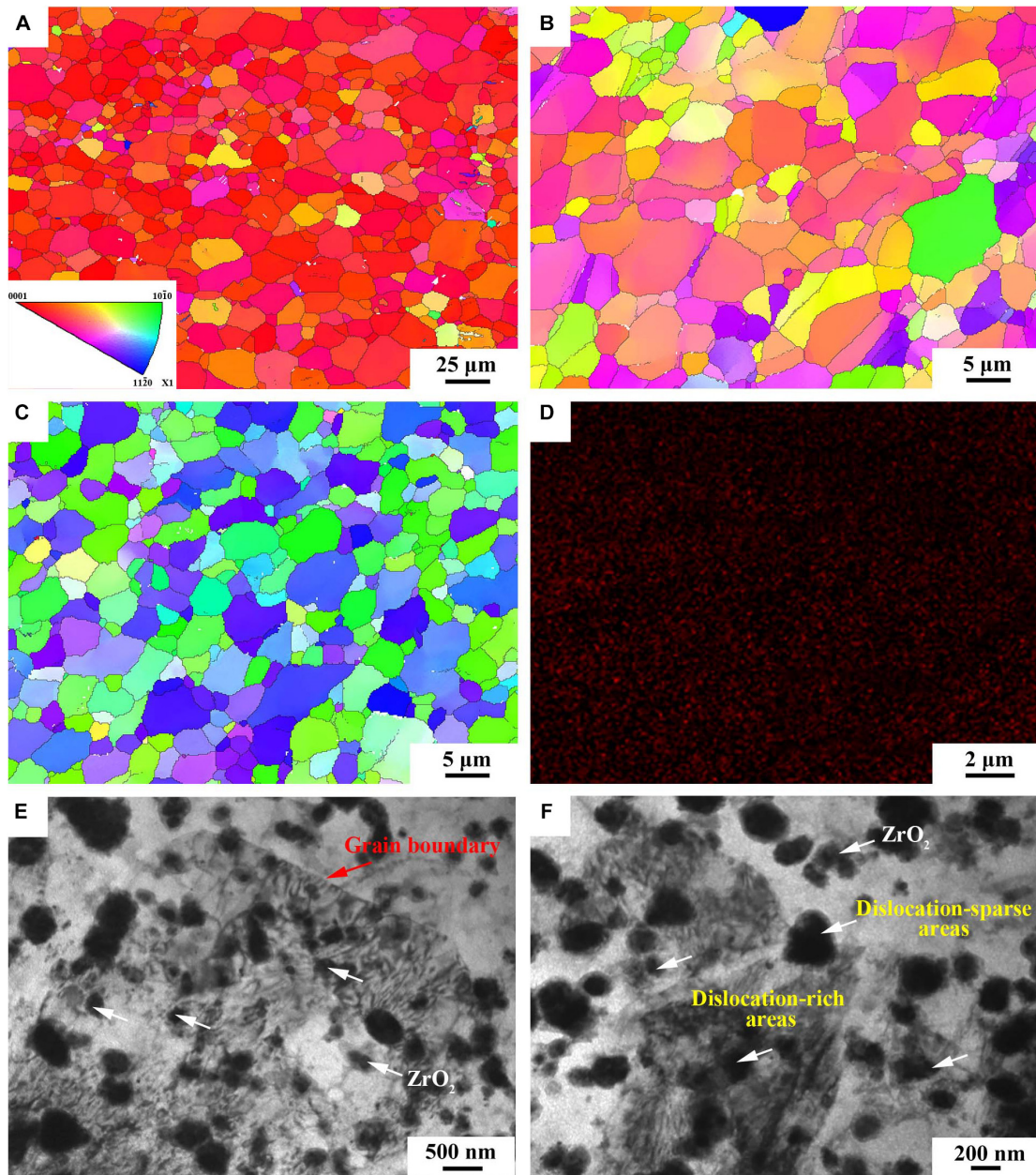


FIGURE 3 | The IPF map of (A) BM, (B) FSP and (C) FSP-ZrO₂; (D) The EDS map of FSP-ZrO₂ sample; (E) and (F) TEM images of FSP-ZrO₂ sample, respectively.

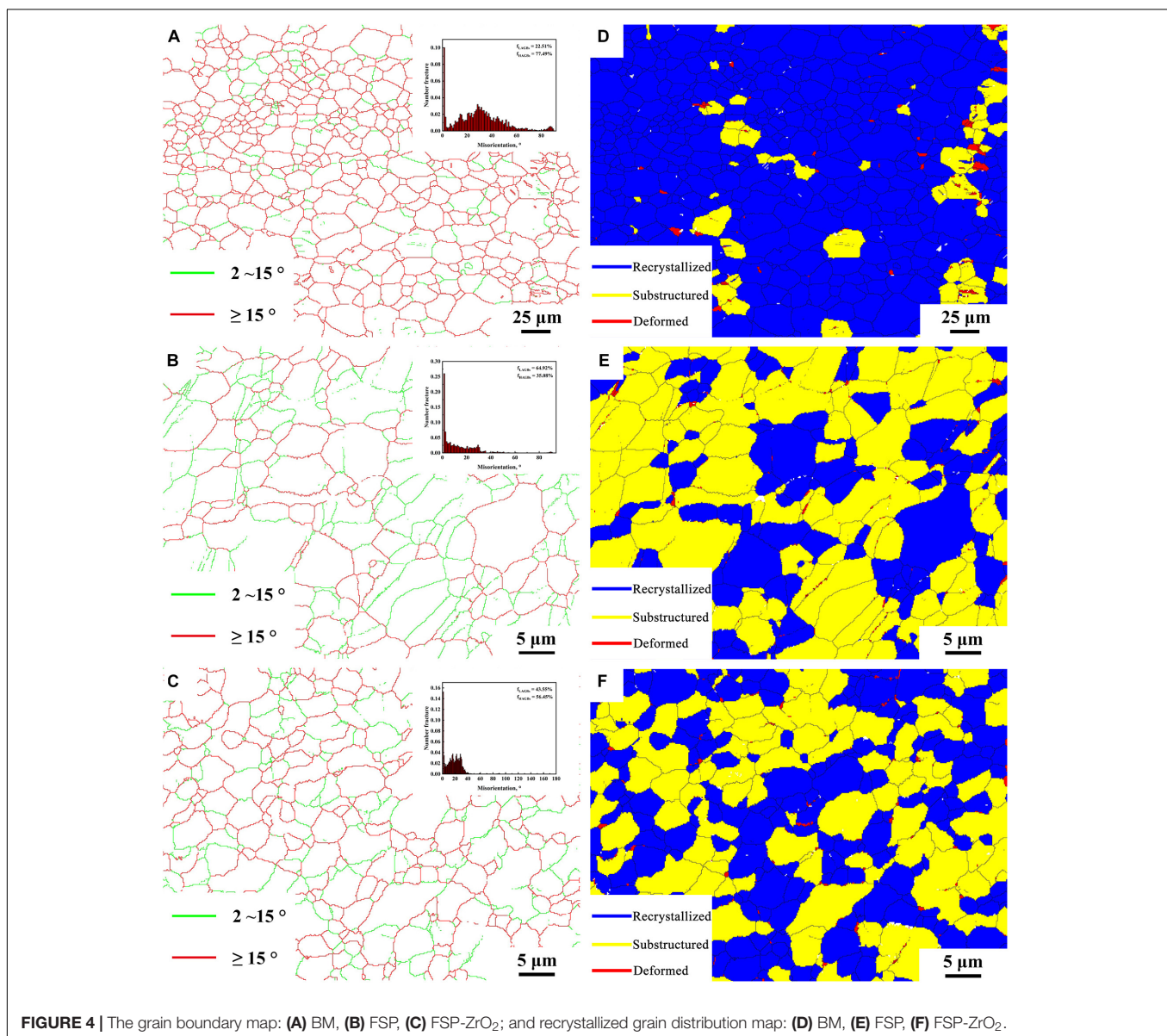
speed was 10 $\mu\text{m/s}$, and the process combined surface scanning and line scanning. The SVET samples were immersed for 1, 3, 6, and 24 h, respectively. The statistical analysis of SVET data was carried out with Origin software. The voltages were displayed in a three-dimensional (3D) maps, which showed the spatial distribution of the voltage as a function of the (x, y) position in the scan region. The voltage value in the SVET map is positive for anodic currents and negative for cathodic currents. The contour map of the voltage was located at the bottom of the 3D map.

RESULTS

Microstructure Evolution

Figures 3A–C show the inverse pole figure (IPF) of BM, FSP and FSP-ZrO₂ samples. BM exhibits equiaxed grains with the

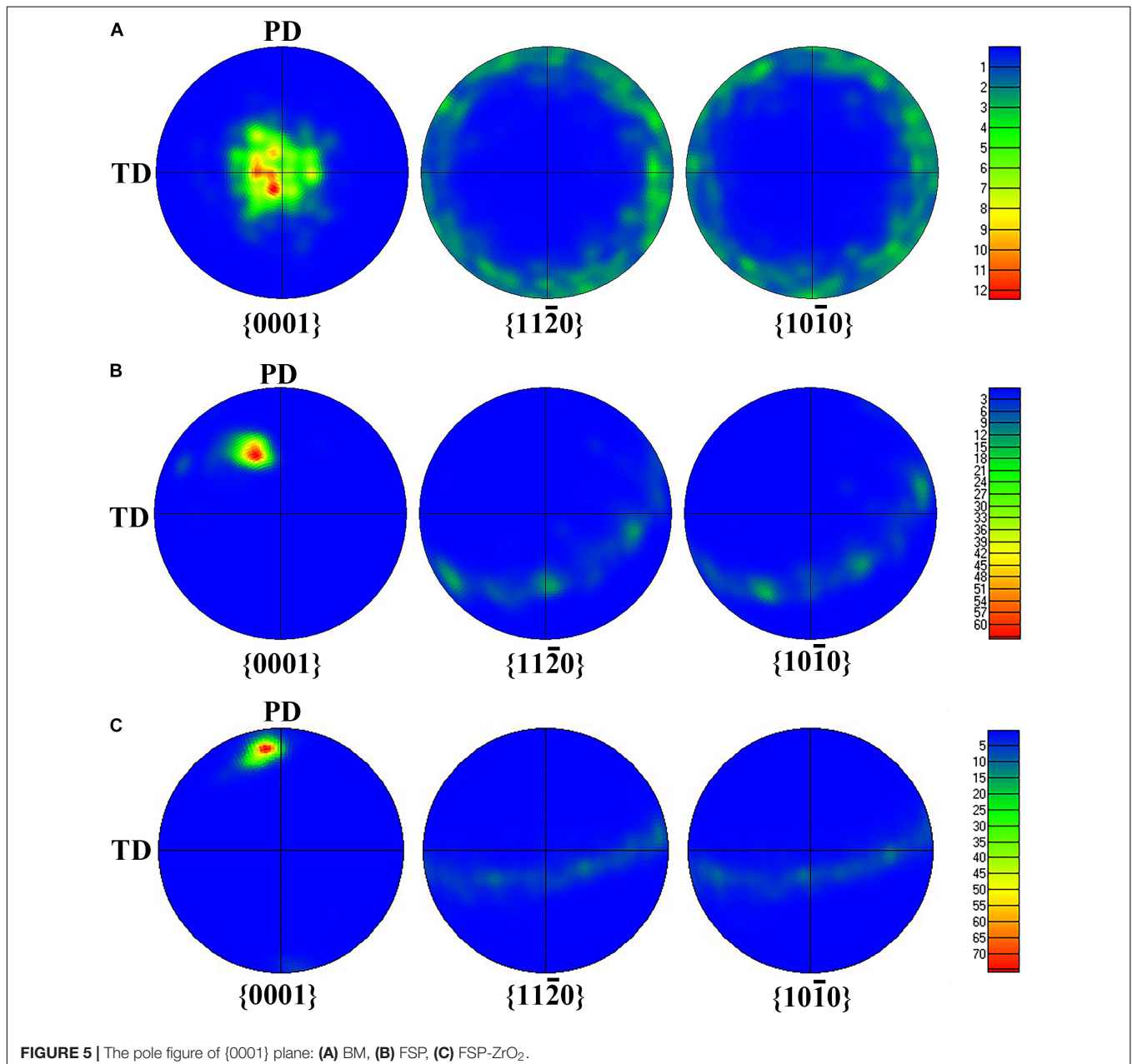
size ranging from 0.2 to 53.5 μm , and the average size is 10 μm (Figure 3A). Compared with BM, FSP displays a more uniform microstructure and finer grain, with a grain size range of 0.1–15 μm and an average size of 4.0 μm (Figure 3B). The microstructure of FSP-ZrO₂ sample is further homogenized and refined, with a grain size range of 0.1–14 μm and an average grain size of 3.2 μm (Figure 3C), which indicates that ZrO₂ particles contribute to reducing grain size. Morisada et al. (2006a) showed that FSP with the SiC particles can refine grains more effectively due to the enhancement of the induced strain and the pinning effect by the SiC particles. Therefore, it can be considered that the ZrO₂ particles in this work play a similar role to the SiC particles in the report. Figure 3D shows the distribution of Zr elements in FSP-ZrO₂ sample. Zr element is uniformly distributed in the Mg matrix without obvious vacancies and aggregation, indicating that the ZrO₂



particles are evenly distributed in the composites after FSP. **Figures 3E,F** are TEM images of FSP-ZrO₂ samples. It can be clearly seen that the ZrO₂ particles (white arrows) are well combined with the matrix, and mainly nucleate within the grains rather than preferentially distribute along the grain boundaries (red arrows). In addition, due to the high temperature and severe plastic deformation during FSP, the dislocation around the ZrO₂ particles is unevenly distributed, forming dislocation-rich areas (i.e., dislocation tangle) and dislocation-sparse areas (**Figure 3F**). During FSP, the stress is concentrated around the ZrO₂ particles due to the significant difference between the elastic modulus of the ZrO₂ particles and Mg matrix, thus a large number of dislocations are generated around ZrO₂ particles. On

the other hand, the dynamic recovery is reduced owing to the low stacking fault energy of Mg alloys, resulting in dense and sparse dislocations (Vignesh et al., 2019).

Figures 4A–F show the grain boundary distribution maps and recrystallized grain distribution maps of BM, FSP, and FSP-ZrO₂ samples, respectively. The insets are the misorientation angle distribution maps. The green and red lines represent low angle grain boundaries (LAGBs) of 2~15° and high angle grain boundaries (HAGBs) of >15°, respectively. Blue indicates recrystallized grains, yellow indicates sub-grains, and red indicates deformed grains. It can be seen that the proportions of HAGBs in BM, FSP, and FSP-ZrO₂ samples are 86.3, 52.8, and 66.5%, respectively. The proportions of recrystallized grains are



89.83, 34.37, and 48.79%, respectively. The HAGB ratios of the above three samples are all reduced because of the dislocations (Figures 3E,F) produced inside the grains during FSP. It is worth noting that there are a large number of $60^\circ \pm 5^\circ$ and $86^\circ \pm 5^\circ$ twins in BM sample, $60^\circ \pm 5^\circ$ twins in FSP sample are reduced, and two twins in FSP-ZrO₂ composites disappear, as shown in the inserts in Figures 4A–C. The grain size affects twin deformation, the finer the grain, the more difficult to twin. Therefore, the main reason for the reduction of twins is that FSP and the

combination of FSP with ZrO₂ particles makes the grain refined (Figures 3B,C).

Figures 5, 6 display {0001}, {11 $\bar{2}$ 0}, and {10 $\bar{1}$ 0} pole figures, and the {0001} orientation distribution function (ODF) map of BM, FSP, and FSP-ZrO₂ samples, respectively. The c-axis of {0001} plane of BM parallel to ND (Figure 5A), showing a typical rolled texture with the polar density of 14.63, and the texture component is {11 $\bar{2}$ 0} < 0001 > or {10 $\bar{1}$ 0} < 0001 > texture (Figure 6A). The c-axis of {0001} plane of FSP sample is deflected

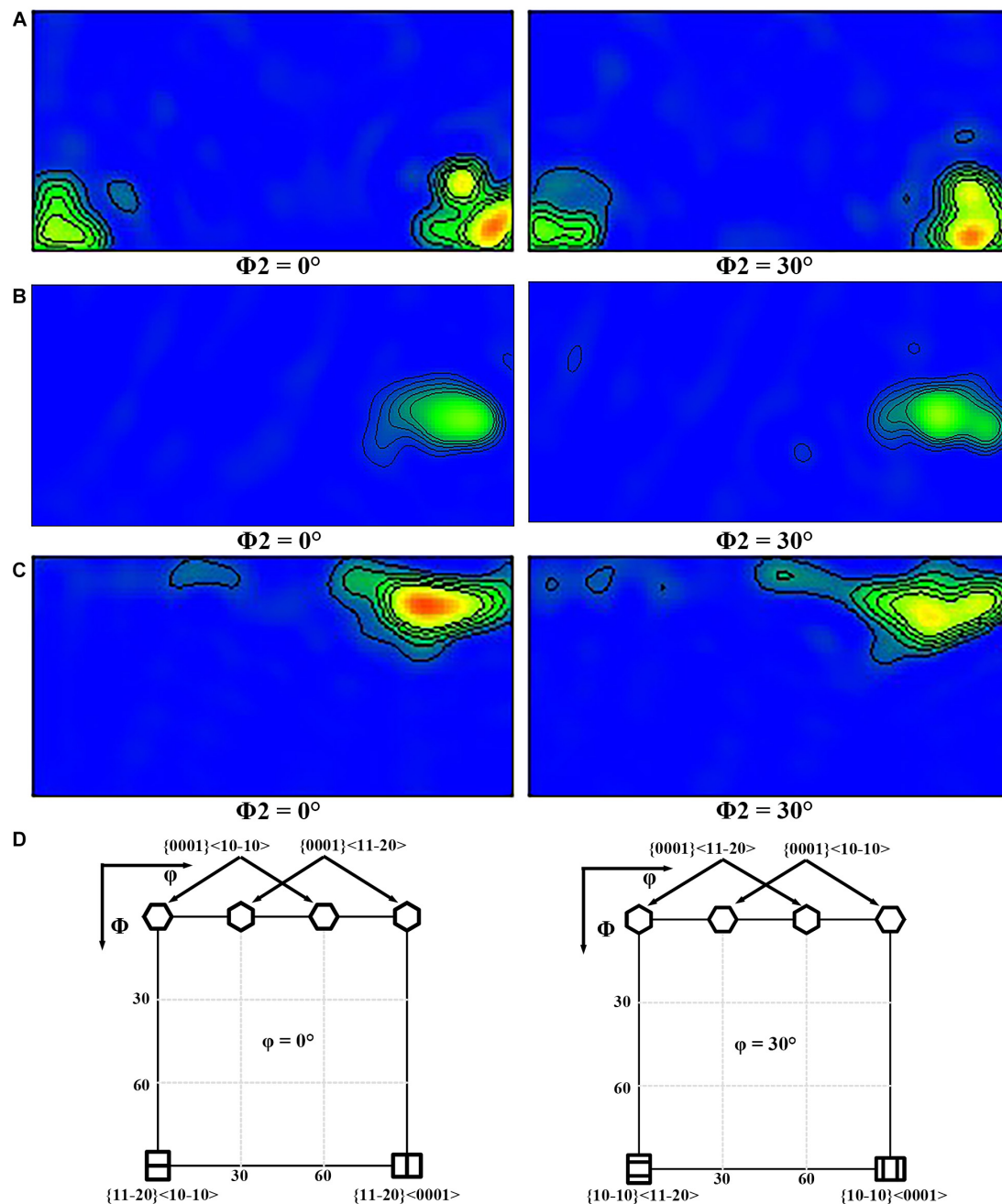


FIGURE 6 | The ODF map of {0001} plane: (A) BM, (B) FSP, (C) FSP-ZrO₂; (D) the standard ODF map of hcp structure.

from PD and TD approximately 45° and 80°, respectively (**Figure 5B**), and the texture component consists of {10 $\bar{1}$ 0} or {1120} fiber texture with the polar density of 60.25 (**Figure 6B**). The c-axis of {0001} plane of FSP-ZrO₂ sample is deflected from PD and TD approximately 15° and 85°, respectively (**Figure 5C**), and the texture component consists of {0001} < 1120 or {0001} < 10 $\bar{1}$ 0 texture with the polar density of 77.21 (**Figure 6C**). The detailed statistical results about the texture of three samples on the {0001} planes are shown in **Table 1**. It has been reported that the deflection of c-axis on the {0001} plane of FSP sample is mainly due to the shear stress induced by shoulder and stir pin (Huang et al., 2019). It is worth noting that the deflection angle of c-axis of FSP-ZrO₂ sample is larger than that of FSP sample, which may be due to the fact that ZrO₂ particles increase the friction coefficient of the material during the plastic flow process, causing more grains on the {0001} plane to deflect.

Figure 7 presents the Schmidt factor (SF) distribution of {0001} basal slip along TD and PD of BM, FSP and FSP-ZrO₂ specimens. The average SFs of BM, FSP, and FSP-ZrO₂ specimens along TD are 0.21, 0.28, and 0.17, respectively, and the average SFs along PD are 0.21, 0.45, and 0.30, respectively. BM has the same SF value along TD and PD, and both samples after FSP have different SFs along TD and PD due to the different angles between their c-axis and TD / PD. In addition, the average SF of FSP sample is higher than that of BM, and the average SF of FSP-ZrO₂ sample is lower than that of BM. In addition, the average SF is arranged from large to small as FSP > BM > FSP-ZrO₂. This indicates that FSP make material soften, while ZrO₂ particles make material harden. This phenomenon has been confirmed in the studies of Navazani and Dehghani (2016) and Jin et al. (2019).

Figure 8 shows the microhardness distribution of the cross section of BM, FSP, and FSP-ZrO₂ samples. The average microhardness of BM is 71 HV. The average microhardness of the FSP sample is reduced to 53 HV, which is mainly because the SF increases along PD (**Figures 7C,D**), causing the material to soften. The average microhardness of FSP-ZrO₂ samples is 99 HV, which is about 40% higher than that of BM. On the one hand, ZrO₂ particles further refine the grains of the Mg alloy during FSP (**Figure 3C**), and improve the strengthening effect of the refined grains. On the other hand, ZrO₂ particles increase the resistance of dislocation movement (Vignesh et al., 2019), so that more dislocations accumulate when the material undergoes plastic deformation (**Figures 3E,F**), thereby strengthening the matrix.

Figure 9 shows the stress-strain curves of BM, FSP, and FSP-ZrO₂ samples. The ultimate tensile strength (UTS) of BM, FSP,

and FSP-ZrO₂ samples is 283, 265, and 427 MPa, the yield strength (YS) is 137, 91, and 217 MPa, and the elongation is 15.5, 13.6, and 9.5%, respectively. Compared to BM, the YS and elongation for FSP specimens reduces, and the YS of FSP-ZrO₂ specimens increases by 80 MPa, while the elongation significantly reduces by about 6%. Since the ZrO₂ particles impede the strain around the matrix (**Figures 3E,F**), thus a plastic deformation gradient is generated on the ZrO₂/matrix interface, resulting in the uneven plasticity and the lower elongation for FSP-ZrO₂ composites. The mechanical properties of materials are usually determined by the microstructure, and detailed analysis will be discussed later. **Figure 10** shows the fracture morphology of BM, FSP, and FSP-ZrO₂ samples after tensile testing. It can be seen that the fracture of BM is composed of dimples with different depths and cleavage surfaces (**Figure 10A**), showing a typical quasi-cleavage fracture. The fracture of FSP sample also presents quasi-cleavage fracture characteristics, with more uniform and fewer dimples, while more cleavage surfaces (**Figure 10B**), indicating a decrease in plasticity. The fracture of FSP-ZrO₂ sample is composed of dimples and a small amount of cleavage surfaces (**Figure 10C**). There are a large number of ZrO₂ particles in the dimples (**Figure 10D**), showing the microporous aggregate fracture characteristics. This is consistent with the previous stress-strain curve results (**Figure 9**).

Electrochemical Corrosion Performance

Figure 11A shows the curves of open circuit potential (OCP) of BM, FSP and FSP-ZrO₂ samples in SBF solution with time. It can be seen that the corrosion potential of the sample increases as time increases. In the initial stage of corrosion, the OCP of BM and FSP samples are similar, while the OCP of FSP-ZrO₂ is higher, indicating that the FSP-ZrO₂ sample is easier to form a passivation film and has a lower self-corrosion tendency.

Figure 11B shows the potentiodynamic polarization curves of BM, FSP, and FSP-ZrO₂ samples in SBF solution. The corrosion potential of BM and FSP samples are the same, while the corrosion potential of FSP-ZrO₂ is lower, suggesting that FSP-ZrO₂ samples are more sensitive to corrosion and easier to form passivation films. According to the corrosion current density, the order of samples is FSP < FSP-ZrO₂ < BM. Corrosion rate (P_i) that can be calculated according to Eq. (1).

$$P_i = 22.85i_{\text{corr}} \quad (1)$$

This means that BM presents the fastest corrosion rate and FSP sample exhibits the slowest. The results of corrosion potential (E_{corr}), corrosion current density (i_{corr}) and corrosion rate (P_i) of BM, FSP and FSP-ZrO₂ samples are listed in **Table 2**.

Figure 11C exhibits the Nyquist plots of BM, FSP and FSP-ZrO₂ samples in SBF solution. All samples are characterized by a capacitive loop in high and medium frequency range, and an inductive loop in the low frequency range. The capacitive loop is caused by the charge transfer process on the surface of the passive film, and the inductive loop is formed by the adhesion of Mg⁺ ions and Mg(OH)⁺ ions on the surface of the sample (Zhuang et al., 2015). FSP samples show the largest radius of capacitive and inductive loop, followed by FSP-ZrO₂ samples,

TABLE 1 | Detailed statistical results about the texture of three samples of {0001} plane.

Samples	{0001}		
	The angle between c-axis and TD (°)	The angle between c-axis and PD (°)	Polar density
BM	0	90	14.63
FSP	80	45	60.25
FSP-ZrO ₂	85	15	77.21

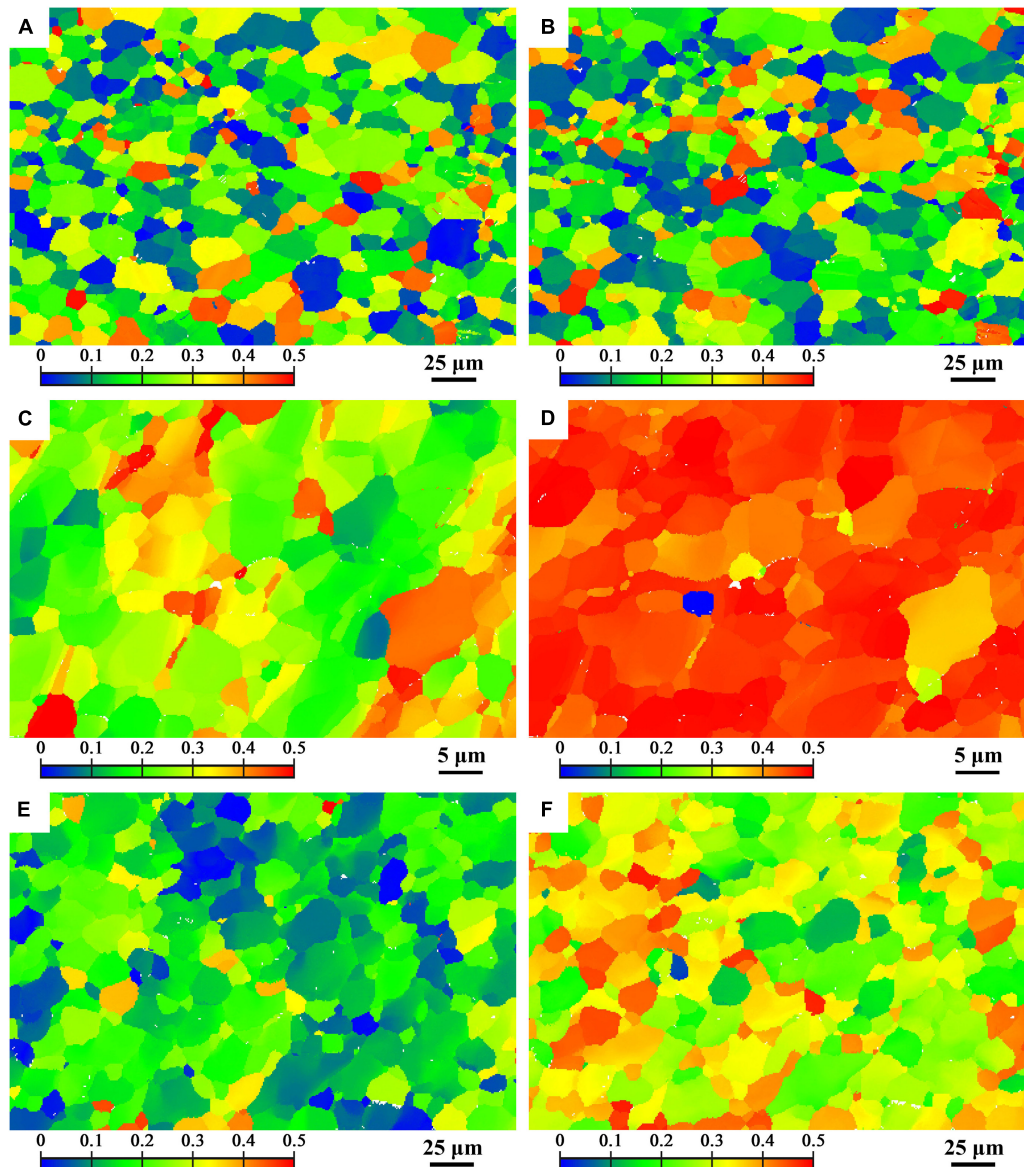
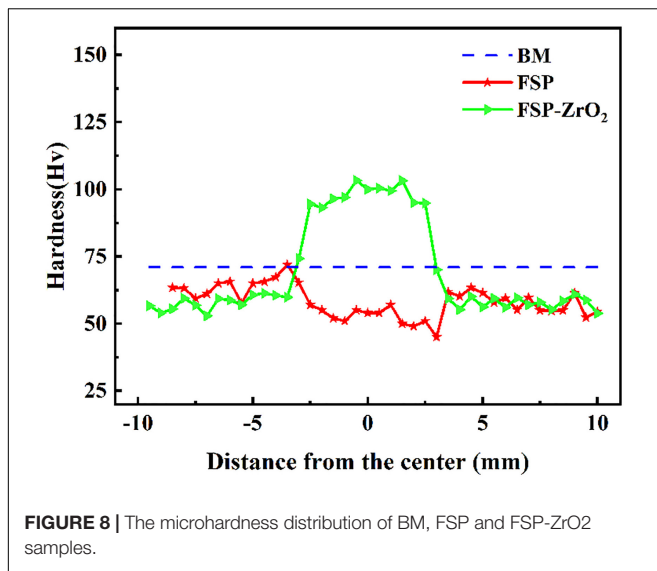


FIGURE 7 | Schmid factor distribution map of TD (on the left side) and PD (on the right side) of (0001) basal slip system (A,B) BM, (C,D) FSP, (E,F) FSP-ZrO₂.

and finally BM. Generally, the larger the radius of capacitive and inductive loop, the better corrosion resistance of the sample (Wang et al., 2018). Furthermore, the dislocation density at the ZrO₂ particles is too large (Figures 3E,F), and thus the local corrosion is aggravated (Liu et al., 2008). It has been reported that dislocations are easily formed between the ZrO₂ particles and the matrix due to a large mismatch of thermal expansion coefficient between them (ZrO₂ particles is $\sim 7.5 \times 10^{-6} \text{ K}^{-1}$, Mg matrix is $\sim 27.1 \times 10^{-6} \text{ K}^{-1}$) (Liu et al., 2008; Vedabouriswaran and Aravindan, 2018). Therefore, the FSP-ZrO₂ composite exhibits worse corrosion performance than FSP sample. In summary, it can be considered that the corrosion resistance of FSP samples is the best, followed by FSP-ZrO₂, and the corrosion resistance of BM is the worst.

SVET Voltage Maps

Figure 12 shows the SVET maps of BM, FSP and FSP-ZrO₂ samples soaked in SBF at 0, 1, 3, 6, and 24 h, respectively. It can be seen that a local violent reaction occurs in BM when it is just soaked in SBF, the maximum voltage is 0.122 mv. When they are soaked for 24 h, the voltage drops to 0.017 mv. The maximum voltage for FSP samples is 0.024 mv when they are just soaked in SBF, and the voltage is reduced to 0.000 mv for 24 h. The maximum voltage for FSP-ZrO₂ sample just immersed in SBF is -0.004 mv, and the voltage first increases and then decreases during the corrosion process. After being soaked for 24 h, the voltage drops to -0.005 mv. The above results indicate that FSP-ZrO₂ samples are more prone to passivation during the corrosion process, followed by FSP and BM is the worst.



DISCUSSION

Relationship Between Microstructure and Mechanical Property

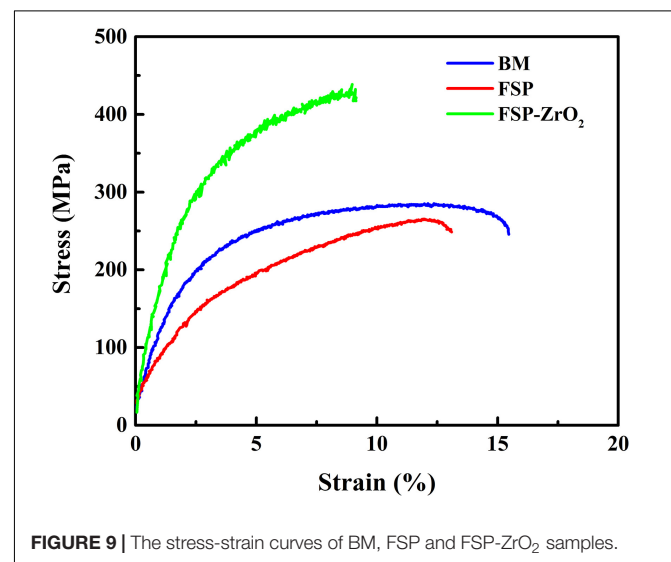
Base metal exhibits coarse grains with inhomogeneous distribution of grain size (Figure 3A), while the FSP sample presents fine and uniform grains. During FSP, the effect of severe plastic deformation, high temperature and strain rate breaks the grains and causes dynamic recrystallization, resulting in the grain refinement of Mg alloy (Figure 3B). LAGBs entangled inside the FSP sample to form fine recrystallized grains (Figures 4A,B), indicating that continuous dynamic recrystallization (CDRX) occurs. Severe plastic deformation increases the dislocation density in grains, and the dislocations rotate or rearrange to form LAGBs in FSP process. These LAGBs gradually transform into HAGBs in the subsequent plastic deformation process (Figures 4A,B).

Compared with FSP sample, grain size of FSP-ZrO₂ sample is refined, and HAGBs and recrystallized grains increase (Figures 3, 4). This is mainly due to the following three reasons. First, the elastic modulus of ZrO₂ particles is different from that of Mg matrix, which will increase dislocation density and provide more nucleation sites for CDRX during FSP (Figures 3E,F). Second, ZrO₂ particles will increase the strain and strain rate, thereby refining the grains (Mukherjee and Ghosh, 2010; Navazani and Dehghani, 2016). Third, ZrO₂ particles pin the dislocations, hindering the movement of dislocations and growth of grain (Figures 3E,F; Mazaheri et al., 2019).

In Figures 5, 6, the grain orientation and texture of three samples have changed significantly. Mg alloy undergoes plastic flow under the combination of the shoulder and stirring pin during FSP, which greatly changes the grain orientation and texture (Yuan et al., 2011). From Figure 5B, it can be seen that the c-axis is deflected and the polar density increases for FSP sample, under the action of the compressive stress induced by the rotation of the shoulder and the shearing force of the stirring pin. For Mg alloy, basal slip has a lower critical resolved shear stress

(CRSS) compared to prismatic slip and pyramidal slip (Park et al., 2003; Woo et al., 2006). Therefore, basal slip is easier to start in FSP, resulting in the formation of obvious basal texture, and the highest polar density is four times that of BM. In addition, the deflected angle of the c-axis on the {0001} plane in FSP-ZrO₂ sample is larger than that of FSP sample, and the polar density is also significantly increased. This indicates that ZrO₂ particles contribute to the initiation of basal slip and increase the strength of basal texture.

In general, the mechanical properties of Mg alloys are mainly affected by grain size, secondary phase and grain orientation. There is hardly precipitates in AZ31 Mg alloy, so the influence of precipitates on the alloy is not considered after FSP. During FSP, the grains of the alloy are significantly refined and uniformed, while the strength is significantly lower than that of BM (Figure 9). The grain refinement strengthening effect is not enough to compensate for the strength loss caused by other factors. Moreover, Mg alloy undergoes severe plastic deformation during FSP, and the texture composition completely different from BM is formed in the processing zone (Figures 5, 6). In addition, compared with BM, the SF value of each area for FSP sample is increased, and the basal slip is easy to proceed, so the strength of FSP sample is reduced. This reduction of strength caused by the softening of grain orientation has been confirmed in our previous studies (Wang et al., 2020). The strength of FSP-ZrO₂ sample is significantly higher than that of BM, as shown in Figure 9. Several strengthening mechanisms of composites have been proposed (Lloyd, 1994). It has been reported that increases in the YS and UTS of FSP-ZrO₂ composites by addition of reinforcing particles may be attributable to three factors as following (Chang et al., 2007; Navazani and Dehghani, 2016; Mazaheri et al., 2019). Firstly, the grains are obviously refined due to the dynamic recrystallization caused by FSP and the pinning effect of ZrO₂, triggering grain refinement strengthening (Morisada et al., 2006a; Cao et al., 2014; Sun et al., 2017). Secondly, ZrO₂ particles uniformly distributed in the matrix are pinned to the grain boundaries, hindering the movement



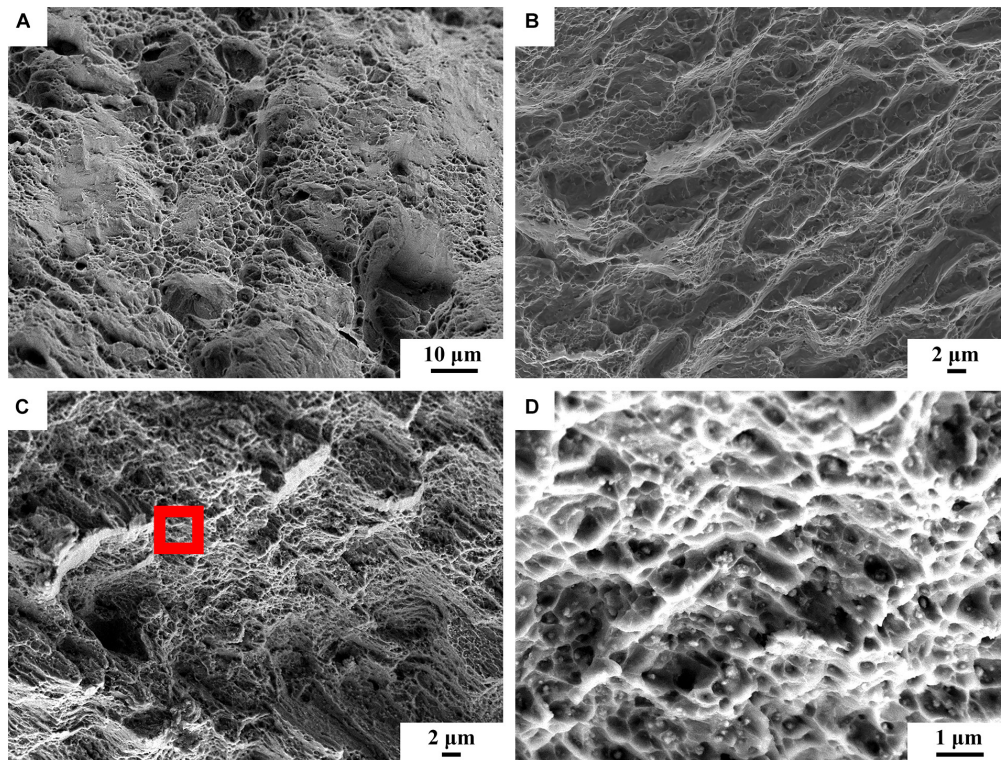


FIGURE 10 | The fracture surfaces of tensile samples: (A) BM, (B) FSP, (C) FSP-ZrO₂, (D) the enlarged view of red rectangle of (c).

of dislocations and causing Orowan strengthening. Thirdly, the load-transfer strengthening caused by the difference in elastic modulus between Mg matrix and ZrO₂ particles.

Furthermore, the contribution of each strengthening mechanism to the YS of FSP-ZrO₂ composites can be calculated using the mathematical equations as following (Hall, 1951; Zhang and Chen, 2006; Shahin et al., 2019):

$$\sigma_y = \sigma_0 + k_y d^{-1/2} \quad (2)$$

where σ_y is the yield strength, σ_0 is the friction stress, k_y is the stress concentration factor (5 MPa mm^{1/2}), and d is the average grain size.

$$\sigma_{\text{orowan}} = \sqrt{3} \frac{Gb}{L} \quad (3)$$

where G is the shear modulus (1.64×10^4 MPa), b is Burgers vector (3.21×10^{-10} m), L is the average distance between ZrO₂ particles (350 nm).

$$\sigma_{LT} = \frac{\sigma_{my} f_v}{2} \quad (4)$$

where σ_{my} is the YS of BM (137 MPa), f_v is the volume fraction of ZrO₂ particles (about 17.6%).

Based on Eqs. (2) – (4), the calculated strength increments between the as-received AZ31 and FSP-ZrO₂ samples were about 39.8, 26.8, and 12.1 MPa, respectively. This indicates that grain refinement strengthening contributes to improve the strength of the material, followed by Orowan strengthening, and finally

load transfer strengthening. This is because the reduction of the grain size for metal matrix directly effects the increase of the strength characteristics of specimens after uniaxial tensile (Vedabouriswaran and Aravindan, 2018). Saikrishna et al. (2017) also proposed the similar conclusion. In addition, the size of the reinforcement particle (Orowan strengthening) contributes in the improvement of strength. Therefore, FSP-ZrO₂ sample in this work presents the highest UTS and YS. Adding the contributions of various strength mechanisms, the strength increment of the material is 78.7 MPa, whereas the measured strength increment is approximately 80 MPa (Figure 9). This indicates a good agreement between the calculated and measured amounts of strength. In conclusion, the grain refinement and Orowan strengthening mechanism can be considered as the major reason of the enhanced strength for FSP-ZrO₂ sample in this work.

Corrosion Mechanism of the FSP-ZrO₂

As shown in Figure 11B, BM, FSP samples and FSP-ZrO₂ composites exhibit similar cathodic reaction and anodic dissolution characteristics. It is known that Mg and its alloys suffer electrochemical corrosion in aqueous solutions, involving cathodic reduction of water (5) and anodic dissolution of Mg (6) (Esmaily et al., 2016).



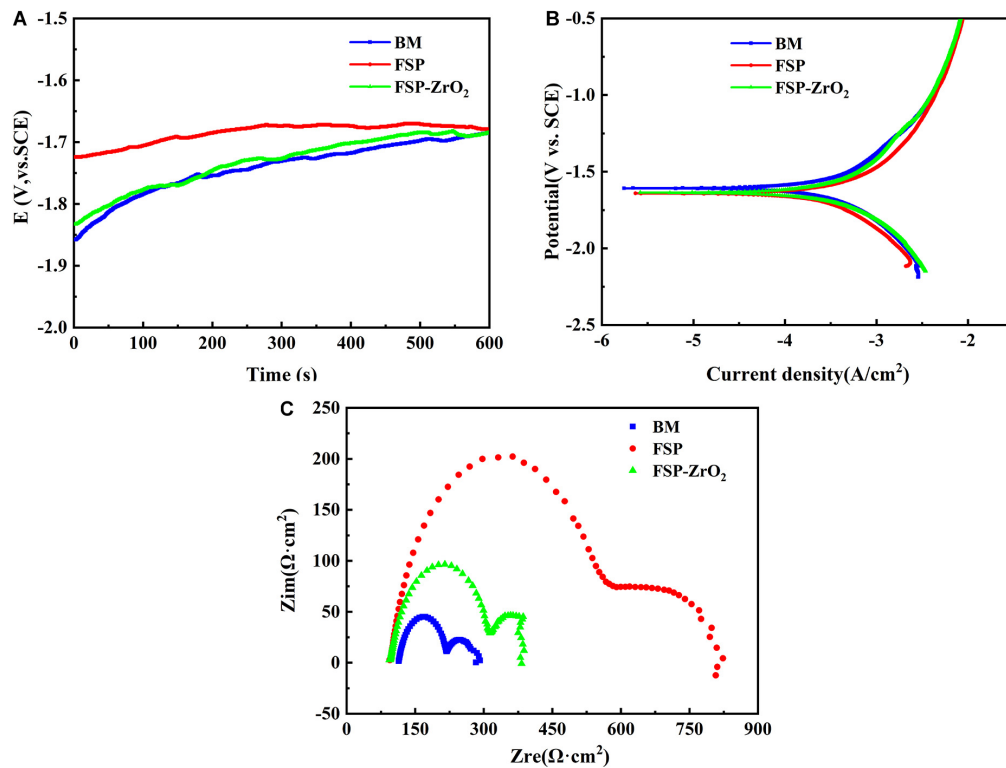
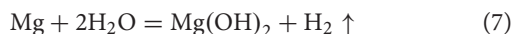


FIGURE 11 | The BM, FSP and FSP-ZrO₂ samples in SBF solution: **(A)** E versus time curves; **(B)** Tafel polarization curves; **(C)** Nyquist plots.

According to Eqs. (5) and (6), the overall corrosion reaction (7) during electrochemical corrosion processing as following:



Mg dissociates in aqueous environments to form Mg hydroxide (Mg(OH)₂) and hydrogen (H₂) gas. The Mg(OH)₂ corrosion film product formed on the alloy surface is a very poor electronic conductor and the rate of corrosion is hence strongly reduced (Esmaily et al., 2016).

The electrochemical corrosion test and SVET measurement of BM, FSP, and FSP-ZrO₂ samples were carried out (Figures 11, 12) in this work. In both tests, the corrosion rate of FSP-ZrO₂ sample is lower than that of BM (Table 2), which indicates that it has better corrosion resistance. In the electrochemical corrosion test, the corrosion resistance of FSP sample is better than that of FSP-ZrO₂ sample, while the opposite result appears in the SVET measurement. For Mg alloys, grain size and grain orientation are the main factors affecting their corrosion resistance (Huang et al., 2019). For Mg matrix composites, in addition to the above two factors, reinforced particles also affect the corrosion resistance significantly (Vignesh et al., 2019).

Generally, grain refinement is considered to effectively improve the corrosion resistance of Mg alloys (Saikrishna et al., 2017; Wang et al., 2018; Huang et al., 2019). The corrosion resistance depends on the grain size, via the grain boundary defects. The high grain boundary energy and chemical activity promote rapid transfer rate of electrons and materials, resulting

in a strong chemical reaction, so the grain boundary can provide more nucleation sites for the passive film. Fine-grained structure can provide more grain boundaries, and the smaller grain size can promote the formation of the protective Mg(OH)₂ layer. Moreover, Choi and Kim (2015) reported that the grain boundary is conducive to stress release and can reduce the number of cracks in the protective film or corrosion layer. Therefore, grain refinement can improve the biological corrosion resistance of Mg alloy. In constant, it has been reported that the grain refinement and the increase of grain boundaries are harmful to corrosion properties. Because of the high defect density at the grain boundary, the material has a greater tendency to corrosion. According to Figures 11, 12, the grain size of FSP and FSP-ZrO₂ samples in this study is smaller than that of BM, which means that they have better corrosion resistance, so it can be considered that grain refinement contributes to improve the corrosion resistance of FSP-ZrO₂ composites.

On the other hand, grain orientation is also a critical factor for influencing the corrosion behavior of FSP-ZrO₂ composites.

TABLE 2 | The results of E_{corr} , i_{corr} and P_i of samples in SBF solution.

Sample	E_{corr} (V)	i_{corr} (mA/cm ²)	P_i (mm/y)
BM	-1.61 ± 0.02	0.271 ± 0.003	6.19 ± 0.02
FSP	-1.61 ± 0.01	0.090 ± 0.002	2.06 ± 0.04
FSP-ZrO ₂	-1.64 ± 0.01	0.217 ± 0.001	4.96 ± 0.02

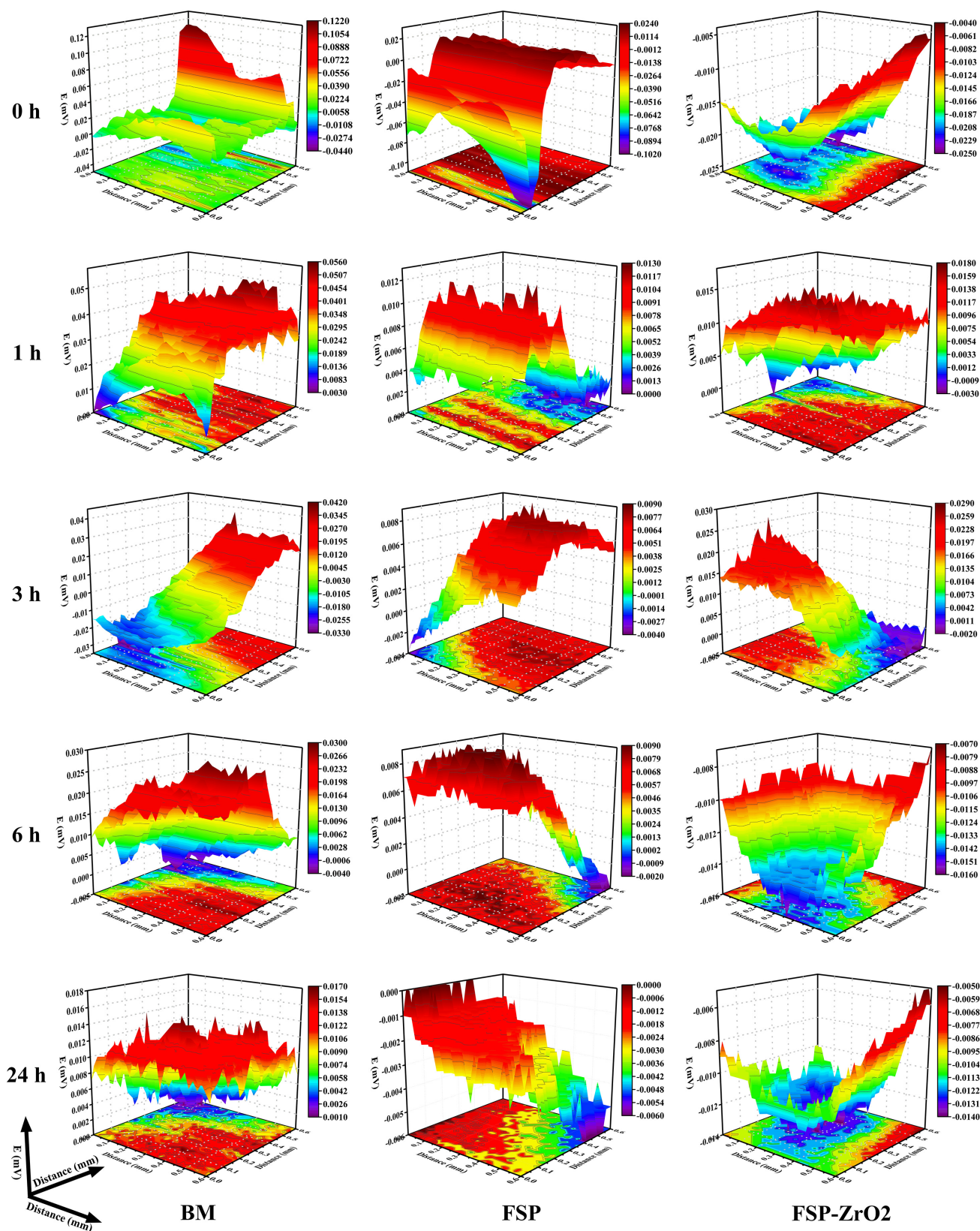


FIGURE 12 | The SVET voltage maps of BM, FSP and FSP-ZrO₂ samples in SBF solution for 0 h, 1 h, 3 h, 6 h, 24 h, respectively.

Previous studies have shown that the (0001) plane of Mg alloy is more resistant to corrosion than (10–10) and (11–20) plane (Liu et al., 2008; Campo et al., 2014; Huang et al., 2019). The (0001) plane of Mg alloy exhibits the highest atomic density (1.13×10^{19} , atom/m²) and the lowest surface energy, which leads to a low atomic dissolution rate during the corrosion. Besides, Micro-zone primary cells are formed between different grain orientations, which in turn affects the OCP (Song et al., 2010). In this study, the micro-galvanic effect in FSP and FSP-ZrO₂ samples leads to preferential dissolution of grains with (10–10) and (11–20) orientations, resulting in the increase of OCP (**Figure 11A**), thus improving the corrosion resistance of the materials.

In addition, the effect of ZrO₂ particles on the corrosion performance of FSP-ZrO₂ sample cannot be ignored. The secondary particles improve the corrosion resistance of Mg alloy mainly in the following two ways. One is to promote grain refinement, and the other is to play a role in obstacle. According to the previous experimental results (**Figures 3, 4**), adding ZrO₂ particles into AZ31 Mg with FSP can promote grain refinement, and then improve the corrosion performance. Similar results have been reported (Esmaily et al., 2016; Wang et al., 2018; Huang et al., 2019). Moreover, Vignesh et al. (2019) believed that the dispersion distribution of ZrO₂ particles in composites increases the cumulative corrosion potential of the material, which increases the corrosion resistance of the composite. Mensah-Darkwa et al. (2013) studied the corrosion properties of Mg-hydroxyapatite (HA) composites and found that HA provides greater resistance to electrons and ions on the surface of Mg, so it essentially has greater corrosion resistance. In this study, during the corrosion process of FSP-ZrO₂ sample, there are many dislocations (**Figures 3E,F**) around ZrO₂ particles. Corrosion is more likely to occur at the position where the dislocation intersects the surface of the matrix (Liu et al., 2008). Therefore, ZrO₂ particles can be used as obstacles to effectively prevent the penetration of corrosion and ultimately improve the corrosion resistance of the alloy. It is reported that reinforced particles can also reduce the corrosion resistance of the composites (Liu et al., 2008). For example, Saikrishna et al. (2017) prepared MWCNT/Mg composites by FSP, but its corrosion resistance was reduced because the added carbon nanotubes provide a nucleation site for galvanic corrosion. Meanwhile, this effect suppresses the effect of grain size and grain orientation on corrosion properties.

In summary, grain size, ZrO₂ particles and grain orientation all influence the corrosion properties. Among them, the grain size is the main factor affecting the corrosion performance. According to the microstructure results, the size of FSP-ZrO₂ (3.2 μm) is smaller than that of FSP (4 μm) and should have better corrosion resistance, which had been confirmed by SVET measurement (**Figure 11**). However, its electrochemical corrosion performance is lower than that of FSP sample, which may be due to the stress concentration caused by the pits left by the shedding of ZrO₂ particles, which accelerates the corrosion rate. When the grain size is similar, ZrO₂ particles are easy to fall off and affect the corrosion performance. In addition, grain orientation has little effect on the corrosion performance because it affects the corrosion performance by affecting the surface energy.

CONCLUSION

- (1) AZ31/ZrO₂ composites with fine, densified and homogenized microstructure can be prepared by FSP. The grain size is refined from 10 μm of BM to 3.2 μm. After FSP, a strong basal texture is produced, and the c-axis of the grain is deflected under the action of compressive stress of shoulder and shear stress of pin.
- (2) With the addition of ZrO₂ particles, the microhardness of FSP-ZrO₂ composites increases from 71 HV (BM) to 99 HV, UTS from 273 MPa (BM) to 427 MPa, YS from 137 MPa (BM) to 217 MPa. The strengthening mechanisms of the composites are mainly fine grain strengthening and Orowan strengthening. Compared with BM, the addition of ZrO₂ particles increase the brittleness but decrease the elongation. BM and FSP samples show quasi-cleavage fracture characteristics, while FSP-ZrO₂ composites present microporous polymerization fracture characteristics.
- (3) The electrochemical corrosion behavior of three samples in SBF solution shows that the i_{corr} of FSP-ZrO₂ composites decreases and the radius of capacitive loop increases, indicating that the corrosion rate decreases but the corrosion resistance increases for the composites. The main factors affecting the corrosion performance are grain size and ZrO₂ particles.

DATA AVAILABILITY STATEMENT

The raw data supporting the conclusions of this article will be made available by the authors, without undue reservation.

AUTHOR CONTRIBUTIONS

KQ and TZ performed the experiments and wrote the manuscript. SY and SZ designed the research. ZW and PP analyzed the data. JC analyzed the data and reviewed the manuscript. LW, CL, and WW contributed to the design and data analysis. All authors read and approved the final manuscript.

FUNDING

The authors gratefully acknowledge the sponsorship from the National Natural Science Foundation of China (Nos. U1760201 and 51974220). National Key Research and Development Program of China (No. 2017YFB0306202). Key Research and Development Program of Shaanxi Province (No. 2017ZDXM-GY-037). Natural Science Foundation of Shaanxi Province (Nos. 2019JQ-769 and 2019JQ-111). Royal Society via an International Exchange program (Grant No: IEC\NSFC\191253). The Youth Innovation Team of Shaanxi Universities (2019-2022). Engineering and Physical Sciences Research Council (EPSRC) (Grant No: EP/T517793/1) for their support this research.

REFERENCES

- Ammouri, A. H., Kridli, G., Ayoub, G., and Hamade, R. F. (2015). Relating grain size to the Zener–Hollomon parameter for twin-roll-cast AZ31B alloy refined by friction stir processing. *J. Mater. Process. Technol.* 222, 301–306. doi: 10.1016/j.jmatprotec.2015.02.037
- Arab, S. M., Zebajrad, S. M., and Jahromi, S. A. J. (2017). Fabrication of AZ31/MWCNTs surface metal matrix composites by friction stir processing: investigation of microstructure and mechanical properties. *J. Mater. Eng. Perform.* 26, 5366–5374. doi: 10.1007/s11665-017-2763-y
- Azizieh, M., Larki, A. N., Tahmasebi, M., Bavi, M., Alizaden, E., and Kim, H. S. (2018). Wear behavior of AZ31/Al₂O₃ magnesium matrix surface nanocomposite fabricated via friction stir processing. *J. Mater. Eng. Perform.* 27, 2010–2017. doi: 10.1007/s11665-018-3277-y
- Balakrishnan, M., Dinaharan, I., Palanivel, R., and Sivaprakasam, R. (2015). Synthesize of AZ31/TiC magnesium matrix composites using friction stir processing. *J. Magnes. Alloy.* 3, 76–78. doi: 10.1016/j.jma.2014.12.007
- Campo, R., Savoini, B., Muñoz, A., Monge, M. A., and Garcés, G. (2014). Mechanical properties and corrosion behavior of Mg–HAP composites. *J. Mech. Behav. Biomed. Mater.* 39, 238–246. doi: 10.1016/j.jmbbm.2014.07.014
- Cao, L., Liu, W. C., Li, Z. Q., Wu, G. H., Xiao, L., Wang, S. H., et al. (2014). Effect of heat treatment on microstructures and mechanical properties of sand-cast Mg–10Gd–3Y–0.5Zr magnesium alloy. *Trans. Nonferrous Met. Soc. China* 24, 611–618. doi: 10.1016/S1003-6326(14)63102-2
- Castellani, C., Lindtner, R. A., Hausbrandt, P., Tschegg, E., Tschegg, S. E. S., Zanoni, G., et al. (2011). Bone–implant interface strength and osseointegration: biodegradable magnesium alloy versus standard titanium control. *Acta Biomater.* 7, 432–440. doi: 10.1016/j.actbio.2010.08.020
- Chang, C. I., Wang, Y. N., Pei, H. R., Lee, C. J., Du, X. H., and Huang, J. C. (2007). Microstructure and mechanical properties of nano-ZrO₂ and nano-SiO₂ particulate reinforced AZ31–Mg based composites fabricated by friction stir processing. *Key Eng. Mater.* 351, 114–119. doi: 10.4028/www.scientific.net/KEM.351.114
- Choi, H. Y., and Kim, W. J. (2015). Effect of thermal treatment on the bio-corrosion and mechanical properties of ultrafine-grained ZK60 magnesium alloy. *J. Mech. Behav. Biomed. Mater.* 51, 291–301. doi: 10.1016/j.jmbbm.2015.07.019
- Daniel, B. S. S., Murthy, V. S. R., and Murty, G. S. (1997). Metal–ceramic composites via in-situ methods. *J. Mater. Process. Technol.* 68, 132–155. doi: 10.1016/S0924-0136(96)00020-9
- Davis, E. A., and Ward, I. M. (1993). *An Introduction to Metal Matrix Composites*. New York, NY: Cambridge University Press.
- Esmaily, M., Mortazavi, N., Svensson, J. E., Halvarsson, M., Jarfors, A. E. W., Wessén, M., et al. (2016). On the microstructure and corrosion behavior of AZ91/SiC composites produced by rheocasting. *Mater. Chem. Phys.* 180, 29–37. doi: 10.1016/j.matchemphys.2016.05.016
- Gobara, M., Shamekh, M., and Akid, R. (2015). Improving the corrosion resistance of AZ91D magnesium alloy through reinforcement with titanium carbides and borides. *J. Magnes. Alloy.* 39, 112–120. doi: 10.1016/j.jma.2015.03.002
- Hall, E. O. (1951). The deformation and ageing of mild steel: III discussion of results. *Proc. Phys. Soc. B* 64:747. doi: 10.1088/0370-1301/64/6/305
- Hashim, J., Looney, L., and Hashmi, M. S. J. (1999). Metal matrix composites: production by the stir casting method. *J. Mater. Process. Technol.* 92–93, 1–7. doi: 10.1016/S0924-0136(99)00118-1
- Henderson, S. E., Verdelis, K., Maiti, S., Pal, S., Chung, W. L., Chou, D. T., et al. (2014). Magnesium alloys as a biomaterial for degradable craniofacial screws. *Acta Biomater.* 10, 2323–2332. doi: 10.1016/j.actbio.2013.12.040
- Huang, L. Y., Wang, K. S., Wang, W., Peng, P., Qiao, K., and Liu, Q. (2019). Microstructural evolution and corrosion behavior of friction stir processed fine-grained AZ80 Mg alloy. *Mater. Corros.* 71, 93–108. doi: 10.1002/maco.201911108
- Jin, Y. Y., Wang, K. S., Wang, W., Peng, P., Zhou, S., Huang, L. Y., et al. (2019). Microstructure and mechanical properties of AE42 rare earth-containing magnesium alloy prepared by friction stir processing. *Mater. Charact.* 150, 52–61. doi: 10.1016/j.matchar.2019.02.008
- Kokubo, T., and Takadama, H. (2006). How useful is SBF in predicting in vivo bone bioactivity? *Biomaterials* 27, 2907–2915. doi: 10.1016/j.biomaterials.2006.01.017
- Lan, J., Yang, Y., and Li, X. (2004). Microstructure and microhardness of SiC nanoparticles reinforced magnesium composites fabricated by ultrasonic method. *Mater. Sci. Eng. A* 386, 284–290. doi: 10.1016/j.msea.2004.07.024
- Lavernia, E. J., and Grant, N. J. (1988). Spray deposition of metals: a review. *Mater. Sci. Eng.* 98, 381–394. doi: 10.1016/0025-5416(88)90191-7
- Liu, M., Qiu, D., Zhao, M. C., Song, G. I., and Atrens, A. (2008). The effect of crystallographic orientation on the active corrosion of pure magnesium. *Scr. Mater.* 58, 421–424. doi: 10.1016/j.scriptamat.2007.10.027
- Lloyd, D. J. (1994). Particle reinforced aluminium and magnesium matrix composites. *Int. Mater. Rev.* 39, 1–23. doi: 10.1179/095066094790150982
- Mazaheri, Y., Jalilvand, M. M., Heidarpour, A., and Jahani, R. A. (2019). Tribological behavior of AZ31/ZrO₂ surface nanocomposites developed by friction stir processing. *Tribol. Int.* 143:106062. doi: 10.1016/j.triboint.2019.106062
- Mensah-Darkwa, K., Gupta, R. K., and Kumar, D. (2013). Mechanical and corrosion properties of magnesium–hydroxyapatite (Mg–HA) composite thin films. *J. Mater. Sci. Technol.* 29, 788–794. doi: 10.1016/j.jmst.2013.04.019
- Mishra, R. S., and Ma, Z. Y. (2005). Friction stir welding and processing. *Mater. Sci. Eng. R* 50, 1–78. doi: 10.1016/j.mser.2005.07.001
- Morisada, Y., Fujii, H., Nagaoka, T., and Fukusumi, M. (2006a). Effect of friction stir processing with SiC particles on microstructure and hardness of AZ31. *Mater. Sci. Eng. A* 433, 50–54. doi: 10.1016/j.msea.2006.06.089
- Morisada, Y., Fujii, H., Nagaoka, T., and Fukusumi, M. (2006b). MWCNTs/AZ31 surface composites fabricated by friction stir processing. *Mater. Sci. Eng. A* 419, 344–348. doi: 10.1016/j.msea.2006.01.016
- Mukherjee, S., and Ghosh, A. K. (2010). Flow visualization and estimation of strain and strain-rate during friction stir process. *Mater. Sci. Eng. A* 527, 5130–5135. doi: 10.1016/j.msea.2010.04.091
- Navazani, M., and Dehghani, K. (2015). Investigation of microstructure and hardness of Mg/TiC surface composite fabricated by Friction Stir Processing (FSP). *Proc. Mater. Sci.* 11, 509–514. doi: 10.1016/j.mspro.2015.11.082
- Navazani, M., and Dehghani, K. (2016). Fabrication of Mg–ZrO₂ surface layer composites by friction stir processing. *J. Mater. Process. Technol.* 229, 439–449. doi: 10.1016/j.jmatprotec.2015.09.047
- Ni, D. R., Wang, J. J., and Ma, Z. Y. (2016). Shape memory effect, thermal expansion and damping property of friction stir processed NiTi/Al composite. *J. Mater. Sci. Technol.* 32, 162–166. doi: 10.1016/j.jmst.2015.12.013
- Park, S. H. C., Sato, Y. S., and Kokawa, H. (2003). Basal plane texture and flow pattern in friction stir weld of a magnesium alloy. *Metall. Mater. Trans. A* 34, 987–994. doi: 10.1007/s11661-003-0228-4
- Saikhishna, N., Pradeep, K. R. G., Munirathinam, B., Ravikumar, D., Jagannatham, M., and Sunil, B. R. (2017). An investigation on the hardness and corrosion behavior of MWCNT/Mg composites and grain refined Mg. *J. Magnes. Alloy.* 6, 83–89. doi: 10.1016/j.jma.2017.12.003
- Shahin, M., Munir, K., Wen, C., and Li, Y. (2019). Magnesium matrix nanocomposites for orthopedic applications: a review from mechanical, corrosion, and biological perspectives. *Acta Biomater.* 96, 1–19. doi: 10.1016/j.actbio.2019.06.007
- Song, G. L., Mishra, R., and Xu, Z. Q. (2010). Crystallographic orientation and electrochemical activity of AZ31 Mg alloy. *Electrochem. Commun.* 12, 1009–1012. doi: 10.1016/j.elecom.2010.05.011
- Staiger, M. P., Pietak, A. M., Huadmai, J., and Dias, G. (2006). Magnesium and its alloys as orthopedic biomaterials: a review. *Biomaterials* 27, 1728–1734. doi: 10.1016/S0921-4526(00)00577-9
- Sun, J., Zhang, D. F., Tang, T., Yu, D. L., Xu, J. Y., and Pan, F. H. (2017). Effect of aging treatment before extrusion on microstructure and mechanical properties of AZ80 magnesium alloy. *Rare Metal Mater. Eng.* 46, 1768–1774. doi: 10.1016/S1875-5372(17)30164-9
- Ugandhar, S., Gupta, M., and Sinha, S. K. (2006). Enhancing strength and ductility of Mg/SiC composites using recrystallization heat treatment. *Compos. Struct.* 72, 266–272. doi: 10.1016/j.compstruct.2004.11.010
- Vedabouriswaran, G., and Aravindan, S. (2018). Development and characterization studies on magnesium alloy (RZ 5) surface metal matrix composites through friction stir processing. *J. Magnes. Alloy.* 6, 145–163. doi: 10.1016/j.jma.2018.03.001
- Vignesh, R. V., Padmanaban, R., Govindaraju, M., and Priyadharshini, S. G. (2019). Investigations on the corrosion behaviour and biocompatibility of magnesium

- alloy surface composites AZ91D-ZrO₂ fabricated by friction stir processing. *Trans. Inst. Metal Finish.* 97, 261–270. doi: 10.1080/00202967.2019.1648005
- Wang, H. Y., Jiang, Q. C., Wang, Y., Ma, B. X., and Zhao, F. (2004). Fabrication of TiB₂ particulate reinforced magnesium matrix composites by powder metallurgy. *Mater. Lett.* 58, 3509–3513. doi: 10.1016/j.matlet.2004.04.038
- Wang, W., Han, P., Peng, P., Zhang, T., Liu, Q., Yuan, S. N., et al. (2020). Friction stir processing of magnesium alloys: a review. *Acta Metall. Sin.* 33, 43–57. doi: 10.1007/s40195-019-00971-7
- Wang, W., Xu, R. Q., Hao, Y. X., Wang, Q., Yu, L. L., Che, Q. Y., et al. (2018). Corrosion fatigue behavior of friction stir processed interstitial free steel. *J. Mater. Sci. Technol.* 34, 148–156. doi: 10.1016/j.jmst.2017.11.013
- Woo, W., Choo, H., Brown, D. W., Liaw, P. K., and Feng, Z. (2006). Texture variation and its influence on the tensile behavior of a friction-stir processed magnesium alloy. *Scr. Mater.* 54, 1859–1864. doi: 10.1016/j.scriptamat.2006.02.019
- Xu, N., and Bao, Y. (2016). Enhanced mechanical properties of tungsten inert gas welded AZ31 magnesium alloy joint using two-pass friction stir processing with rapid cooling. *Mater. Sci. Eng. A* 655, 292–299. doi: 10.1016/j.msea.2016.01.009
- Yuan, W., Mishra, R. S., Carlson, B., Mishra, R. K., Verma, R., and Kubic, R. (2011). Effect of texture on the mechanical behavior of ultrafine grained magnesium alloy. *Scr. Mater.* 64, 580–583. doi: 10.1016/j.scriptamat.2010.11.052
- Zhang, Z., and Chen, D. L. (2006). Consideration of Orowan strengthening effect in particulate-reinforced metal matrix nanocomposites: a model for predicting their yield strength. *Scr. Mater.* 54, 1321–1326. doi: 10.1016/j.msea.2006.10.184
- Zhuang, J. J., Guo, Y. Q., Xiang, N., Xiong, Y., Hu, Q., and Song, R. G. (2015). A study on microstructure and corrosion resistance of ZrO₂-containing PEO coatings formed on AZ31 Mg alloy in phosphate-based electrolyte. *Appl. Surf. Sci.* 357(Pt B), 1463–1471. doi: 10.1016/j.apsusc.2015.10.025

Conflict of Interest: The authors declare that the research was conducted in the absence of any commercial or financial relationships that could be construed as a potential conflict of interest.

Copyright © 2021 Qiao, Zhang, Wang, Yuan, Zhang, Wang, Wang, Peng, Cai, Liu and Wang. This is an open-access article distributed under the terms of the Creative Commons Attribution License (CC BY). The use, distribution or reproduction in other forums is permitted, provided the original author(s) and the copyright owner(s) are credited and that the original publication in this journal is cited, in accordance with accepted academic practice. No use, distribution or reproduction is permitted which does not comply with these terms.



Metal Material, Properties and Design Methods of Porous Biomedical Scaffolds for Additive Manufacturing: A Review

Yuting Lv^{1,2}, Binghao Wang¹, Guohao Liu¹, Yujin Tang^{3*}, Eryi Lu^{4*}, Kegong Xie³, Changgong Lan³, Jia Liu^{3*}, Zhenbo Qin⁵ and Liqiang Wang²

¹ College of Mechanical and Electronic Engineering, Shandong University of Science and Technology, Qingdao, China, ² State Key Laboratory of Metal Matrix Composites, Shanghai Jiao Tong University, Shanghai, China, ³ Affiliated Hospital of Youjiang Medical University for Nationalities, Baise, China, ⁴ Renji Hospital, Shanghai Jiao Tong University, Shanghai, China, ⁵ Tianjin Key Laboratory of Composite and Functional Materials, School of Material Science and Engineering, Tianjin University, Tianjin, China

OPEN ACCESS

Edited by:

João Conde,
New University of Lisbon, Portugal

Reviewed by:

Qiang Chen,
Southeast University, China
Monica Mattioli-Belmonte,
Marche Polytechnic University, Italy

*Correspondence:

Yujin Tang
tangyujin196709@163.com
Eryi Lu
lueryi222@126.com
Jia Liu
liujia0111@live.cn

Specialty section:

This article was submitted to
Biomaterials,
a section of the journal
Frontiers in Bioengineering and
Biotechnology

Received: 13 December 2020

Accepted: 23 February 2021

Published: 26 March 2021

Citation:

Lv Y, Wang B, Liu G, Tang Y, Lu E,
Xie K, Lan C, Liu J, Qin Z and Wang L
(2021) Metal Material, Properties
and Design Methods of Porous
Biomedical Scaffolds for Additive
Manufacturing: A Review.
Front. Bioeng. Biotechnol. 9:641130.
doi: 10.3389/fbioe.2021.641130

Design an implant similar to the human bone is one of the critical problems in bone tissue engineering. Metal porous scaffolds have good prospects in bone tissue replacement due to their matching elastic modulus, better strength, and biocompatibility. However, traditional processing methods are challenging to fabricate scaffolds with a porous structure, limiting the development of porous scaffolds. With the advancement of additive manufacturing (AM) and computer-aided technologies, the development of porous metal scaffolds also ushers in unprecedented opportunities. In recent years, many new metal materials and innovative design methods are used to fabricate porous scaffolds with excellent mechanical properties and biocompatibility. This article reviews the research progress of porous metal scaffolds, and introduces the AM technologies used in porous metal scaffolds. Then the applications of different metal materials in bone scaffolds are summarized, and the advantages and limitations of various scaffold design methods are discussed. Finally, we look forward to the development prospects of AM in porous metal scaffolds.

Keywords: metal material, additive manufacturing, porous scaffold, design, bone tissue engineering

INTRODUCTION

Bone defects caused by pathologies such as fracture, bone tumor, or external trauma are among the main problems in clinical treatment (Moiduddin et al., 2017). Autologous bone transplantation is considered to be a good choice, but the mismatched performance of different bone sites and the limited number of useful bone grafts limit the application of autologous bone transplantation (Henkel et al., 2013). In contrast, allogeneic bone transplantation has an obvious risk of immune rejection and infection, which affects bone formation and is prone to bone resorption. Therefore, it is ideal to seek natural bone replacement for bone transplantation in orthopedics.

As an alternative material, porous metal scaffolds avoid a series of adverse reactions in natural bone grafting and have gradually attracted researchers' attention. To simulate the mechanical properties and biocompatibility of real bone, porous metal scaffolds not only have interconnected

porous structures but also have good mechanical properties and biocompatibility (Li et al., 2020a). Mechanical properties mainly include better yield strength, matching elastic modulus, and better fatigue strength (Yuan et al., 2019). Common biomedical metal materials such as Ti and Ti alloys can completely meet bone implants needs in terms of strength. Nevertheless, the elastic modulus of dense metals is much greater than that of human bones, which is prone to bone resorption and leads to bone loosening in the human body (Bundy, 2008). The porous scaffolds can obtain matching elastic modulus with human bone by adjusting the pore size and porosity (Kelly et al., 2019), and at the same time have better yield and fatigue strength (Chen et al., 2018). Porous metal scaffolds should also have good biocompatibility, which not only can promote cell attachment, growth, proliferation, and differentiation, but also facilitates the transport of nutrients and metabolic wastes (Little et al., 2011; Saint-Pastou Terrier and Gasque, 2017).

Traditional processing methods are challenging to prepare porous metal scaffolds with complex structures, while additive manufacturing (AM) technology can prepare the scaffolds with controllable structures, shape, and properties (Wang et al., 2020a). Thus AM is one of the most effective methods to prepare porous metal scaffolds. The design of porous metal scaffolds is another crucial problem because scaffold features such as unit type, pore size, porosity, and distribution have significantly influence on their mechanical properties and biocompatibility. Therefore, this article introduces the AM technologies for preparing metal scaffolds and summarizes the research progress in relative metal materials, including non-biodegradable metals (Ti alloys, Ta alloy, and stainless steel), and biodegradable metals (Fe, Mg alloy, and Zn alloy). Besides, we review the structural characteristics of porous metal scaffolds and their design methods in detail, and evaluate the advantages and limitations of these methods. Finally, we prospect the future development direction of bone scaffolds.

BASIC REQUIREMENTS FOR METAL POROUS SCAFFOLDS

For metal implants, the elastic modulus is a very important mechanical performance (Ngo et al., 2018). Large elastic modulus differences between the implants and the bone tissue can result in “stress shielding” effect, which will gradually trigger the loosening of the implant, finally leading to the failure of implant. As known to all, solid metals has much higher elastic modulus than bone tissue (Li et al., 2020a). Obviously, the solid metals are not suitable to use as implants. Thus porous structures were designed in order to reduce the elastic modulus of the solid metals. Metal porous implants should be non-toxic, non-rejection, and non-allergenic, which requires us to select suitable metal as raw material (Roseti et al., 2017). Good biocompatibility is also reflected in the reasonable porous shape and distribution, which can promote the adhesion and growth of bone tissue cells (Shor et al., 2007). In addition, metal porous scaffolds should have good wear and corrosion resistance. Worse wear resistance can cause loosening of the scaffolds, and metal particles caused by wear or metal ions

formed due to the corrosion effect can lead to tissue reactions and lesions (Wang et al., 2020a). Furthermore, the scaffolds should have good machinability, and the structures can be obtained using existing processing technologies.

ADDITIVE MANUFACTURING TECHNOLOGY

Additive manufacturing (AM) technologies, also known as 3D printing, attracts extensive attention in the fabrication of biomedical implants due to their capability of manufacturing porous scaffolds with irregular shapes (Chen et al., 2020b). AM prepares products by layer-by-layer stacking method, which divides into the following three steps. Firstly, the entity model is established by commercial software such as UG, Pro/Engineer, SolidWorks, and Materialise 3-Matic, etc. Secondly, the model is imported into slicing software for slicing and layering. Finally, the layered file is imported into a 3D printer, and the parts are formed layer by layer from bottom to top. At present, the AM technologies suitable for preparing porous metal scaffolds mainly divides into two categories: powder bed fusion technology (PBF) and directional deposition technology (DED) (Chen et al., 2020a). Compared with DED, PBF can prepare the parts with better manufacturing accuracy and surface quality and are more prevalent in the biomedical field. Therefore, this article focuses on powder bed fusion technologies, including selective laser sintering (SLS), selective laser melting (SLM), and electron beam melting (EBM) (Chen et al., 2020b). The differences in these AM technologies are summarized, as shown in Table 1.

Selective Laser Sintering (SLS) and Selective Laser Melting (SLM)

Figure 1A show the schematic diagram of SLS. SLS uses a laser as an energy source to sinter the powder materials (Szymczyk-Ziółkowska et al., 2020). After melting one layer, the equipment descends to fabrication platform and raises the powder delivery platform. Then the roller rolls out powders on the fabrication platform, and a new layer of sintering begins. This process is repeated until entirely formation of the part. When using SLS, prepared material need introduce binder materials (alloys with a low melting point) to reduce the melting point, promoting sintering (Lee et al., 2017). SLS can prepare a variety of materials such as polymers (Goodridge et al., 2012), metals and alloys (Bae et al., 2014), etc. but it is challenging to prepare metal materials with a high melting points.

Selective laser melting is developed based on SLS technology, and its principles are the same. Nevertheless, powder material and the bonding mechanisms in the two technologies are different. In SLS technology, the powder materials are heated to partly melt by laser beams instead of completely melting (Bose et al., 2018). Powders with a low melting points are used as binders for bonding high melting point metals (Qu, 2020). Compared with SLS, the laser of SLM has higher energy (Dogan et al., 2020), which can completely melt the powder. Thus it can prepare metals or alloys with a high melting points. The parts prepared by SLM have higher dimensional accuracy and density,

and their mechanical properties are comparable to those of forged one. Due to the high sintering temperature, the powder sintering needs to be performed under the protection of inert gas to prevent metal oxidation (Wang et al., 2017).

Selective laser melting technology also has shortcomings. The surface of parts prepared by SLM can adhere to some particles that do not melt completely (Zadpoor, 2019), resulting in its high surface roughness. It is necessary to smooth the surface by sandblasting or chemical corrosion (Ahmadi et al., 2019; Zadpoor, 2019). Besides, when the SLM is used to process brittle materials, residual stresses are easily generated inside the parts

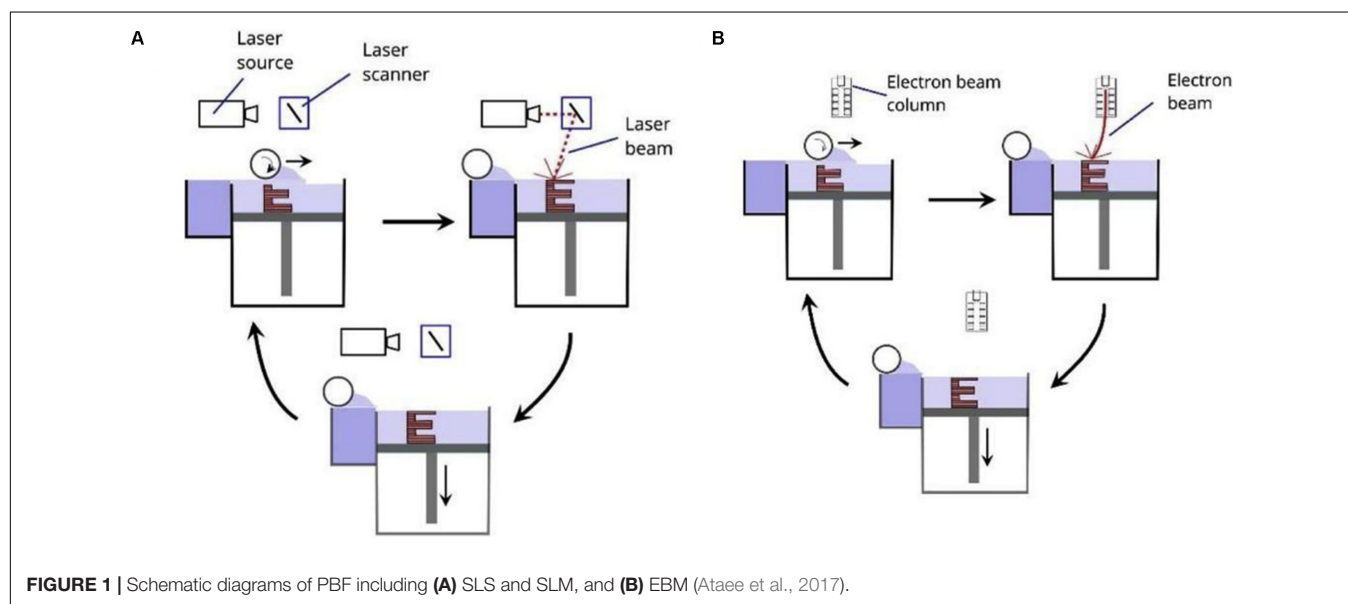
during the cooling process. Thus it is often necessary to adopt isobaric sintering or heat treatment to eliminate residual stress (Fang et al., 2020).

Electron Beam Melting (EBM)

Electron beam melting, like SLS and SLM, is a powder bed fusion technology (PBF). The significant differences between SLM and EBM are the source of energy, and their energy sources are laser and high-energy, high-speed electron beams, respectively. **Figure 1B** show the principle of EBM. The electron gun emits electrons, and then the electron beam is accelerated by the heated

TABLE 1 | Summaries of four different additive manufacturing technologies: selective laser sintering (SLS), selective laser melting (SLM), electron beam melting (EBM), and directional deposition technology (DED).

Category	Materials	Application	Resolution (μm)	Advantages	Disadvantages	References
SLS	Polymers Metals Alloys	<ul style="list-style-type: none"> • Biomedical fabrication • Shipbuilding • Auto industry • Aerospace 	76–100	<ul style="list-style-type: none"> • Superior mechanical properties • Complex geometry • No supporting • High utilization of powder Materials 	<ul style="list-style-type: none"> • Low energy efficiency • Expensive • Low density 	Chohan et al., 2017; Ngo et al., 2018
SLM	Metals Alloys	<ul style="list-style-type: none"> • Biomedical fabrication • Shipbuilding • Auto industry • Aerospace 	80–250	<ul style="list-style-type: none"> • Superior mechanical properties • Complex geometry • No supporting • High density 	<ul style="list-style-type: none"> • Expensive • Residual stress • Rough surface • Time consuming process 	Sood et al., 2010; Tofail et al., 2018
EBM	Metals Alloys	<ul style="list-style-type: none"> • Biomedical fabrication • Shipbuilding • Auto industry • Aerospace 	50–100	<ul style="list-style-type: none"> • Superior mechanical properties • Complex geometry • No supporting 	<ul style="list-style-type: none"> • Expensive • Rough surface • Time consuming process 	Ngo et al., 2018; Qu, 2020
DED	Metals Alloys Ceramics Glass Polymers	<ul style="list-style-type: none"> • Aerospace • Repair of bespoke parts • Biomedical application 	250	<ul style="list-style-type: none"> • Good mechanical properties • Rapid cooling rates • Effective time and cost of repairs 	<ul style="list-style-type: none"> • Low resolution • Low surface quality • Producing less complex parts 	Gibson et al., 2015; Mohamed et al., 2015



tungsten wire, and the direction and diameter of the electron beam are controlled by a magnetic lens (or coil) (Yuan et al., 2019). During sintering, the metal powder melts entirely, and then the electron beam sweeps the powder along the preset path and processing parameters. The powders can be melted and solidified into a metal entity, finally forming a thin layer with a thickness of 0.05–0.2 mm. Then the powders are spread and sintered again and this operation was repeated until the formation of parts entirely. To prevent the oxidation of the metal powder, the entire process needs to be carried out in a vacuum (Gokuldoss et al., 2017). EBM's advantages are lies in the higher energy density of the electron beam, faster rate of powder melting and forming (Liu et al., 2016). Due to the high energy density, EBM technology can prepare refractory metals with high melting points. During processing, EBM usually heats the powder bed, which can reduce the temperature differences between the powder bed and the metal. Thus the residual stress of parts is small (Gokuldoss et al., 2017). Like the SLM technology, the parts prepared by EBM have high surface roughness (Gong et al., 2014), and the dimensional error and surface integrity are worse than those of the cast one.

THE METAL MATERIAL USED IN POROUS SCAFFOLDS

Non-biodegradable Metals

The non-biodegradable metal materials currently used in porous scaffolds mainly include pure Ti (Wauthle et al., 2015a), Ti alloy (Kapat et al., 2017; Onal et al., 2018; Cutolo et al., 2020), Ta (Wauthle et al., 2015b), 316L stainless steel (Yan et al., 2014), NiTi alloy (Habijan et al., 2013), and Co-Cr alloy (Demir and Previtali, 2017), etc. **Table 2** lists the mechanical properties of

different non-biodegradable porous scaffolds (Peng et al., 2019). Ti alloys are widely used in orthopedic implants due to the better biocompatibility, corrosion resistance, and excellent mechanical properties (Zhu et al., 2016). Ti-6Al-4V has more matching elastic modulus with human bone and relatively low price (Yang et al., 2018; Lv et al., 2019), which is the most studied biomedical Ti alloy (Cheng et al., 2014; Zhu et al., 2018). However, cytotoxicity experiments of Ti-6Al-4V scaffolds also indicate that the release of Al and V ions occurs in the human body, which affects cell proliferation and causes cytotoxicity (Surmeneva et al., 2019). Pure Ti, as a good biometal material, avoids the release of harmful ions (Liu J. et al., 2020). Wauthle et al. (2015b) and Liu S. et al. (2020) prepared pure Ti scaffolds with a dodecahedral unit structure and found that the scaffolds have higher fatigue cycle strength and ductility than that of Ti-6Al-4V. The Nb and Zr elements also have good biocompatibility (Sing et al., 2016) and have been used as alloying elements to improve the biological and mechanical properties of Ti alloys (Lin et al., 2013). Liang et al. (2020) prepared Ti-25Nb porous scaffolds with a hydrophilic surface structure. They found that Ti-25Nb scaffold can promote the expression of phagocyte M2 type and enhance the activity of anti-inflammatory phagocytes. Luo et al. (2020) found that the Ti-30Nb-5Ta-8Zr scaffold exhibits similar fatigue strength, compression, and tensile properties with cortical bone, and they also established the functional relationship between the porosity, yield strength, and elastic modulus of the alloy. Wauthle et al. (2015b) and Wang H. et al. (2019) prepared three type porous metal scaffolds, including Ta, pure Ti, and Ti-6Al-4V. They found that Ta porous scaffolds have the same cell proliferation, survival and osteogenic properties as Ti scaffolds. Moreover, the Ta scaffolds have better toughness and fatigue limit than Ti-6Al-4V scaffolds (Guo et al., 2013). However, Ta scaffold has a higher price, which limits its wide application.

TABLE 2 | Mechanical properties of different porous metal scaffolds.

Mechanical properties of porous metal scaffolds			
Materials(structure)	Elastic modulus (GPa)	Yield strength (MPa)	References
Ti-6Al-4V (Gyroid and Diamond)	3.8	152.6 145.7	Liu et al., 2018
Ti-6Al-4V (Octahedral)	2.1–4.7	71–190	Yan et al., 2019
Pure Ti (Diamond)	0.557–0.661	50	Taniguchi et al., 2016
Pure Ti (FGPS)	0.28–0.59	3.79–17.75	Han et al., 2018
Pure Ta (Diamond)	3.1	393.62	Wang H. et al., 2019
Pure Ta (Dodecahedron)	1.22	12.7	Wauthle et al., 2015b
Ti-30Nb-5Ta-8Zr (Rhombic dodecahedron, Body diagonals)	0.7–4.4	12.5–67	Luo et al., 2020
Ti35Zr28Nb (Face centered cubic)	1.1	27	Li et al., 2019a
Ti-35Nb-2Ta-3Zr	3.1 3.5 3.9	136 137 149	Hafeez et al., 2020
CoCr F75 (Diamond)	3.43 2.32 2.22	116.34 75.97 78.57	Hooreweder et al., 2017
NiTi (Octahedron, Cellular gyroid, Sheet gyroid)		21 29 44	Speirs et al., 2017
NiTi	3.7–13.5		Bartolomeu et al., 2020; Liu S. et al., 2020
316L (Gyroid)	2.04 2.48 2.71	55 72.1 89.4	Ma et al., 2019
316L (Gyroid)	14.41–15.53	251–302	Yan et al., 2014
Fe (Diamond)	2.81 0.89 1.77 1.75	53.1 10.7 32.9 30.5	Li et al., 2019b
Fe-35Mn (Schwarz Primitive)	33.5	304	Carluccio et al., 2020
Zn (Diamond)	0.786	10.8	Li et al., 2020c
Mg WE43 (Diamond)	0.7–0.8	23	Li et al., 2018

Ma et al. (2019) prepared 316L stainless steel porous scaffolds and studied the influence of the pore size and porosity on their elastic modulus, yield strength, and permeability. They also established the functional relationship of the above parameters and predicted the permeability of the scaffold. Čapek et al. (2016) also obtained 316L stainless steel scaffolds with good mechanical properties and found that the mechanical properties are close to that of trabecular bone. However, compared with Ti alloy and Ta, stainless steel has a higher elastic modulus, which easily leads to stress shielding (Yamamoto et al., 2004). Thus how to adjust the pore size and porosity of scaffolds and balance their relationship between strength and elastic modulus is the crucial point for 316L stainless steel porous scaffolds.

NiTi alloy has the characteristics of superelasticity and shape memory, which have a good application prospect in biomedical field (Wang L. et al., 2016; Liu et al., 2019). Nevertheless, the Ni ions in the alloy have cytotoxicity, which is a concerning matter to people. Habijan et al. (2013) prepared NiTi scaffolds with different porosity and surface morphology, and cultivated stem human mesenchymal stem cells (hMSC) on NiTi scaffolds. They found that the amount of Ni released in the porous scaffold is higher than that of the dense sample, but all were below the cytotoxic concentration. They also found that changing the spot diameter can improve the scaffold surface morphology, and reducing the spot diameter can reduce Ni ions' release. They believed that NiTi scaffolds are suitable carriers for hMSC, but the process parameters and post-processing still need to be optimized before *in vivo* studies (Liu et al., 2021).

The Co–Cr alloy has good biocompatibility (Baldwin and Hunt, 2006), corrosion resistance, and wear resistance, and is widely used in orthopedic surgery, especially in hip replacement or knee replacement. However, the osseointegration and biomechanical properties of Co–Cr alloy are inferior to Ti–6Al–4V. Shah et al. (2016) prepared Co–Cr and Ti–6Al–4V porous scaffolds by EBM. *In vivo* implantation experiments found that the bone-implant bonding rate of the Co–Cr scaffold is lower than that of the Ti–6Al–4V, but they have similar bone cell density and distribution in a newly formed bone. Caravaggi et al. (2019) prepared Co–Cr scaffolds with different porous structures by SLM, and found that the elastic modulus of porous structure is about 32 GPa, which is close to the elastic modulus of human bone. Cell culture experiments showed that the number of cells on the porous structure continued to increase over the course of 1 week, indicating that the Co–Cr alloy had good biocompatibility.

Biodegradable Metals

The biodegradable metal can effectively avoid chronic local inflammation (Moravej and Mantovani, 2011), continuous physical stimulation (Song and Song, 2007), and implant-related infections, which has broad prospects in the biomedical field. At present, Fe, Mg, and Zn alloys are widely studied as materials for degradable scaffolds (Li et al., 2020b). How to match the rate of metal degradation to that of bone tissue ingrowth is the main challenge. **Table 2** lists the mechanical properties of Fe, Mg, and Zn porous scaffolds.

Fe is an element needed by the human body, and also has good biocompatibility. The main problem for Fe is the slower degradation rate in the human body, which can inhibit the ingrowth rate of bone tissue. Li et al. (2019b) prepared gradient porous Fe scaffolds and the pore size of scaffolds are 600 μm (S0.4), 600–800 μm (Dense-out), 800–600 μm (Dense-in), and 800–600 μm (S0.2). They found that the scaffold of S0.2 and Dense-out had exactly the same structure in the center (**Figure 2B**), but the weight loss of the Dense-out scaffold in the center was higher than that of the S0.2 scaffold, as shown in **Figure 2C**. They believe that the Dense-out scaffold has higher flow velocities in the center than on the periphery, as shown in **Figure 2D**. Adding alloy elements into the Fe can also affect its degradation rate. Carluccio et al. (2019) prepared Fe and Fe–Mn porous scaffolds. They found that the corrosion rate of Fe–Mn scaffold is much higher than that of pure Fe. They believed that a galvanic cell is formed between the different metal scaffolds, which accelerates Fe–Mn alloy's degradation. The Fe–Mn alloy scaffold has good biocompatibility and vitality to mammalian cells.

Mg alloy porous scaffolds have a higher degradation rate, leading to its complete degradation before bone tissue fully grows into the scaffolds. To decrease the degradation rate, surface modification (plasma electrolytic oxidation), and heat treatment of the scaffold were performed by Kopp et al. (2019). They found that Mg hydroxide and oxide are formed on the scaffold surface, which slows down the degradation rate in the simulated body fluid. Mg is more active, and there are problems such as difficulty in preparation, powder splashing, cracks, and so on (Wang et al., 2020d). The degradation rate of Mg scaffolds also can produce hydrogen that affects cell proliferation. They believed that if the problems mentioned above can be dealt with, Mg alloys will have a more significant impact in the biomedical field.

Zn alloys have gradually attracted extensive attention from researchers because their degradation rate is closest to bone tissue (Su et al., 2019; Fu et al., 2020), which is very beneficial to the healing of bone tissue. Li et al. (2020c) prepared Zn scaffolds with a diamond structure and found that the mechanical properties are similar to cancellous bone. The volume loss is 7.8 and 3.6%, respectively, after 28 days of dynamic and static immersion *in vitro*, and the degradation rate is between Mg and Fe, as shown in **Figure 2A**. The mechanical properties of the Zn scaffolds after soaking can be improved after a small amount of degradation. Cockerill et al. (2020) prepared Zn scaffolds with different pore sizes through combination methods of AM and casting and found that the Zn scaffolds have good biocompatibility and antibacterial properties.

High Entropy Alloys

Compared with traditional metals and alloys, high-entropy alloys are gradually becoming a focus of attention due to their better comprehensive properties. These alloys are no longer based on a particular component, but are made of a variety of metal to provide better properties such as strength, corrosion resistance, and biocompatibility (Ma et al., 2020).

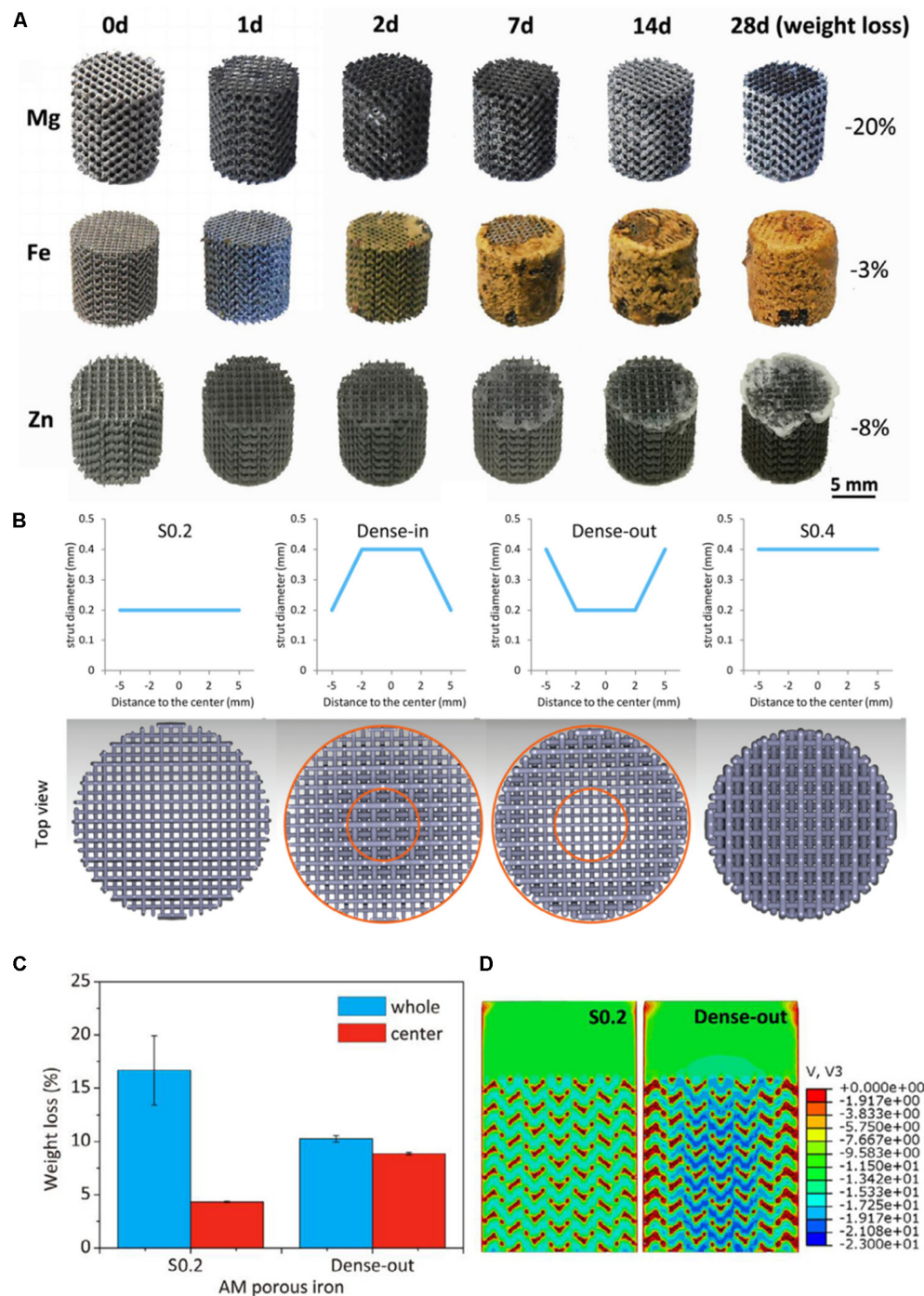


FIGURE 2 | (A) The morphologies of samples after *in vitro* immersion tests (Li et al., 2020b). **(B)** Functionally graded structure of porous Fe scaffolds. **(C)** The weight of S0.2 and Dense-out for 28 days. **(D)** The flow distributions in S0.2 and Dense-out according to CFD modeling (Li et al., 2019b).

Motallebzadeh et al. (2019) prepared TiZrTaHfNb and Ti_{1.5}ZrTa_{0.5}Hf_{0.5}Nb_{0.5} high entropy alloys and compared their properties with 316L, CoCrMo, and Ti6Al4V alloys. They found that the high entropy alloy show higher wear resistance and corrosion resistance. They attributed the higher mechanical properties to the “cocktail effect” of the high entropy

alloy. Nagase et al. (2019) developed novel TiZrHfCr_{0.2}Mo and TiZrHfCo_{0.07}Cr_{0.07}Mo high-entropy alloys for metallic biomaterials based on the combination of Ti–Nb–Ta–Zr–Mo and Co–Cr–Mo alloy systems. The experimental results showed that newly developed high entropy has comparable biocompatibility with pure Ti.

THE STRUCTURE DESIGN OF POROUS METAL SCAFFOLDS

The ideal scaffold should be a porous structure in space that provides space for cells to adhere, grow and proliferate, and have mechanical properties similar to the bone tissue (Cheng et al., 2014). Pore size and porosity are very important structural parameters, which have a direct impact on mechanical properties and biocompatibility of bone scaffolds. Proper pore size can provide growth space for cells, and proper porosity can ensure transportation of nutrients and metabolites in bone tissue (Cheng et al., 2014). Besides, the shape of the porous scaffold structure is also related to the biocompatibility and mechanical properties. The continuous and smooth porous structure can avoid stress concentration and facilitate the attachment of cells to the scaffold surface.

Porous scaffold prepared by the traditional foaming (Murray, 2003) and sintered microsphere methods (Mark et al., 2002) has a single structural unit, and the shape, size, and spatial distribution can not be precisely controlled. With the development of computer-aided design and AM technologies, problems as mentioned above have gradually been improved. AM technologies not only can accurately control the porous scaffold size and spatial structure distribution but also can obtain ideal mechanical properties and biocompatibility of porous scaffold by adjusting the pore size and porosity. In this section, the pore size and porosity of the scaffold are described, and the influence of pore size and porosity on the scaffold's performance are summarized. Then current design methods for porous metal scaffold including CAD structure, topology optimization, minimal surface structure, Voronoi mosaic method, CT imaging method, etc. are systematically reviewed.

Pore Size and Porosity of the Porous Metal Scaffold

The porous scaffold's pore size is generally defined by the inscribed circle method, as shown in **Figure 3**. The definition of porosity is the percentage of pore space in the solid structure given by the following formula:

$$\text{Porosity} = (1 - V_p/V_s) \times 100\%$$

Among them: V_p is the volume of the porous structure and V_s is the volume of the dense structure.

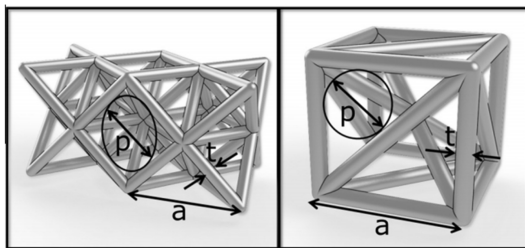


FIGURE 3 | Basic structural unit: p: aperture, t: pillar thickness (Arabnejad et al., 2016).

The Influence of Pore Size and Porosity on Biocompatibility

Many investigations reported that the optimal pore size and porosity of the porous scaffold are about 200–1200 μm (Ataee et al., 2018) and 60–95% (Zhou et al., 2015), respectively. To explore a more specific range of porosity, Ma et al. (2020b) prepared convolute structured scaffolds with a porosity of 75–88% to study the effect of different porosity on cell proliferation. They found that a scaffold with a porosity of 88.8% has the largest number of cells, and they believed that increasing porosity could increase the specific surface area of the porous scaffold and improve its permeability.

Ouyang et al. (2019) explored the pore size's effect on the biocompatibility of porous scaffolds and designed Ti-6Al-4V scaffolds with pore sizes of 400, 650, 850, and 1100 μm , respectively. They found that increasing pore size can reduce the thickness and specific surface area of the pillar and increase the scaffold's permeability. Cell proliferation and *in vivo* bone formation first increase and then decrease with the increase of pore size, and the best pore size is 650 μm . Ran et al. (2018) compared the bone ingrowth of Ti-6Al-4V scaffolds with a different pore sizes (400, 600, and 800 μm). They found that the bone ingrowth properties of the scaffold with pores size of 800 μm and 600 μm is significantly better than that of 400 μm .

Wang S. et al. (2019) compared the biocompatibility of Ti-6Al-4V scaffold with different structures, including OTC, TC, and OTC+TC (PFGS) structures. They found that the OTC structure has the fastest cell proliferation in 1–4 days, and the PFGS structure has the fastest cell proliferation in 4–7 days. In contrast, TC structure has slowest cell proliferation in 1–7 days. They believed that increasing the pore size can improve the permeability of the structure and high permeability can transport more oxygen and nutrients, which is conducive to cell growth in the early stage of cell culture (Wang et al., 2020c). PFGS has a smaller inner hole that is conducive to cell adhesion and differentiation, so the PFGS structure shows a higher cell proliferation rate in the later stage of cell culture.

The Influence of Pore Size and Porosity on Mechanical Properties

The dense metal materials have a much higher elastic modulus than human bone. For example, the elastic modulus of pure Ti and Ti-6Al-4V are 112 and 132 GPa, respectively (Sing et al., 2016). While the elastic modulus of trabecular or cancellous bone is between 0.02 and 2 GPa (Wang X. et al., 2016), cortical bone is higher, ranging from 7.7 to 21.8 GPa (Zhang et al., 2018). At present, the implant's elastic modulus is mainly controlled by adjusting the pore size and porosity. Yan et al. (2015) prepared Ti-6Al-4V scaffolds with G and D structures with a porosity of 80–95%, a pore size of 480–1600 μm , and found that the elastic modulus is about 0.12–1.25 GPa. The pore size and porosity of scaffold also have immediate impact on strength (Ran et al., 2018). Zhao et al. (2019) prepared octahedral structured Ti-6Al-4V porous scaffolds with pore sizes of 500 and 1000 μm and found that increasing pore size can decrease the tensile strength and fatigue strength. Therefore, increasing the pore size and can

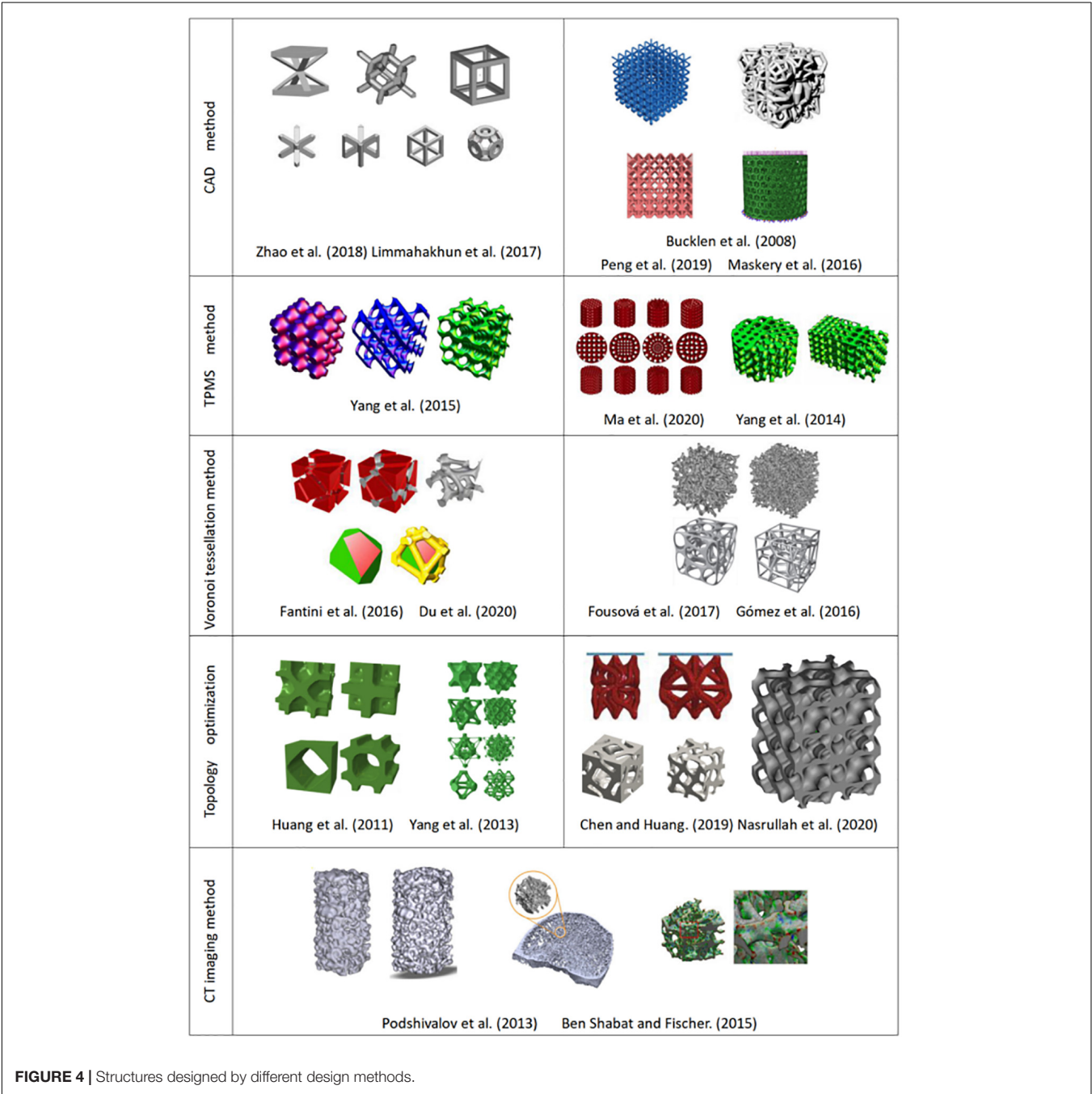
reduces the elastic modulus, but it will also cause a decrease in the tensile strength and fatigue strength of the scaffold.

Structure Design Methods of Porous Metal Scaffold

CAD Method

The main principle of the CAD method is to design different types of hole-making units and then create a porous scaffold through the Boolean operation (Zhao et al., 2018). As the basic unit of a porous scaffold, the shape, porosity, pore

size, and surface area have a direct impact on the overall performance. Thus in the early stage, researchers mainly focused on the design of the hole-making unit. Based on bionic characteristics of different parts of human bones, Sun et al. (2005) designed structural units with disk and rod shapes using computer-aided tissue technology (CATE). They obtained a combination of different units by adding the same circular boundary on different units. Finally, a unit library that can combine multiple structural units was established. Chua et al. (2003) used the CAD method to develop a standard unit library containing 11 kinds of hole elements and developed



an automatic assembly unit to match the anatomical shape of bone tissue. Polyhedra and lattice structure play an important role in CAD design due to their simple structure and good mechanical properties. Maskery et al., 2016 designed a gradient BCC (body centered cubic) lattice model (see **Figure 4**) to compare their mechanical properties and energy absorption with a uniform one. They found that the gradient structure is able to absorb around 114% higher energy than uniform structure. Li et al. (2019a) established the FCC (face-centered cubic structure) and BCC lattice models, and they considered that this simple and reliable models can obtain the desired mechanical properties and biocompatibility. Limmahakhun et al. (2017) established four structures (octahedron, column octahedron, cube and truncated octahedron), as shown in **Figure 4**. The mechanical tests and *in vitro* cellular experiments showed that the column octahedron structure can balance mechanical and biological properties, and are more suitable as the basic unit of bone scaffold. Although created units using CAD method are simple and have a low mechanical property (Wettergreen et al., 2005; Chantarapanich et al., 2012), the method still provides ideas for the following research.

Triple Periodic Minimal Surface (TPMS) Structure

A minimal surface is an implicit equivalent surface with zero mean curvature. If the minimal surface is periodic in three independent directions, it is usually called triple periodic minimal surface (TPMS). TPMS can be expressed by a trigonometric

function, as shown in **Table 3**. Changing the TPMS's threshold value can accurately control the internal pore structure, optimize the gradient pore structure, and maximize the specific surface area of the scaffold.

Yoo (2011b) proposed a three-dimensional bone scaffold design method that integrated distance field algorithms and TPMS curved surfaces. This method can automatically obtain a bone scaffold model with complex microstructures and high quality free-form external surfaces. Yoo (2011a) proposed another TPMS design method that two different TPMS structures can be combined by using a linear interpolation algorithm. Yang et al. (2014) reported that smooth transition between multiple different TPMS substructures could be combined by sigmoid and Gaussian radial basis functions (Yang and Zhou, 2014; Yang et al., 2015). Ma et al. (2020a) proposed a new method for designing heterogeneous porous scaffolds, that is, TPMS units were combined with grid units using shape functions, and they obtained a conformal refined discrete scaffold of a full hexahedral grid. After finite element analysis, they found that the elastic modulus, strength, and energy absorption of the heterogeneous scaffolds are significantly improved than uniform structure.

Nature bone has a porous gradient structure; thus, the gradient TPMS structure is a hot spot in scaffolds design (Almeida and Bartolo, 2014; Zhou et al., 2020). Wang et al. (2020c) designed a symmetrical gradient Ti-6Al-4V scaffolds with a P structure. They found that the gradient structure has better mechanical performance than that of the uniform structure.

TABLE 3 | Common minimal surface structures.

TPMS unit	Mathematical expressions	
P (SchwarzP) structure	$\varphi(x,y,z)=\cos(\omega_x x)+\cos(\omega_y y)+\cos(\omega_z z)=C$	
D (Diamond) structure	$\varphi(x,y,z)=\cos(\omega_x x)\cos(\omega_y y)\cos(\omega_z z)-\sin(\omega_x x)\sin(\omega_y y)\sin(\omega_z z)=C$	
G (Gyroid) structure	$\varphi(x,y,z)=\sin(\omega_x x)\cos(\omega_y y)+\sin(\omega_y y)\cos(\omega_z z)+\sin(\omega_z z)\cos(\omega_x x)=C$	
F-RD structure	$\varphi(x,y,z)=4\cos(\omega_x x)\cos(\omega_y y)\cos(\omega_z z)-[\cos(2\omega_x x)\cos(2\omega_y y)+\cos(2\omega_z z)2(\omega_x x)+\cos(2\omega_y y)\cos(2\omega_z z)]=C$	
I-WP structure S	$\varphi(x,y,z)=2[\cos(\omega_x x)\cos(\omega_y y)+\cos(\omega_z z)\cos(\omega_x x)+\cos(\omega_y y)\cos(\omega_z z)]-[\cos(2\omega_x x)+\cos(2\omega_y y)+\cos(2\omega_z z)]=C$	

Zhang X.Y. et al. (2020) proposed a new method that flexible control of structural parameters can be realized by changing the TPMS equation and found that those structure design parameters have obviously effects on the scaffold performance.

Voronoi Tessellation Method

Voronoi tessellation is a space division method based on seed points (Du et al., 2020). The seed points are connected through a specific algorithm to form a space polygon surrounding the seed points. Based on these polygonal edges, irregular porous scaffolds are generated (Xiao and Yin, 2016). Thus the internal structure of natural bone can be well simulated by irregular porous scaffolds based on the Voronoi tessellation principle.

Kou and Tan (2010) proposed a design method with controllable shape and distribution by using the two-dimensional Voronoi diagram and they obtained irregular concave and convex polygons through the merging of Voronoi units. Then the boundaries of the concave and convex polygons were interconnected to form a bracket. The method makes a heterogeneous porous structure easier and maintain the irregularities in natural bone. Fantini et al. (2016) and Fantini and Curto (2017) used the three-dimensional Voronoi tessellation method to design porous structures, and obtained the three-dimensional Voronoi unit by processing the three-dimensional coordinates, and established the porous structure by Boolean operation on Voronoi unit, as shown in **Figure 4**. Lei et al. (2020) proposed a new Voronoi tessellation method to control the distribution of seed points and established a function relationship of the porosity and the number of seed points. Through this method, they obtained a Voronoi tessellation scaffold with a gradient distribution of seed points, which realizes the global control of the lattice porous structure.

The Voronoi tessellation method can generate an irregular pore model with controllable pore size and distribution, and the automation degree of generating the model is relatively higher. However, this method can not generate complicate porous structure due to the difficulty in the visualization of the porous scaffolds (Wang et al., 2020b).

Topology Optimization

Topology optimization technology is a mathematical method based on finite elements (Marinela et al., 2019), which can rearrange materials or structures to obtain the required mechanical properties (Zhao et al., 2014). It is a powerful method for the design of complex structures with multi-scale features (Chen and Huang, 2019).

Yang et al. (2013) proposed a topology optimization method of periodic hole unit structure and designed a porous scaffold with a required Young's modulus, as shown in **Figure 4**. Radman et al. (2012) specified the volume or shear modulus of units, and optimized the primary unit through the anti-homogeneous two-way advanced optimization technology, and established functionally gradient porous structure by the proper connection between adjacent basic units. Xiao et al. (2012) rearranged the structure of the model under the constraint of volume fraction to achieve the ideal stiffness through the topology

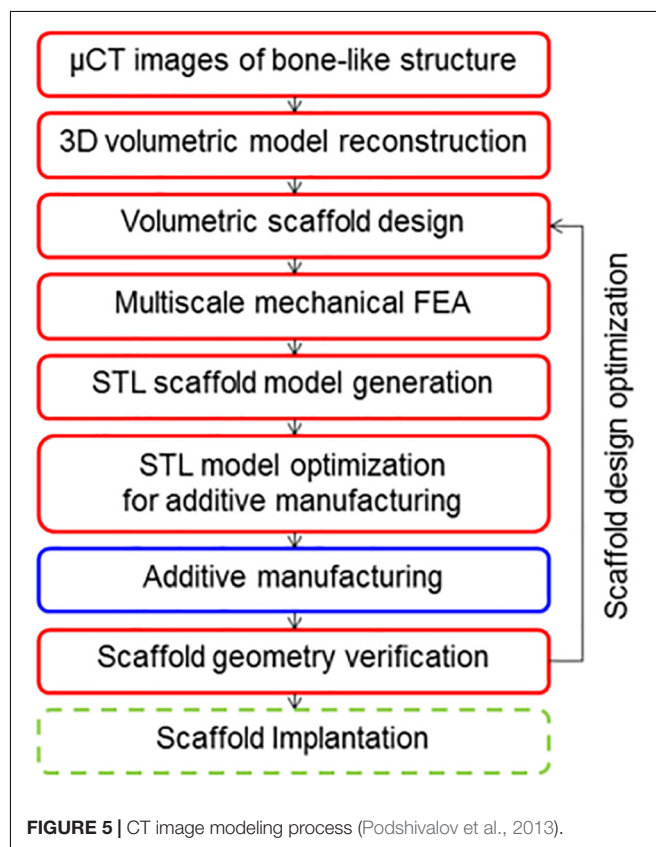
optimization method and obtain optimal three-dimensional structure of porous scaffolds (Xiao et al., 2013). Nasrullah et al. (2020) established 11 kinds of porous structures by topology optimization of lattice structures, and reported a conical lattice structure that can provide energy absorption of up to 127 kJ/kg. Zhang L. et al. (2020) combined the topology optimization with numerical homogenization method to design high stiffness lattice structure, and successfully obtained a new lattice structure with high load-bearing and energy absorption capacity, and the relative elastic modulus can reach 0.037.

Topology optimization methods can combine with a variety of design methods to achieve required mechanical properties and biocompatibility (Wang X. et al., 2016; Park et al., 2018). Nevertheless, the design methods have many variables and high calculations (Zhang X.Y. et al., 2019). How to balance the relationship between structural design and calculation efficiency remains to be resolved (Dias et al., 2014).

CT Imaging Method

The main principle of CT imaging method is to analysis and processing of CT or MRI images (Feinberg et al., 1999) and to extract key features by various reconstruction algorithms to perform three-dimensional reconstruction. The modeling flow chart is shown in **Figure 5**.

Hollister (2005) performed gray-scale processing of medical images and obtained the distribution of solid voxel and void information using a binarization segmentation algorithm. Then



they established the porous structure by mapping the defined porous structure unit to the solid voxel. Podshivalov et al. (2013) segmented the CT image and removed the redundant shadow part, then repaired hole on the model, and finally obtained ideal bone scaffold model, as shown in **Figure 4**. Ben and Fischer (2015) made important progress in CT image adaptive model reconstruction. They introduced the quadtree and octree algorithms into the process of adaptive model reconstruction, which greatly simplifies the modeling process. Zheng et al. (2020) scanned skull samples, extracted the shape of the skull and reconstructed inside structure of the trabecular. Cell cultures experiment showed that the model restores the internal structure of the skull, and has good biocompatibility. The CT imaging method can produce porous structure closest to the three-dimensional structure inside the bone tissue (Cai, 2008; Cai and Xi, 2009; Cai et al., 2012). However, the method has a high dependence on the image resolution (Li et al., 2006), and the simplification processing of CT or MRI data is relatively cumbersome, which leads to certain restrictions on its clinical application (Jones et al., 2007).

Comparison of Porous Scaffold Design Methods

At present, CAD design and topology optimization methods are the widely used methods in the design of porous scaffolds because these methods are simple and reliable, and simultaneously meeting the basic requirements of reducing the modulus of the scaffolds. The structures designed by TPMS and Voronoi methods are more similar to the internal structure of human bone, and they have better permeability and mechanical properties than the structure designed by CAD method. The


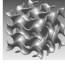

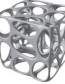
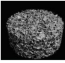
CT imaging method can reflect the real structure of bone. If the reconstruction process of the model can be simplified, it is believed that the CT imaging method can be further developed. The comparisons of these modeling methods are summarized, as shown in **Table 4**.

The above is the comparison and summary of structural unit design methods. In addition, we also pay attention to the overall design of the scaffold, and the hierarchical structure is the hot spot in the overall design of the scaffold (He et al., 2021). The real shape of bone in human body is the porous structure with gradient distribution. According to the size and porosity of the pores, bone can be divided into dense and cancellous bone from the outside to the inside (Du et al., 2019). Only vascular and nerve channels remain in dense bone, with a porosity of about 5–30%. Cancellous bone has a porosity of 30–90%, and can deform under stress and absorb energy shocks from outside (Liu et al., 2018). The hierarchical structure of natural bone in human body can not only meet the needs of material transportation, but also meet the requirements of mechanical properties. Singh et al. (2010) and Huang et al. (2014) demonstrated that the hierarchical structure of the scaffold can produce anisotropic mechanical properties, which are more similar to the mechanical properties of human bones than the homogeneous structure. If the unit design is combined with the overall hierarchical design, scaffolds with better comprehensive performance can be obtained.

SUMMARY AND OUTLOOK

Additive manufacturing technology provides unprecedented opportunities for the production of customized biomedical

TABLE 4 | Comparison of porous scaffold design methods.

Methods	Structures	Design principle	Advantages	Disadvantages	References
CAD method		Boolean operations between unit structures	<ul style="list-style-type: none"> • Low cost • High efficiency • Good permeability 	<ul style="list-style-type: none"> • Poor controllability of parameters • Poor mechanical properties • Small function coverage 	Zhao et al., 2018; Maconachie et al., 2019; Ren et al., 2019
TPMS method		Modeling of trigonometric function expression of minimal surface	<ul style="list-style-type: none"> • Smooth transition • Large specific surface area • Good controllability of parameters 		Yoo, 2011b; Abueidda et al., 2019; Yu et al., 2019
Topology optimization method		According to requirements, optimized by finite element method	<ul style="list-style-type: none"> • Combine with multiple design methods • Good mechanical properties • Good permeability 	<ul style="list-style-type: none"> • Variable and complex parameters 	Challis et al., 2010; Yang et al., 2013
Voronoi tessellation method		Based on the seed point, surround the seed point to form a spatial polygon, and build a support based on the edge of the polygon	<ul style="list-style-type: none"> • Simulate the irregular porosity of natural bone • Good controllability of parameters 	<ul style="list-style-type: none"> • Poor mechanical performance • Complex relationship between parameters and performance 	Gómez et al., 2016; Fantini et al., 2016; Fantini and Curto, 2017
CT imaging method		Extract the key shape features of the CT images and perform 3D reconstruction	<ul style="list-style-type: none"> • Internal structure closest to natural bone • Good permeability 	<ul style="list-style-type: none"> • Complex data processing • High equipment requirements 	Gómez et al., 2016

implants. With the development of materials science and computer-assisted technologies, metal porous scaffolds produced by AM, additive manufacturing have been applied in clinical practice. In the future, the preparation of porous metal scaffolds by AM, additive manufacturing still has great potential in the following fields.

- (1) The metal scaffolds with degradable materials can effectively reduce the subsequent maintenance problems of the implant. However, the most widely used materials for metal porous scaffolds are still non-degradable metals such as pure Ti, Ti alloys, 316L and so on. So it is particularly important to design and prepare new biodegradable materials that matching degradation rate with bone tissue.
- (2) Real bone in the human body has gradient microstructures; thus the development of porous scaffolds with gradient structure is a future development trend. At present, it is challenging to obtain a gradient scaffold with better performance with a single design method. Therefore, combination methods of topology optimization, CAD and minimal surface and so on. Can be tried to design the gradient structure in the future.
- (3) Surface modification can effectively improve the osteogenesis, bacteriostasis, and biocompatibility of porous scaffolds. At present, preparation of inorganic and organic surfaces, or changing the surface morphologies of bone implants are the main surface modification methods. In the future, new surface modification materials and methods used for porous scaffolds should be developed in order to improve its biocompatibility or realize the treatment of certain diseases.
- (4) At present, most of the researches on the biocompatibility of the scaffold only stays in cell experiments, which lacks accurate evaluation of the scaffold performances. Thus effective *in vivo* osteogenic experiment should be introduced and biological standards should be established

to more scientifically evaluate the osteogenic ability of porous scaffolds.

- (5) 4D printing is a concept that has emerged in recent years, which generally refers to programmatical change in shape and function of 3D printed scaffolds over time. The change can adjust the mechanical properties or structure characteristics of the porous scaffolds and expand its functions and applications, providing a broader prospect for the development of porous scaffolds.

AUTHOR CONTRIBUTIONS

YT carried out the conception of the idea of the manuscript. ZQ and JL provided the data and advice. BW and GL collected and collated the data. YL wrote the original draft. EL reviewed and revised the original draft. KX and CL provided guidance for the revision of the manuscript. LW provided the financial support for the project to this publication. All the authors contributed to the article and approved the submitted version.

FUNDING

The authors would like to acknowledge the financial supports provided by National Science Foundation under Grant No. 51801115, the China Postdoctoral Science Foundation (Grant No. 2020M671112), High-level Innovation team and Outstanding Scholars Program of Colleges and Universities in Guangxi: innovative team of basic and Clinical Comprehensive Research on Bone and Joint degenerative Disease, Project of Science and Technology Innovation Base under the Central Guidance of local Science and Technology Development (Guikexi [2020] No. 198): Science and Technology Innovation Base for basic Research and Transformation of bone and joint degenerative diseases.

REFERENCES

- Abueidha, D. W., Elhebeary, M., Shiang, C.-S., Pang, S., Abu Al-Rub, R. K., and Jasiuk, I. M. (2019). Mechanical properties of 3D printed polymeric gyroid cellular structures: experimental and finite element study. *Mater. Des.* 165:107597. doi: 10.1016/j.matdes.2019.107597
- Ahmadi, S. M., Kumar, R., Borisov, E. V., Petrov, R., Leeflang, S., Li, Y., et al. (2019). From microstructural design to surface engineering: a tailored approach for improving fatigue life of additively manufactured meta-biomaterials. *Acta Biomater.* 83, 153–166. doi: 10.1016/j.actbio.2018.10.043
- Almeida, H. A., and Bártolo, P. J. (2014). Design of tissue engineering scaffolds based on hyperbolic surfaces: structural numerical evaluation. *Med. Eng. Phys.* 36, 1033–1040. doi: 10.1016/j.medengphy.2014.05.006
- Arabnejad, S., Burnett Johnston, R., Pura, J. A., Singh, B., Tanzer, M., and Pasini, D. (2016). High-strength porous biomaterials for bone replacement: a strategy to assess the interplay between cell morphology, mechanical properties, bone ingrowth and manufacturing constraints. *Acta Biomater.* 30, 345–356. doi: 10.1016/j.actbio.2015.10.048
- Ataee, A., Li, Y., Fraser, D., Song, G., and Wen, C. (2018). Anisotropic Ti-6Al-4V gyroid scaffolds manufactured by electron beam melting (EBM) for bone implant applications. *Mater. Des.* 137, 345–354. doi: 10.1016/j.matdes.2017.10.040
- Ataee, A., Li, Y., Song, G., and Wen, C. (2017). Metal scaffolds processed by electron beam melting for biomedical applications. *Metallic Foam Bone* 3, 83–110. doi: 10.1016/b978-0-08-101289-5.00003-2
- Bae, E.-J., Kim, J.-H., Kim, W.-C., and Kim, H.-Y. (2014). Bond and fracture strength of metal-ceramic restorations formed by selective laser sintering. *J. Adv. Prosthodont.* 6, 266–271. doi: 10.4047/jap.2014.6.4.266
- Baldwin, L., and Hunt, J. A. (2006). Host inflammatory response to NiCr. CoCr, and Ti in a soft tissue implantation model. *J. Biomed. Mater. Res. A* 79, 574–581. doi: 10.1002/jbm.a.30856
- Bartolomeu, F., Costa, M. M., Alves, N., Miranda, G., and Silva, F. S. (2020). Engineering the elastic modulus of NiTi cellular structures fabricated by selective laser melting. *J. Mech. Behav. Biomed. Mater.* 110:103891. doi: 10.1016/j.jmbbm.2020.103891
- Ben, S. Y., and Fischer, A. (2015). Design of porous micro-structures using curvature analysis for additive-manufacturing. *Procedia CIRP* 36, 279–284. doi: 10.1016/j.procir.2015.01.057
- Bose, S., Ke, D., Sahasrabudhe, H., and Bandyopadhyay, A. (2018). Additive manufacturing of biomaterials. *Prog. Mater. Sci.* 93, 45–111. doi: 10.1016/j.pmatsci.2017.08.003
- Bundy, K. J. (2008). Biomaterials and the chemical environment of the body. *Joint Replacement Technology* 44, 56–80. doi: 10.1533/9781845694807.1.56

- Cai, S. (2008). A control approach for pore size distribution in the bone scaffold based on the hexahedral mesh refinement. *Comput. Aided Des.* 40, 1040–1050. doi: 10.1016/j.cad.2008.09.004
- Cai, S., and Xi, J. (2009). Morphology-controllable modeling approach for a porous scaffold structure in tissue engineering. *Virtual Phys. Prototyp.* 4, 149–163. doi: 10.1080/17452750903208467
- Cai, S., Xi, J., and Chua, C. K. (2012). A novel bone scaffold design approach based on shape function and all-hexahedral mesh refinement. *Comput. Aided Tissue Eng.* 868, 45–55. doi: 10.1007/978-1-61779-764-4_3
- Čapek, J., Machová, M., Fousová, M., Kubásek, J., Vojtěch, D., Fojt, J., et al. (2016). Highly porous, low elastic modulus 316L stainless steel scaffold prepared by selective laser melting. *Mater. Sci. Eng. C* 69, 631–639. doi: 10.1016/j.msec.2016.07.027
- Caravaggi, P., Liverani, E., Leardini, A., Fortunato, A., Belvedere, C., Baruffaldi, F., et al. (2019). CoCr porous scaffolds manufactured via selective laser melting in orthopedics: topographical, mechanical, and biological characterization. *J. Biomed. Mater. Res. Part B* 107, 2343–2353. doi: 10.1002/jbm.b.34328
- Carluccio, D., Demir, A. G., Caprio, L., Previtali, B., Bermingham, M. J., and Dargusch, M. S. (2019). The influence of laser processing parameters on the densification and surface morphology of pure Fe and Fe-35Mn scaffolds produced by selective laser melting. *J. Manuf. Processes* 40, 113–121. doi: 10.1016/j.jmapro.2019.03.018
- Carluccio, D., Xu, C., Venezuela, J., Cao, Y., Kent, D., Bermingham, M., et al. (2020). Additively manufactured iron-manganese for biodegradable porous load-bearing bone scaffold applications. *Acta Biomater.* 103, 346–360. doi: 10.1016/j.actbio.2019.12.018
- Challis, V. J., Roberts, A. P., Grotowski, J. F., Zhang, L.-C., and Sercombe, T. B. (2010). Prototypes for bone implant scaffolds designed via topology optimization and manufactured by solid freeform fabrication. *Adv. Eng. Mater.* 12, 1106–1110. doi: 10.1002/adem.201000154
- Chantarapanich, N., Puttawibul, P., Sucharitpwatskul, S., Jeamwattthanachai, P., Inglam, S., and Sitthiseripratip, K. (2012). Scaffold library for tissue engineering: a geometric evaluation. *Comput. Math. Method. M.* 2012, 1–14. doi: 10.1155/2012/407805
- Chen, S. Y., Kuo, C. N., Su, Y. L., Huang, J. C., Wu, Y. C., Lin, Y. H., et al. (2018). Microstructure and fracture properties of open-cell porous Ti-6Al-4V with high porosity fabricated by electron beam melting. *Mater. Charact.* 138, 255–262. doi: 10.1016/j.matchar.2018.02.016
- Chen, W., and Huang, X. (2019). Topological design of 3D chiral metamaterials based on couple-stress homogenization. *J. Mech. Phys. Solids* 131, 372–386. doi: 10.1016/j.jmps.2019.07.014
- Chen, Y., Li, W., Zhang, C., Wu, Z., and Liu, J. (2020b). Recent developments of biomaterials for additive manufacturing of bone scaffolds. *Adv. Healthc. Mater.* 9:2000724. doi: 10.1002/adhm.202000724
- Chen, Z., Yan, X., Yin, S., Liu, L., Liu, X., Zhao, G., et al. (2020a). Influence of the pore size and porosity of selective laser melted Ti6Al4V ELI porous scaffold on cell proliferation, osteogenesis and bone ingrowth. *Mater. Sci. Eng. C* 106:110289. doi: 10.1016/j.msec.2019.110289
- Cheng, A., Humayun, A., Cohen, D. J., Boyan, B. D., and Schwartz, Z. (2014). Additively manufactured 3D porous Ti-6Al-4V constructs mimic trabecular bone structure and regulate osteoblast proliferation, differentiation and local factor production in a porosity and surface roughness dependent manner. *Biofabrication* 6:045007. doi: 10.1088/1758-5082/6/4/045007
- Chohan, J. S., Singh, R., Boparai, K. S., Penna, R., and Fraternali, F. (2017). Dimensional accuracy analysis of coupled fused deposition modeling and vapour smoothing operations for biomedical applications. *Compos. Part B Eng.* 117, 138–149. doi: 10.1016/j.compositesb.2017.02.045
- Chua, C. M., Chua, C. K., Cheah, C. M., and Chua, S. W. (2003). Development of a tissue engineering scaffold structure library for rapid prototyping. Part 2: parametric library and assembly program. *Adv. Manuf. Technol.* 21, 303–312.
- Cockerill, I., Su, Y., Sinha, S., Qin, Y. X., Zheng, Y., Young, M. L., et al. (2020). Porous zinc scaffolds for bone tissue engineering applications: a novel additive manufacturing and casting approach. *Mater. Sci. Eng. C Mater. Biol. Appl.* 110:110738. doi: 10.1016/j.msec.2020.110738
- Cutolo, A., Engelen, B., Desmet, W., and Van Hooreweder, B. (2020). Mechanical properties of diamond lattice Ti-6Al-4V structures produced by laser powder bed fusion: on the effect of the load direction. *J. Mech. Behav. Biomed. Mater.* 104:103656. doi: 10.1016/j.jmbbm.2020.103656
- Demir, A. G., and Previtali, B. (2017). Additive manufacturing of cardiovascular CoCr stents by selective laser melting. *Mater. Des.* 119, 338–350. doi: 10.1016/j.matdes.2017.01.091
- Dias, M. R., Guedes, J. M., Flanagan, C. L., Hollister, S. J., and Fernandes, P. R. (2014). Optimization of scaffold design for bone tissue engineering: a computational and experimental study. *Med. Eng. Phys.* 36, 448–457. doi: 10.1016/j.medengphy.2014.02.010
- Dogan, E., Bhusal, A., Cecen, B., and Miri, A. K. (2020). 3D Printing metamaterials towards tissue engineering. *Appl. Mater. Today* 20:100752. doi: 10.1016/j.apmt.2020.100752
- Du, Y., Guo, J. L., Wang, J., Mikos, A. G., and Zhang, S. (2019). Hierarchically designed bone scaffolds: from internal cues to external stimuli. *Biomaterials* 218:119334. doi: 10.1016/j.biomaterials.2019.119334
- Du, Y., Liang, H., Xie, D., Mao, N., Zhao, J., Tian, Z., et al. (2020). Design and statistical analysis of irregular porous scaffolds for orthopedic reconstruction based on voronoi tessellation and fabricated via selective laser melting (SLM). *Mater. Chem. Phys.* 239:121968. doi: 10.1016/j.matchemphys.2019.121968
- Fang, Z.-C., Wu, Z.-L., Huang, C.-G., and Wu, C.-W. (2020). Review on residual stress in selective laser melting additive manufacturing of alloy parts. *Optics Laser Technol.* 129:106283. doi: 10.1016/j.optlastec.2020.106283
- Fantini, M., and Curto, M. (2017). Interactive design and manufacturing of a Voronoi-based biomimetic bone scaffold for morphological characterization. *Int. J. Interact. Des. Manuf.* 12, 585–596. doi: 10.1007/s12008-017-0416-x
- Fantini, M., Curto, M., and De Crescenzo, F. (2016). A method to design biomimetic scaffolds for bone tissue engineering based on Voronoi lattices. *Virtual Phys. Prototyp.* 11, 77–90. doi: 10.1080/17452759.2016.1172301
- Feinberg, S., Hollister, S., Chu, T., and Halloran, J. (1999). An image-based approach to design and manufacture of scaffolds for maxillofacial reconstruction. *Maxillofacial Reconstruction* 28:55. doi: 10.1016/S0901-5027(99)80817-0
- Fu, J., Su, Y., Qin, Y.-X., Zheng, Y., Wang, Y., and Zhu, D. (2020). Evolution of metallic cardiovascular stent materials: a comparative study among stainless steel, magnesium and zinc. *Biomaterials* 230:119641. doi: 10.1016/j.biomaterials.2019.119641
- Gibson, I., Rosen, D., and Stucker, B. (2015). Directed energy deposition processes. *Addit. Manuf. Technol.* 10, 245–268. doi: 10.1007/978-1-4939-2113-3_10
- Gokuldoss, P. K., Kolla, S., and Eckert, J. (2017). Additive manufacturing processes: selective laser melting, electron beam melting and binder jetting—selection guidelines. *Materials* 10:672. doi: 10.3390/ma10060672
- Gómez, S., Vlad, M. D., López, J., and Fernández, E. (2016). Design and properties of 3D scaffolds for bone tissue engineering. *Acta Biomater.* 42, 341–350. doi: 10.1016/j.actbio.2016.06.032
- Gong, X., Anderson, T., and Chou, K. (2014). Review on powder-based electron beam additive manufacturing technology. *Manuf. Rev.* 1:2. doi: 10.1051/mfreview/2014001
- Goodridge, R. D., Tuck, C. J., and Hague, R. J. M. (2012). Laser sintering of polyamides and other polymers. *Prog. Mater. Sci.* 57, 229–267. doi: 10.1016/j.pmatsci.2011.04.001
- Guo, Y., Chen, D., Cheng, M., Lu, W., Wang, L., and Zhang, X. (2013). The bone tissue compatibility of a new Ti35Nb2Ta3Zr alloy with a low Young's modulus. *Int. J. Mol. Med.* 31, 689–697. doi: 10.3892/ijmm.2013.1249
- Habijan, T., Haberland, C., Meier, H., Frenzel, J., Wittsiepe, J., Wuwer, C., et al. (2013). The biocompatibility of dense and porous Nickel–Titanium produced by selective laser melting. *Mater. Sci. Eng. C* 33, 419–426. doi: 10.1016/j.msec.2012.09.008
- Hafeez, N., Liu, J., Wang, L., Wei, D., Tang, Y., Lu, W., et al. (2020). Superelastic response of low-modulus porous beta-type Ti-35Nb-2Ta-3Zr alloy fabricated by laser powder bed fusion. *Addit. Manuf.* 34:101264. doi: 10.1016/j.addma.2020.101264
- Han, C., Li, Y., Wang, Q., Wen, S., Wei, Q., Yan, C., et al. (2018). Continuous functionally graded porous titanium scaffolds manufactured by selective laser melting for bone implants. *J. Mech. Behav. Biomed. Mater.* 80, 119–127. doi: 10.1016/j.jmbbm.2018.01.013
- He, J., Fang, J., Wei, P., Li, Y., Guo, H., Mei, Q., et al. (2021). Cancellous bone-like porous Fe@Zn scaffolds with core-shell-structured skeletons for biodegradable bone implants. *Acta Biomater.* 121, 665–681. doi: 10.1016/j.actbio.2020.11.032

- Henkel, J., Woodruff, M. A., Epari, D. R., Steck, R., Glatt, V., Dickinson, I. C., et al. (2013). Bone regeneration based on tissue engineering conceptions — a 21st century perspective. *Bone Res.* 1, 216–248. doi: 10.4248/br201303002
- Hollister, S. J. (2005). Porous scaffold design for tissue engineering. *Nat. Mater.* 4, 518–524. doi: 10.1038/nmat1421
- Hooreweder, B. V., Lietaert, K., Neirincx, B., Lippiatt, N., and Wevers, M. (2017). CoCr F75 scaffolds produced by additive manufacturing: Influence of chemical etching on powder removal and mechanical performance. *J. Mech. Behav. Biomed. Mater.* 70, 60–67. doi: 10.1016/j.jmbbm.2017.03.017
- Huang, S., Chen, Z., Pugno, N., Chen, Q., and Wang, W. (2014). A novel model for porous scaffold to match the mechanical anisotropy and the hierarchical structure of bone. *Mater. Lett.* 122, 315–319. doi: 10.1016/j.matlet.2014.02.057
- Jones, A. C., Arns, C. H., Sheppard, A. P., Hutmacher, D. W., Milthorpe, B. K., and Knackstedt, M. A. (2007). Assessment of bone ingrowth into porous biomaterials using MICRO-CT. *Biomaterials* 28, 2491–2504. doi: 10.1016/j.biomaterials.2007.01.046
- Kapat, K., Srivas, P. K., Rameshbabu, A. P., Maity, P. P., Jana, S., Dutta, J., et al. (2017). Influence of porosity and pore-size distribution in Ti6Al4V foam on physicochemical properties, osteogenesis, and quantitative validation of bone ingrowth by micro-computed tomography. *ACS Appl. Mater. Inter.* 9, 39235–39248. doi: 10.1021/acsami.7b13960
- Kelly, C. N., Francovich, J., Julmi, S., Safranski, D., Guldborg, R. E., Maier, H. J., et al. (2019). Fatigue behavior of As-built selective laser melted titanium scaffolds with sheet-based gyroid microarchitecture for bone tissue engineering. *Acta Biomater.* 94, 610–626. doi: 10.1016/j.actbio.2019.05.046
- Kopp, A., Derra, T., Muther, M., Jauer, L., Schleifenbaum, J. H., Voshage, M., et al. (2019). Influence of design and postprocessing parameters on the degradation behavior and mechanical properties of additively manufactured magnesium scaffolds. *Acta Biomater.* 98, 23–35. doi: 10.1016/j.actbio.2019.04.012
- Kou, X. Y., and Tan, S. T. (2010). A simple and effective geometric representation for irregular porous structure modeling. *Comput. Aided Des.* 42, 930–941. doi: 10.1016/j.cad.2010.06.006
- Lee, H., Lim, C. H. J., Low, M. J., Tham, N., Murukeshan, V. M., and Kim, Y.-J. (2017). Lasers in additive manufacturing: a review. *Int. J. Pr. Eng. Man GT.* 4, 307–322. doi: 10.1007/s40684-017-0037-7
- Lei, H.-Y., Li, J.-R., Xu, Z.-J., and Wang, Q.-H. (2020). Parametric design of Voronoi-based lattice porous structures. *Mater. Des.* 191:108607. doi: 10.1016/j.matdes.2020.108607
- Li, J., Cui, X., Hooper, G. J., Lim, K. S., and Woodfield, T. B. F. (2020a). Rational design, bio-functionalization and biological performance of hybrid additive manufactured titanium implants for orthopaedic applications: a review. *J. Mech. Behav. Biomed. Mater.* 105:103671. doi: 10.1016/j.jmbbm.2020.103671
- Li, Y., Jahr, H., Zhou, J., and Zadpoor, A. A. (2020b). Additively manufactured biodegradable porous metals. *Acta Biomater.* 115, 29–50. doi: 10.1016/j.actbio.2020.08.018
- Li, Y., Pavanram, P., Zhou, J., Lietaert, K., Taheri, P., Li, W., et al. (2020c). Additively manufactured biodegradable porous zinc. *Acta Biomater.* 101, 609–623. doi: 10.1016/j.actbio.2019.10.034
- Li, X., Li, D., and Zhang, Y. (2006). Investigation of bone tissue microstructure and indirect fabrication of biomimetic scaffold via stereolithography. *Beijing Biomed. Eng.* 25, 164–167.
- Li, Y., Ding, Y., Munir, K., Lin, J., Brandt, M., Atrens, A., et al. (2019a). Novel β -Ti35Zr28Nb alloy scaffolds manufactured using selective laser melting for bone implant applications. *Acta Biomater.* 87, 273–284. doi: 10.1016/j.actbio.2019.01.051
- Li, Y., Jahr, H., Pavanram, P., Bobbert, F. S. L., Puggi, U., Zhang, X. Y., et al. (2019b). Additively manufactured functionally graded biodegradable porous iron. *Acta Biomater.* 96, 646–661. doi: 10.1016/j.actbio.2019.07.013
- Li, Y., Zhou, J., Pavanram, P., Leeflang, M. A., Fockaert, L. I., Pouran, B., et al. (2018). Additively manufactured biodegradable porous magnesium. *Acta Biomater.* 67, 378–392. doi: 10.1016/j.actbio.2017.12.008
- Liang, H., Zhao, D., Feng, X., Ma, L., Deng, X., Han, C., et al. (2020). 3D-printed porous titanium scaffolds incorporating niobium for high bone regeneration capacity. *Mater. Des.* 194:108890. doi: 10.1016/j.matdes.2020.108890
- Limmahakhun, S., Oloyede, A., Sithithiripratip, K., Xiao, Y., and Yan, C. (2017). 3D-printed cellular structures for bone biomimetic implants. *Addit. Manuf.* 15, 93–101. doi: 10.1016/j.addma.2017.03.010
- Lin, Z., Wang, L., Xue, X., Lu, W., Qin, J., and Zhang, D. (2013). Microstructure evolution and mechanical properties of a Ti-35Nb-3Zr-2Ta biomedical alloy processed by equal channel angular pressing (ECAP). *Mater. Sci. Eng. C. Mater. Biol. Appl.* 33, 4551–4561. doi: 10.1016/j.msec.2013.07.010
- Little, N., Rogers, B., and Flannery, M. (2011). Bone formation, remodelling and healing. *Surgery* 29, 141–145. doi: 10.1016/j.mpsur.2011.01.002
- Liu, F., Mao, Z., Zhang, P., Zhang, D. Z., Jiang, J., and Ma, Z. (2018). Functionally graded porous scaffolds in multiple patterns: new design method, physical and mechanical properties. *Mater. Des.* 160, 849–860. doi: 10.1016/j.matdes.2018.09.053
- Liu, J., Liu, J., Attarilar, S., Wang, C., Tamaddon, M., Yang, C., et al. (2020). Nano-modified titanium implant materials: a way toward improved antibacterial properties. *Front. Bioeng. Biotechnol.* 8:576969. doi: 10.3389/fbioe.2020.576969
- Liu, S., Han, S., Wang, L., Liu, J., and Tang, H. (2019). Effects of Nb on the microstructure and compressive properties of an As-Cast Ni44Ti44Nb12 eutectic alloy. *Materials* 12:4118. doi: 10.3390/ma12244118
- Liu, S., Han, S., Zhang, L., Chen, L., Wang, L., Zhang, L., et al. (2020). Strengthening mechanism and micropillar analysis of high-strength NiTi-Nb eutectic-type alloy prepared by laser powder bed fusion. *Compos. Part B Eng.* 200:108358. doi: 10.1016/j.compositesb.2020.108358
- Liu, S., Liu, W., Liu, J., Zhang, L., Tang, Y., Zhang, L., et al. (2021). Compressive properties and microstructure evolution in NiTiNb alloy with mesh eutectic phase. *Mater. Sci. Eng. A* 801:140434. doi: 10.1016/j.msea
- Liu, Y. J., Li, S. J., Wang, H. L., Hou, W. T., Hao, Y. L., Yang, R., et al. (2016). Microstructure, defects and mechanical behavior of beta-type titanium porous structures manufactured by electron beam melting and selective laser melting. *Acta Mater.* 113, 56–67. doi: 10.1016/j.actamat.2016.04.029
- Luo, J. P., Huang, Y. J., Xu, J. Y., Sun, J. F., Dargusch, M. S., Hou, C. H., et al. (2020). Additively manufactured biomedical Ti-Nb-Ta-Zr lattices with tunable Young's modulus: mechanical property, biocompatibility, and proteomics analysis. *Mater. Sci. Eng. C* 114:110903. doi: 10.1016/j.msec.2020.110903
- Lv, Y., Ding, Z., Sun, X., Li, L., Sha, G., Liu, R., et al. (2019). Gradient microstructures and mechanical properties of Ti-6Al-4V/Zn composite prepared by friction stir processing. *Materials* 12:2795.
- Ma, N., Liu, S., Liu, W., Xie, L., Wei, D., Wang, L., et al. (2020). Research progress of titanium-based high entropy alloy: methods, properties, and applications. *Front. Bioeng. Biotechnol.* 8:603522. doi: 10.3389/fbioe.2020.603522
- Ma, S., Song, K., Lan, J., and Ma, L. (2020a). Biological and mechanical property analysis for designed heterogeneous porous scaffolds based on the refined TPMS. *J. Mech. Behav. Biomed. Mater.* 107:103727. doi: 10.1016/j.jmbbm.2020.103727
- Ma, S., Tang, Q., Han, X., Feng, Q., Song, J., Setchi, R., et al. (2020b). Manufacturability, mechanical properties, mass-transport properties and biocompatibility of triply periodic minimal surface (TPMS) porous scaffolds fabricated by selective laser melting. *Mater. Des.* 195:109034. doi: 10.1016/j.matdes.2020.109034
- Ma, S., Tang, Q., Feng, Q., Song, J., Han, X., and Guo, F. (2019). Mechanical behaviours and mass transport properties of bone-mimicking scaffolds consisted of gyroid structures manufactured using selective laser melting. *J. Mech. Behav. Biomed. Mater.* 93, 158–169. doi: 10.1016/j.jmbbm.2019.01.023
- Maconachie, T., Leary, M., Lozanovski, B., Zhang, X., Qian, M., Faruque, O., et al. (2019). SLM lattice structures: properties, performance, applications and challenges. *Mater. Des.* 183:108137. doi: 10.1016/j.matdes.2019.108137
- Marinela, P., Erick Ramirez-Cedillo, C., Adriana, H., and Hector, R. S. (2019). Structural design optimization of knee replacement implants for additive manufacturing. *Procedia Manuf.* 34, 574–583. doi: 10.1016/j.promfg.2019.06.222
- Mark, B., Mohamed, A., Yusuf, K., and Laurencina, C. T. (2002). Tissue engineered microsphere-based matrices for bone repair: design and evaluation. *Biomaterials* 23, 551–559.
- Maskery, I., Hussey, A., Panesar, A., Aremu, A., Tuck, C., Ashcroft, I., et al. (2016). An investigation into reinforced and functionally graded lattice structures. *J. Cell. Plast.* 53, 151–165. doi: 10.1177/0021955x16639035
- Mohamed, O. A., Masood, S. H., and Bhowmik, J. L. (2015). Optimization of fused deposition modeling process parameters: a review of current research and future prospects. *Adv. Manuf.* 3, 42–53. doi: 10.1007/s40436-014-0097-7
- Moiduddin, K., Darwish, S., Al-Ahmari, A., ElWatidy, S., Mohammad, A., and Ameen, W. (2017). Structural and mechanical characterization of custom

- design cranial implant created using additive manufacturing. *Electron. J. Biotechnol.* 29, 22–31. doi: 10.1016/j.ejbt.2017.06.005
- Moravej, M., and Mantovani, D. (2011). Biodegradable metals for cardiovascular stent application: interests and new opportunities. *Int. J. Mol. Sci.* 12, 4250–4270. doi: 10.3390/ijms12074250
- Motallebzadeh, A., Peighambaroust, N. S., and Sheikh, S. (2019). Microstructural, mechanical and electrochemical characterization of TiZrTaHfNb and Ti1.5ZrTa0.5Hf0.5Nb0.5 refractory high-entropy alloys for biomedical applications. *Intermetallics* 113:106572. doi: 10.1016/j.intermet.2019.106572
- Murray, N. (2003). Microstructure evolution during solid-state foaming of titanium. *Compos. Sci. Technol.* 63, 2311–2316. doi: 10.1016/s0266-3538(03)00264-1
- Nagase, T., Iijima, Y., Matsugaki, A., Ameyama, K., and Nakano, T. (2019). Design and fabrication of Ti–Zr–Hf–Cr–Mo and Ti–Zr–Hf–Co–Cr–Mo high-entropy alloys as metallic biomaterials. *J. Pre Proof* 107:110322. doi: 10.1016/j.msec.2019.110322
- Nasrullah, A. I. H., Santosa, S. P., and Dirgantara, T. (2020). Design and optimization of crashworthy components based on lattice structure configuration. *Structures* 26, 969–981. doi: 10.1016/j.istruc.2020.05.001
- Ngo, T. D., Kashani, A., Imbalzano, G., Nguyen, K. T. Q., and Hui, D. (2018). Additive manufacturing (3D printing): a review of materials, methods, applications and challenges. *Compos. Part B Eng.* 143, 172–196. doi: 10.1016/j.compositesb.2018.02.012
- Onal, E., Frith, J., Jurg, M., Wu, X., and Molotnikov, A. (2018). Mechanical properties and in vitro behavior of additively manufactured and functionally graded Ti6Al4V porous scaffolds. *Metals* 8:200. doi: 10.3390/met8040200
- Ouyang, P., Dong, H., He, X., Cai, X., Wang, Y., Li, J., et al. (2019). Hydromechanical mechanism behind the effect of pore size of porous titanium scaffolds on osteoblast response and bone ingrowth. *Mater. Des.* 183:108151. doi: 10.1016/j.matdes.2019.108151
- Park, J., Sutradhar, A., Shah, J. J., and Paulino, G. H. (2018). Design of complex bone internal structure using topology optimization with perimeter control. *Comput. Biol. Med.* 94, 74–84. doi: 10.1016/j.compbiomed.2018.01.001
- Peng, W.-M., Liu, Y.-F., Jiang, X.-F., Dong, X.-T., Jun, J., Baur, D. A., et al. (2019). Bionic mechanical design and 3D printing of novel porous Ti6Al4V implants for biomedical applications. *J. Zhejiang Univ. Sci. B* 20, 647–659. doi: 10.1631/jzus.B1800622
- Podshivalov, L., Gomes, C. M., Zocca, A., Guenster, J., Bar-Yoseph, P., and Fischer, A. (2013). Design, analysis and additive manufacturing of porous structures for biocompatible micro-scale scaffolds. *Procedia Cirp* 5, 247–252. doi: 10.1016/j.procir.2013.01.049
- Qu, H. (2020). Additive manufacturing for bone tissue engineering scaffolds. *Mater. Today Commun.* 24:101024. doi: 10.1016/j.mtcomm.2020.101024
- Radman, A., Huang, X., and Xie, Y. M. (2012). Topology optimization of functionally graded cellular materials. *J. Mater. Sci.* 48, 1503–1510. doi: 10.1007/s10853-012-6905-1
- Ran, Q., Yang, W., Hu, Y., Shen, X., Yu, Y., Xiang, Y., et al. (2018). Osteogenesis of 3D printed porous Ti6Al4V implants with different pore sizes. *J. Mech. Behav. Biomed. Mater.* 84, 1–11. doi: 10.1016/j.jmbbm.2018.04.010
- Ren, D., Li, S., Wang, H., Hou, W., Hao, Y., Jin, W., et al. (2019). Fatigue behavior of Ti-6Al-4V cellular structures fabricated by additive manufacturing technique. *J. Mater. Sci. Technol.* 35, 285–294. doi: 10.1016/j.jmst.2018.09.066
- Roseti, L., Parisi, V., Petretta, M., Cavallo, C., Desando, G., Bartolotti, I., et al. (2017). Scaffolds for bone tissue engineering: state of the art and new perspectives. *Mater. Sci. Eng. C* 78, 1246–1262. doi: 10.1016/j.msec.2017.05.017
- Saint-Pastou Terrier, C., and Gasque, P. (2017). Bone responses in health and infectious diseases: a focus on osteoblasts. *J. Infection* 75, 281–292. doi: 10.1016/j.jinf.2017.07.007
- Shah, F. A., Omar, O., Suska, F., Snis, A., Matic, A., Emanuelsson, L., et al. (2016). Long-term osseointegration of 3D printed CoCr constructs with an interconnected open-pore architecture prepared by electron beam melting. *Acta Biomater.* 36, 296–309. doi: 10.1016/j.actbio.2016.03.033
- Shor, L., Güçeri, S., Wen, X., Gandhi, M., and Sun, W. (2007). Fabrication of three-dimensional polycaprolactone/hydroxyapatite tissue scaffolds and osteoblast-scaffold interactions in vitro. *Biomaterials* 28, 5291–5297. doi: 10.1016/j.biomaterials.2007.08.018
- Sing, S. L., Yeong, W. Y., and Wiria, F. E. (2016). Selective laser melting of titanium alloy with 50 wt% tantalum: microstructure and mechanical properties. *J. Alloy. Compd.* 660, 461–470. doi: 10.1016/j.jallcom.2015.11.141
- Singh, R., Lee, P. D., Jones, J. R., Poologasundarampillai, G., Post, T., Lindley, T. C., et al. (2010). Hierarchically structured titanium foams for tissue scaffold applications. *Acta Biomater.* 6, 4596–4604. doi: 10.1016/j.actbio.2010.06.027
- Song, G., and Song, S. (2007). A possible biodegradable magnesium implant material. *Adv. Eng. Mater.* 9, 298–302. doi: 10.1002/adem.200600252
- Sood, A. K., Ohdar, R. K., and Mahapatra, S. S. (2010). Parametric appraisal of mechanical property of fused deposition modelling processed parts. *Mater. Des.* 31, 287–295. doi: 10.1016/j.matdes.2009.06.016
- Speirs, M., Van Hooreweder, B., Van Humbeeck, J., and Kruth, J. P. (2017). Fatigue behaviour of NiTi shape memory alloy scaffolds produced by SLM, a unit cell design comparison. *J. Mech. Behav. Biomed. Mater.* 70, 53–59. doi: 10.1016/j.jmbbm.2017.01.016
- Su, Y., Cockerill, I., Wang, Y., Qin, Y.-X., Chang, L., Zheng, Y., et al. (2019). Zinc-based biomaterials for regeneration and therapy. *Trends Biotechnol.* 37, 428–441. doi: 10.1016/j.tibtech.2018.10.009
- Sun, W., Starly, B., Nam, J., and Darling, J. (2005). Bio-CAD modeling and its applications in computer-aided tissue engineering. *Comput. Aided Des.* 37, 1097–1114. doi: 10.1016/j.cad.2005.02.002
- Surmeneva, M., Lapanje, A., Chudinova, E., Ivanova, A., Koptuyg, A., Loza, K., et al. (2019). Decreased bacterial colonization of additively manufactured Ti6Al4V metallic scaffolds with immobilized silver and calcium phosphate nanoparticles. *Appl. Surf. Sci.* 480, 822–829. doi: 10.1016/j.apsusc.2019.03.003
- Szymczyk-Ziółkowska, P., Łabowska, M. B., Detyna, J., Michalak, I., and Gruber, P. (2020). A review of fabrication polymer scaffolds for biomedical applications using additive manufacturing techniques. *Biocybern. Biomed. Eng.* 40, 624–638. doi: 10.1016/j.bbe.2020.01.015
- Taniguchi, N., Fujibayashi, S., Takemoto, M., Sasaki, K., Otsuki, B., Nakamura, T., et al. (2016). Effect of pore size on bone ingrowth into porous titanium implants fabricated by additive manufacturing: an in vivo experiment. *Mater. Sci. Eng. C* 59, 690–701. doi: 10.1016/j.msec.2015.10.069
- Tofail, S. A. M., Koumoulos, E. P., Bandyopadhyay, A., Bose, S., O'Donoghue, L., and Charitidis, C. (2018). Additive manufacturing: scientific and technological challenges, market uptake and opportunities. *Mater. Today* 21, 22–37. doi: 10.1016/j.mattod.2017.07.001
- Wang, C., Huang, W., Zhou, Y., He, L., He, Z., Chen, Z., et al. (2020a). 3D printing of bone tissue engineering scaffolds. *Bioact. Mater.* 5, 82–91. doi: 10.1016/j.bioactmat.2020.01.004
- Wang, S., Ding, Y., Yu, F., Zheng, Z., and Wang, Y. (2020b). Crushing behavior and deformation mechanism of additively manufactured Voronoi-based random open-cell polymer foams. *Mater. Today Commun.* 25:101406. doi: 10.1016/j.mtcomm.2020.101406
- Wang, S., Shi, Z. A., Liu, L., Zhou, X., Zhu, L., and Hao, Y. (2020c). The design of Ti6Al4V primitive surface structure with symmetrical gradient of pore size in biomimetic bone scaffold. *Mater. Des.* 193:108830. doi: 10.1016/j.matdes.2020.108830
- Wang, Y., Fu, P., Wang, N., Peng, L., Kang, B., Zeng, H., et al. (2020d). Challenges and solutions for the additive manufacturing of biodegradable magnesium implants. *Engineering* 6, 1267–1275. doi: 10.1016/j.eng.2020.02.015
- Wang, H., Su, K., Su, L., Liang, P., Ji, P., and Wang, C. (2019). Comparison of 3D-printed porous tantalum and titanium scaffolds on osteointegration and osteogenesis. *Mater. Sci. Eng. C* 104:109908. doi: 10.1016/j.msec.2019.109908
- Wang, S., Liu, L., Li, K., Zhu, L., Chen, J., and Hao, Y. (2019). Pore functionally graded Ti6Al4V scaffolds for bone tissue engineering application. *Mater. Des.* 168:107643. doi: 10.1016/j.matdes.2019.107643
- Wang, L., Wang, C., Zhang, L. C., Chen, L., Lu, W., and Zhang, D. (2016). Phase transformation and deformation behavior of NiTi-Nb eutectic joined NiTi wires. *Sci. Rep.* 6:23905. doi: 10.1038/srep23905
- Wang, X., Jiang, M., Zhou, Z., Gou, J., and Hui, D. (2017). 3D printing of polymer matrix composites: a review and prospective. *Compos. Part B Eng.* 110, 442–458. doi: 10.1016/j.compositesb.2016.11.034
- Wang, X., Xu, S., Zhou, S., Xu, W., Leary, M., Choong, P., et al. (2016). Topological design and additive manufacturing of porous metals for bone scaffolds and orthopaedic implants: a review. *Biomaterials* 83, 127–141. doi: 10.1016/j.biomaterials.2016.01.012

- Wauthle, R., Ahmadi, S. M., Amin Yavari, S., Mulier, M., Zadpoor, A. A., Weinans, H., et al. (2015a). Revival of pure titanium for dynamically loaded porous implants using additive manufacturing. *Mater. Sci. Eng. C* 54, 94–100. doi: 10.1016/j.msec.2015.05.001
- Wauthle, R., van der Stok, J., Amin Yavari, S., Van Humbeeck, J., Kruth, J.-P., Zadpoor, A. A., et al. (2015b). Additively manufactured porous tantalum implants. *Acta Biomater.* 14, 217–225. doi: 10.1016/j.actbio.2014.12.003
- Wettergreen, M. A., Bucklen, B. S., Starly, B., Yuksel, E., Sun, W., and Liebschner, M. A. K. (2005). Creation of a unit block library of architectures for use in assembled scaffold engineering. *Comput. Aided Des.* 37, 1141–1149. doi: 10.1016/j.cad.2005.02.005
- Xiao, D., Yang, Y., Su, X., Wang, D., and Sun, J. (2013). An integrated approach of topology optimized design and selective laser melting process for titanium implants materials. *Bio Med. Mater. Eng.* 23, 433–445. doi: 10.3233/bme-130765
- Xiao, D.-M., Yang, Y.-Q., Su, X.-B., Wang, D., and Luo, Z.-Y. (2012). Topology optimization of microstructure and selective laser melting fabrication for metallic biomaterial scaffolds. *T. Nonferr. Metal. Soc.* 22, 2554–2561. doi: 10.1016/s1003-6326(11)61500-8
- Xiao, F., and Yin, X. (2016). Geometry models of porous media based on Voronoi tessellations and their porosity–permeability relations. *Comput. Math. Appl.* 72, 328–348. doi: 10.1016/j.camwa.2015.09.009
- Yamamoto, A., Kohyama, Y., Kuroda, D., and Hanawa, T. (2004). Cytocompatibility evaluation of Ni-free stainless steel manufactured by nitrogen adsorption treatment. *Mater. Sci. Eng. C* 24, 737–743. doi: 10.1016/j.msec.2004.08.017
- Yan, C., Hao, L., Hussein, A., and Young, P. (2015). Ti–6Al–4V triply periodic minimal surface structures for bone implants fabricated via selective laser melting. *J. Mech. Behav. Biomed. Mater.* 51, 61–73. doi: 10.1016/j.jmbbm.2015.06.024
- Yan, C., Hao, L., Hussein, A., Young, P., and Raymont, D. (2014). Advanced lightweight 316L stainless steel cellular lattice structures fabricated via selective laser melting. *Mater. Des.* 55, 533–541. doi: 10.1016/j.matdes.2013.10.027
- Yan, X., Li, Q., Yin, S., Chen, Z., Jenkins, R., Chen, C., et al. (2019). Mechanical and in vitro study of an isotropic Ti6Al4V lattice structure fabricated using selective laser melting. *J. Alloy. Compd.* 782, 209–223. doi: 10.1016/j.jallcom.2018.12.220
- Yang, N., Quan, Z., Zhang, D., and Tian, Y. (2014). Multi-morphology transition hybridization CAD design of minimal surface porous structures for use in tissue engineering. *Comput. Aided Des.* 56, 11–21. doi: 10.1016/j.cad.2014.06.006
- Yang, N., Tian, Y., and Zhang, D. (2015). Novel real function based method to construct heterogeneous porous scaffolds and additive manufacturing for use in medical engineering. *Med. Eng. Phys.* 37, 1037–1046. doi: 10.1016/j.medengphys.2015.08.006
- Yang, N., and Zhou, K. (2014). Effective method for multi-scale gradient porous scaffold design and fabrication. *Mater. Sci. Eng. C* 43, 502–505. doi: 10.1016/j.msec.2014.07.052
- Yang, X. Y., Huang, X., Rong, J. H., and Xie, Y. M. (2013). Design of 3D orthotropic materials with prescribed ratios for effective Young's moduli. *Comp. Mater. Sci.* 67, 229–237. doi: 10.1016/j.commatsci.2012.08.043
- Yang, Z., Gu, H., Sha, G., Lu, W., Yu, W., Zhang, W., et al. (2018). TC4/Ag metal matrix nanocomposites modified by friction stir processing: surface characterization, antibacterial property, and cytotoxicity in vitro. *ACS Appl. Mater. Interfaces* 10, 41155–41166. doi: 10.1021/acsami.8b16343
- Yoo, D.-J. (2011a). Three-dimensional surface reconstruction of human bone using a -spline based interpolation approach. *Comput. Aided Des.* 43, 934–947. doi: 10.1016/j.cad.2011.03.002
- Yoo, D. J. (2011b). Porous scaffold design using the distance field and triply periodic minimal surface models. *Biomaterials* 32, 7741–7754. doi: 10.1016/j.biomaterials.2011.07.019
- Yu, S., Sun, J., and Bai, J. (2019). Investigation of functionally graded TPMS structures fabricated by additive manufacturing. *Mater. Des.* 182:108021. doi: 10.1016/j.matdes.2019.108021
- Yuan, L., Ding, S., and Wen, C. (2019). Additive manufacturing technology for porous metal implant applications and triple minimal surface structures: a review. *Bioact. Mater.* 4, 56–70. doi: 10.1016/j.bioactmat.2018.12.003
- Zadpoor, A. A. (2019). Mechanical performance of additively manufactured meta-biomaterials. *Acta Biomater.* 85, 41–59. doi: 10.1016/j.actbio.2018.12.038
- Zhang, L., Song, B., Fu, J. J., Wei, S. S., Yang, L., Yan, C. Z., et al. (2020). Topology-optimized lattice structures with simultaneously high stiffness and light weight fabricated by selective laser melting: design, manufacturing and characterization. *J. Manuf. Process* 56, 1166–1177. doi: 10.1016/j.jmapro.2020.06.005
- Zhang, X.-Y., Fang, G., Leeflang, S., Zadpoor, A. A., and Zhou, J. (2019). Topological design, permeability and mechanical behavior of additively manufactured functionally graded porous metallic biomaterials. *Acta Biomater.* 84, 437–452. doi: 10.1016/j.actbio.2018.12.013
- Zhang, X.-Y., Yan, X.-C., Fang, G., and Liu, M. (2020). Biomechanical influence of structural variation strategies on functionally graded scaffolds constructed with triply periodic minimal surface. *Addit. Manuf.* 32:101015. doi: 10.1016/j.addma.2019.101015
- Zhang, X. Z., Leary, M., Tang, H. P., Song, T., and Qian, M. (2018). Selective electron beam manufactured Ti-6Al-4V lattice structures for orthopedic implant applications: current status and outstanding challenges. *Curr. Opin. Solid St. M.* 22, 75–99. doi: 10.1016/j.cossms.2018.05.002
- Zhao, D., Han, C., Li, Y., Li, J., Zhou, K., Wei, Q., et al. (2019). Improvement on mechanical properties and corrosion resistance of titanium-tantalum alloys in-situ fabricated via selective laser melting. *J. Alloy. Compd.* 804, 288–298. doi: 10.1016/j.jallcom.2019.06.307
- Zhao, L., Ha, S., Sharp, K. W., Geltmacher, A. B., Fonda, R. W., Kinsey, A. H., et al. (2014). Permeability measurements and modeling of topology-optimized metallic 3-D woven lattices. *Acta Mater.* 81, 326–336. doi: 10.1016/j.actamat.2014.08.037
- Zhao, S., Hou, W. T., Xu, Q. S., Li, S. J., Hao, Y. L., and Yang, R. (2018). “Ti-6Al-4V lattice structures fabricated by electron beam melting for biomedical applications,” in *Titanium in Medical and Dental Applications*, eds F. Froes, and M. Qian (Cambridge: Woodhead Publishing), 277–301. doi: 10.1016/b978-0-12-812456-7.00013-5
- Zheng, S., Li, J., Jing, X., and Gong, Z. (2020). Parameterized design and fabrication of porous bone scaffolds for the repair of cranial defects. *Med. Eng. Phys.* 81, 39–46. doi: 10.1016/j.medengphys.2020.05.002
- Zhou, C., Deng, C., Chen, X., Zhao, X., Chen, Y., Fan, Y., et al. (2015). Mechanical and biological properties of the micro-/nano-grain functionally graded hydroxyapatite bioceramics for bone tissue engineering. *J. Mech. Behav. Biomed. Mater.* 48, 1–11. doi: 10.1016/j.jmbbm.2015.04.002
- Zhou, H., Zhao, M., Ma, Z., Zhang, D. Z., and Fu, G. (2020). Sheet and network based functionally graded lattice structures manufactured by selective laser melting: design, mechanical properties, and simulation. *Int. J. Mech. Sci.* 175:105480. doi: 10.1016/j.ijmecsci.2020.105480
- Zhu, C., Lv, Y., Qian, C., Ding, Z., Jiao, T., Gu, X., et al. (2018). Microstructures, mechanical, and biological properties of a novel Ti-6V-4V/zinc surface nanocomposite prepared by friction stir processing. *Int. J. Nanomed.* 13, 1881–1898. doi: 10.2147/IJN.S154260
- Zhu, C., Lv, Y., Qian, C., Qian, H., Jiao, T., Wang, L., et al. (2016). Proliferation and osteogenic differentiation of rat BMSCs on a novel Ti/SiC metal matrix nanocomposite modified by friction stir processing. *Sci. Rep.* 6:38875. doi: 10.1038/srep38875

Conflict of Interest: The authors declare that the research was conducted in the absence of any commercial or financial relationships that could be construed as a potential conflict of interest.

Copyright © 2021 Lv, Wang, Liu, Tang, Lu, Xie, Lan, Liu, Qin and Wang. This is an open-access article distributed under the terms of the Creative Commons Attribution License (CC BY). The use, distribution or reproduction in other forums is permitted, provided the original author(s) and the copyright owner(s) are credited and that the original publication in this journal is cited, in accordance with accepted academic practice. No use, distribution or reproduction is permitted which does not comply with these terms.



Enhancement of Bone Regeneration on Calcium-Phosphate-Coated Magnesium Mesh: Using the Rat Calvarial Model

Shuang Wu, Yong-Seok Jang^{*†} and Min-Ho Lee^{*†}

Department of Dental Biomaterials, Institute of Oral Bioscience, Institute of Biodegradable Material, School of Dentistry, Jeonbuk National University, Jeonju-si, South Korea

OPEN ACCESS

Edited by:

Chaozong Liu,
University College London,
United Kingdom

Reviewed by:

Sergey V. Dorozhkin,
Independent Researcher, Moscow,
Russia
Jennifer Patterson,
Instituto IMDEA Materiales, Spain
Yu-Lung Chiu,
University of Birmingham,
United Kingdom

*Correspondence:

Yong-Seok Jang
yjjang@jbnu.ac.kr
Min-Ho Lee
mh@jbnu.ac.kr

[†]These authors have contributed
equally to this work and share last
authorship

Specialty section:

This article was submitted to
Biomaterials,
a section of the journal
Frontiers in Bioengineering and
Biotechnology

Received: 12 January 2021

Accepted: 22 March 2021

Published: 29 April 2021

Citation:

Wu S, Jang Y-S and Lee M-H
(2021) Enhancement of Bone
Regeneration on
Calcium-Phosphate-Coated
Magnesium Mesh: Using the Rat
Calvarial Model.
Front. Bioeng. Biotechnol. 9:652334.
doi: 10.3389/fbioe.2021.652334

Metallic biodegradable magnesium (Mg) is a promising material in the biomedical field owing to its excellent biocompatibility, bioabsorbability, and biomechanical characteristics. Calcium phosphates (CaPs) were coated on the surface of pure Mg through a simple alkali-hydrothermal treatment. The surface properties of CaP coatings formed on Mg were identified through wettability, direct cell seeding, and release tests since the surface properties of biomaterials can affect the reaction of the host tissue. The effect of CaP-coated Mg mesh on guided bone regeneration in rat calvaria with the critical-size defect was also evaluated *in vivo* using several comprehensive analyses in comparison with untreated Mg mesh. Following the application of protective CaP coating, the surface energy of Mg improved with higher hydrophilicity and cell affinity. At the same time, the CaP coating endowed Mg with higher Ca affinity and lower degradation. The Mg mesh with CaP coating had higher osteointegration and bone affinity than pristine Mg mesh.

Keywords: magnesium mesh, surface modification, calcium phosphate, guided bone regeneration, rat calvarial defect

INTRODUCTION

Guided bone regeneration (GBR) is an osteogenesis technique that has been developed from guided tissue regeneration, and it is used for regenerating new bone at sites with insufficient dimensions, heights, and bone volumes. Bone regeneration procedures, such as reconstruction of the bone structure after excision of ameloblastoma and jaw tumors, augmentation of the deficient height of alveolar ridges caused by periodontics, sinus elevation before implantation, and increase in jaw bone size horizontally or vertically before implantation at the site of tooth loss, are required in many patients undergoing oral and maxillofacial or orthopedic surgery (Miura et al., 2012). Using barrier membranes to form a secluded space is the key to this reconstructive procedure because the newly formed bone can be forced to collapse by the upper soft tissue of a large bone defect. Titanium alloys, cobalt-chromium alloys, and stainless steel are widely used as implant materials in traditional surgery. They have excellent mechanical strength, biostability, and durability, but they can cause stress-shielding effects, and additional surgery is often required to remove the implant after healing. Moreover, they can lead to the visualization of artifacts in magnetic resonance imaging and three-dimensional computed tomography technology, which is not conducive

to bone structure monitoring and image evaluation (Hargreaves et al., 2011). Compared with the non-absorbable materials, the advantages of absorbable materials are evident. The latter can degrade in a physiological environment, reducing the need for additional removal surgeries and decreasing the incidence of secondary injuries to the wound; therefore, absorbable materials have been widely used in the biomedical field. However, the unpredictable resorption and unstable rigidity of absorbable materials can affect the structural integrity and barrier function of membranes (Rakhmatia et al., 2013). Therefore, a suitable GBR membrane is expected to not only have sufficient rigidity to reserve anatomic space at the site and exhibit bioactivity to boost new bone formation but also be able to degrade after bone regeneration is complete.

Magnesium (Mg) is a promising biomaterial and has attracted considerable research attention due to its excellent biodegradability, biocompatibility, and biomechanical properties (Staiger et al., 2006). Mg is the fourth most abundant metal ion in the human body, half of which is stored in the bone tissue, and the remaining excess ions are excreted through urine (De Baaij et al., 2015). The density of lightweight Mg is approximately 1.74 g/cm³, and elastic modulus is 41–45 GPa. Both of these parameters are similar to those of the human bone (1.8–2.1 g/cm³, 3–20 GPa) and better than those of commonly used materials, such as titanium alloys (4.4–4.5 g/cm³, 110–117 GPa) and stainless steel (7.9–8.1 g/cm³, 189–205 GPa) (Walker et al., 2014). Moreover, Mg also plays a regulatory role as a calcium-sensing receptor in the bone and calcium metabolism (Schlingmann, 2007). The history of biodegradable Mg implants began shortly after the discovery of Mg by Sir Humphrey Davy in 1808 (Witte, 2010). In 1878, Huse used Mg wire as a ligature to successfully stop bleeding in three patients and discovered the corrosive characteristics of Mg in the body (Bettman and Zimmerman, 1935). Since then, many studies have attempted to explore the *in vivo* application of Mg as miniscrews and cardiovascular stents (Witte, 2010). However, the rapid degradation of Mg in the physiological environment raises the problem of changing the pH around the implant and releasing gas, which not only reduces the mechanical strength but also increases the metabolic burden on human organs, thereby limiting its clinical applicability. Hence, many studies have focused on improving the corrosion resistance of Mg and its alloys using various methods.

Surface modification and alloying are the main methods used to control degradation and maintain mechanical properties in pure Mg (PM); however, it is difficult to achieve the required degree of corrosion resistance by alloying alone (Tian and Liu, 2015). Therefore, surface modification is used to form a degradable dynamic interface on Mg-based materials, improving biocompatibility, imparting corrosion resistance, and maintaining mechanical strength; ultimately, such materials can be degraded without the release of any toxic by-products. Calcium phosphates (CaPs) have been used as coatings on implant surfaces because of their biocompatibility, bioactivity, and osteoconductive and osteoinductive properties (Jeong et al., 2019). CaP ceramics may also have the ability to induce

appropriate host reactions to connect bone and materials via chemical bonding (Surmenev et al., 2014). Additionally, CaPs have chemical composition and properties similar to those of the mineral phase of human bones and teeth (Yang et al., 2005). Recently, CaPs have been successfully coated on AZ31, Mg–Zn, and AZ91D to improve their corrosion performance to different degrees of success (Xu et al., 2012).

The novelty of the current study is that the effect of CaP coating on pure Mg, in the field of surface performance and *in vivo* osteointegration, was studied from the perspective of the material interface, as this is the first step when the implant material interacts with the host. A uniform and dense CaP protective coating was formed on the surface of PM meshes using a simple alkali-hydrothermal treatment. Surface-modified Mg meshes have excellent biocompatibility and improved corrosion resistance compared with untreated Mg meshes. In particular, samples treated for 2 h showed the best biological activity among various groups stratified according to treatment time. Based on the results, the 2-h group samples were selected to further investigate their application potential as biomedical materials using an animal model. The present study aimed to evaluate the performance difference between the Mg mesh subjected to alkali-hydrothermal treatment for 2 h and original Mg mesh, using *in vivo* and *in vitro* tests. The effect of the CaP coating layer on surface wettability, direct cell seeding, and ion release was evaluated. To further confirm and verify the advantages of CaP coating on the Mg surface over the untreated surface, a critical-size rat calvarial defect was used to evaluate the GBR of CaP-coated Mg mesh and the pure Mg mesh. Osteogenesis was assessed via quantitative and qualitative analyses of GBR employing microcomputed tomography (micro-CT) scanning, histomorphometry, and three-dimensional reconstruction.

MATERIALS AND METHODS

Sample Preparation and Surface Modification

Magnesium foils (99.9% high purity) (Goodfellow, England), 100 mm × 100 mm × 0.1 mm in dimensions, were prepared by rolling and used as the substrate. The Mg foil was subjected to laser microprocessing to form a Mg mesh with a diameter of 10 mm and hole diameter of 0.4 mm. According to the American Society for Testing and Materials (ASTM) standard (G1-03), chemical cleaning procedures were performed to remove the surface corrosion products and revitalize the surface. The Mg samples were directly placed into a beaker filled with a solution containing 0.25 mol/L Ca-ethylenediaminetetraacetic acid (EDTA) (C₁₀H₁₂CaN₂Na₂O₈) and 0.25 mol/L KH₂PO₄, and the solution was adjusted to a pH value of 8.9 with NaOH. The alkaline-hydrothermal treatment was conducted at 90°C for 2 h.

The microstructure and morphology of the CaP coating were identified using scanning electron microscopy (SEM; JSM-5900, JEOL, Japan). The cross-section of surface-modified Mg was sputtered with platinum coating, following which

the cross-sectional morphological microstructure was observed using field emission scanning electron microscopy (FE-SEM; SU-70, HITACHI, Japan), while the elemental composition of the designated localized area on the cross-section was investigated using energy dispersive spectroscopy with FE-SEM.

Implant–Body Fluid Interface Analysis

The initial contact between the implant and host is at the interface between the sample and body fluid. The surface property of the implant is an important consideration for its clinical applicability, which can affect the surface wettability, tissue adhesion, and the release of active ingredients of biomaterials. Therefore, the surface difference between PM and coated Mg (CM) was evaluated by the contact angle, direct cell seeding, and ion release tests.

Wettability

The hydrophilicity of the sample surface was evaluated by the contact angles of dropping the cell culture medium on prepared samples to determine the wettability of the sample. To prevent oil or pollution from the skin and environment from affecting the sample surfaces, it was necessary to use 70% ethanol to clean the sample placement plane and use forceps to place the samples. Contact angles and images were obtained by the touch drop method using a contact angle analyzer (Phoenix-300 Touch, Surface Electro Optics, South Korea).

Cell Adhesion

The mouse osteoblast cell line, MC3T3-E1, obtained from the American Type Culture Collection, was used directly for seeding onto the prepared sample surface to evaluate cell adhesion and the changes in surface morphological. MC3T3-E1 cells were maintained in a culture medium at 37°C in a humidified atmosphere containing 5% CO₂. Cells were cultured in α -minimum essential medium (Gibco Co., Carlsbad, CA, United States) supplemented with 10% fetal bovine serum (Gibco Co.), 500 U/ml penicillin (Gibco Co.), and 500 mg/ml streptomycin (Gibco Co.).

After sterilizing the prepared samples with ultraviolet (UV) radiation for 30 min per side, the samples were placed in 24-well cell culture plates. Next, MC3T3-E1 cells at a density of 1.5×10^4 cells/ml were carefully seeded onto the sample surfaces (three wells per group). The cultures were incubated at 37°C in a 5% CO₂ incubator for 3 days. The morphology of the cells adhered to the samples was observed using SEM. The samples were washed twice with phosphate-buffered saline (PBS) and fixed with 2.5% glutaraldehyde (GA) for 2 h at 4°C. After removing GA and washing twice with PBS, the cells were fixed with 1% osmium for 2 h at 4°C. Following dehydration with gradient ethanol (30, 50, 70, 80, 90, and 100%) for 10 min each at 4°C, the samples were ion sputtered and analyzed by SEM.

Release Test

Both sides of PM and CM were sterilized by UV radiation for 30 min before performing corrosion tests. The tests were performed by soaking the prepared samples in Earle's balanced salt solution (EBSS) and incubating at 37°C in 5% CO₂. EBSS

(1×) was prepared following the manufacturer's instructions of commercial EBSS 10× (E7510, Sigma, United States). Prepared samples were immersed in a solution in which the ratio of media volume to sample surface area is 0.255 ml/mm² [more than the minimum of 0.20 ml/mm² (ASTM International, 2012)]. Mg and Ca concentrations in EBSS, before and after immersion, were quantitatively analyzed using an inductively coupled plasma-optical emission spectrometer (ICP-OES; Agilent 7500a, Agilent Technologies, Wilmington, DE, United States). Samples were collected after by taking out 1-ml aliquots and then replacing them with 1 ml of fresh EBSS. All measurements were performed in triplicate.

In vivo Analyses

Sixteen Mg meshes manufactured were divided into PM and CM mesh groups for *in vivo* studies. Male Sprague–Dawley rats, aged 8 weeks and weighing 250 ± 20 g, were used as experimental subjects. One week before the experiment, the rats were housed in the animal room at a constant temperature, humidity, and standard light–dark schedule to acclimatize them to the environment.

All animal experiments were conducted under ethical clearance, which was approved by the Institutional Animal Care and Use Committee of the Jeonbuk National University, Laboratory Animal Center, Jeonju-si, South Korea (approval number: CBNU 2020-008).

Procedures

The surgery was conducted under aseptic conditions. All samples were sent to the hospital disinfection room (Jeonbuk National University Hospital) for ethylene oxide sterilization before performing the *in vivo* tests.

An 8-mm critical size defect was created surgically, as described in previous studies (Wu et al., 2019). After intramuscular injection of 50 mg/kg of Zoletil (Zoletil 50, Virbac Laboratories, France) and 15 mg/kg of xylazine hydrochloride (Rompun, Bayer, South Korea) to induce general anesthesia, the skin at the surgical site was shaved and then disinfected with iodine scrubs. Additional local anesthesia (0.5 ml of 1% lidocaine) was injected on the calvaria to aid the effects of anesthesia and reduce hemorrhaging. A 2-cm incision was created from the lambda to the middle of the nasal bones, and the periosteum was bluntly dissected to expose the calvaria. The critical-size defect was performed using a trephine bur connected to an endodontic motor (X-SMART, Dentsply, Switzerland) under copious saline irrigation. The edges of the 8-mm-diameter defect were checked carefully and washed to remove residual bone debris. Care was taken to avoid damaging the dura or brain under the bone. The defect was completely covered by mesh, and the periosteum was positioned over the mesh and sutured with bioabsorbable silk (5–0 glyconate monofilament, B. Braun, Rubí, Spain), following which the skin was closed using a non-absorbable nylon silk (4/0 blue nylon, Ailee Co., Ltd., Busan, South Korea). To prevent infection, antibiotics (amikacin; Samu Median Co., Ltd., South Korea) were administered subcutaneously for 3 days postoperatively. The rats were sacrificed at 4 and 8 weeks by euthanization

with an overdose of thiopental sodium (Choongwae Pharma Corporation, Seoul, South Korea).

Micro-CT

The excised blocks, 20 mm × 20 mm in dimensions, were stored in 10% formalin before being dispatched to the Center for University-Wide Research Facilities at Jeonbuk National University. For quantitative and qualitative analyses, micro-CT (Skyscan 1076) was used to examine the dissected specimens at an 18-μm resolution with a 1-mm aluminum filter. The blocks were scanned at 100 kV voltage and 100 μA current with 360° scanning rotation. The three-dimensional images were reconstructed and analyzed using the NRecon reconstruction program and CT-analyzer software (SkyScan, Aartselaar, Belgium). Regions of interest (ROIs) were created by manually drawing in the region of the 8-mm critical defect to distinguish the newly formed bone and Mg mesh. Three-dimensional images were reconstructed using the CTvox program (SkyScan).

Histological Analysis

After micro-CT scanning, the blocks obtained in each group were subjected to a series of fixation, staining, and embedding processes for performing histological analysis.

After micro-CT scanning, the blocks were fixed in fresh 10% formalin for 2 days and stained using Villanueva solution (Polysciences, Inc., Eppelheim, Germany). The blocks were then dehydrated with gradient ethanol (80, 90, 95, and 100%) and 100% acetone. To embed the blocks in resin, the blocks were prepermeated with methylmethacrylate (MMA, Yuruki Pure Chemicals Co., Ltd., Kyoto, Japan) under vacuum for 2 h and then infiltrated with the polymerization mixture (PMMA) at 35°C for 3 days followed by 60°C for 1 day. Prepared resin blocks were cut into 0.7-mm-thick slices through the central line of the defect using a low-speed saw (EXAKT 300 CP, EXAKT Technologies

Inc., Norderstedt, Germany). Slices were ground to 70-μm thickness for histological analysis using a microgrinding system (EXAKT 400 CS, EXAKT Technologies Inc.). Histomorphometric analysis was conducted using optical microscopy (10× magnification and 30× magnification; EZ4D, Leica, Wetzlar, Germany).

Statistical Analyses

The data are presented as the mean ± standard deviation (SD). One-way ANOVA with *post hoc* Tukey's test was performed, and $p < 0.05$ was considered statistically significant.

RESULTS

Figure 1 shows the results of the surface morphology and cross-sectional elemental distribution of CM. After 2 h of alkali-hydrothermal treatment, the rod-like particles assembled to form a dense and uniform coating layer with a cauliflower-like structure. The thickness of the coating was in the range of 1.5–2.2 μm, and two distinct strata consisting of the dense inner layer and rod-like irregular orientation outer layer were visible. Elemental mapping showed the distribution of Ca, P, O, and Mg in the cross-section. The line profiles of Ca and P showed broad peaks in the outer layer of the coating, while those of Mg and O showed broad peaks in the inner layer. The interface between the Mg substrate and coating was not straight, indicating that a corrosion reaction occurred. The elemental distribution of the point profile showed that Mg mainly existed in the inner layer of the coating, indicating that Mg(OH)₂ was formed at the interface between the Mg substrate and coating after 2 h of alkali-hydrothermal treatment.

The wettability of the sample surface (**Figure 2**) was evaluated by the touch drop method and presented as optical images and contact angles. The results show that the hydrophilic CaP

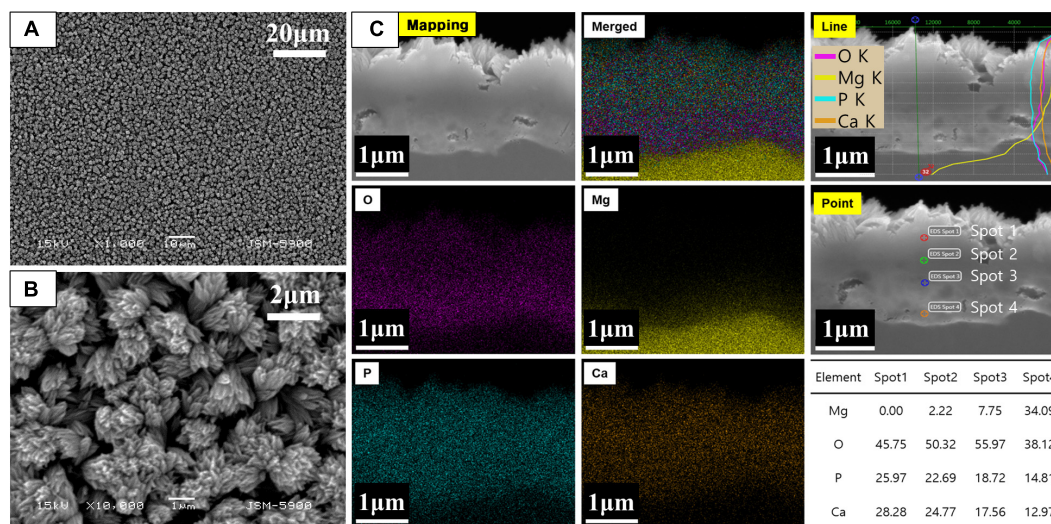


FIGURE 1 | (A,B) Surface morphology and **(C)** cross-sectional elemental analysis of CaP-coated Mg after alkali-hydrothermal treatment for 2 h.

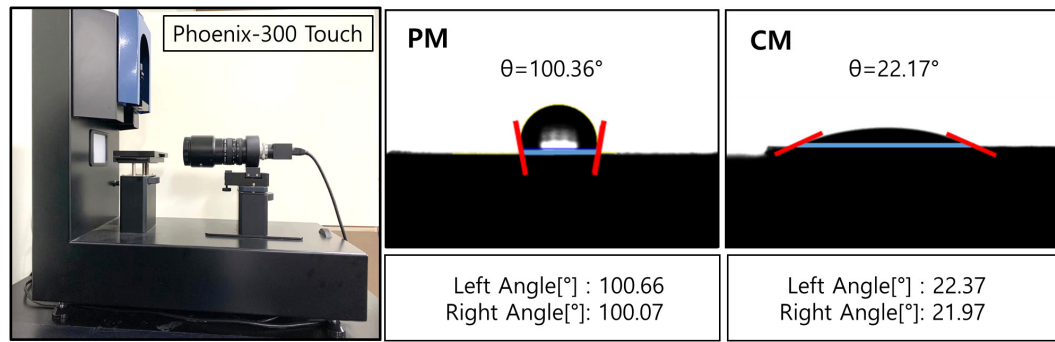


FIGURE 2 | Contact angles of PM and CM were measured using Phoenix-300 Touch, representing the hydrophilicity of the sample surface. PM, pure magnesium; CM, calcium-phosphate-coated magnesium.

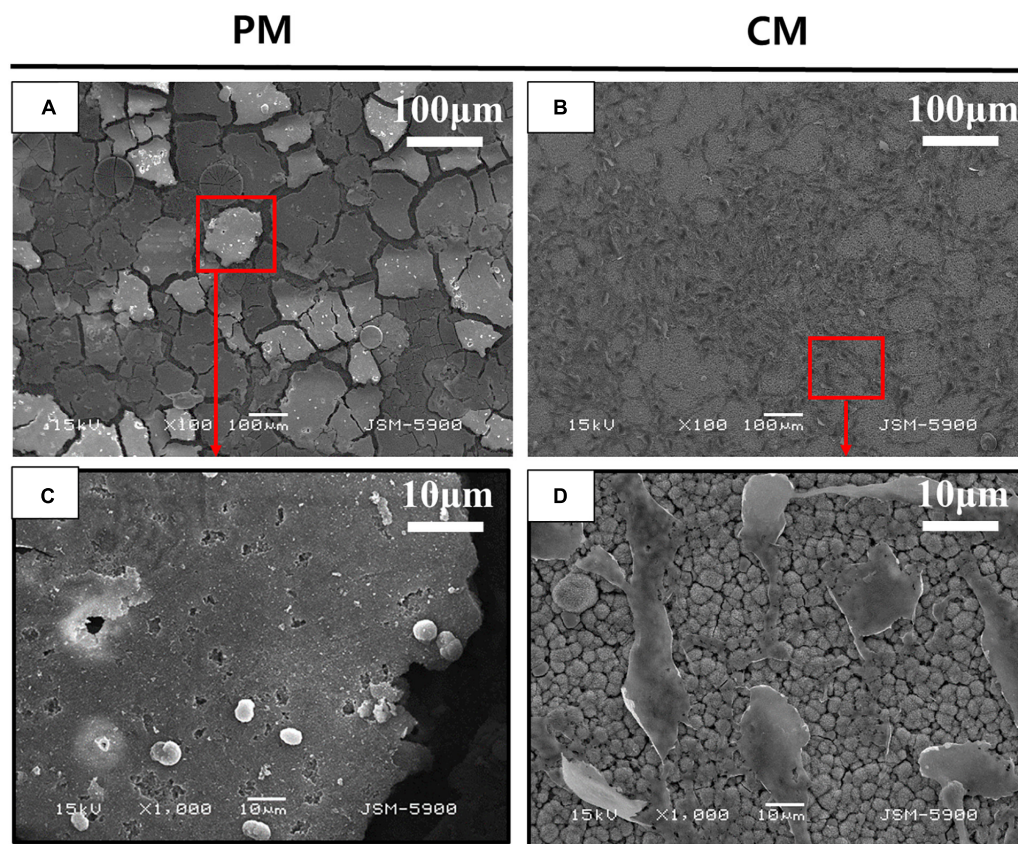


FIGURE 3 | Scanning electron microscopy (SEM) analysis of MC3T3-E1 cells cultured on (A,C) pure magnesium (PM) and (B,D) calcium-phosphate-coated magnesium (CM) for 3 days. Red color box of A and B enlarged in C and D respectively.

coating reduced the contact angle of CM to $22.69 \pm 2.27^\circ$, which significantly improved the wettability of CM compared to that of PM ($105.66 \pm 7.86^\circ$).

Figure 3 shows the attachment of MC3T3-E1 cells on PM and CM after 3 days of cell culture observed by FE-SEM. Images obtained at $100\times$ magnification showed the attachment of numerous cells and improved cell distribution on the surface of

CM compared to that of PM. The morphology of MC3T3-E1 cells cultured on CM showed an elongated shape without filopodia extensions, indicating that the cells were in a state of proliferation. However, in PM, many cells were not found on the surface; in addition, the material appeared to be severely degraded. The few cells detected on PM were white in color and round in shape, indicating cell death and detachment.

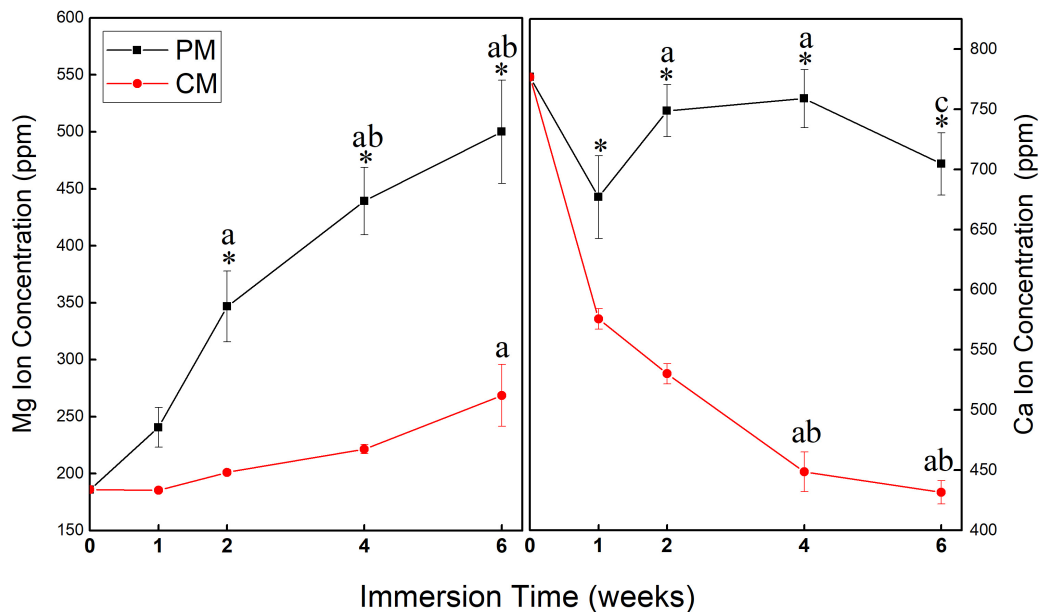


FIGURE 4 | Changes in the concentration of Mg and Ca ions in Earle's balanced salt solution (EBSS) during the 6-week ion release test of pure magnesium (PM) and calcium-phosphate-coated magnesium (CM) (* indicates significant difference between PM and CM; a indicates significant differences compared to 1 week; b indicates significant differences compared to 2 weeks; c indicates significant differences compared to 4 weeks).

Figure 4 shows changes in the concentration of Mg and Ca ions in EBSS during the 6-week ion release test of PM and CM. ICP-OES test data showed that the release amount and rate of Mg ions from PM were significantly higher than those from CM, indicating that CM had excellent corrosion resistance. At 1 week of immersion in EBSS, the concentration of Ca ions in the PM (677.04 ± 34.46) and CM (575.82 ± 8.50) groups was lower than that in EBSS initially (776.88 ppm). However, the concentration of Ca ions in the PM group began to increase after 1 week, which indicated that deposited Ca ions continued to be released along with the degradation of PM. The concentration of Ca ions in the CM group continued to decrease throughout the test period, which indicated that CaP coating significantly improved the corrosion resistance of Mg and made surface-modified Mg with favorable calcium affinity.

Quantitative assessment was performed using micro-CT to investigate bone reconstruction within the ROI in rat calvaria. As shown in **Figure 5**, both the new bone volume and mineral density in the 8-mm critical-size defect of rat calvaria placed with PM and CM increased with time. New bone volume in the CM group was significantly higher than that in the PM group at 4 weeks postsurgery ($p \leq 0.05$). From 4 to 8 weeks, even if the amount of new bone formation in the CM group increased significantly, there was no significant difference compared with the PM group. In terms of bone mineral density, there was no significant difference between the CM and PM groups.

To confirm the residual amount of Mg mesh, the ROI was manually drawn to mark the placement of Mg mesh in the rat calvarial model based on micro-CT data. The Mg meshes of all groups showed time-dependent degradation, and the volume of Mg in all groups decreased during each assessed period. As

shown in **Figure 6**, the corrosion speed of PM was fast. The residual Mg volume of PM was $3.74 \pm 0.12 \text{ mm}^3$ at 8 weeks, and the percentage of Mg degradation reached 58.49%. However, the residual Mg volume of CM was $7.02 \pm 0.75 \text{ mm}^3$, and percentage of Mg degradation reached 21.98%. These results were consistent with the three-dimensional reconstructed micro-CT image showing that the PM meshes experienced severe degradation after implantation (**Figure 6B**).

Figures 7, 8 show bone formation in the rat calvarial defect from the perspective of overall and partial views, respectively. In the three-dimensional reconstruction image of CTvox (see **Figure 7**), new bone formation can be observed above and beneath the Mg mesh, and both the area of new bone and residual mesh volume in the CM group were higher than those in the PM group. In addition, the partial views in **Figure 8** show the relationship between the membrane and new bone in the CM group in which CM led to the generation of a dense and regular new bone layer and also had a direct contact between the mesh and newly formed bones. However, because gas was released when Mg was degraded in the physiological environment, it created a gap between the new bone layer and mesh (**Figure 8**). In particular, the severe degradation of PM led to a large gap between the new bone and mesh in the PM group.

DISCUSSION

Previous studies on Mg have mainly focused on the development of Mg alloys to improve surface properties and corrosion protection because alloying is an effective method to improve the mechanical strength of Mg. However, it is difficult to achieve

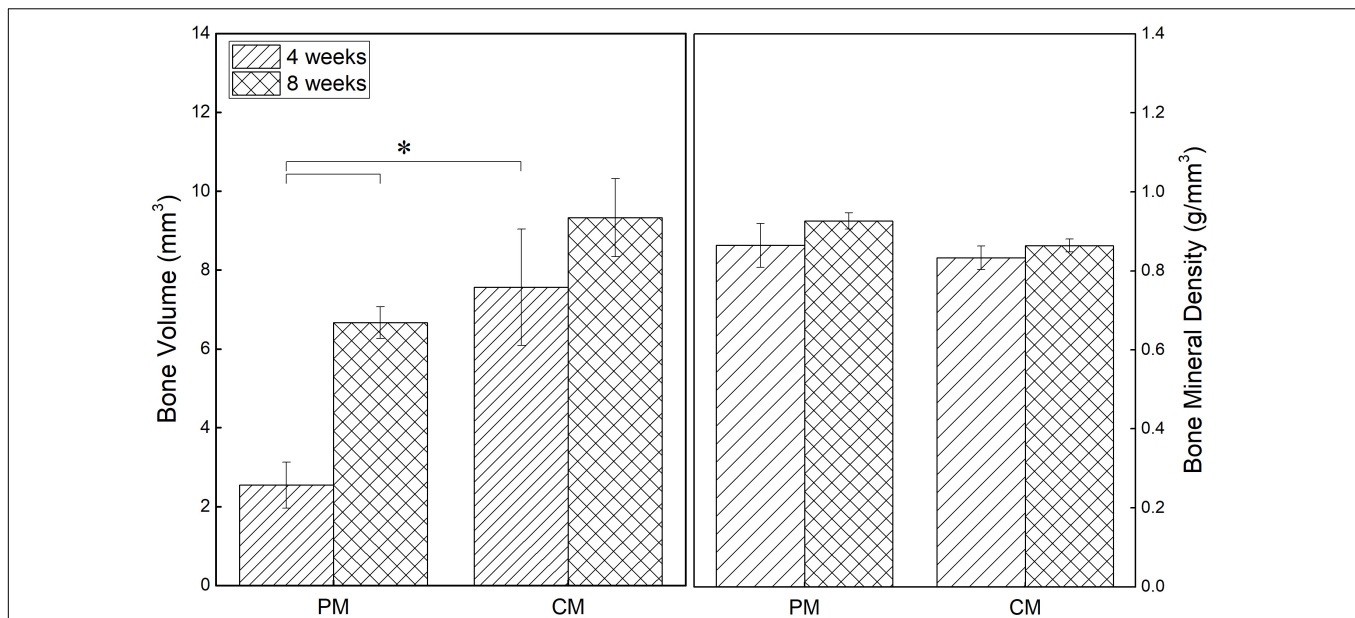


FIGURE 5 | Quantitative analysis results of new bone volume and mineral density in the critical-size defects of rat calvaria obtained from micro-CT data (* $p \leq 0.05$).

the desired degree of corrosion resistance by alloying alone since thin $\text{Mg}(\text{OH})_2$ formed spontaneously on the surface can be easily destroyed in the physiological environment including chloride ions, as well as microgalvanic corrosion can occur due to the different potential between Mg matrix and alloy elements (Gusieva et al., 2015). Furthermore, to improve the mechanical strength of Mg alloys, some components such as aluminum (Abd El-Rahman, 2003) are added, which increases the uncertain toxicity of commercial Mg alloys (Song, 2007). Therefore, to improve not only corrosion resistance but also biostability and biosafety, CaP coating was produced on PM, which has been previously confirmed to be effective in controlling early corrosion (Gan et al., 2013) and improving bioactivity (Lorenz et al., 2009).

Recent studies have investigated CaPs as a long-term biocompatibility coating on PM. Zhang et al. (2009) found that biomimetic CaP coating could increase corrosion protection compared with untreated Mg. Gan et al. (2013) showed that bioactive coating with Ca and P on PM was relatively dense and uniform and significantly enhanced corrosion resistance in Hank's solution. In the study conducted by Lorenz, the protective layer containing CaP was formed by soaking Mg in simulated body fluid for 5 days, leading to favorable initial cell adhesion to samples, but poor protective properties of this layer prevented long-term cell survival (Lorenz et al., 2009). Research on the biocompatibility, biosafety, and biostability of Mg also plays a role in the study of bioabsorbable implants for biomedical applications. It has been shown that amorphous CaP coating on PM mesh significantly retards the biodegradation of PM and improves bone formation in rat calvaria (Wu et al., 2019). A protective CaP coating was formed on PM through a simple alkali-hydrothermal treatment, which not only effectively increased the ratio of Ca and P but also improved corrosion

resistance and biocompatibility. In particular, Mg after alkali-hydrothermal treatment for 2 h induced excellent differentiation and proliferation of MC3T3-E1 cells, indicating that Mg has high biocompatibility and biosafety and is suitable for further exploration in bone tissue engineering.

In tissue engineering, the scaffold substrates are mostly dependent on the surface features of materials. The initial interaction immediately occurs between the host tissue and surface of the barrier membrane when the material is placed in the human body and exposed to body fluid, followed by a series of cell-material interactions. Hence, the implant-body fluid interface has a profound impact on the biocompatibility of biomaterials, and the surface properties of materials influence the biological response of the host. Following the application of CaP coating, a series of experiments were performed on the implant-body fluid interface to determine the energy of the surface of Mg in this study. The surface energy generated by the external unsaturated bond is higher than its internal energy. Therefore, when a liquid is placed on a low-energy surface metal, the contact angle is higher than that of a high-energy surface metal (Mekayarajananonth and Winkler, 1999). When the hydrophobic solid surface of PM with a contact angle of $105.66 \pm 7.86^\circ$ (higher than 90°) changed to a hydrophilic surface of CM with a contact angle of $22.68 \pm 2.27^\circ$, the CaP coating significantly improved the wettability and surface energy of Mg (Figure 2). Moreover, HAp coating can induce cell attachment, proliferation, and differentiation and increase the activity of osteoblasts (Kim et al., 2014). As shown by the results of the direct cell test (Figure 3), the stable hydrophilic surface of CM has the advantage of inducing cell attachment and cell spreading compared to the hydrophobic surface of PM. This is consistent with previous studies showing that hydrophilic materials with

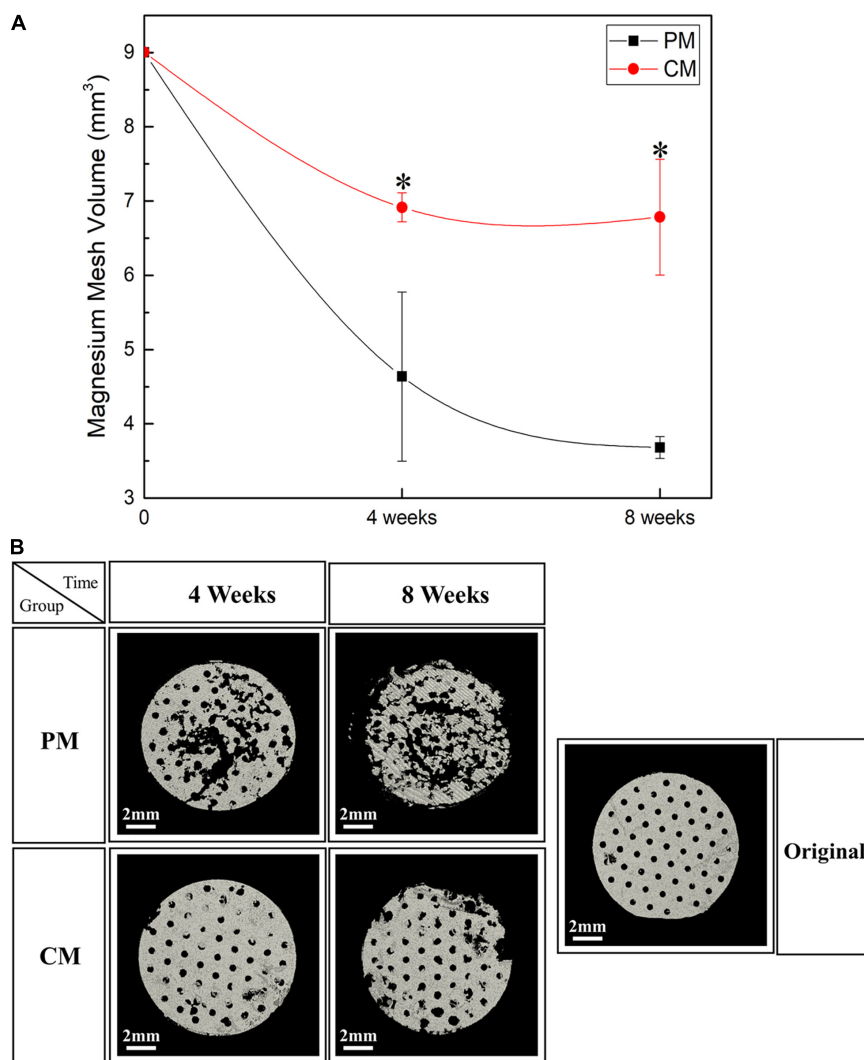


FIGURE 6 | (A) Quantitative analysis results and **(B)** three-dimensional reconstruction images of the Mg meshes used in the rat calvarial model for guided bone regeneration obtained using micro-CT [* indicates significant difference between pure magnesium (PM) and calcium-phosphate-coated magnesium (CM)].

low water contact angles can promote cell adhesion (Ishizaki et al., 2010), spreading (Amornsudthiwat et al., 2013), and proliferation (Watanabe et al., 2012; Kim et al., 2016). Cell adhesion and surface interaction with biomaterials in tissue engineering are mainly attributed to the wettability of materials (Aronov et al., 2006).

During the 6 weeks of the release test, the concentration of Mg ions in the PM group continuously increased to 500.12 ± 45.26 , while the concentration of Mg ions in the CM group did not increase (268.56 ± 27.07). This indicates that the release of Mg ions was significantly reduced by the protective CaP coating in the CM group. At 1 week of immersion, Mg ion concentration in the CM group was 185.46 ± 1.87 , which was close to the initial Mg ion concentration of 185.81 due to the deposition of Mg ions on the surface of CM owing to their affinity toward electronegative ions such as OH^- and PO_4^{3-} . Ca ion concentration in all groups decreased after

1 week of EBSS immersion. In previous studies, CaP coating has displayed bioactivity in simulated body solutions. Ca ions were released into the peri-implant region in the initial stage of implantation, resulting in local supersaturation of Ca ions. Next, the ions were redeposited from the simulated body solution into the implant, which triggered HAp formation (Cazalbou et al., 2005; Paital and Dahotre, 2009). However, the first ion assessment in the current study was carried out after 1 week of immersion, which is markedly beyond the 2 days of immersion assessed in the previous study (Nguyen et al., 2013). This might be the reason why the initial release of Ca ions was not detected in the current study, yet the deposition and concentration reduction in Ca ions were detected (Figure 6). The redeposition layer was a biological apatite layer produced by a biomimetic coating method. Two factors contributed to this layer: (i) CaP coating in CM provided nucleation sites for further deposition of apatite and (ii) the alkaline environment

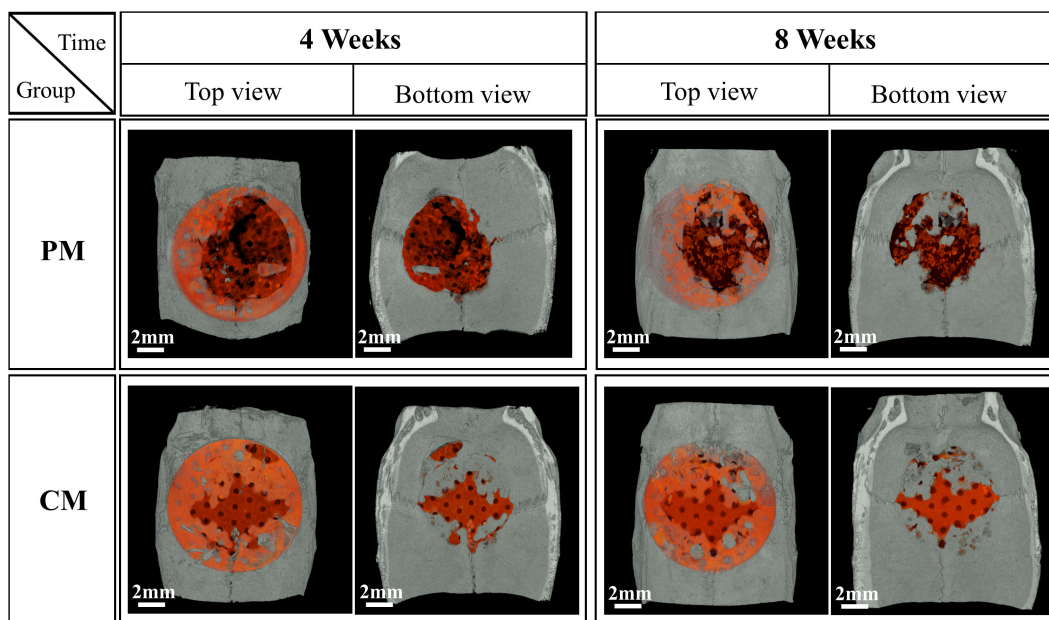


FIGURE 7 | Micro-CT images of the morphology of degraded Mg mesh and newly formed bone in the rat calvaria. The degraded Mg mesh is highlighted in orange.

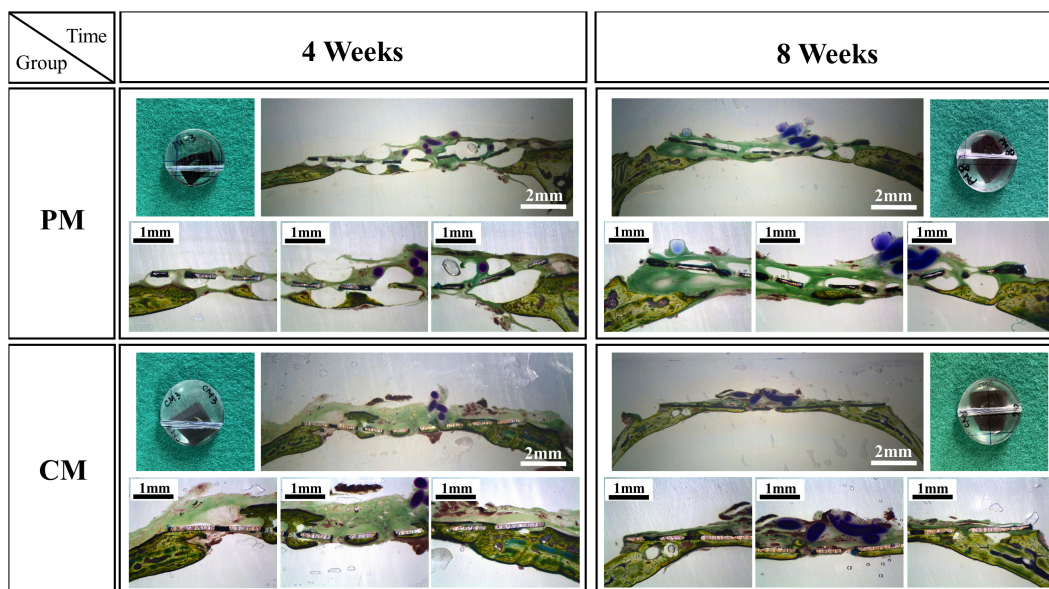


FIGURE 8 | Histological cross-sectional images of bone formation in the pure magnesium (PM) and calcium-phosphate-coated magnesium (CM) groups after 4 and 8 weeks of implantation. Histomorphology is presented as 10× magnification of coronal slices and focal areas of the center and side points (30×).

processed into CM provided the necessary functional groups (such as H_2PO_4^- and OH^-) for apatite formation (Tanahashi and Matsuda, 1997). As a result (**Figure 3D**), the structure of CM changed slightly after incubation for 3 days and could induce cell attachment, proliferation, and differentiation to form new bones (Paital and Dahotre, 2009).

After placing meshes for 4 and 8 weeks (**Figures 7, 8**), a new bone was formed above and beneath the surface-treated

meshes and was in close contact. This indicates that the CaP coating has a high affinity for osteoblasts, resulting in osteointegration at the implant–host tissue interface. The degradation of Mg is inevitably accompanied by gas release ($\text{Mg} + 2\text{H}_2\text{O} \rightarrow \text{Mg}^{2+} + 2\text{OH}^- + \text{H}_2\uparrow$), which results in the detachment of newly formed bone or osteoblasts from the mesh. Especially in PM (**Figure 8**), the large amount of gas produced pushed osteoblasts far away from the mesh, generating

a gap between the new bone layer and mesh. After implantation in rat models, the mesh volume of CM and PM decreased after the biodegradation of Mg. By calculating the residual Mg volume, the extent of degradation in CM was lower than that in PM (Figure 6); this is because CM with a protective CaP coating exhibited high corrosion resistance. In addition, excessive Mg ion release during corrosion of the uncoated sample possibly inactivated new bone formation (Serre et al., 1998; Wong et al., 2010), thereby resulting in less new bone formation around the PM compared with the CM. The high osteoblast affinity of coating in CM also contributed to the higher bone volume in CM. Within 4–8 weeks, even if the volume of new bone formed in CM significantly increased, there was no significant difference compared with PM. This may be attributed to the time-dependent degradation of the CaP coating.

CONCLUSION

The results of this study demonstrate that the corrosion rate and osteogenesis capability of Mg in the physiological environment can be tailored by using a simple alkali-hydrothermal treatment. CaP coating of Mg favors cell attachment and cell spreading. The formation of a bioactive CaP coating can endow Mg with higher surface energy and osteogenesis capability and lower degradation than PM.

REFERENCES

- Abd El-Rahman, S. S. (2003). Neuropathology of aluminum toxicity in rats (glutamate and GABA impairment). *Pharmacol. Res.* 47, 189–194. doi: 10.1016/s1043-6618(02)00336-5
- Amornsudthiwat, P., Mongkolnavin, R., Kanokpanont, S., Panpranot, J., San Wong, C., and Damrongsakul, S. (2013). Improvement of early cell adhesion on Thai silk fibroin surface by low energy plasma. *Colloids Surfaces B: Biointerfaces* 111, 579–586. doi: 10.1016/j.colsurfb.2013.07.009
- Aronov, D., Rosen, R., Ron, E., and Rosenman, G. (2006). Tunable hydroxyapatite wettability: effect on adhesion of biological molecules. *Process Biochem.* 41, 2367–2372. doi: 10.1016/j.procbio.2006.06.006
- ASTM International. (2012). *NACE/ASTMG31-12a Standard Guide for Laboratory Immersion Corrosion Testing of Metals*. West Conshohocken, PA: ASTM International. doi: <https://doi.org/10.1520/NACEASTMG0031-12A>
- Bettman, R. B., and Zimmerman, L. M. (1935). The use of metal clips in gastrointestinal anastomosis. *Am. J. Digest. Dis.* 2, 318–321. doi: 10.1007/bf03000817
- Cazalbou, S., Eichert, D., Ranz, X., Drouet, C., Combes, C., Harmand, M., et al. (2005). Ion exchanges in apatites for biomedical application. *J. Materials Sci.: Materials Med.* 16, 405–409. doi: 10.1007/s10856-005-6979-2
- De Baaij, J. H., Hoenderop, J. G., and Bindels, R. J. (2015). Magnesium in man: implications for health and disease. *Physiol. Rev.* 95, 1–46. doi: 10.1152/physrev.00012.2014
- Gan, J., Tan, L., Yang, K., Hu, Z., Zhang, Q., Fan, X., et al. (2013). Bioactive Ca–P coating with self-sealing structure on pure magnesium. *J. Materials Sci.: Materials Med.* 24, 889–901. doi: 10.1007/s10856-013-4850-4
- Gusieva, K., Davies, C., Scully, J., and Biribilis, N. (2015). Corrosion of magnesium alloys: the role of alloying. *Int. Materials Rev.* 60, 169–194. doi: 10.1179/1743280414y.00000000046
- Hargreaves, B. A., Worters, P. W., Pauly, K. B., Pauly, J. M., Koch, K. M., and Gold, G. E. (2011). Metal-induced artifacts in MRI. *Am. J. Roentgenol.* 197, 547–555.

DATA AVAILABILITY STATEMENT

The original contributions presented in the study are included in the article/supplementary material, further inquiries can be directed to the corresponding authors.

ETHICS STATEMENT

The animal study was reviewed and approved by the Institutional Animal Care and Use Committee of the Jeonbuk National University, Laboratory Animal Center, Jeonju-si, South Korea.

AUTHOR CONTRIBUTIONS

SW and Y-SJ conceived and designed the experiments. SW performed the experiments, analyzed the data, and drafted the manuscript. Y-SJ and M-HL revised the manuscript. All authors contributed to the article and approved the submitted version.

FUNDING

This research was supported by the Grant of the National Research Foundation of South Korea (NRF) (No. 2018R1D1A1B07049491).

- Ishizaki, T., Saito, N., and Takai, O. (2010). Correlation of cell adhesive behaviors on superhydrophobic, superhydrophilic, and micropatterned superhydrophobic/superhydrophilic surfaces to their surface chemistry. *Langmuir* 26, 8147–8154. doi: 10.1021/la904447c
- Jeong, J., Kim, J. H., Shim, J. H., Hwang, N. S., and Heo, C. Y. (2019). Bioactive calcium phosphate materials and applications in bone regeneration. *Biomaterials Res.* 23, 1–11.
- Kim, S. M., Jo, J. H., Lee, S. M., Kang, M. H., Kim, H. E., Estrin, Y., et al. (2014). Hydroxyapatite-coated magnesium implants with improved in vitro and in vivo biocorrosion, biocompatibility, and bone response. *J. Biomed. Materials Res. Part A* 102, 429–441. doi: 10.1002/jbm.a.34718
- Kim, S.-Y., Kim, Y.-K., Jang, Y.-S., Park, I.-S., Lee, S.-J., Jeon, J.-G., et al. (2016). Bioactive effect of alkali-heat treated TiO₂ nanotubes by water or acid treatment. *Surface Coatings Technol.* 303, 256–267. doi: 10.1016/j.surfcoat.2016.03.074
- Lorenz, C., Brunner, J. G., Kollmannsberger, P., Jaafar, L., Fabry, B., and Virtanen, S. (2009). Effect of surface pre-treatments on biocompatibility of magnesium. *Acta Biomaterialia* 5, 2783–2789. doi: 10.1016/j.actbio.2009.04.018
- Mekayarajananonth, T., and Winkler, S. (1999). Contact angle measurement on dental implant biomaterials. *J. Oral Implantol.* 25, 230–236. doi: 10.1563/1548-1336(1999)025<0230:camodi>2.3.co;2
- Miura, K., Matsui, K., Kawai, T., Kato, Y., Matsui, A., Suzuki, O., et al. (2012). Octacalcium phosphate collagen composites with titanium mesh facilitate alveolar augmentation in canine mandibular bone defects. *Int. J. Oral Maxillofacial Surg.* 41, 1161–1169. doi: 10.1016/j.ijom.2012.05.020
- Nguyen, T.-D. T., Park, I.-S., Lee, M.-H., and Bae, T.-S. (2013). Enhanced biocompatibility of a pre-calcified nanotubular TiO₂ layer on Ti–6Al–7Nb alloy. *Surface Coatings Technol.* 236, 127–134. doi: 10.1016/j.surfcoat.2013.09.038
- Patil, S. R., and Dahotre, N. B. (2009). Calcium phosphate coatings for bio-implant applications: materials, performance factors, and methodologies. *Materials Sci. Eng.: R: Rep.* 66, 1–70. doi: 10.1016/j.mser.2009.05.001
- Rakhmatia, Y. D., Ayukawa, Y., Furuhashi, A., and Koyano, K. (2013). Current barrier membranes: titanium mesh and other membranes for guided bone

- regeneration in dental applications. *J. Prosthodontic Res.* 57, 3–14. doi: 10.1016/j.jpor.2012.12.001
- Schlingmann, K. P. (2007). “Calcium-sensing receptor and magnesium,” in *New Perspect in Magnesium Research*, eds J. Durlach, Y. Nishizawa, and H. Morii (Berlin: Springer), 272–285. doi: 10.1007/978-1-84628-483-0_22
- Serre, C., Papillard, M., Chavassieux, P., Voegel, J., and Boivin, G. (1998). Influence of magnesium substitution on a collagen-apatite biomaterial on the production of a calcifying matrix by human osteoblasts. *J. Biomed. Materials Res.* 42, 626–633. doi: 10.1002/(sici)1097-4636(19981215)42:4<626::aid-jbm20>3.0.co;2-s
- Song, G. (2007). Control of biodegradation of biocompatible magnesium alloys. *Corrosion Sci.* 49, 1696–1701. doi: 10.1016/j.corsci.2007.01.001
- Staiger, M. P., Pietak, A. M., Huadmai, J., and Dias, G. (2006). Magnesium and its alloys as orthopedic biomaterials: a review. *Biomaterials* 27, 1728–1734. doi: 10.1016/j.biomaterials.2005.10.003
- Surmenev, R. A., Surmeneva, M. A., and Ivanova, A. A. (2014). Significance of calcium phosphate coatings for the enhancement of new bone osteogenesis—a review. *Acta Biomaterialia* 10, 557–579. doi: 10.1016/j.actbio.2013.10.036
- Tanahashi, M., and Matsuda, T. (1997). Surface functional group dependence on apatite formation on self-assembled monolayers in a simulated body fluid. *J. Biomed. Materials Res.* 34, 305–315. doi: 10.1002/(sici)1097-4636(19970305)34:3<305::aid-jbm5>3.0.co;2-o
- Tian, P., and Liu, X. (2015). Surface modification of biodegradable magnesium and its alloys for biomedical applications. *Regenerative Biomaterials* 2, 135–151.
- Walker, J., Shadanbaz, S., Woodfield, T. B., Staiger, M. P., and Dias, G. J. (2014). Magnesium biomaterials for orthopedic application: a review from a biological perspective. *J. Biomed. Materials Res. Part B: Appl. Biomaterials* 102, 1316–1331. doi: 10.1002/jbm.b.33113
- Watanabe, H., Saito, K., Kokubun, K., Sasaki, H., and Yoshinari, M. (2012). Change in surface properties of zirconia and initial attachment of osteoblastlike cells with hydrophilic treatment. *Dental Materials J.* 31, 806–814. doi: 10.4012/dmj.2012-069
- Witte, F. (2010). The history of biodegradable magnesium implants: a review. *Acta Biomaterialia* 6, 1680–1692. doi: 10.1016/j.actbio.2010.02.028
- Wong, H. M., Yeung, K. W., Lam, K. O., Tam, V., Chu, P. K., Luk, K. D., et al. (2010). A biodegradable polymer-based coating to control the performance of magnesium alloy orthopaedic implants. *Biomaterials* 31, 2084–2096. doi: 10.1016/j.biomaterials.2009.11.111
- Wu, S., Jang, Y.-S., Kim, Y.-K., Kim, S.-Y., Ko, S.-O., and Lee, M.-H. (2019). Surface modification of pure magnesium mesh for guided bone regeneration: in vivo evaluation of rat calvarial defect. *Materials Design* 12:2684. doi: 10.3390/ma12172684
- Xu, L.-P., Zhang, E.-L., and Ke, Y. (2012). Biocorrosion property and cytocompatibility of calcium phosphate coated Mg alloy. *Trans. Nonferrous Metals Soc. China* 22, 2014–2020. doi: 10.1016/s1003-6326(11)61422-2
- Yang, Y., Kim, K.-H., and Ong, J. L. (2005). A review on calcium phosphate coatings produced using a sputtering process—an alternative to plasma spraying. *Biomaterials* 26, 327–337. doi: 10.1016/j.biomaterials.2004.02.029
- Zhang, Y., Zhang, G., and Wei, M. (2009). Controlling the biodegradation rate of magnesium using biomimetic apatite coating. *J. Biomed. Materials Res. Part B: Appl. Biomaterials* 89, 408–414. doi: 10.1002/jbm.b.31228

Conflict of Interest: The authors declare that the research was conducted in the absence of any commercial or financial relationships that could be construed as a potential conflict of interest.

Copyright © 2021 Wu, Jang and Lee. This is an open-access article distributed under the terms of the Creative Commons Attribution License (CC BY). The use, distribution or reproduction in other forums is permitted, provided the original author(s) and the copyright owner(s) are credited and that the original publication in this journal is cited, in accordance with accepted academic practice. No use, distribution or reproduction is permitted which does not comply with these terms.

Advantages of publishing in Frontiers



OPEN ACCESS

Articles are free to read
for greatest visibility
and readership



FAST PUBLICATION

Around 90 days
from submission
to decision



HIGH QUALITY PEER-REVIEW

Rigorous, collaborative,
and constructive
peer-review



TRANSPARENT PEER-REVIEW

Editors and reviewers
acknowledged by name
on published articles

Frontiers

Avenue du Tribunal-Fédéral 34
1005 Lausanne | Switzerland

Visit us: www.frontiersin.org

Contact us: frontiersin.org/about/contact



REPRODUCIBILITY OF RESEARCH

Support open data
and methods to enhance
research reproducibility



DIGITAL PUBLISHING

Articles designed
for optimal readership
across devices



FOLLOW US

@frontiersin



IMPACT METRICS

Advanced article metrics
track visibility across
digital media



EXTENSIVE PROMOTION

Marketing
and promotion
of impactful research



LOOP RESEARCH NETWORK

Our network
increases your
article's readership